Seamount structure and subduction at the Louisville Ridge – Tonga-Kermadec collision

ROBINSON, ADAM,HACKETT

ROBINSON, ADAM,HACKETT (2017) *Seamount structure and subduction at the Louisville Ridge – Tonga-Kermadec collision*, Durham theses, Durham University. Available at Durham E-Theses Online: http://etheses.dur.ac.uk/12497/

Seamount structure and subduction at the Louisville Ridge – Tonga-Kermadec collision

Adam Hackett Robinson

A dissertation submitted for the degree of
Doctor of Philosophy
at the University of Durham

September 2017

Software used:

Seismic processing was conducted using *Seismic Unix* (Cohen and Stockwell, 2000) and *GLOBE Claritas*. Forward and inverse travel time modelling were conducted using *RAYINVR* (Zelt and Smith, 1992) and *FAST* (Zelt and Barton, 1998) respectively. Most images in this thesis were produced using the *Generic Mapping Tools* (Wessel and Smith, 1991), and post-processed using *Adobe Illustrator*.

Declaration

This dissertation describes my original work, except where acknowledgement is made in the text. It is not substantially the same as any work that has been or is being submitted to any other university for any degree, diploma, or any other qualification.

A. H. Robinson
September 2017

Seamount structure and subduction at the Louisville Ridge – Tonga-Kermadec collision

Adam Hackett Robinson

The Louisville Ridge (LRSC) is an ~4000 km-long SW Pacific seamount chain currently being subducted at the Tonga-Kermadec Trench (TKT). Both the trend of the LRSC and the subduction of the Pacific plate are oblique to the trench, resulting in southward migration of the intersection point at a rate of 120-180 mm yr^{-1}, and producing significant along-strike variation in forearc structure and seismicity.

The LRSC-TKT intersection was investigated by a multi-disciplinary geophysical experiment aboard the R/V Sonne in 2011, acquiring multichannel and wide-angle seismic, gravity, and bathymetry data, to better understand the effect of subducting bathymetric features on forearc deformation. As part of this, it is necessary to determine the structure and characteristics of the incoming seamounts, and how they are deformed during subduction. This study is underpinned by an ~725 km-long profile traversing the oldest extant LRSC seamounts, that continues along its projection into the trench and forearc.

LRSC seamounts display a range of internal structures, including shallow, high-velocity (≥6 km s^{-1}) cores. The also sit on crust that is not significantly thickened. At the trench, Osbourn seamount is experiencing bend-induced normal faulting which suggests that each seamount may be disarticulated to a size smaller than the imaging resolution. Observed similarity between the P-wave velocity structure of seamount flank material and ordinary subducting oceanic crust also suggests that distinguishing between these in the trench-forearc region is challenging. Consequently, it is not unequivocally possible to determine, within the confines of the profile locations and model resolution, whether the last LRSC seamount to have subducted, was subducted intact along the continuation of the trend of the extant chain.

Along-margin observations indicate that significant seamount-related forearc deformation is superimposed on pre-existing crustal structures, with the maximum deformation occurring in the wake of the migration of active collision. Observations of forearc morphology at the present-day intersection point support those from seismicity and plate reconstruction, which suggests that this location may also coincide with a westerly rotation in the trend of the chain.

Acknowledgements

First and foremost, I would like to greatly and sincerely thank Christine Peirce for having supervised this work over the past four years. Without your outstanding effort, commitment, patience, good humour, advice and encouragement, this would not have been possible. I will not forget the important lessons that you have taught me, particularly with regard to planning, rigor and keeping the troops happy, and I expect you will not easily forget how energised I looked starting my watchkeeping shifts at 0345 every morning in the Panama Basin.

I would also like to thank Richard Hobbs for his support, particularly with regard to the processing of MCS data. Also, my thanks go to Tony Watts, for giving me the start in marine geophysics that led me to this point. My research has been funded by the UK's Natural Environment Research Council.

In addition, my thanks go to the scientific parties, masters and crews of R/V Sonne cruise SO215, on which this project is based, and RSS James Cook cruises JC109, JC114 and JC132. In particular, I would like to thank the staff of the UK Ocean Bottom Instrumentation Consortium for their patience, training and the thoroughly enjoyable night shifts. After a slightly false start, and a baptism of fire through the Bay of Biscay in my first 36 hours at sea, I can absolutely say that many of my best memories from my time doing my PhD will be from my time at sea.

Over the past four years, I have always been able to rely on Matt Funnell to provide assistance, advice, constructive discussion, humour, and most critically, vast quantities of coffee. It has been a pleasure to work and travel with you. Also in the Department of Earth Sciences, I would particularly like to thank my fellow inmates in 'Geophysics Corner' – Emma, Dimitrios and Olly – Dean, and the many other students and postdocs with whom I've shared lunch, coffee, cake and beer-breaks.

In Durham I would like to thank the following: Van Mildert College, Talking Changes (for sanity), Durham University Improvised Comedy Society (for insanity), Su Hirst, and the management and staff of the Swan and Three Cygnets and The Station House. Beyond Durham I wish to thank Ben and Naomi, Peter, Dan, and Craig for keeping me grounded in the world outside academia. Also, my gratitude goes to Stanley Hackett, for the newspapers and for keeping me solvent with beer money.

Finally, thanks go to my parents, Susan and David, whose unwavering support throughout has been much needed, and could not be more appreciated. It fills me with a deep sadness that Dad will never be able to see me graduate and call me a doctor. Everything I have achieved, both here and elsewhere, is dedicated to them both.

Contents

Abstract **iv**
Acknowledgements **v**
List of Figures **x**
List of Tables **xiv**

Chapter 1 – Introduction **1**
1.1. Introduction 1
1.2. Seamount constructional processes 3
1.3. Seamounts and subduction zones 4
  1.3.1. Observations of seamount subduction 5
  1.3.2. Modes of seamount accommodation and effects on seismicity 5
1.4. Louisville Ridge Seamount Chain 8
  1.4.1. Pre-hotspot geological history 11
  1.4.2. Geological and geochronological studies of the LRSC 13
1.5. Tonga-Kermadec Trench and LRSC subduction 15
1.6. Cruise SO215 16
1.7. Study aims 18
1.8. Summary 19

Chapter 2 – Multichannel Seismic Reflection Data – Acquisition and Processing **21**
2.1. Introduction 21
2.2. MCS data acquisition 21
  2.2.1. Profile C seismic data acquisition 21
  2.2.2. Challenges during acquisition 23
2.3. MCS data processing 25
  2.3.1. Geometry 25
  2.3.2. CMP binning 25
  2.3.3. Brute stack 27
  2.3.4. Results of brute stacking 28
  2.3.5. Velocity analysis 30
  2.3.6. Removal of high amplitude, shallow sub-seabed noise 31
  2.3.7. Post-stack deconvolution 36
2.4. Results of MCS data processing 39
2.5. Summary 52

Chapter 3 – Wide-Angle Seismic Data – Acquisition and Forward Modelling **54**
3.1. Introduction 54
3.2. WA seismic dataset acquisition 54
3.3. WA arrival picking strategy 55
3.4. WA seismic dataset characteristics 57
  3.4.1. Pacific plate 58
    3.4.1.1. Background oceanic crust – OBSs C15-C18 60
    3.4.3.2. Seamount chain – OBSs C14-C35 60
  3.4.2. Overriding plate 63

- 3.4.2.1. Upper forearc – OBSs C52-C58 63
- 3.4.2.2. Middle trench slope – OBSs C44-51 70
- 3.4.2.3. Lower trench slope/trench-transition – OBSs C37-C46 72

3.5. Model construction 73
- 3.5.1. Initial model 73
- 3.5.2. Ray-tracing around bend 76
  - 3.5.2.1. Criterion 1 – travel path length and travel time difference 77
  - 3.5.2.2. Criterion 2 – sampling the correct features 79
  - 3.5.2.3. Applying the criteria to selecting travel time picks 82
- 3.5.3. Instrument relocation using P_w arrivals 84

3.6. Forward modelling 85
- 3.6.1. Water wave modelling 86
- 3.6.2. Modelling of subsurface arrivals 90
- 3.6.3. Ray coverage 91
  - 3.6.3.1. P_g arrivals 100
  - 3.6.3.2. P_mP arrivals 103
  - 3.6.3.3. P_n arrivals 103
  - 3.6.3.4. Total ray coverage 104
- 3.6.4. Effect of ray selection at profile bend 105

3.7. Preliminary interpretation of model features 107

3.8. Summary 108

Chapter 4 – Forward Model Testing and Verification 110

4.1. Introduction 110

4.2. Inverse modelling 111
- 4.2.1. Principles of inverse modelling 111
- 4.2.2. Starting model 113
- 4.2.3. Inverse model parameterisation 115
- 4.2.4. Inverse modelling results 115
- 4.2.5. Comparison with the forward model 121
- 4.2.6. Ray coverage 124

4.3. Resolution testing 125
- 4.3.1. Adding noise to picks 127
- 4.3.2. Checkerboard testing procedure 128
- 4.3.3. Results of checkerboard testing 130
- 4.3.4. Checkerboard phase shifts and edge effects 133
- 4.3.5. Implication of checkerboard testing 137

4.4. Sensitivity testing 138
- 4.4.1. Perturbations 138
- 4.4.2. Input pick selections 140
- 4.4.3. Results 140
  - 4.4.3.1. Velocity sensitivity 146
  - 4.3.3.2. Depth sensitivity 147
  - 4.4.3.3. Testing the significance of depth sensitivity on the Moho 148
- 4.4.4. Sensitivity testing the bend in Profile C 150

4.5. Gravity modelling 154
- 4.5.1. Conversion of the forward model to the density model 154
- 4.5.2. Modelling procedure 157

4.5.3. Initial results 158
4.5.4. Model refinements 158
4.5.5. Long-wavelength misfit 162
4.5.6. Lower forearc 167
4.6. MCS data restacking 169
4.7. Summary 169

Chapter 5 – Model Description and Interpretation 173
5.1. Introduction 173
5.2. Pacific plate 173
5.3. LRSC 176
5.3.1. Seamount internal structure 176
5.3.2. Seamount flanks 176
5.3.3. Intra-seamount saddles 181
5.3.4. Crustal thickness 181
5.3.5. Subduction related faulting of LRSC seamounts 184
5.4. Indo-Australian plate 186
5.4.1. Is there a seamount in the trench? 191
5.4.2. Is there evidence for seamount accommodation? 193
5.5. Summary 193

Chapter 6 – Discussion 195
6.1. Introduction 195
6.2. Seamount constructional processes 196
6.2.1. Formation of densely cored seamounts 196
6.2.2. Δt and the LRSC 196
6.2.3. Role of melting and crystallisation processes in crustal structural variability 197
6.2.4. Seamount structures arising from alternative magmatic origins 199
6.2.5. Additional controls on seamount structure 201
6.3. Subduction of the LRSC 202
6.3.1. Behaviour and imaging of subducting seamounts 202
6.3.2. Effects of LRSC subduction 203
6.3.2.1. Pre-collisional forearc structure 203
6.3.2.2. Syn-collisional forearc structure 204
6.3.3.3. Post-collisional forearc structure 206
6.3.3.4. Arc and back arc structure 209
6.3.4. Seismicity observations 209
6.3.5. Continuation of the LRSC 210
6.3.6. Significance of the Osbourn Trough 212
6.3.7. Location of the initial collision 214
6.4. Summary 215

Chapter 7 – Conclusions 218
7.1. Seamount structure 218
7.2. Subduction of the LRSC 219
7.3. Further work 220
7.4. Summary 223

References **224**

Appendix

Appendix A 237
Appendix B 281
Appendix C 284

List of Figures

1.1. Pacific seamount chains 2
1.2. Modes of seamount accommodation in subduction zones 7
1.3. Full extent of the LRSC in the SW Pacific 9
1.4. SO215 study area 10
1.5. Satellite-derived free-air gravity anomaly for the LRSC-TKT intersection 12
1.6. Plate age along the LRSC 14

2.1. Seismic acquisition equipment configuration 22
2.2. Seismic source array configuration 22
2.3. MCS acquisition and shot point locations 24
2.4. MCS geometry assignment and checking 26
2.5. Profile C MCS brute stack 29
2.6. Brute stacks showing the removal of high amplitude dipping events in the upper Tonga forearc region. 32
2.7. Upper Tonga forearc MCS data, stacked using the velocity model developed from velocity analysis, showing the effects on high amplitude dipping events 34
2.8. Screenshots from the Claritas testing application showing the front mute for CMP gathers 1240-1242 35
2.9. Test panels showing the effects of deconvolution in the middle Tonga forearc region 37
2.10. Test panels showing the effects of deconvolution for LRSC seamounts and intra-seamount saddles 38
2.11. Definition and calculation of autocorrelation functions for stacked CMP gathers 6130-6260 40
2.12. Screenshots from Claritas autocorrelation function calculator for stacked CMP gathers 14430-14560 41
2.13. Profile C MCS data for Tonga upper forearc region 43
2.14. Profile C MCS data for Tonga middle forearc region 44
2.15. Profile C MCS data for Tonga lower forearc and trench axis region 45
2.16. Profile C MCS data for Osbourn seamount summit and flanking regions 46
2.17. Profile C MCS data for Canopus seamount, and intra-seamount basin immediately to the south 47
2.18. Profile C MCS data for 27.6˚S seamount and adjacent region 48
2.19. Profile C MCS data for southernmost part of profile, including last sampled seamount (flank crossing) and ‘background’ Pacific plate 49

3.1. Profile C OBS locations 59
3.2. Combined swath-satellite bathymetry for ‘background’ Pacific plate, adjacent to the LRSC, gridded at 50m, and illuminated only in regions of swath coverage 60
3.3. WA seismic data from OBS C17, located at 705.6 km d.a.p. 61
3.4. Combined swath-satellite bathymetry for the LRSC along Profile C 62
3.5. WA seismic data from OBS C04, located at 543.6 km d.a.p. 64
3.6. WA seismic data from OBS C20, located at 481.1 km d.a.p. 65
3.7. WA seismic data from OBS C33, located at 318.8 km d.a.p. 66

3.8. Combined swath-satellite bathymetry for Tonga upper forearc, at northernmost end of Profile C 67
3.9. WA seismic data from OBS C56, located at 31.8 km d.a.p. 68
3.10. WA seismic data from OBS C53, located at 69.2 km d.a.p. 69
3.11. Combined swath-satellite bathymetry for Tonga middle forearc terrace 70
3.12. WA seismic data from OBS C50, located at 106.4 km d.a.p. 71
3.13. Combined swath-satellite bathymetry for Tonga lower forearc slope and trench, at point of present LRSC collision 72
3.14. WA seismic data from OBS C36, located at 281.5 km d.a.p. 74
3.15. WA seismic data from OBS C41, located at 218.5 km d.a.p. 75
3.16. Generalized schematic geometry for calculating the path length difference 77
3.17. Across- versus around-corner ray-path differences 79
3.18. Generalized schematic of Profile C bend geometry, where the bend is not centred on the seamount 80
3.19. Test intrusive core radii for 27.6˚S seamount with Profile C overlain 81
3.20. Maximum permissible shot offsets for ray tracing from one segment of Profile C to the other 82
3.21. Maximum permissible shot offset, $S_{max,}$ versus maximum travel time difference, τ_{max} 83
3.22. Cartoon of the effect of a OBS drifting out-of-plane on the time corrections which need to be applied 85
3.23. Water column properties along Profile C, determined using expendable bathymetric thermographs (XBTs) 87
3.24. RAYINVR ray tracing output from built in plotting tools, for P_w arrivals 89
3.25. Best-fit P-wave forward velocity-depth model for water column along Profile C 90
3.26. RAYINVR ray tracing output for P_s arrivals 92
3.27. RAYINVR ray tracing output for $P_{g,l}$ arrivals, tracing towards the left (northwest) of model 93
3.28. RAYINVR ray tracing output for $P_{g,r}$ arrivals, tracing towards the right (southeast) of model 94
3.29. RAYINVR ray tracing output for P_mP arrivals 95
3.30. RAYINVR ray tracing output for P_n arrivals 96
3.31. Depth to subduction interface along the Tonga-Kermadec subduction system from SLAB1.0 97
3.32. Best-fit WA forward model 98
3.33. Forward velocity model ray coverage for a) $P_{g,l}$ – refracted phases through the oceanic crust towards the left (northwest), and b) $P_{g,r}$ – refracted phases through the oceanic crust towards the right (southeast) 101
3.34. Forward velocity model ray coverage for a) P_mP – reflected phases from the Moho, and b) P_n – refracting phases through the mantle 102
3.35. Forward velocity model ray coverage for all 60736 reflected and refracted travel time picks used for modelling 102
3.36. Number of rays per 0.2 x 0.2 km cell of the forward model 105
3.37. Comparing the effects of ray selection at bend on ray coverage 106

4.1. Example starting models for inversion illustrating different general groups 114

4.2. Inversion modelling results 116
4.3. Graph of improving χ^2 value with each iteration during inversion procedure 117
4.4. Intermediate inversion modelling steps, showing development of model structures with number of iterations 118
4.5. Comparison between results of forward (RAYINVR) and inverse (FAST) modelling approaches 122
4.6. Histogram of P-wave velocity difference between forward and inverse models where both are sampled by rays 124
4.7. Comparison between forward (RAYINVR) and inverse (FAST) model ray coverage 126
4.8. Generation of random numbers for addition of noise to picks 128
4.9. Results of checkerboard testing for 15 x 4 km input anomaly 129
4.10. Checkerboard testing for vertical anomaly sizes ≥5 km 131
4.11. Checkerboard testing with a vertical anomaly size of 4 km 132
4.12. Checkerboard testing with a vertical anomaly size of 3 km 134
4.13. Effect of phase-shifting the 20 x 4 km anomaly size input checkerboard pattern 135
4.14. Effect of phase-shifting the 25 x 5 km anomaly size input checkerboard pattern 136
4.15. Summary of perturbation types that were applied during forward model sensitivity testing 139
4.16. Results of sensitivity testing of the sediment layer 142
4.17. Results of sensitivity testing for Indo-Australian plate crust 143
4.18. Results of sensitivity testing for Pacific plate crust 144
4.19. Results of sensitivity testing for the Indo-Australian and Pacific mantle 145
4.20. Frequency spectra for a) OBS C17 and b) OBS C18 149
4.21. Comparison between sensitivity testing results with and without inclusion of picks at the bend 152
4.22. Comparison between sensitivity testing results with inclusion of picks at the bend for different applied uncertainties 153
4.23. Empirically derived velocity-density conversion curves 155
4.24. Assessment of forward model uniqueness using gravity modelling 159
4.25. Gravity modelling with adjusted mantle densities 160
4.26. Parameters used to determine the effects of the subducting slab on the fit of the density model 161
4.27. Depths to the top of the slab for a range of slab dip scaling factors 162
4.28. Gravity model testing for varying slab dip and overriding plate taper scaling factors 163
4.29. Gravity model testing with varying slab dip and changing density contrast between Pacific and Indo-Australian mantle 165
4.30. Candidate best-fitting density model 166
4.31. Preferred density model 168
4.32. Conversion of P-wave velocity-depth model to stacking velocity-TWTT model 170
4.33. Forward model restacked MCS record section 171

5.1. Best-fit P-wave velocity-depth models for oceanic crust adjacent to seamount edifices 174
5.2. Best-fit P-wave velocity-depth models for large LRSC seamounts 177
5.3. Comparison of velocity structures of seamount flank-crossings 178

5.4. 3D satellite-derived FAA 180
5.5. Restacked MCS data in saddles between seamounts 182
5.6. Comparison of velocity structures of through inter-seamount saddles 183
5.7. Effects of outer-rise normal faulting 185
5.8. P-wave velocity-depth models crossing Tonga-Kermadec forearc and trench 187
5.9. Profile C Tonga forearc structure 188
5.10. Restacked MCS data using the forward velocity model for trench/lower forearc region 192

6.1. Processes of tectonic erosion resulting from background plate and seamount subduction 205
6.2. Evidence for proposed continuation of the LRSC 206
6.3. Previous studies identifying a subducted seamount (Motuku) beneath the Tonga forearc 213

7.1. Potential further study locations in the LRSC-TKT intersection region 221

A.1. WA seismic data from OBS C57 hydrophone channel 238
A.2. WA seismic data from OBS C58 hydrophone channel 239
A.3. WA seismic data from OBS C55 hydrophone channel 240
A.4. WA seismic data from OBS C54 hydrophone channel 241
A.5. WA seismic data from OBS C52 hydrophone channel 242
A.6. WA seismic data from OBS C51 hydrophone channel 243
A.7. WA seismic data from OBS C49 hydrophone channel 244
A.8. WA seismic data from OBS C48 hydrophone channel 245
A.9. WA seismic data from OBS C47 hydrophone channel 246
A.10. WA seismic data from OBS C46 hydrophone channel 247
A.11. WA seismic data from OBS C45 hydrophone channel 248
A.12. WA seismic data from OBS C44 hydrophone channel 249
A.13. WA seismic data from OBS C43 hydrophone channel 250
A.14. WA seismic data from OBS C40 hydrophone channel 251
A.15. WA seismic data from OBS C38 hydrophone channel 252
A.16. WA seismic data from OBS C37 hydrophone channel 253
A.17. WA seismic data from OBS C35 hydrophone channel 254
A.18. WA seismic data from OBS C34 hydrophone channel 255
A.19. WA seismic data from OBS C32 hydrophone channel 256
A.20. WA seismic data from OBS C30 hydrophone channel 257
A.21. WA seismic data from OBS C29 hydrophone channel 258
A.22. WA seismic data from OBS C28 hydrophone channel 259
A.23. WA seismic data from OBS C27 hydrophone channel 260
A.24. WA seismic data from OBS C26 hydrophone channel 261
A.25. WA seismic data from OBS C25 hydrophone channel 262
A.26. WA seismic data from OBS C24 hydrophone channel 263
A.27. WA seismic data from OBS C22 hydrophone channel 264

A.28. WA seismic data from OBS C21 hydrophone channel 265
A.29. WA seismic data from OBS C19 hydrophone channel 266
A.30. WA seismic data from OBS C01 hydrophone channel 267
A.31. WA seismic data from OBS C02 hydrophone channel 268
A.32. WA seismic data from OBS C03 hydrophone channel 269
A.33. WA seismic data from OBS C05 hydrophone channel 270
A.34. WA seismic data from OBS C06 hydrophone channel 271
A.35. WA seismic data from OBS C07 hydrophone channel 272
A.36. WA seismic data from OBS C08 hydrophone channel 273
A.37. WA seismic data from OBS C09 hydrophone channel 274
A.38. WA seismic data from OBS C11 hydrophone channel 275
A.39. WA seismic data from OBS C12 hydrophone channel 276
A.40. WA seismic data from OBS C13 hydrophone channel 277
A.41. WA seismic data from OBS C14 hydrophone channel 278
A.42. WA seismic data from OBS C15 hydrophone channel 279
A.43. WA seismic data from OBS C18 hydrophone channel 280

C.1. Results of checkerboard testing for 40 x 4 km input anomaly 285
C.2. Results of checkerboard testing for 40 x 3 km input anomaly 286
C.3. Results of checkerboard testing for 30 x 4 km input anomaly 287
C.4. Results of checkerboard testing for 30 x 3 km input anomaly 288
C.5. Results of checkerboard testing for 20 x 4 km input anomaly 289
C.6. Results of checkerboard testing for 20 x 3 km input anomaly 290
C.7. Results of checkerboard testing for 15 x 5 km input anomaly 291
C.8. Results of checkerboard testing for 15 x 3 km input anomaly 292
C.9. Results of checkerboard testing for 12 x 5 km input anomaly 293
C.10. Results of checkerboard testing for 12 x 4 km input anomaly 294

List of Tables

3.1. Forward model ray tracing statistics and fit parameters for the entire model 99
3.2. Forward model ray tracing statistics and fit parameters for the Indo-Australian plate 99
3.3. Forward model ray tracing statistics and fit parameters for the Pacific plate 100

4.1. Forward model sensitivity testing results 141
4.2. Velocity and density bounds for density model blocks, and best fitting values 156

B.1. OBS deployment, recovery and relocated (model) positions 281

Glossary of terms and abbreviations

Δt	plate age at time of volcanism
CMP	common mid-point
2D	two-dimensional
b.s.b.	below seabed
b.s.s.	below sea surface
χ^2	normalised chi-squared statistic
d.a.p.	distance along profile
d.p.t.	distance perpendicular to trench
FAA	free air gravity anomaly
FAST	First Arrival Seismic Tomography
LRSC	Louisville Ridge Seamount Chain
MCS	multi-channel seismic
NMO	normal moveout
OBS	ocean-bottom seismograph
ODP	Ocean Drilling Program
OT	Osbourn Trough
P_s	P-wave sediment refraction
P_g	P-wave crustal refraction
P_mP	P-wave Moho reflection
P_n	P-wave mantle refraction
P_w	P-wave water wave direct arrival
R/V	research vessel
RBA	residual bathymetric anomaly
RFGA	residual free air gravity anomaly
RMS/rms	root mean square
S_{max}	maximum shot offset
SNR	signal to noise ratio
τ	travel time difference
T_e	lithospheric elastic thickness
TKT	Tonga-Kermadec Trench
TOTAL	Tonga Thrust earthquake Asperity at Louisville Ridge
TWTT	two-way travel time
WA	wide angle
XBT	expendable bathymetric thermograph

Chapter 1 - Introduction

1.1. Introduction

Seamount chains represent a record of the modification of the oceanic crust by intrusive and extrusive magmatism, and are near-ubiquitous features of the seafloor (e.g. Wessel, 2001; Hillier and Watts, 2007; Tetreault and Buiter, 2014), observed in all major oceanic regions (Fig. 1.1). A range of processes can give rise to these features, including hotspot magmatism (Wilson, 1963; Morgan, 1971), small-scale mantle convection (Buck and Parmentier, 1986; Haxby and Weissel, 1986; Ballmer et al., 2007), and localised lithospheric extension (Winterer and Sandwell, 1987; Sandwell et al., 1995), where the mode of origin and motion of the overriding plate relative to the magma source may result in the formation of linear chains or broader, more scattered seamount fields. Geophysical studies have identified a diversity in the crustal and upper mantle structure of seamounts (Watts et al., 1985; Caress et al., 1995; Weigel and Grevemeyer, 1999; Contreras-Reyes et al., 2010; Kaneda et al., 2010; Wang et al., 2016), where there is an apparent first-order correlation between the type of internal velocity structure observed and the age of the oceanic lithosphere at the time of seamount volcanism (Gass et al., 1978; Pollack et al., 1981).

Seamounts also represent significant plate topography, and when subducted it is likely that they affect inter-plate boundary processes (e.g. Rosenbaum and Mo, 2011), inducing along-strike variation in trench and forearc morphology (e.g. Kopp, 2013), seismicity (e.g. Habermann et al., 1986) and arc volcanism (e.g. McGeary et al., 1985). During subduction, the seamounts themselves may become decapitated (Cloos, 1992; Cloos and Shreve, 1996) or disaggregated by faulting, and deform the overriding forearc (e.g. Funnell et al., 2014; 2017) orthogonal to the trench.

The Louisville Ridge Seamount Chain (LRSC) intersects with, and is being subducted at, the Tonga-Kermadec subduction system in the SW Pacific. The oblique collision of the Pacific plate with the Indo-Australian plate causes a southward migration of the point of LRSC collision, and along-strike variations in forearc structure. A multi-disciplinary geophysical investigation of the LRSC was undertaken aboard the R/V Sonne in 2011 (cruise SO215), acquiring multichannel and wide-angle seismic, gravity, and bathymetry data (Peirce and Watts, 2011). In combination with the results of the earlier *TOTAL* (*To*nga *T*hrust earthquake *A*sperity at *L*ouisville Ridge;

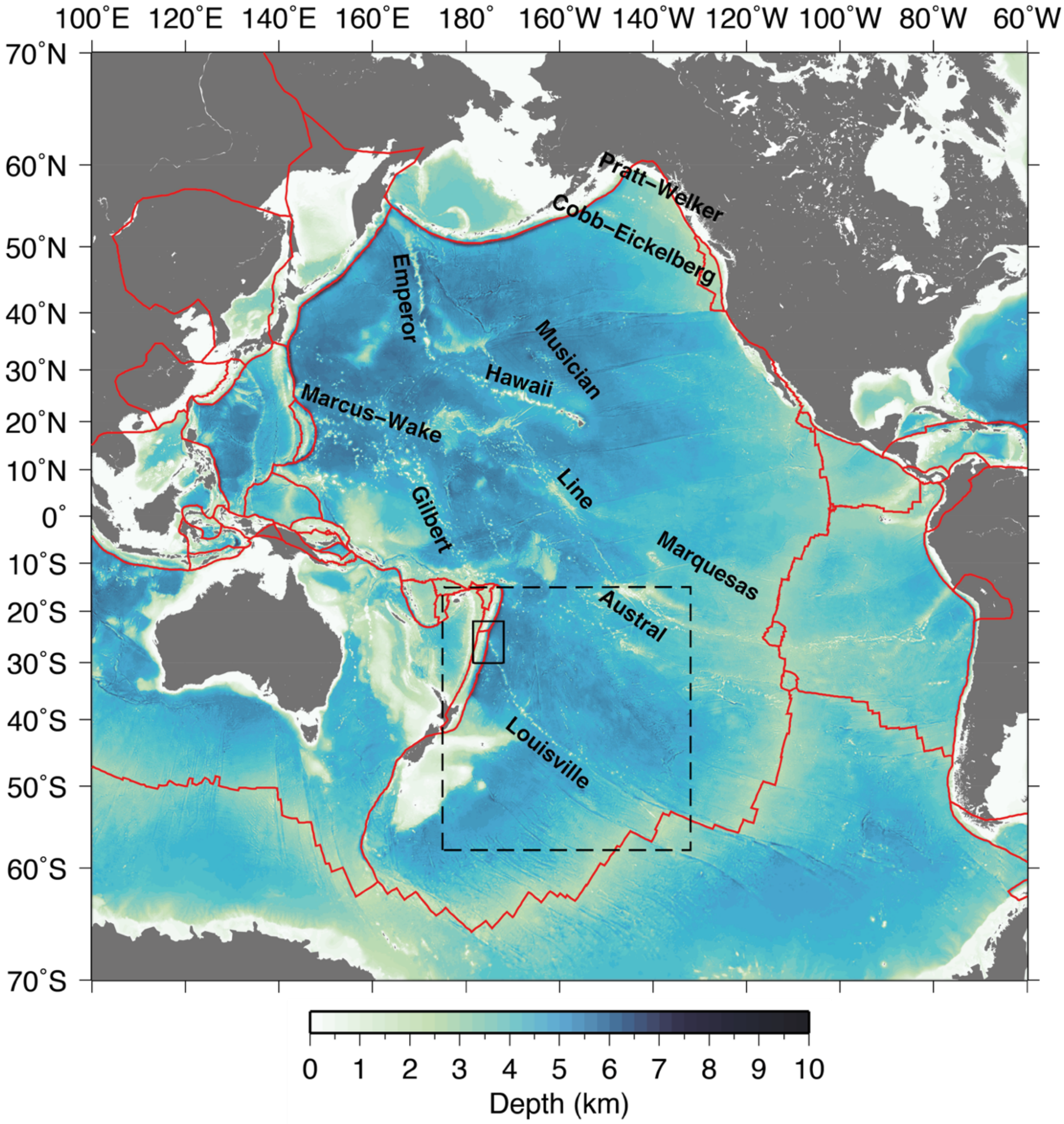

Figure 1.1: *Pacific seamount chains. Bathymetry from the GEBCO 30 second grid (IOC et al., 2003). Major WNW-to-NNW trending seamount chains are labelled, as are some minor chains (e.g. Marcus-Wake) which will be discussed further in the text. Dashed black box indicates area shown in Figs 1.3 and 1.6. Solid black box indicates the SO215 study region shown in Fig. 1.4. Red lines are plate boundaries from Bird (2003).*

Grevemeyer and Flueh, 2008) project, this experiment sought to address the question of how the subducting LRSC affects plate boundary processes and overriding plate deformation. In this study, part of the SO215 dataset is modelled and interpreted to form a robustly tested velocity-depth model of ~500 km of the extant Louisville Ridge, and ~225 km of the adjacent Tonga forearc. This model reveals the internal structure of the largest distinct seamounts that comprise the chain, and how already subducted seamounts may interact with the overriding plate and influence forearc structure.

1.2. Seamount constructional processes

Seamounts are built by a combination of intrusive and extrusive volcanic processes, the balance of which results in variations in crustal structure. The principal factors which govern the eruptive style include the:

- temperature, viscosity and crystal:liquid ratio of the magma (e.g. Bonatti, 1967; Bonatti and Harrison, 1988);
- volatile content and the manner of degassing (e.g. Gill et al., 1990; Kokelaar, 1986; Bonatti and Harrison, 1988; Devine and Sigurdsson, 1995; Dixon et al., 1997; Head and Wilson, 2003); and
- confining (hydrostatic) pressure exerted by the water column (e.g. Staudigel and Clague, 2010),

all of which may vary throughout seamount growth. As a result of the variability in these factors, when the eruption depth reaches ~0.7-1.0 km below sea surface a transition occurs from dominantly effusive to more explosive behaviour (McBirney, 1963; Peckover et al., 1973; Staudigel and Schminke, 1984). The depth at which this change occurs is known as the volatile fragmentation depth (Fisher and Schmincke, 1984). The guyot morphology of the Louisville seamounts indicates that they were once emergent and have subsequently subsided and been eroded by wave action, thus they must have passed through this transition. Differences in eruptive character may also lead to changes in the proportions of different volcanic products produced, and their associated seismic velocity characteristics (e.g. Staudigel and Schminke, 1984, Carlson and Herrick, 1990; Planke et al., 1999).

A number of measures can be used to attempt to express the diversity in seamount structure in terms of measurable characteristics relating to the location and timing of their formation. The response of a plate to loading by intraplate volcanism can be expressed in terms of its lithospheric elastic thickness (T_e). This characteristic of a plate is strongly governed by age and, hence, the thermal state of the lithosphere at the time of loading (Watts, 1978; Calmant et al., 1990). Variation in lithospheric thickness also has implications for melting and fractionation depths, which can lead to magma compositional variability (Ellam, 1992; Haase, 1996; Farnetani et al., 1996; Ito and Mahoney, 2005; Humphreys and Niu, 2009).

It has been suggested that the response of the lithosphere to point sources of magmatism can be expressed as a non-dimensional 'vulnerability' to shallow vertical intrusion, where this tendency scales proportionally to the age of the lithosphere at the time of volcanism (hereafter denoted by Δt) and to the square root of the plate velocity over the source of magma (Gass et al., 1978; Pollack et al., 1981). Hence, it is argued that old, cold and thick crust is more resistant to the action of point sources of magmatism beneath it, and hence large volumes of magmatic material are emplaced at the base of the crust. In contrast, younger, hotter and thinner crust would correlate with more significant magmatic intrusion into the relatively more vulnerable crust. A slower moving plate will also be more vulnerable to penetrative magmatism, as it will be in contact with the magma source for longer. However, to affect the same change in 'vulnerability' as a doubling or halving of plate thickness, plate velocity must be multiplied or divided by a factor of four respectively.

Whether the along-hotspot track morphology is rough, dominated by individual volcanic edifices, or smooth appears to show a dependency that is proportional to the root of magmatic buoyancy flux, and inversely proportional to T_e and the square root of plate velocity (Orellana-Rovirosa and Richards, 2017). It has also been proposed that intra-volcanic spacing along hotspot chains, r, is related to lithospheric rigidity, and hence T_e, where $r \propto T_e^{3/4}$ (ten Brink, 1991). This arises as a result of the compressive stresses associated with volcanic loading being unfavourable for further upwelling, thus causing the locus of upwelling to shift to the nearest transition between radially compressive and tensile stress.

1.3. Seamounts and subduction zones

Where seamounts subduct it is likely that they have an effect on plate boundary processes. Observations of subducting bathymetric features exist worldwide (e.g. Kelleher and McCann, 1976; Rosenbaum and Mo, 2011; Bassett and Watts, 2015), with the associated impacts including along-strike variations in:

- trench and forearc morphology (e.g. Dupont and Herzer, 1985; McCann and Habermann, 1989; Fleury et al., 2009; Kopp, 2013; Funnell et al., 2014; 2017);
- seismicity (Kelleher and McCann, 1976; Habermann et al., 1986; Scholz and Small, 1997; Bassett and Watts, 2015); and
- arc volcanism (e.g. McGeary et al., 1985, Rosenbaum and Mo, 2011).

It has also been variously suggested that subducting bathymetry may be accommodated within subduction zones by:

- truncation, or 'decapitation', of the seamount from its host plate (Cloos, 1992; Cloos and Shreve, 1996);
- elastic deformation of the overriding plate (Scholz and Small, 1997); or
- distributed plastic deformation of the forearc (Dominguez et al., 1998; Wang and Bilek, 2011).

1.3.1. Observations of seamount subduction

Large-scale subducted seamount-like features have been imaged at a number of margins. These include the Japan (Kodiara et al., 2000), Mediterranean Ridge (von Huene et al., 1997) and Mariana (Oakley et al., 2007; 2008) forearcs. Forearc slopes show morphological evidence for uplift, head scars, slumps, and re-entrant features along the projection of incoming seamount-like features at locations including the Mariana (Fryer and Smoot, 1985) and Japan trenches (Lallemand and Le Pichon, 1987; Kobayashi et al., 1987), the Nankai Trough (Kodaira et al., 2000; Bangs et al., 2006), and the Costa Rica margin (Dominguez et al., 1998; Ranero and von Huene, 2000; von Huene et al., 2000) margins. In addition, magnetic anomalies have been traced into the overriding plates in the Japan (Cadet et al., 1987), Costa Rica (Barckhausen et al., 1998) and Cascadia (Tréhu et al., 2012) subduction zones.

1.3.2. Modes of seamount accommodation and effects on seismicity

The role of subducting plate topography has been implicated as a factor in the seismic behaviour of a number of earthquake events (e.g. Abercrombie et al., 1994; Kodiara et al., 2000; Bilek et al., 2003; Bell et al., 2014). Various proposed modes of interaction between subducting features and the overriding plate exist to explain the changes in seismicity observed (Kelleher and McCann, 1976; Habermann et al., 1986; Scholz and Small, 1997).

It has been suggested that truncation of seamounts from their host plate may occur (Fig. 1.2a – Cloos, 1992; Cloos and Shreve, 1996), where the depth and hence confining pressure at which this occurs govern whether the stress release produces a large earthquake. However, given the relatively small base:height ratio for seamounts (10:1 or larger), this is now held to be mechanically unlikely (Wang and Bilek, 2011; 2014). In addition, there are only limited observations of large-scale seamount accretion (e.g. MacPherson, 1983), with accreted volcanic fragments typically one to two orders of magnitude smaller than would be expected if they represented full seamount edifices (e.g. Isozaki et al., 1990). This indicates that whole scale removal of the seamount from its host plate is uncommon, although it may be possible where the seamount was built on a surface that acts as a décollement (Got et al., 2008; Watts et al., 2010). An additional control on whether seamounts are removed intact from their host plates may be their mode of isostatic compensation. In general, seamounts which form off-ridge are regionally supported, whereas on-ridge seamounts have local compensating roots (Watts et al., 1980). Upon approach to a trench, any supporting root will be progressively removed. Hence, regionally compensated off-ridge seamounts be less buoyantly supported and tend to subduct, whereas the locally compensated on-ridge seamounts will not undergo progressive removal of their roots, leaving them more liable to obduction onto the overriding plate (Das and Watts, 2009).

Seamounts have been proposed to act both as asperities or barriers to seismic rupture. The asperity model (e.g. Scholz and Small, 1997) proposes that the overriding plate deforms elastically in response to the subducting seamount, locally increasing normal stress on the interface (Fig. 1.2b). This accumulated stress may then be released as large moment seismic events. A side-effect of the stress build-up necessary for this to occur is that earthquake reoccurrence intervals may be increased such that the timescales over which instrumental records are available do not contain evidence for them. However, asperity models of seamount earthquake nucleation are often criticised (e.g. Wang and Bilek, 2011) for treating the subduction interface as planar with a spatially varying normal stress. This is contrary to reality where the interface is generally non-planar, and it is the interface irregularity that is the principal contributor to normal stress increase.

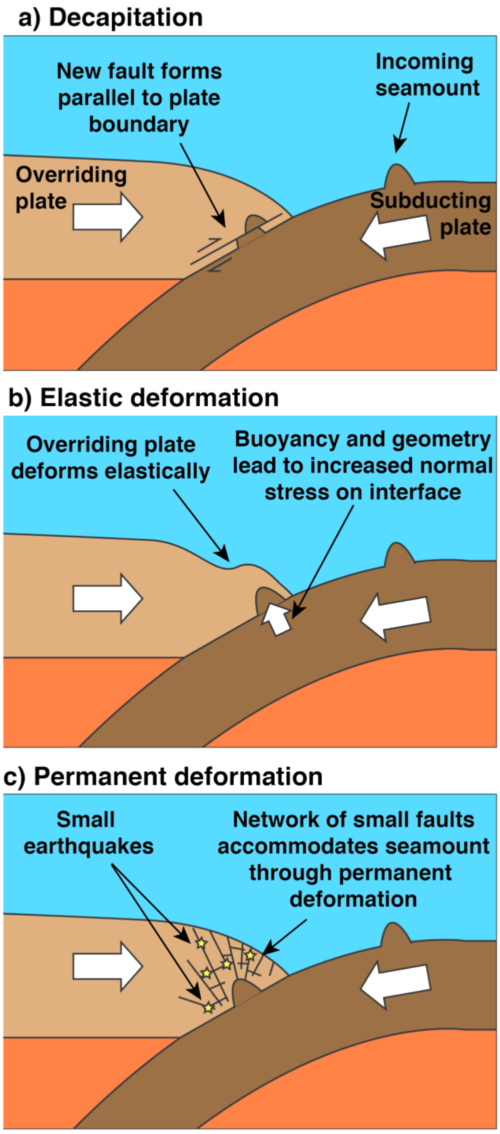

Figure 1.2: *Modes of seamount accommodation in subduction zones. a) Seamount decapitation by a newly formed fault parallel to the plate boundary (e.g. Cloos and Shreve, 1996). Note that the base:height ratio shown is ~1:1, which is unrealistic compared to the value of ≥10:1 which is more typically observed in reality (e.g. Wang and Bilek, 2011). b) Buoyancy and geometry of the incoming seamount increase the normal stress on the subduction interface, acting either as an asperity or barrier to rupture (see text). Overriding plate deformation is purely elastic, and after stress release the forearc will return to its previous morphology. c) Overriding plate deforms permanently (plastically) through the generation of a large number of small-scale antithetic normal faults on which small movements may lead to small earthquakes. After the seamount passes beyond this region, the weakened forearc is likely to undergo collapse.*

Where fluid-rich sediments on the summits of seamounts are subducted, inter-plate coupling may be reduced. This can cause the seamount to act as a barrier to rupture propagation, causing segmentation of the seismic zone along strike (Cummins et al., 2002; Singh et al., 2011). It is also suggested that the presence of a seamount on the subduction interface may act as a barrier to seismic rupture following a classical view of great subduction zone earthquakes, where the moment magnitude (M_w) of a seismic event is related to the area over which rupture occurs (Kanamori and Anderson, 1975; Kanamori, 1977). If the down-dip rupture area is considered to remain constant and the presence of topography along-strike from the hypocentre prevents co-seismic slip propagation, the along-strike rupture length and, hence, M_w are reduced. If a large amount of sediment is subducted with the seamount in a subduction channel, the smoothing of the interface can restore the rupture area to a larger value (e.g. Chilean-type margin – Cloos and Shreve, 1996), with many large subduction zone earthquakes having occurred in these regions of excess trench sediment (Ruff, 1989).

An alternative to elastic deformation of the overriding plate is permanent damage by generation of a forearc fracture network (FFN – Fig. 1.2c). In this model, passage of the seamount beneath the leading edge of the overriding plate is accommodated by the generation of, and movement on, a large network of relatively small-scale faults. Whilst some of these faults may appear to generate earthquakes, their short lengths and cross-cutting relationships will limit event magnitude. This hypothesis is supported by laboratory analogue modelling (Dominguez et al., 1998; Dominguez et al., 2000) and field observations in locations including Costa Rica (e.g. Wang and Bilek, 2011) and Japan (e.g. Lallemand and Le Pichon, 1987).

1.4. Louisville Ridge Seamount Chain

The Louisville Ridge Seamount Chain (LRSC) is a >4000 km-long chain of Cretaceous-Cenozoic seamounts and guyots trending in a broadly NW-SE orientation in the SW Pacific (Fig. 1.3 – Lonsdale, 1986; 1988). LRSC guyots typically have summit plains <20 km wide, suggesting that their emergent area when islands would have been <50 km^2 (Lonsdale, 1988). Their planform is generally ellipsoidal-to-stellate (Fig. 1.4), with radiating ribs interpreted as traces of flanking rift zones and the result of large-scale sector collapse (Vogt and Smoot, 1984; Mitchell, 2001). The oldest extant seamount, Osbourn, has an ^{40}Ar/^{39}Ar age of between 76.7 ± 0.8 Ma and

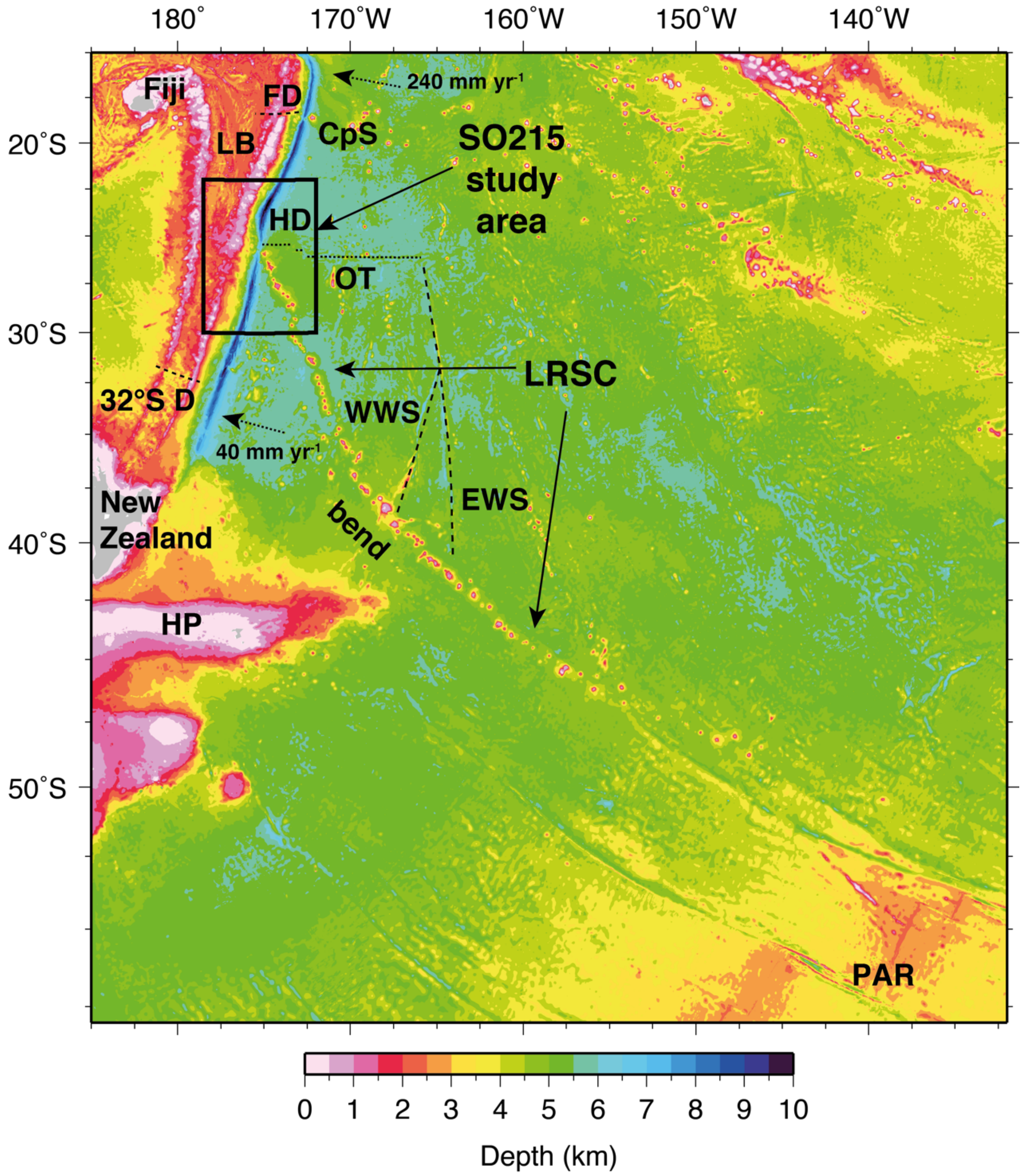

***Figure 1.3:** Full extent of the LRSC in the SW Pacific. Bathymetry from the GEBCO 30 second grid (IOC et al., 2003). Black box is the SO215 study area shown in Fig. 1.4. Dotted/dashed lines are major linear tectonic features discussed in the text. Features labelled are: CpS – Capricorn seamount, EWS – East Wishbone Scarp, FD – Fonualei Discontinuity, HD – Horizon Deep, HP – Hikurangi Plateau, LB – Lau Basin, LRSC – Louisville Ridge Seamount Chain, OT – Osbourn Trough, PAR – Pacific-Antarctic Ridge, WWS – West Wishbone Scarp, 32˚S D – 32˚S Discontinuity. Dotted arrows show subduction direction and velocity.*

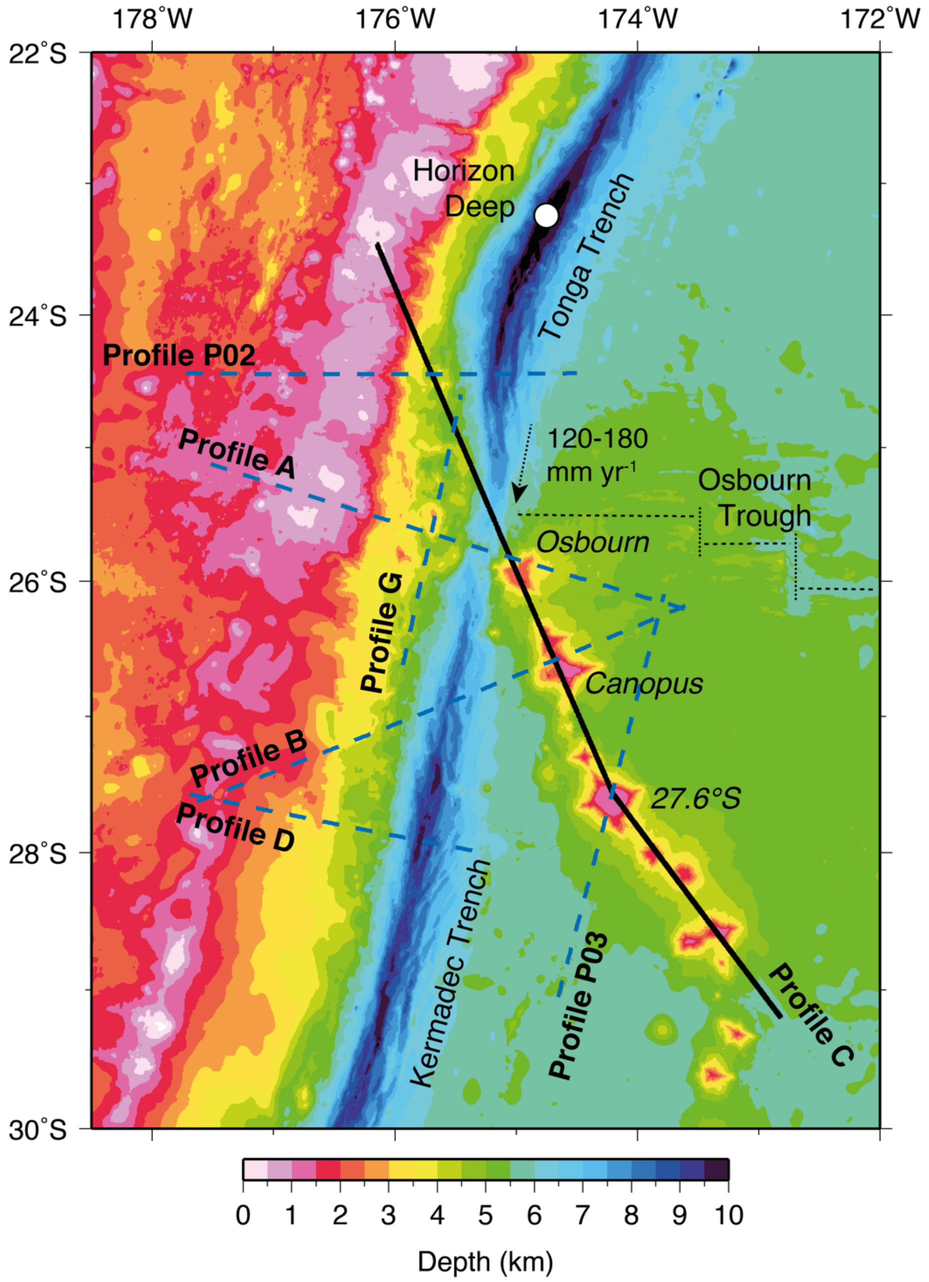

Figure 1.4: *SO215 study area, as shown by black boxes in Figs 1.1 and 1.3. Bathymetry is a composite of 50 m gridded swath bathymetry from all cruises to this region (see Section 1.6), with gaps filled using the GEBCO 30 second grid (IOC et al., 2003). Profile C shown as solid black line. Additional SO215 and TOTAL profiles shown as dashed blue lines. Osbourn Trough plotted as dashed black line and transforms between segments as dotted lines. Horizon Deep shown as white circle. Profiles (bold), seamounts (italics) and tectonic features are labelled. Dotted arrow shows the direction and rate of migration of the LRSC-TKT intersection point.*

78.8 ± 1.3 Ma (Koppers et al., 2004), and lies proximal to the Tonga Kermadec Trench (TKT) at ~25.8˚S (Fig. 1.4). Throughout the Palaeogene, the magmatic supply rate appears to have been generally constant at 3-4 x 10^3 km^3 Myr^{-1}, but has waned since 25 Ma, and post-11 Ma there is no evidence for emergent volcanism (Lonsdale, 1988). The youngest main-chain LRSC seamount is located at ~146˚W, and has an estimated age of ~8.5 Ma (Lonsdale, 1988). At 139.1˚W, a large, isolated seamount with an uneroded summit at a depth of 540 m, an $^{40}Ar/^{39}Ar$ age of 1.11 ± 0.04 Ma (Koppers et al., 2004; Lonsdale, 1988) and an isotopic signature consistent with other LRSC seamounts (Cheng et al., 1987; Hawkins et al., 1987) has been suggested as a candidate for the extension of the chain. Between the 146˚W and 139.1˚W seamounts Koppers et al. (2011) identify a field of very small volcanic cones, suggesting that the two may be linked. Lonsdale (1988) suggests a 750 m-high unsampled edifice at 138.2˚W as a candidate for the present hotspot location. A small chain of 1 km-high seamounts around 135˚W has been suggested as a further continuation with a best-fit present hotspot location suggested at 52.0˚S, 134.5˚W based on linear extrapolation of the trail from the dated seamount at 139.1˚W (Koppers et al., 2011). The chain morphology topographically resembles a linear hotspot chain such as the Hawaii-Emperor, with the LRSC also displaying a conspicuous (~25˚) bend at ~37.5˚S (Fig. 1.3). $^{40}Ar/^{39}Ar$ dating of dredge samples from either side of this break in trend show it to be approximately coeval with the 60° bend in the Hawaii-Emperor seamount chain at 50-44 Ma (Watts et al., 1988), supporting reconstructions for past motions of the Pacific plate.

1.4.1. Pre-hotspot geological history

Osbourn seamount is located adjacent to the Osbourn Trough (OT), an E-W oriented linear feature which exhibits only a weak bathymetric expression (Figs 1.3 and 1.4), but is much more clearly observed in gravity data (Fig. 1.5). The most likely interpretation of this feature is that it represents a palaeo-spreading centre related to the rifting apart of the Hikurangi and Manihiki plateaux (Downey et al., 2007). However, constraints on the age of initiation and cessation of OT spreading are limited due to its temporal coincidence with the Cretaceous Normal Superchron (Cande and Kent, 1992), meaning that there are no magnetic reversal patterns for dating. However, dated dredge samples yield a range of spreading cessation ages of:

- 93-87 Ma (Worthington et al., 2006; Downey et al., 2007) to 83-71 Ma

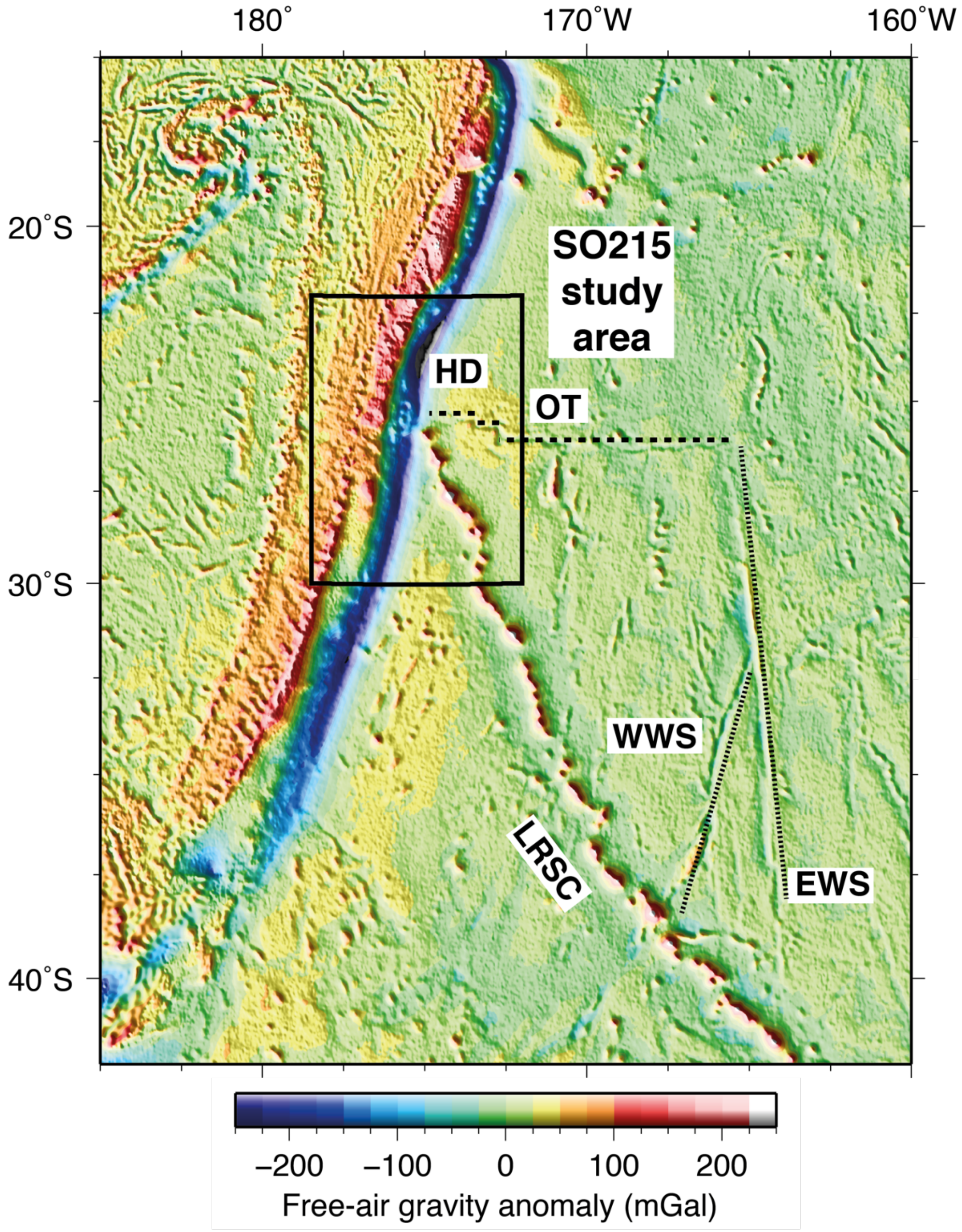

Figure 1.5: *Satellite-derived free-air gravity anomaly for the LRSC-TKT intersection. Data from Sandwell et al. (2014) v23, illuminated from the SW, which allows better identification of linear features (Wishbone Scarp and Osbourn Trough – plotted as dashed lines) which are not well imaged in bathymetry data (cf. Fig. 1.3). Features labelled are: EWS – East Wishbone Scarp, HD – Horizon Deep, LRSC – Louisville Ridge Seamount Chain, OT – Osbourn Trough, WWS – West Wishbone Scarp. Black box shows the location of the SO215 study area shown in Fig 1.4.*

(Billen and Stock, 2000), corresponding to a full spreading rate of 60-80 mm yr^{-1} and initiation at ~121 Ma; and

- ~105-115 Ma (Mortimer et al., 2006; Beier et al., 2011) corresponding to a faster full spreading rate of 150 mm yr^{-1}.

Taking the age of Osbourn seamount from Koppers et al. (2004), these spreading cessation ages result in a plate age at the time of volcanism (Δt) of between 10-35 Ma. The Müller et al. (2008) global plate age model (Fig. 1.6) supports the lower end of this range, with a seafloor age of ≤90 Ma in region of the Osbourn Trough.

1.4.2. Geological and geochronological studies of the LRSC

The LRSC exhibits an increasing age progression along-chain, although the rate of ageing is not always linear (Watts et al., 1988; Koppers et al., 2004; 2011), and little overall chemical and isotopic variation (Beier et al., 2011; Nichols et al., 2014). Small, sparsely spaced volcanoes between 167-171˚W show more variable lava (Lonsdale, 1988), trace element and isotope compositions, and higher Nb/Zr and La/Yb values (Beier et al., 2011), and are associated with a region of older underlying seafloor (Fig. 1.6; Müller et al., 2008) located to the northwest of the Wishbone Scarp, which represents the boundary between crust formed by spreading at the OT and at the Pacific-Antarctic Ridge (Watts et al., 1988). Beier et al. (2011) suggest that this variability could result from the same homogenous mantle source but with laterally smaller degrees of melting, but may also be related to the waning of the magma source from the Neogene to present (Lonsdale, 1988).

Dredged and drilled lava samples from LRSC volcanoes show that they display a dominantly alkalic composition throughout their lifespan (Hawkins et al., 1987; Beier et al., 2011; Koppers et al., 2013), in contrast to Hawaiian volcanoes (e.g. Clague and Dalrymple, 1988) which progress from an alkaline pre-shield through to a dominant tholeiitic shield-building stage and then back to a relatively alkaline post-shield over a time span of up to ~6 Ma. Trace element (Zr/Y, Zr/Nb, Ba/La, and La/Ce; Hawkins et al., 1987) and isotopic (Nd and Sr; Cheng et al., 1987) records indicate that the LRSC source has remained homogeneous over long timescales.

Together, these studies indicate that the mantle source for the LRSC does not appear to be significantly affected by variable degrees of melting and/or source fertility (Chen and Frey, 1985; Phipps Morgan, 1999; Koppers et al., 2011). The relatively

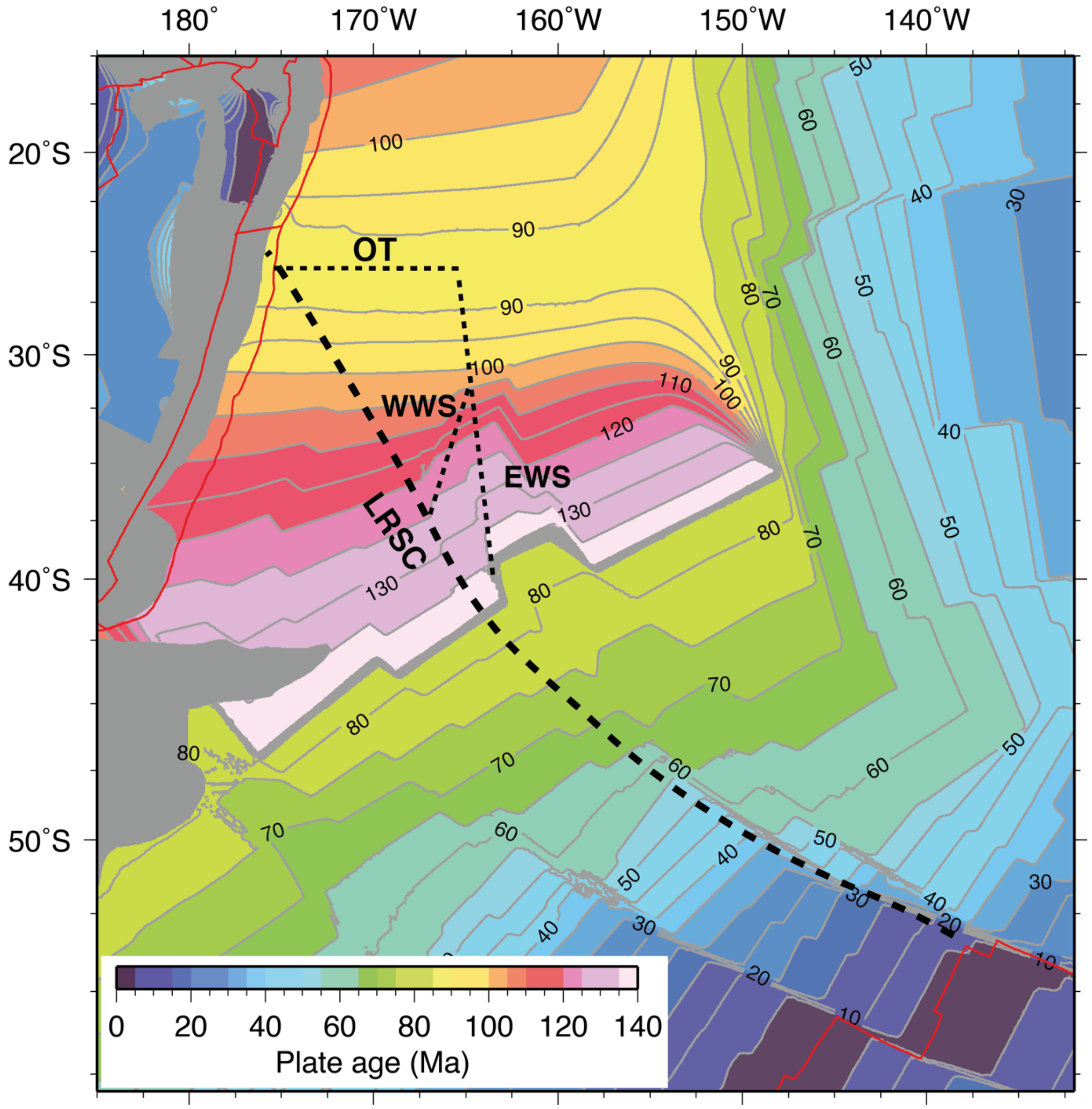

Figure 1.6: Plate age along the LRSC from Müller et al. (2008). Contours in grey, plotted at 5 Ma and labelled at 10 Ma intervals. Red lines are plate boundaries from Bird (2003). Labelled dashed lines show locations of principal features described in the text and their relation to underlying plate age. Label abbreviations as in Fig. 1.5.

uniform melting conditions along-chain may instead be explained simply by limited variation in lithospheric thickness (Beier et al., 2011), however this does not explain the lack of a tholeiitic shield stage unless different melting processes are considered. In addition to these studies which identify the relative homogeneity of the LRSC volcanism through time, it has also been observed that the seamounts display a distinctive $^{206}Pb/^{204}Pb$ signature, which can be used as a tracer to follow LRSC material through the subduction system (Cheng et al., 1987).

1.5. Tonga-Kermadec Trench and LRSC subduction

Initiation of subduction at the Tonga-Kermadec Trench (TKT) occurred at around 52 Ma (Meffre et al., 2012), contemporaneously with initiation of the Izu-Bonin-Mariana system to the north (Figs 1.1, 1.3 and 1.4 – Ishizuka et al., 2011; Reagan et al., 2013). A record of subduction initiation is preserved in the form of the buried Tonga Ridge, as manifest in the vertical gravity gradient, which extends north from the LRSC-TKT intersection to the ~18-19°S Fonualei Discontinuity and south to the 32°S Discontinuity respectively (Fig. 1.3 – Pelletier and Dupont, 1990; Collot and Davy, 1998; Ballance et al., 1999; Bassett et al., 2016; Funnell et al., 2017). Subduction of the Pacific plate beneath the Indo-Australian plate is oblique, with convergence rates ranging from 240 mm yr^{-1} at the northern part of the Tonga Trench, to 40 mm yr^{-1} at the southern part of the Kermadec Trench (Fig. 1.3 – Bevis et al., 1995). Coupled with the thin trench sediment fill (<100 m – Hayes and Ewing, 1971) and incoming plate horst and graben structure, subduction here meets the general definition of being tectonically erosive (e.g. Clift and Vannucchi, 2004). In other words, removal of material from the front and base of the forearc represents the 'background' subduction behaviour at this margin.

The LRSC presently intersects the Tonga-Kermadec subduction system at ~25.8°S (Fig. 1.4). In addition to the oblique direction of subduction described above, the strike of the incoming LRSC is also oblique to the plate boundary (~50°), resulting in southwards migration of the intersection point at a rate of 120-180 mm yr^{-1} (Lonsdale et al., 1986; Ballance et al., 1989). This results in the generation of along-margin variability in structure of the:

- trench (Pointoise et al., 1986; Ballance et al., 1989; Clift et al., 1998);
- forearc (Lonsdale, 1986; Ballance et al., 1989; Pelletier and Dupont, 1990; Clift and MacLeod, 1999; Funnell et al., 2014; 2017);

- arc (Dupont and Herzer, 1985; McGeary et al., 1985; England et al., 2004); and
- back arc (Bevis et al., 1995; Ruellan et al., 2003; Bonnardot et al., 2007).

In addition, the LRSC-TKT intersection is marked by an ~200 km-wide zone of seismic quiescence (Scholz and Small, 1997), a feature which has been observed at other margins where bathymetric features are subducted (Kelleher and McCann, 1976; Habermann et al., 1986). However, the location of this zone is offset to the south from the point of the intersection (Timm et al., 2013), which suggests that more complex geometry or processes may be controlling the reduced seismicity.

These observations of along-strike variability in forearc and trench morphology and seismicity have been directly attributed to the subduction of the LRSC at the margin. However, a number of significant unknowns remain regarding the nature and history of the already subducted part of the chain, namely when and where the initial collision occurred, (von Huene and Scholl, 1991; Lallemand et al., 1992; Wright et al. 2000; Ruellan et al., 2003; Bonnardot et al., 2007; Contreras-Reyes et al., 2011; Stratford et al., 2015), and in what direction and what manner the LRSC continues to the northwest of Osbourn seamount, where it has already been subducted (e.g. Ruellan et al., 2003; Timm et al., 2013; Bassett and Watts, 2015; Stratford et al., 2015).

1.6. Cruise SO215

A marine geophysical survey of the LRSC and the adjacent Indo-Australian plate was conducted aboard R/V Sonne between April-June 2011 (Peirce and Watts, 2011), during which a series of multichannel seismic (MCS) reflection and wide-angle seismic (WA) refraction profiles was acquired (Profiles A, B, C, D, and G). The co-incident MCS-WA profile that underpins this study, Profile C (Fig. 1.4), traverses ~500 km of the oldest extant part of the LRSC, and then crosses into the overriding Indo-Australian plate along the continuation of the extant chain. The acquisition, processing and modelling of this data will be discussed in Chapters 2 (MCS) and 3 (WA). The data acquired during this experiment complement that collected part of the earlier *TOTAL* experiment (Fig 1.4. – Profiles P02 and P03; Grevemeyer and Flueh, 2008).

In addition to the combined seismic dataset, multibeam swath bathymetry and gravity data were acquired throughout the cruise, together with a number of measurements of water column properties made using a sound velocity probe (SVP) and expendable bathymetric thermographs (XBT). The swath bathymetry and acoustic backscatter data, acquired port-to-port using the R/V Sonne's Kongsberg Simrad EM120 multibeam echosounder, were combined with all available swath bathymetry data from previous studies in the region dating back to 1998. Each cruise's data were processed using *MB-System* (Caress and Chayes, 2006) to remove large artefacts and then gridded on a cruise-by-cruise basis at 50 m node spacing. Data were then progressively combined such that more recently acquired data were used preferentially to older data, and gaps in coverage were filled using the GEBCO 30 second grid (IOC et al., 2003). This combined bathymetry dataset is used as the input to modelling and as the underlay for all figures in this thesis, unless otherwise identified in the figure caption.

Gravity data were also acquired port-to-port throughout the cruise using a NERC National Marine Facilities Sea Systems' (NMFSS) LaCoste & Romberg air-sea gravimeter. Base ties, where the ship gravimeter was calibrated against established absolute gravity reference points, were conducted in Auckland (New Zealand) and Townsville (Australia) at beginning and end of the cruise respectively, allowing an instrument drift of 3.02 mGal month^{-1} to be calculated. This drift was removed assuming it accumulated linearly over time. Eötvos correction and filtering, to remove the high-frequency noise component, completed the data processing. As part of the post-cruise data QC process, cross-over analysis of >2200 ship track intersections was undertaken to assess the survey error. The determined mean difference between crossing tracks is -0.6 mGal, and the RMS difference is ±10.2 mGal (Peirce and Watts, 2011). This RMS value represents largest uncertainty case given that it is based on using all cross-over points, including those during OBS deployments and recoveries when the vessel motion is quite variable during manoeuvring. It is anticipated, therefore, that the actual uncertainty on the measured FAA is better than this. The gravity data will be used in Chapter 4 to provide an independent verification on the uniqueness of the WA seismic modelling result, by converting this structure to a density model and comparing the FAA associated with this to the measured data. It may also allow further appraisal and constraint to be made on parts of the model which are less well resolved by WA seismic travel time modelling.

1.7. Study aims

Overall, and in their broadest sense, the aims of the *TOTAL* project, and SO215 in particular, of which this work forms part, were to address the following two primary questions:

- what is the mechanical response to loading associated with seamount chains and subduction?; and
- do bathymetric features on the subducting oceanic plate control margin seismicity (Kelleher and McCann, 1976)?

Therefore, geophysical data were acquired to determine:

- the crustal and uppermost mantle structure across and along the Louisville Ridge Seamount Chain (Profiles A, B, C, P03);
- the 'background' crustal and uppermost mantle structure of the subducting plate, for comparison with the above, in relation to both how intraplate volcanism modifies the crust and how seamount subduction differs from 'background' subduction in terms of its effects on the plate boundary and overriding plate (A, B, C, D, P02, P03);
- the mechanical properties of the subducting and overriding plates, the state of isostasy, and the degree of seamount chain related flexure (A, B, C, P03);
- the structure and behaviour of the subducting and overriding plates immediately adjacent to the trench (A, B, C, P02); and
- the seafloor morphology and crustal structure along the Kermadec forearc (B, D), which is yet to be affected by seamount collision, and the collision-related deformation and structure in the Tonga forearc (A, C, G, P02).

This study focuses on Profile C and, of the above goals, there are three principal scientific aims which governed its design and which will be investigated in this study. These aims are:

1) to characterize the structure of the LRSC and pre-subduction crust, identifying any along-ridge variation in crustal structure or magmatic underplating;
2) to identify how seamounts interact with the overriding plate during subduction; and

3) to understand how along-ridge variation in topography and crustal structure relate to post-collisional forearc uplift.

Further to this, by integrating the results of this study with other models from the region (Contreras-Reyes et al., 2010; 2011; Bassett, 2014; Stratford et al., 2015; Funnell et al., 2017) this study will:

4) further constrain the along- and across-chain crustal and upper mantle structure of the large LRSC seamounts (Osbourn, Canopus and 27.6˚S), in order to determine whether there is any consistency in crustal structure and thickness along-chain which may provide further insight into their constructional origin; and
5) determine the most likely continuation direction of the LRSC beneath the forearc, and where, if seamounts remain sufficiently intact to be imaged, these may be observed.

1.8. Summary

Throughout the following chapters, the geophysical data acquired along Profile C will be used to address the above goals. In Chapter 2 the MCS reflection data will be processed to provide an image of the shallow subsurface structures, in particular those associated with faulting and sediment cover. This will also permit identification of the top of the oceanic basement along-profile, which will provide an input for forward modelling of the WA seismic dataset in Chapter 3. The best-fitting model generated by this approach will then be extensively tested in Chapter 4, by applying a number of independent techniques and modelling of additional datasets. This is necessary in order to verify whether the model represents a valid and unique solution to the fitting of observed to modelled WA travel times, and to determine the minimum resolvable feature size and the confidence limits on the depths of layer interfaces and layer velocities. In Chapter 5 the results of modelling Profile C will be discussed in detail, with reference made where appropriate to additional data profiles from the SO215 and *TOTAL* experiments (Fig. 1.4) which allow the observations to be extended to understanding both across- and along-chain seamount structure and along-margin variability in overriding plate structure in response to the different stages of seamount subduction. Finally, in Chapter 6 the results of this study, and the experiment as a whole, will be discussed with reference to the general models governing seamount formation and structural variability, seamount interaction with the overriding plate, and overriding plate response to seamount subduction, which have been outlined in this chapter. In Chapter 7, the conclusions of this study will be set in the context of the wider experiment, and outstanding questions which have either not been answered, or have arisen from this study, will be identified. Finally, suggested further work to address the remaining uncertainties will be described in outline.

Chapter 2 - Multichannel Seismic Reflection Data – Acquisition and Processing

2.1. Introduction

In the previous chapter, the acquisition and broad composition of the geophysical dataset from R/V Sonne cruise SO215, and the motivations which governed the experiment were described. The principal focus of this chapter is the processing of the multichannel seismic (MCS) reflection component of this dataset, which will be used primarily to image the thickness and location of the sediment cover along-profile. Identification of the top of the oceanic crust will allow the starting point of wide-angle forward modelling to be informed. In addition, it may also reveal any structures which are present within the crust which may be further investigated during wide-angle forward modelling.

In this chapter, a simple workflow will be used to explain the various stages of the MCS data processing. Mitigation steps are applied as necessary to correct for features of the dataset which arise as a direct result of the acquisition geometry, the topography of the seabed, and the complex geology of the study area. The primary features shown by the resulting record section are briefly summarized, and will be discussed in more detail in Chapter 5, in relation to the interpretation of the final crustal velocity-depth model.

2.2. MCS data acquisition

In Section 1.6, the geophysical survey of the LRSC and the adjacent Indo-Australian plate undertaken during cruise SO215 was outlined. In this section, acquisition of the multichannel seismic (MCS) reflection component of this dataset, which was performed concurrently with the wide-angle (WA) seismic refraction and other geophysical datasets, will be described.

2.2.1. Profile C seismic data acquisition

Figure 2.1 shows a schematic of the equipment configuration used to acquire the MCS and WA seismic data contemporaneously along Profile C. The airgun array comprised 12 Sercel G-guns, with a total volume of 5440 in^3 (Fig. 2.2), and was towed at a depth of 7.5 m. Shots were recorded using a 240-channel, 3000 m-long multichannel

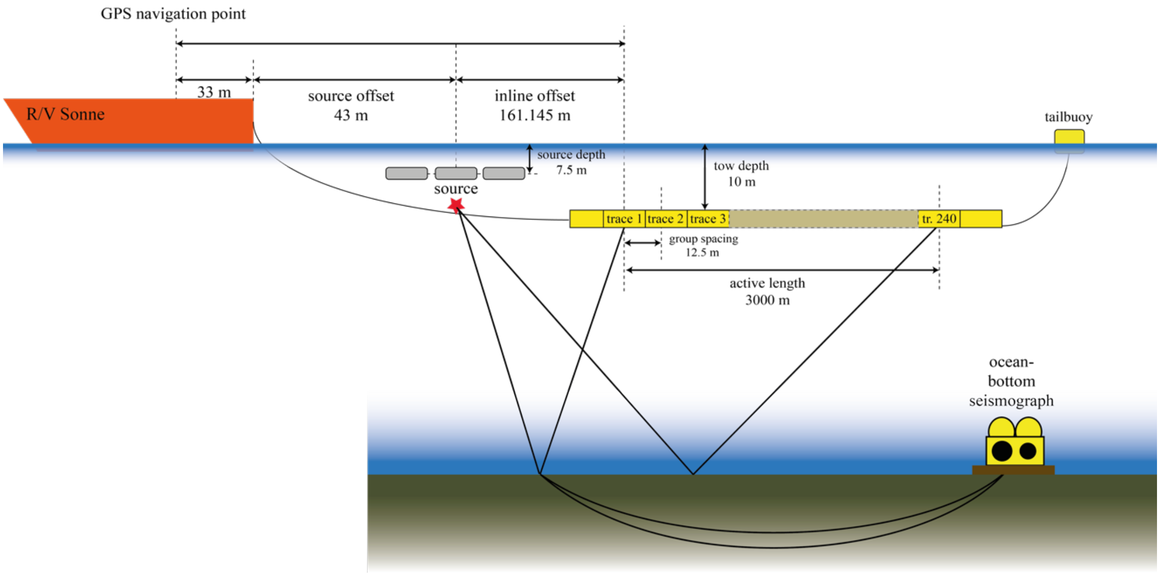

Figure 2.1: *Seismic acquisition equipment configuration. Source offset is the distance between stern of vessel and centre of source array (see Fig. 2.2, below). Inline offset is the distance between centre of source array and centre of first streamer active group.*

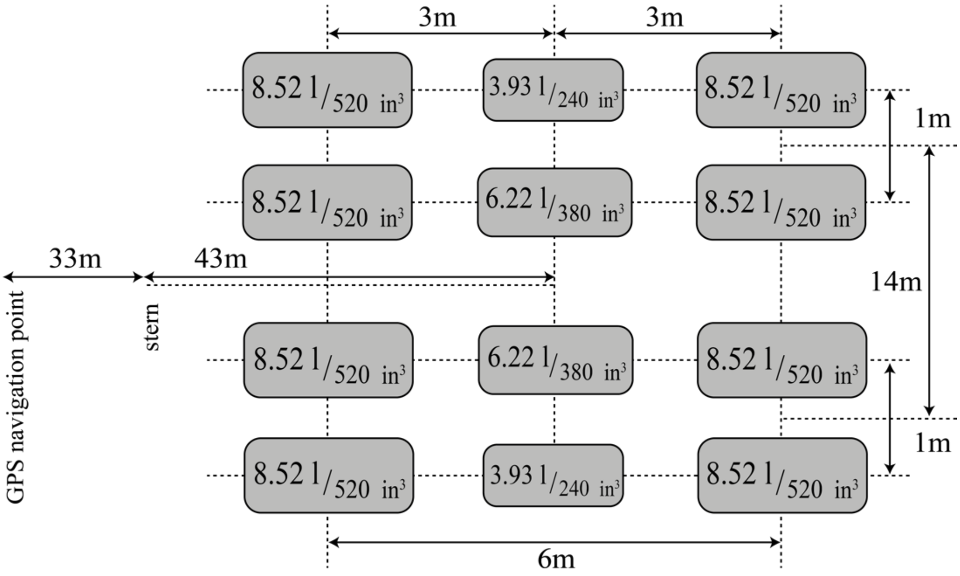

Figure 2.2: *Seismic source array configuration. Grey boxes represent Sercel G-guns, labelled with chamber sizes. The centre of the array is located 43 m astern, or 76 m aft of the point at which the recording of navigation is defined.*

streamer with a 12.5 m active group length. The streamer was towed at 10 m depth. Individual shots were recorded in SEG-D format, at a sampling rate of 2 ms over a trace length of 29 s. Shots were fired at 60 s intervals which, at a survey speed of 4.5 kn, results in a shot spacing of ~150 m (~12 streamer groups). Shots were triggered using a Longshot airgun array shot controller and their timings recorded using a Zypher GPS clock. A trigger pulse trailing versus leading edge mismatch between the firing and recording systems resulted in a 560 ms delay between the aim point and the trace start, which was removed by applying a bulk static shift to all traces. The 60 s firing rate was a compromise between achieving an acceptable fold of MCS data and minimising the effect of water wave wrap-around in the WA data, and is a direct result of the contemporaneous acquisition of these two data sets. The consequences of this firing rate on the nominal data fold will be addressed in Section 2.3.2.

2.2.2. Challenges during acquisition

Approximately 21 hours into the acquisition of Profile C, a valve failure in a compressor unit turbo-charger resulted in a loss of air pressure, and acquisition was suspended to affect repairs. A loop-back turn was conducted in parallel, which returned the vessel to a point on the profile before failure occurred once repairs were complete (Fig. 2.3a,b).

To produce a single reflection profile, shots from the first and second phases of shooting were spliced together (Fig. 2.3c). The selection of the point at which to splice the two phases of shooting had to satisfy two criteria. Firstly, the sets of shots comprising each phase of shooting must join without overlap and, secondly, shots selected from each phase of shooting must be located on-profile, rather than on turns onto- or off-profile at the beginning and end of the shooting phases respectively. Finally, the splice point must be a full streamer length before and after each turn to ensure it was fully straight astern, i.e. such that each channel was inline and on-profile.

The shot numbering for each of the two phases of shooting begins at 100. For the first phase of shooting shots 100-1321 (1222 shots) are included, and for the second phase, shots 232-4444 (4213 shots) are included (Fig. 2.3d). The location of the join is 24.80˚S, 175.53˚W, and the resulting profile comprises a total of 5435 shots. These shots were combined into a single SEG-Y file and the shot numbers in the headers renumbered sequentially starting at 1 (Fig 2.3e). A single file containing the corresponding shot locations was compiled, and used to assign the profile geometry.

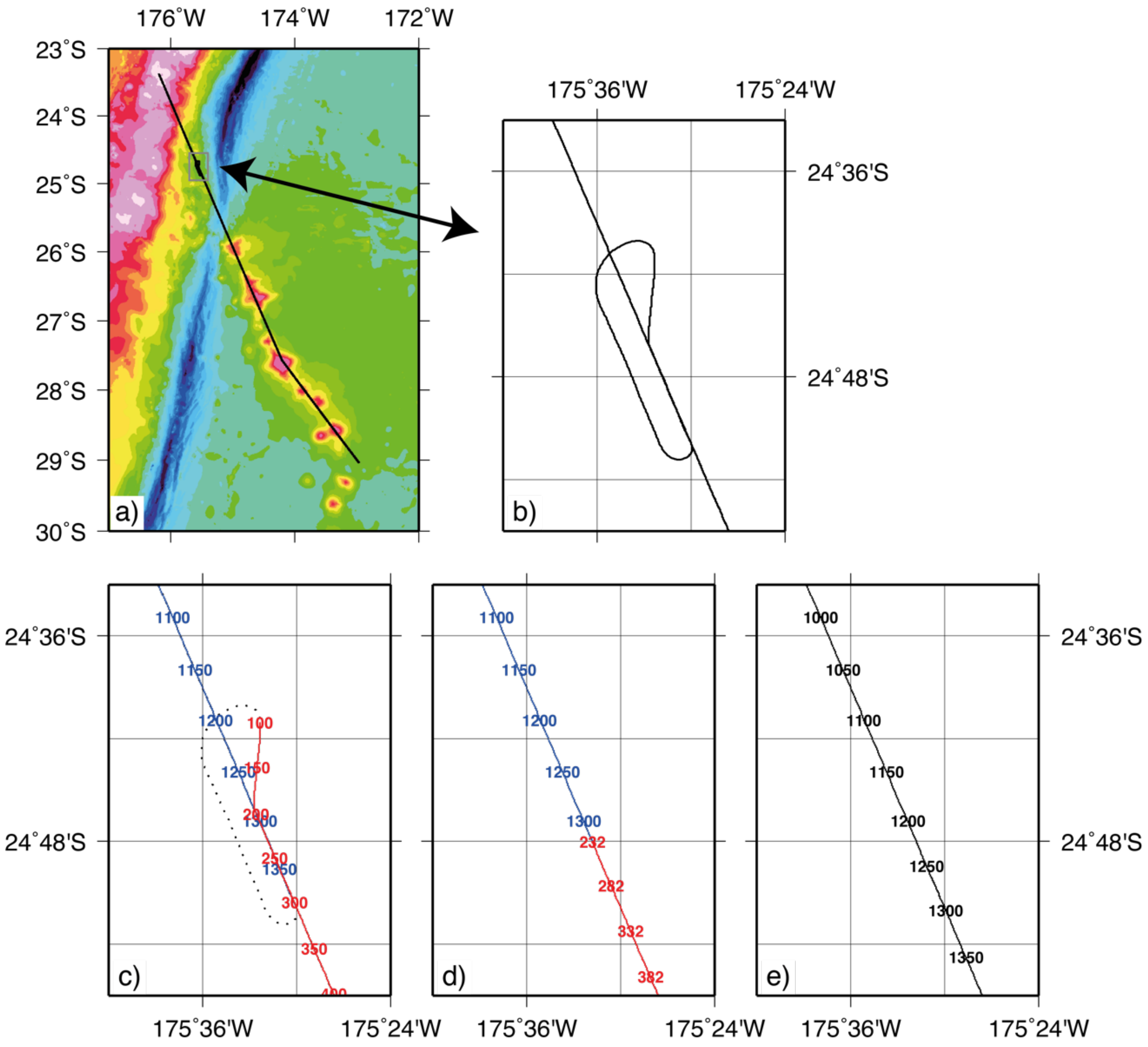

Figure 2.3: *MCS acquisition and shot point locations. a) Profile C (black line) in the SO215 study area. Bathymetry from GEBCO 30 second grid (IOC et al., 2003). Grey box centred on 24.75˚S, 175.50˚W and indicated with arrow shows the location of the compressor failure and turn, shown in detail in panels b) to e). b) Ship track for the period of repairs. Shooting occurred from south to north, with airgun compressor failure followed by three turns to starboard to return to profile at a point prior to failure. c) MCS shooting phases during acquisition. Blue line = first phase. Red line = second phase, following repairs. Shot numbers are labelled every 50 shots, starting from 100 for both phases of shooting. Ship track is plotted as dotted black line. d) As for c) but the overlap and off-line parts of shooting phases have been removed. e) Resulting single-profile shot locations for Profile C (black line). Shots have been sequentially renumbered, beginning at 1, and are labelled at every 50 shots.*

2.3. MCS data processing

2.3.1. Geometry

All MCS data processing was conducted using *Claritas*, and commenced with geometry assignment, by initially converting all shot locations from geographical co-ordinates in degrees (Fig. 2.4a) to Universal Transverse Mercator (UTM) co-ordinates, and then subtracting a false origin from all northing and easting values to remove the least significant figure. This ensured that the *Claritas* geometry application was able to handle the numerical values with sufficient precision (Fig. 2.4b). Due to the bend in Profile C, it was necessary to adopt the 'wiggly-line' geometry approach, which generates CMP locations from a set of hit points defined along-profile, using either straight or curved line segments. The *Claritas* geometry application includes an automated hit point generator. This was used to create a population of equally spaced hit point locations to faithfully define the trend of the profile. These 400 hit points were then used to generate the geometry database. This relatively large number of 1 hit point per 13.5 shots (or ~2 km), is necessary to sufficiently replicate the profile bend. The locations of CMP bins were then calculated using these hit points. The bin centre positions were cross-checked against the shot positions, with particular attention paid to the area in the vicinity of the profile bend at ~27.6˚S (Fig. 2.4c-i), to ensure that the CMP locations follow the shot locations and produce the shape of the bend with sufficient sharpness.

2.3.2. CMP binning

The compromise firing interval of 60 s (Section 2.2.1) results in the MCS data having a relatively low nominal fold of ~10. Coupled with the highly variable seabed topography and complex subsurface geological features, this results in a relatively poor signal-to-noise ratio (SNR). By increasing the CMP bin size to 25 m, the fold can be increased by a factor of ~4, and re-binning results in an improvement of the vertical image resolution, achieved without excessively compromising the horizontal resolution because the characteristic horizontal scales of both seabed features and imaging targets are significantly larger than 25 m. The mean fold in each CMP bin using this interval is 44, and the maximum is 66.

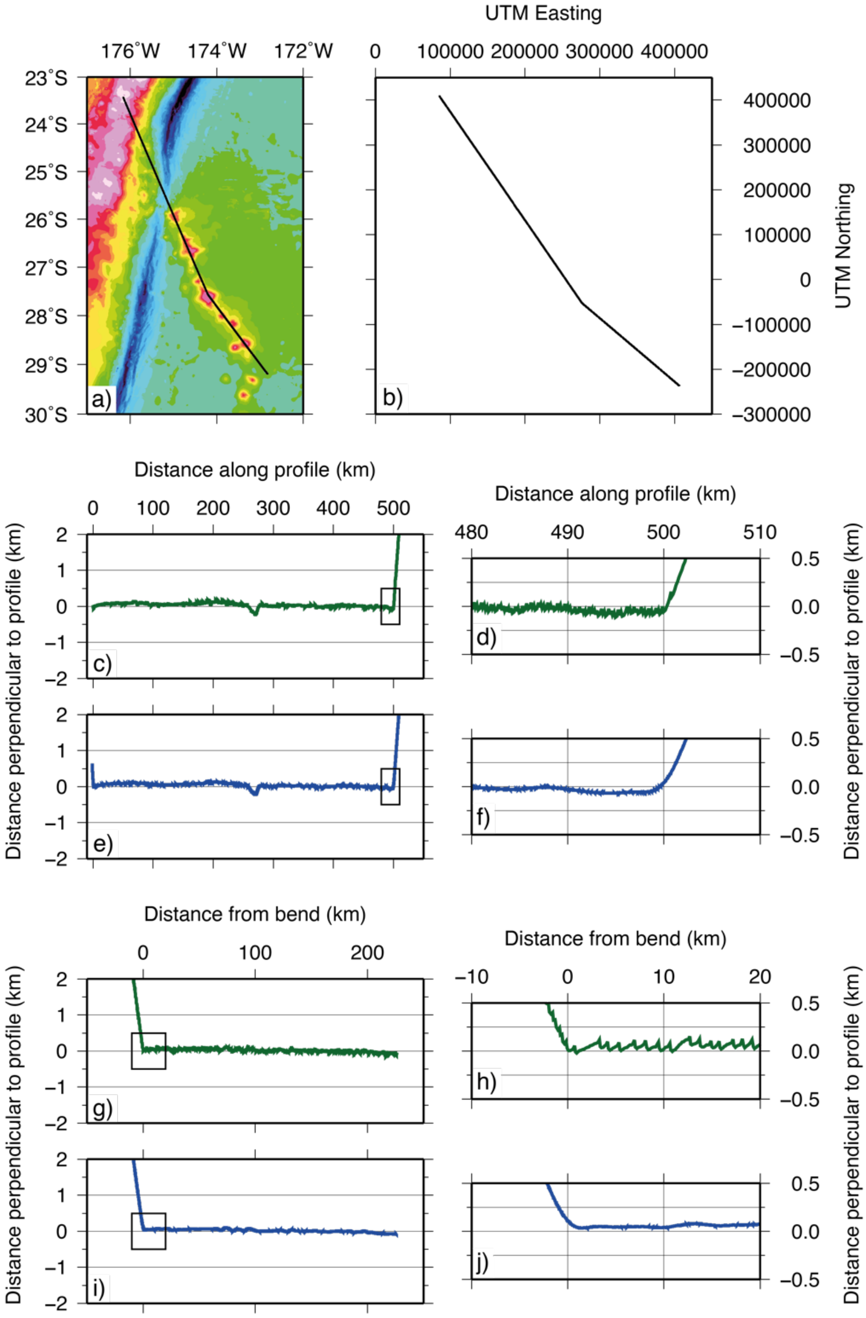

Figure 2.4: *MCS geometry assignment and checking. a) Location of Profile C (black line) in the SO215 study area. Bathymetry from GEBCO 30 second grid (IOC et al., 2003). b) Profile C location projected into UTM co-ordinates and with subtraction of false origins from northing and easting values c) MCS shot locations during acquisition, rotated into zero across-profile offset, for shots located to north of the bend in profile. Black box indicates location of zoomed region shown in d). d) Zoomed region at profile bend as indicated by black box in c). e) and f) As for c) and d) but plotting calculated CMP bin locations. g)-j) As for c)-f), for shots located to the south of the bend in profile. Rotated locations are plotted in terms of distance from the bend in the profile, not adjusted to distance along profile.*

2.3.3. Brute stack

In order to produce a first-pass image of Profile C, and determine what further processing needed to be applied, a brute stack of the data was produced. A simple processing workflow was adopted, which included the following steps:

- Resampling - The data were resampled from 2 ms to 4 ms, after low pass anti-alias filtering with a high cut at 125 Hz, which reduced the data volume for processing considerably. As frequency analysis showed no significant signal content above 100 Hz, resampling did not compromise data fidelity.
- Bulk shift - A static correction of 560 ms was is applied to all traces, to account for the observed lag between the triggering of the MCS recording system and the firing of the airgun array, as discussed in Section 2.2.1.
- Filtering - A zero-phase band-pass Butterworth filter, with a pass-band of 3-10-100-120 Hz, and amplitudes of 0.05, 0.95, 0.95, and 0.05, was used to remove significant low-frequency swell noise encountered during acquisition due to the sea state.
- Geometry assignment - The geometry was added to the trace headers and the data sorted into common midpoint gathers.
- Normal moveout correction - To generate the brute stack, a normal moveout (NMO) correction with a constant velocity of 1500 m s^{-1} was applied. This value represents a mean seismic velocity for seawater, and should coherently stack the seabed reflector, resulting in the generation of a first-pass image of the sub-seabed.
- Stacking - The NMO corrected CMP data were then stacked.

At this stage, additional operators can be applied. These principally serve to improve the appearance of the stack for display purposes. The post-stack processes applied in this study comprise:

- Migration - Kirchhoff post-stack time migration was applied at 1500 m s^{-1}. This process acts to collapse diffraction events, and results in significant improvement to the appearance and the shape of the seafloor, especially in areas of rough and irregular bathymetry.
- Muting - Kirchhoff post-stack time migration generates an above-seabed artefact, which was removed using a cosmetic top mute.

- Trace balancing - In order to balance trace amplitudes, an automatic gain control (AGC) may be applied. This technique calculates an average amplitude value within a time-window, progressively sliding the window along the trace length, then applies scaling to normalize the amplitudes to a fixed value. Although fast to calculate, mean scaling generates a shadow above and below strong reflections.

2.3.4. Results of brute stacking

Figure 2.5 shows the brute stack, with the additional processing steps applied to improve the stack for display. The principal forearc structural divisions, and named seamounts along the LRSC on the Pacific plate have been labelled.

Where seamount summits are relatively flat, prominent seabed reflectivity is observed. This reflectivity may correspond to: recently deposited pelagic sediments; summit breccias, conglomerates, or other products of reworking; or reef material, associated with periods when the seamount summit was located within the photic zone. IODP Expedition 330 (Koppers et al., 2011) drilled the summits of a number of Louisville Ridge seamounts, both within and beyond the SO215 study area, and revealed such facies. Generally, sediment accumulations on the Pacific plate are only found in the saddles between seamounts, and on the ‘background’ plate beyond the southernmost seamount imaged along-profile. In between, the steep seamount slopes prohibit significant accumulation.

The overriding plate can be divided structurally into three principal regions. Sloping towards the trench, the upper forearc contains the only significant sediment accumulations along-profile. The seabed of the middle forearc region is generally rougher, but its average depth does not vary by more than 1 km. The lower forearc is uplifted at its northwestern end, and dips steeply toward the trench.

Appraisal of the brute stack, unsurprisingly given the rough and significant seabed topography and lack of sediment cover, shows quite significant seabed scatter and numerous strong seabed multiples, together with an apparent lack of geologically-related reflectivity at depth. Consequently, the focus of the subsequent processing will be: velocity analysis to optimise stacking and migration; long-offset trace muting to reduce reflector smear within gathers; and deconvolution to minimise source-generated reverberation.

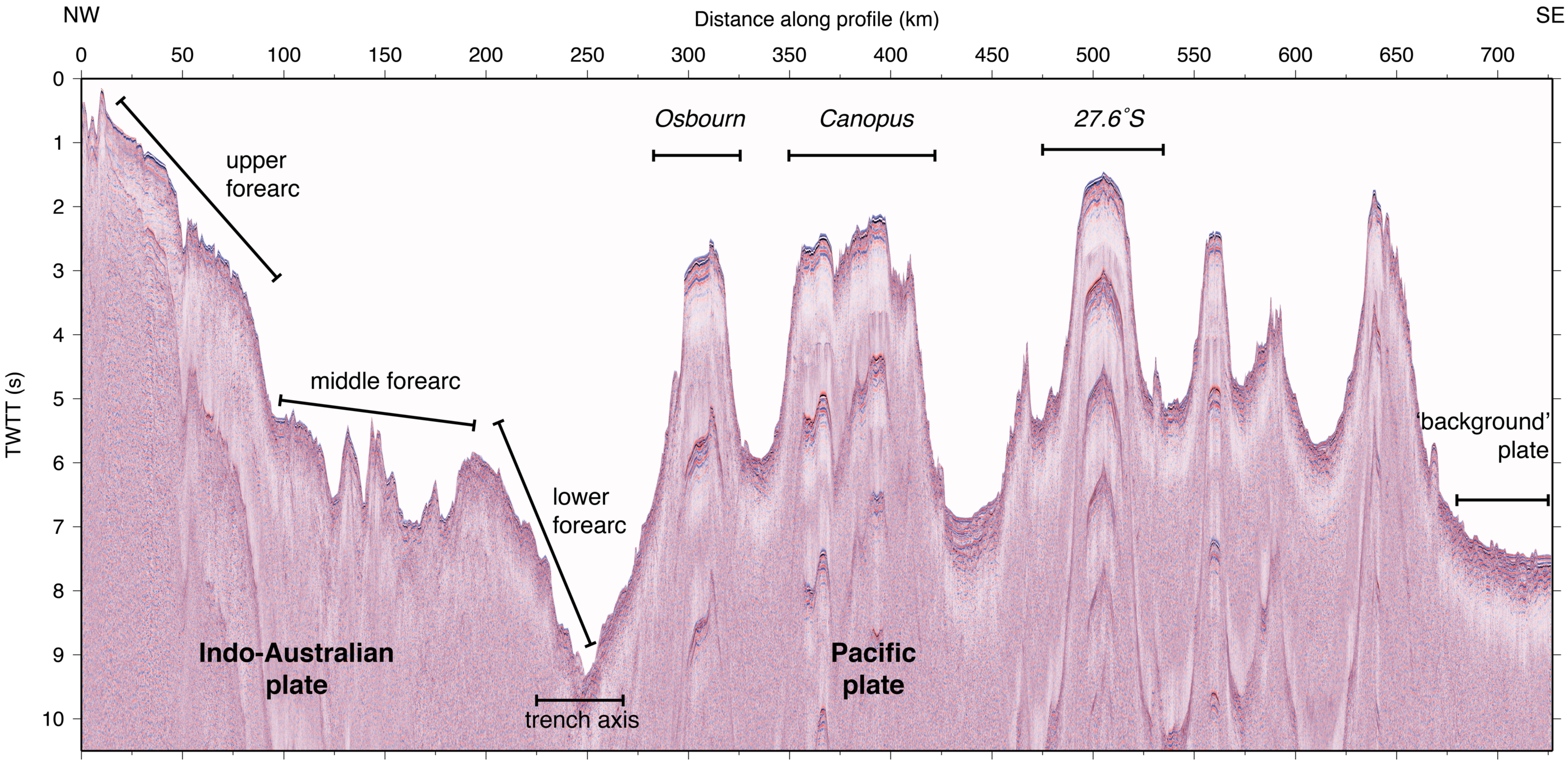

Figure 2.5: *Profile C MCS brute stack generated following procedure outlined in Section 2.3.3., and displayed with Kirchoff post-stack time migration at 1500 m s^{-1}, seabed mute, and AGC with 2000 ms time gate. Principal structural regions in the forearc and named seamounts are labelled.*

2.3.5. Velocity analysis

Following appraisal of the brute stack, detailed velocity analysis was conducted to produce an improved stacking velocity model. In particular, this was targeted at better resolving structures within the sediment covered parts of the profile, and reducing the appearance of seabed scatter.

Due to the large bathymetric gradients along the profile associated with the seamount chain, velocity analysis on the Pacific plate region concentrated on areas such as the seamount summits and saddles in between. These were the likely locations of pelagic, and pelagic and flank-derived sediments respectively. Sediments do not readily accumulate on steep slopes and correspondingly, the brute stack shows that there is virtually no sediment on the seamount flanks.

On the overriding plate, the most significant sedimentary accumulations appear to be located within a number of down-stepping, fault-bounded terraces on the upper forearc. Consequently, at the northwesternmost end of the profile, it was important to ensure that only primary reflection events were stacked as, given the relatively shallow water depth, the first seabed multiple arrives shortly after the primary reflections. Application of a stacking velocity function at depth with $V_{stack} > 1500$ m s^{-1} would also result in the suppression of the seabed multiple. Within the middle and lower forearc regions, the relatively steep slopes prohibit large scale sediment accumulation. However, the irregular bathymetry may act as a potential sediment trap, depending on the relative timing of the generation of the trapping features (oblique, transverse ridges) and the erosion of the upper slopes.

Velocity analysis was conducted within the *Claritas* constant velocity analysis (cva) environment. Stacking velocity picks were made at 50-100 CMP (1.25-2.5 km) intervals, depending on the degree of sediment cover, with those areas with more sediment being more closely sampled. A number of techniques were used to aid velocity picking. These comprised:

- constant velocity gathers (CVG) – where the CMP was displayed in a series of panels, with each NMO corrected using a different constant velocity. The user then picks the stacking velocity which best flattens the gather at a given two-way travel time (TWTT);
- constant velocity stacks (CVS) – where a range of CMPs centred on the analysis location were displayed as panels, and each was NMO corrected using

a different constant velocity. The user then picks the best stacked image on a velocity panel versus TWTT basis;

- semblance – which is a measure of trace-to-trace coherency over a range of stacking velocities and TWTTs. Bright spots in the semblance spectrum represent coherence maxima, and were picked as a velocity function; and
- live NMO corrected gathers – where a single gather was viewed with and without NMO correction using the current stacking velocity function. These gathers were recomputed automatically, so that reflector across-gather flattening could be checked and picks adjusted accordingly.

Once velocity analysis was complete, the resulting stacking velocity model was substituted into the processing scheme described in Section 2.3.3, then the data were reprocessed, migrated and displayed using the same parameters.

2.3.6. Removal of high amplitude, shallow sub-seabed noise

In the upper forearc region, the brute stacked section displays a band of steeply-dipping reflectors (Fig. 2.6a), which do not appear to represent a feature which could be interpreted as geological in origin. These features are limited to the first ~2000 CMPs, or 50 km along the profile, where water depths are shallowest. These dipping features appear to be bounded by a pair of consistent reflectors whose depth mirrors the water depth, implying that they are related to the shape of the seafloor.

During the initial stages of velocity analysis, stacking velocity picks were made on the consistent reflectors located above and below this band, and the stacking velocity field interpolated between picks. When this stacking velocity model was applied as a normal moveout correction, the steeply-dipping features appeared to be mostly removed. This observation suggests that they likely represent a signal which travels only through the water column, as they principally appear only when normal moveout is applied at a constant V_{stack} of 1500 m s^{-1}. It is also possible that heterogeneous across-profile bathymetry has generated diffractions and/or reflections from out-of-plane features that have mapped back onto the profile given the in-plane assumption that underpins the applied processing. Due to the relatively shallow water depth, such out-of-plane reflections and diffractions would have high signal amplitude, and would arrive at the receiver at a similar TWTT range to the primary reflections of interest. This may explain why these features only appear to be observed in this part

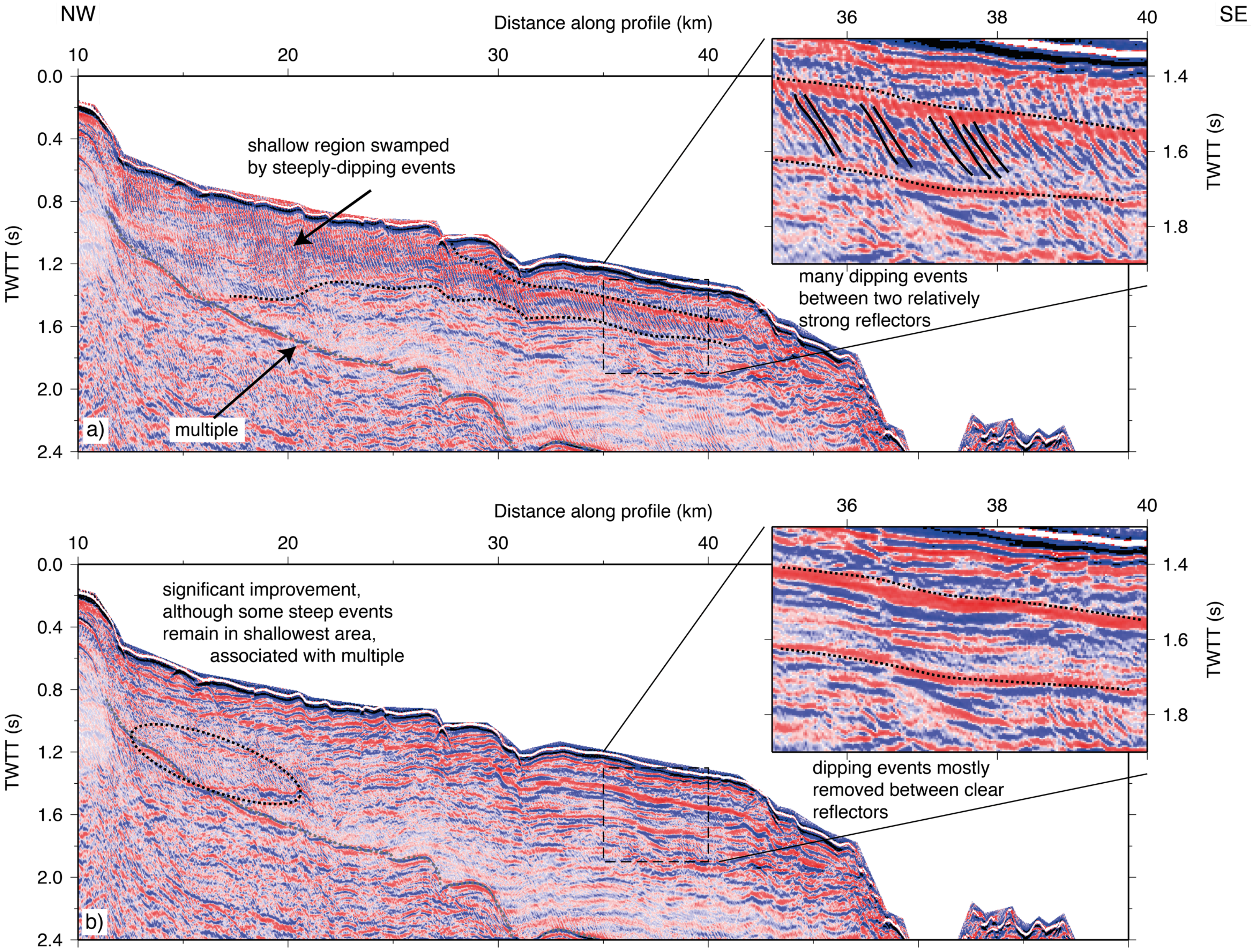

Figure 2.6: *Brute stacks showing the removal of high amplitude dipping events in the upper Tonga forearc region. a) Brute stack, displaying high amplitude, steeply-dipping events which mirror the seabed to ~40 km distance along profile. Up to 25 km d.a.p., almost all the section above the multiple is masked by these dipping events. Strong seabed multiple is labelled m. Dashed box shows the location of inset. Inset: Zoom-in of steeply-dipping events. b) As a) but following application of front mute to remove the large amplitude events at far-offsets (Fig. 2.8) Inset shows zoom-in of same area as in a), and that most of the events have been removed Some dipping events still remain in some locations, particularly in proximity of the seabed multiple.*

of the profile. A side effect of the application of NMO correction using the velocity analysis-derived stacking velocity model is a distortion of several reflectors in areas which were previously associated with this probable out-of-plane reflectivity (Fig. 2.7a). In order to attempt to determine the cause of the dipping events, and that of the distortion of the reflectors during stacking, an inspection of individual shot gathers was conducted focusing on the near and far offset channels. Unstacked, sorted CMP gathers were also inspected, with and without normal moveout correction (Fig. 2.8a,b). Following the application of a normal moveout correction, both at 1500 m s^{-1} (Fig. 2.8c) and using the velocity analysis-derived stacking velocity, it is possible to identify a cause of one or both of these features. This ‘event’ is located below the primary seafloor reflector, dips (in time) towards the front of the streamer, appears to be associated with CMP traces originating from receivers in the rear half of the streamer (far offset channels), and is relatively large in amplitude. A front mute was therefore designed in an attempt to remove this signal.

To test the suitability of this approach, an initial mute comprising a single TWTT-offset profile at which to make the cut, was applied to all CMPs along the profile. The parameters of this initial mute are:

Offset (m)	**TWTT (s)**
0	0
1650	1
2000	4
3200	6

This muting profile was applied after NMO correction, and prior to stacking, both for the 1500 m s^{-1} (Fig. 2.8d) and the velocity analysis-derived stack. Inspection of the resulting stacks indicated that this approach appeared to successfully reduce or remove both the dipping events in the brute stack (Fig. 2.6b) and the smearing of reflectors (Fig. 2.7b). Some dipping events were still visible in both stacks, and these were identified as short-path seabed multiples. Following this proof of concept, an improved muting profile was developed to account for the variable bathymetry in the region of interest.

In the upper forearc, between the start-of-profile and CMP ~2000, where these events no longer appear, the seabed gradually deepens from ~0.4 s to ~1.6 s TWTT.

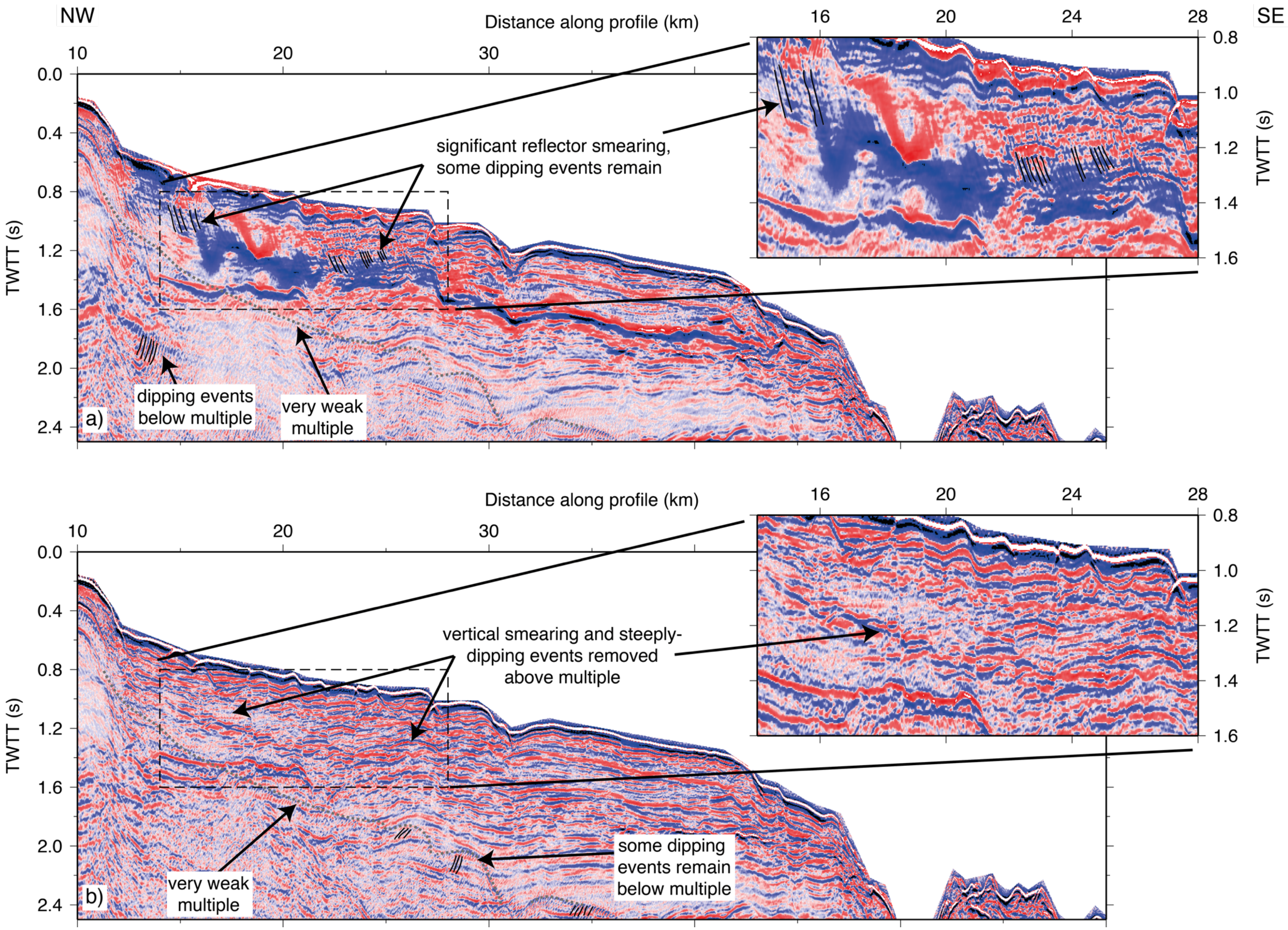

Figure 2.7: Upper Tonga forearc MCS data, stacked using the velocity model developed from velocity analysis, showing the effects on high amplitude dipping events. a) Some steeply-dipping events can be seen (cf. Fig. 2.6a), particularly between 10-25 km d.a.p.. There is vertical smearing of the seabed reflector between 12-18 km d.a.p., and of a dipping reflector between ~27-40 km d.a.p. and 1.4-1.6 s TWTT. Inset: Zoom-in of part of this smeared reflector. Some steeply-dipping reflectors are still present up to ~ 20 km distance, and above 1 s TWTT. b) Stacked section as in a), but with application of front mute as described in Section 2.3.6 and as applied in Fig. 2.6b). Areas of uppermost forearc steeply-dipping events are suppressed, and there is significant improvement to the appearance of the reflectors which were smeared in a). Some events can still be seen at the bottom of this figure, and appear to be associated with the seabed multiple.

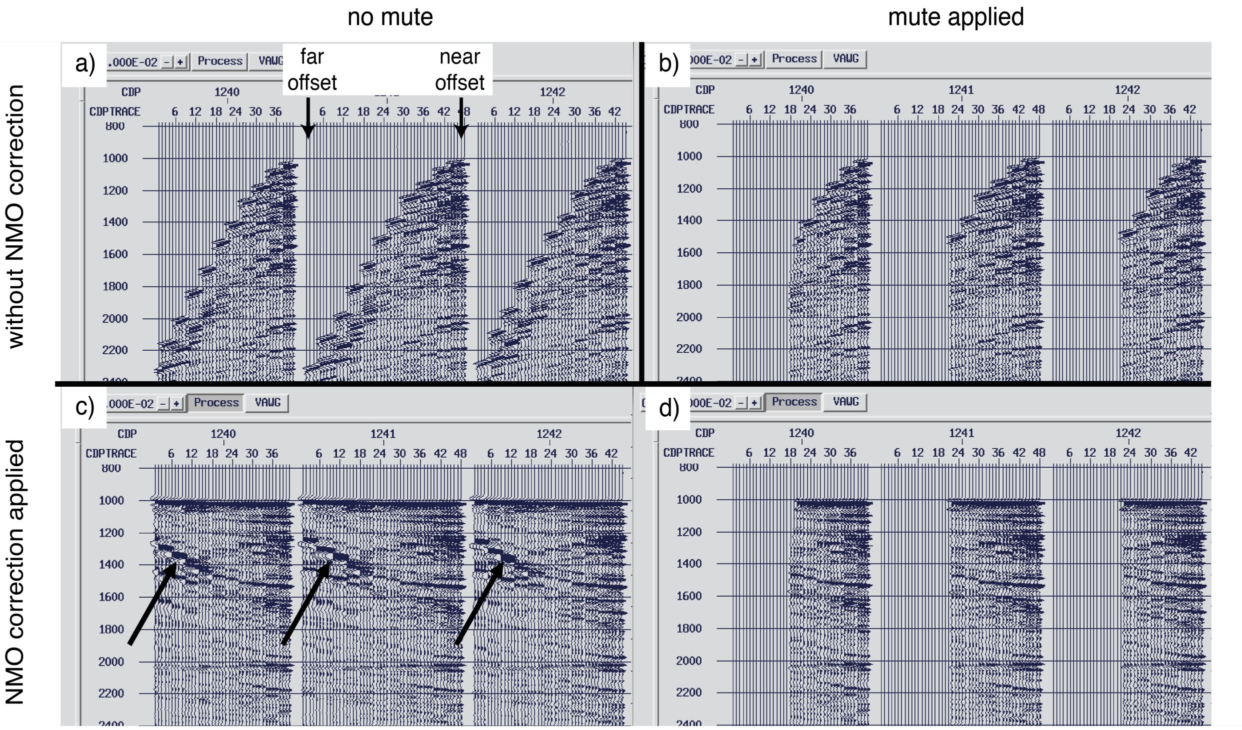

Figure 2.8: *Screenshots from the Claritas testing application showing the front mute for CMP gathers 1240-1242. Traces recorded on near-offset channels are on right of each gather, and far-offsets on the left. Vertical axes are in milliseconds TWTT. The seabed primary reflection occurs at ~ 1000 ms TWTT. Both a) and b) show gathers without application of NMO correction. The apparently stepped profile of each hyperbola is a result of the spacing between blocks of 4-5 adjacent offset traces in each CMP gather being displayed by CMP trace number. No features immediately identifiable as a potential source of the artefacts observed in brute and velocity analysis-derived stacks are visible. Panels c) and d) have NMO correction applied at 1500 m* s^{-1}*, in preparation for brute stack. Arrows in c) indicate location of large amplitude dipping noise, which is located on far-offset channels (CMP traces <18). d) Results of application of a pre-stack mute to remove the far-offset traces. At the seabed, muting begins at 1650 m offset.*

The onset of the mute, which was defined by the time of the event arrival at 1650 m streamer offset, was adjusted to follow the seafloor at intervals of 100-200 CMPs depending on how quickly seabed depth varied. Below this, the offset and time values of the lower two points defining the muting profile were held constant. Beyond CMP 2000, the event appears to be negligible or absent, so the muting profile was no longer applied. Based on the hypothesis that these features are manifestations of signals travelling only through the water column, as discussed above, this observation may be expected, since beyond CMP 2000 the significant increase in water depth results in a greater path length and, hence, a larger TWTT delay behind the primary immediately-sub-seabed geological reflectors and greater suppression due to stacking alone.

Following the identification and removal of these artefacts, a further pass of velocity analysis was made for the northern part of Profile C, in the CMP range where the features were observed. The resulting stacking velocity model was used for NMO correction to produce the final reflection stack.

2.3.7. Post-stack deconvolution

In areas where there is very little or no sedimentary cover, the stacked MCS section shows evidence for a weak reflector, which follows the primary seabed reflector, at a lag of ~200 ms. This event is attributed to the bubble pulse from the seismic source. The concurrent MCS-WA acquisition necessitated the design of a source array, the characteristics of which had to represent a compromise between the ideal parameters for each individual data type. In order to be able to record long offset refracted arrivals with OBSs as part of the WA experiment, and hence be able to determine the velocity structure of the lower crust and uppermost mantle, it was necessary the seismic source needed to have a powerful low frequency signal component. A side effect of this, however, is the generation of a bubble pulse, as a result of using airguns with a large chamber size (Figs 2.9a-c and 2.10a-d). Pre-cruise modelling of the source array used in this experiment (Peirce and Watts, 2011) showed an expected peak-to-bubble amplitude ratio for the seismic source of ~13. The onset of the bubble occurs at ~200 ms lag behind the primary pulse, and has a duration of 100-150 ms.

To suppress the bubble pulse reverberation, autocorrelation functions were calculated for the stacked data at various points along the profile. Autocorrelation is a technique used to detect repeating patterns, such as periodic signals. It works by correlating the signal with a copy of itself over a range of delays, or time-lags, between

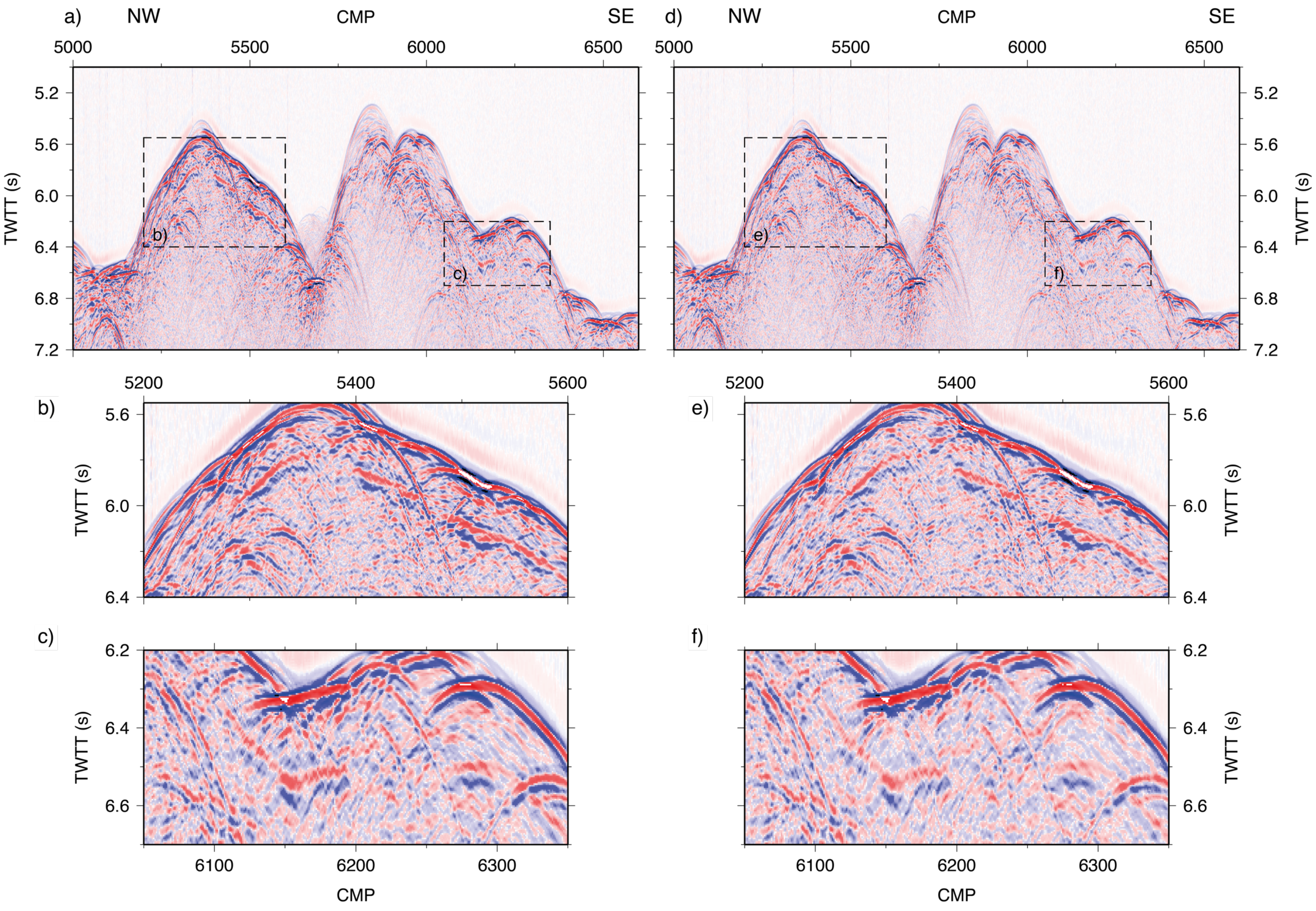

Figure 2.9: *Test panels showing the effects of deconvolution in the middle Tonga forearc region. a) Velocity-analysis stacked section, plotted without migration or AGC. Dashed boxes show locations of zoomed regions in b) and c. b) Oblique, transverse ridge, displaying strong 200 ms-lag reverberation following the seabed reflection. c) As b) for a small region on flank of the transverse ridge. d)-f) As for a)-c) following application of post-stack statistical Weiner deconvolution, with 60 ms gap and 300 ms operator length.*

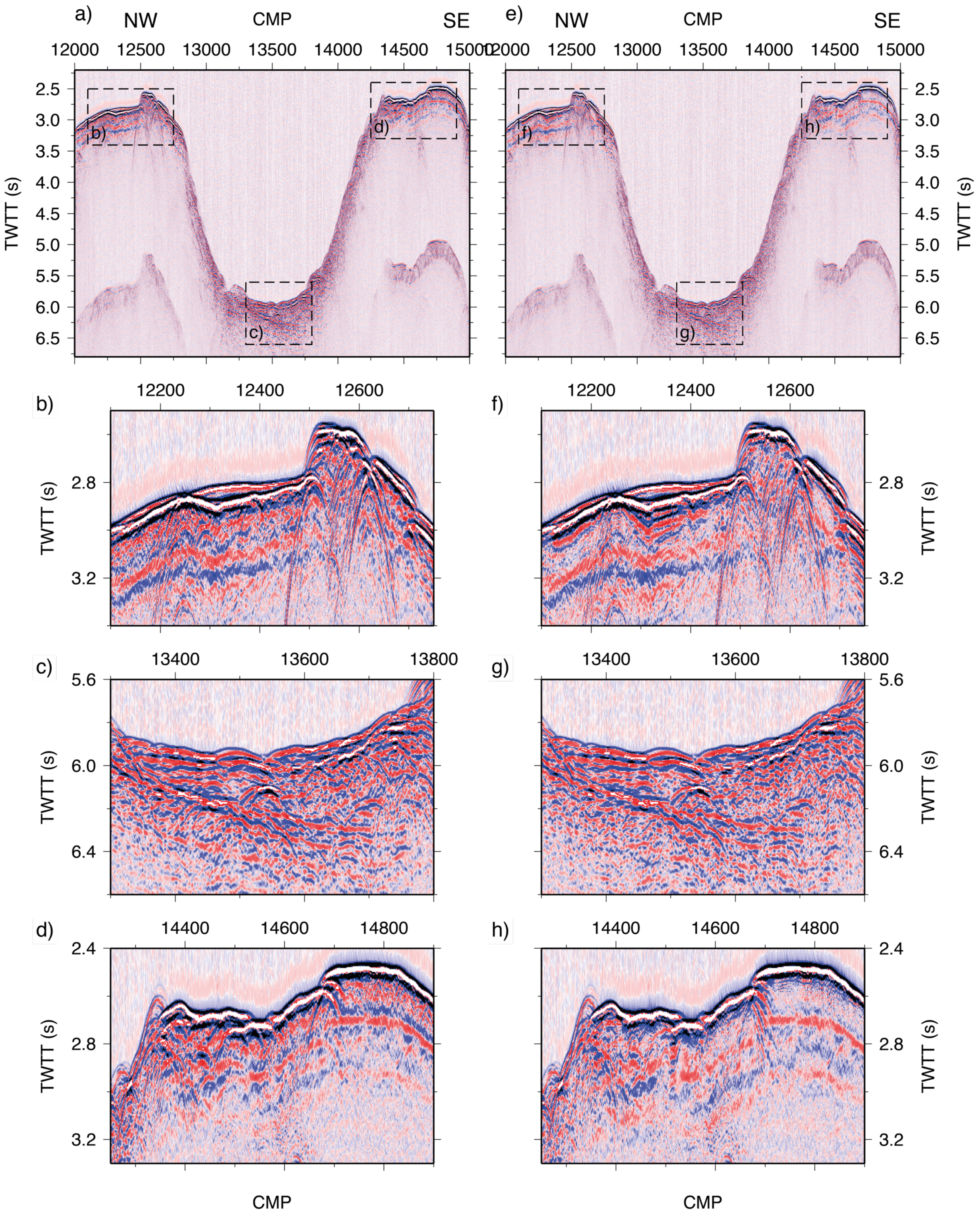

Figure 2.10: *Test panels showing the effects of deconvolution for LRSC seamounts and intra-seamount saddles. a) Velocity-analysis stacked section, plotted without migration or AGC. Dashed boxes show locations of zoomed regions in b-d). b) Summit of Osbourn seamount with strong 200 ms-lag reverberation located below the bright summit reflection. c) Intra-seamount saddle with sediment accumulations. No strong evidence for bubble pulse reverberation is present, which is likely a result of the abundance of sediment primary reflectors. d) Summit of Canopus seamount with bubble reverberation clearly visible between CMPs 14700-14800. e)-h) As for a)-d) following application of post-stack statistical Weiner deconvolution, with 60 ms gap and 300 ms operator length.*

the two signals being compared. The peak signal of the autocorrelation function for each stacked CMP trace is, therefore, centred at 0 ms. Where periodic signals are present in the traces, peaks are produced in the autocorrelation function at time lags from 0 ms where the signal peaks are present (Fig 2.11a). Coherent autocorrelation occurs when many adjacent traces all show peaks at the same time lag.

Calculation of autocorrelation functions was conducted at a number of locations along Profile C, where the stacked sections show evidence for bubble pulse reverberation. In some cases, for example between CMPs 6150-6200 on the middle forearc region (Fig. 2.11b), it was possible to identify a clear peak in the autocorrelation function at 200 ms. However, this was not always the case. In addition, where there did appear to be a clear autocorrelation peak at ~200 ms, the amplitude of the correlation was relatively low compared to that of the peak signal (Fig 2.12a). This observation is consistent with the pre-cruise source modelling, which indicated a high peak-to-bubble ratio, but may also indicate variation in the peak-to-bubble period, for example due to variable tow depth.

In an attempt to remove, or reduce, the effects of the bubble pulse, a simple post-stack statistical Weiner deconvolution method was tested. The design window was set to 10 s, encompassing the seabed along the entire profile. The deconvolution operator was designed following the principle of setting the gap length to be the time of the second zero-crossing following the peak of the autocorrelation function at 0 ms, and the operator length to encompass the first bubble pulse. A range of operators were iteratively tested with gaps of between 50-60 ms and lengths of 300-350 ms, which all appeared to produce results which were mostly visually indistinguishable. In some parts of the profile, these tests showed that this deconvolution method produced minor improvement (Figs 2.9d-f, 2.10e-h, 2.11c, 2.12b). However, the bubble pulse reverberation was not entirely removed.

Given that only limited geological interpretations will be made in areas of little-to-no sediment, where the bubble reverberation is most abundant, and that the primary reason for MCS data acquisition was to estimate the sediment layer thickness for WA data modelling, it was considered acceptable to apply this simple deconvolution process to provide some, but not total, improvement.

2.4. Results of MCS data processing

Profile C is ~750 km in length and has a bathymetric variation of ~6 km. Consequently,

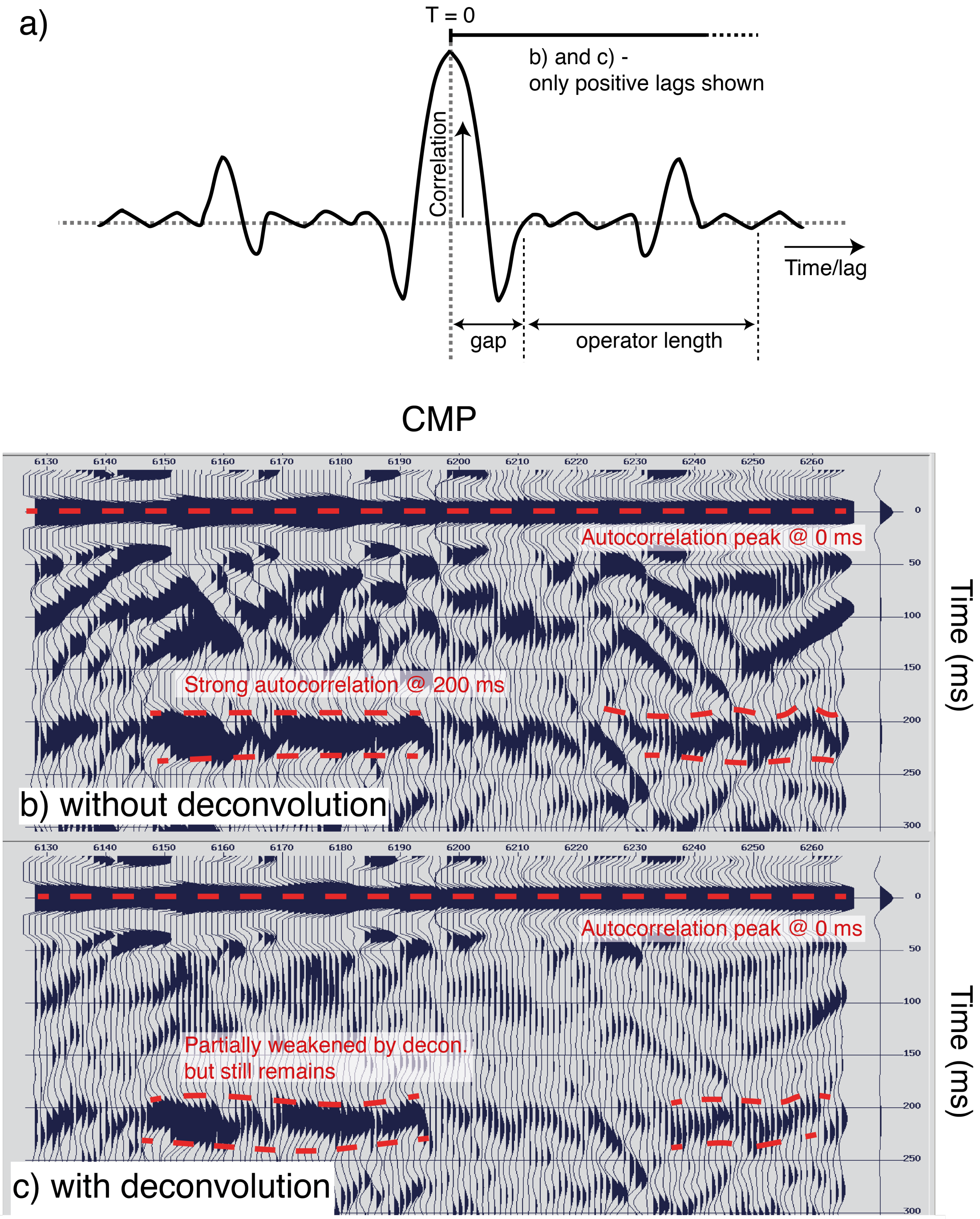

Figure 2.11: *Definition and calculation of autocorrelation functions. a) Sketch autocorrelation function showing symmetry about 0 ms, and definition of gap and operator length. b) Screenshot from Claritas autocorrelation function calculator for stacked CMP gathers 6130-6260, plotted without deconvolution, and c) following application of post-stack statistical Weiner deconvolution, with 60 ms gap and 300 ms operator length. Both panels are displayed only for positive lags and with same gain. A patch of relatively concordant autocorrelation peaks is present between CMPs 6150-6180, at ~200 ms. Following application of the deconvolution operator (c) these are weakened, but still remain.*

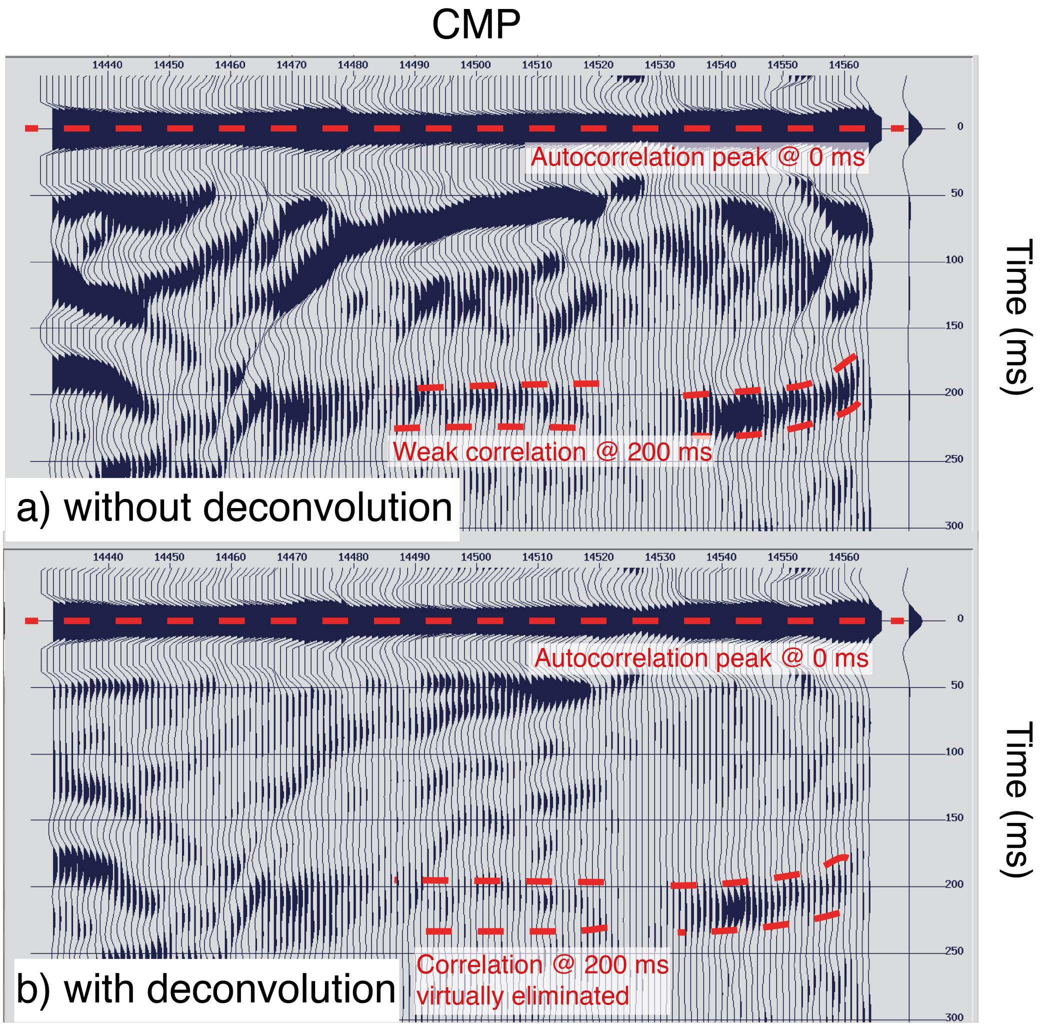

Figure 2.12: *Screenshots from Claritas autocorrelation function calculator for stacked CMP gathers 14430-14560, plotted a) without any deconvolution applied, and b) following application of post-stack statistical Weiner deconvolution, with 60 ms gap and 300 ms operator length. Both panels are displayed only for positive lags and with same gain. A low-amplitude autocorrelation is present between CMPs 14490-14520, at ~200 ms. This is almost entirely removed following application of the deconvolution filter (b). However, Fig 2.10e-g shows that the bubble pulse reverberation is not totally removed.*

it is challenging to display the entire profile at a scale dictated by this thesis, such that the its features are readily visible. Therefore, the profile has been divided based on tectonic region in Figures 2.13-2.19. A full interpretation of the key features of the final processed MCS section will be discussed in Chapter 5, together with the interpretation of the WA crustal velocity-depth model which will be developed Chapters 3 and 4. In addition, the crustal velocity-depth model will be used to restack the MCS data as part of its robustness testing (Section 4.6), which may enhance any reflectivity associated with sub-basement geological features. However, a preliminary description of the principal features of the stacked image developed in this chapter will now be provided to underpin its use to estimate the thickness of the sediment layer to be included as part of the WA seismic data modelling (Section 3.5.1), by defining the location of the top of the oceanic igneous basement.

Along parts of the profile, the sediment cover is very thin-to-negligible, and the crystalline basement is effectively the seabed. These areas are typically characterized by high slopes and when viewed without post-stack Kirchhoff time migration show strong diffraction hyperbolae. At the northwesternmost end of the profile, in the upper forearc region between ~10-50 km distance along profile (hereafter abbreviated to d.a.p.), the sedimentary sequences appear to comprise generally flat lying, planar, concordant reflectors, and the uppermost layers are offset by small trenchward-dipping normal faults (Fig. 2.13). The shallow water depth makes it challenging to define the basement with absolute confidence given the arrival time of the seabed multiple. A range of candidate basements are identified, and the wide-angle data modelling (Chapter 3) will be used to resolve which of these represents the true basement, and what the others may correspond to. However, generally the basement appears to increase in depth towards the trench, mirroring the bathymetry. Between ~12-18 km d.a.p. it is located at ~1.5 s TWTT, increasing to 2.5-3.4 s TWTT at ~50 km d.a.p. depending which of the candidate basement reflectors is selected. A large fault, or pair of antithetic faults, at ~50 km separate the flatter-lying sediments of the uppermost part of the upper forearc from those of the lower part of the upper forearc. Within this region, reflectors are less clearly defined, but appear to dip towards the trench. Normal faults progressively cut this part of the forearc, producing a downward-stepping pattern. The fault offsets here are larger, cutting deeper into the sediments, with may indicate increasing degrees of deformation towards the trenchward end of this part of the forearc.

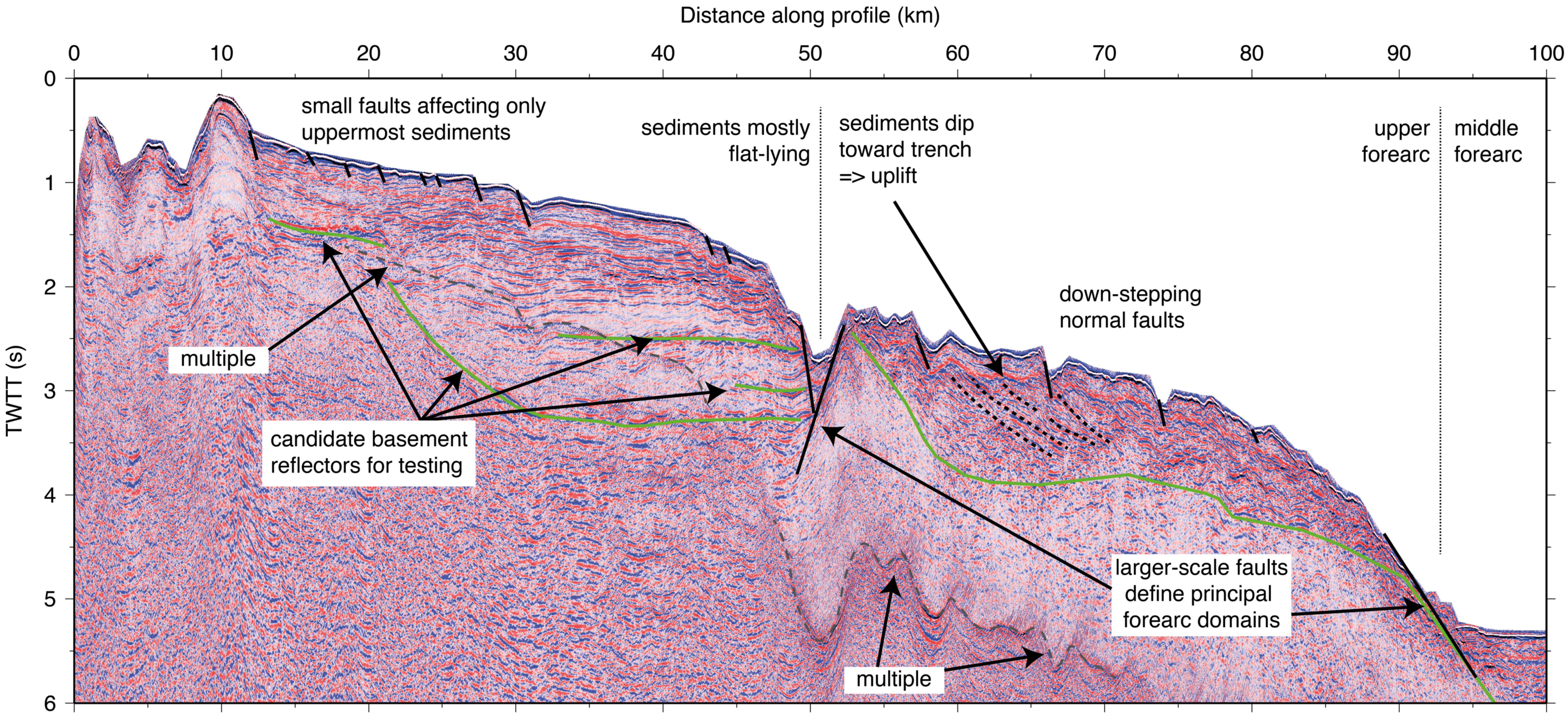

Figure 2.13: *Profile C MCS data for Tonga upper forearc region, stacked using velocity analysis-derived stacking velocity model. Displayed with post-stack time migration at 1500 ms^{-1}, seabed mute, and AGC with 2000 ms time gate. Dotted grey line indicates seabed multiple. Green line is chosen as the basement, for inclusion in the initial WA model to be constructed in Chapter 3. Black lines indicate faults. Principal features labelled are discussed within the text.*

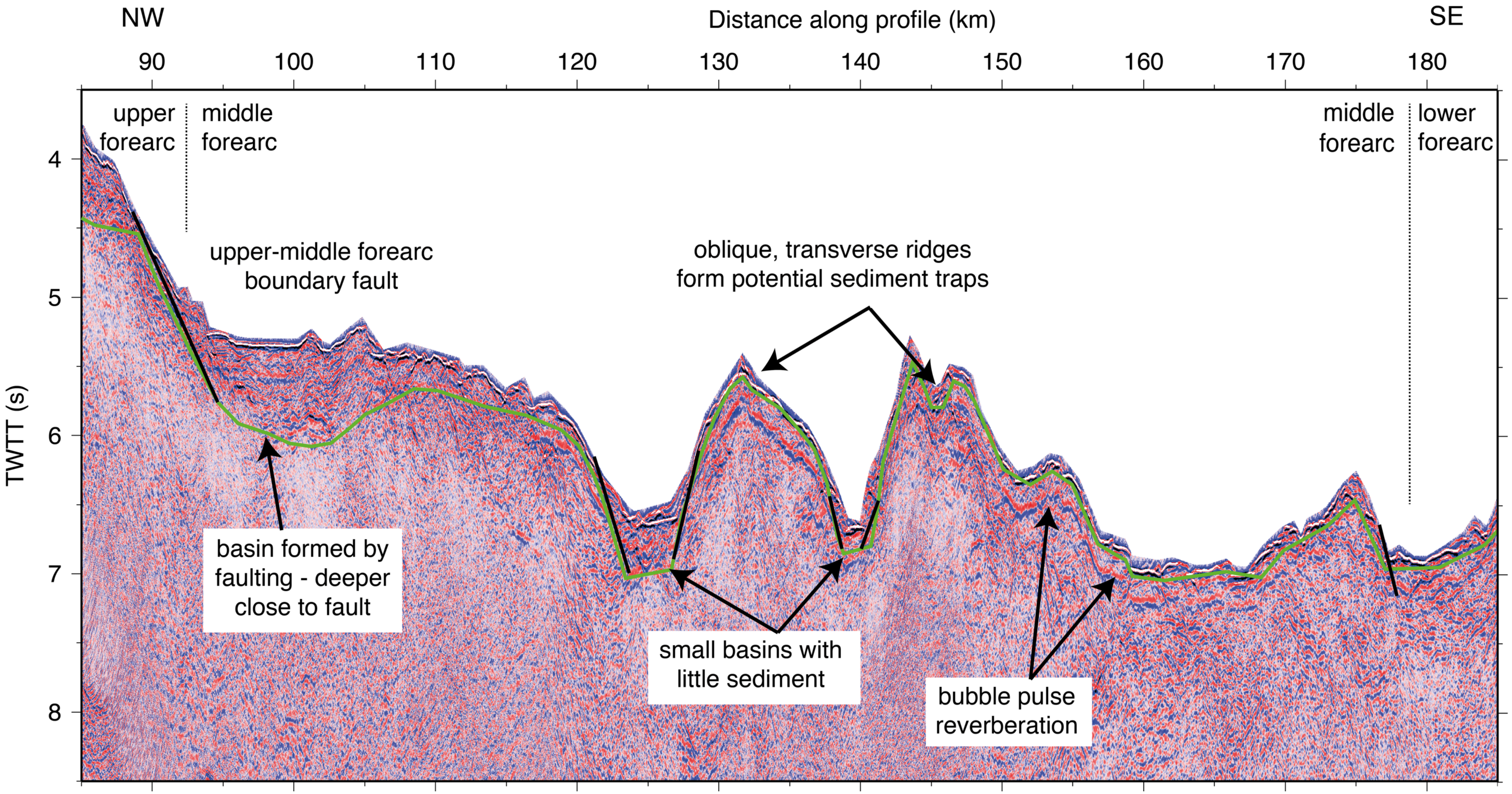

Figure 2.14: *Profile C MCS data for Tonga middle forearc region, stacked using velocity analysis-derived stacking velocity model. Plotted as for Fig. 2.13.*

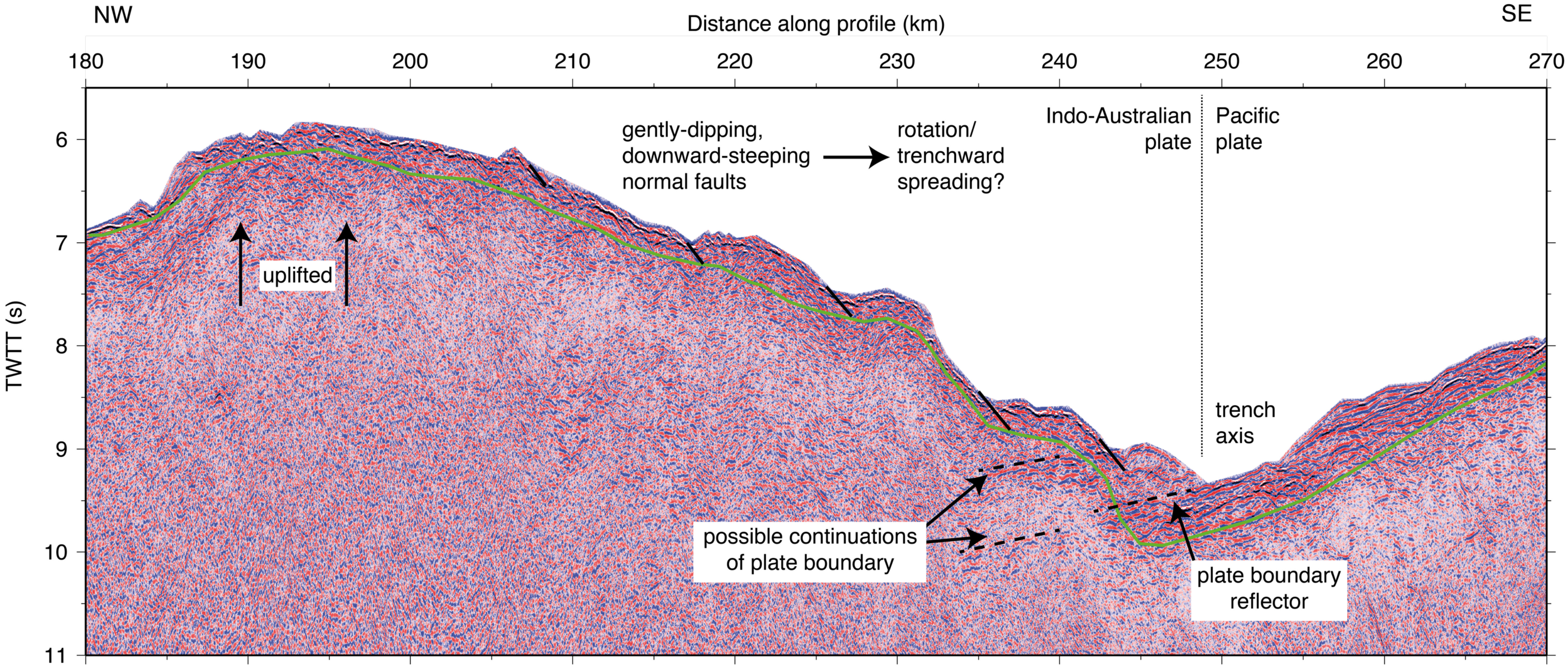

Figure 2.15: *Profile C MCS data for Tonga lower forearc and trench axis region, stacked using velocity analysis-derived stacking velocity model. Plotted as for Fig. 2.13.*

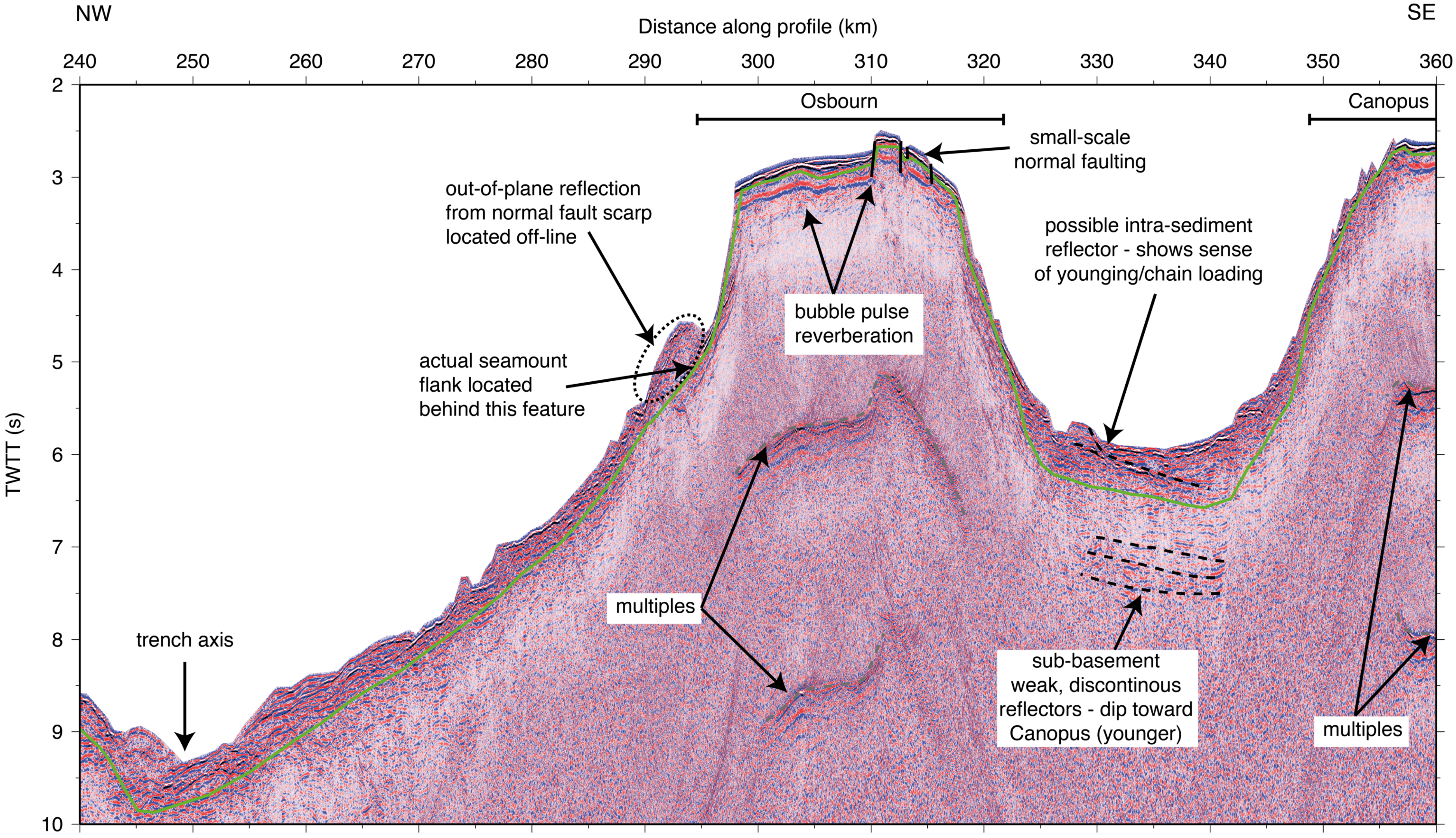

Figure 2.16: *Profile C MCS data for Osbourn seamount summit and flanking regions, stacked using velocity analysis-derived stacking velocity model. Plotted as for Fig. 2.13.*

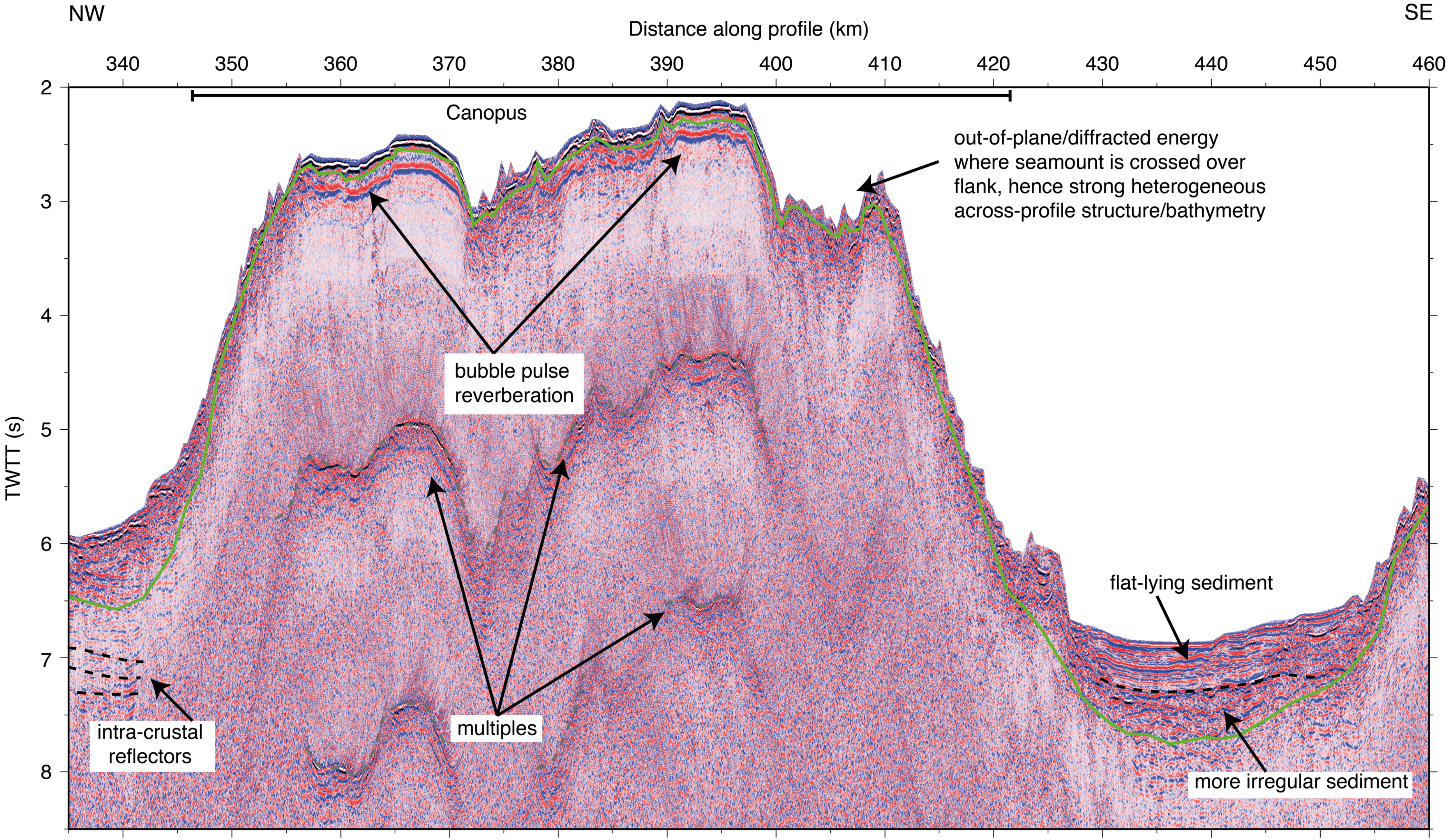

Figure 2.17: *Profile C MCS data for Canopus seamount, and intra-seamount basin immediately to the south, stacked using velocity analysis-derived stacking velocity model. Plotted as for Fig. 2.13.*

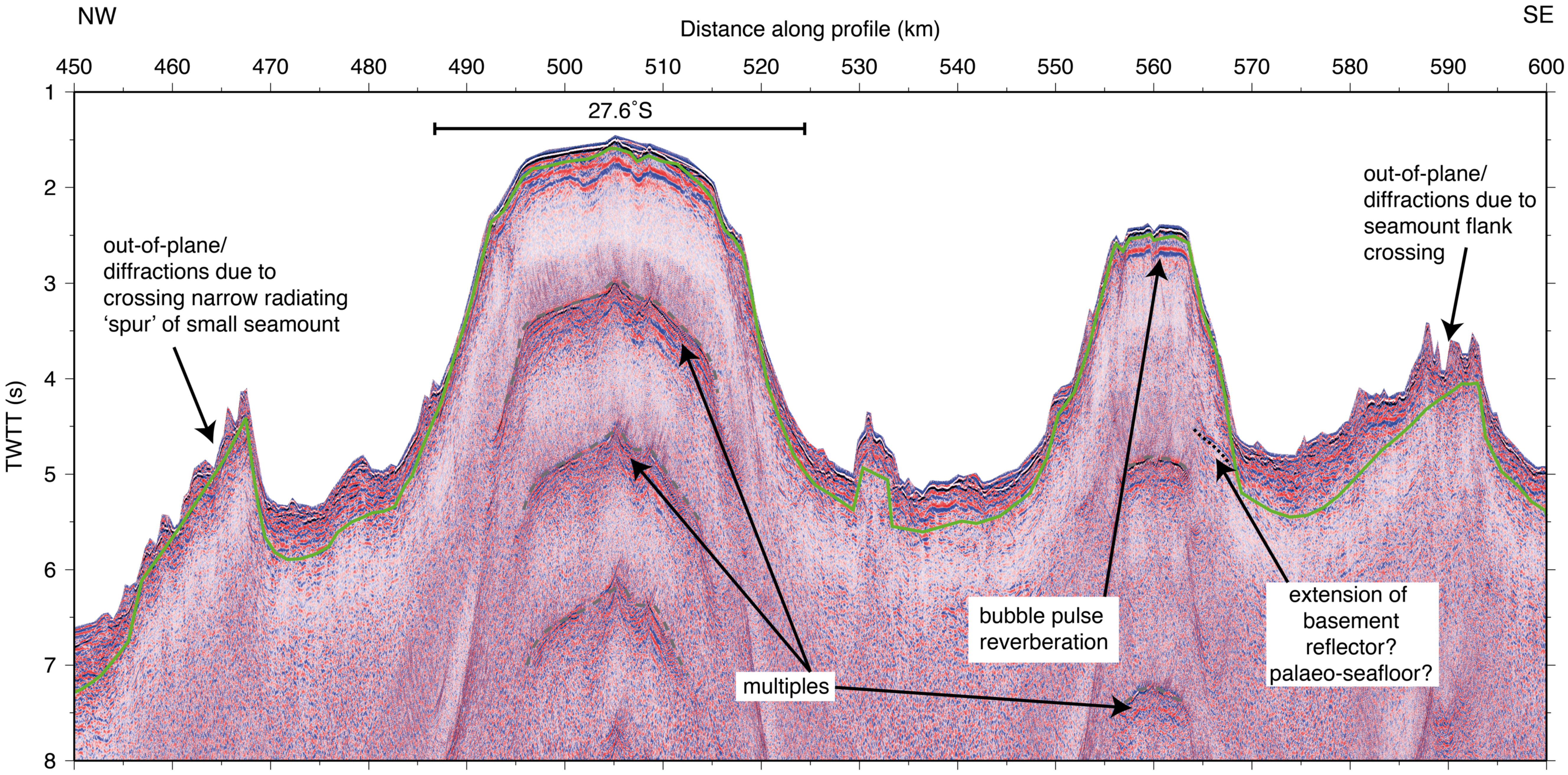

Figure 2.18: *Profile C MCS data for 27.6˚S seamount and adjacent region, stacked using velocity analysis-derived stacking velocity model. Plotted as for Fig. 2.13.*

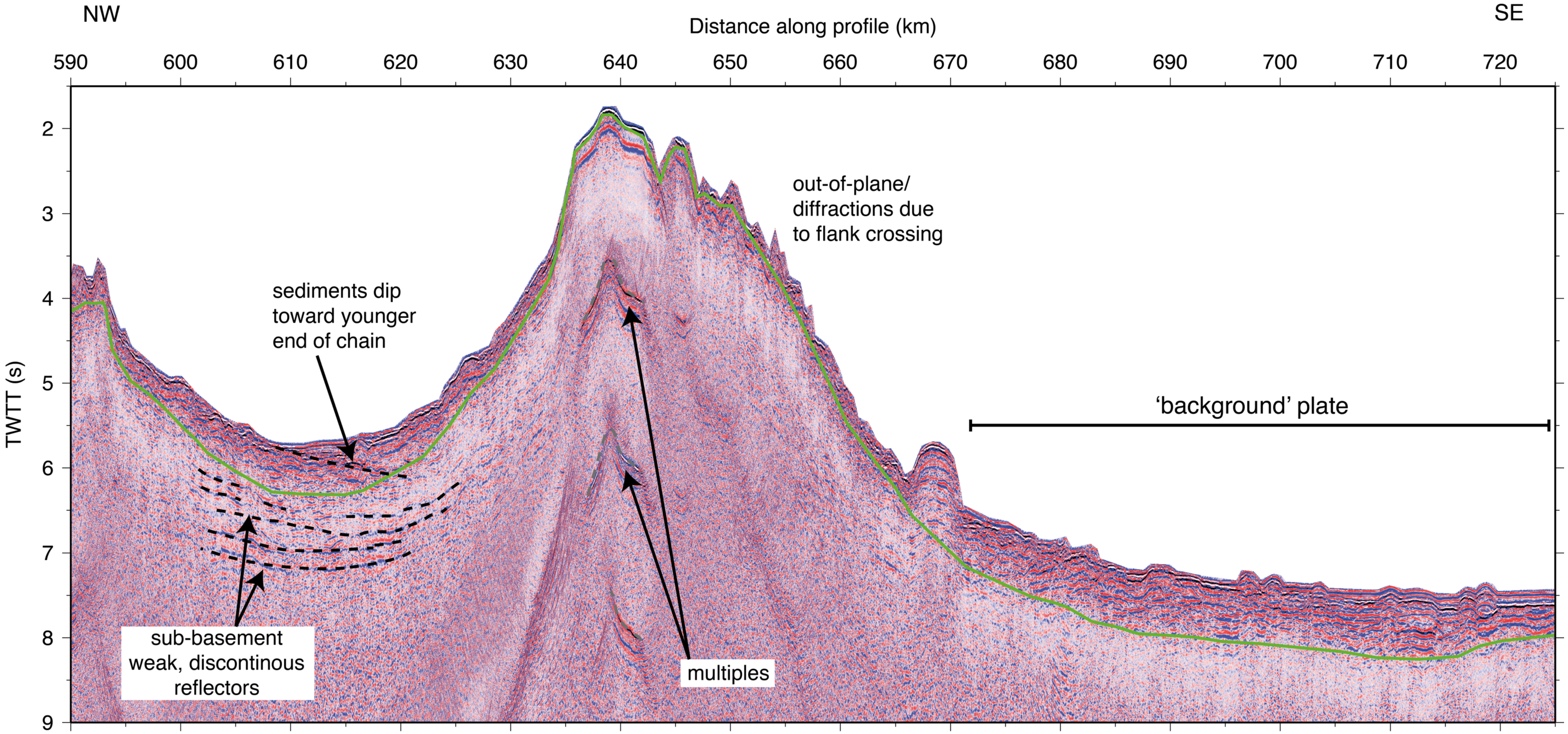

Figure 2.19: *Profile C MCS data for southernmost part of profile, including last sampled seamount (flank crossing) and 'background' Pacific plate, stacked using velocity analysis-derived stacking velocity model. Plotted as for Fig. 2.13.*

At ~90 km d.a.p., the seabed abruptly deepens from ~4.0 to ~5.4 s TWTT, across what appears to be a large-scale normal fault dividing the upper and middle forearc regions. The hanging wall of the fault contains a basin which is deepest (~0.8 s TWTT) close to the fault, which may indicate a component of block-rotation associated with movement on this fault, and the generation of accommodation space (Fig. 2.14). A series of 1 s TWTT-high ridges, which are oriented obliquely to the strike of the profile, and run through the middle forearc sub-parallel to the trench axis, forming small potential basins between them. As these basins show only very limited sediment accumulation (Fig. 2.15 – ~125 and ~140 km d.a.p.), this may indicate that these features are either relatively contemporary, or there is little erosion and transport of material into this region.

The lower forearc slope (Fig. 2.15) is uplifted at its upper, northwestern end. The seabed of this region is cut by a number of small, down-stepping normal faults, which show a shallow dip compared normal faults further up the forearc. Together, these observations of uplift and low-angle faults suggest possible rotation of the lowermost part of the forearc as its trenchward end is uplifted over incoming bathymetric features, and trenchward advance or spreading of this part of the slope as a result of weakening and/or collapse as bathymetric anomalies pass beneath and beyond this region. Adjacent to the trench axis, between 235-240 km d.a.p. and 9-10 s TWTT, there are a number of weak reflectors which may represent the continuation of the plate boundary at depth. The potential origin of these reflectors will be further investigated once the crustal velocity structure has been determined by wide-angle seismic data modelling, as this should provide additional constraint in determining the exact location and shape of the plate boundary in this region.

The seamounts of the LRSC (Figs 2.16-2.19) show very little sediment accumulated on their flanks, with the top of the basement effectively being the seafloor. Bright reflectors on the summits most likely represent the sedimentary caps sampled by ocean drilling (e.g. Koppers et al., 2013) which, alongside the guyot morphology, support the interpretation that the largest LRSC seamounts became emergent at some point during their history. Further to this, the relatively strong bubble pulse reverberations beneath the summits indicate that these caps may be relatively hard. The summit of Osbourn seamount appears to be cut by several small normal faults, which are most likely associated with the bending of the Pacific plate as it passes over the trench outer rise (Fig. 2.16). The trenchward flank of this seamount shows an out-of-plane feature which is seen in the MCS record section but not in the along-profile bathymetry. Comparison with the across-profile bathymetry suggests that this out-of-plate feature is likely to have arisen as a result of energy being reflected from the scarp of a normal fault which cuts the seamount flank to the west of the path of the profile.

Where the seamounts are crossed over their flanks, e.g. Canopus seamount, across its entire span, but particularly between 400-410 km d.a.p. (Fig. 2.17), and the small seamounts to the south of the bend (570-595 km d.a.p. – Fig. 2.18; 645-660 km d.a.p. – Fig. 2.19) there is significant scattering of energy from out-of-plane features, which maps back onto the 2D profile. Post-stack Kirchhoff time migration provides only a limited improvement to the stacked image in these regions, and the seabed mute must be defined by the bathymetry along-profile. Consequently, it is unfeasible to identify any primary reflector events in these areas. However, since they are correlated with relatively steep and, hence, un-sedimented seamount flanks, the basement can be taken to be located at the seabed.

The sediment accumulations in the saddles between seamounts (325-340 km d.a.p. – Fig. 2.16; 430-450 km d.a.p. – Fig. 2.17; 525-545 km and 570-580 km d.a.p. – Fig. 2.18; and 600-620 km d.a.p. – Fig. 2.19) occasionally show dipping features which reflect the sense of loading of the Pacific plate by the LRSC. These reflectors always appear to dip towards the younger (southeastern) end of the chain. This makes sense from a loading perspective, as it suggests that once a seamount has formed and the next youngest volcano in the chain begins to form, the latter applies a load on the plate focused in the plate motion direction away from the previous seamount (Wessel et al., 2014).

There is also some evidence for sub-basement, discontinuous intra-crustal reflections visible between 330-345 km and 600-625 km d.a.p. (Figs 2.16 and 2.19). It is likely that these events indicate that there is not massive basalt present in these locations, and that they may be related to volcanic, rather than magmatic, crustal thickening. These features will be investigated further as part of the WA seismic velocity-depth model interpretation (Chapter 5), since their P-wave velocity may help to indicate their likely origin.

The background Pacific plate shows sediment accumulations of ~0.7 s TWTT in thickness (Fig. 2.19). Assuming a velocity of 2-3 km s^{-1}, this corresponds to thicknesses of up to 1 km, which is large compared to the typical sediment cover on the Pacific plate of ~200 m (e.g. Funnell et al., 2014). It is likely that the thicker accumulation here arises as a result of the proximity to the seamount chain, which provides a loading force on the plate generating a flexural moat. The loading effect on the crust will be considered further in a later chapter.

2.5. Summary

In this chapter the processing steps which have been applied to the Profile C MCS dataset have been described. In Sections 2.3.3-2.3.5, a standard, simple reflection processing procedure was followed, progressively developing the stacking velocity model. However, inspection of the stacked sections revealed the presence of data artefacts, which required suppression or removal. These artefacts arise as a result of:

- the challenging environment in which the acquisition was conducted, with shallow water depths and heterogeneous across-profile bathymetry leading to the recording of steeply-dipping events on far-offset channels in the northwesternmost part of the profile; and
- the need to mitigate the effects of contemporaneously acquiring MCS and WA seismic data, which resulted in a source array design with a strong low-frequency component. The side effect of using large chambered airguns is that a strong, reverberative bubble pulse is generated, despite pre-acquisition array output modelling having been performed in an attempt to minimize this.

These artefacts were removed by applying far-offset channel muting within the CMP gathers (Section 2.3.6) and post-stack Weiner deconvolution (Section 2.3.7), to produce the final record section. The features of the final section were described in brief in Section 2.4.

The results of the processing described in this chapter will now be applied in two principal ways. The first, which will follow in the next chapter, will be to provide an initial basis for the modelling of the WA seismic dataset, which will use the location of the top of the oceanic basement to initially define this interface in the initial WA velocity-depth model. This sediment layer will then be tested by modelling corresponding WA arrival travel times. Secondly, the WA-derived velocity-depth model will be used to restack the MCS data in Chapter 4, which may provide additional insight into the origin of some of the preliminarily identified intra-crustal reflection features, particularly those in the vicinity of the plate boundary, and the intra-crustal reflections observed beneath the sediment-filled saddles between seamounts. By correlating the locations of these reflection events with the WA seismic velocity-depth model, it may be possible to reach an improved understanding of their nature and/or origin. This comparison will be conducted as part of the full profile description and interpretation, using all available datasets, which will be presented in Chapter 5.

Chapter 3 – Wide-Angle Seismic Data – Acquisition and Forward Modelling

3.1. Introduction

In this chapter, the acquisition of the wide-angle (WA) seismic dataset, which was conducted concurrently with the MCS data acquisition along Profile C, will be described. The focus of this chapter will be the development, using this dataset and some initial constraints from other data sources, of a best-fitting velocity-depth crustal structure model of the LRSC, and adjacent forearc region.

First, the acquisition and general characteristics of the dataset will be reviewed. The mechanism by which the travel times, recorded by an array of ocean-bottom seismographs (OBSs), are used to develop the best-fitting crustal-structure velocity-depth model, hereafter referred to as the *forward model,* will be described, including how the initial model was constructed and constrained. Forward ray-trace modelling was undertaken using the *RAYINVR* code (Zelt and Smith, 1992), adopting an iterative approach starting at the top of the model and working downwards and laterally. A number of modelling issues were encountered in accommodating the acquisition geometry. How these problems were overcome, and how the model was evolved to account for the tectonic setting will be described in Section 3.5.

Finally, an outline description of the *forward model* will be discussed. However, this model requires robustness and sensitivity testing before final conclusions can be drawn. This process will be described in Chapter 4. Primarily, this further testing will be tailored to appraise and determine the resolution of key features of the *forward model*, and then test it for uniqueness using the free-air gravity anomaly. The final *forward model* will be described and discussed in Chapter 5, in the context of all other WA seismic profiles from the SO215 and *TOTAL* projects, and the results set in a regional context in Chapter 6.

3.2. WA seismic dataset acquisition

The deployed ocean-bottom seismograph array consisted of 58 instruments; 46 of the "LC" type provided by the NERC Ocean-Bottom Instrumentation Facility (Minshull et al., 2005) and 12 of the KUM 8000m type, provided by IFM-GEOMAR, suitable for use in deep water. The latter group were deployed in the trench-proximal region.

Each instrument was fitted with a hydrophone and three-component geophone package. Data were recorded at sampling rates of 250 Hz (4 ms) and 200 Hz (5 ms) for the OBIF and IFM-GEOMAR instruments respectively, and with a trace length of 60 s for both.

Prior to deployment, instruments were synchronised to UTC (Co-ordinated Universal Time). Following instrument recovery, a further time tie was performed, which allowed correction for clock drift. Data were then converted from the raw format recorded by the instruments, into a single SEG-Y format file for each instrument, during which the shot-receiver geometry was applied. The UTC time and location of each shot was logged throughout acquisition using a Zypher GPS clock and Verif-I logger.

The airgun array and firing parameters for the WA seismic survey along Profile C are identical to those for the MCS survey as described in Chapter 2, as these datasets were acquired concurrently. In particular, the shot interval of 60 s was selected to prevent wrap-around of the water-wave direct arrival into the trace recording the following shot, over the range of offsets where the primary sub-seabed turning arrivals were expected.

3.3. WA arrival picking strategy

For travel time picking, each OBS SEG-Y record section was converted to z-format for input to *zplot* – a semi-automated travel time picking tool, that has a graphical user interface that enables the variation of display parameters, such as filtering and scaling, to underpin pick quality control. For each trace, the point at which an arrival was picked was determined by the first onset of energy; that is, the first excursion from zero. The hydrophone channel was picked by preference, as this has the highest frequency range and, hence, should have the highest resolution record, in the absence of background environmental noise, when compared to any of the geophone channels. Where picking on the hydrophone channel was not possible, or to check arrival assignments in particularly noisy regions, the vertical geophone channel was used as an alternative. Ultimately, no travel time picks from vertical geophone data needed to be used in this study, as the only instrument with an unusable hydrophone record also displayed an unusable vertical geophone record, due to hardware failure.

Whenever possible, arrival identifications and travel time picks were made using unfiltered data. Filtering causes modification of the wavelet and, hence, position of the first-arrival onset in time. In practise, significant low-frequency water column noise makes this impractical, in particular when picking long offset, refracted arrivals, where the low-frequency water column noise swamps the signal. In reality, picks were made having compared filtered and unfiltered data, that had had minimum-phase, with a low cut of 1-2 Hz, Butterworth high-pass filtering applied, that effectively removed this noise without significantly affecting the onset of the first-arrival, within the picking errors.

Picks were assigned to one of a number of phase type categories, which would be used to determine the statistical fit of the modelled to observed arrivals. The phase category definitions were as follows:

1) P_w – water wave direct arrival;
2) P_{wm} – water wave first multiple;
3) $P_{s,l}$ – sediment refracted arrivals towards the left (northwest) of the model (negative relative to instrument);
4) $P_{s,r}$ – sediment refracted arrivals towards the right (southeast) of the model (positive relative to instrument);
5) $P_{g,l}$ – crustal refracted arrivals towards the left of the model;
6) $P_{g,r}$ – crustal refracted arrivals towards the right of the model;
7) P_mP – reflections from the Moho; and
8) P_n – mantle refracted arrivals.

During the picking process, two additional phase categories were defined as spares, to be used as necessary for additional arrival types if these were observed, and during the phase assignment testing process. The latter were not used in the final modelling.

Each travel time pick was assigned an uncertainty, or error, that accounts for the ability to pick the first onset, and any uncertainties which may arise as a result of instrument location (or relocation). The assigned uncertainties for the travel time picks modelling in this study were defined as:

- P_w – 30 ms;
- $P_{s,l}$ and $P_{s,r}$ – 40 ms;
- $P_{g,l}$ and $P_{g,r}$ – 70 ms; and
- P_mP and P_n – 100 ms.

However, for the OBSs located closest to the trench (C38-C43) an additional error was added to the P_g, P_mP and P_n arrival picks, such that these had the assigned values 100 ms, 120 ms, and 120 ms respectively, due to the poorer signal-to-noise ratio (SNR). In addition, OBSs located close to the bend in Profile C would require the addition of further travel time pick error to P_g and P_n arrivals. The rationale for, and application of the additional uncertainty will be discussed in Section 3.5.2.

P_mP arrivals are particularly useful in defining the transition between P_g and P_n arrival branches since, by definition, the three phases should meet at a triplication point. It should be noted here though, that P_mP arrivals were not always readily observed in the dataset, particularly as the alternative slope break technique was hampered by the significant bathymetric variability along the profile. Phase assignment will be discussed in a following section, using example OBS record sections from each of the primary tectonic domains along the profile.

3.4. WA seismic dataset characteristics

Of the 58 instruments deployed along Profile C, 52 were used for travel time modelling. The excluded instruments were:

- C10, C16, C39 and C42, which were not recovered;
- C23, which displays a very low signal-to-noise ratio on all channels, which was most likely related to a fault with the cabling connecting the sensors to the data logger; and
- C31, which drifted significantly off-profile during deployment, and cannot be reliably relocated without the incursion of large additional errors due to the significant differences in seabed topography.

The OBS which successfully recorded data can be divided into subgroups along-profile, based on tectonic setting. Each setting has a difference influence on the noise characteristics, topography, and sub-surface geological and structural complexity, which all affected the offset ranges to which arrivals could be identified.

Instruments C1-C38 are located on the subducting ‘background’ Pacific plate and, with the exception of C35-C38, were all LC-type instruments. Instruments C35-C46 were of the KUM-type, and straddled the plate boundary/trench, with C35-C38 located on the Pacific plate and C39-C46 on the Indo-Australian plate. Instruments

C47-C58 were LC-type instruments located on the overriding plate. Figure 3.1 shows the OBS locations along each of the two segments of the profile, in geographic context (part a), and where the two segments have been projected into the modelling space (parts b and c).

The characteristics of the OBS records along-profile will now be reviewed, taking into account the different settings in which instruments are located, and how this appears to impact on the data they record. This description will be ordered from the least bathymetrically and/or structurally complex regions, and progress to the more challenging environments, beginning at the southeasternmost end of the profile on the Pacific plate adjacent to the LRSC, before moving northwestwards toward the trench. The discussion will then focus on the northwestern end of the profile, and progress across the forearc slope, and conclude with the trench region. Descriptions of the dataset characteristics in this section will be supplemented by example OBS record section plots, where an example for each setting has an enlarged inset that shows the further-offset arrival phases, with the remaining OBS record sections provided in Appendix A.

3.4.1. Pacific plate

The OBSs located on the subducting Pacific plate are numbered from northwest to southeast, beginning at C38, which is located closest to the Tonga Trench, and ending with C19, located just to the north of the bend in the profile coincident with the summit of 27.6˚S seamount. The instrument numbering then returns to C1, before increasing to C18 at the southeasternmost end of the profile. These instruments are located in a wide range of bathymetric settings, with significant lateral variability both along- and across-profile. Changes in bathymetry of 3-4 km occur over relatively short length scales, of the order of ~ 50 km. The bathymetric settings include:

- on the summits of seamounts (e.g. C1, C27, C29, C34);
- on the seamount flanks (e.g. C2, C5-8, C11-C13, C19-C21, C30, C33, C35);
- in the saddles between seamounts (e.g. C9, C22-C25, C31-C32); and
- on the 'background' oceanic crust of the Pacific plate to the south of the LRSC, which is relatively unaffected by volcanism (e.g. C14-C18).

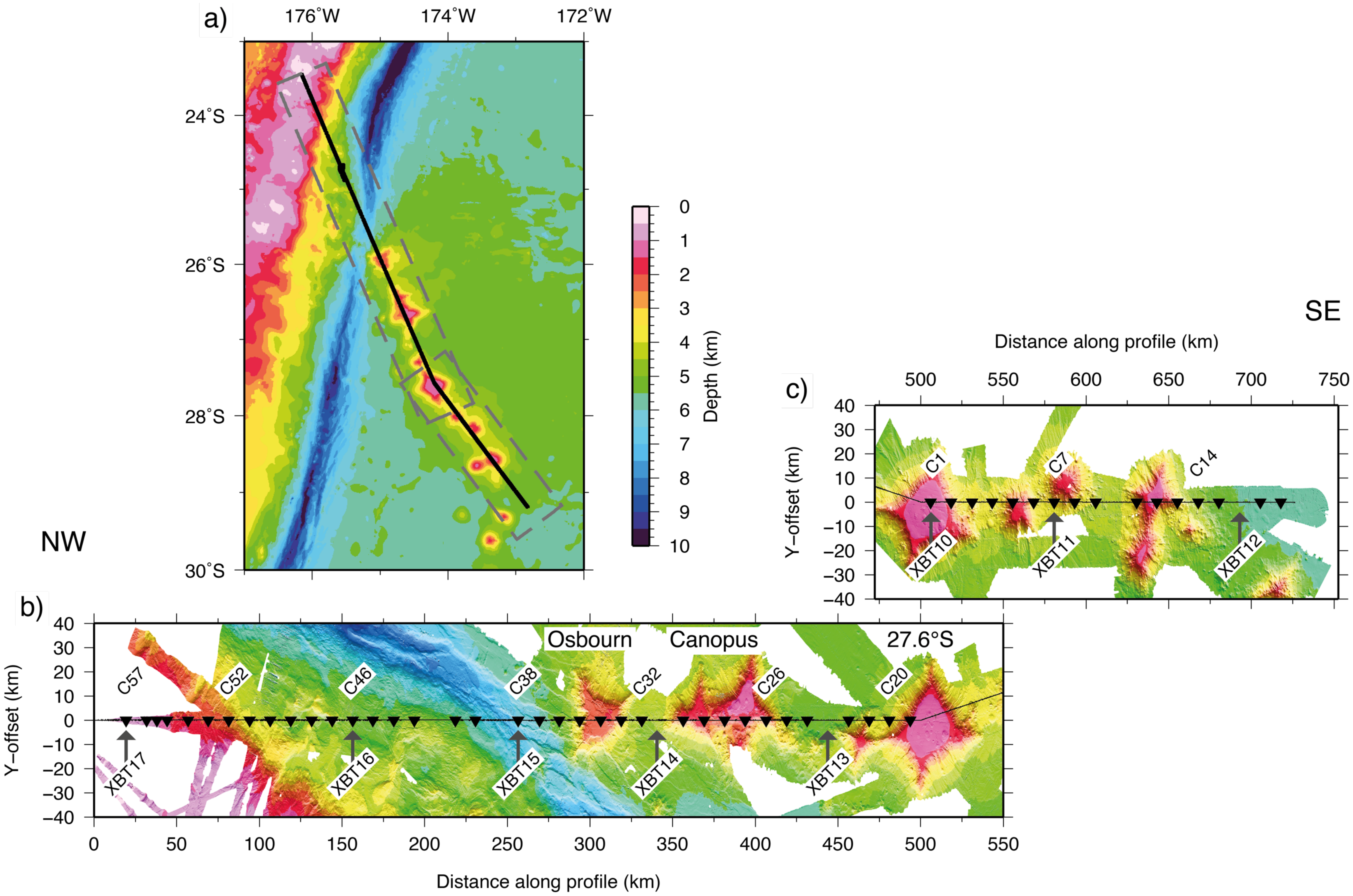

Figure 3.1: *Profile C OBS locations. a) Regional bathymetry of the SO215 study area. Profile C is marked as a black line. Dashed grey boxes are the areas covered by b) and c). b) Bathymetry along the northwestern part of Profile C (solid black line). c) As for b), but for southern part of Profile C. b) and c) are offset such that the bend in the profile is aligned. Inverted triangles are OBS locations, plotted only where they are included in the modelling. XBT locations shown with grey arrows. All XBT and only selected OBS locations are labelled for clarity and brevity.*

3.4.1.1. Background oceanic crust – OBSs C14-C18

As noted above, only instruments C17 and C18 truly lie on the Pacific plate away from the LRSC (Fig. 3.2). As one of the few locations of relatively flat seafloor, this region represents what is most likely the simplest tectonic environment along the profile. Based on their record characteristics, OBSs C14 and C15 may also warrant consideration for inclusion in this grouping, as they appear to share general trends. An example OBS record section from this region, C17, is shown in Figure 3.3.

It is only possible to pick P_s arrivals over short offsets (< 9 km) from each OBS, as a result of the limited sediment accumulation (~0.7 s TWTT) on the Pacific plate, despite its age. P_g first-arrivals tend to extend to only approximately ±30-40 km from each instrument. P_mP arrivals are also identified, also typically over relatively short offset ranges of <10-15 km. P_n arrivals are observed at shot-receiver offsets of up to 100 km, and thus for ~60 km as first-arrivals.

3.4.3.2. Seamount chain – OBSs C14-C35

A significant contributing factor to the appearance of the OBS records along Profile C is the large along-profile bathymetric variation (Fig. 3.4). These are particularly

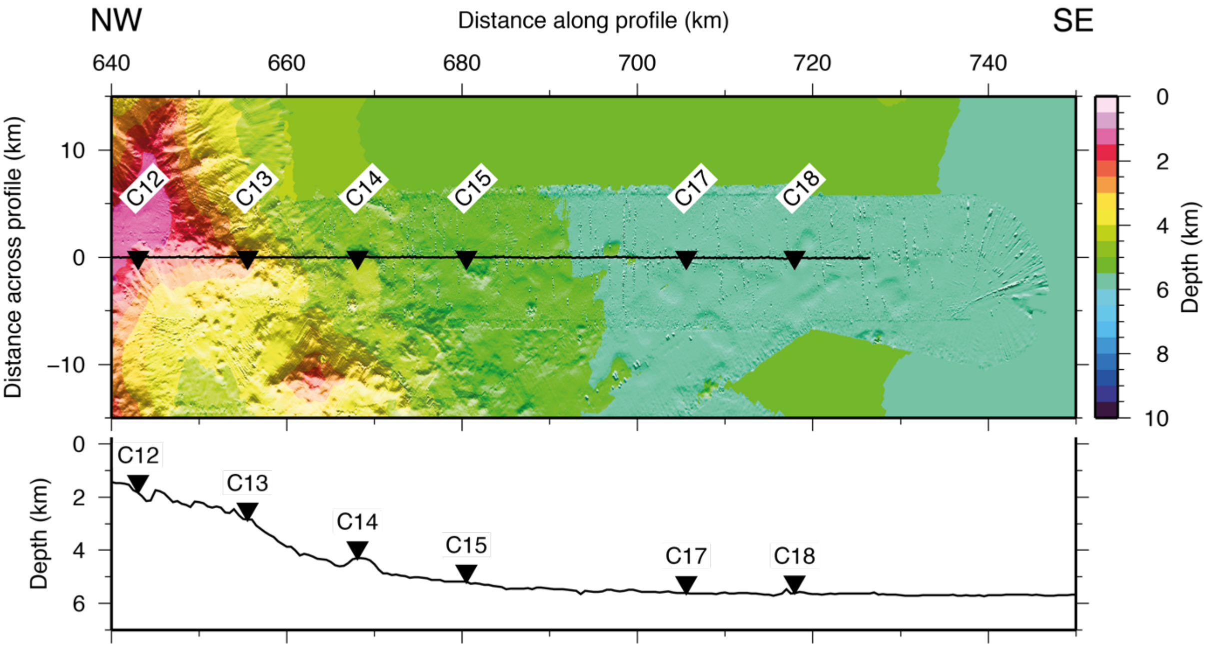

Figure 3.2: *Combined swath-satellite bathymetry for 'background' Pacific plate, adjacent to the LRSC, gridded at 50m, and illuminated only in regions of swath coverage. Relocated OBSs are indicated by inverted black triangles, with instrument numbers labelled. Black line indicates the trend of Profile C.*

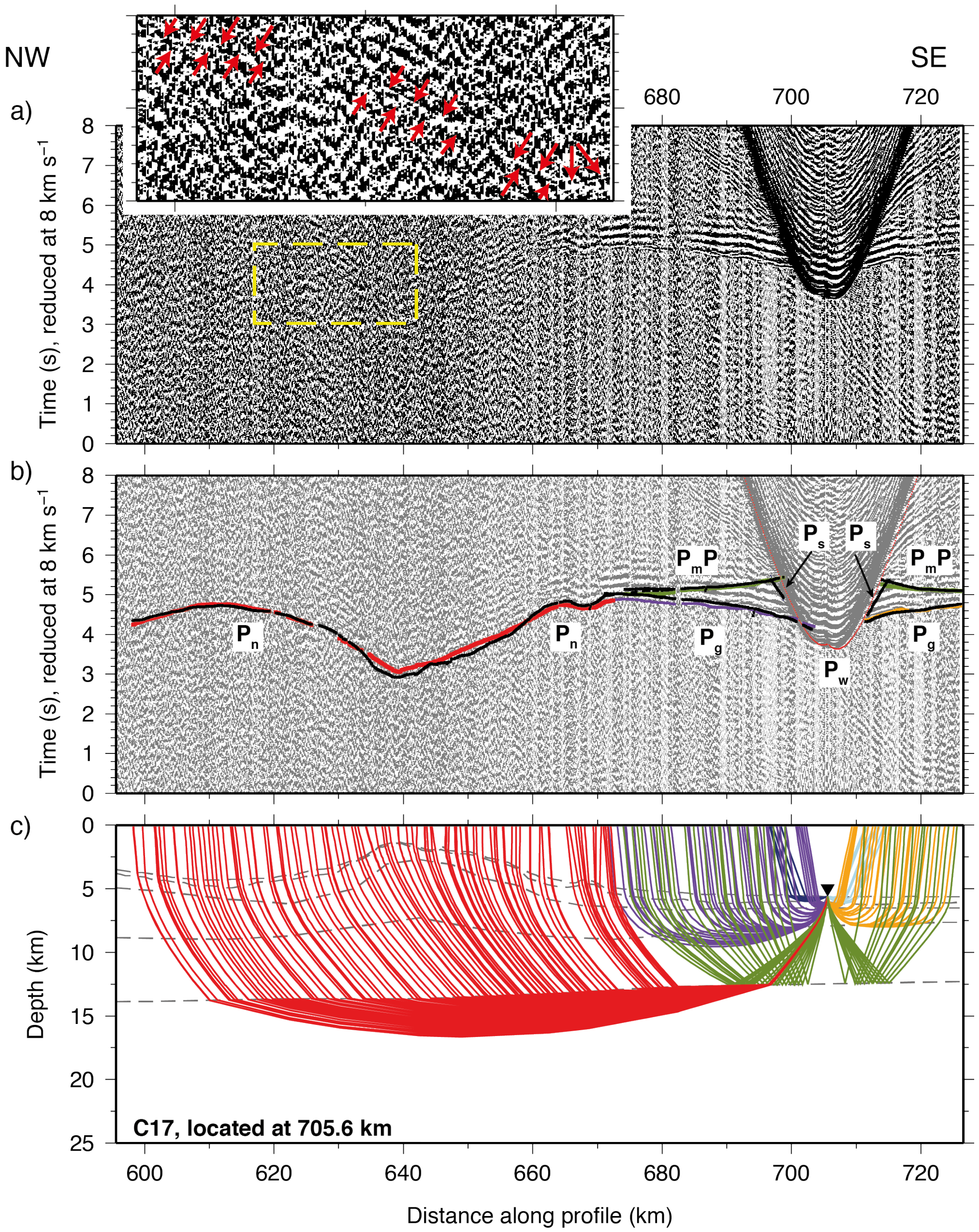

Figure 3.3: *WA seismic data from OBS C17 hydrophone channel, located at 705.6 km d.a.p., on the background Pacific plate (see Fig. 3.2). a) OBS record section, displayed using a minimum-phase Butterworth band-pass filter (2-3-20-30 Hz), trace normalized amplitudes, and reduced at 8.0 km s^{-1}. Inset: Zoom-in of far-offset arrivals in region indicated by dashed yellow box. Arrows show the location of the arrival branch, with colours corresponding to the phase type listed in b). b) OBS record section plotted as in a), with picked phases annotated as coloured bars (dark blue and light blue – P_s; purple and orange – P_g; green – P_mP; red – P_n). Coloured bar length corresponds to pick uncertainty. Black lines show the modelled travel times. c) Calculated rays traced through the best-fit forward model, where the ray colours match picked phase sets in b). Forward modelling layer boundaries plotted as grey dashed lines. Black inverted triangle indicates OBS location on model.*

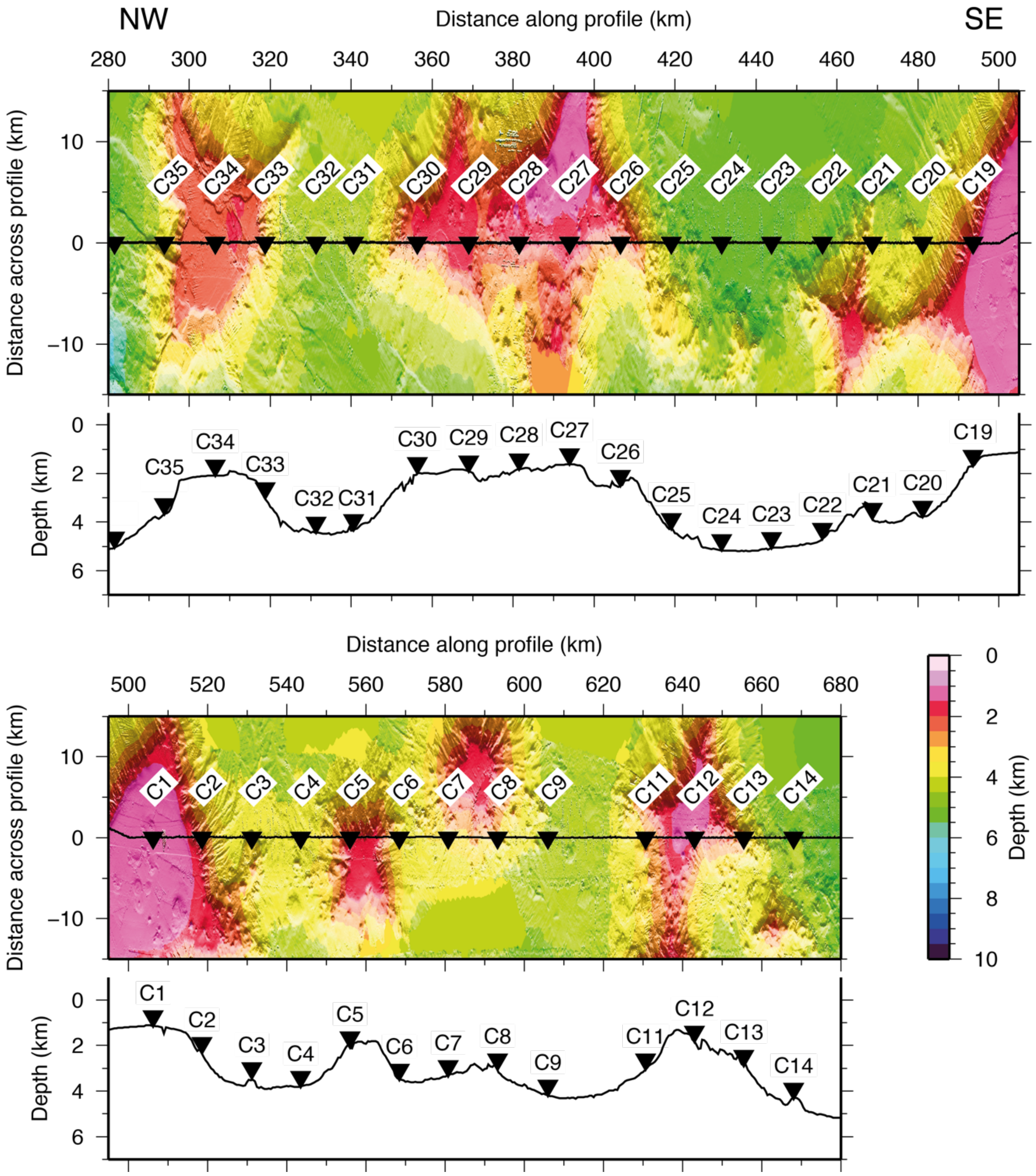

Figure 3.4: Combined swath-satellite bathymetry for the LRSC along Profile C, a) between Tonga-Kermadec trench and 27.6˚S seamount, and b) 27.6˚S seamount and south. Gridded at 50m, and illuminated only in regions of swath coverage. Relocated OBSs indicated as inverted black triangles, with instrument numbers labelled. Black line along y=0 indicates path of Profile C.

apparent on the Pacific plate between the seamounts and the saddles between seamounts, where there may be a 3-4 km difference in depth over relatively short (20-30 km) along-profile distances. In parts of the OBS records the variation in arrival travel time mirrors these variations, making phase assignment based on apparent velocity alone effectively impossible (Fig. 3.5 – 490-520 km d.a.p.). Generally, record sections from this part of the profile display relatively low SNRs, which most likely is a result of the significant bathymetric variability, and the resulting strong water column currents passing over this seabed topography.

P_s arrivals occur rarely along this part of the profile, as a result of the seamount slopes which discourage sediment from accumulating. Hence, where these phases are observed, it is by instruments located either on seamount summits, or in the saddles between seamounts. P_g arrivals are observed to broadly similar maximum offsets to those for the OBSs located on the 'background' Pacific plate, being in the range ±30-50 km. In some cases, for example OBS C20 (Fig. 3.6), P_n arrivals are also observed to ~100 km offset, similar to OBSs C14-18, although 70-80 km is more typical. On the whole, for instruments located between 300-650 km d.a.p., there does not appear to be a significant variability in the maximum offsets to which arrivals can be identified, nor does there appear to be a significant difference in the character of record sections between those for OBSs located on seamount summits or those located in the saddles in between. However, as the proximity of instruments to the trench increases, the maximum offsets to which P_g and P_n arrivals can be identified reduces to <30 km and ~45 km respectively (Fig. 3.7 – OBS C33), indicating that the water depth and geological complexity associated with the trench setting affects the ability to identify refracted arrival phases in this region.

3.4.2. Overriding plate

Eighteen instruments, numbered between C40-C58, were deployed on the overriding Indo-Australian plate. OBSs C47-58 are LC-type instruments, and C40-C46 were of the KUM-type. This latter, trenchmost subset will be discussed in detail as part of the trench-transition grouping in a following section.

3.4.2.1. Upper forearc – OBSs C52-C58

The OBSs located on the upper forearc, C52-C58, are situated on gently sloping bathymetry (Fig. 3.8). Water depth increases from <1 km at the northwesternmost end

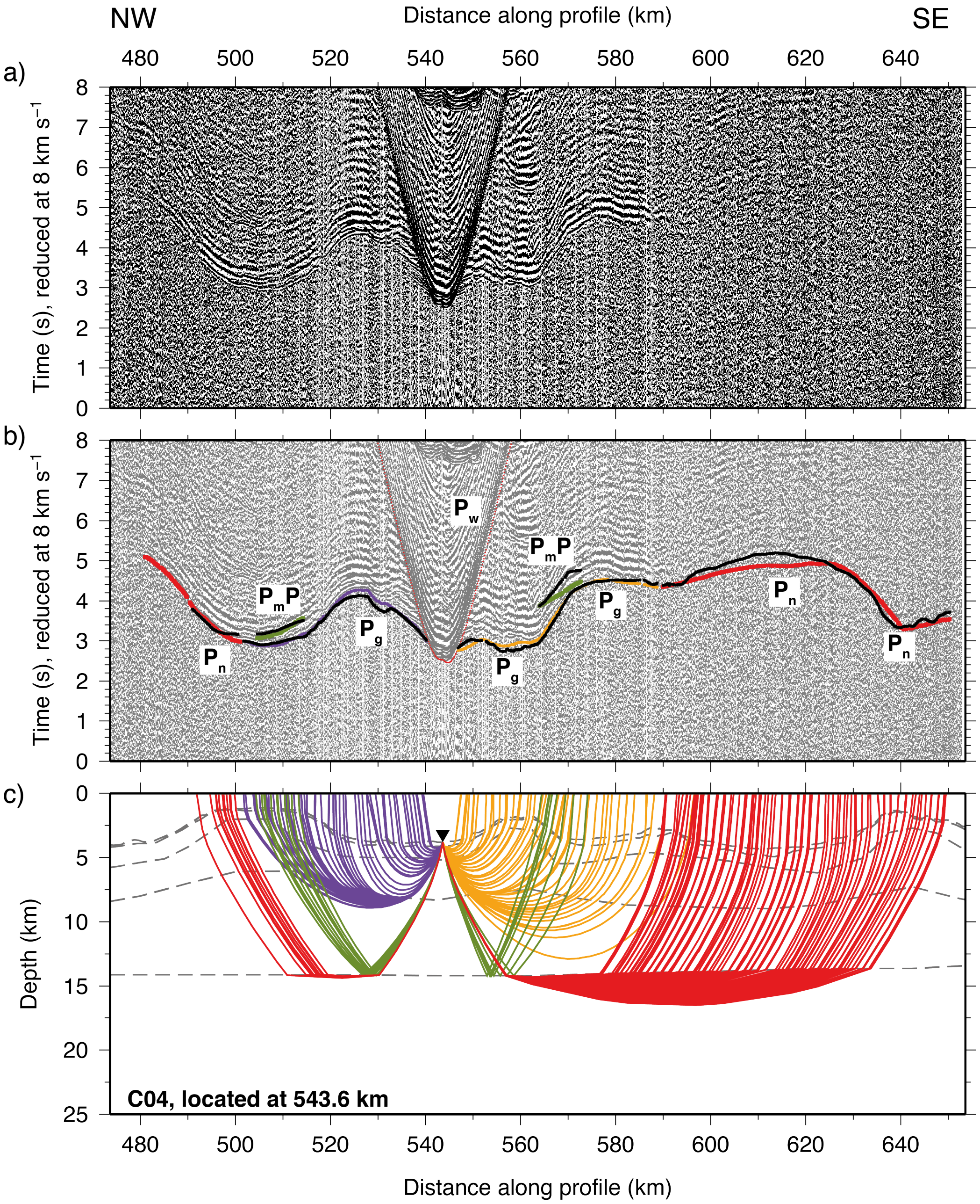

Figure 3.5: *WA seismic data from OBS C04 hydrophone channel, located at 543.6 km d.a.p., on the background Pacific plate (see Fig. 3.4). Plotted as for Fig. 3.3. Ray-tracing ends before all picked travel times are modelled, due to ray selection at bend procedure discussed in Section 3.5.2.*

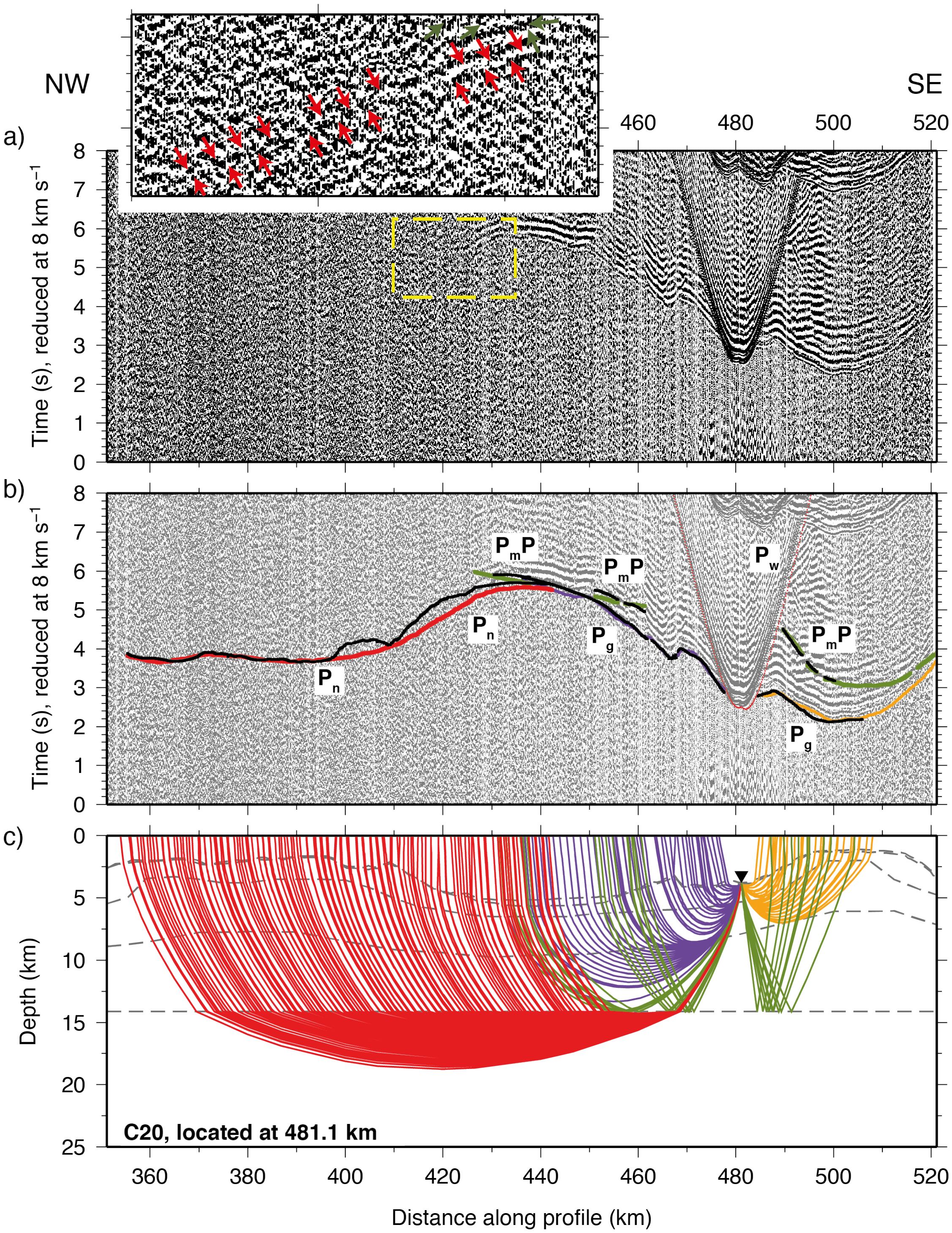

Figure 3.6: *WA seismic data from OBS C20 hydrophone channel, located at 481.1 km d.a.p., located on the north flank of 27.6˚S seamount (see Fig. 3.4). Plotted as for Fig. 3.3. Ray-tracing ends before all picked travel times are modelled, due to ray selection at bend procedure discussed in Section 3.5.2.*

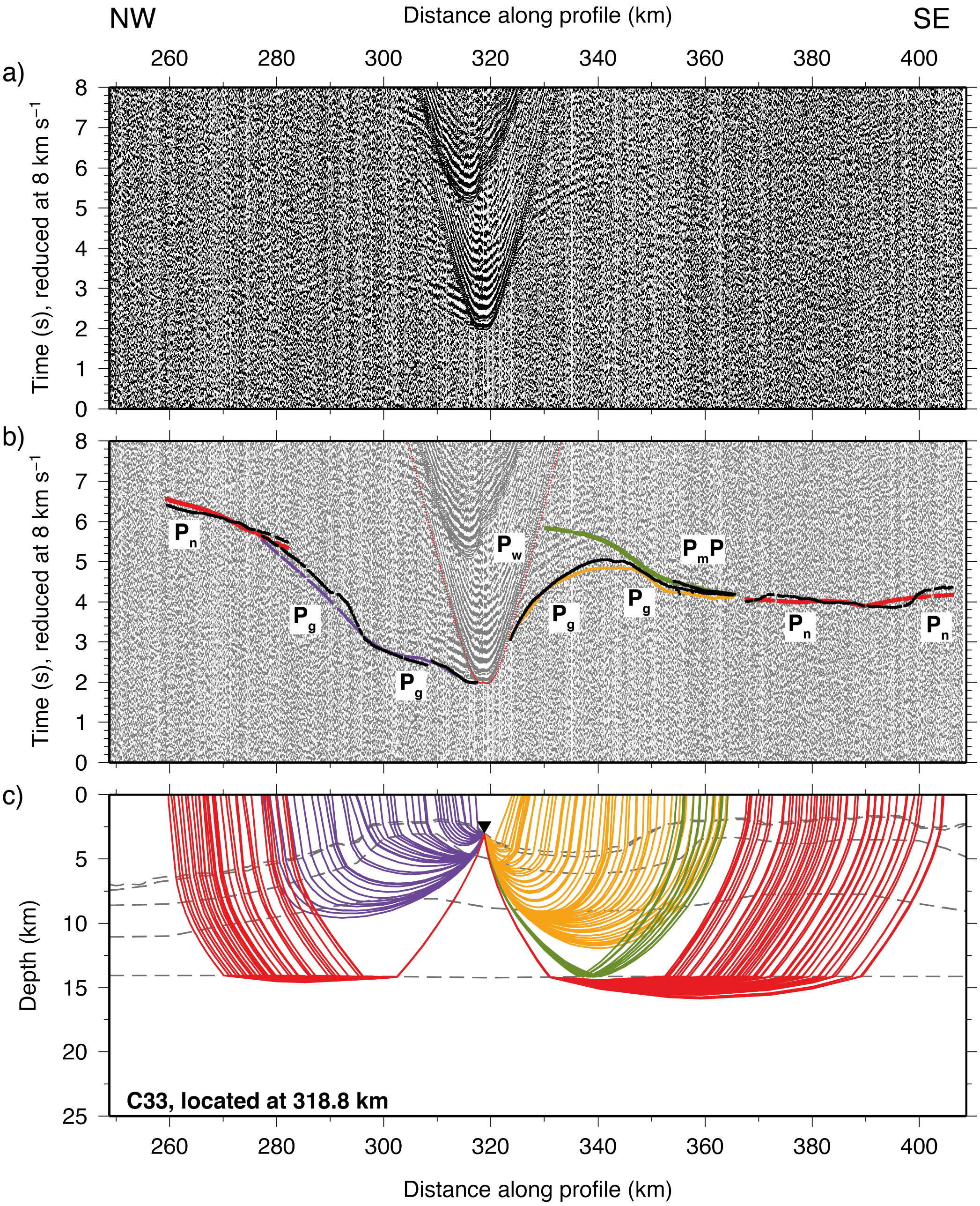

Figure 3.7: *WA seismic data from OBS C33 hydrophone channel, located at 318.8 km d.a.p., on the southern flank of Osbourn seamount (see Fig. 3.4). Plotted as for Fig. 3.3.*

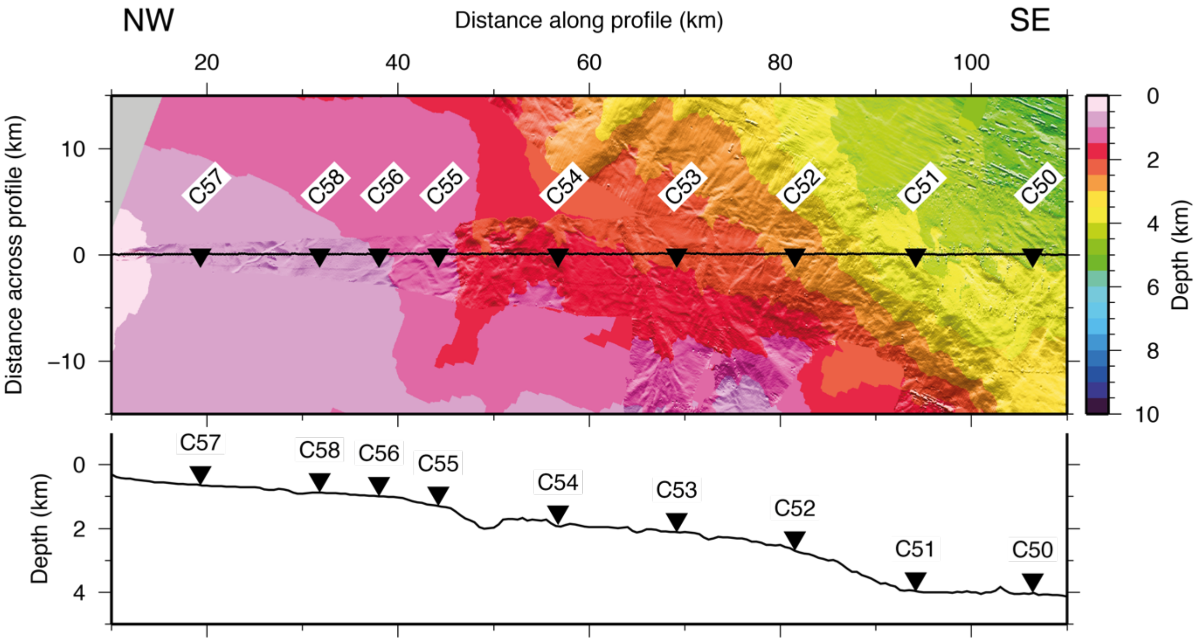

Figure 3.8: Combined swath-satellite bathymetry for Tonga upper forearc, at northernmost end of Profile C. Gridded at 50m, and illuminated only in regions of swath coverage. Relocated OBSs indicated as inverted black triangles, with instrument numbers labelled. Black line along y=0 indicates path of Profile C.

of the profile (0 km d.a.p.) to 3 km at ~85 km d.a.p.. At this point there is a downward step in the bathymetry to the middle trench slope, which appears in the MCS data as a large-scale fault (Figs 2.13 and 2.14). The SNR is generally high for instruments located in this region, which is most likely a result of the much simpler bathymetry generating much less scattering of energy.

Given the degree of sediment cover observed on the MCS record section (Fig. 2.13), coupled with the relatively flat, only gently sloping bathymetry, and the relative proximity to the volcanic arc which represents an important potential source for sediments, observation of refracted arrivals through the sediment layer is most likely expected here. P_s first-arrivals can be picked on most, but not all instruments, and are limited to offset ranges of <8 km from each instrument.

P_g arrivals show maximum offsets of ~90 km (Fig. 3.9 – C56), however more typical values are of the order of ~40 km (Fig. 3.10 – C53). For some instruments, for example C56, the P_g arrival continues as a secondary arrival after the P_n arrivals appear. P_n arrivals are observed to 100 km offset (e.g. OBS C57), however, the typical maximum offset is ~70 km. P_mP arrivals are observed at offsets of between ~30-50 km.

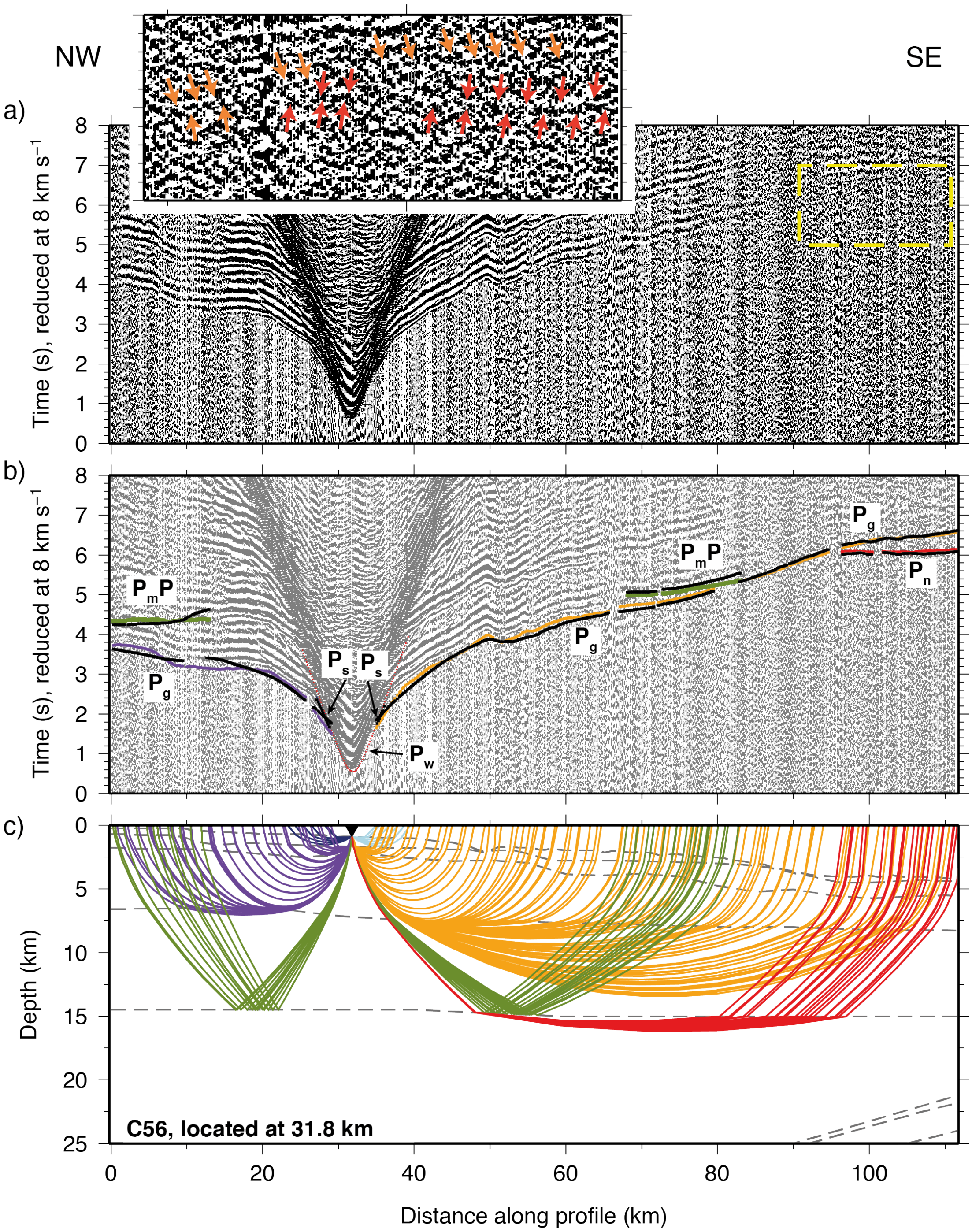

Figure 3.9: *WA seismic data from OBS C56 hydrophone channel, located at 31.8 km d.a.p., on the Tonga upper forearc (see Fig. 3.8). Plotted as for Fig. 3.3.*

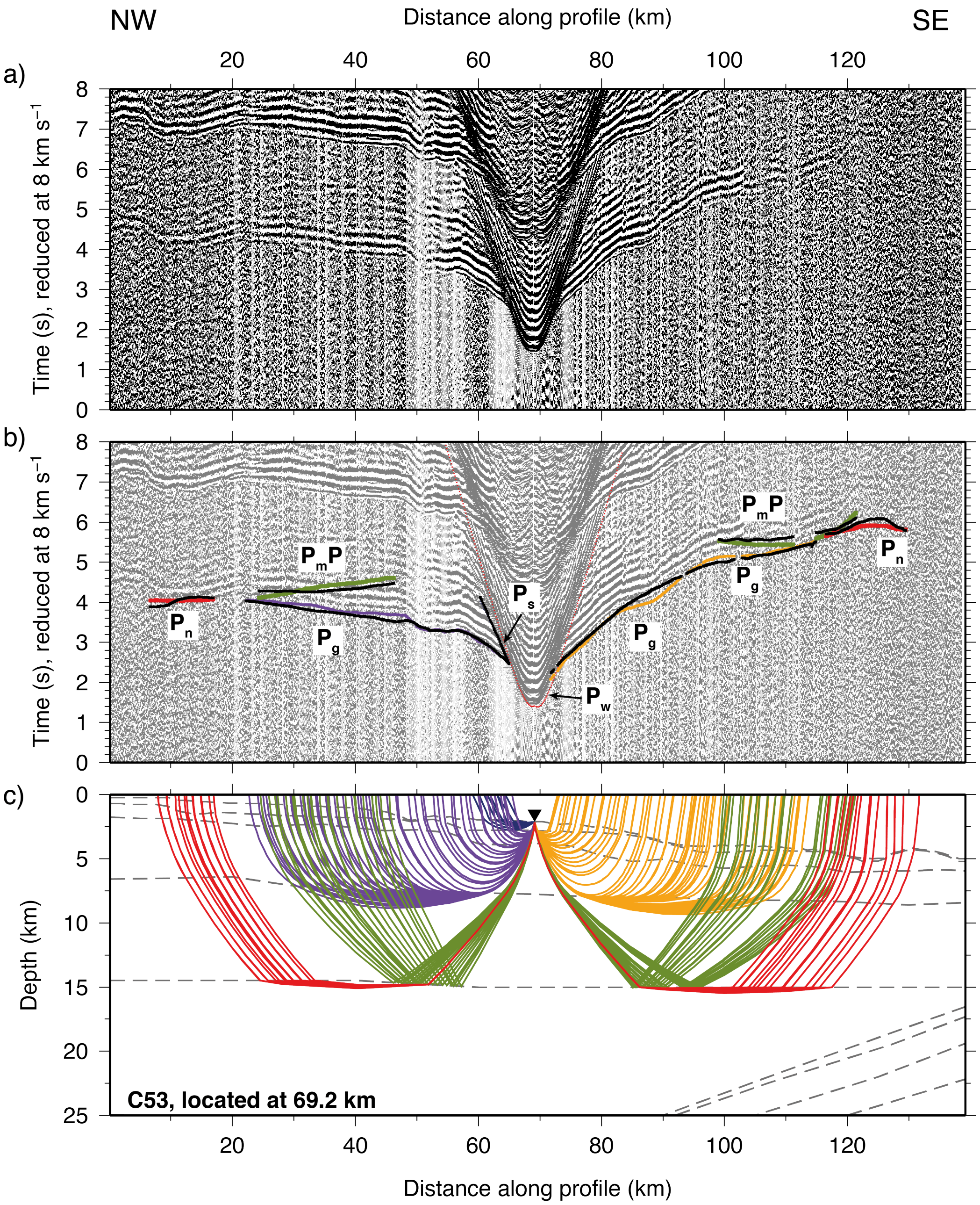

Figure 3.10: *WA seismic data from OBS C53 hydrophone channel, located at 69.2 km d.a.p., on the Tonga upper forearc (see Fig. 3.8). Plotted as for Fig. 3.3.*

3.4.2.2. Middle trench slope – OBSs C44-51

OBSs C44-C51 are located on the middle trench slope, although the lower numbered instruments here are in the transition to the lower trench slope region. This part of the forearc extends from ~90 km d.a.p., where the bathymetry steps down from the upper forearc, to ~190 km d.a.p., where the topmost part of the lower forearc slope is uplifted, before it descends steeply toward the trench. The bathymetry of this region is rough, characterised by a number of ~0.8 km-high ridges which are oriented obliquely to the strike of the trench (Fig. 3.11), on top of which are sited OBSs C47 and C48. These ridges may define a series of small potential depocentres, hence spatially limited P_s arrivals are observed although, broadly, the MCS record section shows this area to be very sediment poor (Fig. 2.14). The seabed in this part of the profile lies at a relatively consistent depth, with only a 1 km increase from 4 km in the upper part of this region, to 5 km at the middle to lower trench slope transition.

Record sections for instruments in this region generally show characteristics similar to those in the upper forearc (Fig. 3.12). As the instrument proximity to the trench increases, the offset ranges of all crustal refracted phases tends to decrease, such

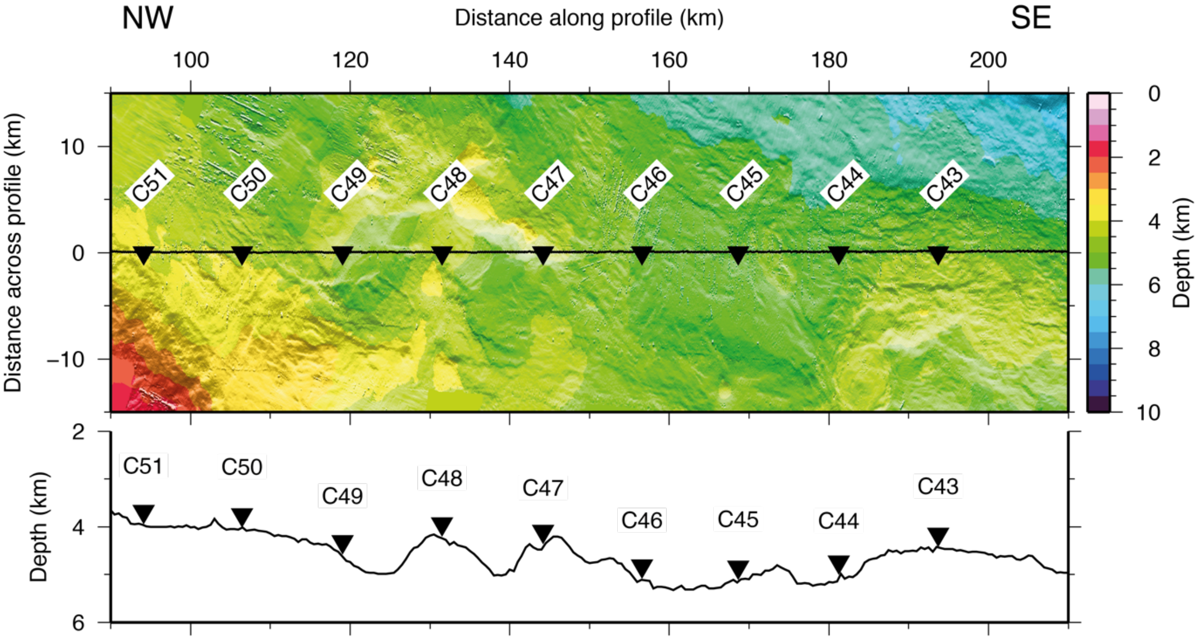

Figure 3.11: Combined swath-satellite bathymetry for Tonga middle forearc terrace. Gridded at 50m, and illuminated only in regions of swath coverage. Relocated OBSs indicated as inverted black triangles, with instrument numbers labelled. Black line along y=0 indicates path of Profile C.

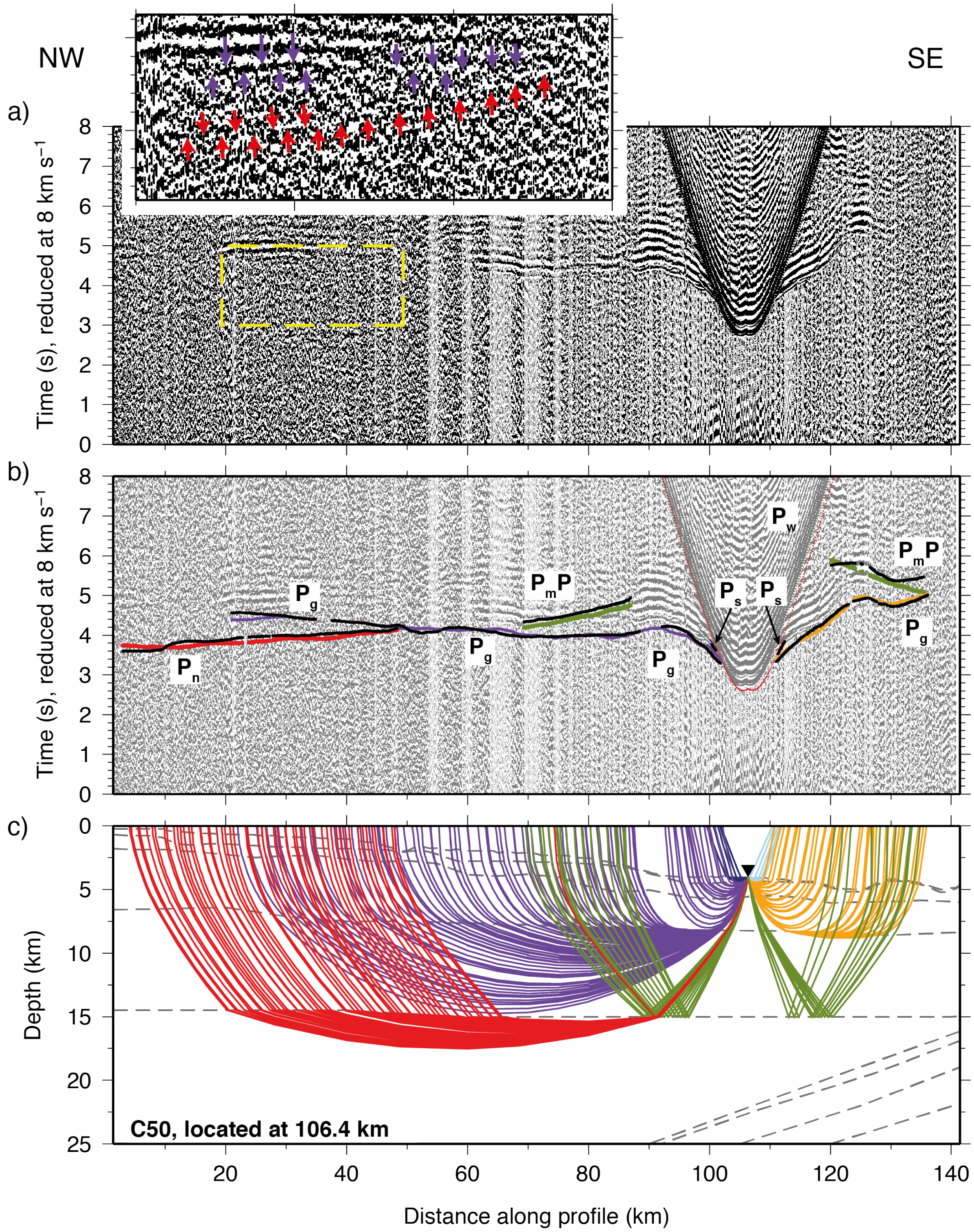

Figure 3.12: *WA seismic data from OBS C50 hydrophone channel, located at 106.4 km d.a.p., on the Tonga middle forearc (see Fig. 3.11). Plotted as for Fig. 3.3.*

that for some instruments, P_g arrivals are limited to offsets <20 km. For the two instruments between ~180-215 km d.a.p. (C43-C44), no P_n arrivals can be confidently identified, although P_n arrivals are found on other instruments, with increasing maximum offsets with greater distance from the trench.

3.4.3. Lower trench slope/trench-transition – OBSs C37-C46

The trench-transition instruments are represented by OBSs C37 and C38 on the Pacific plate and C40-C46 on the lower trench slope of the overriding Indo-Australian plate (Fig. 3.13). These instruments are all of the IFM-Geomar KUM deep water type and, therefore, should have relatively similar characteristics. In this region, the maximum offsets are likely to be highly limited both as a result of signal attenuation caused by the deep water setting, steep bathymetry, and the complex structural variations associated with the subduction zone.

The relatively steep slopes in this region are not conducive to sediment accumulation, sourced either from the forearc or Osbourn seamount. Consequently, the seabed here is underlain by virtually no sediment (Figs 2.15 and 2.16), and hence

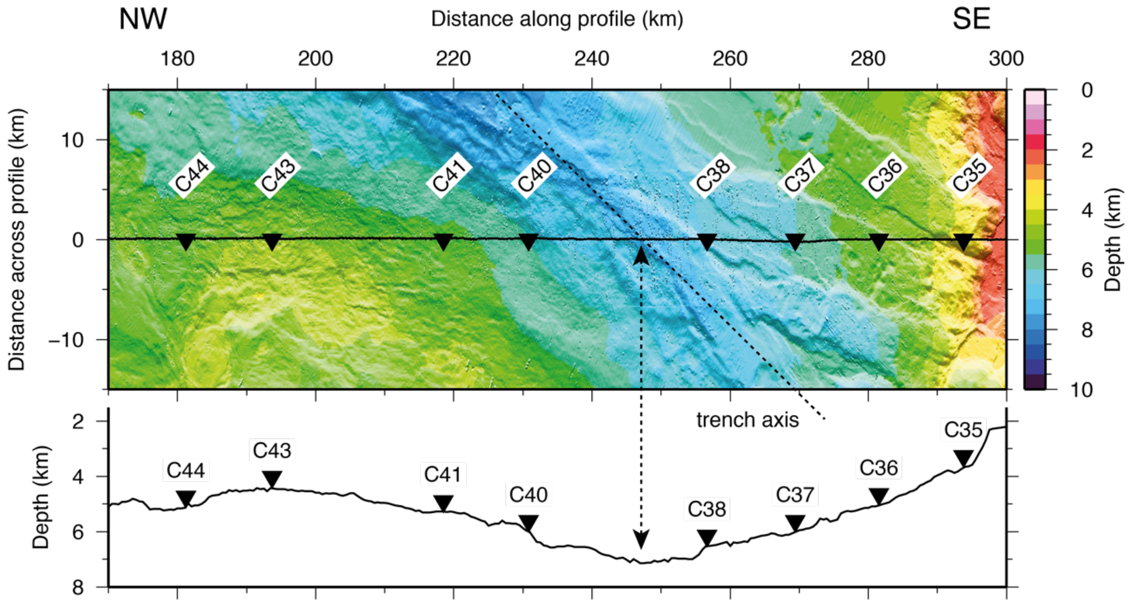

Figure 3.13: *Combined swath-satellite bathymetry for Tonga lower forearc slope and trench, at point of present LRSC collision. Gridded at 50m, and illuminated only in regions of swath coverage. Relocated OBS indicated as inverted black triangles, with instrument numbers labelled. Black line along y=0 indicates path of Profile C. Dashed black line indicates location of trench axis.*

virtually no P_s arrivals are observed. For P_g arrivals, offset ranges are generally short, at less than 40-50 km, particularly so in the direction, relative to the instrument, of the trench. For OBS C44, for example, P_g arrivals are observed to offsets of ~40 km away from the trench; however, in the towards the trench direction this is limited to ~20 km. This pattern is observed more strongly for instruments located on the overriding plate, between 150-200 km d.a.p., and likely represents the increasing subsurface structural complexity that might be anticipated. For the instruments located closest to the trench, P_g offsets in both directions are typically short (<30 km).

The trench-proximal instruments tend to show the shortest maximum P_mP and P_n offsets, rarely reaching >25 km and >50 km respectively (Fig. 3.14). Reflected phases are not commonly identified in the towards the trench direction from the instrument. However, OBSs C44 and C46 show arrivals which are best modelled as reflections from the plate boundary. As these arrivals represent reflections from the lowermost Indo-Australian crust, despite it now being bounded at its base not by mantle but by the Pacific plate, these arrivals are treated in the modelling in the same way as P_mP arrivals. A small number of instruments, for example C41 (Fig. 3.15), show arrivals which seem to indicate the transmission of rays through the subduction interface and downgoing slab, into the Pacific mantle. As the P_n arrivals from the different plate are not distinguished, these are treated in the modelling in the same way as P_n arrivals passing through only one of the two plates.

3.5. Model construction

3.5.1. Initial model

Due to the two-dimensional nature of the modelling approaches being used in this study, it was necessary to translate all OBS and shot locations onto straight line segments with variation only in one lateral dimension. All geographical co-ordinate systems were projected, using an oblique Mercator projection, into a kilometre-offset modelling space (Fig. 3.1b,c). The distance along the profile was defined as the x-dimension, and all y values are set to zero.

The geometry of the LRSC meant that it could not easily be represented by a single, straight line segment. Instead, the trend of Profile C has a single bend, which represented an acceptable compromise between maintaining profile simplicity, which is important for data processing, and seamount imaging capability. The bend is located over the summit of 27.6˚S seamount, at 27.59 ˚S, 174.20 ˚W (Fig. 3.1). Two separate

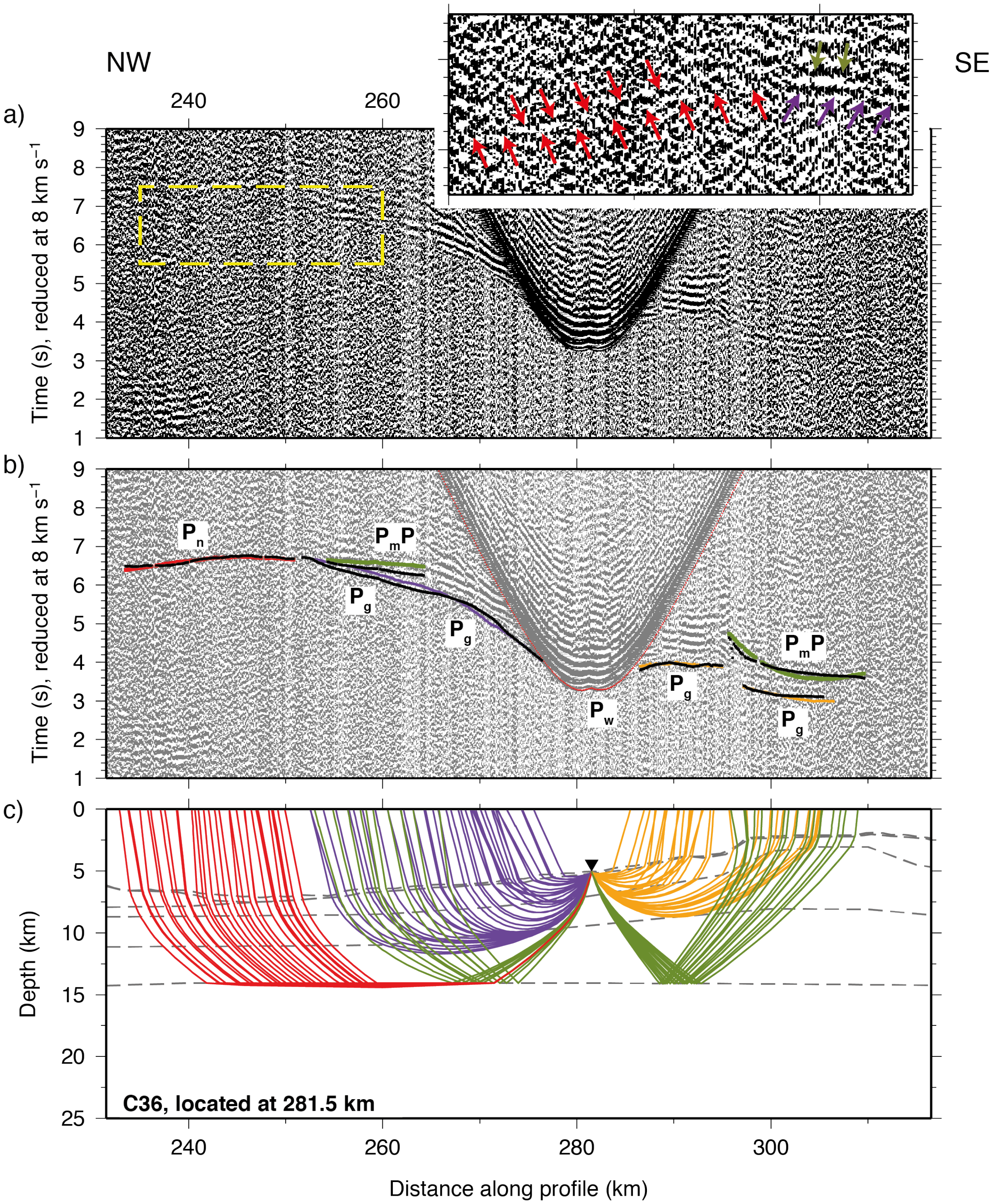

Figure 3.14: *WA seismic data from OBS C36 hydrophone channel, located at 281.5 km d.a.p., on the northern flank of Osbourn seamount, adjacent to the Tonga Trench (see Fig. 3.13). Plotted as for Fig. 3.3.*

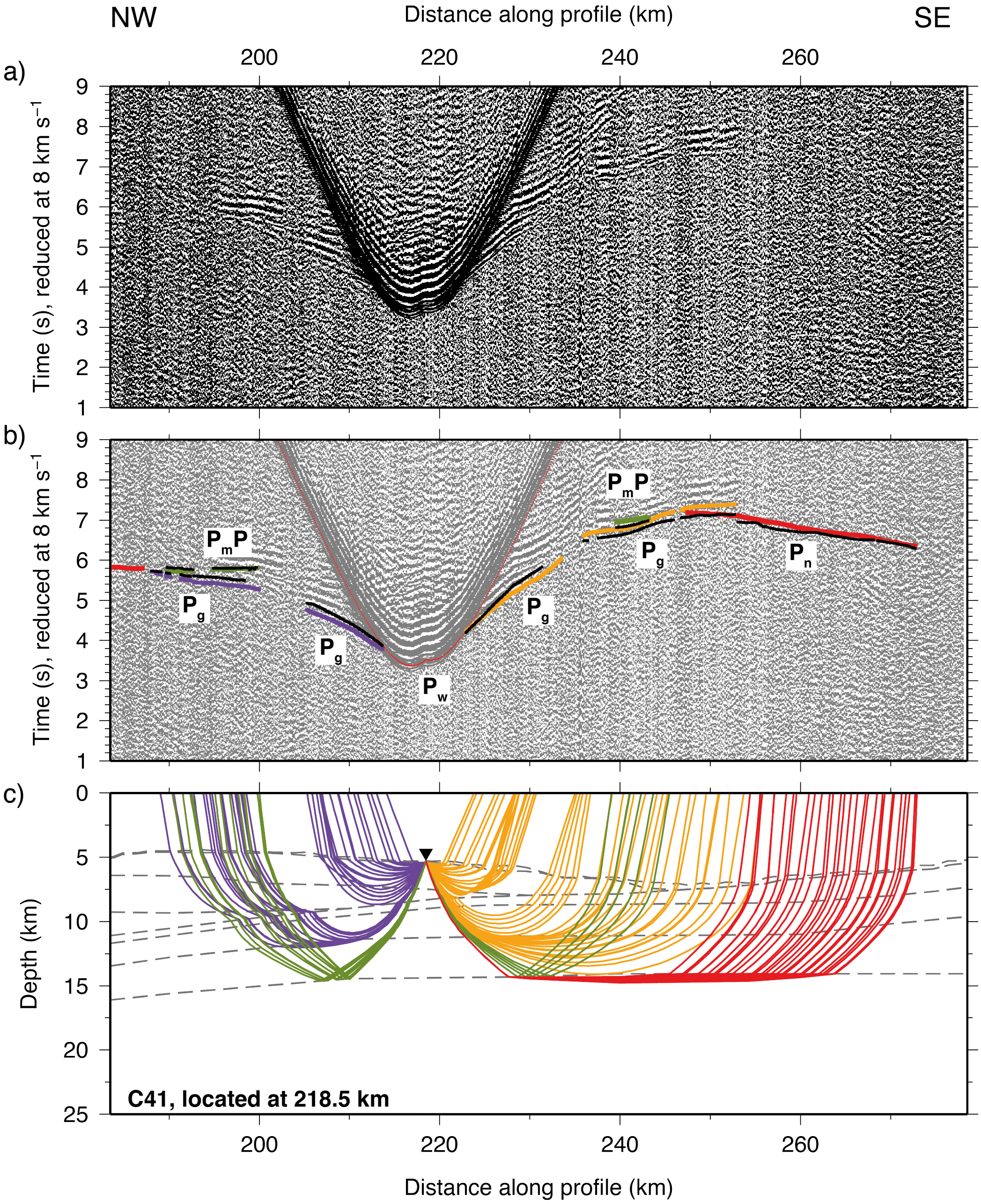

Figure 3.15: *WA seismic data from OBS C41 hydrophone channel, located at 218.5 km d.a.p., on the Tonga lower forearc slope region, adjacent to the Tonga trench (see Fig. 3.13). Plotted as for Fig. 3.3.*

rotations of the co-ordinate system were thus required, and the resulting two straight-line segments are 500.21 km and 225.83 km in length. The zero point of the model was defined as the northwesternmost end of Profile C, and the bend initially acted as an apparent zero point for the southeastern part of the profile, which would be initially modelled separately. The model offsets would then be translated by 500.21 km, the length of the northern segment, before being appended to produce a single profile for final stage modelling.

The seabed depth along the profile was sampled from the swath bathymetry data to a model node spacing of ~750 m (5 shots). This was sufficient to match the longer wavelength variation to within the resolution of the WA seismic data and modelling approach. Above the bathymetry, an initial average seawater velocity of 1500 m s^{-1} was applied. The further development of the water column velocity structure will be discussed in Section 3.6.1.

Below the bathymetry, the sediment-basement interface is added using the picked interface from the processed MCS data (Figs 2.13-2.19), sampled to a node spacing of ~0.75-2.0 km (30-80 CMPs). The spacing used depends on the resolution required to well represent the interface depth variability. The initial velocity structure for the sediment layer was derived by converting the stacking velocities derived from the MCS velocity analysis to interval velocities using the Dix (1955) relationship and averaging.

3.5.2. Ray-tracing around bend

One of the principal aims of this study is to image and understand the internal structure of the Louisville Ridge seamounts, to determine along-ridge variability. However, a result of the selection of the path of Profile C, as a compromise given the complex geometry of the LRSC, is that only two of the largest seamounts are crossed directly over their summits. It is critical, therefore, that these two seamounts, Osbourn and 27.6˚S, have their velocity structure well resolved. Additionally, SO195 Profile P03 (Contreras-Reyes et al., 2010) also traverses the 27.6˚S seamount, and intersects Profile C, thus providing a degree of three-dimensionality.

The bend in Profile C at 27.59˚S, 174.20˚W complicates the internal imaging of 27.6˚S seamount, as to resolve its velocity structure it was necessary to trace rays from shots to the north of the bend into instruments to the south, and vice versa. Since these rays no longer follow the exact path of Profile C, only suitable shot-receiver pairs that minimize the associated error to within acceptable limits were selected. There were two key criteria for the selection of rays for use in this part of the modelling:

1) that the difference in travel time between the direct (across-the-corner) and along-profile (around-the-bend) paths could be suitably accounted for in the model errors; and,
2) that the rays sampled approximately the same velocity structure as they would by travelling around the bend, i.e. they pass close enough to the seamount centre.

To calculate the difference in travel time for criterion 1, an estimate of the crustal seismic velocity was needed, indicating that it is dependent on the second criterion being satisfied. That is, if the rays are not sampling a similar part of the seamount then they may travel at a different velocity, and hence their travel time may also be very different.

3.5.2.1. Criterion 1 – Travel path length and travel time differences

A means of determining the difference in travel time, τ, between the direct (across-the-corner) and along-profile (around-the-bend) paths was derived, which was applicable to any shot-receiver geometries and a bend of arbitrary angle, θ (Fig. 3.16).

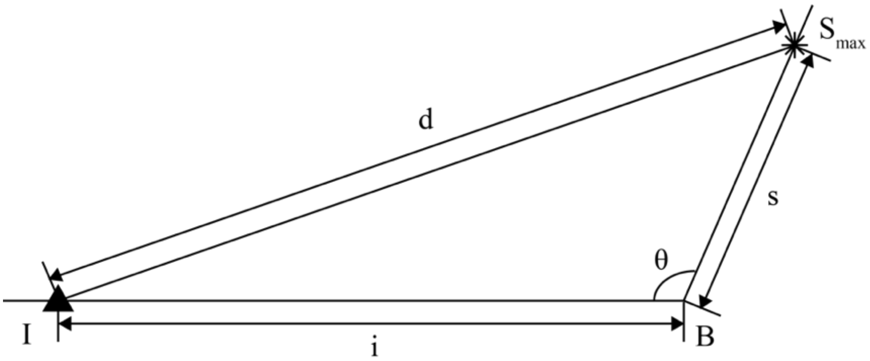

Figure 3.16: *Generalized schematic geometry for calculating the path length difference, δ, between direct, across-the-corner, arrivals (d) and around-the-corner arrivals (i+s). Black triangle I is an OBS location. Star S_{max} is the location of the maximum offset shot from the bend at B.*

This calculation does not require the consideration of the location of the bend point relative to the seamount, as is takes into account only the distances of shots and receivers either side of the bend point, and the angle of the bend. From the value of θ, and the known shot (S) and receiver (I) positions on the profile, the direct path distance taken by the rays, d, can be calculated using the cosine rule. Comparison with the around-the-bend distance for each shot-receiver pair (s + i) allows the path length difference, δ, to be determined. By assuming a suitable value for the velocity of the medium through which the rays are travelling, the travel time difference, τ, can then be derived.

It was necessary to define a threshold for the additional error which may be added to travel time picks, based on their travel path (and time) difference. For P_g arrivals the error assigned to picks for the rest of the model was 70 ms. An addition of 50% of this was deemed an acceptable threshold, and, hence, a maximum τ of 35 ms was permitted for P_g arrivals. For P_n arrivals the pick error for the rest of the model was 100 ms, and an addition of a 100% threshold was deemed acceptable. Therefore, picks were accepted which had a maximum $\tau = 100$ ms. Whether these limits and additional pick uncertainties are appropriate will be assessed as part of the model robustness testing discussed in Chapter 4.

In order to calculate τ for each shot-receiver pair, to ensure that it lies below the defined thresholds, an estimate of the velocity of the medium through which the rays were travelling was required. Using the observations of Contreras-Reyes et al. (2010) for 27.6˚S seamount, and preliminary results arising from this study of the interior velocity structure of Osbourn seamount, it could be argued that a suitable P-wave velocity for the internal higher-velocity component of the seamount is 6 km s^{-1}. Figure 3.17 shows the calculated path length (a,b) and travel time (c,d) differences for instruments tracing from north-to-south and vice versa. It can be seen that shot-receiver pairings can be divided into a number of groupings. The first contains instruments which are located very close to the bend, and thus have a τ <35 ms for shots located at all distances from the bend. The second group contains instruments which are located further from the bend, and which have τ <35 ms only for shots located relatively close to the bend.

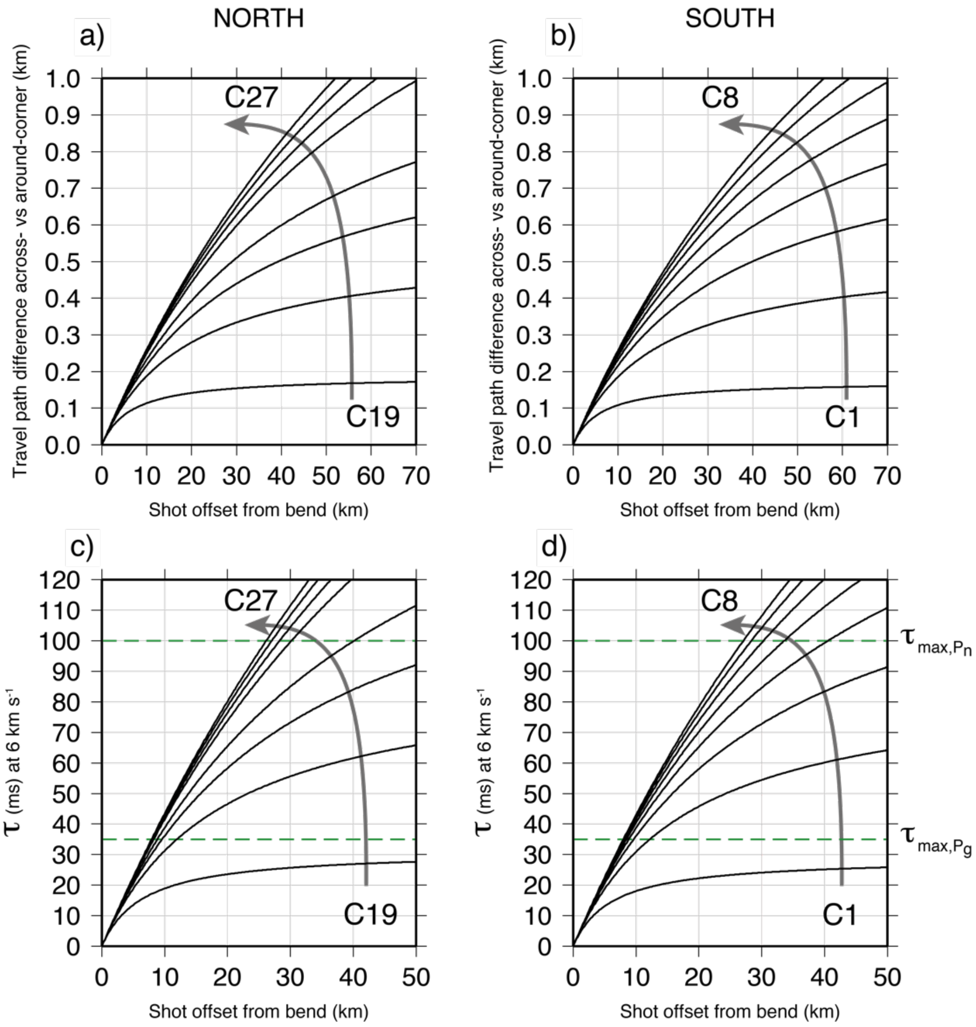

Figure 3.17: *Across- versus around-corner ray path differences. a) Ray path length difference between travelling directly across corner or around bend, along line of profile, with varying shot offset on opposite side of bend, for instruments C19-C27, located to the north of the bend. Values are not shown for OBS C23 as this instrument is excluded from modelling (see text). Instrument distance from bend increases in direction of arrow. b) As a), for instruments C1-C8 located south of bend. c) Calculated* τ *arising due to path length difference in a), calculated assuming a velocity of 6 km* s^{-1}*. Dashed lines at* $\tau = 35$ *ms and* $\tau = 100$ *ms are thresholds for* $\tau_{max,Pg}$ *and* $\tau_{max,Pn}$ *respectively. d) As c), for instruments on southern part of profile.*

3.5.2.2. Criterion 2 – sampling the correct features

It is possible to calculate the maximum shot offset, S_{max} for an instrument at any given position, where the ray path between the instrument and S_{max} is a tangent to a circle of radius r, centred on the seamount centre, C. Figure 3.18 defines the subsequent terms and shows a generalized geometry for performing this calculation.

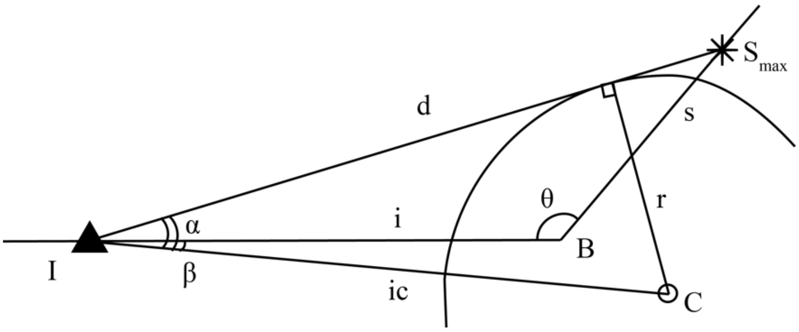

Figure 3.18: *Generalized schematic of Profile C bend geometry, where the bend is not centred on the seamount. Black triangle I is an OBS location. Star* S_{max} *is the maximum shot offset for a seamount with radius r, centred at C. B is the bend in the profile, which runs along the lines IB and* BS_{max}*.* θ *is the angle of the bend in the profile. i, ic, s, d,* α*, and* β *are quantities which need to be calculated to define* S_{max}*.*

Since r and ic are known, the sine rule can be used to calculate angle $\alpha+\beta$. The value of β can then be calculated from the declination of the line joining the instrument and the seamount centre, IC, from the plane of the profile, IB. Hence, it is possible to determine the value of α and, by extension, all of the angles within the triangle IBS_{max}. Using the sine rule,

$$\frac{\sin(180 - \theta - \alpha)}{i} = \frac{\sin \alpha}{s}$$

allows determination of the distance, s, of the point S_{max}. Using the cosine rule as above allows calculation of the values of d, δ and τ.

To understand how this criterion governs the selection of rays in this study, the actual shot-receiver and bend geometry of Profile C must be considered. From published (Contreras-Reyes et al., 2010) and preliminary observations arising this study, it appears that where seamounts contain intrusive cores, these have a radius of approximately half of the seamount basal radius. The core radii tested were 5.0 km, 5.5 km, and 6.0 km (Fig. 3.19). The smallest of these values was selected as it corresponds to a case where a circle of twice this radius fits entirely within the summit area of 27.6°S seamount. The larger value of 6 km corresponds to a 12 km-radius outer circle, which lies predominantly within the main body of the seamount, although there is some extension beyond the summit and onto the NE and SW facing flanks.

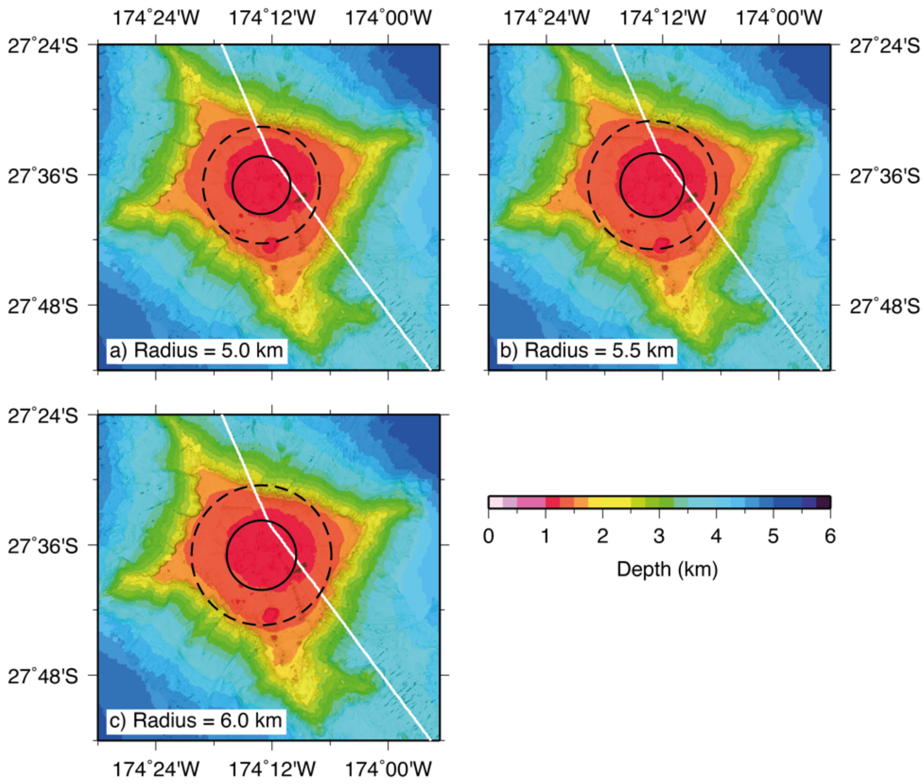

Figure 3.19: *Test intrusive core radii for 27.6˚S seamount with Profile C overlain (white line). Solid circles centred at 27.62˚ S, 174.22˚ W represent the intrusive cores and have a radius of a) 5.0 km, b) 5.5 km, and c) 6.0 km. Dashed outer circles have a radius of two times that of inner circle, and are centred at the same point on the seamount, illustrating the proposed core to total diameter ratio of ~0.5.*

The above calculations were performed for each of the three test radii to determine S_{max} for each instrument within ~100 km of the bend to the northwest and southeast. The results are shown in Figure 3.20. As the profile bend is not centred on the seamount, instead lying close to the northernmost edge of the inner (core) circle, there is an asymmetry in the trend of S_{max} between rays tracing from north to south, and vice versa. Where instruments are located sufficiently proximal to the bend, they may lie within the circles used to calculate S_{max}, or adjacent to them in such a way that a line tangent to the circle from the instrument location is always divergent to the profile. In this case, all shots for this instrument pass the S_{max} criterion (e.g. for C1 at all radii, and C19 for a radius of 6.0 km). All shots which were fired within the area covered by the inner circle also, by definition, pass the S_{max} criterion.

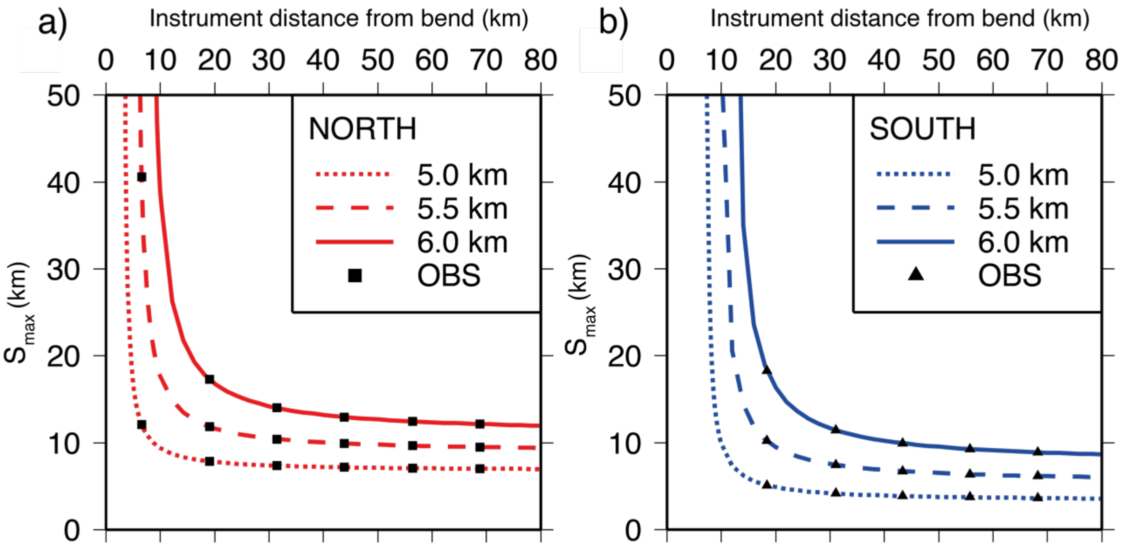

Figure 3.20: *Maximum permissible shot offsets for ray-tracing from one segment of Profile C to the other. a) Instruments located north of the bend in profile. Lines represent synthetic instrument locations, and black squares actual instrument locations, for 5.0, 5.5 and 6.0 km seamount core radii. b) As a), for instruments located south of the bend in profile. Actual instrument locations are identified by black triangles.*

3.5.2.3. Applying the criteria to selecting travel time picks

Figure 3.21 shows τ plotted against shot distance from bend, s, for each of the instruments within 100 km of the bend on the north and south segments of Profile C. By overlaying the value of τ corresponding to S_{max} for each instrument, it is possible to define the maximum shot offset for each instrument which passes criterion 2. For the range of radii tested, the stronger limiting factor for travel time pick selection is that its path travels close to the centre of the seamount, rather than the threshold limit on the additional error. Hence, generally, the S_{max} criterion has a significantly larger control than τ_{max}, on whether shot-receiver pairs straddling the bend are included or not, because all the τ-S_{max} curves for each tested seamount core radius lie below the $\tau_{max,Pn}$ = 100 ms criterion, and only for the 6.0 km radius do they regularly lie above the $\tau_{max,Pg}$ = 35 ms criterion. However, for differing bend angles and locations relative to the seamount centre, this may not always be the case.

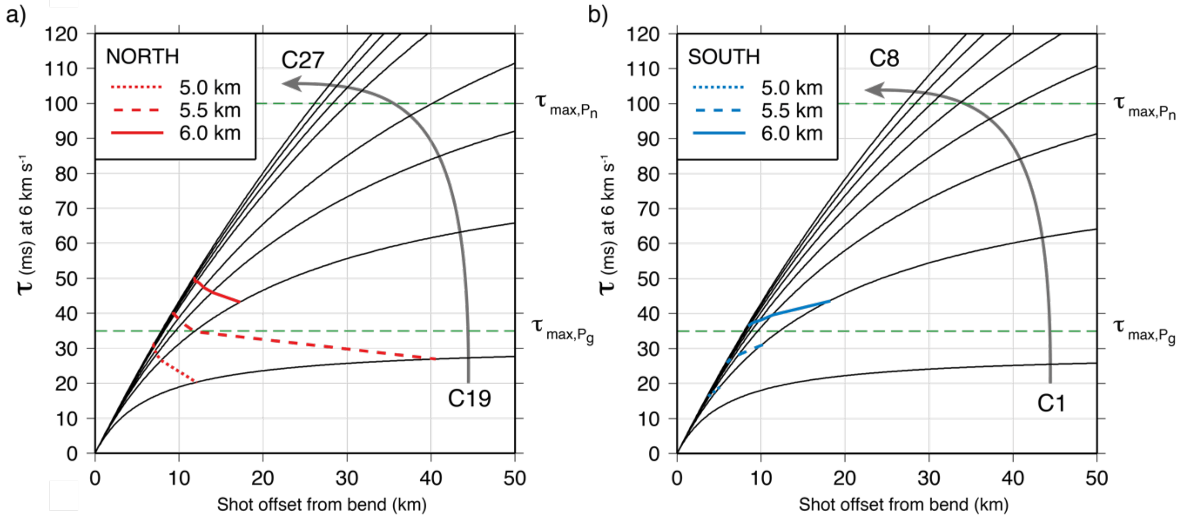

Figure 3.21: *Maximum permissible shot offset, S_{max}, versus maximum travel time difference, τ_{max}, for a) instruments located north of the bend in profile, and b) instruments located to the south. Black lines show τ calculated for all shot offsets <50 km, with instrument distance from bend increasing upwards, as in Fig. 3.17. Coloured lines identified in the key represent the τ value at the calculated S_{max} for each instrument. Only shot-receiver pairs located below each line pass the S_{max} criterion. If the coloured line does not cross an instrument line, then no shot-receiver pairs fail the S_{max} criterion.*

Using the limits derived for defining the suitability of picks proximal to the bend, the pick files for individual instruments were filtered to remove shots which do not pass the criteria. A summary of the conditions applied is as follows:

- if the pick represents a P_g arrival from a shot located closer to the bend than S_{max} for its instrument, and which has a travel time difference, τ, of <35 ms, the pick is included and an additional pick uncertainty of 35 ms is applied;
- if the pick represents a P_g arrival from a shot located further from the bend than S_{max} for its instrument, or it is has a τ of >35 ms, the pick is excluded;
- if the pick represents a P_n arrival from a shot located closer to the bend than S_{max} for its instrument, and which has travel time difference, τ, of < 100 ms, the pick is included and an additional pick uncertainty of 100 ms is applied; or,
- if the pick represents a P_n arrival from a shot located further from the bend than S_{max} for its instrument, or it is has a τ of >100 ms, the pick is excluded.

3.5.3. Instrument relocation using P_w arrivals

As discussed in Section 3.2, the shot-receiver offsets for each OBS are derived from each OBS's deployment location. However, as OBSs fall and rise through the water column they may drift, such that their actual position on the seafloor is not the same as their deployment or recovery position. Consequently, it is necessary to accurately locate each OBS on the seafloor, a process that is known as relocation. In addition, the relocated OBS positions must also be projected onto the two-dimensional profile along which ray-trace modelling will take place. The relocated instrument positions and depths on the model along Profile C are provided in Appendix B.

A closest approach method was employed to determine the actual seafloor instrument locations. As shots were fired progressively at the sea surface while the ship passed over the instruments, there would be a point where the source was closest to being directly over each instrument. By inspecting the OBS record sections, the shot number (or numbers) of this point of closest approach were identified, and the location of the zero-offset shot point can be determined from the GPS locations of those shots. By this method it is possible to determine the lateral position along the profile of an instrument to no worse than half a shot spacing (75 m). If the instrument drifted along-profile during either deployment or recovery, the zero-offset shot location will not coincide with the documented deployment location. By comparing these two locations, a lateral shift can be applied to to correct the 'instrument zero' to the point of closest approach.

In addition to drifting along-profile, instruments may also drift in or out of the plane, which must also be corrected for. Where this occurs for Profile C, given the significant out-of-plane variation in seabed topography, it manifests in the OBS record sections as a difference between the observed travel times of the water waves and those calculated (the hodochron) based on the measured seabed depth on deployment. The application of a static time correction can also be used to account for instances where an instrument which has drifted out of the profile plane is no longer located on seabed which is of the same depth as the projected on-profile location. From an application point of view, it does not matter whether this correction arises purely as a result of instrument off-profile drift, or includes a component of changing depth, which may act to further increase, or balance out the path length difference (Fig. 3.22). As shot-receiver offsets increase the significance of the travel time error associated with instrument depth and location decreases due to the increasing arrival path length.

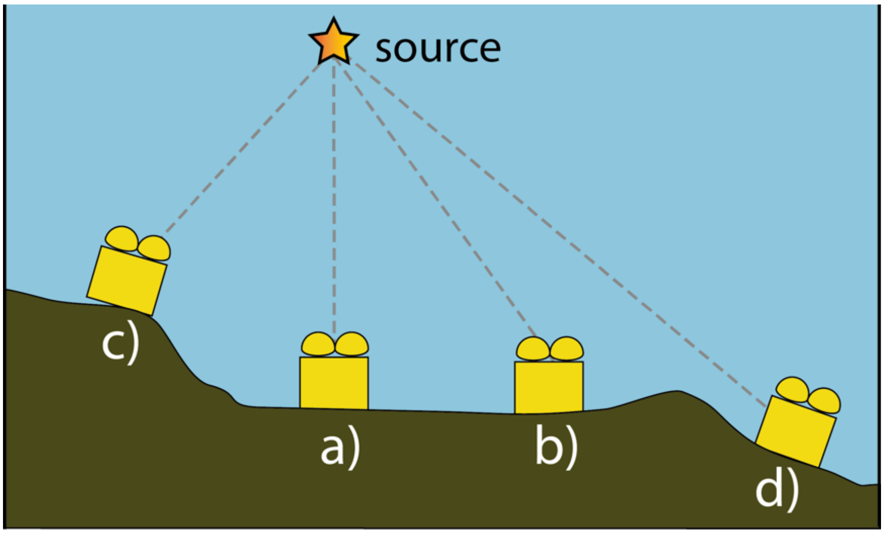

Figure 3.22: *Cartoon of the effect of a OBS drifting out-of-plane on the time corrections which need to be applied. Profile is oriented into/out of the page. Seismic source indicated by labelled orange star. a) Instrument is located directly on-profile, and no correction is required. b) Instrument has drifted out-of-plane, but is on a seabed of the same depth as that directly beneath the profile. A time correction is required, to account for the path length difference, which will be longer than a). c) Instrument has drifted out-of-plane, and lies on seabed shallower than that directly beneath the profile. A time correction is required which will depend on the balance between how far out-of-plane the instrument is located and the depth difference. This may, therefore, be a positive or negative time correction. d) Instrument has drifted out-of-plane, and lies on deeper seabed. A time correction is required to account for both the distance out-of-plane and depth difference, both of which will have the effect of increasing the path length.*

3.6. Forward modelling

Forward modelling of the WA seismic dataset is performed using *RAYINVR* (Zelt and Smith, 1992) in which a model is defined by a number of layer boundaries with an arbitrary depth and velocity node spacing, which need not necessarily be constant with depth or defined at the same model locations along any layer. For ray-tracing, the model is divided into an array of trapezoids with velocities defined at each corner. The velocity field within each trapezoid is calculated by linear interpolation along each of its sides, such that both vertical and horizontal velocity gradients can exist. Forward modelling is a user-driven iterative process, whereby locations and velocities of depth nodes are manually changed between each iteration, with the process repeated until an acceptable fit (to within the travel time pick uncertainties) between modelled and observed arrivals is achieved. Forward modelling was chosen as it allows the use of arrival phase assignment information, concurrent modelling of refracted and reflected phases, and the inclusion of features such as the plate boundary, which is required by the tectonic setting of this study.

Modelling was conducted a top-down manner. Shallow layers were modelled first until they showed a good fit between modelled and observed travel time picks, before moving on to deeper layers. Additional model layers were only added when necessary to generate suitable fit. Ray-tracing was performed in two ways. Initially, rays were traced from each instrument through all ray take-off angles ±90° upwards (for P_w) and downwards (for all crustal phases) in the positive (southeast) and negative (northwest) directions from each instrument. The initial stage of modelling aimed to test the assignment of arrivals to the correct phase type, and to achieve a good visual fit within the uncertainties.

Following this 'take-off angle' stage of modelling, point-to-point ray-tracing was conducted. In this stage, only rays forming shot-receiver pairs with matching pick phase assignments were included. Point-to-point ray-tracing enables a statistical determination of the fit between modelled and picked travel times. Two measures of fit were used:

- the root mean squared travel time residual (T_{rms}), which is a measure of the total misfit between the picked and modelled travel times; and
- the chi-squared statistic (χ^2), which is a measure of the fit between modelled and picked travel times, taking into account the pick uncertainties. A value of $\chi^2 = 1$ represents a model with uncertainties equivalent to those of the picks, and $\chi^2 <1$ represents an over-fit to the observed data. Hence, the modelling goal was a χ^2 as close to 1 as possible, but no less than 1.

3.6.1. Water wave modelling

Before modelling the sub-seabed, it was first necessary to include in the model a good representation of the water column velocity structure, since every arrival must travel through this region at least once. Eight expendable bathymetric thermographs (XBTs) were deployed along Profile C during OBS deployment (Fig. 3.1). XBTs measure the temperature of the water column down to a maximum depth of ~1800 m below sea surface (b.s.s.). In addition, a sound velocity profile (SVP) was also taken to a depth of 3 km b.s.s. to permit calibration of the XBT data, and the EM120 swath bathymetry system. The temperature data acquired by the XBTs were converted into vertical velocity profiles through the water column using an assumed salinity of 35 parts per thousand (Fig. 3.23).

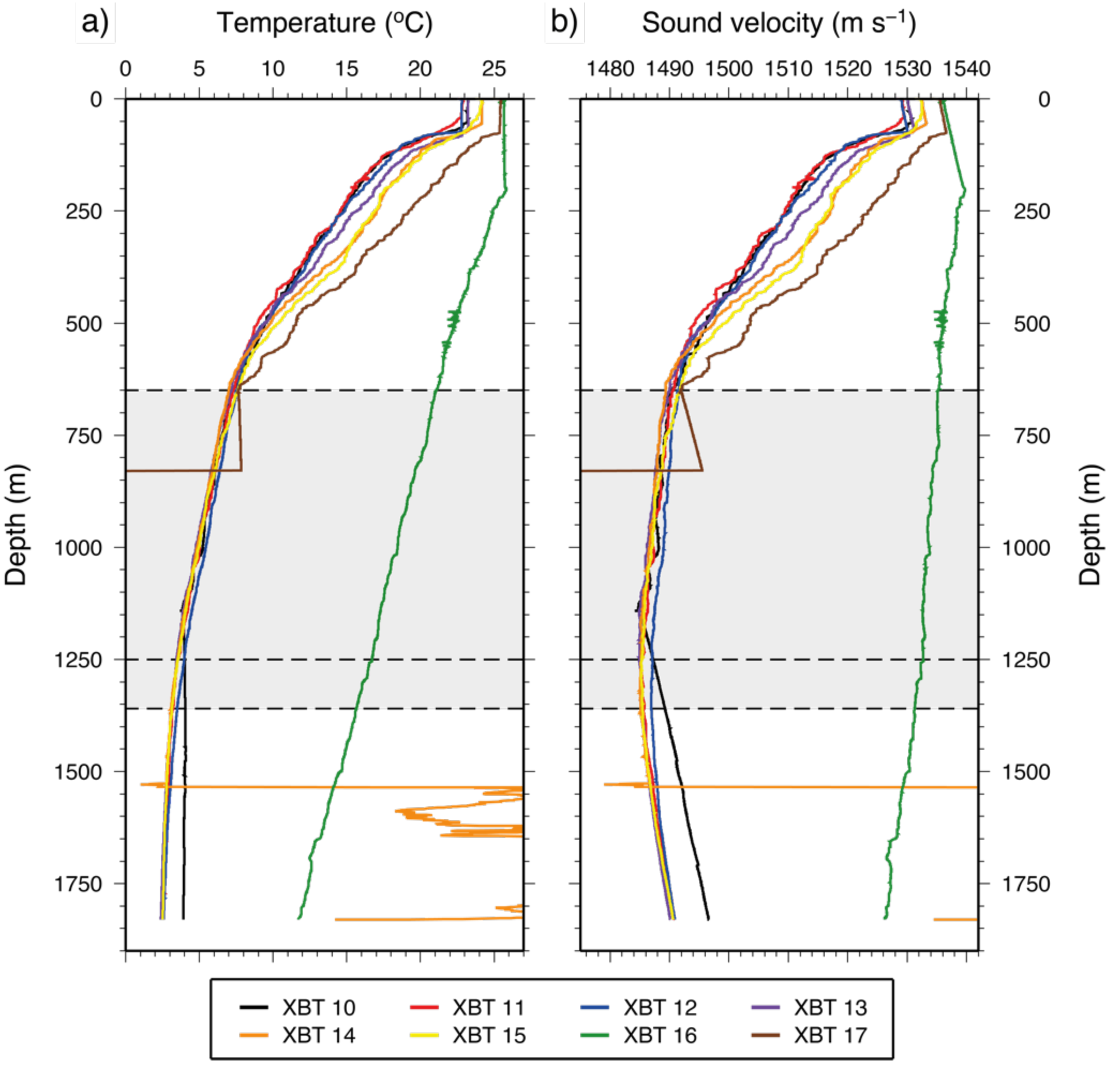

Figure 3.23: *Water column properties along Profile C, determined using expendable bathymetric thermographs (XBTs). a) Directly measured water temperature. b) Calculated sound velocity, using a salinity of 35 parts per thousand. Line colours are identified in the legend. Dashed lines at 650 m, 1250m, and 1360 m show where changes in velocity gradient have been incorporated into the water column of the forward model to match the XBT measurements.*

XBT 16 did not record any usable data, and appears to have malfunctioned throughout deployment. XBTs 14 and 17 recorded useful data to ~1500 m and ~650 m depth respectively, beyond which their behaviour becomes erratic, which is attributed to their landing on the seabed. Five XBTs recorded temperature to their full depth of ~1.8 km.

The principal features of the XBT profiles can be summarized by dividing the water column into three layers. The top layer from the sea surface to ~650 m b.s.s. shows a decreasing P-wave velocity from ~1530 m s^{-1} to ~1490 m s^{-1}. In the second layer between ~650 km and ~1250-1360 km b.s.s., velocity decreases from 1490 to 1485 m s^{-1}. Below 1360 m b.s.s., velocity begins to increase, until the XBT maximum depth is reached at 1800 m. In this lower layer, velocity appears to linearly increase with depth. Consequently, below 1800 m b.s.s., the velocity of the water column was simply extrapolated to the seabed using the gradient of the layer above, which is found to be ~1.25 x10^{-2} s^{-1}. This does not produce a significant misfit outside the pick uncertainties.

The water column velocity structure was added into the initial model to be used for ray-tracing, and the suitability of this structure was tested by tracing all P_w arrivals through the model. The three-layer water column velocity structure required little iterative adjustment to produce a good fit of the modelled to picked travel times. The best-fitting ray-tracing model results from a fit to 14621 travel time picks, with a T_{rms} = 32 ms and χ^2 = 1.11, and is shown in Figure 3.24. The water column velocity structure corresponding to this model is shown in Figure 3.25. 1D velocity profiles are calculated at the XBT locations, and compared to show the fit of this model to both datasets.

Figure 3.24c also shows that the full range of offsets of P_w arrivals is not always matched, with longer-offset arrivals on some instruments not replicated by modelled arrivals. The most likely cause of this mismatch is the coarseness of the water column velocity structure, controlled by the model node spacing of either ~7 km or ~14 km depending on location within the model. However, as all crustal arrivals pass through the water column effectively vertically, any results from the node spacing should have little effect.

To test this hypothesis, a single, fixed value of velocity was assigned at the seabed along the entire model, such that the model was smooth. In this case, the far-offset P_w arrivals are traced successfully. Testing with different single velocity values

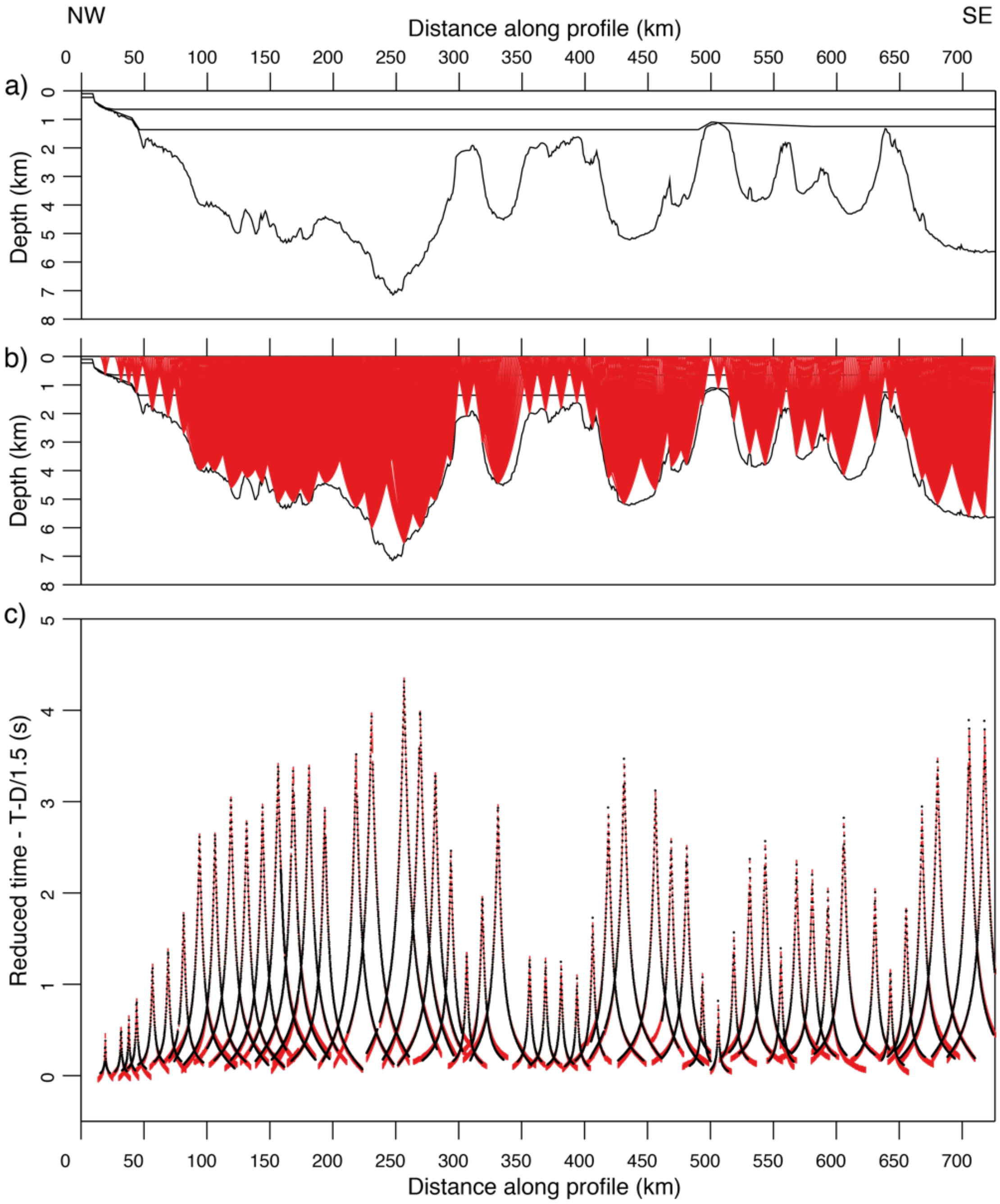

Figure 3.24: *RAYINVR ray-tracing output from built in plotting tools, for P_w arrivals. a) Water column model layers and bathymetry plotted as black lines. b) Locations of rays included in model during point-to-point ray-tracing. For clarity, only every 20th ray is plotted. c) P_w picked arrivals plotted as red bars, where bar height indicates the applied pick uncertainty. Black lines represent modelled arrivals calculated. Vertical axis is in reduced time, after application of a reducing velocity of 1.5 km s^{-1}, which is a typical average value for seawater velocity.*

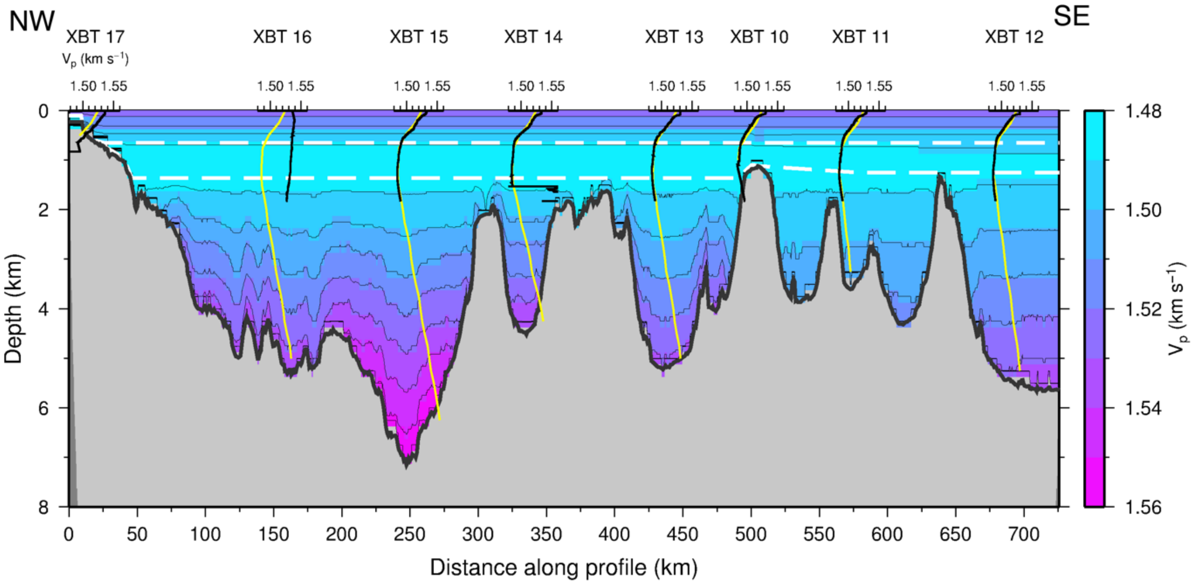

Figure 3.25: *Best-fit P-wave forward velocity-depth model for water column along Profile C. Contours drawn at 0.01 km s^{-1} (10 m s^{-1}) intervals. Sub-seabed shaded in light grey. Seabed marked as thick dark grey solid line. Dashed white lines are the locations of layer boundaries in the forward model (see Figs 3.23 and 3.24). XBT profiles plotted over velocity structure at each sampled location, with XBT cast numbers labelled. Black lines = XBT derived water column velocity. Yellow lines = 1-D vertical sample through velocity model at XBT sample location, taken to full water depth. Velocities are labelled in km s^{-1}.*

at the seabed resulted in variable fits, with a tendency for the modelled arrivals to be either too early or too late correlating with the water depth in which the instrument is located. This is not surprising since the P-wave velocity of seawater has a dependency on pressure. Overall, therefore, the generally good fit achieved between the observed and modelled travel time picks also shows that each OBS had been correctly relocated in terms of position along-profile and seabed depth.

3.6.2. Modelling of subsurface arrivals

Beneath the sediment layer, the initial model was configured with three layers representing the upper (basaltic), and lower (gabbroic) standard layer definitions of the oceanic crust (White et al., 1992) overlying a mantle layer. As modelling progressed it quickly became clear that it would be necessary to further divide these layers to improve the fit. Consequently, below the sediment layer the oceanic basement for each plate comprises three layers, with the upper and middle layer separated by a first-order velocity discontinuity (step in velocity), and the middle and lower crust separated by a second-order velocity discontinuity (change in gradient). The depth-velocity trade-off associated with second-order discontinuities is addressed during iterative forward modelling. however, it is the depth at which the velocity gradient change occurs at that the ray tracing process is sensitive to. Hence, the best fit occurs when both an appropriate velocity gradient and depth of gradient change are found. With increasing depth, the spacing for velocity and depth nodes increases, to 5 km in the upper parts of the crust, and to a maximum of 20 km at the Moho. These spacings were defined, using iterative forward modelling, to be the minimum necessary to adequately model lateral variability in structure within the errors, without use of an excessively large number of nodes. Figures 3.26-3.30 show the output from *RAYINVR* modelling of each arrival phase-type, and demonstrate the goodness of fit, excepting in the vicinity of the trench.

As modelling progressed, it became clear that the observed travel times could not be matched without introducing a representation of the downgoing plate. The SLAB1.0 global model (Hayes et al., 2012) was used to provide initial constraint on the location and dip of the plate boundary. This model was projected into the modelling space and the depth to the top of the slab sampled along Profile C, extending ~100 km to the northwest, beyond the end of the profile (Fig 3.31). These depths were used to define the subducting slab in the forward, extending from its shallowest depth (~8 km) downward. Why the SLAB1.0 was sampled beyond the northwest of the profile will be discussed in Chapter 4.

Figure 3.32 shows the *forward model* with the layer boundaries overlaid. The best-fitting *forward model* is based on a fit to a total of 60736 travel time picks and has an overall T_{rms} = 140 ms and $\chi^2 = 2.45$. The individual contributions of each phase to the overall fit are shown in Table 3.1 for the whole model, and Tables 3.2 and 3.3 for the separate plates.

In Chapter 4, this model will be rigorously tested to assess the error bounds which are present on the depths of and velocities at the model interfaces. This will inform the degree to which interpretations and inferences about model features can be made.

3.6.3. Ray coverage

Ray diagrams for selected OBSs are shown in Figures 3.3, 3.5-3.7, 3.9-3.10, 3.12 and 3.14-3.15, with the remainder provided in Appendix A. The *forward model* ray density

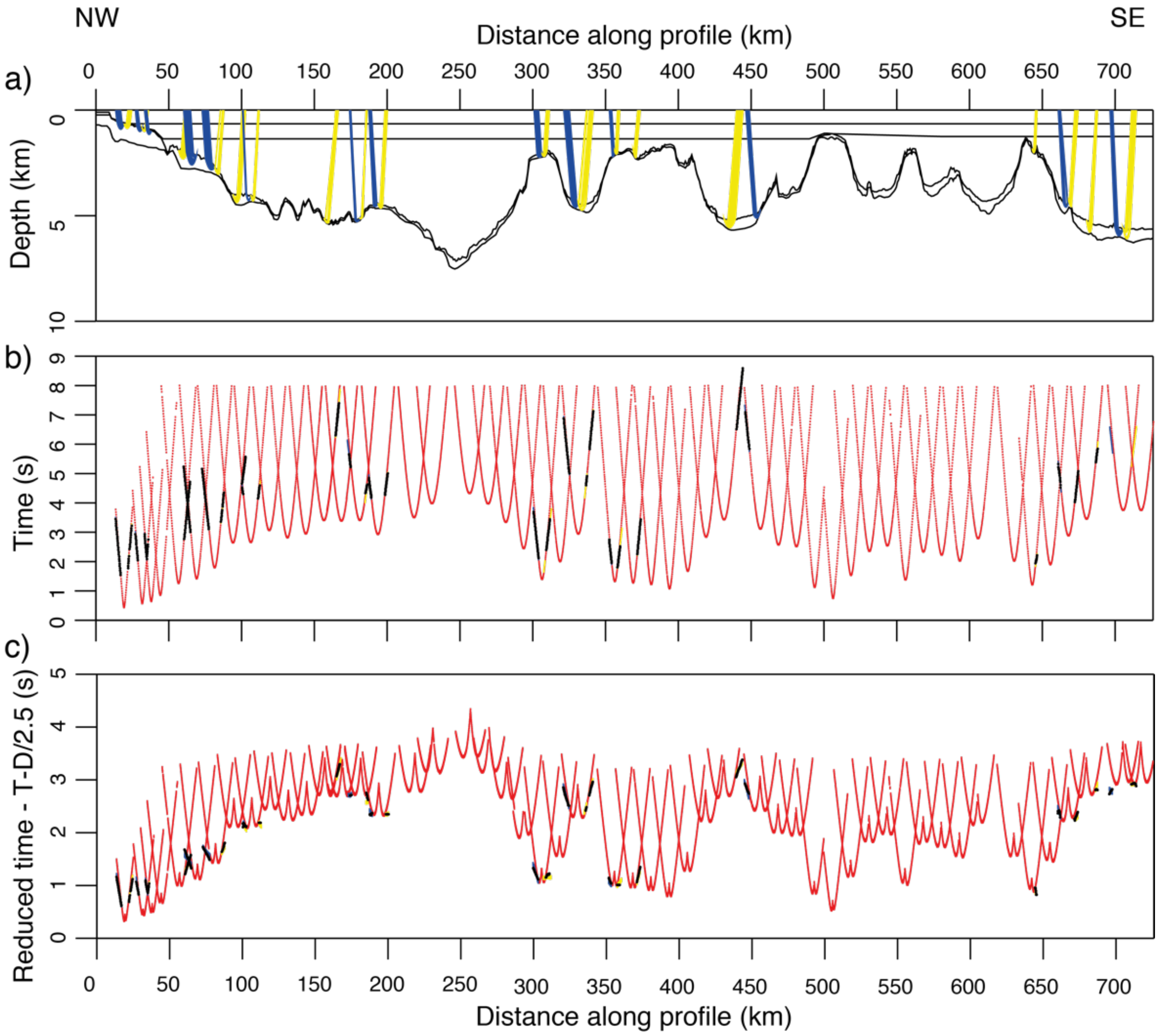

Figure 3.26: *RAYINVR ray-tracing output for P_s arrivals. a) Rays for point-to-point ray-tracing. Blue – P_s tracing towards left (northwest) of model; yellow – P_s tracing towards right (southeast) of model. Model layers are plotted as black lines, with only the water column, seabed and basement layer boundaries shown. b) P_s travel time picks plotted as coloured bars, where bar height indicates the pick uncertainty. Coloured as in a). Black lines represent modelled arrivals. P_w arrivals are shown in red to indicate instrument positions. c) As b) with picked and modelled travel times plotted in reduced time, with a reducing velocity of 2.5 km s^{-1} to match the phase type.*

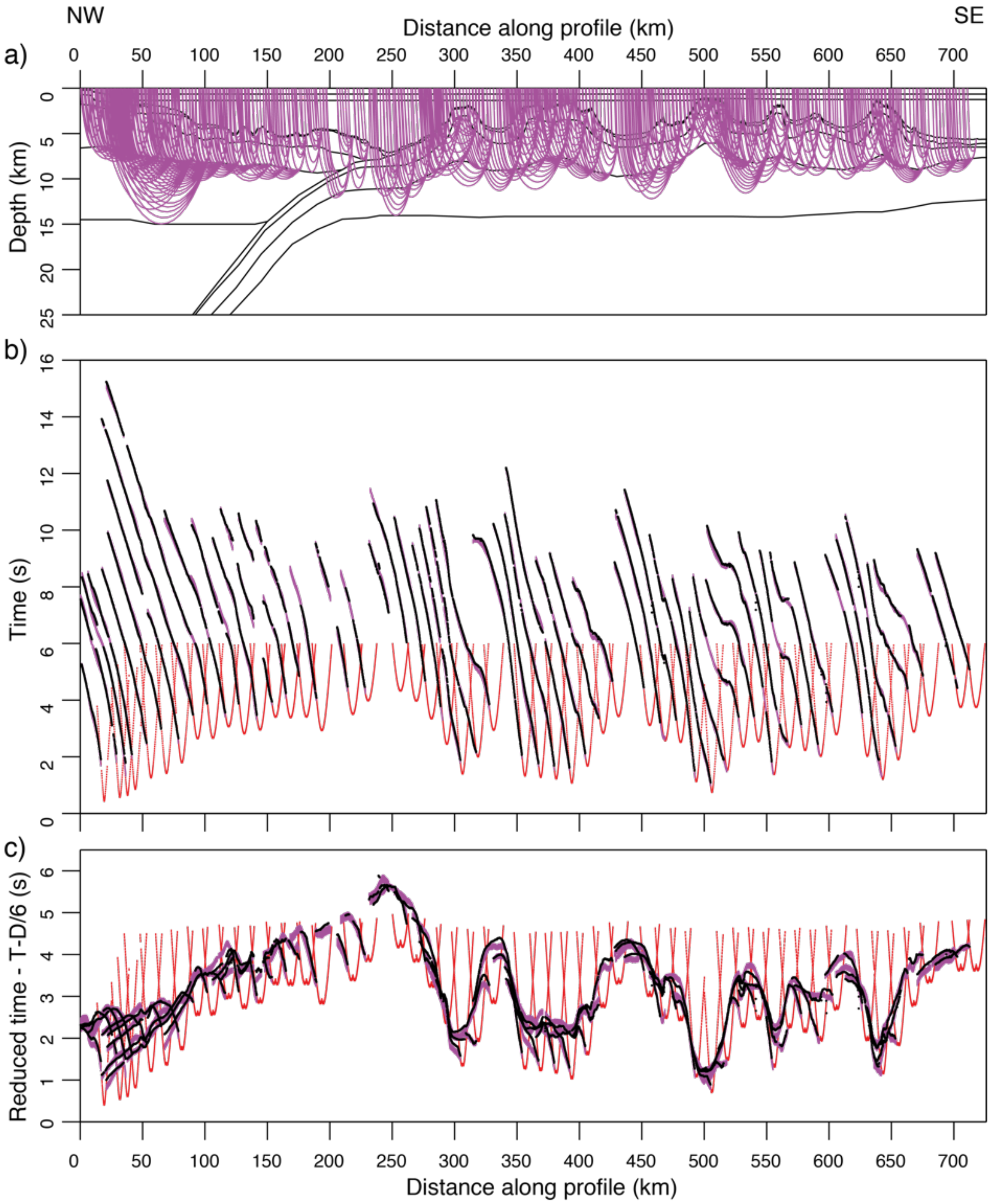

Figure 3.27: *RAYINVR ray-tracing output for $P_{g,1}$ arrivals, tracing towards the left (northwest) of model. a) Rays included for point-to-point ray-tracing, with only every 20th ray plotted for clarity. Model layers are plotted as black lines. b) $P_{g,1}$ travel time picks plotted as coloured bars, where bar height indicates the pick uncertainty. Coloured as in a). Black lines represent modelled arrivals. P_w arrivals are shown in red to indicate instrument positions. c) As b) with picked and modelled travel times plotted in reduced time, with a reducing velocity of 6 km s^{-1} to match the phase type. Note the variation in first-arrival travel time due to the variation in topography along-profile.*

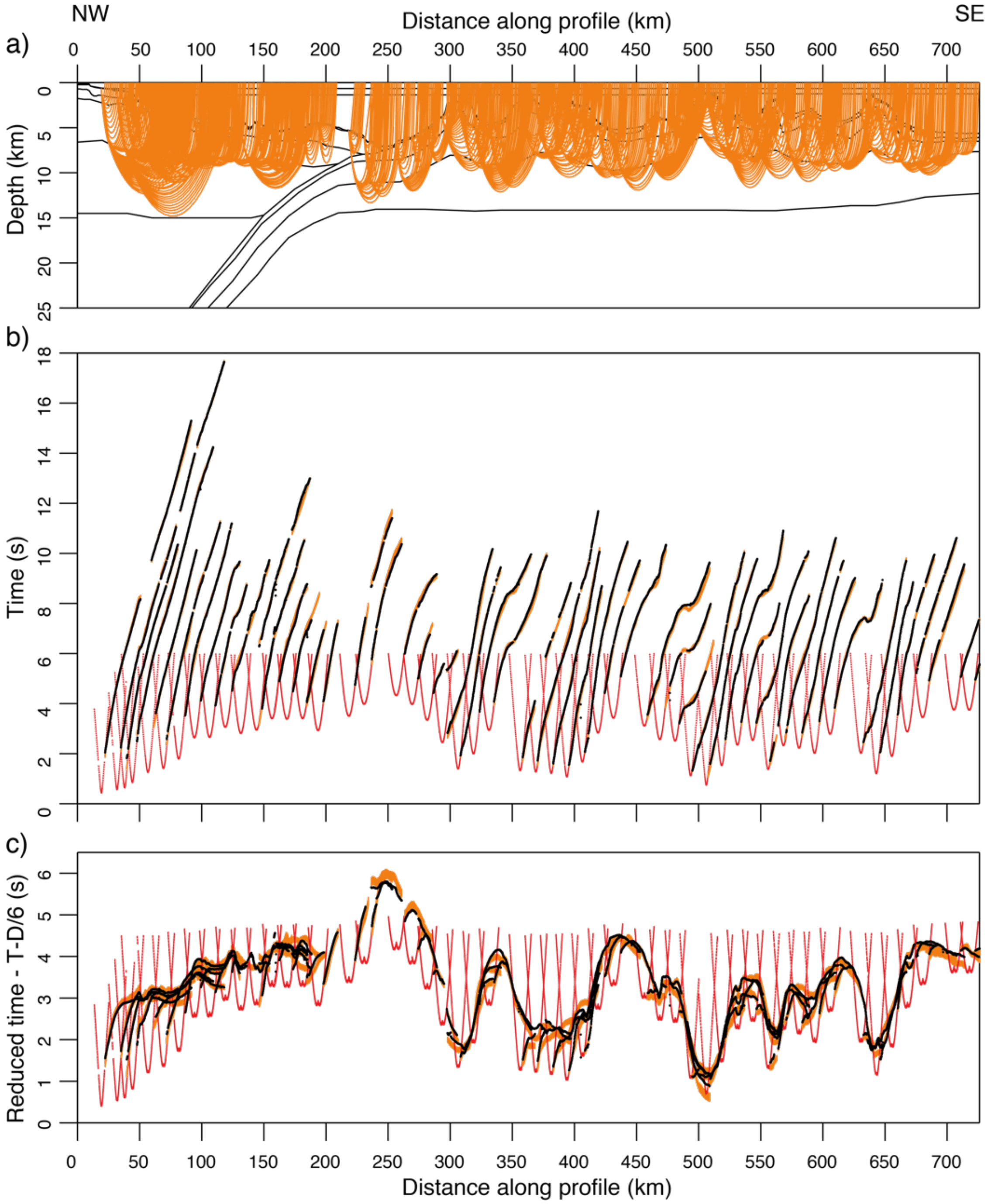

Figure 3.28: *RAYINVR ray-tracing output for $P_{g,r}$ arrivals, tracing towards the right (southeast) of model. a) Rays included for point-to-point ray-tracing, with only every 20^{th} ray plotted for clarity. Model layers are plotted as black lines. b) $P_{g,r}$ travel time picks plotted as coloured bars, where bar height indicates the pick uncertainty. Coloured as in a). Black lines represent modelled arrivals. P_w arrivals are shown in red to indicate instrument positions. c) As b) with picked and modelled travel times plotted in reduced time, with a reducing velocity of 6 km s^{-1} to match the phase type. Note the variation in first-arrival travel time due to the variation in topography along-profile.*

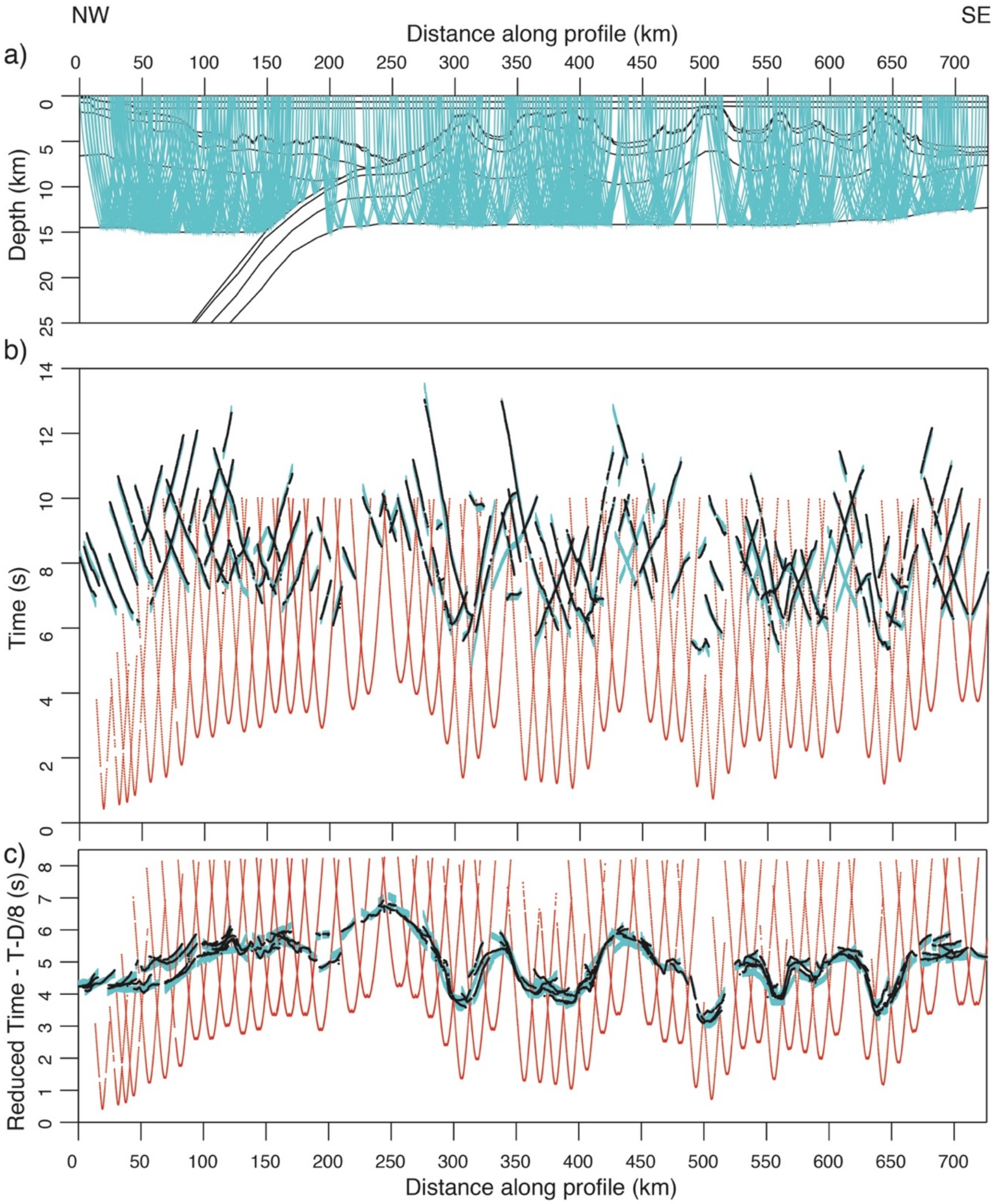

Figure 3.29: *RAYINVR ray-tracing output for P_mP arrivals. a) Rays included for point-to-point ray-tracing, with only every 20th ray plotted for clarity. Model layers are plotted as black lines. b) P_mP travel time picks plotted as coloured bars, where bar height indicates the pick uncertainty. Coloured as in a). Black lines represent modelled arrivals. P_w arrivals are shown in red to indicate instrument positions. c) As b) with picked and modelled travel times plotted in reduced time, with a reducing velocity of 8 km s^{-1} to match the phase type. Note the variation in first-arrival travel time due to the variation in topography along-profile.*

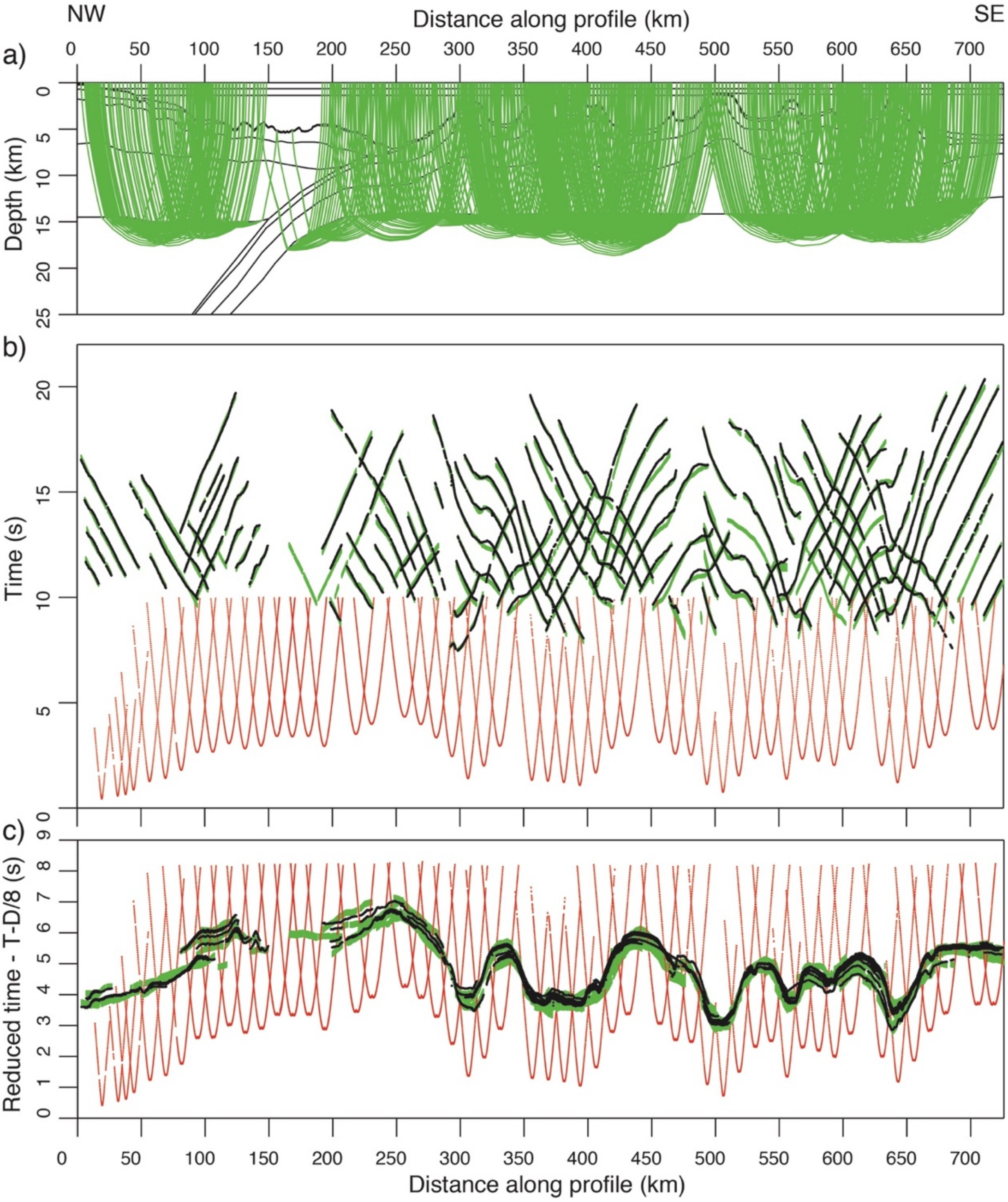

Figure 3.30: *RAYINVR ray-tracing output for P_n arrivals. a) Rays included for point-to-point ray-tracing, with only every 20th ray plotted for clarity. Model layers are plotted as black lines. b) P_n travel time picks plotted as coloured bars, where bar height indicates the pick uncertainty. Coloured as in a). Black lines represent modelled arrivals. P_w arrivals are shown in red to indicate instrument positions. c) As b) with picked and modelled travel times plotted in reduced time, with a reducing velocity of 8 km s^{-1} to match the phase type. Note the variation in first-arrival travel time due to the variation in topography along-profile.*

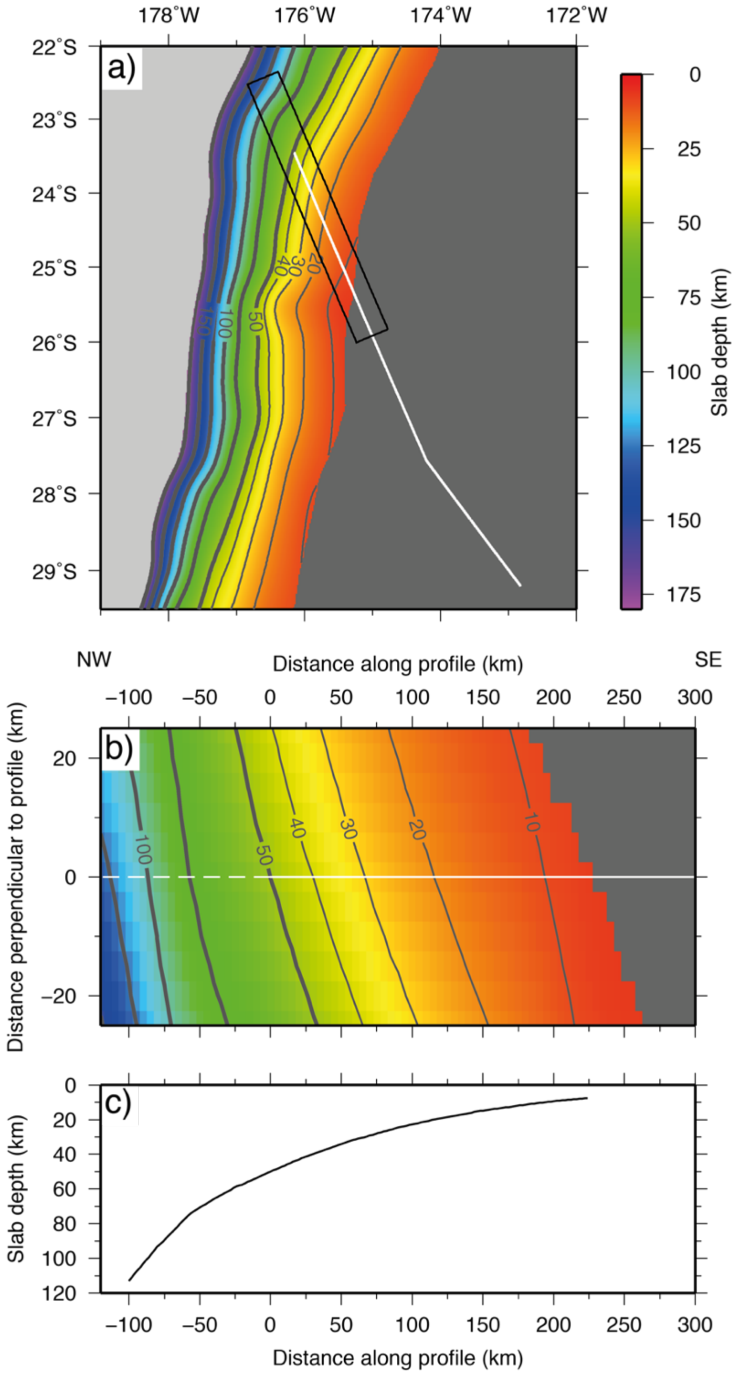

Figure 3.31: *Depth to subduction interface along the Tonga-Kermadec subduction system from SLAB1.0 (Hayes et al., 2012). a) SLAB1.0 model plotted for the study region. Dark and light grey backgrounds represent the model shallow and deep limits respectively. Thin contours are drawn at 10 km intervals between 0-40 km depth, and thick contours at 25 km intervals from 50 km depth. Profile C is plotted as a white line. Black box indicates the area shown in b). b) SLAB1.0 model projected into model space. Solid white line shows the position of Profile C, with the dotted white line the extension beyond the NW end of the profile which will be used in gravity modelling (see Section 4.5). c) Depth to subduction interface plotted against distance along profile.*

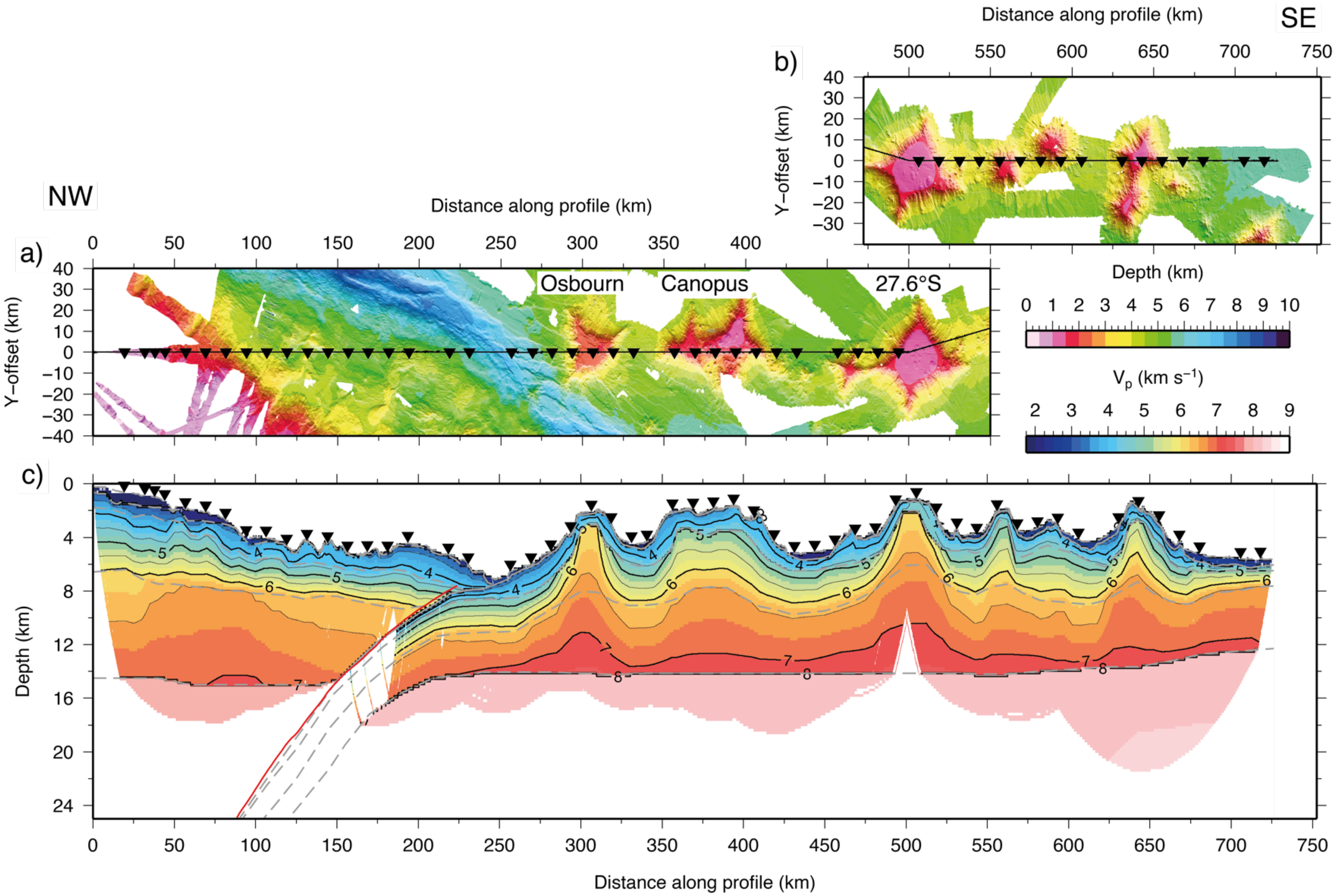

Figure 3.32: *Best-fit WA forward model and acquisition configuration. a) Bathymetry of the northern section of Profile C (forearc to 27.6˚S seamount), and b) southern section (27.6˚S seamount southwards), projected into kilometer-offset modelling space. In both cases, Profile C is oriented along y = 0, with shot locations marked by the solid black line. Relocated-onto-profile OBS positions are plotted as black inverted triangles. a) and b) are offset such that the bend in the profile is aligned c) Profile C best-fit P-wave velocity-depth forward model, masked to show ray coverage. Major velocity contours are annotated at 1 km s^{-1} intervals, and minor contours are drawn at 0.5 km s^{-1} intervals. Dashed grey lines are defined model layer boundaries. Solid red line represents the location of the subduction interface sampled from SLAB1.0 (Hayes et al., 2012).*

Phase	**Error (ms)**	**Number**	**T_{rms} (ms)**	**χ^2**
P_w	30	14621	32	1.11
$P_{s,l}$	40	270	80	4.03
$P_{s,r}$	40	336	43	1.18
$P_{g,l}$	70[1,2]	12694	109	2.37
$P_{g,r}$	70[1,2]	12369	117	2.63
P_mP	100[1,2]	11619	132	1.72
P_n	100[1,2]	23448	168	2.76
Crustal total (excl. P_w)		**60736**	**140**	**2.45**

Table 3.1: *Forward model ray-tracing statistics and fit parameters. Subscripts l and r for P_s and P_g phases indicate where these phase assignments have been split for the purposes of modelling. Notes: [1]OBSs C38-C43 have P_g travel time pick uncertainties of 100 ms and P_mP and P_n have uncertainties of 120 ms. [2]OBSs located close to the bend in Profile C have an additional travel time pick uncertainty applied to P_g and P_n selected having met the criteria outlined in Section 3.5.2.*

Phase	**Error (ms)**	**Number**	**T_{rms} (ms)**	**χ^2**
$P_{s,l}$	40	151	100	6.32
$P_{s,r}$	40	159	48	1.43
$P_{g,l}$	70[1]	5355	108	2.25
$P_{g,r}$	70[1]	4914	113	2.37
P_mP	100[1]	4465	125	1.50
P_n	100[1]	5314	132	1.67
Indo-Australian plate total		**20358**	**119**	**1.99**

Table 3.2: *Forward model ray-tracing statistics and fit parameters for the Indo-Australian plate. Note: [1]OBSs C38-C43 have P_g travel time pick uncertainties of 100 ms and P_mP and P_n have uncertainties of 120 ms.*

Phase	Error (ms)	Number	T_{rms} (ms)	χ^2
$P_{s,l}$	40	119	43	1.15
$P_{s,r}$	40	177	39	0.96
$P_{g,l}$	70[2]	8297	109	2.35
$P_{g,r}$	70[2]	7832	123	2.80
P_mP	100	7793	135	1.80
P_n	100[2]	19722	174	2.95
Pacific plate total		**43940**	**147**	**2.59**

Table 3.3: *Forward model ray-tracing statistics and fit parameters for Pacific plate. Note:* [2]*OBSs located close to the bend in Profile C have an additional travel time pick uncertainty applied to* P_g *and* P_n *selected having met the criteria outlined in Section 3.5.2.*

in 0.2 x 0.2 km sampled cells for $P_{g,l}$ and $P_{g,r}$, and P_mP and P_n phases are shown in Figures 3.33 and 3.34 respectively. A plot is not included for P_s arrivals given the limited sediment cover along-profile. The coverage of the entire *forward model*, is shown in Figure 3.35. The characteristics of the ray coverage for each of these ray groups will now be briefly described, and will later be considered with respect to their contributions to informing the reliability of model interpretation which will be made. For the individual phases, only qualitative descriptions will be made. However, for the coverage of the entire model, some quantitative measures will also be calculated.

3.6.3.1. P_g arrivals

P_g arrivals for the majority of instruments sample the lowermost crustal layer in the model (Fig. 3.33). Rarely do rays sample the base of this layer, except between 40-80 km model offset, beneath the lower part of the upper forearc slope, where the lower crust is modelled with a velocity >7 km s^{-1}. The upper and middle parts of the oceanic crust of the Pacific plate are well sampled, together with the interiors of the seamounts to at least the half of their total crustal thickness.

For the overriding plate, P_g ray coverage is good in both directions from each instrument between the start of the profile and ~100 km d.a.p., covering the upper forearc slope and the first part of the middle forearc. Ray coverage begins to decrease between 100-200 km d.a.p., as the trench is approached. Coverage is poor between

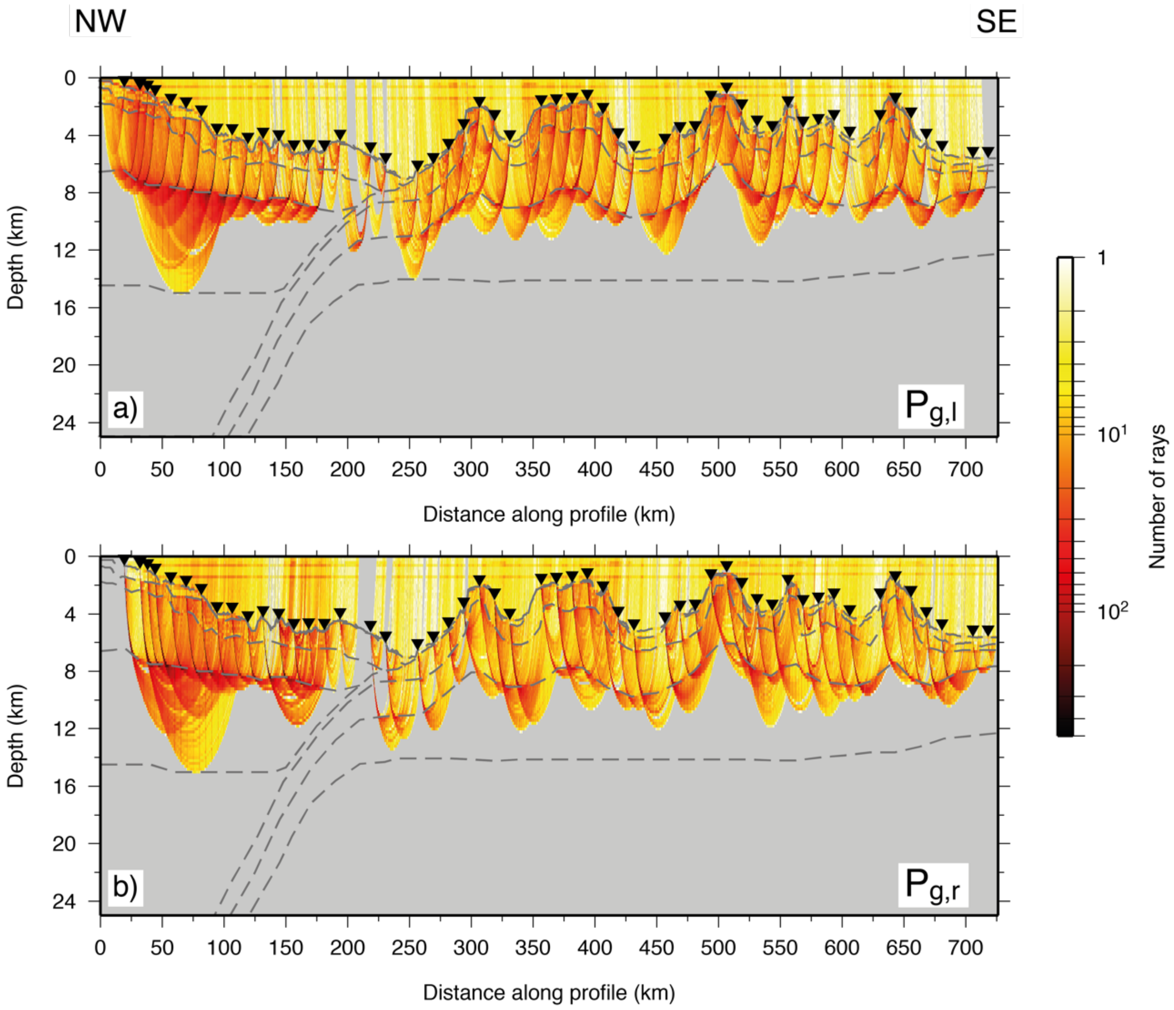

Figure 3.33: *Forward velocity model ray coverage for a)* $P_{g,l}$ *– refracted phases through the oceanic crust towards the left (northwest), and b)* $P_{g,r}$ *– refracted phases through the oceanic crust towards the right (southeast), plotted using a logarithmic colour scale, where dark colours indicate higher ray coverage. Grey areas indicate no coverage. The number of rays are counted in 0.2 x 0.2 km cells. Model layer boundaries are shown as grey dashed lines. Black inverted triangles indicate OBS locations along-profile.*

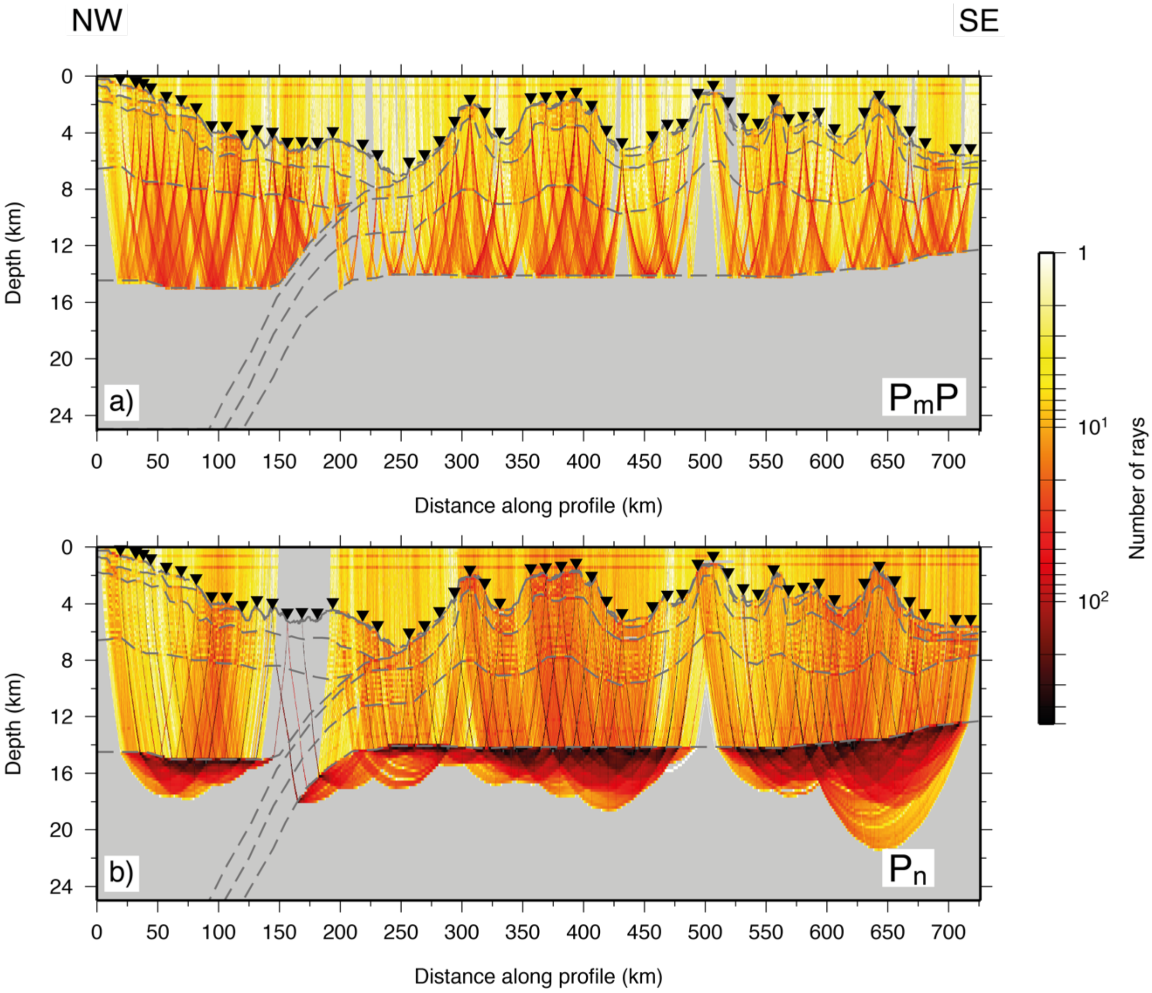

Figure 3.34: *Forward velocity model ray coverage for a) P_mP – reflected phases from the Moho, and b) P_n – refracting phases through the mantle, plotted as for Fig. 3.33.*

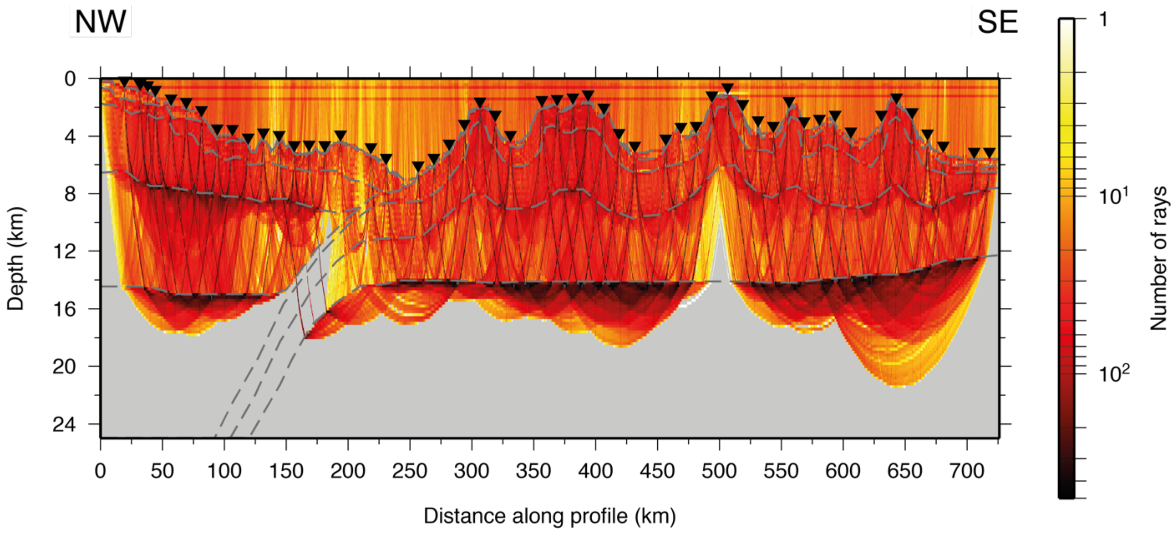

Figure 3.35: *Forward velocity model ray coverage for all 60736 reflected and refracted travel time picks used for modelling, plotted as for Fig 3.34.*

180-270 km d.a.p., in the vicinity of the trench axis, which can be attributed to the challenges of imaging in the complex environment of a subduction zone, where the deep water and complex geological structures will have a significant impact on signal propagation. Sampling of the Pacific plate beyond the trench axis by P_g rays is highly variable.

3.6.3.2. P_mP arrivals

P_mP coverage is variable throughout the model (Fig. 3.34a). Coverage is best beneath the overriding plate. For the first 100 km of the model, the crustal structure is generally simpler, and signal-to-noise higher, hence these arrivals are more easily identified. Closer to the trench, reflected phases from the base of the overriding plate where this represents the subduction interface are modelled and, thus, provide some constraint on the geometry of this feature. The Moho of the Pacific plate is not sampled along its entire model length, with 10-20 km-wide gaps, especially between Canopus (375 km d.a.p.) and 27.6˚S (500 km d.a.p.) seamounts. An ~40 km-wide gap is present centred at 500 km, beneath 27.6˚S seamount since P_mP travel times of arrivals from this region were excluded from the bend criteria assessment. At the southeasternmost end of the profile, P_mP coverage is good and helps to constrain the crustal thickness in the transition between the LRSC and the background Pacific plate.

3.6.3.3. P_n arrivals

P_n phases travel through the crust and into the uppermost mantle, and to the furthest offsets from the instruments, constraining the Moho along almost the entire model length (Fig. 3.34b). The limited penetration depth of ray coverage into the mantle (<18 km b.s.s.) likely arises as a result of changes in the seismic velocity and interface geometry at the Moho and the velocity gradient in the upper mantle. Throughout the Pacific plate, the coverage is generally even between 300 km d.a.p. and the southeasternmost end of the profile, with the exception of a gap beneath 27.6˚S seamount. This gap begins to appear as a region of reducing ray coverage at ~6 km depth, and is offset towards the north of the bend initially, as a result of it not being centred on the seamount summit (see Section 3.5.2). No rays are traced through a region between 8-9 km depth, and centred on the bend, as a result of these arrival travel time picks being excluded from modelling as they failed the bend criteria. At the Moho, this gap is 20-30 km in width. Trenchward of 300 km, P_n arrival ray coverage through the crust becomes patchier, although it does appear to be generally well sampled as far as 220 km d.a.p., ~30 km to the northeast of the trench axis.

P_n ray coverage of the crust of the overriding plate is generally poorer than the Pacific plate, despite the generally better SNR for instruments here. There is effectively no ray coverage through the crust between 140 km and 200 km, because there is no underlying Indo-Australian mantle. Instead, the subducting plate is located below the base of this crust, and for instruments on the Pacific plate there are insufficient P_n arrivals in the direction of the trench observed at appropriate offsets for this region to be well sampled.

3.6.3.4. Total ray coverage

The total ray coverage for the entire model, including the ~600 modelled sediment arrivals, is shown in Figure 3.35. Overall, the model appears to be well sampled by rays throughout, with the exception of the two regions of lower ray coverage which have already been described in relation to the P_mP and P_n phases (Fig. 3.34). Particularly dense ray coverage is achieved just below the middle-lower crustal layer interface, and just beneath the Moho. These represent the parts of the model at which the majority of P_g and P_n rays turn. These areas are also associated with reductions in the velocity gradient from the layer above to the layer below the boundary.

To assess the ray coverage quantitatively, the water column layer was ignored, and the number of ray hits per 0.2 x 0.2 km model cell counted for a series of constant depth slices (Fig. 3.36). Above 22 km, which is approximately the depth of maximum ray penetration, only 70% of the 0.2 x 0.2 km cells are sampled at all. However, above 18 km, the average depth of P_n ray coverage throughout the model, ray coverage reaches ~87%. Shallower than 14 km, which approximates the crustal part of the model, over 96% of cells have at least some ray coverage, with over one third of those containing more than 50 rays. Shallower than the middle crust (8 km) 98.8% of nodes contain at least a single ray, 96% contain 10 or more, and 75% contain 30 or more. Including only those cells where there is at least a single ray (Fig. 3.36 – dashed black line), i.e. ignoring any gaps in ray coverage, the median ray hit count is 40 (Fig. 3.36 – dotted grey line). However, fewer than 10% of cells contain more than 150 rays.

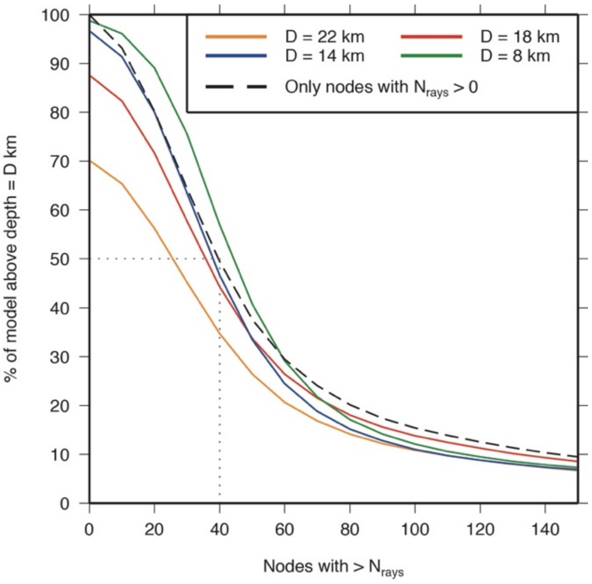

Figure 3.36: *Number of rays per 0.2 x 0.2 km cell of the forward model. Coloured lines represent constant depth slices above which the ray coverage is counted, excluding the water column layer. Colours correspond to values in the legend. Dashed black line is for cells which contain at least a single ray, so areas of no ray coverage are ignored. Dotted grey line indicates the median number of ray hits for all cells with* $N_{rays} > 0$.

3.6.4 Effect of ray selection at profile bend

In Section 3.5.2, the approach to selection of rays for inclusion in the ray-tracing across the bend in Profile C was described. Figure 3.37 shows the best-fit *forward model* in this region, where; a) all rays which have to pass across the bend are excluded, and b) only rays that fail the test criteria are excluded. Without including rays which cross the bend, the coverage gap extends from the seabed downwards reaching a width of ~30 km. Including the rays which pass the criteria test limits the gap to a maximum of ~15 km, starting just ~4 km above the Moho.

By comparing these models, it is possible to determine whether the additional ray coverage constrains any feature which may not have otherwise been imaged had this procedure not been followed. Fig. 3.37 suggests that there is unlikely to be any anomalous feature within the 27.6˚S seamount edifice that is not already well sampled but that the selective inclusion of the additional travel time picks does provide a more complete image of the crustal structure beneath this seamount. Modelling of these additional picks also gives confidence in the interpretation that the crust also does not thicken beneath this seamount either. The remaining coverage gap in the lower crust and upper mantle is not, therefore, a cause for concern.

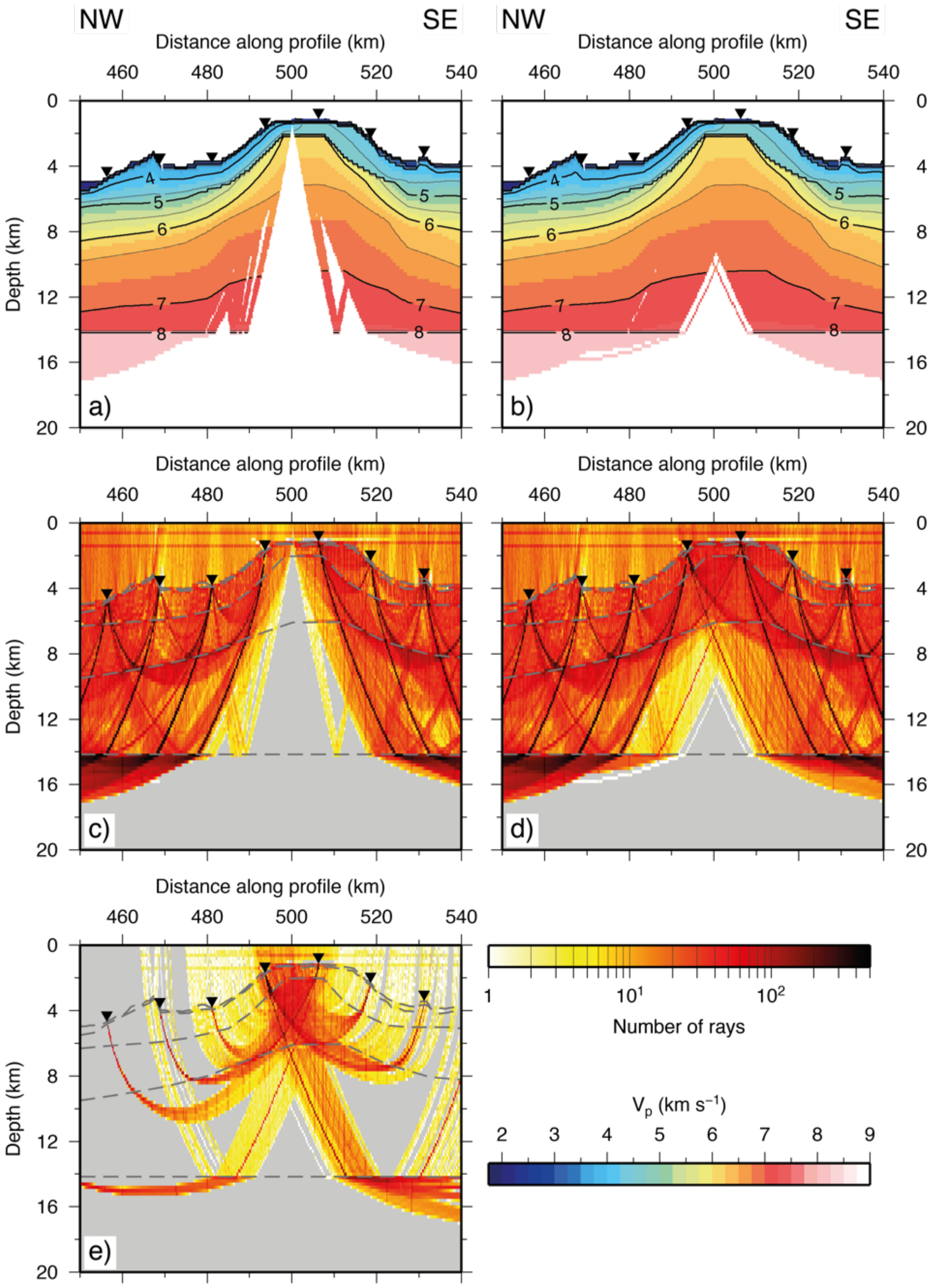

Figure 3.37: *Comparing the effects of ray selection at bend on model coverage. a) Coverage masked best-fit velocity-depth model for 27.6˚S seamount/Profile C bend region. Rays are only traced between shots and instruments located on the same side of the bend. b) Coverage masked best-fit velocity-depth model including additional rays which fit the criteria outlined in section 3.5.2. c) Ray coverage for a), where ray hits are counted in 0.2 x 0.2 km cells. d) Ray coverage for b). e) Difference in ray coverage between two sets of selected rays. Rays plotted in e) are those which are present in d), but not c). OBS locations plotted as inverted black triangles. Model layers plotted as dashed grey lines.*

By plotting the ray coverage for the most bend-proximal instruments, it is possible to identify where the improvement in sampling of the model structure occurs (Fig. 3.37c,d). The majority of the improvement in ray coverage appears to be provided by travel time picks from instruments C1-C3 and C19-C22, located ≤45 km from the bend, that constrain a region 20 km-wide beneath the seamount summit, down to a depth of 6 km b.s.s. (Fig. 3.37e). A total of ~7500 more rays were included in the best-fit model as a result of the ray-selection procedure. Additional ray coverage deeper than 6 km is provided by instruments located at >50 km from the bend, and results in a narrowing, by 8-10 km, of the coverage gap at the Moho, although the actual ray coverage either side of the gap is not particularly high.

3.7. Preliminary interpretation of model features

A full description and interpretation of the best-fit *forward model* will be presented in Chapter 5, once robustness, sensitivity and uniqueness testing has been undertaken in Chapter 4. However, by identifying key structures that appear in the *forward model* at this stage, the model testing can be appropriately designed and set in the context of the primary goals of this research.

A notable feature of the *forward model*, is that the internal velocity structure of the Louisville Ridge seamounts appears to vary along-strike. Comparison with the bathymetry along-profile suggests that this may be governed by where the profile crosses each seamount. Osbourn and 27.6°S seamounts, located at 280-325 km and 480-525 km d.a.p. respectively, display seismic velocities of ≥6 km s^{-1} at relatively shallow levels within the volcanic edifice (Fig. 3.32). Indeed, the 6 km s^{-1} contour within these seamounts shallows above the depth of the seabed at the southeasternmost end of the profile. However, Canopus seamount, located between 345-420 km d.a.p., and not clearly crossed directly over its summits, does not show a similarly high-velocity internal core.

The *forward model* does not indicate the presence of significant downward-focused crustal thickening beneath the LRSC. The Moho appears to deepen by ~2 km beneath the LRSC, however this could be a result of flexure due to the loading of the plate by the seamounts. In addition, there does not appear to be any evidence of, for example, a magmatic underplate, and instead, beneath the seamount chain the Moho appears to be best represented as a flat interface.

There is no compelling evidence for a subducted seamount in the trench, or along the continuation of Profile C beneath the forearc. However, identification of trench features will inevitably be controlled by model resolution which will be discussed in the following chapter. Resolution testing will seek to determine if the lack of an obvious seamount-like structure in this part of the model is a true observation, or whether it is a function of the dataset and/or modelling technique used in this study, limiting the spatial and/or velocity resolution rendering such seamounts beyond the imaging limits.

The upper and middle crustal velocity structure of the overriding plate appears to be relatively homogeneous along the length of the model. In the upper crustal layer of the lower forearc there is evidence of a reduction in P-wave velocity, which may be associated with the thickening and uplift of this layer. However, given that this part of the model has the most limited model ray coverage, the significance of this requires further investigation.

In the lower crust, there appears to be a feature which displays elevated velocities of >7 km s^{-1}. Due to the oblique direction (40° between the trench axis and profile strike) in which Profile C crosses the subduction zone, the features seen in this part of the model are visually distorted and must be considered in terms of their distance perpendicular to the trench.

3.8. Summary

In this chapter, the WA seismic data along Profile C has been forward ray-trace modelled to produce a velocity-depth model for the crust and uppermost mantle of the Louisville Ridge Seamount Chain, and adjacent Tonga forearc that best fits the observed travel time picks to within their pick uncertainties. This has been achieved through the application of a user-driven, iterative, forward modelling method, utilising the travel time modelling code *RAYINVR* (Zelt and Smith, 1992) as described in Section 3.5.

Due to the specific geometry of the study targets, and hence the variation in the trend of the data acquisition profile, a significant portion of this chapter has been concerned with addressing how this affects the approach to (Section 3.5.2) and results of (Section 3.6.4) modelling.

Preliminary interpretation of the resulting *forward model* (Section 3.7) indicates the presence of a number of features of interest. Most striking of these is the observation that the internal seismic velocity structure of the Louisville seamounts does not appear to be consistent along the profile, and that this inconsistency mirrors where seamount summits are traversed over their centres and where they are not.

Prior to the full interpretation and discussion of the modelling results presented in this chapter, rigorous model testing will be applied and discussed in the following chapter. This testing will seek to determine if more features are geologically valid and a unique solution of the travel time picks, and will be achieved by the use of an alternative modelling approach and an independent dataset. In addition, a thorough assessment of the error bounds associated with the layer boundaries and velocities of the *forward model* will be undertaken, which will determine the degree of confidence to which the model can interpreted.

Chapter 4 – Forward Model Testing and Verification

4.1. Introduction

In Chapter 3, a best-fit crustal velocity-depth model (the *forward model*) was developed based on the Profile C WA seismic data by applying an iterative ray-tracing approach. To assess the uniqueness and robustness of this model in order to determine the degree to which interpretations can be made, it was necessary to apply a series of rigorous testing procedures. The principal goals of these tests were to demonstrate whether the model was free of inherent modeller bias, to assess its uniqueness in producing a fit of calculated to observed travel times, and, finally, to determine how well the structural features and velocity anomalies are resolved. These tests and their outcomes will be discussed in this chapter.

An inverse modelling approach will first be applied to the WA seismic travel time picks (Section 4.2). The recovered crustal velocity structure (hereafter referred to as the *inverse model*) will then be appraised for similarity to that of the *forward model*, having applied as little user input to the inversion as possible. If similar results for the same travel time picks are achieved using two different and independent modelling approaches, this will confirm degree of uniqueness of the *forward model*. Further independent support for the uniqueness of the *forward model* solution will be appraised by converting this velocity-depth structure to a density-depth model (henceforth referred to as the *density model*) and calculating the associated free-air gravity anomaly (FAA), and comparing that to the observed shipboard measured FAA (Section 4.5). This approach will also allow testing and verification of aspects of the *forward model* which are not necessarily well constrained by the WA seismic data.

In order to robustly interpret model features, it is also necessary to understand the limits that both the dataset and modelling techniques used place on the imaging capability. Firstly, checkerboard testing will be applied to the *inverse model* to determine where it is well resolved, and what scale of feature and velocity anomaly are distinguishable with confidence (Section 4.3). Secondly, by progressively perturbing the values assigned to depths and velocities along model layer interfaces, the *forward model* will be used to determine their error bounds, by determining how much variability is possible before the modelled travel times no longer fit the observations within acceptable limits (Section 4.4). This information will then be used to guide the degree to which interpretations can be made when all of the modelling results are collectively described in detail in Chapter 5.

4.2. Inverse modelling

There were two principal motivations behind the application of an inverse modelling technique to the Profile C WA seismic data. Firstly, it attempted to ascertain if the results obtained from forward modelling are free of modeller bias. The second, related, purpose was to demonstrate the uniqueness of the *forward model* solution. If inverse modelling produced a similar result to the forward modelling approach, this would indicate that a unique solution to the dataset had, most likely, been found. However, if the inversion reached a fit with a structure very different to that of the *forward model*, but was geologically feasible given the tectonic setting, it would indicate that multiple potential models exist, and that the *forward model* is just one of them. Hence, the *forward model* would be deemed to be non-unique, and further investigation would be warranted.

4.2.1. Principles of inverse modelling

Inverse modelling of the WA seismic data was conducted using *FAST* (*First Arrival Seismic Tomography* – Zelt and Barton, 1998). This method applies a regularized inversion approach to fitting modelled and observed travel times, allowing the user to specify the trade-off between using smallest, flattest, and/or smoothest perturbation constraints to achieve a good fit.

Within each inversion, a nested set of iterations are performed over varying values of the trade-off parameter, λ. These begin with an initial value, λ_0, and reduce by a factor of 1.414 (~$\sqrt{2}$) after each iteration, until the current λ fails to produce a better fit than the previous value. When this occurs, the best-fitting model is recorded as the optimum model for that iteration, and used as the input for the next iterative cycle. This parameter's role is to govern the balance between the fit of the data and the structure of the model. Inversion seeks to reach a final model that only includes the structure necessary to achieve a fit to within the uncertainty, and no more (Scales et al., 1990). This is referred to as a 'minimum structure' model and is characterised by a low model roughness, which is calculated as the second spatial derivative of the model.

The *FAST* inversion procedure is designed to iterate towards a model with a fit of $\chi^2 = 1$, and not to over fit data. If $\chi^2 = 1$ is reached, then the model is 'relaxed' by increasing λ to find the largest value of this that produces $\chi^2 = 1$. The number of iterations during inversion can, therefore, be set relatively large, with the only negative impact being on run-time.

A number of parameters are used to control the way in which the best-fit model is achieved. The principal among these are:

- s_z – a smoothing parameter, which determines the relative importance of maintaining vertical versus horizontal smoothness;
- α – a trade-off parameter, which selects the relative weighting between fitting smallest versus smoothest (or flattest) perturbation constraint equations; and
- s_{edge} – a parameter which controls the constraints which are applied to the cells at the edge of the model, which may be necessary to prevent edge effects that arise due to smoothing from the interior of the model, where there is ray coverage, to the edges, where there is none.

The objective function H, minimized at each iteration by varying the trade-off parameter, λ, is given by Zelt (1998) as

$$\mathrm{H(m)} = \ \mathrm{dtTC_d^{-1}dt} + \lambda(\mathrm{mTC_h^{-1}\,m} + \ \mathrm{s_z C_v^{-1} m})$$

where $\mathrm{dtTC_d^{-1}dt}$ and $\mathrm{mTC_h^{-1}\,m + s_z C_v^{-1} m}$ measure the data misfit and model roughness respectively. Within these terms, m signifies the model vector, dt the traveltime residual vector, C_d the data covariance matrix containing the pick uncertainties, and C_h and C_v the horizontal and vertical roughness matrices. s_z is the smoothing parameter, defined above, which determines the relative importance of maintaining vertical versus horizontal model smoothness.

In addition, the *inverse model* is padded with cells to the left and right (northwest and southeast in geographic terms) of where shots were fired. Primarily, this prevents rays hitting the sides of the model and terminating, and minimises edge effects. By moving the model edges away from the limits of the ray coverage, it also provides a buffer zone over which smoothing can be accommodated without affecting the result.

Throughout the inversion procedure, the bathymetry is defined as an interface, above which the velocity is reset to the values in the starting model between each iteration. This preserves the water column velocity structure throughout the inversion procedure, and prevents upward leaking of crustal velocities above the seabed.

4.2.2. Starting model

The results of inverse modelling are highly sensitive to structures contained within the input velocity model. A number of initial models were tested for suitability, which can broadly be divided into three groups, examples of which are shown in Figure 4.1. The first group comprised models that had a constant depth to an indicative base of crust. Velocity contours initially follow the bathymetry, but become progressively flatter with depth, until they are totally flat at the defined depth of the indicative crustal base (Fig. 4.1a). The second group displayed a constant initial crustal thickness throughout. All the velocity contours above that indicative of the base of crust follow the bathymetry (Fig. 4.1b). The third group is a combination of these two, having an upper layer of initial constant thickness, and a lower layer which has a constant maximum depth (Fig. 4.1c,d).

Each of the different groups of initial model, with a range of thickness and upper and lower velocity bounds, was run through an inversion starting point test procedure. Those which failed to produce any change from the starting model, and those where the results became dominated by rapid lateral and/or vertical variations or instabilities, were rejected. The optimum starting model was that which, with limited variation of other inversion parameters, produced a result which had a first-pass visual similarity to the *forward model*, but which underwent sufficient changes during the iterative inversion process such that the input and output models were not overtly similar.

The selected starting model was of the latter, hybrid group identified above, parameterised on a 0.2 x 0.2 km uniform square grid. The upper layer has a constant thickness, with a velocity of 2.5 km s^{-1} at the seabed, increasing to 6.0 km s^{-1} at 1.5 km b.s.s.. The velocity then increases to 7.5 km s^{-1} at 16 km b.s.s. (Fig. 4.1d). Below 16 km b.s.s., the velocity is assigned an initial value of 7.5 km s^{-1}. At 22 km b.s.s., the

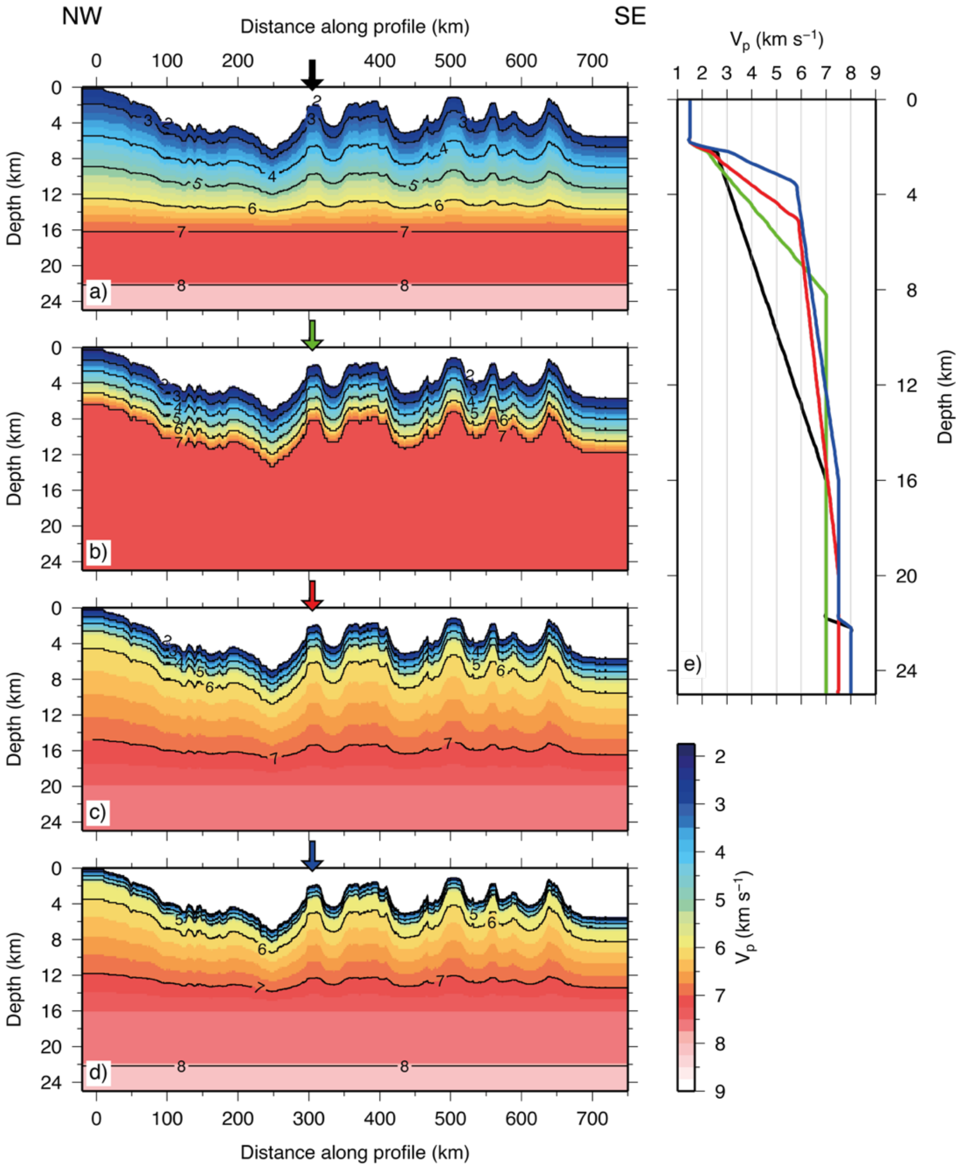

Figure 4.1: *Example starting models for inversion illustrating different general groups. a) Constant depth to indicative base of crust at 16 km b.s.s., with single velocity gradient between seabed and base of crust. b) Constant total crustal thickness of 6 km, draped below bathymetry. c) Hybrid model with a constant 2.5 km-thick upper layer, and linear vertical velocity gradient between 2.5 km s^{-1} and 6.0 km s^{-1} along profile. Lower layer with linearly interpolated velocity between that of the base of upper layer and 7.5 km s^{-1} at 20 km b.s.s.. d) As for c) with higher velocity gradients. 1.5 km-thick upper layer, with linear velocity gradient between 2.5 km s^{-1} and 6.0 km s^{-1}. Base of lower layer has a velocity of 7.5 km s^{-1}, set at 16 km b.s.s.. Below this, the velocity is set at 8 km s^{-1} at 22 km b.s.s. to prevent upward leaking of high velocity artefacts. Coloured arrows in a-d) indicate locations at which velocity-depth profiles are sampled in e). e) Velocity-depth profiles from models a-d), with colours corresponding to arrows at 305 km d.a.p., directly over the summit of Osbourn seamount.*

maximum depth of any turning rays in the *forward model*, the velocity is fixed at 8.0 km s^{-1} throughout inversion modelling to prevent smearing upwards of high velocity regions.

4.2.3. Inverse model parameterisation

Tests were performed to determine the optimal values of the required input parameters which govern the trade-off between fitting and smoothing. Testing of a range of s_z and α values indicated a relative insensitivity to changes in these within ±0.1 of the recommended values suggested by Zelt and Barton (1998). The values assigned were, therefore, $s_z = 0.95$, and $\alpha = 0.125$.

Performing tests with a large value for λ_0, of 500, failed to produce either a good quantitative ($\chi^2 \approx 5.00$) or visual fit. For example, it failed to produce a feature which could be interpreted as trench-like. A better visual fit was achieved with λ_0 values between 100 and 200, with values less than 100 rejected because the iteration process failed to progressively reduce λ over each subsequent cycle. The optimum value of λ_0 was found to be 100.

Testing also indicated that it was not necessary to bound the degree to which velocities could change between iterations. It is likely that this arises as a result of the inclusion of the fixed velocity at 22 km b.s.s., which limits the absolute velocity values and velocity gradients which can result by preventing upward smear artefacts. Otherwise, in order to provide the least biased starting model parameterisation, the model was allowed the freedom to update velocities as necessary.

Once the starting point was determined, the inversion procedure was run over two different inversion cell sizes. The first cell size was set to 8 x 3 km (horizontal x vertical), and had eight iterations which produced the longer wavelength model features. The second inversion cell size was set to 4 x 2 km, with five iterations, and refined more detailed features.

4.2.4. Inverse modelling results

A total of 49779 travel time picks were used in the inversion modelling process. The resulting final *inverse model* has a T_{rms} = 129 ms, and $\chi^2 = 2.29$ (Fig. 4.2a,b). Changes in the value of χ^2 over subsequent iterative cycles (Fig. 4.3) show that the greatest improvements to fit occur during the first two iterations. The fit decreases from $\chi^2 =$

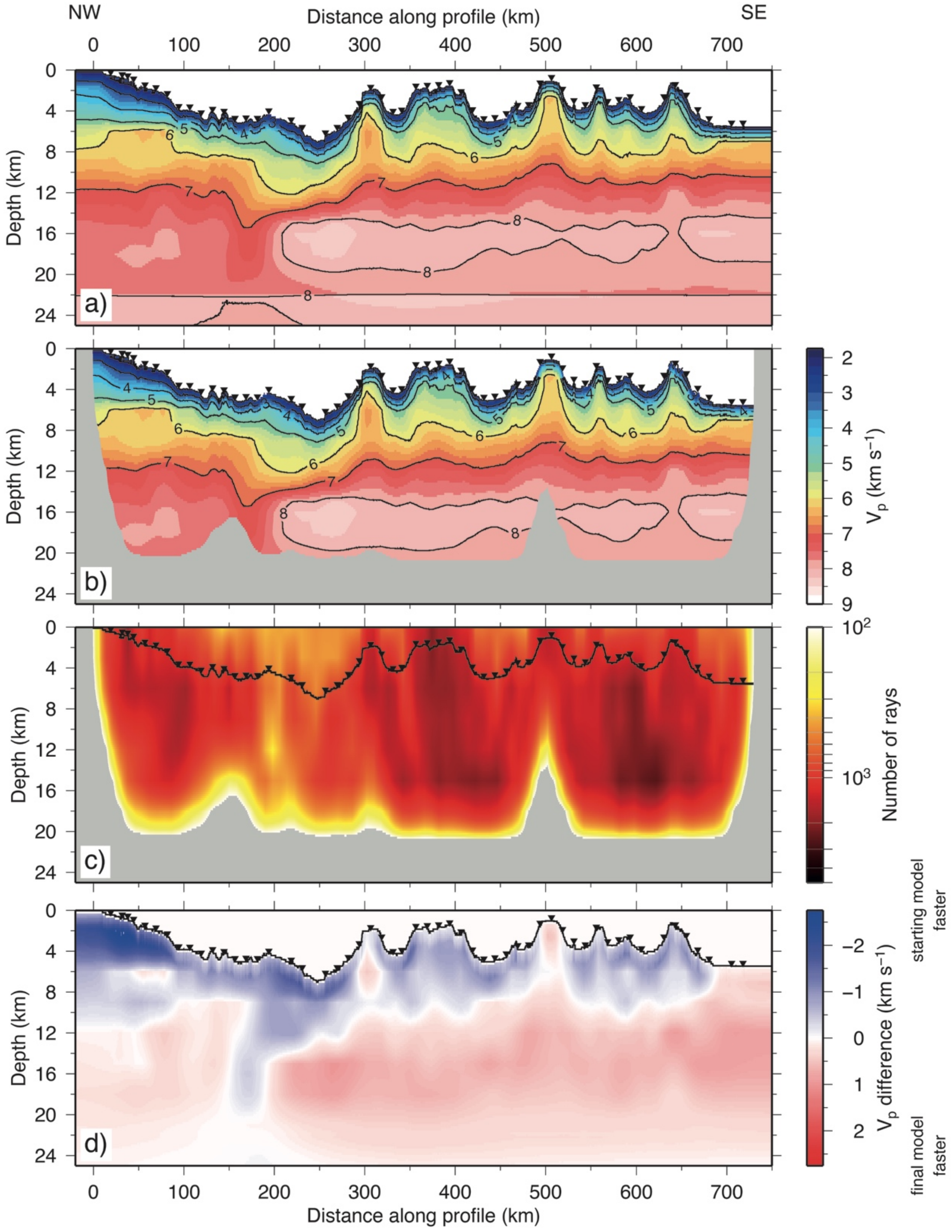

Figure 4.2: *Inversion modelling results. a) Best-fit inverse model, with* T_{rms} *= 129 ms and* χ^2 *= 2.424. Whole model is plotted, regardless of whether the area is sampled by rays or not. b) As for a), with masking to show only those areas which are sampled by rays. c) Ray coverage used for generating the mask for b), plotted using a logarithmic colour scale. Black line indicates location of the seabed. d) Difference between starting and final models. Blue indicates that the starting model has a higher and red a lower velocity than the final model. OBS locations shown by inverted triangles.*

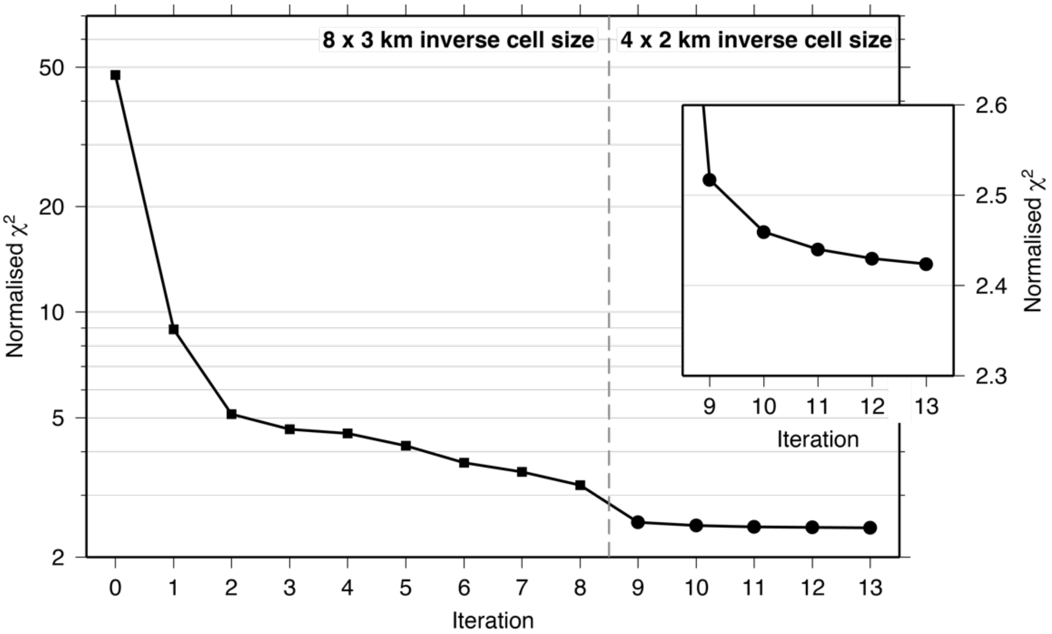

Figure 4.3: *Graph of improving χ^2 value with each iteration during inversion procedure. χ^2 values plotted using a logarithmic scale. Dashed vertical grey line indicates the point at which the inverse cell size changes from 8 x 3 km for iterations 1-8 to 4 x 2 km for iterations 9-13. Value at iteration 0 represents starting model. Inset: Values of χ^2 for iterations 9-13 plotted using a linear vertical scale, showing the rapid improvement achieved during the initial iterations at each inverse cell size as a result of adopting a two phased inversion procedure.*

47.5 for the starting model (Fig. 4.4a), to $\chi^2 = 8.9$ after the first iteration (Fig. 4.4b), and $\chi^2 = 5.1$ following the second iteration.

Between the starting model and result of the first iteration, there are three significant changes to the model. Firstly, the upper crustal velocity of the upper forearc region, between 0-100 km d.a.p., reduces by ≥1 km s^{-1}. The 6 km s^{-1} contour in this region deepens by > 4 km, and less clearly follows the bathymetry as far as the trench. Between the middle forearc and the trench (100-250 km d.a.p.) the upper-to-middle crustal velocity also decreases by ~0.5 km s^{-1}. Within the seamounts of the LRSC, the upper crustal velocity also appears to decrease. This is most noticeable for Canopus seamount (~375 km d.a.p.), and the flank-crossed seamounts to the southeast of the bend, where the 6 km s^{-1} contour deepens by ~2 km. Changes are less noticeable, but still present within Osbourn and 27.6˚S seamounts. The third major change is the

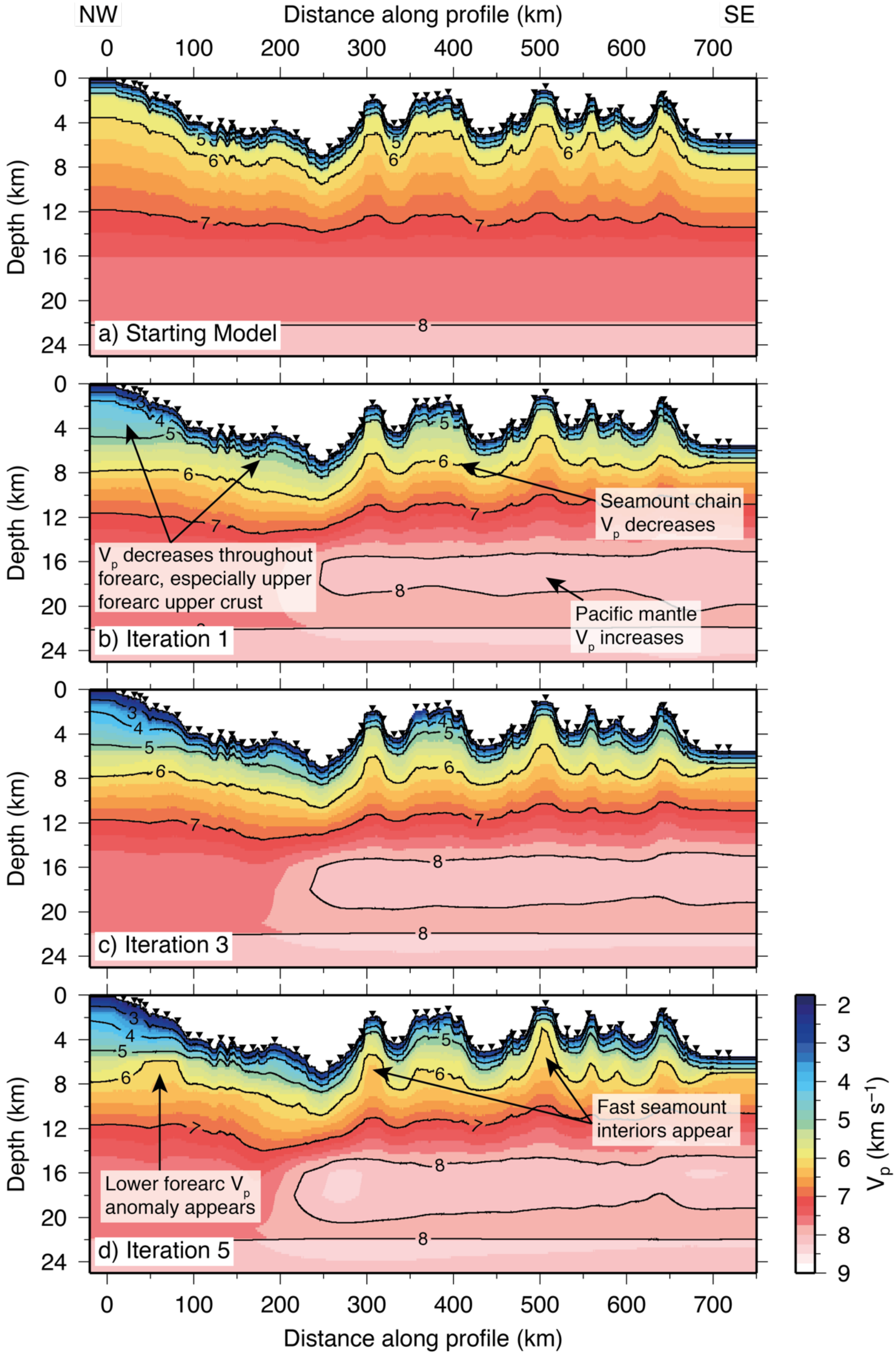

Figure 4.4: *Intermediate inversion modelling steps, showing development of model structures with number of iterations. a) Starting model. b) After 1 iteration at 8 x 3 km inverse cell size. c) and d) As for b) after three and five iterations respectively. OBS locations shown by inverted triangles.*

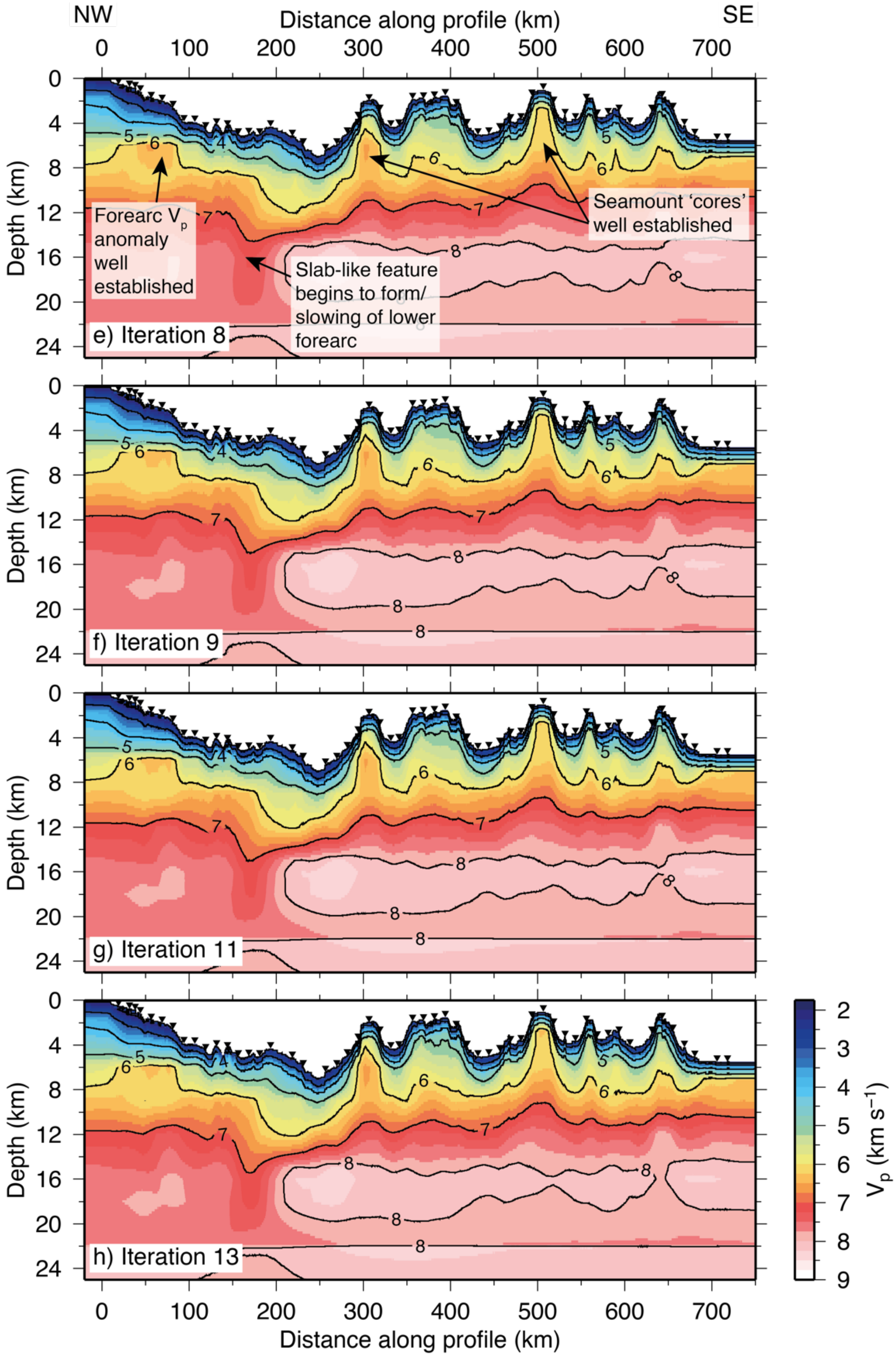

Figure 4.4 cont.: *e) After eight iterations, the final model achieved for the 8 x 3 km inverse cell size, used at the starting point for the five iterations at 4 x 2 km cell size. The models resulting from the first (f), third (g) and final (h) iteration at 4 x 2 km inverse cell size. Note how this second stage of the inversion adds the smaller scale features into the inverse model. OBS locations shown by inverted triangles.*

development of a ≥8 km s^{-1} region between 15-19 km b.s.s., from 230 km d.a.p. towards the southeast.

Following the first two iterations, the fit continues to improve slowly during the remaining iterations at the larger inverse cell size. By the completion of the fifth iteration (Fig. 4.4d), further velocity reduction is observed to have occurred in the upper forearc, with the 4 km s^{-1} contour now reaching depths of 2-4 km b.s.s.. In the mid-to-lower crust of the forearc, between ~40-80 km d.a.p., a 2 km shallowing of the 6 km s^{-1} P-wave velocity contour begins to appear. Within the seamount chain, the velocity within Canopus seamount also continues to decrease, particularly so at shallower depths. Within Osbourn and 27.6˚S seamounts, the initial reduction in velocity relative to the starting model is reversed, with the 6 km s^{-1} contour shallowing to ~5.5 and ~3.0 km b.s.s. respectively. Between the fifth and eighth iterations (Fig. 4.4e) χ^2 continues to decrease from 4.2 to 3.2, accommodated principally by enhanced definition of features which started to appear in iteration 5, alongside the development of a sub-vertical, reduced velocity divide between the Pacific (≥8 km s^{-1}) and Indo-Australian (<7.8 km s^{-1}) mantles. This feature is effectively the representation of the subducting slab in the *inverse model*. A discussion of why this is the limit to which this feature can be imaged using the inversion technique employed in this study will be provided in Section 4.2.5.

Following reduction of the inversion cell size to 4 x 2 km, there is an immediate improvement in fit to a χ^2 of 2.5. The remaining iterations at the smaller inversion cell size continue to improve the quantitative model fit to a minor degree (<0.01 decrements in χ^2) until the final iteration. It is not possible to readily distinguish the changes between different iterations visually at this stage (Fig. 4.4f-h).

Comparing the final and starting models, it can be seen that the inversion process both increases and decreases the velocity in parts of the model (Fig. 4.2d). The interiors of Osbourn and 27.6˚S seamounts both display higher velocity relative to the starting model, whilst Canopus and the smaller seamounts to the south of 27.6˚S, which are only crossed over their flanks, show decreases. The largest difference between the starting and final models is observed in the uppermost forearc, where the resulting velocities are lower by >2 km s^{-1} in some parts. The observed changes to the initial velocity structure support the conclusion that the *inverse model* parameterisation is free from preconceived bias. While the starting model does appear to be one of the key controls on the success of an inversion it does not appear to have a significant control on the exact nature of the result, since the final *inverse model* has a number of key and distinct features resulting from the inversion, which are not present in the starting model.

A number of small velocity inversions are present in the final inversion model (Fig. 4.2a,b). Two are located within the high velocity interiors of Osbourn (~300 km d.a.p.) and 27.6°S (~500 km d.a.p.) seamounts, below the 6 km s^{-1} contour. Two further velocity inversions are located between 50-80 km d.a.p., and at 6-8 km depth, in the mid-to-lower crust of the overriding plate, associated with the shallowed 6 km s^{-1} region. In all of these cases these velocity inversions have small magnitudes (<0.25 km s^{-1}) and their small spatial dimension indicates that they are highly likely to fall below the model resolution limits, which will be assessed in Section 4.3. These features likely arise as a result of small scale instabilities in the model, which are not smoothed.

Velocity inversions at the base of the model arise as a result of the setting of a fixed velocity interface at 22 km b.s.s. between inversion iterations, to prevent high velocity leakage upwards. It can be seen that if the output model is masked only to show the regions where there is ray coverage, the majority of this region is not sampled by rays (Fig. 4.2b,c). The lowermost part of the masked velocity model continues to show a velocity inversion. However, inspection of these regions in tandem with the magnitude of ray coverage shows them to be poorly sampled by rays. Consequently, this velocity inversion at depth is, therefore more likely to be a smoothing effect between the more well constrained parts of the model directly above, and the 8 km s^{-1} velocity fix at 22 km b.s.s. directly below.

4.2.5. Comparison with the *forward model*

In regions where both the *forward* (Fig. 4.5a) and *inverse* (Fig. 4.5b) *models* have good ray coverage, visual inspection suggests that the two models are in good agreement. Analytically taking the difference between the models allows more detailed analysis of the spatial distribution of differences (Fig. 4.5c).

Generally, the *inverse model* does not appear to generate as high velocities for the seamount interiors as the *forward model*. This is the case for all of the sampled seamounts, regardless of what their internal structure appears to be. This relative

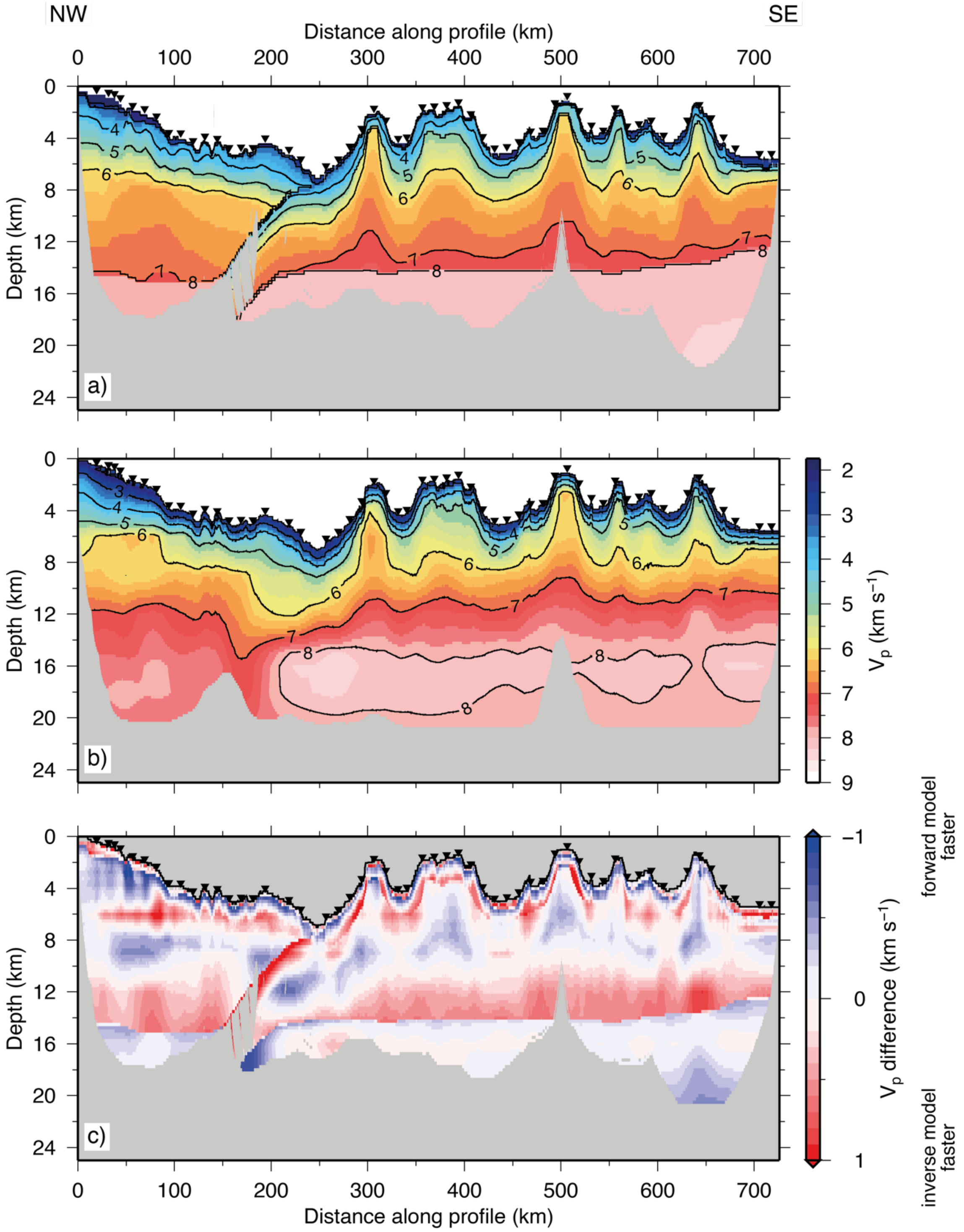

Figure 4.5: *Comparison between results of forward (RAYINVR) and inverse (FAST) modelling approaches. a) Best-fit forward model, masked to show only those areas sampled by rays. b) Best-fit inverse model, masked to show only those areas sampled by rays. c) Difference between forward and inverse models for regions where only both models are sampled by rays, and ignoring the water column. Blue indicates forward model is faster than inverse model, and red slower. OBS locations shown by inverted triangles.*

slowness is particularly observed shallower than 10 km b.s.s., with a gradual change to the *inverse model* being faster deeper than 10 km until the *forward model*-derived Moho.

The largest observed differences between the *forward* and *inverse models* can be explained as principally arising from the limitations of the inverse modelling technique. The plate boundary region represents almost the entirety of the model where the velocity difference is greater than +1 km s^{-1} (Fig. 4.5c). As this is a spatially discrete feature, is it poorly constrained by the *FAST* inversion technique, which cannot produce sharp boundaries. The misfit in this region therefore arises as a result of the smoothed and continuous nature of the velocity field in the *inverse model*, compared to the *forward model* where there is a discrete plate boundary at this location.

Ignoring the regions above the bathymetry and where there is only ray coverage from one of the modelling methods, both of which would bias the results, an initial quantitative velocity difference between the two modelling approaches can be calculated. This was achieved by sampling the difference between the two models over an array of 0.5 km wide by 0.25 km deep windows (Fig. 4.6). Negative values of velocity difference indicate that the *forward model* is faster than the *inverse model*, and positive, slower. Both the mean and median velocity differences are close to 0 km s^{-1}, while the variability, as defined by the standard deviation, is 0.34 km s^{-1}. Comparison with the error bounds on the layer velocities of the *forward model* will be made in Section 4.4., which will indicate whether the observed differences lie within the uncertainties of travel time picks and the modelling approaches or whether they are real features.

As *FAST* is limited to using only first-arrivals, P_mP phases, which are used in the forward modelling approach to define the Moho, are excluded from the inversion. A small number of P_g arrivals are also excluded as they arrive after the P_n arrival at the same instruments (e.g. OBS C56). However, the contribution of these picks to the modelling is negligible. Consequently, when considered as solely a test of forward modeller bias on modelling outcome, the *FAST* approach to inversion, even if limited to first arriving phases, is considered valid.

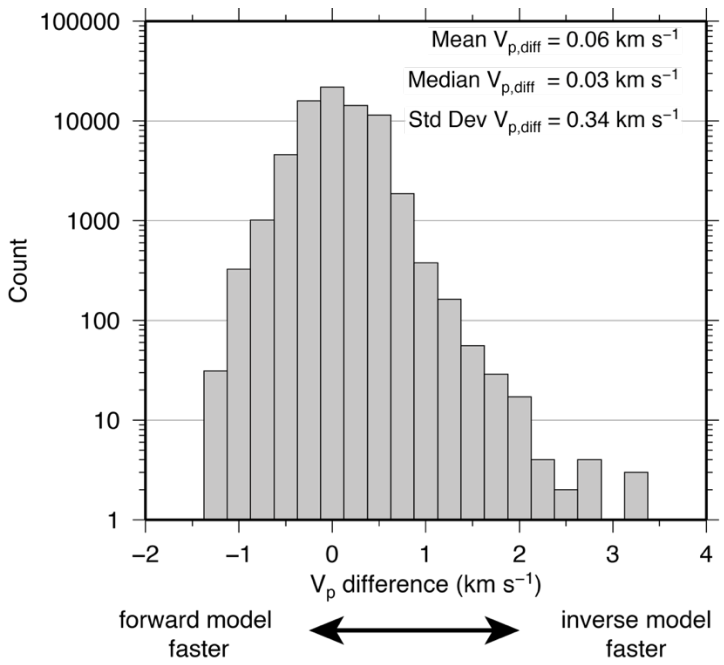

Figure 4.6: *Histogram of P-wave velocity difference between forward and inverse models where both are sampled by rays, calculated using a 0.5 km wide by 0.25 km deep sampling window and ignoring regions above the bathymetry. Window counts binned at 0.25 km* s^{-1} *intervals. Negative values indicate that the forward model is faster than the inverse model, and positive slower. Statistics of the distribution are labelled.*

4.2.6. Ray coverage

The *inverse model* ray coverage, shown in Fig. 4.2c, extends to a maximum depth of ~18-20 km b.s.s.. Coverage is generally uniformly high across the lateral extent of the model, except for two areas of reduced coverage. The first area occurs between ~180-210 d.a.p., which corresponds to the part of the overriding plate immediately above the shallow subduction interface. Here, P_g arrivals could be picked only at short shot-receiver offsets (OBSs C36-C44), and there is an associated lack of deeper penetrating P_n arrivals. A further gap in ray coverage is present beneath the summit of 27.6˚S seamount, where the bend in the profile is located, and arises for the reasons discussed in Section 3.5.2.

Differences between the *forward* and *inverse model* ray coverage can only be expressed qualitatively. This is because the *FAST* inversion technique excludes reflected and second-arrival refracted phases in the modelling and, hence, the ray coverage through this model. The total number of rays in the inverse set is, therefore, smaller at ~50000 versus ~61000 for the forward model, and so a quantitative comparison between the two model coverages is not possible.

Secondly, the method by which ray coverage is calculated is different between the two modelling techniques. In the *RAYINVR* forward modelling technique, the node spacing of the model governs the block size in which ray hits are counted (Fig. 4.7a). In contrast, in the *FAST* inverse modelling process, ray coverage is calculated for each of the inversion cells (i.e. the 4 x 2 km second phase cell size), and then interpolated onto the inversion process's grid of forward nodes, producing a smoothing effect. In order to better compare the characteristics of the ray coverage between the two modelling techniques, the forward ray coverage was recalculated over blocks with the same dimensions as the inversion cells (Fig. 4.7b). For the purpose of comparison, the layer boundaries of the *forward model* are overlaid over each panel, including the inverse ray coverage (Fig. 4.7c).

The coarsely sampled *forward model* (Fig. 4.7b) shows a higher ray density per 4 x 2 km cell in the upper and middle crust. Likely causes for this observation include the lack of phase information associated with the picks in the inverse modelling technique, which does not allow them to be forced to turn within a certain layer, and the lack of P_mP phases. Generally, both the forward and inverse methods show similar patterns of ray coverage, or lack thereof. The region of lower coverage between 180-220 km d.a.p., associated with the plate interface-adjacent part of the lower forearc, is observed in both models. The maximum depth of coverage in the *inverse model* is generally constant along the profile at 20 km b.s.s.. This contrasts with the forward ray coverage, which has more variable maximum depths between 18-24 km. This latter value is an artefact of the block size used for sampling, as the finely spaced ray coverage (Fig. 4.7a) does not show rays reaching beyond 22 km b.s.s..

4.3. Resolution testing

To determine the minimum resolvable feature size in the *inverse model*, resolution testing was performed using the checkerboard method (e.g. Hearn and Ni, 1994; Zelt, 1998; 1999). The *inverse model* was convolved with a regular checkerboard of alternating polarity velocity anomalies. Using the real experiment shot-receiver geometry, a set of synthetic travel times was generated by applying forward finite difference ray-tracing through this perturbed model. Gaussian noise was then added to the synthetic travel times, with the magnitude of the noise scaled such that the standard

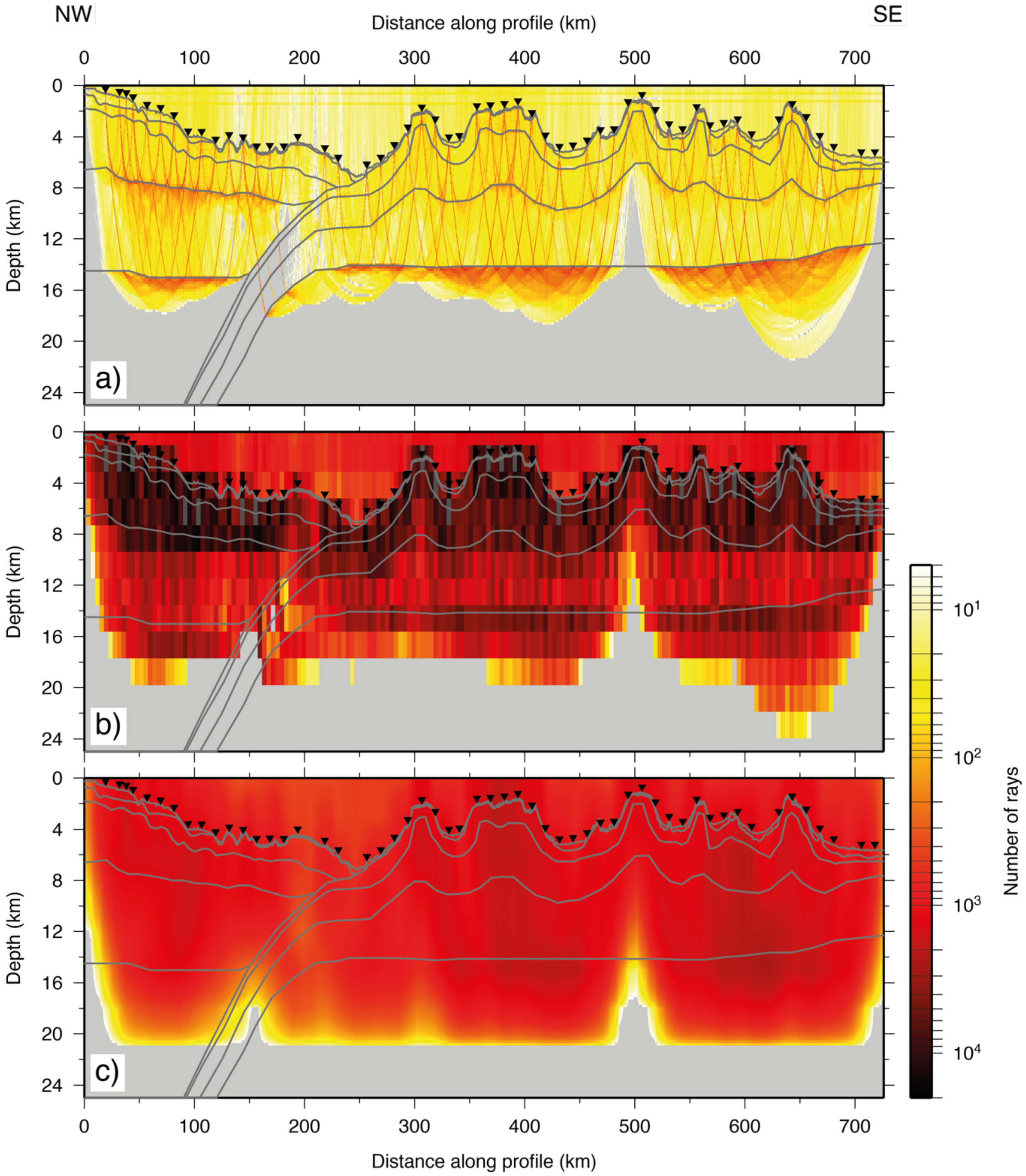

Figure 4.7: *Comparison between forward (RAYINVR) and inverse (FAST) model ray coverage. a) RAYINVR forward model ray coverage sampled at velocity model grid spacing (0.2 x 0.2 km). b) Forward model ray coverage resampled to final inverse cell spacing (4 x 2 km). c) FAST inverse model ray coverage, sampled in inverse cells (4 x 2 km) and smoothed. All panels are plotted using same logarithmic colour scheme. Grey lines are the forward model layer boundaries. OBS locations shown by inverted triangles.*

deviation of the noise is equal to the pick uncertainties. The procedure for generating this noise will be described in Section 4.3.1.

The noise-added synthetic arrivals were then traced through the unperturbed final inversion model using the same inversion parameters that were used to generate this model. The ability of the model to resolve anomalies with dimensions equal to the anomaly pattern can then be estimated by appraisal of the recovered anomaly pattern. Where the ray coverage is insufficient to resolve small, local structure, it will be smoothed by the regularization process towards lateral homogeneity (Zelt and Barton, 1998), resulting in the removal of the checkerboard component from the output.

The magnitude of the velocity anomaly is defined relative to the absolute velocity of the background anomaly at each point in the model, so that the perturbation is unbiased. It is important that the magnitude of the velocity perturbation is not excessively large, as this may result in the alteration of ray paths, which is not the object of testing. An input velocity perturbation of ±5% of the background model was chosen as suitable for this goal.

4.3.1. Adding noise to picks

A set of random numbers, uniformly distributed between 0 and 1 (~U(0,1) – Fig. 4.8a), were generated using a computer pseudo-random number generator. To convert this set into normally (Gaussian) distributed numbers, a Box-Muller transform method was used (Box and Muller, 1958). The desired parameters for normally distributed random numbers are that they have a mean of zero and unit variance (~N(0,1) – Fig. 4.8b). The abundance of values within the random set therefore correlates to numbers of standard deviations (σ) from the mean (μ, $\mu=0$), according to a normal distribution.

The random σ values are used to add noise to the synthetic travel times by multiplying the assigned uncertainty for each travel time pick by σ, and then adding this value to the travel time, thus the original magnitude of the uncertainty is maintained. The result is, for example, that the applied noise is larger for P_n arrivals than for P_g.

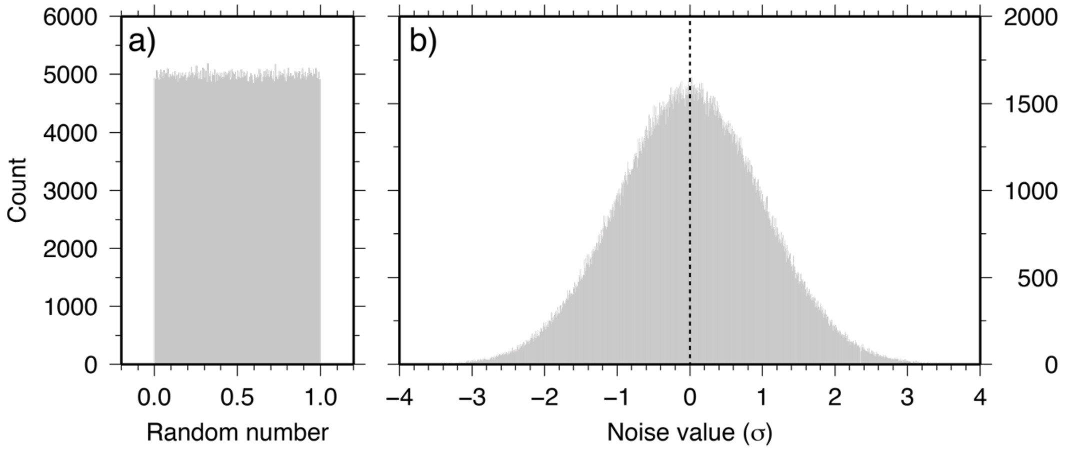

Figure 4.8: *Generation of random numbers for addition of noise to picks. a) Uniformly distributed random numbers, between 0 and 1 [~U(0,1)] b) Normally distributed random number population, with a mean of zero and unit variance [~N(0,1)], generated by applying the Box-Muller transform method to the population in a).*

4.3.2. Checkerboard testing procedure

For each checkerboard size tested, the process was repeated with lateral and vertical shifts to the input pattern of 0.5, 1.0, and 1.5 times the anomaly width and depth. This resulted in the testing of a total of 16 checkerboard sets for each size. A number of these represent the same checkerboard-edge geometries, but with opposite polarities of the applied anomalies. The motivation for applying these phase shifts to the input anomaly was the observation that checkerboard recovery could be strongly dependent on the alignment of checkerboard centres and edges with bathymetric contrasts (Section 4.3.4). An example set of 16 checkerboards for a single input anomaly size is shown in Fig. 4.9. Further recovered checkerboards for an array of tested input anomaly sizes are provided, for reference, in Appendix C.

Figure 4.9 (over page): *Results of checkerboard testing for 15 x 4 km input anomaly size. 0.5, 1.0, and 1.5 x horizontal and vertical anomaly size phase shifts are applied to the initial model (top left, shown without shift), and labelled on each panel with the magnitude of the shift in km, and h or v corresponding to horizontal and vertical shifts respectively. Positive shifts are defined as toward the right of the model and downwards.*

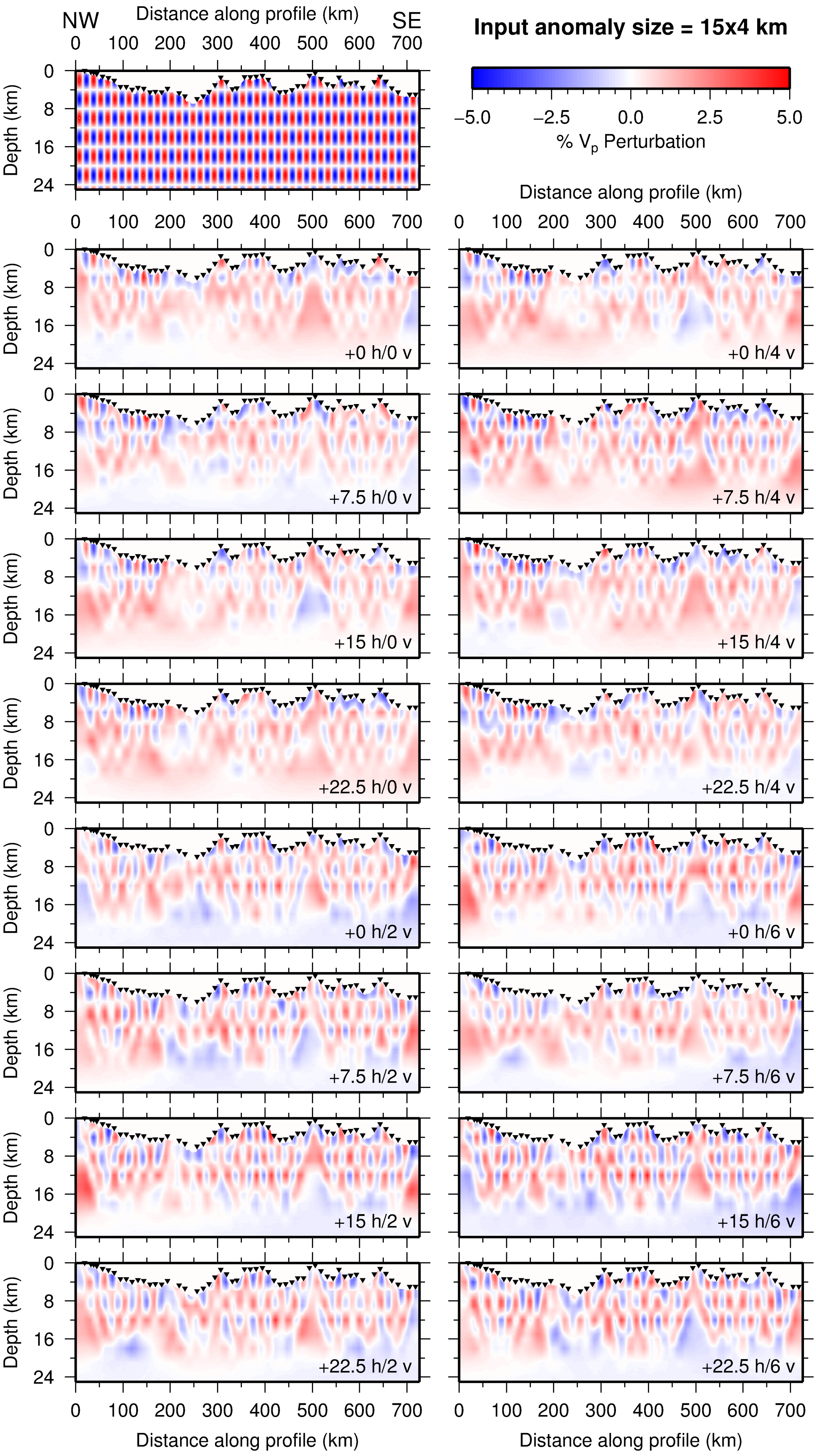
NW
Distance along profile (km)
SE
0
100
200
300
400
500
600
700
Depth (km)
0
8
16
24
Input anomaly size = 15x4 km
−5.0
−2.5
0.0
2.5
5.0
% V_p Perturbation
+0 h/0 v
+0 h/4 v
+7.5 h/0 v
+7.5 h/4 v
+15 h/0 v
+15 h/4 v
+22.5 h/0 v
+22.5 h/4 v
+0 h/2 v
+0 h/6 v
+7.5 h/2 v
+7.5 h/6 v
+15 h/2 v
+15 h/6 v
+22.5 h/2 v
+22.5 h/6 v

Figure 4.9

4.3.3. Results of checkerboard testing

All checkerboard tests appear to share a common limitation in their recovery pattern, located in two parts of the model, namely the forearc and subducting plate region immediately adjacent to the trench/subduction interface and beneath the bend at 27.6˚S seamount. These locations would be expected to have the most limited recovery, and hence spatial resolution, as a result of the lower ray coverage (Fig. 4.2c). In the first case, this arises as a result of structural complexity and the deep water environment, which make it challenging to identify and correctly assign arrival picks to their correct phases. In the latter case, the cause is a direct result of the profile geometry, and the steps that were taken to mitigate the effects of the bend for forward modelling (see Section 3.5.2)

An initial appraisal can be determined by comparing the vertical checkerboard sizes to the crustal thickness of the *forward model*, since the *inverse model* does not produce a boundary at the base of the crust. For the Indo-Australian plate the total crustal thickness is between 10-14 km, and the Moho is located at a depth of ~15 km b.s.s.. The crustal thickness of the Pacific plate is harder to define due to the presence of the seamount chain. The total thickness from seamount summits to the Moho is between 12-13 km, and between 8-9 km in the saddles between seamounts. At the southeasternmost end of the profile, where the plate has not been affected by seamount volcanism, the crustal thickness is between 6.0-6.5 km. The Moho depth along the model varies between ~12-15 km b.s.s.. Checkerboard testing over a range of input anomaly sizes indicates that the principal limiting factor on the size of recoverable features appears to be the vertical dimension of the input anomaly.

For 5 km and greater vertical anomaly sizes, recovery is normally good in all areas, with the exception of the two regions referred to above, for horizontal anomaly sizes ≥15 km (Fig. 4.10a-f). Velocity anomalies 12 x 5 km in size are recovered only in the upper parts of the crust, particularly beneath the upper and middle forearcs, and in some instances in the region of the seamount chain (Fig. 4.10g,h). However, generally at this input size, recoverability is limited. Therefore, 12-15 km appears to represent the minimum horizontal anomaly size that can be recovered for 5 km vertical anomalies.

A similar pattern is observed for 4 km vertical anomalies. Recovery is generally good down to horizontal anomaly dimensions of 15-20 km (Fig. 4.11), but

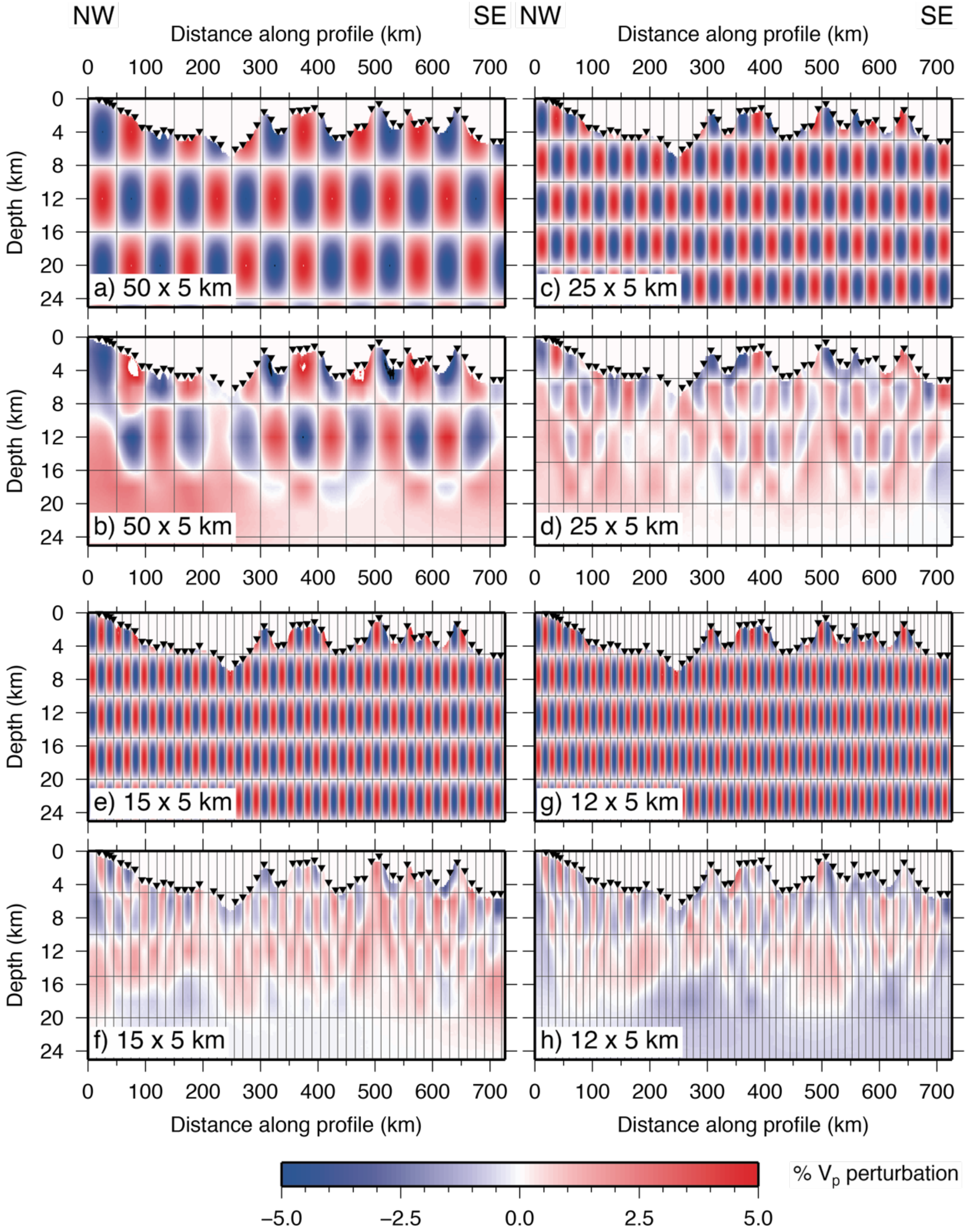

Figure 4.10: *Checkerboard testing for vertical anomaly sizes ≥5 km. a) Input horizontal anomaly size of 50 km and vertical anomaly size of 8 km. b) Recovered checkerboard following inversion with input pattern from a). c) Input horizontal anomaly size of 20 km and vertical anomaly size of 5km. d) Recovered checkerboard with input pattern from c). e) Input horizontal anomaly size of 15 km and vertical anomaly size of 5km. f) Recovered checkerboard with input pattern from e). g) Input horizontal anomaly size of 12 km and vertical anomaly size of 5km. h) Recovered checkerboard with input pattern from g). OBS locations shown by inverted triangles.*

]

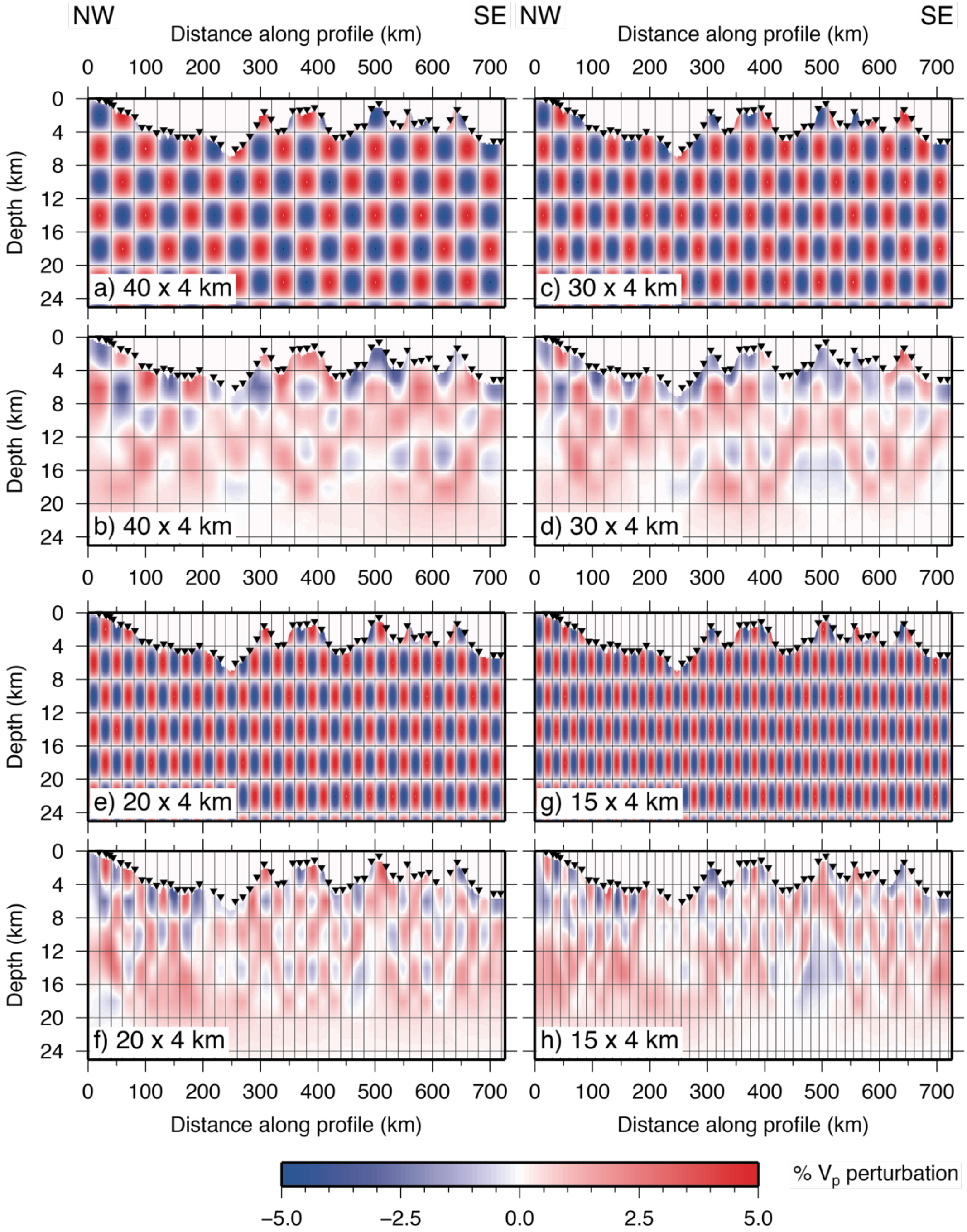

Figure 4.11: *Checkerboard testing with a vertical anomaly size of 4 km. Input horizontal anomaly sizes of a) 40 km, c) 30 km, e) 20 km, and g) 15 km, with matching recovered anomaly patterns in b), d), f), and g) respectively. OBS locations shown by inverted triangles.*

is more limited in some areas where there is significant bathymetry. Good recovery is observed at some input patterns when phase shifted for the 15 x 4 km input size throughout the oceanic crustal regions of both plates, down to depths of up to 12 km b.s.s. (Fig. 4.11g,h). Recovery is observed in some, but not all, of checkerboard sets at 12 x 4 km input anomaly dimensions, however, as with the 5 km vertical anomaly size, recovery tends to fail at horizontal dimensions below this. Thus, 12-15 km appears to represent the minimum horizontal feature sizes that can be resolved for vertical features 4 km in height or greater.

For vertical input anomaly sizes of 3 km, checkerboard recovery is highly limited at horizontal anomaly sizes as high as 40 km (Fig. 4.12). On occasion, phase shifts to the input pattern provide improved recoverability over the wide range of horizontal anomaly sizes. However, this is uncommon, and indicates that 3 km falls below the vertically recoverable feature size for the dataset in this study.

4.3.4. Checkerboard phase shifts and edge effects

Figures 4.13 and 4.14 show examples of checkerboard tests where phase shifts to the input anomaly pattern have been applied. In each figure, the shifts displayed are 0.5 times the anomaly width (c,d) and anomaly depth (e,f) independently, and applied both at once (g,h). The model semblance (i) is calculated by averaging the results for all 16 half-phase shifts, with values >0.7 indicating the model is well resolved (Zelt, 1998).

For the 20 x 4 km input pattern, recovery is noticeably poorer when horizontal phase shifts are applied (Fig. 4.13c,d,g,h). This is particularly noticeable in the mid-to-lower crust of the Pacific plate. Without horizontal phase shifts, the checkerboard pattern can be recovered to depths of 16-18 km b.s.s., depending on location within the model. Better recovery is achieved between 340-420 km d.a.p. beneath Canopus seamount for the vertically phase shifted input pattern (Fig. 4.13e,f), as opposed to the un-shifted (Fig. 4.13a,b). In this case, the tops of the anomalies approximately align with the seamount summit, and the vertical thickness corresponds well to edifice prominence. For the small seamounts located south of 27.6˚S seamount (540-660 km d.a.p.), recovery within seamount edifices is better without horizontal shifts (Fig. 4.13a,b,e,f), but with vertical shifts (Fig. 4.13e,f). The tops of the anomalies appear to approximately align with the tops of the edifices, and the boundaries (zeroes) between

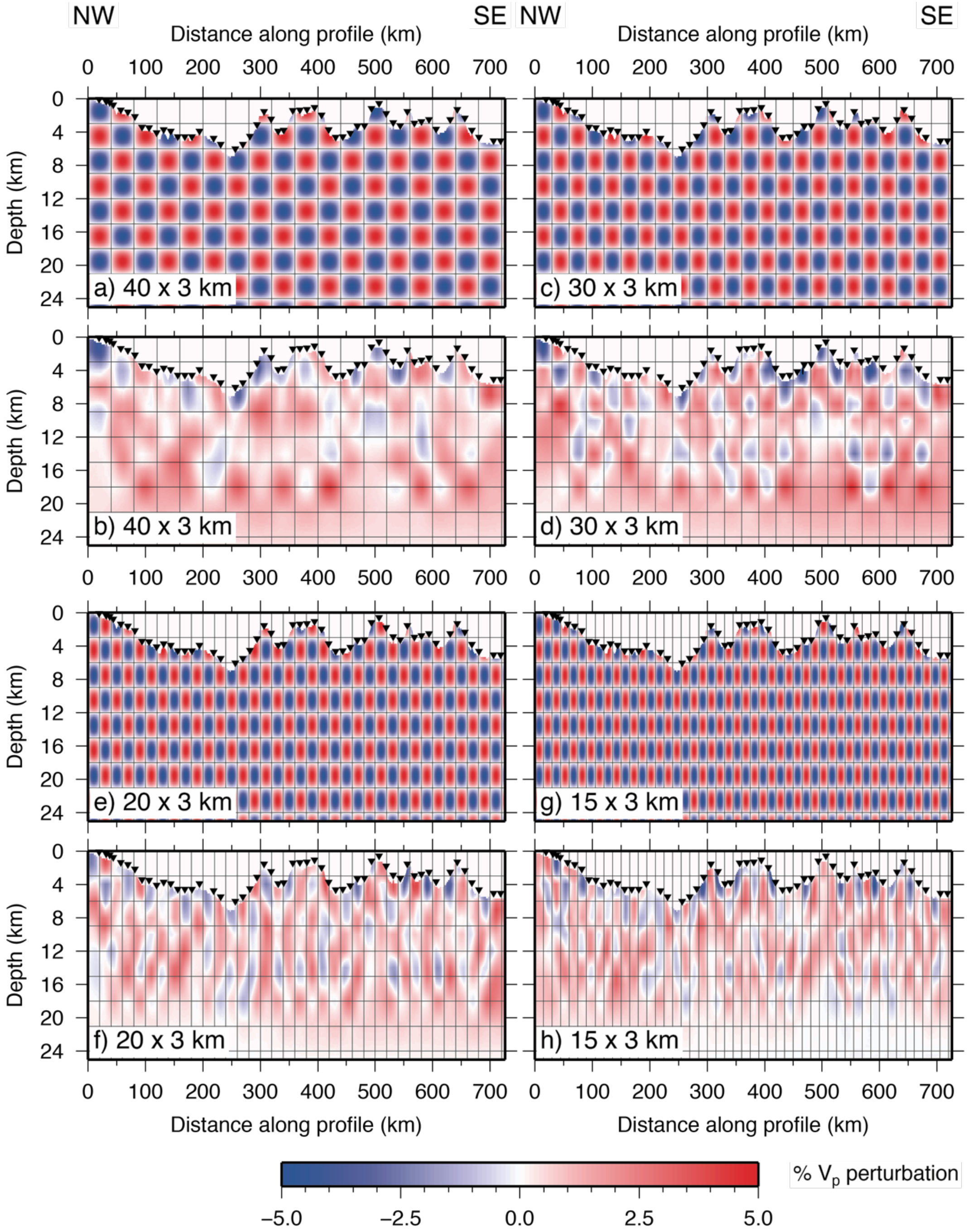

Figure 4.12: *Checkerboard testing with a vertical anomaly size of 3 km. Input horizontal anomaly sizes of a) 40 km, c) 30 km, e) 20 km, and g) 15 km, with matching recovered anomaly patterns in b), d), f), and g) respectively. OBS locations shown by inverted triangles.*

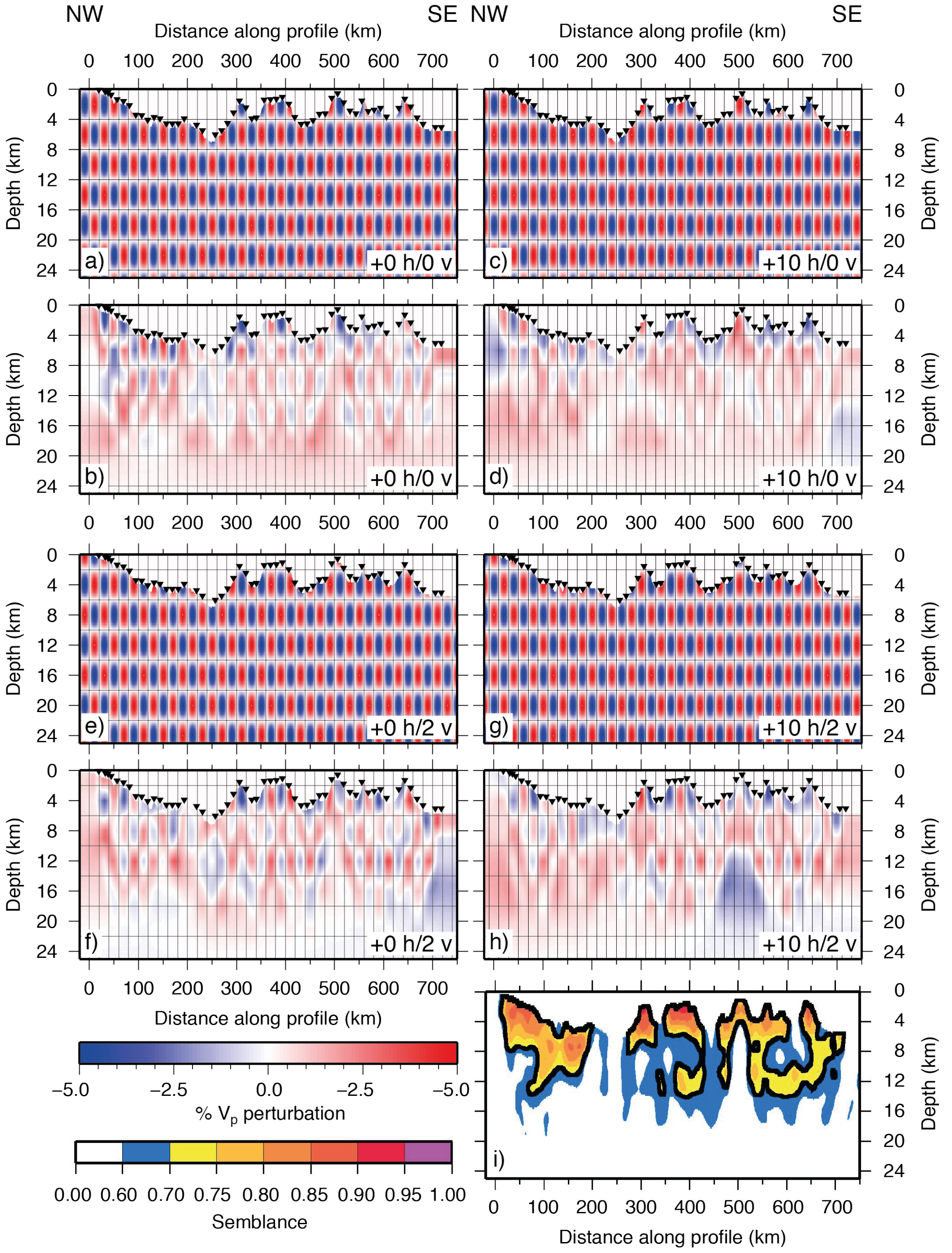

Figure 4.13: *Effect of phase shifting the 20 x 4 km anomaly size input checkerboard pattern. Input anomalies with a) no phase shift, c) 0.5 times horizontal anomaly size (10 km) phase shift, e) 0.5 times vertical anomaly size (2 km) phase shift, and g) 0.5 times horizontal and vertical anomaly size phase shifts, with matching recovered anomaly patterns in b), d), f), and g) respectively. OBS locations shown by inverted triangles. i) Average semblance from 16 half-phase shifted anomalies. Black contour indicates the 0.70 threshold value of Zelt (1998), taken to indicate that the model is well resolved.*

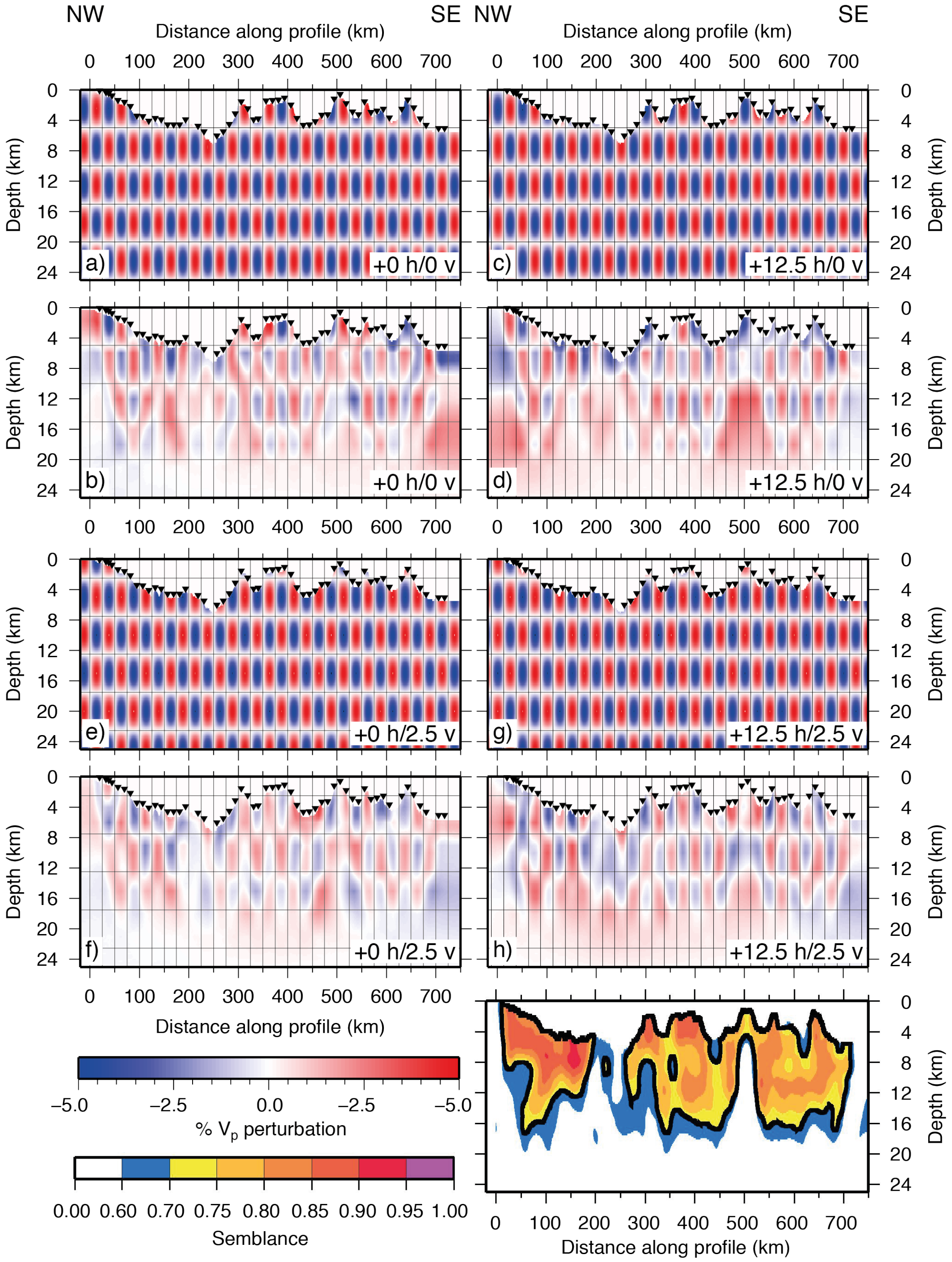

Figure 4.14: *Effect of phase shifting the 25 x 5 km anomaly size input checkerboard pattern. Input anomalies with a) no phase shift, c) 0.5 times horizontal anomaly size (12.5 km) phase shift, e) 0.5 times vertical anomaly size (2.5 km) phase shift, and g) 0.5 times horizontal and vertical anomaly size phase shifts, with matching recovered anomaly patterns in b), d), f), and g) respectively. OBS locations shown by inverted triangles. i) Average semblance from 16 half-phase shifted anomalies. Black contour indicates the 0.70 threshold value of Zelt (1998), taken to indicate that the model is well resolved.*

adjacent anomalies in the horizontal direction align to the centre of edifices, rather than being associated with their edges.

For the overriding plate, good recovery is generally limited to shallower crustal depths than beneath the Pacific plate. Here, the bathymetry is much simpler and, as a result, horizontal phase shifts appear to have less of an impact, with the upper crust (<8 km b.s.s.) undergoing only a small degradation in recoverability between the un-shifted (Fig. 4.13a,b) and shifted (Fig. 4.13c,d) patterns. Vertical shifts appear to have a stronger impact here, with both vertically shifted patterns (Fig. 4.13e-h) showing poorer recovery than their corresponding non-vertically shifted conjugates (Fig. 4.13a-d). It is likely that this arises as a result of the generally degrading recoverability with depth, and suggests that the lower crust and mantle structure here is less well constrained than at equivalent depths in the Pacific plate.

For larger input anomaly sizes, e.g. 25 x 5 km, there appears to be generally lower sensitivity to phase shifts of the input anomaly pattern (Fig. 4.14). For the overriding plate region, between ~40-180 km d.a.p., and from the seabed to 10-12 km b.s.s., the recovery of the input anomalies appears to be similarly good, regardless of the shifts applied. For the Pacific plate, only the vertically shifted input anomaly appears to show reduced recovery for the middle crustal region downwards (Fig. 4.14e-h). Within the seamounts themselves, there does appear to be a continued pattern of better recovery where the checkerboard edges align with the seamount centres and summits, e.g. 475-525 km d.a.p. – Fig. 4.14b,f; and 550-680 km d.a.p. – Fig. 4.14f,h.

For the largest input anomaly sizes – e.g. 50 x 8 km, 40 x 4 km and 30 x 4 km – shifts to the input pattern appear to have relatively little impact on the recoverability. As the input anomaly size decreases, particularly to horizontal widths that are similar to the horizontal dimensions of the Louisville seamounts such as those described in this section, the checker edge geometry appears to have an increasing impact. Finally, as the horizontal size decreases further, the alignments of checker edges with bathymetric contrasts may continue to play a role, but by this point the checkerboard size is the primary influencing factor on anomaly pattern recovery.

4.3.5. Implication of checkerboard testing

In order to interpret the results of resolution testing, it is necessary to compare the size of the test cells used with the size of the features for which resolvability is being determined. One of the principal goals of this study is to determine if and how a seamount along the continuation/projection of the LRSC is being subducted at the Tonga-Kermadec trench. In turn, this relies on the ability to resolve the velocity-depth structure within and beneath the Louisville Ridge seamounts prior to their subduction. The typical dimensions of a LRSC seamount are:

- a summit diameter of 20-30 km;
- a basal diameter of 40-60 km;
- a prominence above the seafloor of 3-4 km; and
- a total crustal thickness of up to 13 km.

The results of resolution testing described above indicate that seamount-sized structures should be resolvable with the dataset and forward modelling technique applied in this study, provided that they are located in regions which are well sampled by rays. The more limited ray coverage in the region of the shallow subduction interface will undoubtedly, therefore, have an impact on the ability to detect a seamount in this region, if one were present. The consequences for model interpretation will be discussed in Chapter 5.

4.4. Sensitivity testing

Sensitivity testing is an approach which is applied to best-fit forward models to determine how and where a model can be varied before it is deemed to no longer produce an acceptable fit between calculated and observed travel time picks. As such, this process provides a means to put confidence limits on both interface depth and velocity throughout a model space and, thus, qualify its subsequent interpretation. For the sensitivity testing applied in this study, the thresholds of misfit were set in terms of the actual fit of the best-fitting model, as expressed by the travel time residual (T_{rms}) and χ^2 values, the latter of which incorporate the assigned pick uncertainty.

4.4.1. Perturbations

Four types of perturbation were applied to the input model, that represented changes to the depth, velocity at the top of a layer, velocity at the base of a layer, and the bulk velocity of a layer whilst keeping the velocity gradient the same. Figure 4.15 summarises these types of perturbations, indicating which values vary and which remain fixed in each case.

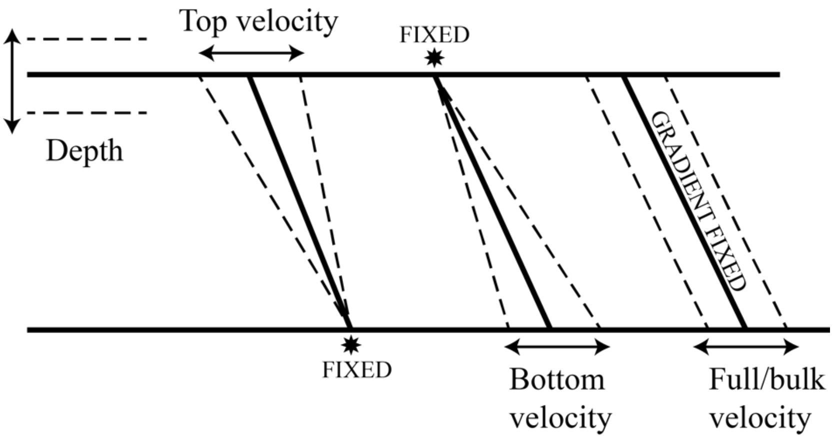

Figure 4.15: *Summary of perturbation types that were applied during forward model sensitivity testing. For velocity perturbations, the slope of line represents the velocity gradient within a layer. Solid lines represent the best-fit forward model values, and dashed lines represent applied changes. Aspects labelled FIXED indicate which were held constant during each type of perturbation.*

The second-order velocity discontinuity between the middle and lower crustal blocks of each plate was preserved throughout the testing procedure, which effectively couples the bottom velocity variation of the middle crustal layer to the upper velocity variation of the lower crustal layer of each plate, such that both tests should have the same effect. In the case of the bulk velocity perturbation, the presence of a second-order discontinuity requires that a variation to the velocity in one of the two layers adjacent to the interface also impacts on the velocity gradient of the other, and so these tests cannot be carried out truly independently. As changing the depth of the lower boundary of a layer corresponds to a matching change of the upper boundary of the layer immediately below, depth changes are defined here as occurring at the upper boundary of each layer.

For the purposes of simplicity, each perturbation tested was applied homogeneously along each interface where the values were altered. This assumption is generally more valid for the overriding plate, where the crustal structure appears to be less laterally variable. However, due to the presence of the seamounts, and their associated large bathymetric and seismic velocity contrasts, this approach can only provide a more approximate estimate of the error bounds, particularly so for shallower layers where the lateral heterogeneity is greater.

4.4.2. Input pick selections

For each perturbed model generated for sensitivity testing, rays were re-traced and the fit re-calculated using the same original ray-tracing approach and parameters. Each plate was independently tested using only instruments and ray groups tracing through that plate to prevent biasing of the calculated fit due to large numbers of rays tracing through an unperturbed part of the model. In the case of a few trench-proximal instruments, that meant that their travel time picks were included in the testing procedure for both plates. The total number of rays in the zero-perturbation tests, therefore, appears higher than the number for the full model (N = 60736), because some travel time picks were included twice. Splitting of P_g, P_mP and P_n phases within the tests for each plate was not conducted.

For P_s arrivals, the travel time pick set was filtered to contain only those for rays which turn in the sediment layer. An additional test was conducted using the entire model pick set, since all rays must pass through the sediment layer at some point along their path. In this latter case, the much increased path length has a buffering effect on the sensitivity, requiring much bigger perturbations to have any significant effect on the fit. Following the definition above, that changes to the depth of a layer were defined as adjustment of the upper interface, applying this test to P_s arrivals is not possible, as the upper boundary of the sediment layer is the seabed, which must be an invariant by definition.

4.4.3. Results

The results of sensitivity testing are shown in Table 4.1 and Figs 4.16-4.19. Due to the difference in fit between the overriding and subducting plates (Tables 3.2 and 3.3) the misfit thresholds must be set independently for each plate. The degree of misfit allowed before the model was no longer deemed to be a good fit was defined as matching the smallest additional travel time pick error assigned to picks at the bend, i.e. 35 ms, for consistency. This corresponds to an ~20% increase in the T_{rms}, or threshold χ^2 values of 3.0 and 3.6 for the overriding and subducting plates respectively, although the exact relationship between these two measures of fit is partly governed by the number of rays, which varies by a plus or minus a few hundred depending on the type of perturbation applied. For further consistency, the thresholds for assessing

Plate		**Number of rays**	**T_{rms} (ms)**	**χ^2**	**χ^2 threshold**
Both	P_s only	606	43	1.17	1.9
	All rays	60736	140	2.45	3.5
Overriding / Indo-Australian		20370	119	1.99	3.0
Subducting / Pacific		43940	147	2.59	3.6

Layer			**Depth (km)**	**Layer top velocity (km s^{-1})**	**Layer bottom velocity (km s^{-1})**	**Layer bulk velocity (km s^{-1})**
Sediment, P_s only		4	not testable†	+0.1/-0.1	+0.3/-0.1	+<0.1/-<0.1
Sediment, all rays			not testable†	$+0.4/-0.3^{fc}$	$+0.3^{fc}/-0.4^{fc}$	+0.2/-0.1
Indo-Australian	Crust	5	$+<0.2/-<0.1^{lv}$	+0.4/-0.2	+0.1/-0.3	$+0.1/-0.4^{fc}$
		6	+0.3/-0.4	+0.4/-0.3	$+0.2/-0.2^{*}$	$+0.2/-0.1^{\#}$
		7	+0.4/-0.5	$+0.2/-0.2^{*}$	+0.4/-0.4	$+0.1/-0.1^{\#}$
	Mantle	8	+0.9/-1.4	insensitive/-0.4	insensitive	+0.4/-0.3
Pacific	Crust	9	$+0.075/\text{fail}^{lv}$	$+0.5^{fc}/-0.4$	$+0.2^{fc}/-0.5$	+0.6/-0.3
		10	$+0.3/-0.2^{lv}$	+0.5/-0.3	$+0.4/-0.1^{*}$	$+0.3/-0.3^{\#}$
		11	$+0.5^{fc}/-0.2$	$+0.4/-0.1^{*}$	+>0.5/-0.3	$+0.3/-0.1^{\#}$
	Mantle	12	+0.2/-0.6	+0.4/-0.2	insensitive	+0.4/-0.2

Table 4.1: *Forward model sensitivity testing. Numbers in layer column correspond to layer identifier number in the RAYINVR forward model. Positive and negative perturbations for each test type that cause the model fit to exceed the threshold values of* $\chi^2 > 3.0$ *and* $\chi^2 > 3.6$ *for the overriding and subducting plates respectively.*

Notes on additional superscripts:

† - tests cannot be performed as the interface represents the seabed, which is an invariant part of the model by definition.

** - test types are identical in nature due to the presence of a second-order velocity discontinuity in the model (see main text).*

 # - due to the second-order discontinuity at the boundary of this layer, this is not a truly independent test of a change to a single layer (see main text).

lv – indicates that this test suffers from layer-crossing violations and therefore either fails or reaches a limit beyond which further variation along the model cannot be made.

fc – a number of tests in this set fail to run before reaching the quoted sensitivity values, therefore it is likely that the true limits are smaller than those listed.

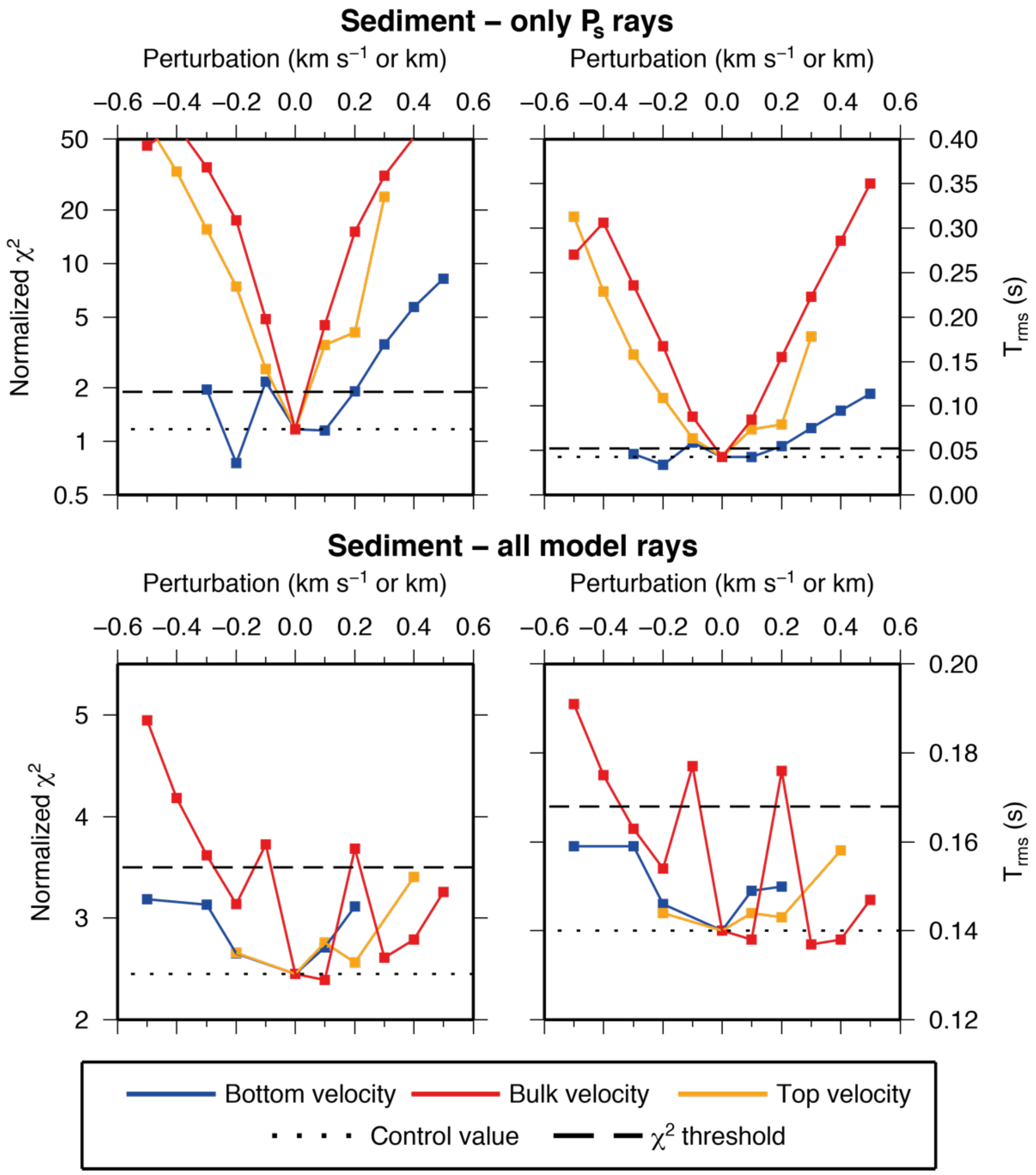

Figure 4.16: *Results of sensitivity testing of the sediment layer, plotted against perturbation in km for depth, and km s^{-1} for velocity. Left column plots are χ^2 values, right column T_{rms}. Control values (non-perturbed) of χ^2 and T_{rms} are plotted as dotted black lines and threshold values as dashed black lines. Line colours correspond to the test type, as identified in the legend. Upper panels – tests using only P_s rays (N = 606), χ^2 plotted using $\log_{10}$ vertical axis. Lower panels – tests using all model rays (N = 60736).*

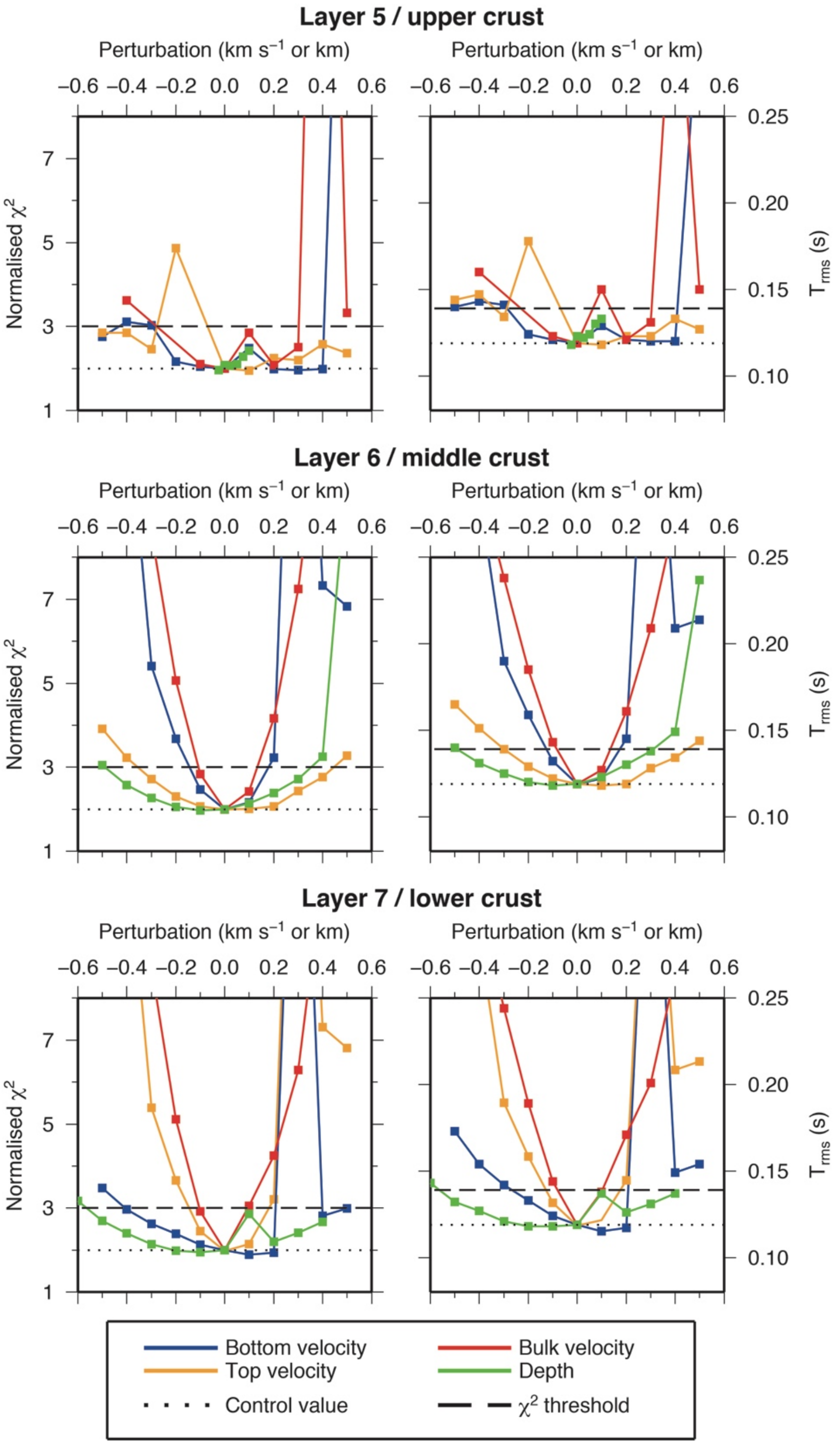

Figure 4.17: *Results of sensitivity testing for Indo-Australian plate crust, plotted against perturbation in km for depth, and km s^{-1} for velocity. Left column plots are χ^2 values, right column T_{rms}. Control values (non-perturbed) of χ^2 and T_{rms} are plotted as dotted black lines and threshold values as dashed black lines. Line colours correspond to the test type, as identified in the legend.*

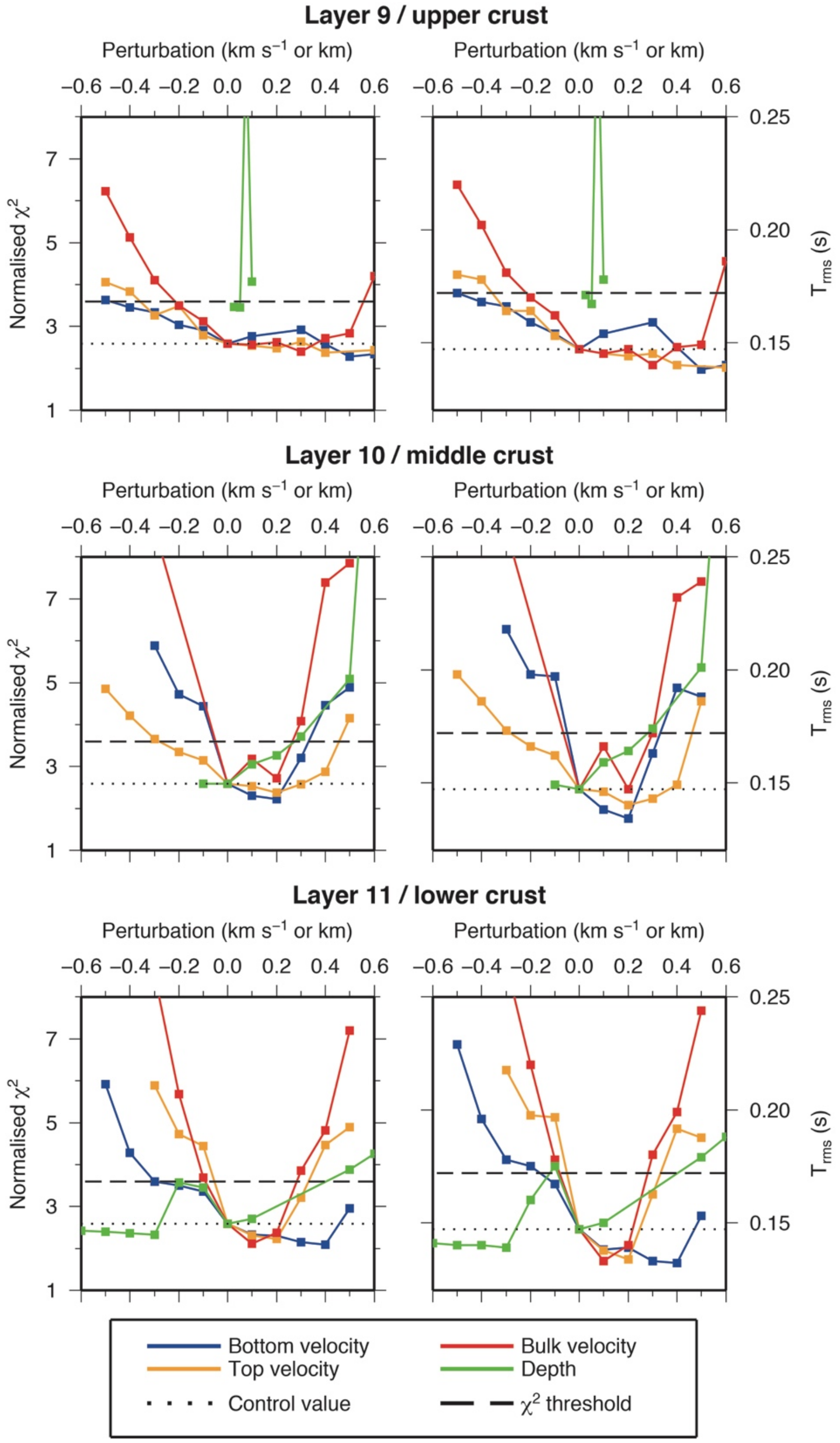

Figure 4.18: *Results of sensitivity testing for Pacific plate crust, plotted against perturbation in km for depth, and km s^{-1} for velocity. Left column plots are χ^2 values, right column T_{rms}. Control values (non-perturbed) of χ^2 and T_{rms} are plotted as dotted black lines and threshold values as dashed black lines. Line colours correspond to the test type, as identified in the legend.*

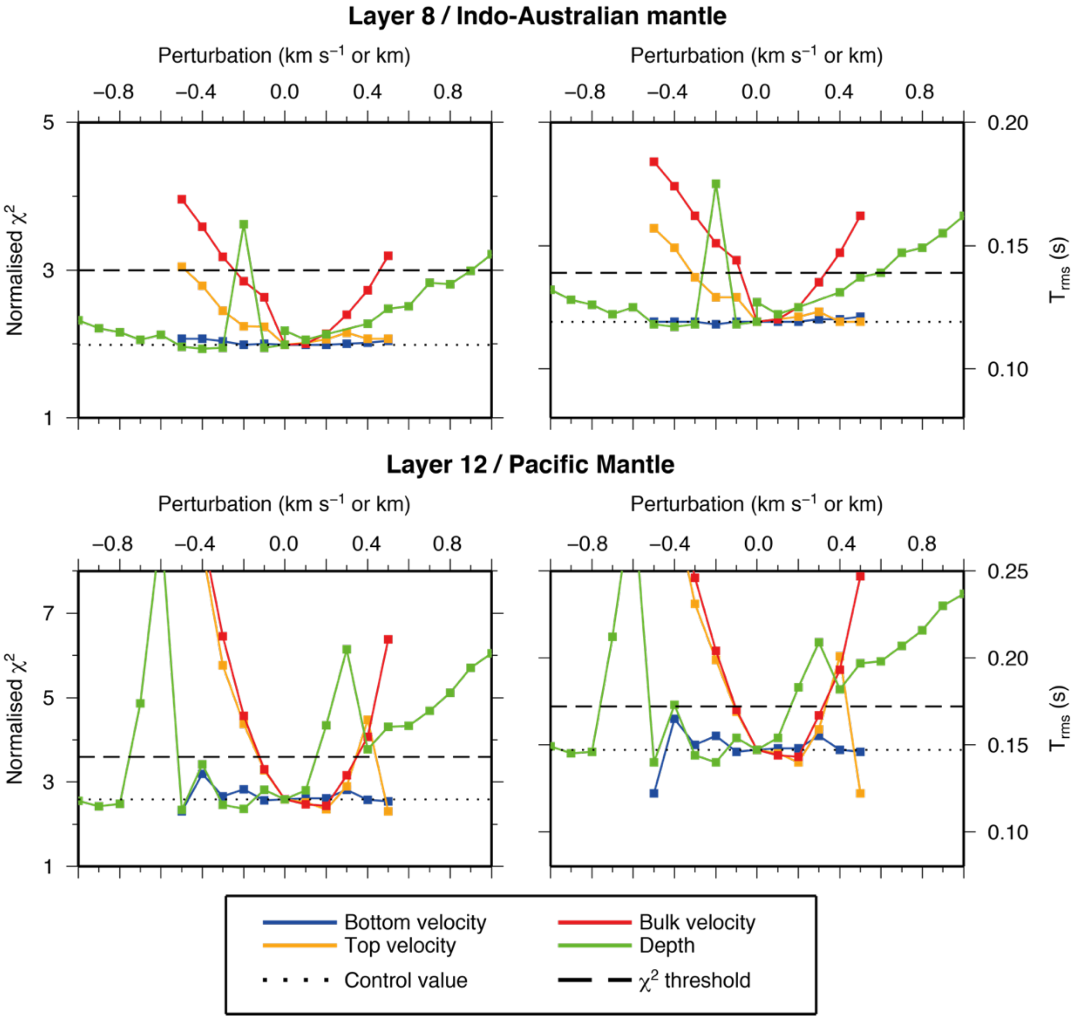

Figure 4.19: *Results of sensitivity testing for the Indo-Australian (top) and Pacific (bottom) mantle, plotted against perturbation in km for depth, and km s*$^{-1}$ *for velocity. Left column plots are* χ^2 *values, right column* T_{rms}. *Control values (non-perturbed) of* χ^2 *and* T_{rms} *are plotted as dotted black lines and threshold values as dashed black lines. Line colours correspond to the test type, as identified in the legend.*

the model sensitivity for the sediment layer (model layer 4) are set at the same ‘20% increase in T_{rms}’ level, with χ^2 thresholds of 1.9 and 3.5 being applied for the cases where only P_s and all model picks are included respectively. However, testing indicated that ray-tracing failed in some cases at perturbation values smaller than those which cause the fit to exceed these thresholds. Where the confidence limits are set at the point that causes ray-tracing to fail, this is indicated in Table 4.1.

In Table 4.1, and subsequently in the text, negative values correspond to either shallower depths or slower velocities, and positive values to increasing depth or faster velocity. These values will subsequently be used throughout the text when describing the *forward model*, to indicate the degree of confidence, or maximum bound of variation, any interpreted feature could have.

4.4.3.1. Velocity sensitivity

Figure 4.16 shows that if only P_s rays were included, the *forward model* shows a high degree of sensitivity to changes in top and bulk layer velocity (±≤0.1 km s^{-1}), and a lesser degree of sensitivity to velocity at the bottom of the layer (+0.3/-0.1 km s^{-1}). The expected buffering effect as a consequence of including all model picks in assessing the confidence in the sediment layer velocity is also observed, with the top (+0.4/-0.3 km s^{-1}), bottom (0.3/-0.4 km s^{-1}), and bulk (+0.2/-0.1 km s^{-1}) layer velocity confidence limits all increasing before the misfit threshold is exceeded.

Velocity sensitivity is generally good throughout the oceanic crust of the Indo-Australian plate, at ≤±0.4 km s^{-1}. In some parts of the crust this improves to ≤±0.2 km s^{-1}. There does not appear to be a strong, consistent pattern which suggests that any one of the three velocity perturbation types plays a distinctly stronger or weaker role in producing model misfit than any other. During testing it was noted that the upper velocity variations for the lower crustal layer caused the ray-tracing to behave erratically (Figs 4.17 and 4.18 – lower panel, orange line). As a result, the confidence limits for this layer were assigned using the sensitivity testing results of the bottom velocity variations for the middle crustal layer, given that these variations are coupled due to the presence of the second-order discontinuity (Section 4.4.1).

The results of sensitivity testing the velocity of the uppermost mantle layer showed common characteristics for both plates, with one difference. Generally, it was found that the model fit was insensitive to changes in velocity at the bottom of the layer and, given the relatively limited ray sampling at depth (Figs 3.34 and 3.35), this was not surprising. Changes to the velocity at the base of this layer will, though, be mirrored by a corresponding change in the velocity gradient. In the uppermost part of the mantle, where the majority of the P_n arrivals turn, the effect will be relatively small compared to the changes in absolute velocity, and will be mostly accommodated within the pick uncertainties. In contrast, changes to the upper velocity of this layer, either independently or as a bulk velocity shift in tandem with the bottom velocity, have a much greater impact. For the Pacific plate, this produced confidence limits of

+0.4/-0.2 km s^{-1} on the uppermost mantle velocity. Equivalent tests on the upper mantle velocity sensitivity for the overriding plate showed that it does not appear to be influenced by increases in velocity at the top of the layer, although the bulk velocity perturbations do reach similar limits of +0.4/-0.3 km s^{-1}.

In Section 4.2.5, the differences between the *forward* and *inverse models* were discussed both qualitatively and quantitatively, the latter only where both have ray coverage. The degree of difference, expressed by the standard deviation in velocity between the two models, was found to be 0.34 km s^{-1}. This is of a similar magnitude to the average velocity confidence limits determined from the sensitivity testing, which indicates that the observed difference between the velocity structures resulting from the two modelling approaches, and the degree of confidence in those structures, can be attributed primarily to the pick uncertainties, and how each approach minimised the misfit between calculated and observed travel time picks.

4.4.3.2. Depth sensitivity

The Indo-Australian plate shows decreasing sensitivity to layer depth with increasing depth in the crust. However, the homogenous layer testing approach applied in this study becomes problematic when reducing (shallowing) the upper crustal layer depth because, where present, the sediment cover is very thin (e.g. between 130-180 km d.a.p.), and layer crossing violations readily occur. Consequently, ray-tracing fails before the sensitivity limits are reached in parts of the model where thicker sediments are present. Middle and lower crustal layer depths can be resolved to within ±0.4 km. The Moho depth appears to be poorly constrained, with calculated confidence limits of +0.9 and -1.4 km. It is likely that this is related to the lack of model sensitivity to changes in velocity in the mantle, suggesting that there is less constraint on the layer as a whole. Whether this is a direct result of the modelling approach used, or occurs as a consequence of the ability of the dataset to resolve features at depth, will be considered in the next section.

For the tests performed on the Pacific plate, layer crossing violations occur for the shallowing of both the upper and middle crustal layers. The former arises for the same reasons as for the overriding plate, whereas the latter is a direct result of the proximity to the top of the apparent high-velocity core within several of the seamounts. The middle and lower crustal layer interfaces show similar sensitivity to depth perturbations as for the overriding plate, with the confidence limits assessed to be +0.5/-0.2 km. The Pacific Moho is much better constrained than the Moho of the Indo-Australian plate, with confidence limits of +0.2/-0.6 km mirroring the better constrained mantle velocity. This observation supports the suggestion that the lower confidence in the overriding plate Moho depth and mantle velocity may be interrelated.

4.4.3.3. Testing the significance of depth sensitivity on the Moho

To determine the significance of the sensitivity testing results on the ability to resolve interface depth, it is necessary to distinguish whether the principal controls on model sensitivity arise as a result of the modelling technique adopted or the characteristics of the dataset being modelled. Such appraisal is informed by analysis of the source characteristics of the seismic data, and how the signal characteristics vary during propagation. The minimum depth variability of an interface that can be resolved by seismic data is considered to be $\lambda/4$, where λ is the wavelength of the seismic signal at the depth of interest. This corresponds to the maximum frequency component of the signal at that depth, which can be determined by frequency analysis of OBS records.

In order to estimate the frequency content of the seismic signal at the depth of interest, frequency spectra were calculated within windows encompassing arrivals which turn at this depth, which were selected based on their phase assignment. Spectra were also calculated in sample windows of water column noise directly preceding the selected arrivals and for the water wave direct arrival, to provide an indication of background noise characteristics, and an indicative frequency content of the signal at source, prior to crustal attenuation, respectively. This approach to assessing the significance of the sensitivity testing-derived confidence limits on the Moho depth is founded on the assumption that significant attenuation of higher frequencies in P_g, P_mP and P_n phases occurs as part of their propagation to and return from this depth. Consequently, the ability of these phases to resolve small changes is compromised as a result.

To estimate the degree to which the seismic signal characteristics limit the imaging of depth variability of the Moho specifically, frequency spectra were calculated for OBSs C17 and C18, at the southeasternmost end of the profile (Fig. 3.2). These OBSs are located in the bathymetrically and structurally simplest part of the profile, and so should, therefore, provide an estimate of the ‘best-case scenario’.

However, such appraisal must be approached with caution because, despite an OBS sitting on the seabed representing a far field measure of the downgoing wavefield, its records in this respect are contaminated by signal resulting from interaction of the wavefield with the seabed on which it sits. For example, the hydrophone would record not only the outbound P-wave passing by before it reaches the seabed, but also the returning P-wave reflection from it very shortly after.

Bearing in mind these caveats, the resulting spectra (Fig. 4.20) show that the bubble pulse dominates the signal at frequencies <5 Hz. The frequency content of the nearest-offset P_n arrivals, and the background noise which immediately precedes these

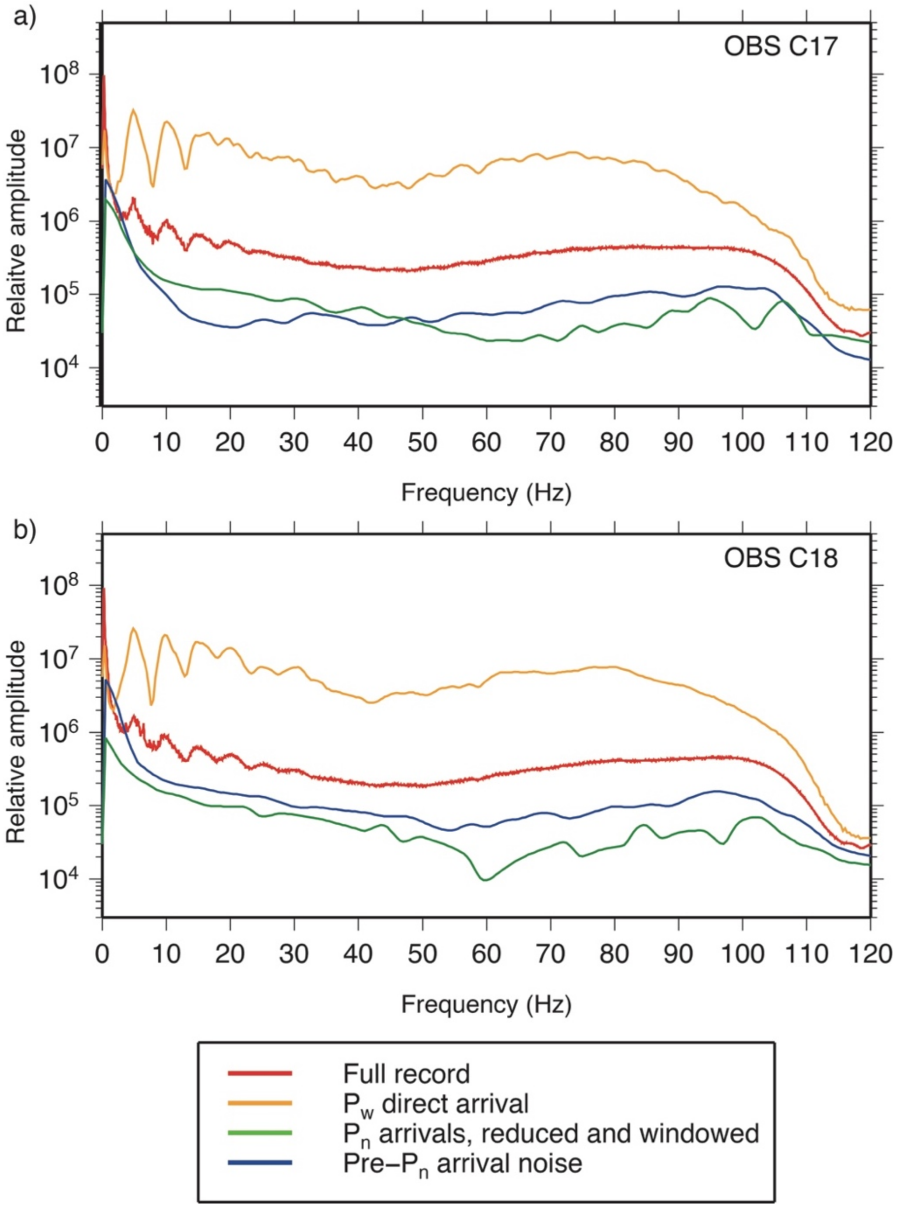

Figure 4.20: *Frequency spectra for a) OBS C17 and b) OBS C18. Line colours correspond to the windowed parts of the record indicated in the legend.*

picks, show similar general trends in signal content with frequency. For the windowed, near-offset P_n arrivals, the calculated spectra are relatively flat, except at the lowest frequencies. OBS C18 shows only a weak increase in relative amplitude for the low frequencies. However, a much clearer increase in amplitude in the P_n spectrum can be observed for frequencies <10 Hz for OBS C17. Taking 10 Hz as an upper, best-case, bound for the frequency range and a velocity at the base of the crust/top of the mantle of 7-8 km s^{-1} provides a range of minimum wavelengths of 0.7-0.8 km. Therefore, the best expected depth resolution for the Moho is of the order of 0.2 km, given the caveats associated with this calculation. When compared to the calculated confidence limits of +0.9/-1.4 km and +0.2/-0.6 km for the Indo-Australian and Pacific Moho depth respectively (Table 4.1) this value is relatively small, indicating that the error bounds on the depth of the Moho are not primarily governed by the source signal frequency content. Instead, it is likely that these confidence limits are influenced by a lack of arrivals sampling the mantle beneath both plates, or by the magnitude of the assigned P_n pick uncertainties. Overall, this conclusion supports the suggestion that the *forward model* is least well constrained in these regions.

4.4.4. Sensitivity testing the bend in Profile C

In Section 3.5.2, a method was devised to facilitate the inclusion of the bend in Profile C, and model it as a single 2D profile. The approach was based on a consideration of the additional pick uncertainties associated with a ray path not being directly along the profile, but instead travelling across the bend, passing close to the centre of 27.6˚S seamount. The inclusion of these picks indicated that there were no significant anomalous features within the upper and middle parts of the seamount. However, it must be considered whether the application of the pick selection procedure affects the confidence with which the crustal velocity structure in this region can be interpreted. This was achieved by testing how the model fit varies as a function of the inclusion of these additional picks, and whether the additional uncertainty applied to them has an effect on the model fit.

The sensitivity testing approach was, therefore, modified to prevent the buffering of the fit by long shot-receiver offset arrivals. Only OBSs located within <100 km either side of the bend were included, and for those OBSs only rays which trace towards the bend, resulting in a subset of ~7300 picks being used in this testing procedure. The same four types of perturbation were applied, and the testing procedure run twice for the same set of model perturbations, with the difference being the input pick set. The first set of picks tested included those that passed the test for inclusion in the forward modelling, and will be referred to in the following discussion as the 'selected picks at bend' test case. The second set excluded all rays which cross the bend, and will be referred to as the 'no picks at bend' test case.

Between the two test cases there is virtually no difference in the T_{rms} measure of fit (Fig. 4.21, right column). This result indicates that, excluding the consideration of additional errors which may be accumulated by arrivals not travelling directly along the profile as they cross the bend, both cases produce an equally good fit. It follows then that any variation in χ^2 between the two test cases arises almost exclusively as a result of the additional uncertainty which is added to the travel times of the arrivals which cross the bend (Fig. 4.21, left column).

The effect of changing the size of the added uncertainty was determined by applying the same testing procedure, using the pick set in for which rays travel across-the-bend. As the only difference is the additional uncertainty added to each pick, the number of rays traced and T_{rms} remain the same between each tested case, hence it is only changes in χ^2 which are considered. The control case in this instance was represented by the best-fit *forward model,* where 35 ms and 100 ms additional uncertainties were applied to P_g and P_n picked arrivals (Section 3.5.2.3). Two different additional uncertainty cases were tested, the first being the 'no additional uncertainty' case, where the rays traced across the bend had the same pick uncertainties as those which did not. This approximates the case where only the proximity to the seamount centre criterion governed whether a travel time pick was selected or not. The second test involved applying 'reduced additional uncertainties' of 35 ms (50% of the initial value) to P_g arrivals, and 50 ms (also 50% of the initial value) to P_n arrivals. The rationale governing the choice of the second test condition was that the path-length difference calculations in Section 3.5.2.2. showed that very few rays which pass the S_{max} criterion displayed a travel time difference (τ) of > 50 ms. The results of this testing scheme are shown in Fig. 4.22.

These tests indicate that, of the two criteria used to determine which picks were selected for inclusion, the proximity of the ray path to the seamount centre has a more significant impact on the final model fit than applying additional pick uncertainties. In

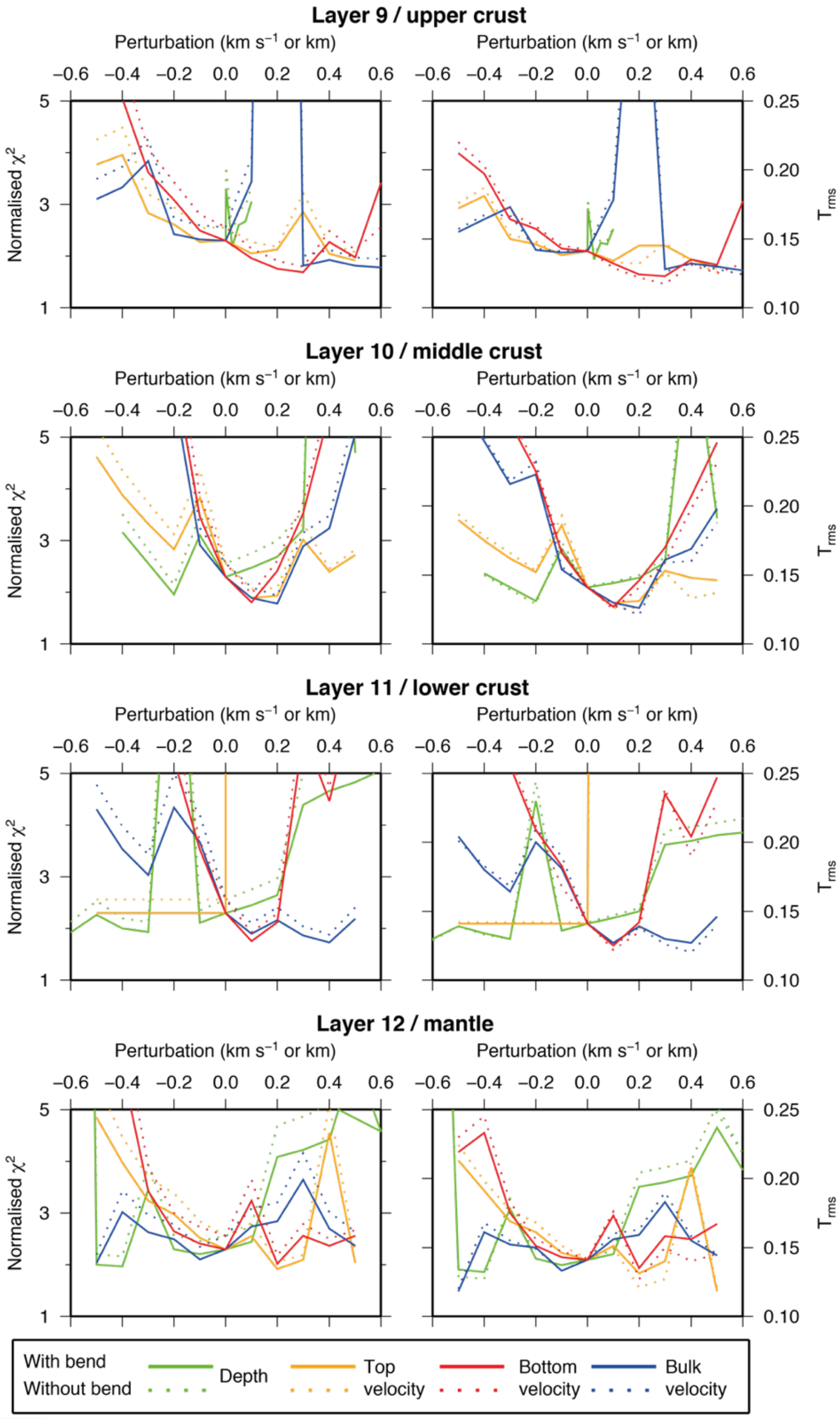

Figure 4.21: *Comparison between sensitivity testing results with and without inclusion of picks at the bend. Left column plots are χ^2 values, right column T_{rms}, plotted against perturbation in km for depth, and km s^{-1} for velocity. Layer depth increases down the page. Solid lines represent testing scheme where picks selected by method in Section 3.5.2 are included, and dotted lines represent where all ray paths crossing the bend are excluded. Colours of lines correspond to layers as identified in legend.*

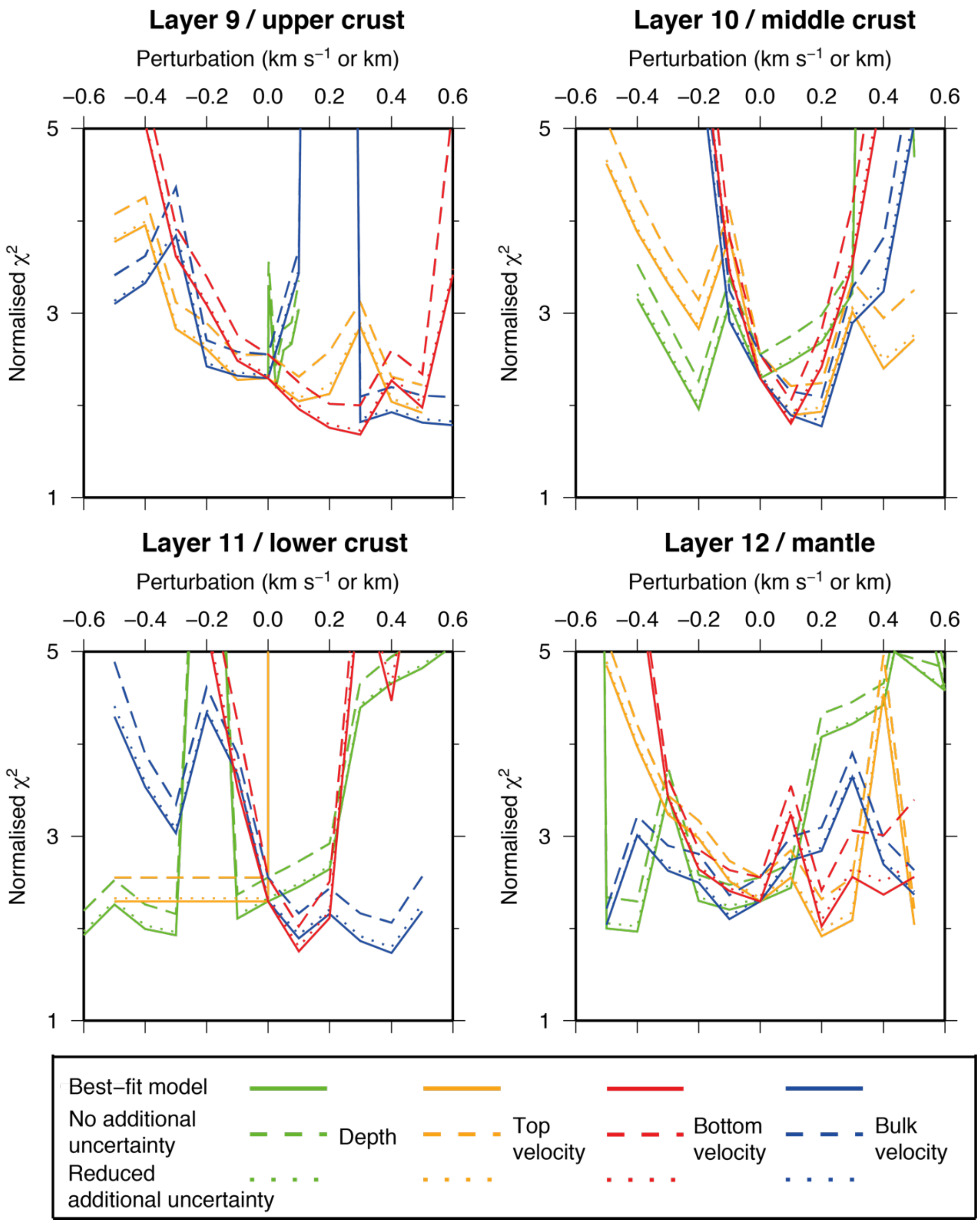

Figure 4.22: *Comparison between sensitivity testing results with inclusion of picks at the bend for different applied uncertainties. Plots are* χ^2 *values, plotted against perturbation in km for depth, and km* s^{-1} *for velocity. Layer depth increases down the page. Colours of lines correspond to layers as identified in legend. Solid lines represent the best-fitting model with 35 ms additional uncertainty applied to* P_g *and 100 ms to* P_n *arrival phases, as described in Section 3.5.2. Dashed lines represent a test where no additional uncertainty is added to arrivals which cross the bend. Dotted lines represent a test where 35 ms additional uncertainty is applied to* P_g *and 50 ms additional uncertainty is applied to* P_n *arrival phases.*

addition, the fact that the control case and 'reduced additional uncertainty' case show an almost identical fit indicates that the 100 ms additional uncertainty applied to the P_n arrivals in the best-fitting model case does not have a significant impact on the overall quantitative model fit. As a result, this value is not, therefore, deemed to represent an over-generous application of additional uncertainty.

Overall, the testing in this section indicates that the pick selection scheme applied in Section 3.5.2 produces only minimal adverse and/or detrimental effects on the modelling result. That is to say, the pick selections which are made appear to be sufficiently conservative, and are handled in a way which does not appear to cause significant changes to the fit of the model.

4.5. Gravity modelling

Gravity modelling was conducted to provide an additional, independent check on the uniqueness of the *forward model*, whereby the FAA associated with the modelled crustal seismic velocity structure was calculated and compared with ship-board acquired FAA. Gravity modelling also allows further appraisal and constraint on parts of the model where the ray coverage is relatively limited, for example the dip of the subducting slab at depth (Section 4.5.4). For gravity modelling, the *forward model* was converted using standard velocity-depth relationships and the model blocks defined by velocity contours representative of principal oceanic crustal layers (e.g. Houtz and Ewing, 1976; White et al., 1992; Kopp et al., 2004). The resulting model is hereafter referred to as the *density model*.

4.5.1. Conversion of the *forward model* to the *density model*

Block geometries within the *density model* were derived from velocity contours representing the first-order oceanic crustal layering. The blocks corresponding to the water and sediment layers extend along the entire length of the profile, and separate sets of crustal and upper mantle blocks were constructed for each plate. The model was extended to 100 km depth using SLAB1.0 (Hayes et al., 2012) to constrain the location of the slab. It was also necessary to extend the model laterally at both ends, to 1000 km, to prevent edge effects. The bathymetry for these extensions was sampled from the GEBCO global bathymetry compilation (IOC et al., 2003).

Each model block was assigned a density based on its average velocity from the *forward model*, with the confidence limits on layer velocities (Section 4.4) also taken into account. A number of empirically calculated, standard velocity-density relationships exist to describe various geological materials. Where listed below, the equations are formulated to convert from P-wave velocity in km s^{-1} to density, ρ, in g cm^{-3}. These units are chosen over the SI units for density of kg m^{-3} for conciseness in discussion and clarity in figure annotation. Figure 4.23 displays the conversion curves for a range of velocities typical for the sedimentary and oceanic crustal layers, and the densities calculated. Table 4.2 shows the range of velocities for each block in the *density model*, the calculated range of density values that these correspond to, and the value assigned to each layer in the best fit *density model* (Sections 4.5.5-4.5.6). The velocity-density relationships which were considered are:

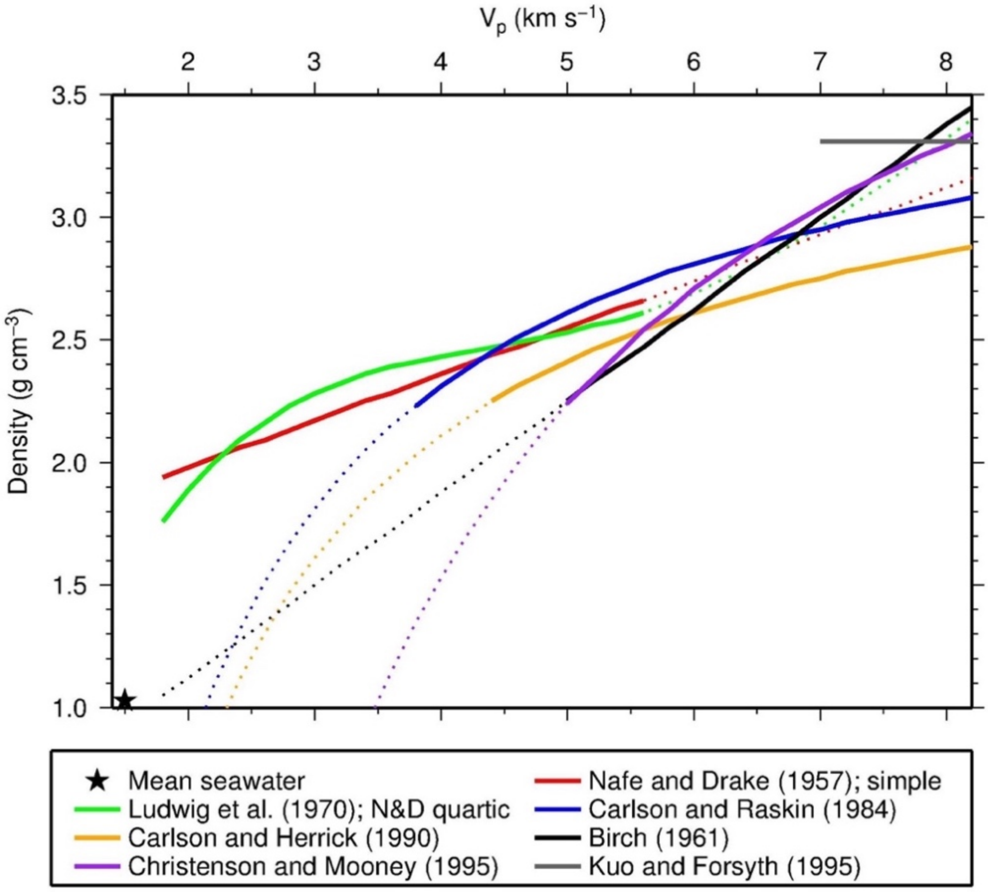

Figure 4.23: *Empirically derived velocity-density conversion curves. Line colours correspond to citations in legend. Values are calculated over full ranges of velocities present in the model, and as drawn as solid lines for velocity ranges between which they are most appropriately applied and as dotted lines elsewhere.*

Plate	Block No.	Layer	Block velocity (km s^{-1})		Density range (g cm^{-3})	Density in model (g cm^{-3})
			Top	Bottom		
n/a	1	water	1.5		1.03	1.03
	2	sediment	2.0	2.6	1.89-2.16	1.90
Indo-Australian	3	upper crust 1	3.0	4.0	1.81-2.31	2.30
	4	upper crust 1*				2.10
	5	upper crust 2	4.0	5.0	2.11.2.61	2.50
	6	upper crust 2*				2.30
	7	middle crust	5.0	6.5	2.41-2.90	2.85
	8	middle crust *				2.50
	9	lower crust 1	6.5	6.8	2.73-3.00	2.95
	10	lower crust 2	6.8	7.5	2.73-3.15	3.05
	11	lower crust 3	7.5	8.0	3.00-3.29	3.20
	12	mantle	>8.0	>8.0	3.31	3.31
Pacific	13	upper crust 1	3.0	4.0	1.81-2.31	2.10
	14	upper crust 2	4.0	5.5	2.11.2.70	2.30
	15	middle crust	5.5	6.5	2.45-2.87	2.60
	16	lower crust 1	6.5	7.0	2.70-3.00	2.90
	17	lower crust 2	7.0	7.5	2.95-3.15	3.00
	18	mantle	>7.5	>8.0	3.31	3.31

Table 4.2: *Velocity and density bounds for density model blocks, and best fitting values. Layer name corresponds to part of the model the layer number represents. * indicates layers which are split laterally to improve fit of short wavelength features in the trench (see section 4.5.6.), where the final column contains both density values used. Density range corresponds to the values calculated from the velocities at the top and bottom of each block, using the relationships in Fig. 4.23 appropriate for the corresponding layer.*

- Nafe and Drake (1957), which applies for sediments, and exists in two forms:
    - simple – $\rho = 0.19v + 1.6$; and
    - quartic – $\rho = 0.00283v^4 + 0.0704v^3 - 0.598v^2 + 2.23v - 0.7$ (Ludwig et al., 1970);
- Carlson and Raskin (1984), for the whole oceanic crust – $\rho = 3.81 - 5.99/v$, and which has been subdivided into:
    - Birch (1961), for the lower oceanic crust – $\rho = 0.375(v + 1)$; and
    - Carlson and Herrick (1990), for the upper oceanic crust – $\rho = 3.61 - 6/v$;
- Christenson and Mooney (1995), for continental crustal material, which may be appropriate for the lower crust of the overriding plate, as subduction is known to be a process by which continental crust is generated – $\rho = 5.055 - 14.094/v$; and
- Kuo and Forsyth (1988), for the mantle, which proposes a fixed density value – $\rho = 3.31$ g cm^{-3}.

4.5.2. Modelling procedure

Calculation of the FAA was performed using *grav2d* based on the method of Talwani et al. (1959). A DC shift is applied to the calculated anomaly to minimise the difference at the SE end of the model, which is chosen as the reference point it displays the least structural complexity. As a two-dimensional computation technique, this method assumes an infinite across-profile width to the blocks, which for the case of the LRSC may not be an entirely valid assumption. However, as a starting point, this method can be used to determine where the model fits well and where further investigation is required where it does not, including considering the consequence of the underlying 2D assumption. A valid test of the uniqueness of the *forward model* would be a fit between the observed and calculated FAA being achieved without the need to make any adjustments to layer interface geometries or velocities beyond the confidence limits of the *forward model*.

4.5.3. Initial results

The initial density model is shown in Figure 4.24, together with the comparison between observed and calculated anomalies. In general, the fit between the amplitude and wavelength of the calculated and observed anomalies is remarkably good for the Pacific plate region of the model. A significant mismatch is observed to the northwest of the trench axis which, given its amplitude, most likely results from the subducting slab not being adequately represented.

The initial representation of the subduction interface with depth was defined using SLAB1.0 (Hayes et al., 2012), with equal densities for the deeper parts of both the Pacific and Indo-Australian mantle of 3.31 g cm^{-3} producing the large, long-wavelength misfit (Fig. 4.24) By reducing the Pacific mantle density by 0.11 g cm^{-3}, to 3.2 g cm^{-3}, much of this large misfit can be eliminated (Fig. 4.25). The limited velocity constraint on the mantle beneath both plates allows these variations in density within the confidence limits. However, based on the observation that the best-fitting velocity for the Pacific mantle is faster than the Indo-Australian, as seen in both the *forward* and *inverse models*, the changes in density described above appear to be contradictory. It is possible that melt depletion as a result of intraplate volcanism may result in small variations in mantle seismic velocity and density (Schutt and Lesher, 2006), However, these are small relative to the model confidence limits of +0.4/-0.2 km s^{-1} calculated for the Pacific mantle in this study and, thus, unresolvable.

Alternatively, the mismatch may arise as a result of the extension of the subduction interface to depth using SLAB1.0 failing to successfully remove a long-wavelength gravity component associated with the subducting plate. The sense of the misfit indicates that the modelled dip of the slab may be too steep. Consequently, in the following section, the relative contributions to misfit of the slab dip, mantle density, and the overriding plate structure will be considered.

4.5.4. Model refinements

The relative contributions of the slab dip, mantle density, and the overriding plate thickness to the modelling misfit can be considered by testing fits for ranges of these quantities. Figure 4.26 shows a schematic of the three types of test which were applied.

Modification to the slab dip was achieved by applying a scaling factor, here referred to as the slab dip scaling factor, which acts linearly with depth, from 25 km b.s.s. downwards. A value of zero corresponds to no change in depth, i.e. the SLAB1.0

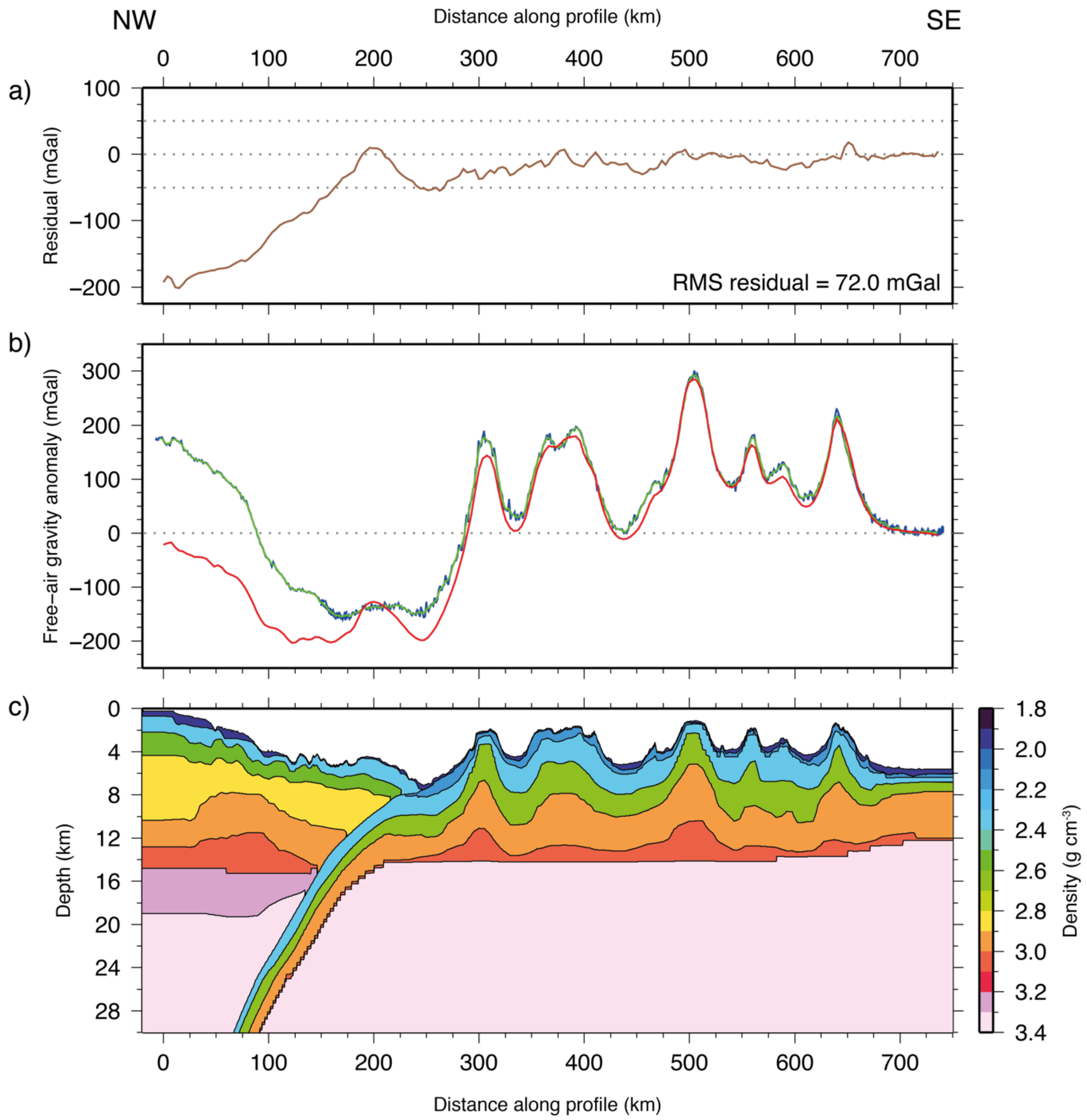

Figure 4.24: *Assessment of forward model uniqueness using gravity modelling. The initial density model maintains layer interface geometries from the forward model and has densities assigned using the standard velocity-density relationships discussed in the text. a) RMS residual between observed and calculated FAA, for the density block model in c). b) Red line is calculated FAA, blue line is the raw observed shipboard gravity and green line is the filtered observed shipboard gravity. c) Density block model used for the calculation of FAA, plotted to 30 km depth.*

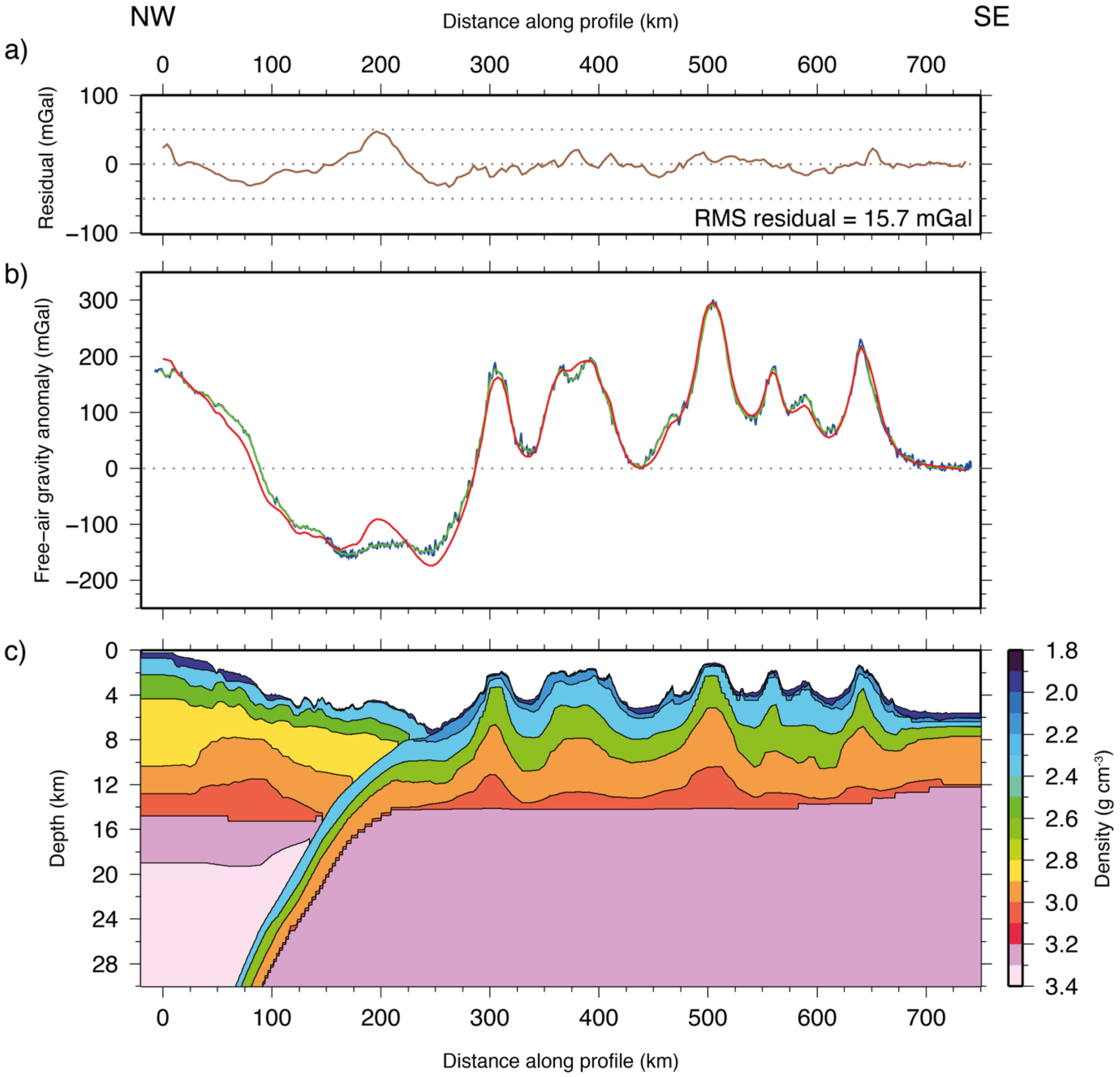

Figure 4.25: *Gravity modelling with adjusted mantle densities. a) RMS residual between observed and calculated FAA, for the density block model in c). b) Red line is calculated FAA, blue line is the raw observed shipboard gravity and green line is the filtered observed shipboard gravity. c) Density block model used for the calculation of FAA, plotted to 30 km depth.*

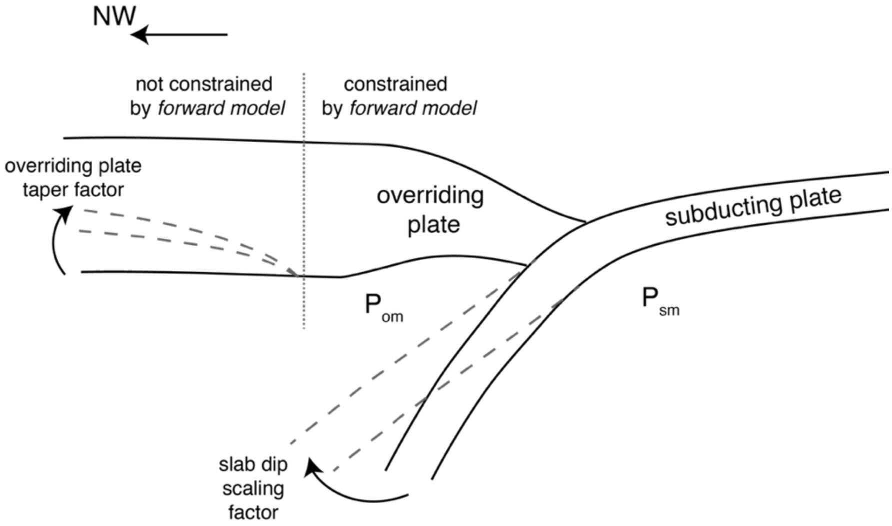

Figure 4.26: *Parameters used to determine the effects of the subducting slab on the fit of the density model. Dotted grey line represents divide between the part of the model constrained by the forward model (right) and that which is not (left). Black lines indicate the location of interfaces in the initial density model, where the slab location is defined by SLAB1.0 (Hayes et al., 2012), and the overriding plate structure to the northwest is extrapolated simply from that at the model edge. Dashed grey lines represent the alterations made to these interfaces, as part of the testing process.* P_{om} *and* P_{sm} *are the densities of the upper mantle beneath each the overriding and subducting plates respectively.*

defined location (Hayes et al., 2012), while values greater than zero correspond to decreasing of the slab dip or reduction of the depth to the top of the slab (Fig. 4.27).

It was also necessary to consider how crustal thickness varies beyond the ends of the profile. As a result of the more heterogeneous tectonic regime, this is more likely an issue to the northwest of the profile, in the Lau back-arc basin, than to the southeast. The crustal structure at the northwest end of the *density model* cannot, therefore, simply be continued from that at 0 km d.a.p., as this represents thickened arc/forearc crust.

For the northwestern extension of the crustal structure, a mechanism for varying the crustal thickness was devised, whereby it was thinned by the square root of the distance from the start of the profile. This means that the thinning initially occurs faster, close to the forearc, and eventually becomes essentially constant beyond 250 km to the northwest of the profile. Previous studies of the crustal structure of the Lau Basin (e.g. Crawford et al., 2003) indicate that the crustal thickness varies between 6-8 km along a profile close to the incoming Capricorn seamount, compared to a

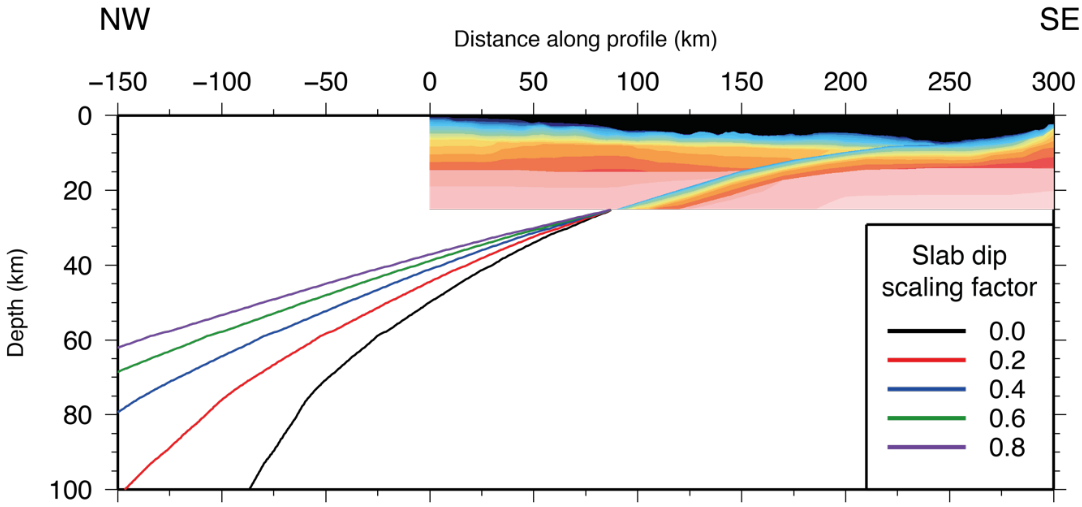

Figure 4.27: *Depths to the top of the slab for a range of slab dip scaling factors, applied below 25 km depth. Black line corresponds to the SLAB1.0 model (Hayes et al., 2012). Forward model is plotted in the region where it is defined (≥0 km d.a.p. and ≤25 km b.s.s.).*

thickness of ~12 km beneath the Tonga Ridge, which represents the thickest part of the arc/forearc unit. These observations, therefore, bound the range of crustal thicknesses to test. A scaling factor – here called the overriding plate thickness taper, or more succinctly the taper – was included which allowed control over what the final thickness at 250 km would be. At the southeastern end of the profile, the crustal structure and bathymetry were simply extended from the structure and seabed depth at the end of the model, since they are much more approximately representative of the background Pacific oceanic crust.

Regarding the observation that, if the SLAB1.0 model is used to constrain the geometry of the plate boundary at depth, the mantle beneath the Pacific plate must have a 0.11 g cm^{-3} lower density than the Indo-Australian mantle in order to remove the long wavelength gravity misfit, it follows that changes in the slab dip may balance out differences in these density values. The dip and taper scaling factors do not themselves correlate directly to values of these parameters. Instead, they provide a means by which these parameters can be iteratively varied to determine their effect on the gravity model.

4.5.5. Long-wavelength misfit

Figure 4.28 shows that with distance to the northwest (i.e. <0 km d.a.p.), the misfit, as

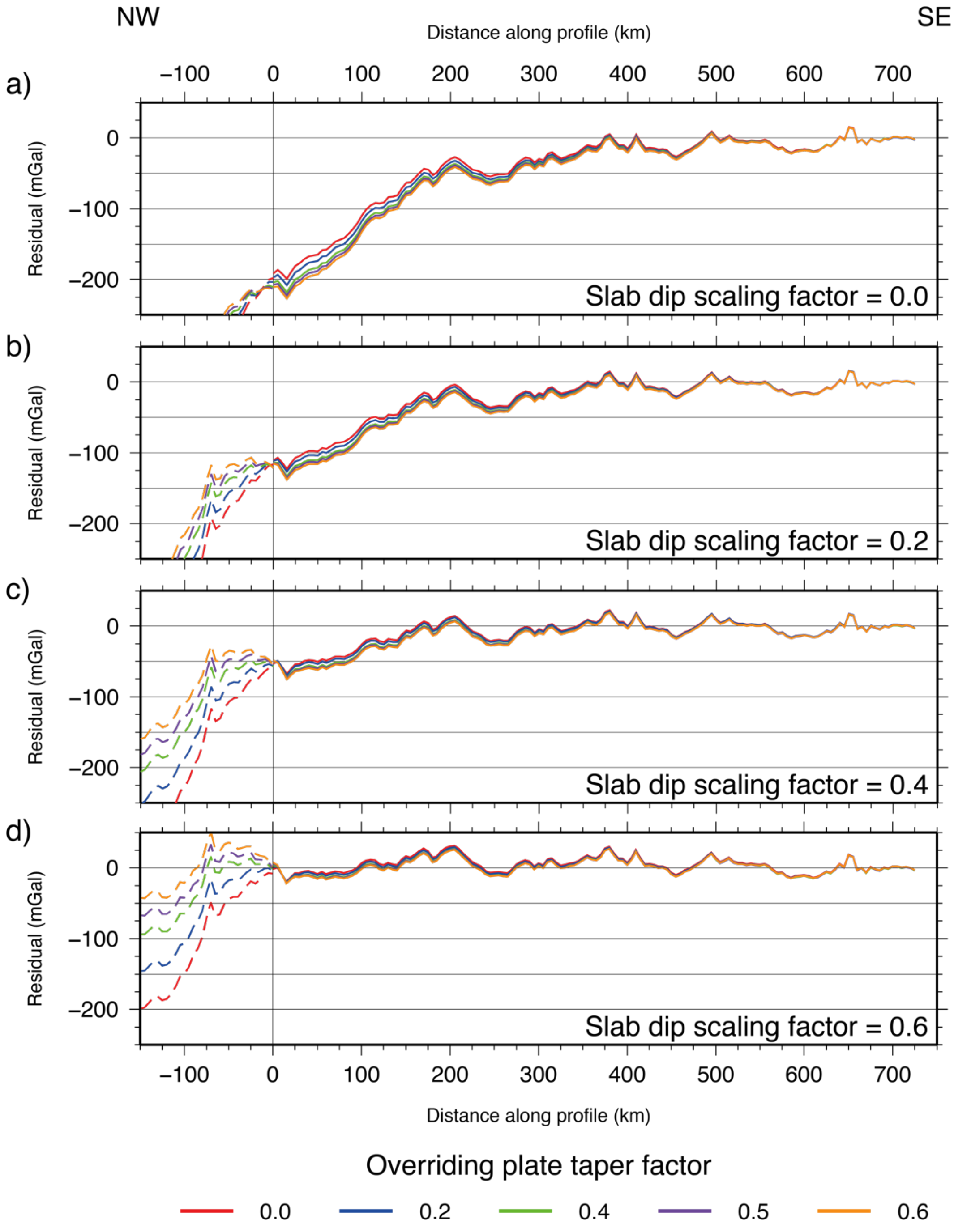

Figure 4.28: *Gravity model testing for varying slab dip and overriding plate taper scaling factors. Line colours correspond to values of taper at bottom of figure. Dashed lines indicate that the residual is calculated relative to the satellite derived (Sandwell et al., 2014) and solid the filtered, shipboard measured FAA. Mantle density beneath both plates is held constant at 3.31 g cm^{-3} for all tests. Slab dip scaling factors are annotated.*

measured by the residual between the modelled and observed FAA, quickly increases. Increasing the value of the slab dip scaling factor from zero to 0.6 results in progressive improvement in the removal of the long-wavelength gravity misfit.

The purpose of testing the overriding plate thickness taper factor is to ensure there is no significant edge effect, arising as a result of the extension of the model crustal structure to the northwest. If there is little difference in the calculated FAA for the parts of the model constrained by the *forward model* over a range of taper values, then edge effects as a result of the unknown crustal structure to the north can be deemed negligible. For increasing values of the slab dip scaling factor, this is seen to be the case, with no notable difference between the residuals between 0-100 km d.a.p. for values ≥0.5. However, differences as large as 25 mGal occur between taper factors of 0.0-0.6 for a slab dip factor of 0.0 (i.e. the SLAB1.0 case). These changes in the taper factor correspond to a change in thickness of ~6 km over 150 km d.a.p. (or ~90 km distance perpendicular to the trench) beyond the end of Profile C.

The relative dominance of changing the slab dip factor over the overriding plate taper factor indicates that the fit trade-off with the density value assigned to the mantle is likely to be dominated much more by the former than the latter. Figure 4.29a shows that for the location of the plate boundary at depth as defined by SLAB1.0, the best fit is achieved with $\Delta\rho = -0.11$ g cm^{-3}, with very little effect arising from variation of the taper factor. Progressively increasing the slab dip scaling factor (Fig. 4.29b-d), and, hence, decreasing the slab dip, results in a tendency towards less negative values of $\Delta\rho$ providing the best fit. It can therefore be seen how the choice of density for the two mantle blocks, or the reliability with which the SLAB1.0 model is held to be true, trade-off against each other with regard to providing the optimum fit. The two end member cases, therefore, appear to be that:

- the plate boundary follows the SLAB1.0 model to 100 km depth, and the Pacific mantle density is 0.11 g cm^{-3} lower than the Indo-Australian mantle density; or
- the plate boundary follows a shallower dip than SLAB1.0, with a non-dimensional scaling factor of 0.6 applied, with the Pacific and Indo-Australian mantle densities equal (±0.01 g cm^{-3}).

For illustrative purposes, Figure 4.30 shows a gravity model constructed with

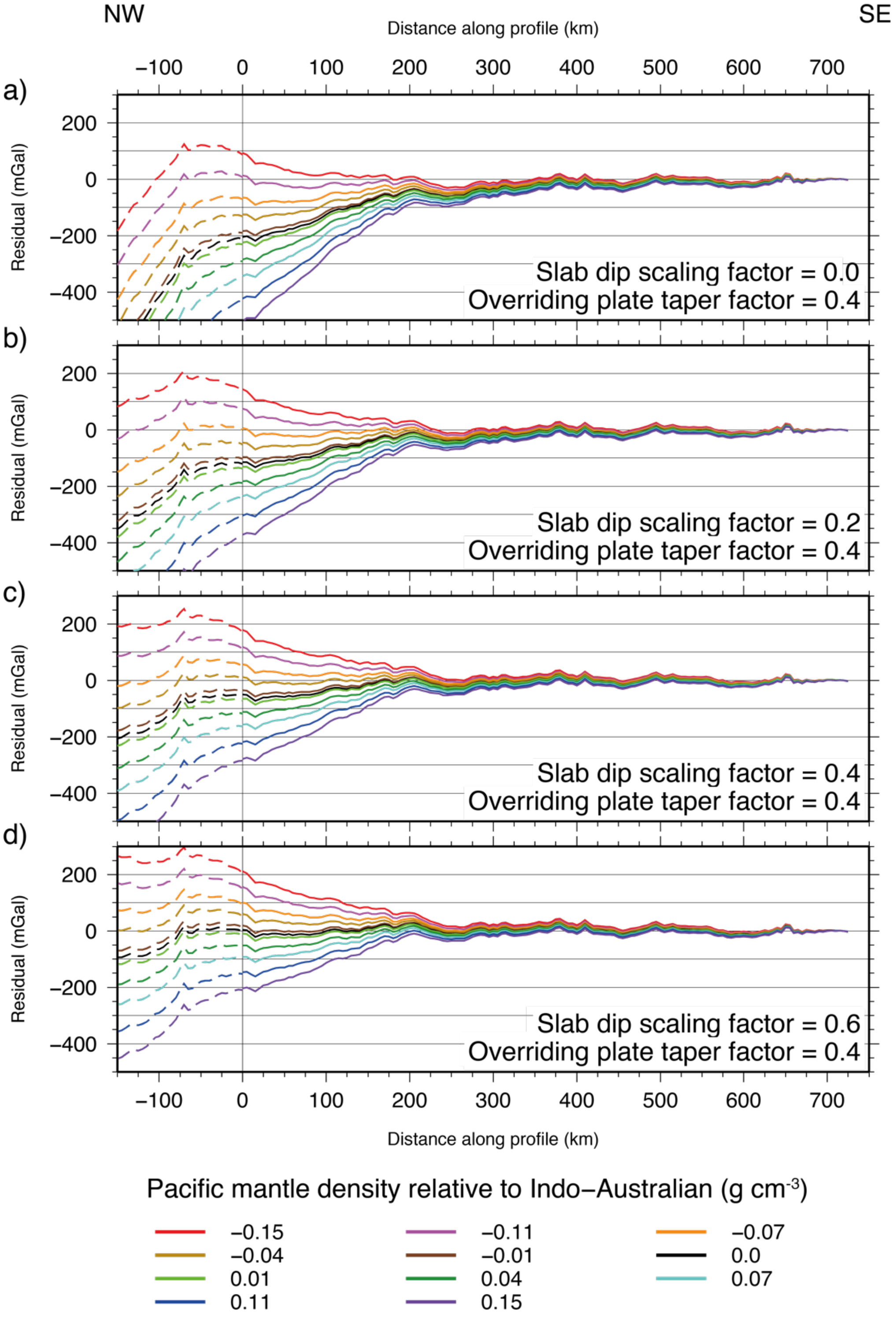

Figure 4.29: *Gravity model testing with varying slab dip and changing density contrast between Pacific and Indo-Australian mantle (Δρ). The density of the Indo-Australian plate mantle remained fixed at 3.31 g cm*$^{-3}$ *throughout, together with the overriding plate taper scaling factor at 0.4 throughout. Slab dip scaling factors are annotated.*

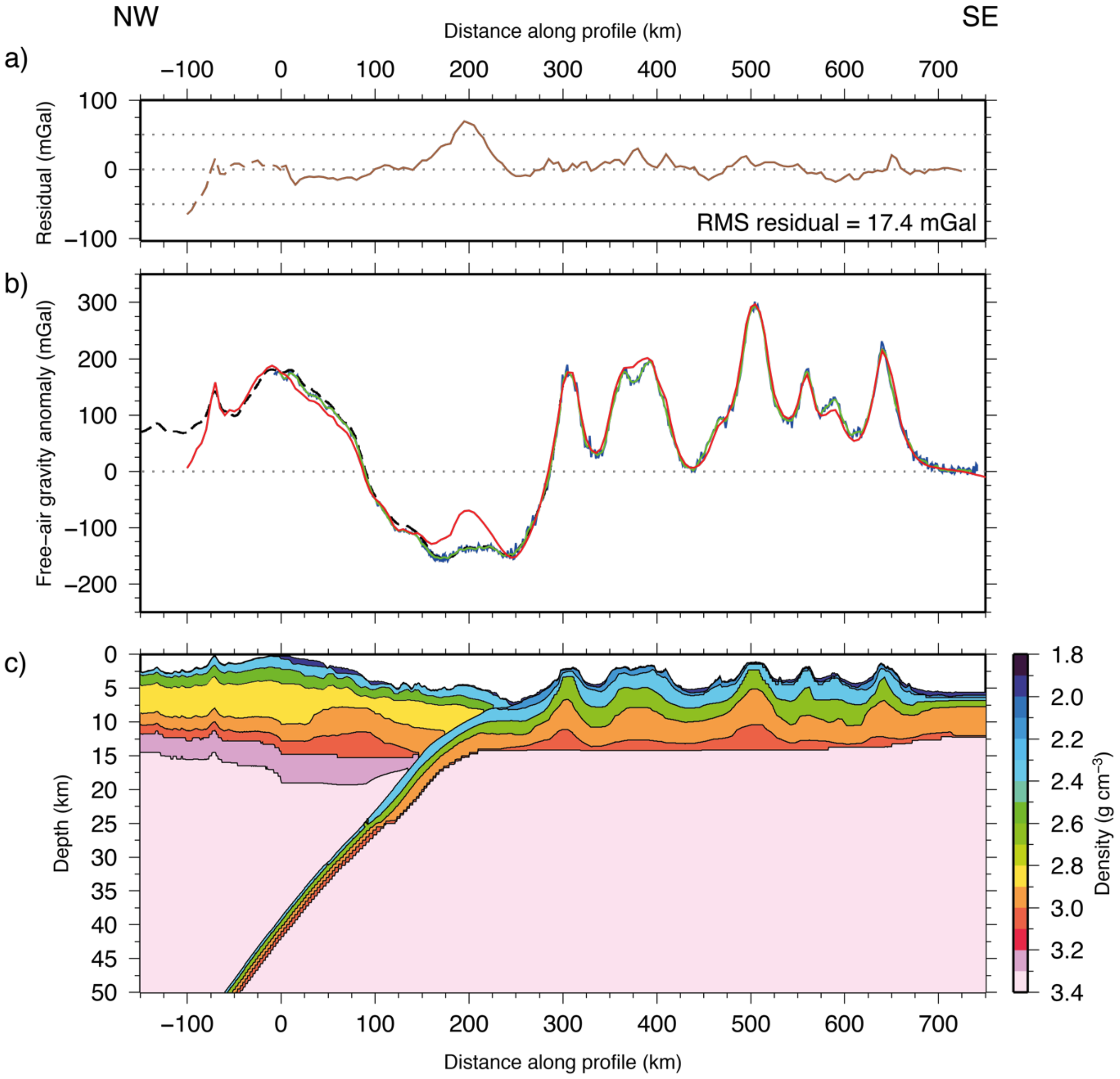

Figure 4.30: *Candidate best-fitting density model, with RMS residual of 17.4 mGal (calculated only for the shipboard measured FAA), slab dip factor of 0.6 and taper factor of 0.4. However, comparison with Fig. 4.29 indicates that slab dip factor can be reduced (slab steepened) if compensated by a density reduction in the Pacific mantle.*

a slab dip factor of 0.6 and taper factor of 0.4, with the mantle density beneath both plates set at 3.31 g cm^{-3}. The misfit between the shipboard FAA and the gravity anomaly calculated from this model has an RMS of 17.4 mGal. This is similar to that (15.7 mGal) calculated for the model shown in Figure 4.25, which has a 0.11 g cm^{-3} difference in the mantle densities between the two plates (the Pacific density being lower), and slab dip and taper factors of zero. Distinguishing between these end member cases is not possible, due to the non-uniqueness problem inherent in the gravity modelling approach. Which is considered more likely will be discussed in Chapter 5 where the combined results of all of the modelling undertaken will be discussed.

4.5.6. Lower forearc

An ~60-70 mGal positive FAA misfit is observed in the region of the trench axis and lower forearc slope (Fig. 4.30). This observation indicates that laterally continuous density blocks across each plate do not produce the best fit in this region. By making minor alterations to block geometries and densities in the lower trench slope region, this misfit can be reduced to an RMS misfit of 11.0 mGal (Fig. 4.31). The rationale for investigating the required changes to the density structure here to achieve a good fit, results from this being one of the regions most poorly constrained by ray-tracing.

Fit improvement was achieved by reducing the density of the upper crustal blocks by 0.2 g cm^{-3} and the middle crustal block by 0.35 g cm^{-3} between 180 km d.a.p. and the trench axis (~250 km d.a.p.). These density reductions correspond to relative velocity decreases of ~0.5 km s^{-1} and ~1.0 km s^{-1} respectively. These velocity reductions lie outside the *forward model* confidence limits for the corresponding layers of +0.4/-0.3 km s^{-1}. However, the challenges associated with imaging seismic velocity structure in deep and structurally complex environments, which manifest in the models as regions of highly variable ray coverage and steep velocity gradients, may indicate that these limits are underestimated. It may also be the case that a homogeneous layer approach to determining the confidence limits of the *forward model* may not be valid for all regions of the model. Alternatively, it is possible that this represents a manifestation of some across-profile structure, which is not considered here as a result of the 2D modelling approach. The potential origin or cause of these reduced densities will be discussed in Chapter 5, where the *forward model* is described and interpreted with relation to its tectonic setting.

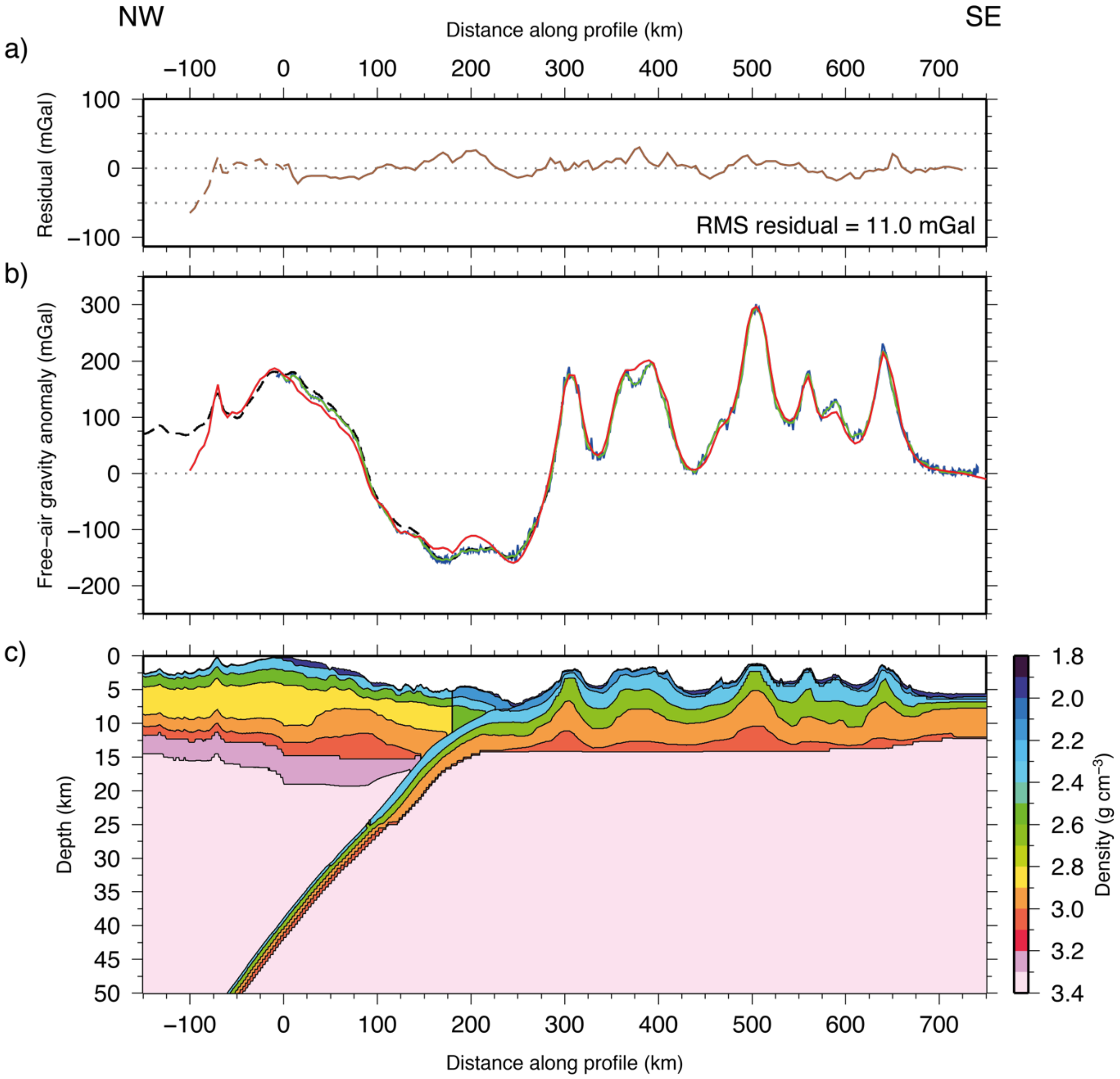

Figure 4.31: *Preferred density model, with RMS residual of 11.0 mGal (calculated only for the shipboard measured FAA). Trench axis/lower forearc slope misfit is minimised by splitting of upper and middle crust blocks and reducing the density of those comprising the lower trench slope, as discussed in the text. Model includes a slab dip factor of 0.6 and taper factor of 0.4, however comparison with Fig. 4.28 indicates that slab dip factor can be reduced (slab steepened) if compensated by a density reduction in the Pacific mantle.*

4.6. MCS data restacking

Following the completion of forward velocity modelling, the derived P-wave velocity-depth structure is used to restack the MCS data. In order to do this, the P-wave velocity-depth (*forward*) model (Fig. 4.32a) needs to be converted to a stacking velocity-TWTT model. This is achieved by calculating the travel time associated with each node of the regularly sampled grid at a 1.0 km horizontal spacing (corresponding to ~40 CMPs), and 0.1 km vertical spacing, and then vertically integrating to produce a cumulative sum with depth. The result is then multiplied by two to account for the two-way travel direction of reflection ray paths. The interval velocity-TWTT model generated is shown in Figure 4.32b.

In order to be used as an input for NMO correction, the interval velocities must be converted to stacking velocity. The *Claritas rmsint* utility is used to apply an inverse form of the Dix (1955) equation which performs this conversion (Fig. 4.32c). The MCS data are NMO corrected and re-stacked using this velocity model, and the same migration, gain and mute parameters that were used in Section 2.3, to produce the image in Figure 4.33. Improvement to the stacked image is generally limited, however there is significant suppression of the shallow seabed multiple in the uppermost forearc between 0-50 km d.a.p. and 1.5-3.0 s TWTT, which may help with producing a better image of the basement in this region. Restacking the MCS data does not appear to improve the ability to image deeper crustal features such as the Moho. It is likely that this occurs as a result of the complex bathymetry and subsurface geology generating significant signal scattering, thus impacting imaging ability at depth. Particular results arising from MCS restacking will be addressed in Chapter 5, alongside detailed description and interpretation of the full WA seismic model developed in Chapter 3 and subsequently tested in this chapter.

4.7. Summary

In this chapter, a series of rigorous model testing procedures have been applied to appraise the *forward model* developed in Chapter 3. These tests have successfully demonstrated that the model represents a valid solution to the WA seismic dataset that is free of bias and effectively unique.

This conclusion has been drawn primarily after the application of an inverse modelling approach, using the inversion code *FAST* (Zelt and Barton, 1998 – Section 4.2). The resulting *inverse model* was achieved with minimal user-defined inputs to

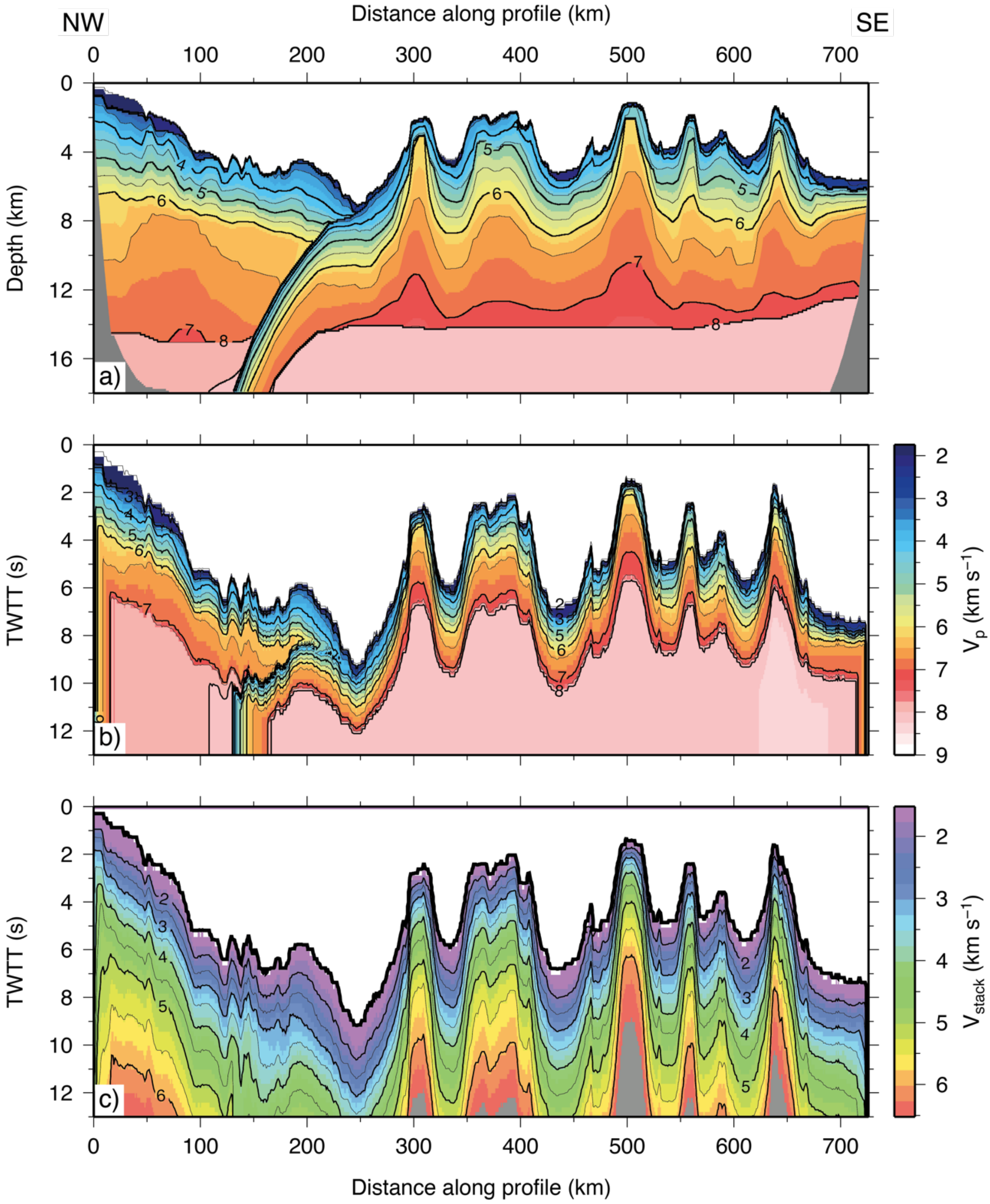

Figure 4.32: *Conversion of P-wave velocity-depth model to stacking velocity-TWTT model. a) Best-fit forward modelling-derived P-wave velocity-depth model. b) P-wave velocity model converted from depth to TWTT at 1 km horizontal and 0.1 km vertical sampling intervals. c) Stacking velocity-TWTT model produced by applying inverse Dix (1955) equation to b), which will be used to restack the MCS data. Contours drawn at 0.5 km s^{-1} and annotated at 1 km s^{-1} intervals.*

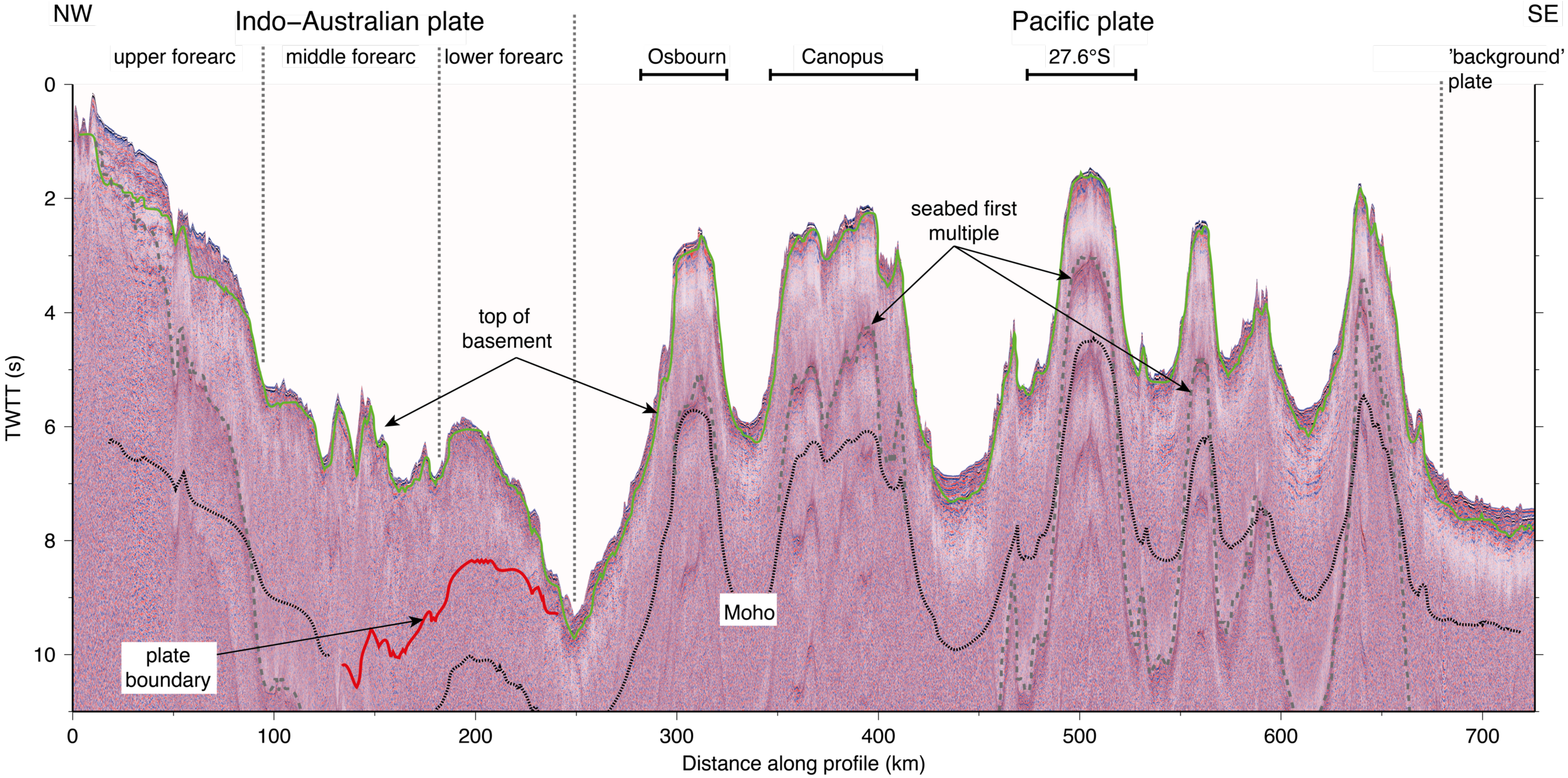

Figure 4.33: *Forward model restacked MCS record section plotted using same parameters as Figs 2.13-2.19. Principal tectonic divisions and seamounts labelled above figure. Green line indicates location of top of oceanic basement in forward model. Dotted black line indicates location of Moho from forward model, however it is not well represented by reflections at any points along-profile. Red line indicates model location of plate boundary. Dashed grey line indicates location of first seabed multiple, where this is visible in the section. The multiple is significantly weakened, particularly in the upper forearc region, as a result of restacking.*

the parameterisation. The only principal input to which the inversion process was found to be sensitive to was the starting model, of which a range were tested to determine the simplest and least free of preconceived bias. Using the ray coverage through the *inverse model*, it was then possible to determine what the smallest resolvable model features are using a checkerboard method (Section 4.3). The results of this testing indicate that seamount-sized structures should be well resolved throughout the model, but least so in the trench axis region. The principal limit on resolution appears to be the vertical dimension of the input velocity anomaly, with cells of 4 km and taller being successfully resolved over a range of horizontal anomaly sizes, but recovery becoming quite limited at 3 km or less in vertical dimension.

The above constraints on minimum resolvable feature size will be considered in the following chapter, to guide the degree to which the results of this study can be interpreted. This interpretation will be conducted in tandem with an appreciation of the confidence limits assessed for the depth and velocity values within the *forward model* (Section 4.4).

Finally, further support for the uniqueness of the *forward model* was provided by applying a gravity modelling technique to a *density model* derived from the *forward model* (Section 4.5). By comparing the modelled free-air gravity anomaly with shipboard and satellite observed FAAs, it has been shown that there are a number of *forward model* features which are not well reconciled.

In the following chapter the results of forward modelling (Chapter 3), will be described and interpreted in full, alongside the MCS record section (Chapter 2 and Section 4.6). The inverse and gravity modelling and model testing procedures conduced in this chapter will be used to inform the robustness of and degree to which these interpretations can be made. In addition, the results of forward modelling of Profile C will be synthesised with additional data profiles in the region, in order to place the observations into a regional tectonic context.

Chapter 5 – Model Description and Interpretation

5.1. Introduction

Chapter 3 provided a description of the forward modelling technique applied to the Profile C wide-angle seismic dataset to produce a best-fit crustal structure velocity-depth *forward model,* where initial constraint was derived from the MCS data presented in Chapter 2. In Chapter 4, this *forward model* was then tested to determine its uniqueness and the limits to which it can be interpreted to. The *forward model* was also tested for its sensitivity to perturbations in the depths of layer interfaces and layer velocities, to determine their confidence. The generation of a velocity-depth model using an inverse modelling technique which displayed consistency with the *forward model*, provided an indication that the *forward model* represents a unique solution to the dataset. The *inverse model* was used to appraise the capability to resolve features of a given size. In this chapter, the results of arising from all aspects of modelling will be described in detail. Where relevant, the confidence limits derived in Section 4.4 will be provided for layer depths and velocities, and the sizes of features will be considered with respect to the minimum resolvable feature size calculated in Section 4.3. In order to extend the observations made from Profile C into pseudo-three-dimensional interpretations of seamount structure and along-margin variability in forearc structure, the results of this study will be synthesised with additional WA profiles from the SO215 experiment (A, Stratford et al., 2015; B, Funnell et al., 2017) and the earlier *TOTAL* experiment (P02, P03, Contreras-Reyes et al., 2010; 2011).

5.2. Pacific plate

Profile C traverses only a short length of the 'background' Pacific oceanic crust (Fig. 5.1a; 690-726 km d.a.p.) which is unmodified by seamount volcanism, limiting the observations that can be made from this profile alone. A thin sedimentary cover (~700 m) with velocity 2.3-2.6 (± 0.1) km s^{-1} overlies an upper crustal layer <0.5 (+0.2/-0.1) km thick with a velocity of 3.5-5.0 (± 0.4) km s^{-1}. Below this, the middle crust thickness varies between 1.5 km close to the LRSC and 1.0 (± 0.4) km at the southernmost end of the profile, and the velocity increases from 5.0 (+0.4/-0.3) km s^{-1} at the top to 6.5 (± 0.2) km s^{-1} at the base. The lower crustal velocity increases from 6.5 (± 0.2) km s^{-1} at the top to 7.0-7.2 (± 0.4) km s^{-1} at the base, over a thickness of

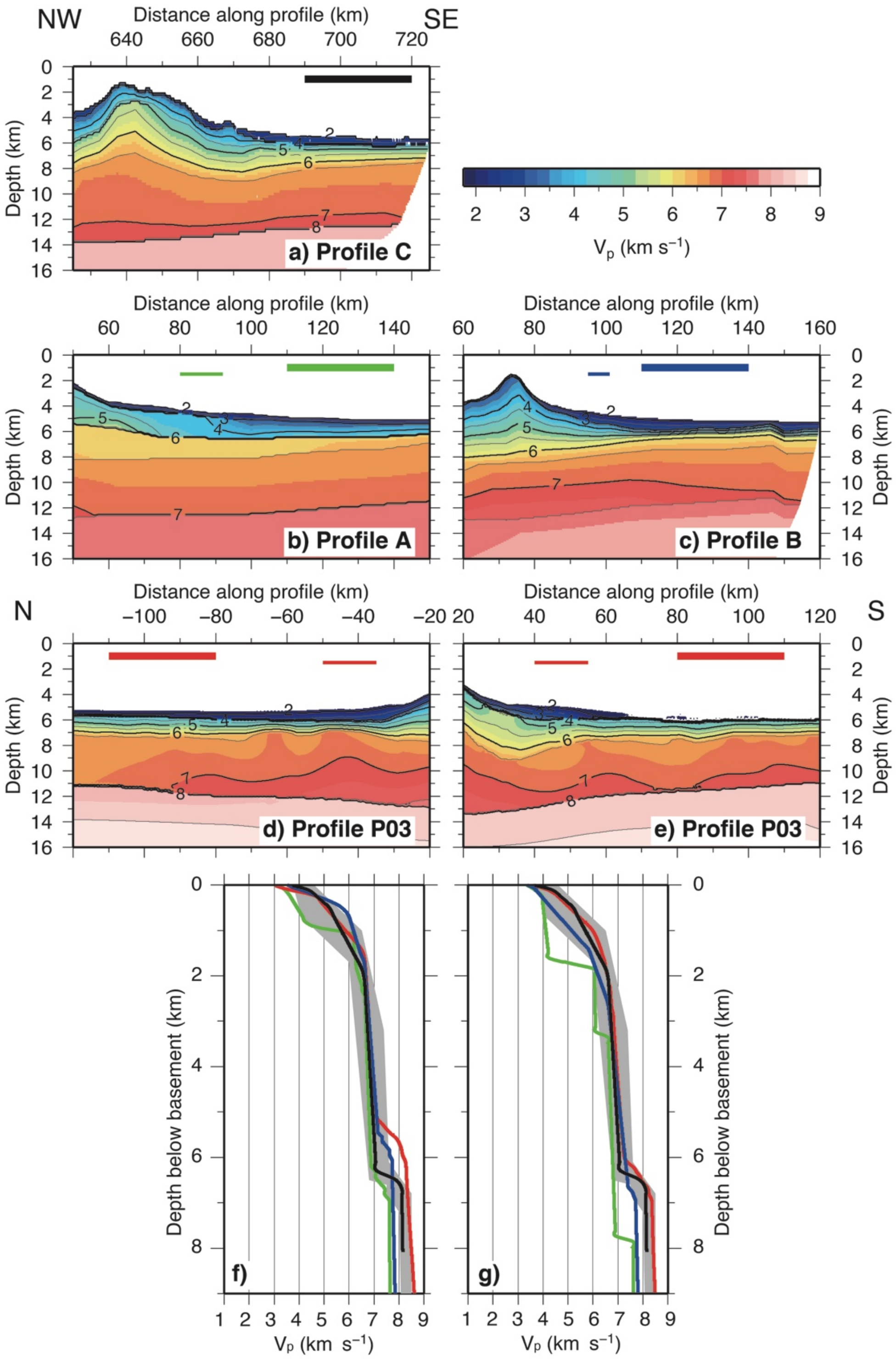

Figure 5.1: *Best-fit P-wave velocity-depth models for oceanic crust adjacent to seamount edifices. a) Profile C, b) Profile A, and c) Profile B, and Profile P03 to the d) south and e) north of 27.6˚S seamount. Horizontal coloured bars represent the offset range over which 1D profiles have been sampled and averaged. f) 1D velocity-depth profiles from the models in a)-e). Colours as for thick coloured bars in a)-e), g) 1D velocity-depth profiles sampled closer to seamount flanks at the locations indicated by thin coloured bars in a)-e). The White et al. (1992) average Pacific oceanic crustal structure is plotted as a grey envelope for reference.*

~4.5 (+0.5/-0.2) km. The total crustal thickness is, therefore, observed to be ~7.0-7.5 (+0.2/-0.6) km.

The additional WA profiles collected as part of the *TOTAL* project all sample the unmodified oceanic crust further from the LRSC. Velocity-depth profiles through these models (Fig. 5.1b-e) show that the ‘background’ Pacific plate crustal structure comprises a thin (few hundred metres) sedimentary cover, a <1 km-thick upper crust with velocity increasing from 3.0 km s^{-1} to 5.0 km s^{-1}, a 1-2 km-thick mid-crust with velocity 5.0-6.0 km s^{-1}, thickening towards the LRSC, and a 5 km-thick lower crust with velocity increasing to >7.0 km s^{-1}. The total crustal thickness is in the range 6.0-7.5 km. This is consistent with the lower bound of observations by White et al. (1992 – Fig. 5.1f), where layer 2 of the oceanic crust, corresponding to the upper and middle crust of the *forward model*, has a P-wave velocity of 2.5-6.6 km s^{-1} and a mean thickness of 2.11 (± 0.55) km, and layer 3, which corresponds to the lower crust of the model, has a velocity of 6.6-7.6 km s^{-1} and a mean thickness of 4.97 (± 0.90) km.

The close proximity of the LRSC volcanoes to the sampled ‘background’ crust on Profile C results in the crustal thickness here appearing greater than that observed on the other profiles. However, velocity-depth profiles from Profiles A, B and P03 taken closer to the seamount edifices show a crustal thickness more consistent with the observations from Profile C (Fig. 5.1g). The crustal structure at the southernmost end of Profile C is not, therefore, truly representative of the ‘background’ Pacific oceanic crust. Evidence for the loading effect of LRSC volcanoes is manifest in the shallow dip of middle and lower crust velocity contours towards the seamount chain, observed in the *forward model* (Fig. 5.1a). This may also account for the apparent thickness of the sediments observed in the MCS record section (Fig. 2.19), which appears greater than the typical values for the incoming Pacific plate (e.g. Funnell et al., 2014), as the loading of the plate by seamount emplacement may be generating additional accommodation space where these may be deposit. There is also an associated ~1 km deepening of the middle-lower crust transition, which corresponds to the distance along profile at which the Moho depth increases from that beneath the ‘background’ crust of 12.5 km b.s.s. to 14.2 km b.s.s. The variations in Moho depth along the profile will be discussed further in a following section.

5.3. LRSC

5.3.1. Seamount internal structure

A striking feature associated with the LRSC is the existence of intrusive bodies with a P-wave velocity >6.0 km s^{-1} within Osbourn and 27.6°S seamounts (Fig. 5.2a,b). The apexes of these features are located 1.0-1.5 km below the seamount summits, have a diameter of ~10 km, about a third to a half of their basal diameter, and protrude 5-6 km above the equivalent velocity contours in the saddles. In the *forward model*, the tops of these intrusive cores are well modelled by a first-order velocity discontinuity (i.e. a step in velocity), with regions of velocity of ≥6 km s^{-1} lying immediately adjacent to upper crustal velocities of ≤4.5 km s^{-1} (Fig 5.2c,e). The mid-lower crust transition, as represented by the 6.5 km s^{-1} velocity contour, reaches to within 4 and 5 km b.s.s. within 27.6°S and Osbourn seamounts respectively. The lowermost crustal velocity beneath these seamounts is 7.2-7.3 km s^{-1}, with velocities ≥7 km s^{-1} extending to 3-4 km above the Moho.

Previous studies over the summits of LRSC volcanoes (Fig. 5.2f; Contreras-Reyes et al., 2010) have observed a similar velocity structure, although the model in this study displays generally slower (by 0.2-0.6 km s^{-1}; Fig. 5.2e) velocities and a lower overall thickness (<1.0 km). The difference in thickness lies beyond the calculated confidence limit of +0.2/-0.6 km, indicating that it cannot fully be accommodated by the model uncertainty. Instead, these differences are probably related to different approaches to modelling. It may also be the case that part of the observed difference is related to features of the model which are below its imaging resolution limit, for example a relatively thin vertical ‘finger’ of 7 km s^{-1} material centred on ~5 km d.a.p. and a small velocity inversion above this (Fig. 5.2f).

5.3.2. Seamount flanks

Not all of the seamounts sampled by Profile C display the same internal structure described above. For example, Canopus seamount (350-410 km d.a.p.) does not display a pronounced higher velocity core, but instead shows 5 km thickness of the <6.0 km s^{-1} component (Fig. 5.3a). Three small (<5 km summit radius) unnamed seamounts to the south of 27.6°S (540-670 km d.a.p.) are also crossed over their flanks by the profile, which passes within 5-8 km of their centres. These seamounts all show a similarity with the flank-crossed Canopus seamount, in that lower crustal velocities (≥6.0-6.5 km s^{-1}) do not reach to shallow depths within the edifices. Profile C crosses

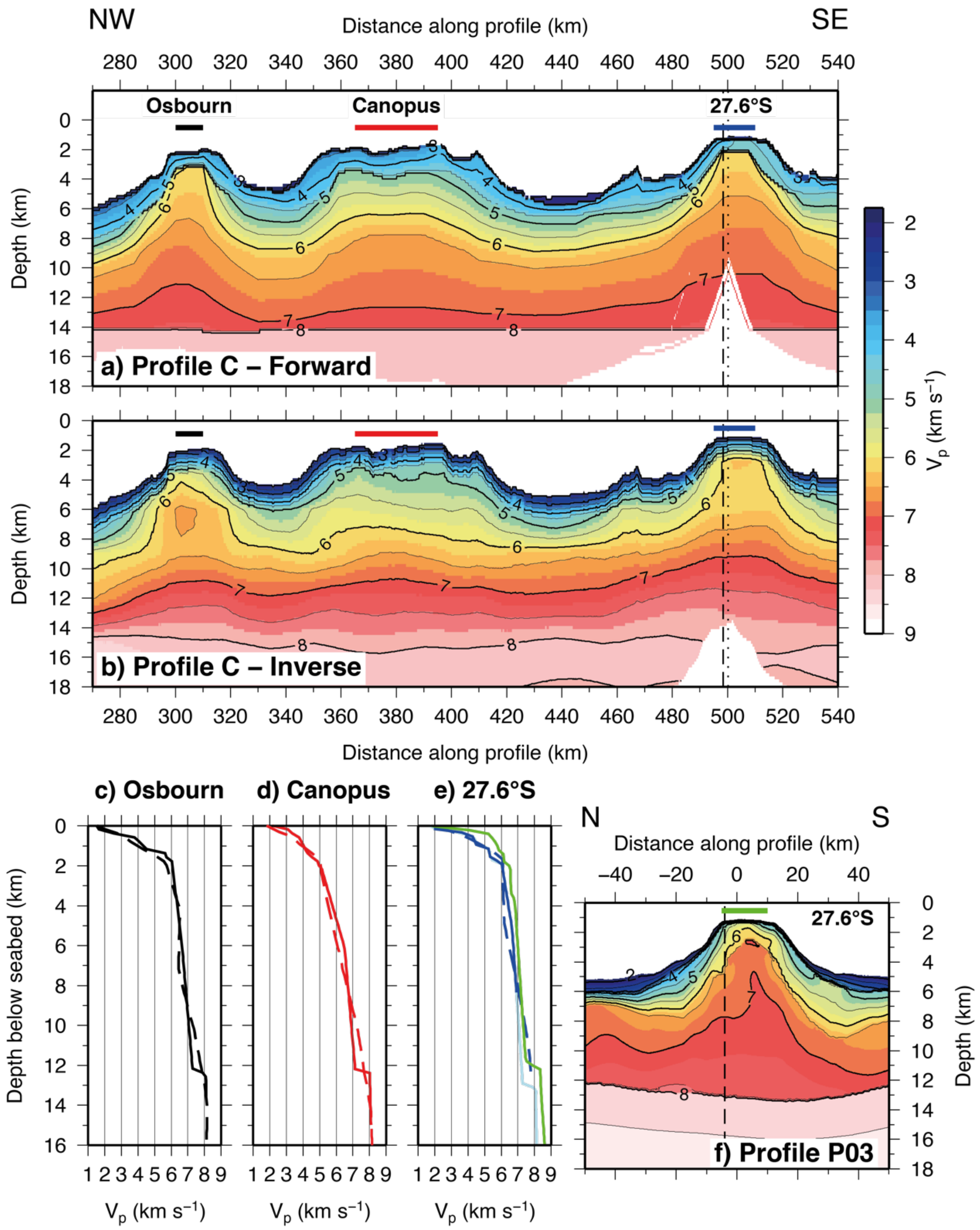

Figure 5.2: *Best-fit P-wave velocity-depth models for large LRSC seamounts. a) Forward model for Osbourn, Canopus and 27.6˚S seamounts. b) As for a), but inverse model. Horizontal coloured bars represent offset ranges over which velocity-depth profiles in c)-e) have been sampled and averaged. Dotted black line indicates location of bend in profile. Dashed black line indicates location of crossing point between Profile C and Profile P03. c) Averaged velocity-depth profiles through summit of Osbourn seamount forward (solid) and inverse (dashed) models. d) As for c), through Canopus seamount. e) As for c) for 27.6˚S seamount. Green line is the velocity-depth profile through the model shown in f). f) Contreras-Reyes et al. (2010) model for 27.6˚S seamount, where crossing point with Profile C is indicated by dashed black line.*

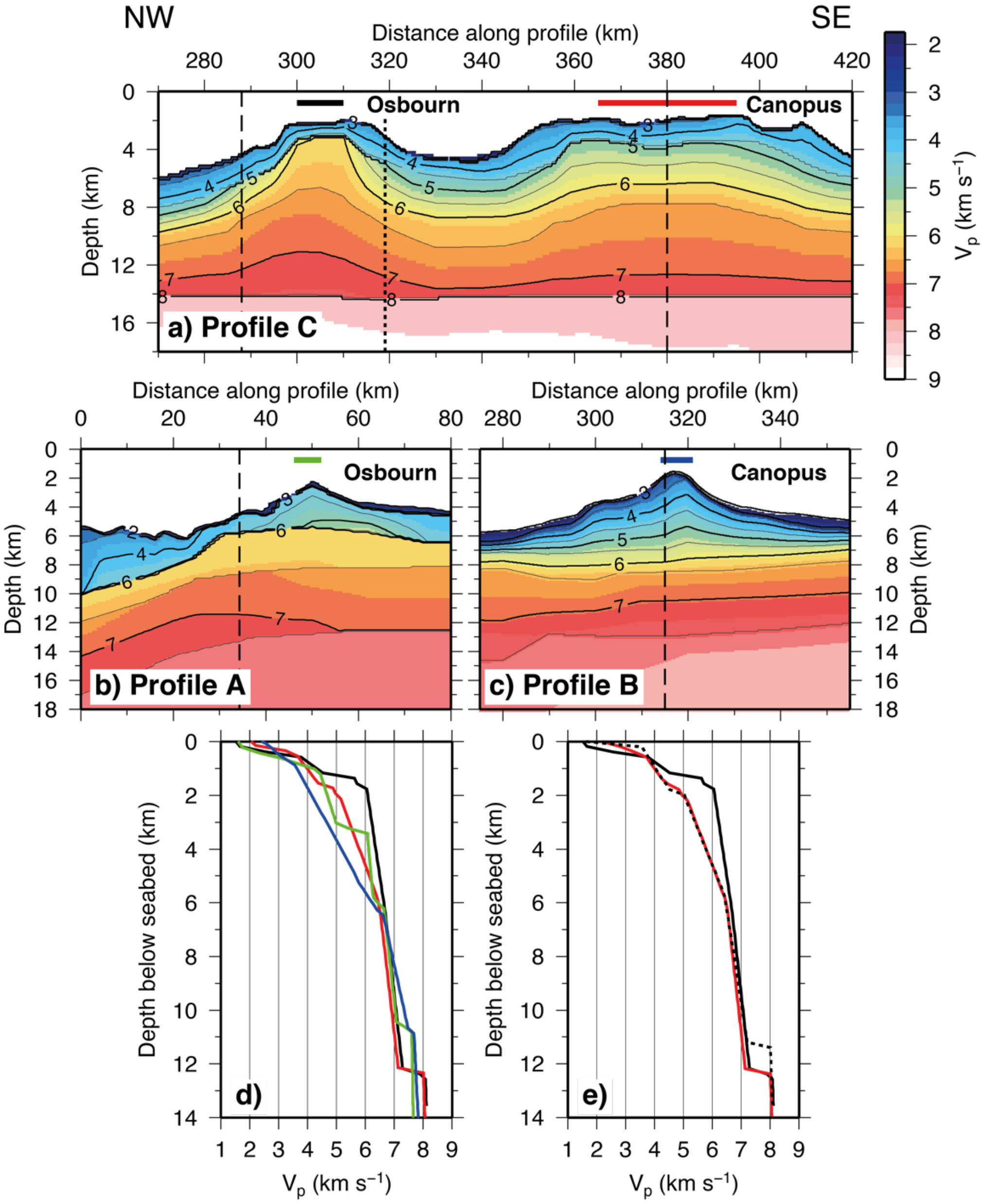

Figure 5.3: *Comparison of velocity structures of seamount flank-crossings. a) Profile C forward model velocity-depth structure of Canopus seamount. b) Funnell et al. (2017) model through Canopus seamount, where Profile B is orientated perpendicular to Profile C and profiles intersect at the dashed black line. c) Stratford et al. (2015) model through the trenchward flank of Osbourn seamount, where Profile A is oblique to Profile C and profiles intersect at the dashed black line. Horizontal coloured bars indicate the location of velocity-depth profiles in d) and e). d) Averaged velocity-depth profiles through seamounts in a-c). e) Velocity profiles through Canopus seamount flank crossing (red) and Osbourn seamount summit (black, solid). Dotted black line is the velocity-depth profile through SE flank of Osbourn seamount at 319 km d.a.p.*

closest to the southernmost seamount's summit, and images a shallowing of the contours to a similar depth to that beneath Canopus seamount.

Where Canopus seamount is crossed by Profile B, that profile also fails to show evidence for elevated shallow velocities (Fig. 5.3b – Funnell et al., 2017). The trenchward flank of Osbourn seamount sampled by Profile A (Fig. 5.3c – Stratford et al., 2015) also follows this pattern. The lack of high velocity interiors may, therefore, be affected by sampling location, and suggest that the intrusive bodies are discrete in size. That Profile C does not observe a shallow intrusive core within Canopus seamount, therefore, neither requires or precludes it having the same structure as Osbourn and 27.6°S. Consequently, based on the WA seismic profiles available, it is not possible to determine whether all LRSC seamounts in this study area share a common internal structure, or whether there are additional governing factors. However, the average *forward model* velocity-depth structure of Canopus seamount is mirrored by a 1D profile sampled at 319 km d.a.p., through the southwestern flank of Osbourn seamount, ~3 km beyond the edge of the summit platform and ~8-9 km beyond the edge of the core 'summit' (Fig. 5.3e).

Gravity modelling (Section 4.5), conducted as a test of model uniqueness, generally produces a good fit between observed and modelled FAA along the entire model. For the seamount chain in particular, the fit between the observed and *forward* (via *density*) *model*-derived FAA is generally ≤10 mGal at best, and at worst ≤30 mGal (Fig. 4.31). Sampling of the satellite-derived FAA (Fig. 5.4a) along and across the chain permits examination of the differences between the measured and peak FAA associated with each seamount. Profile C effectively traverses directly over the summit of Osbourn seamount, so the FAA peak is almost exactly centred on the profile (Fig. 5.4c), and the difference between the FAA along Profile C and along a parallel profile 5 km to the north is small (<10 mGal – Fig. 5.4b), thus providing good evidence that the results of forward modelling are consistent with the gravity field.

In contrast, the centre of Canopus seamount and its associated FAA peak are offset by up to 8 km from the plane of Profile C, and the resulting difference in magnitude is ~40 mGal, while the saddles between seamounts display only small (<10 mGal – Fig. 5.4b) FAA differences. Consequently, it can be concluded that trough-matching the modelled and measured FAA in 2D provides a robust test of fit for the gross crustal structure and that the large misfits are entirely due to profile offset from

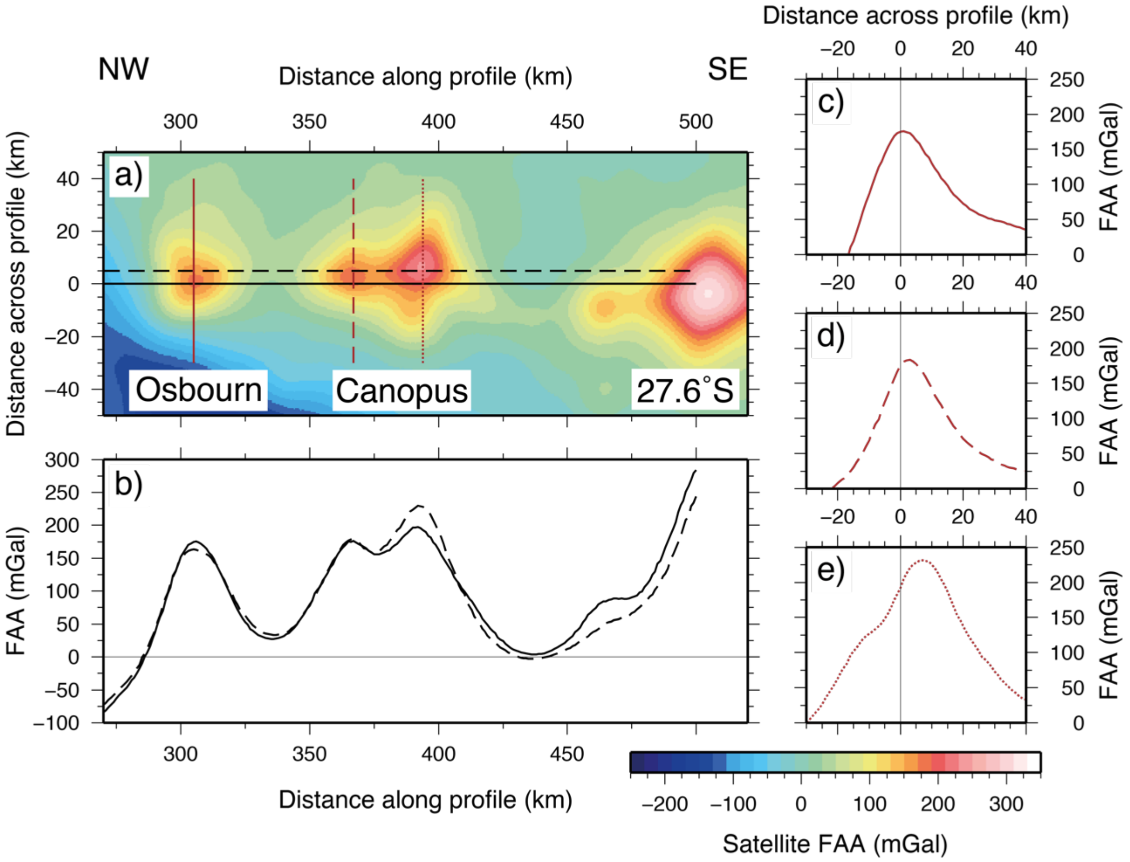

Figure 5.4: *3D satellite-derived FAA (Sandwell et al., 2014) for a) northern segment of Profile C, rotated into modelling co-ordinates. b) FAA sampled along-profile (solid) and 5 km to north (dashed), closer to crossing the summit of Canopus seamount. FAA sampled across profile along c) solid, d) dashed, and e) dotted red lines in a), showing the offset of FAA peaks from Profile C (0 km distance across profile).*

seamount summits rather than inaccuracy in the modelled structure. Overall, the results of gravity modelling, therefore, indicate that the density, and, hence, velocity structure of each summit-traversed seamount can be considered robust.

Distinguishing laterally between the flank of a seamount and 'background' oceanic crust on the basis of their P-wave velocity alone is, therefore, challenging. In addition, because only two of the larger LRSC volcanoes (Osbourn and 27.6˚S) have been imaged in a way that allows robust determination of this structure, it is unclear whether the most recent seamount to have been subducted would display a similar internal velocity structure to these. An outstanding question remains, what determines if a seamount evolves to contain an intrusive core?; this will be discussed in detail in Chapter 6. Furthermore, it will also be considered if it is likely that all seamounts of the LRSC share the same constructional features or processes, as this has implications as to whether sparsely-spaced 2D seismic velocity profiles alone are able to distinguish a seamount subducted at the trench. Additional data, including the MCS and gravity, therefore, may play a significant role in attempting to determine if a subducted seamount is present.

5.3.3. Intra-seamount saddles

In the saddles between the seamounts, the sediment accumulations have a thickness of ~0.4 km. Shallow reflectors between 325-340 km and 610-620 km d.a.p. dip towards the younger end of the seamount chain (Fig. 5.5a,c), and may represent the palaeo-flanks of the seamounts, formed before subsequent younger volcanoes loaded the seafloor downstream and covered this seafloor (e.g. Wessel et al., 2014). The upper and middle crust are thickened to 1.0-1.5 (± 0.2) km and 3.0-4.0 (± 0.3) km respectively (Fig. 5.6a,b,e), accommodated both as an up to 2 km shallowing of the bathymetry relative to the background plate, and downward crustal thickening and/or flexure. There is generally very good agreement between the *forward* and *inverse* modelling results (Fig. 5.6c,d). Much of the thickened crustal component displays a P-wave velocity of <6.0 km s^{-1}, similar to the seamount flanks. It is suggested, therefore, that these are predominantly composed of the same material, namely extrusive volcanics and volcaniclastics, and the products of mass wasting and reworking of seamount flank materials. Partially continuous and irregular reflectors are visible between 330-345 km, 525-550 km and 600-625 km d.a.p. in the *forward model* restacked MCS section (Fig. 5.5). Comparing the locations of these to the P-wave velocity-TWTT structure shows these to occur in areas where the velocity is in the range 4.0-6.0 km s^{-1}. These relatively low velocities support the interpretation above, that the material forming the thickened upper crust in the seamount saddles is not massive basalt, and instead likely represents explosive/extrusive volcanic material and derived products. The mechanism by which this material may be generated will be discussed in Chapter 6.

5.3.4. Crustal thickness

The *forward model* shows that Moho depth increases from 12.5 km b.s.s. in the ‘background’ crust region (Fig. 5.1a – 680-726 km d.a.p.) to ~14.2 km b.s.s. beneath the LRSC (Fig. 5.2a). Other profiles crossing the seamount chain show a similar ~2

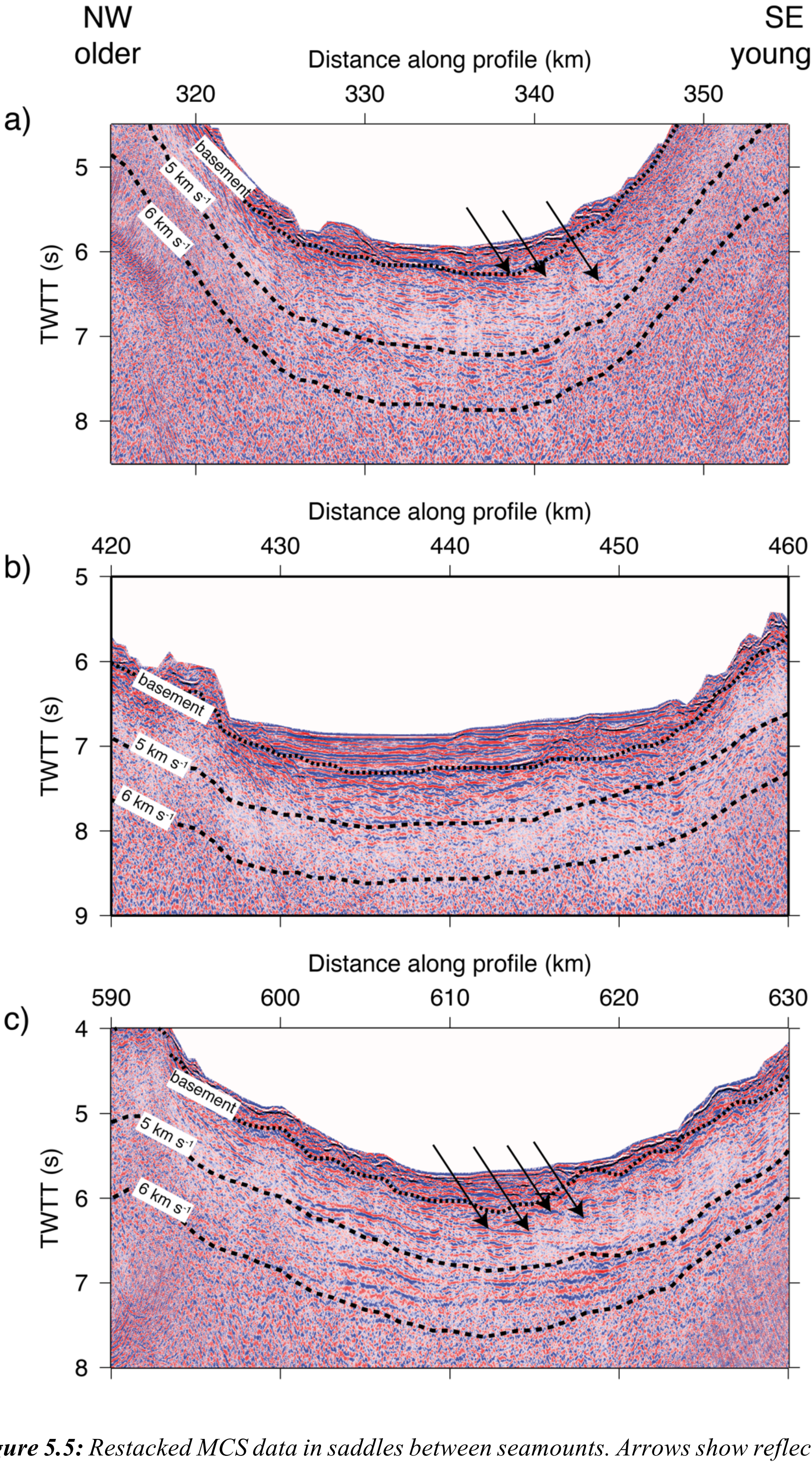

Figure 5.5: *Restacked MCS data in saddles between seamounts. Arrows show reflectors which dip toward the southeast/younger end of the chain. Oceanic basement shown by dotted black line. 5-6 km* s^{-1} *contours shown as dashed black lines, indicating the velocity limits above which sub-basement reflectivity is observed.*

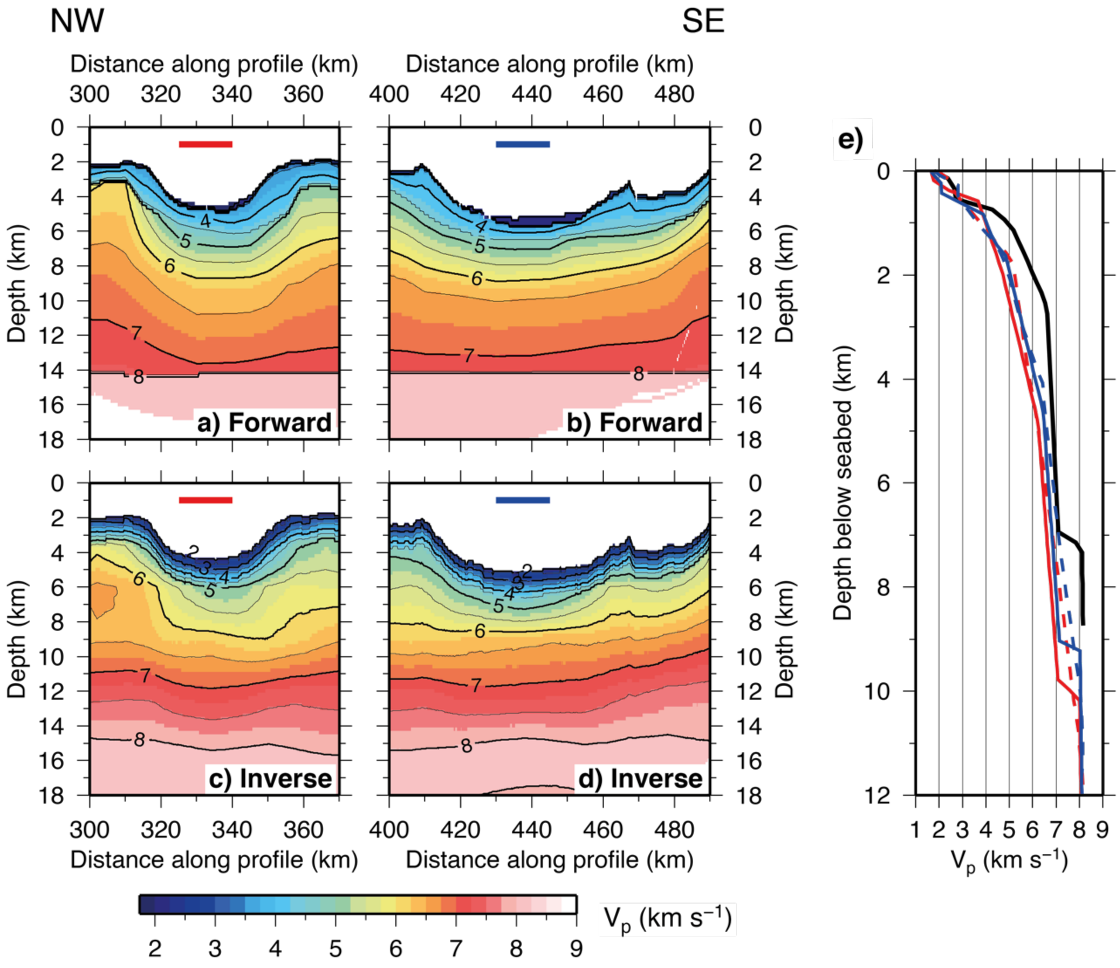

Figure 5.6: *Comparison of velocity structures of through inter-seamount saddles. Profile C forward model between a) Osbourn and Canopus seamounts, and b) Canopus and 27.6˚S seamounts. c-d) As for a-b) for inverse model. Horizontal coloured bars indicate the location of velocity-depth profiles in e). e) Averaged velocity-depth profiles through forward (solid) and inverse (dashed) models a-d). Black line is the Profile C forward model through the 'background' plate region (Fig 5.1a) for comparison.*

km deepening of the Moho beneath the seamounts relative to the adjacent crust (Fig. 5.2f – Contreras-Reyes et al., 2010; Fig. 5.3c – Funnell et al., 2017). This deepening of the Moho does not appear to be related to a significant thickening of the lower crust crust beneath the seamounts (e.g. Hawaii/Marquesas-type underplating – Watts et al., 1985; Caress et al., 1995). The dip of middle and lower crustal velocity contours towards the seamount chain (Fig 5.1 a,c) and the formation of a flexural moat to the north of 27.6˚S seamount (Fig. 5.1e) suggest instead that Moho depth may be affected by flexure of the plate due to the loading effect of the seamount chain. Within the resolution of the model, a good fit of observed to calculated travel times was achieved using an essentially flat Moho beneath the LRSC. The typical spacing between Louisville Ridge seamounts is 40-80 km, and large volcanoes show an across-track flexural half-width of 40-50 km (Contreras-Reyes et al., 2010). It is possible, therefore, that the along-chain crustal flexure signatures may overlap such that the individual flexural contribution of each edifice cannot be individually resolved in this direction. Profiles A and B show that the base of the crust dips gently towards the trench (Fig. 5.3b,c), which may suggest that there is a component of trench-loading acting on the plate and seamount chain. However, the proximity of seamounts to the trench on these profiles makes it challenging to distinguish between the individual contributions of seamount and trench loading.

5.3.5. Subduction related faulting of LRSC seamounts

At the LSRC-trench intersection, swath bathymetry data indicates the presence of large-scale normal faults associated with bending of the Pacific plate as it passes over the outer rise (Fig. 5.7b – Bodine and Watts, 1979; Lonsdale, 1986; Pontoise et al., 1986). Where these faults can be traced adjacent to and into Osbourn seamount, they are spaced approximately 5-8 km apart and display vertical offsets of between 200-800 m (Fig. 5.7d,e). Normal faulting is also observed in the Profile C MCS record section, with the summit of Osbourn seamount being offset by small-scale normal faults. In addition, an out-of-plane reflection feature is observed on the trenchward flank of Osbourn which, when compared to the bathymetry, shows it to be related to one of these fault scarps (Fig. 5.7a,b). To the north and south of the collision zone, larger throws of up to 2 km are observed (Fig. 5.7c,f – Pelletier and Dupont, 1990; Crawford et al., 2003; Funnell et al., 2014; 2017), suggesting that the LRSC moderates bending and bend-related faulting.

Subduction-related bend-faulting may play an important role in the addition of fluids to the subducting crust and mantle. Along Profile B, Funnell et al. (2017) show upper- and mid-crust velocities are reduced by ~1 km s^{-1}, and upper mantle velocity by up to 0.5 km s^{-1}. However, similar reductions are not observed in the Profile C *forward model*, which may indicate that the LRSC is acting to reduce bending and related faulting, due either to buoyancy, increased stiffness, or a combination of both. Faults have been shown to cut >20 km down into the mantle (Ranero et al., 2003; Ranero and Sallares, 2004), which could act as conduits for fluid infiltration. Fluid associated serpentinization has been shown to have the capability to cause velocity

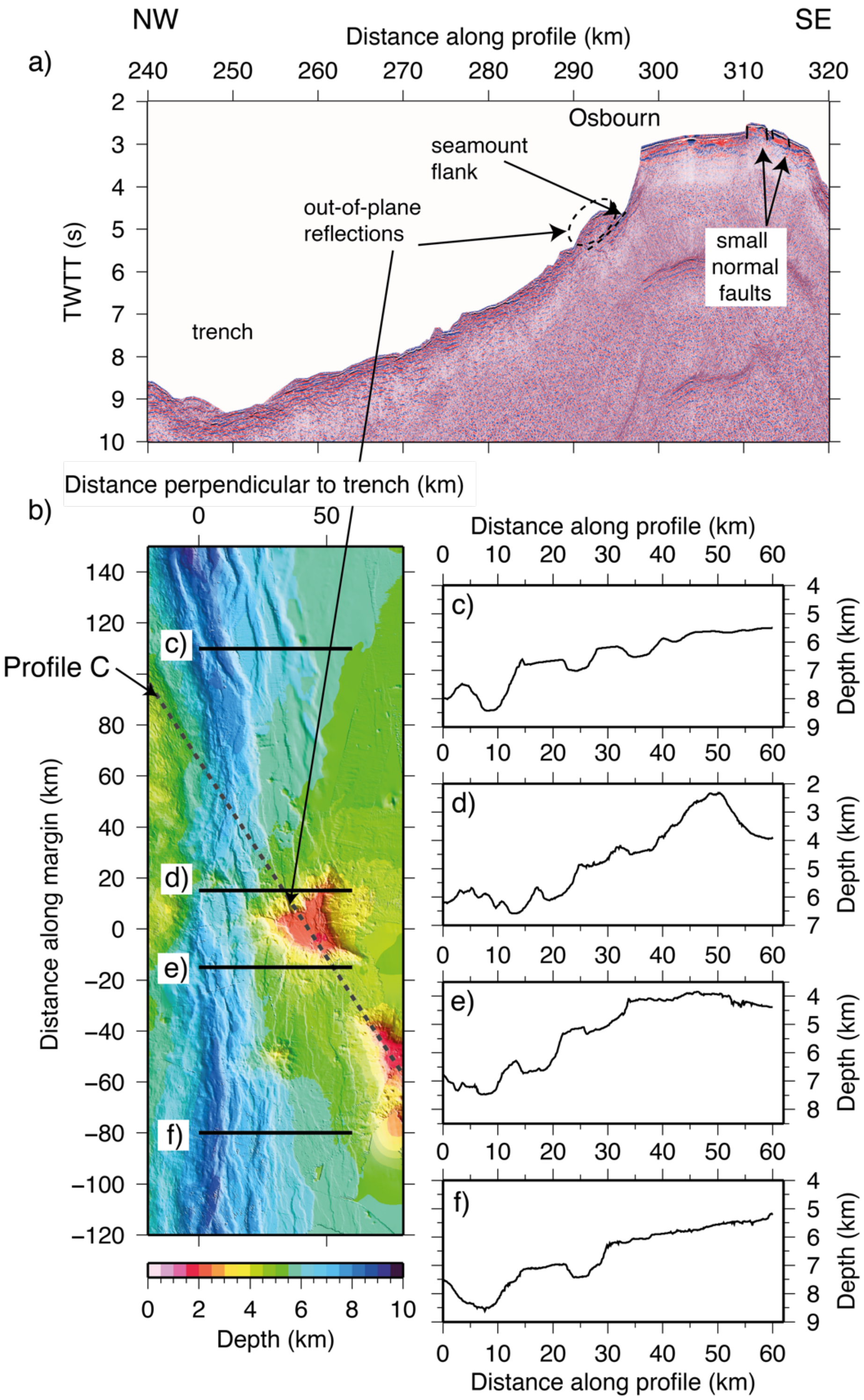

__Figure 5.7:__ Effects of outer-rise normal faulting. a) MCS data restacked using forward model-derived stacking velocity-TWTT model for trenchward flank of Osbourn seamount. Small normal faults cut the flat summit. An out of plane reflection between 290-295 km d.a.p. arises from a fault scarp located trenchward of Profile C at the location shown by the arrow in b). b) Bathymetry of Osbourn seamount and adjacent trench area. Dashed line shows the trace of Profile C. Black lines are sampled bathymetry profiles perpendicular to trench, shown in c-f).

reductions of 0.4-0.7 km s^{-1} and ~0.5 km s^{-1} to the crust and mantle respectively (Ranero et al., 2003; Ivandic et al., 2010; Moscoso and Grevemeyer, 2015).

This mechanism of fluid infiltration, leading to lower crust and upper mantle serpentinization, could account for the 0.11 g cm^{-3} decrease in the density of the Pacific mantle relative to the Indo-Australian mantle, which was found necessary to produce the best-fit *density model* with the slab geometry defined by SLAB1.0 (Figs 4.24 and 4.29 – Section 4.5.5). Applying Birch's Law (1961), this density difference corresponds to a decrease in P-wave velocity of 0.2-0.3 km s^{-1}, which lies within the confidence limits of the mantle velocities for this plate (+0.4/-0.2 km s^{-1}). It is possible, therefore, that this density (and thus velocity) reduction is present, but cannot be resolved by the model. However, given that the faulting (and hence the proposed mechanism for generating the density change) acts only in the trench-proximal region, the use of a single reduced Pacific mantle density along the model space may not be valid.

5.4. Indo-Australian plate

Due to the oblique direction in which Profile C traverses the forearc, it is necessary to consider the results of modelling in terms of distance perpendicular to the trench (d.p.t.), rather than distance along the profile (d.a.p.), in order to prevent horizontal distortion of features making them appear wider than their true width (Fig. 5.8). This will also permit easier comparison between Profile C and the other trench and forearc traversing profiles (A, B, and P02), and allow a better understanding of the length scales over which changes in forearc structure occur. Generally, the Tonga forearc can be divided into three principal domains (Fig. 5.9). The lower trench slope, between 0-35 km d.p.t. (~185-245 km d.a.p.) is uplifted, dips toward the trench at ~3-4°, and is covered by little-to-no sediment (Figs 2.15 and 5.9b). Above this, between ~35-75 km d.p.t. (~120-180 km d.a.p.) the broadly flatter mid-trench slope is crossed by a number of ~800-900 m-high ridges orientated sub-parallel to the trench, which bound small basins. Limited sediment infills in these basins (Figs 2.15 & 5.9b) indicates that they are relatively young features, and that the upper trench slope has not yet begun to be significantly eroded which will lead to the re-equilibration of the slope morphology over time.

WA seismic modelling indicates that the basement of the upper forearc basin (10-50 km d.a.p.) is at ≤2 s TWTT (Fig. 5.9b), corresponding to the shallower of the

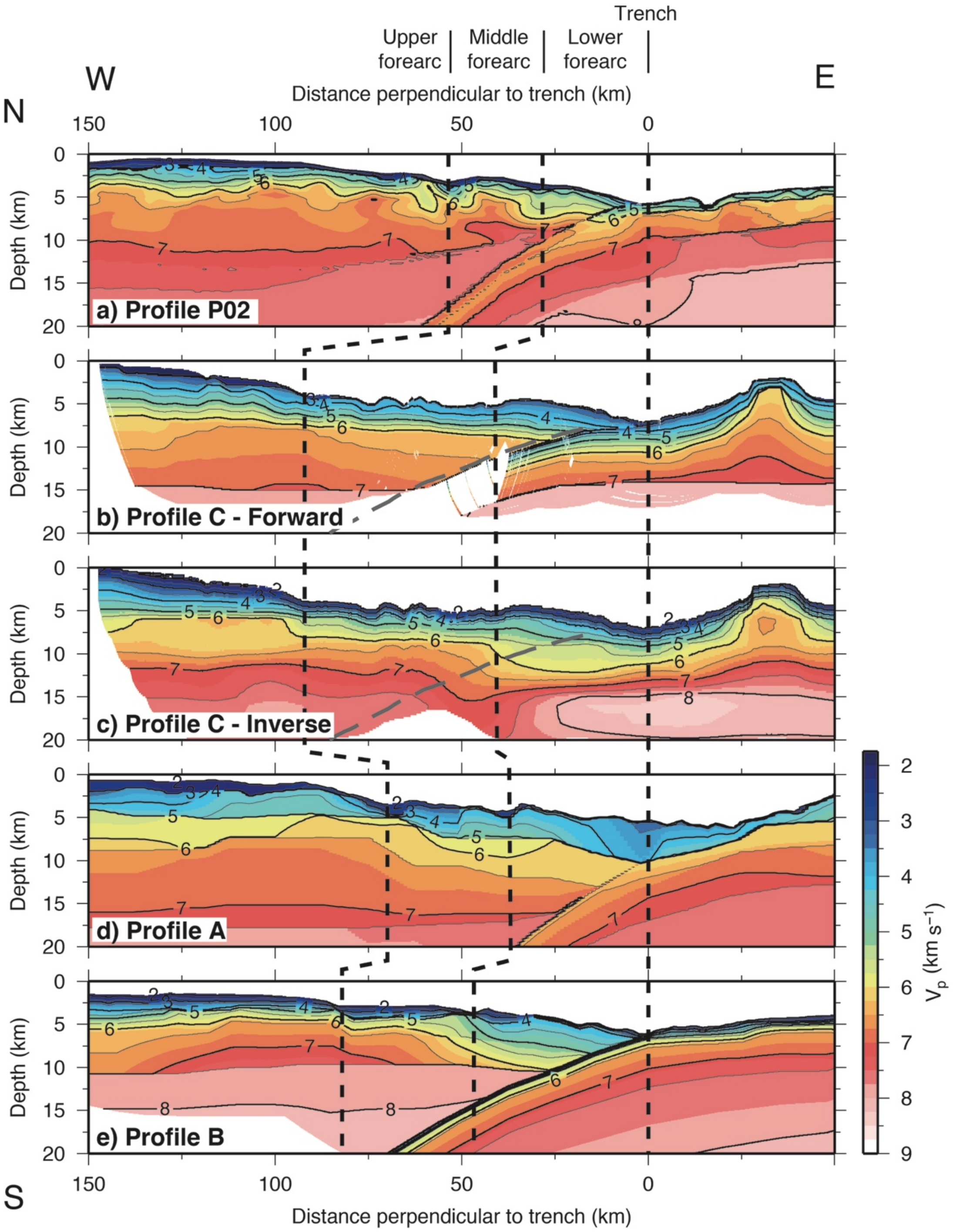

Figure 5.8: *P-wave velocity-depth models crossing Tonga-Kermadec forearc and trench from Profiles a) P02 (Contreras-Reyes et al., 2011), b) C, forward model (this study), c) C, inverse model (this study), dashed grey line indicates the location of the plate boundary in b), d) A (Stratford et al., 2015), and e) B (Funnell et al., 2017). Profiles are ordered from north to south in terms of their trench-crossing location. All profiles have been projected perpendicular to the trench and aligned relative to the trench axis at 0 km d.p.t.. Dashed black lines show subdivisions between forearc domains based on bathymetry and crustal structure.*

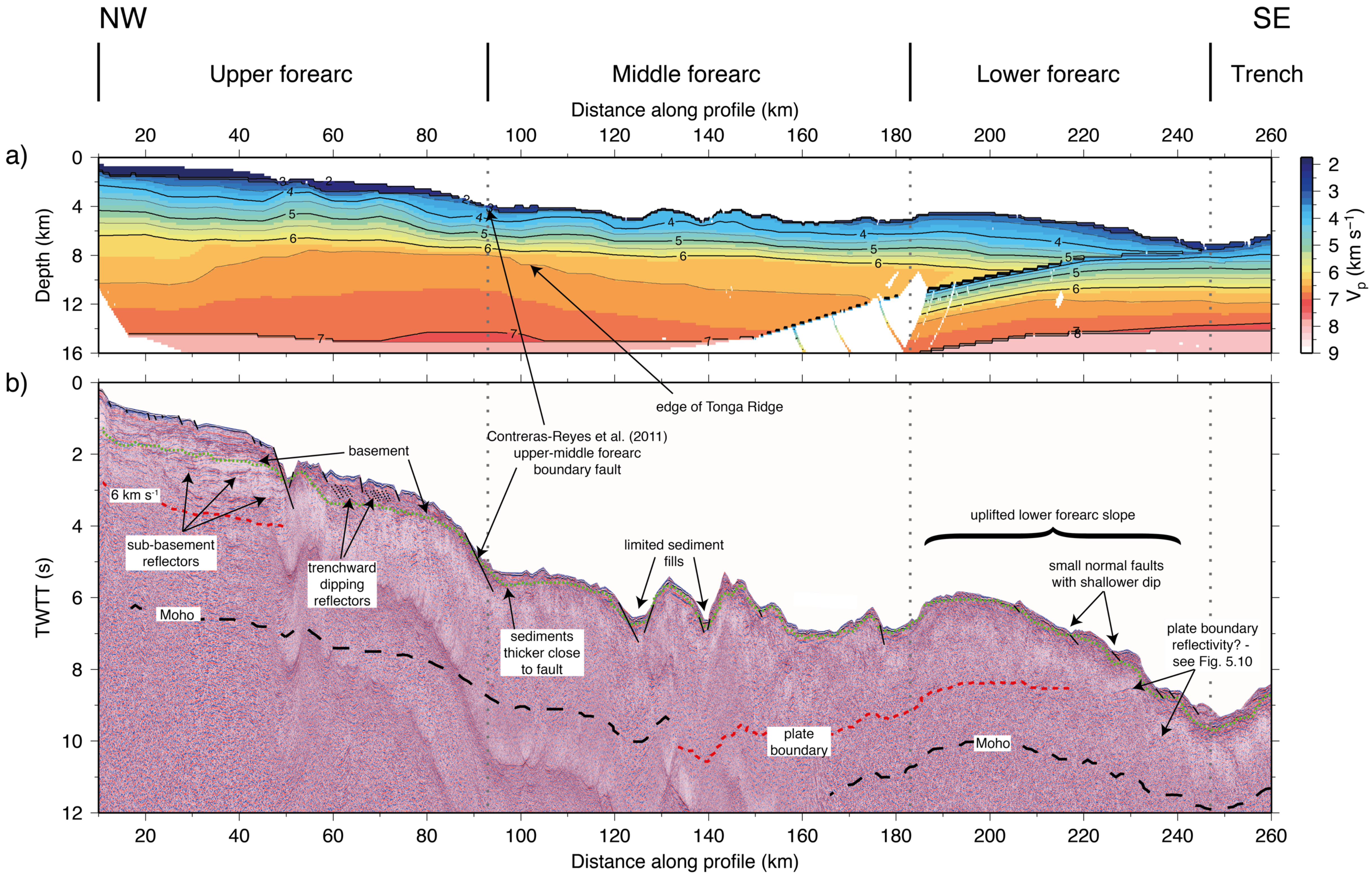

Figure 5.9: *Profile C Tonga forearc structure. a) P-wave velocity-depth model crossing Tonga forearc, plotted in distance along profile. b) Forward model-derived stacking velocity-TWTT restacked MCS section. Basement marked as dotted green line, plate boundary as dashed red line and Moho as dashed black line. Faults shown as solid black lines. In upper forearc (30-50 km d.a.p.) arrows show location of reflectors between basement and 6 km s^{-1} velocity contour which were considered as possible basement locations during iterative forward modelling and subsequently rejected. Arrows between 225-240 km d.a.p. show location of possible plate boundary reflectors shown in detail in Fig 5.10. Principal forearc divisions indicated by dotted grey lines and are labelled at top of figure.*

possibilities identified in Chapter 2 (Fig. 2.13). The basement dips gently towards the trench, mirroring the slope of the bathymetry. The forearc upper crust (V_p <5.0 km s^{-1}) has a minimum thickness of ~2.0-2.5 (± 0.2) km between 50-90 km d.p.t. (~100-180 km d.a.p.), increasing to 4 km at the lower trench slope (0-35 km d.p.t. / 180-250 km d.a.p.) and towards the arc (Figs 5.8b and 5.9a). In the thickened and uplifted lower trench slope region the uppermost crustal velocity is reduced from 3.5 km s^{-1} to 3.2 km s^{-1}. Similar reductions in the lower forearc crustal velocity are also seen in Profiles A, B and P02 (Fig. 5.8a, d and e).

The middle crust is of generally uniform (~2.0 ± 0.3 km) thickness throughout, and dips toward the trench. Between 30-50 km d.a.p. discontinuous bands of reflectivity, that were rejected as the top of the basement, are located in regions where the velocity is ≤6 km s^{-1} (Fig 5.9b). Profiles B and P02, and to a lesser extent A, show slow (<6.0 km s^{-1}) middle crustal velocities between 0-40 km d.p.t. and 8-12 km depth, which lie adjacent to a ~3 km shallowing of the 6.0 km s^{-1} contour at ~40 km d.p.t. (Fig. 5.8a,d,e). These features are not well observed in the Profile C *forward model* (Figs 5.8b & 5.9a), although they are in the *inverse model* (Fig. 5.8c) where they likely arise as an artefact of the continuous and smoothed nature of this model, which does not actually contain a plate boundary. Instead, the lowermost forearc region of the *forward model* appears to be dominated by the upper crust, which may be related to trenchward-directed spreading of this slope accommodated by relatively shallow-dipping normal faults (Fig. 2.15).

The lower crust is up to 8 km thick, with its velocity increasing to ~7.0 (± 0.4) km s^{-1} at the base. Shallowing of the 6.5 km s^{-1} contour from ~10.0 km to ~7.5 km, and a lowermost crustal velocity of ≥7.0 km s^{-1} between 80-130 km d.p.t. (30-120 km d.a.p.) are interpreted as representing the Tonga Ridge, the buried Eocene initial arc. Due to the oblique direction in which the profile traverses the forearc, the apparent width of this feature is greater than its true width of ~40-50 km as observed on Profiles A (Fig. 5.8d – Stratford et al., 2015) and B (Fig. 5.8e – Funnell et al., 2017), whilst Profile P02 (Fig 5.8a, Contreras-Reyes et al., 2011) does not provide a good image of the Tonga Ridge. The trenchward edge of the buried Tonga Ridge is typically associated (±10 km d.a.p.) with the upper-to-middle forearc slope transition along the margin. Despite poorly imaging this feature at depth, Contreras-Reyes et al. (2011) interpret a sharp, trenchward-dipping velocity contrast at ~60 km d.p.t., which separates the middle and upper trench slope domains in their model, as a crustal-scale detachment fault associated with the edge of the Tonga Ridge. Further evidence for this fault is present as a large scarp located ~55 km arcward of the trench, although this does vary along the trench, reaching a maximum of ~90 km where it is crossed by Profile C (Fig. 5.8). It is possible that this feature is represented along Profile C by the large upper-middle forearc fault at ~90 km d.a.p. which is observed in Figs 2.13 and 5.9b. However, the small size of and observation that the shallow fault-like feature in the Profile P02 velocity model appears to be located directly below an OBS position does cast suspicion over its robustness, but overall, if a relatively large-scale forearc-domain boundary does exist, it may well be associated with this feature. Additional studies have shown that the buried Tonga Ridge extends north to the 18-19˚S Fonualei Discontinuity (Fig. 1.3 – Crawford et al., 2003; Contreras-Reyes et al., 2011) and south to the 32˚S Discontinuity (Stratford et al., 2015; Bassett et al., 2016; Funnell et al., 2017), and that its lateral extent indicates that it pre-dates the current tectonic regime of seamount collision.

The Indo-Australian plate mantle represents one of the most poorly constrained parts of the model, both in terms of its velocity and the depth to the Moho (Table 4.1). Hence, there is a strong possibility that this lack of good constraint represents the source of the long-wavelength gravity misfit discussed in Section 4.5.5. and Figs 2.25-4.30. Both the *forward* and *inverse models* show a 0.2-0.3 km s^{-1} difference in the best-fitting mantle velocities between the two mantle regions, however this lies within the ±0.4 km s^{-1} smallest estimate for the confidence limits. As a result, the changes in mantle density which were applied in Fig. 4.25 and Section 4.5.5. can be accounted for entirely within the model errors. Alternatively, it was sought to determine if changes to the geometry of the subducting slab at depth could also contribute, as this was constrained below the model by SLAB1.0 (Hayes et al., 2012). There is a trade-off between the angle of the subduction interface and the density contrast between the two mantle domains, which can be tuned to produce a good fit of observed to modelled FAA (Fig. 4.29). However, it would seem unlikely that sufficient error exists within SLAB1.0 to be the sole generator of the difference. Without improved constraint on the mantle velocities, and thus a reduction of the confidence limits on these values, it is not possible to definitively distinguish the cause of the misfit, which may in fact exist on a spectrum between the two end-member cases of differences in slab dip and density.

5.4.1. Is there a seamount in the trench?

Neither the Profile C *forward* or *inverse models* appear to show compelling evidence for a seamount located in the trench. However, in order to determine whether this represents a robust observation, it is necessary to compare the size of a seamount which could be present here relative to the resolution limits of the models. If the subduction-related normal-faulting described in Section 5.3.5 does successfully cause disarticulation of seamounts into 5-8 km-wide blocks, then even disregarding the more limited resolution afforded in the trench axis region as a result of the lower ray coverage, it would not be possible to identify a seamount since such sized blocks fall below the minimum horizontal resolution of ~12-15 km determined on a whole model basis. However, despite clearly being affected by normal faulting, it is not necessary that Osbourn seamount undergoes total breakup on entering the trench (Ballance et al., 1989), as a range of evidence supports at least some, and in some cases significant, integrity and/or contiguity of subducting seamounts. This evidence, from other seamount subduction localities, will be discussed further in Chapter 6.

By using the *forward model* to restack the MCS data (Section 4.6) a band of reflectivity can be identified between 225-240 km d.a.p. and 8.5-9.5 s TWTT (Fig. 5.10b). On initial inspection it may appear that this feature shows a seamount-like shape, being elevated relative to its surroundings and showing two ~5-8 km-long reflectors which could be interpreted as relating to a seamount summit. However, comparing the location of this reflector to the *forward model* converted to TWTT (Fig. 5.10a) suggests that it may represent the manifestation of the plate boundary in the time domain, which in the depth domain does not contain a convincing anomalous feature which could be called a seamount. In Chapter 6 this feature will be compared to the result of a previous study where similar reflections attributed to a previously subducted seamount at this margin were observed (Ballance et al., 1989).

If a seamount were present in the trench region, it may reasonably be expected to produce a positive FAA. Such an anomaly is not observed, as the FAA appears to be relatively flat in this region. In addition, without the inclusion of a seamount-like feature in the trench, the FAA calculated from the *density model* displays a 60-70 mGal positive (i.e. too high) misfit (e.g. Fig. 4.30), further supporting the absence of a seamount in this location.

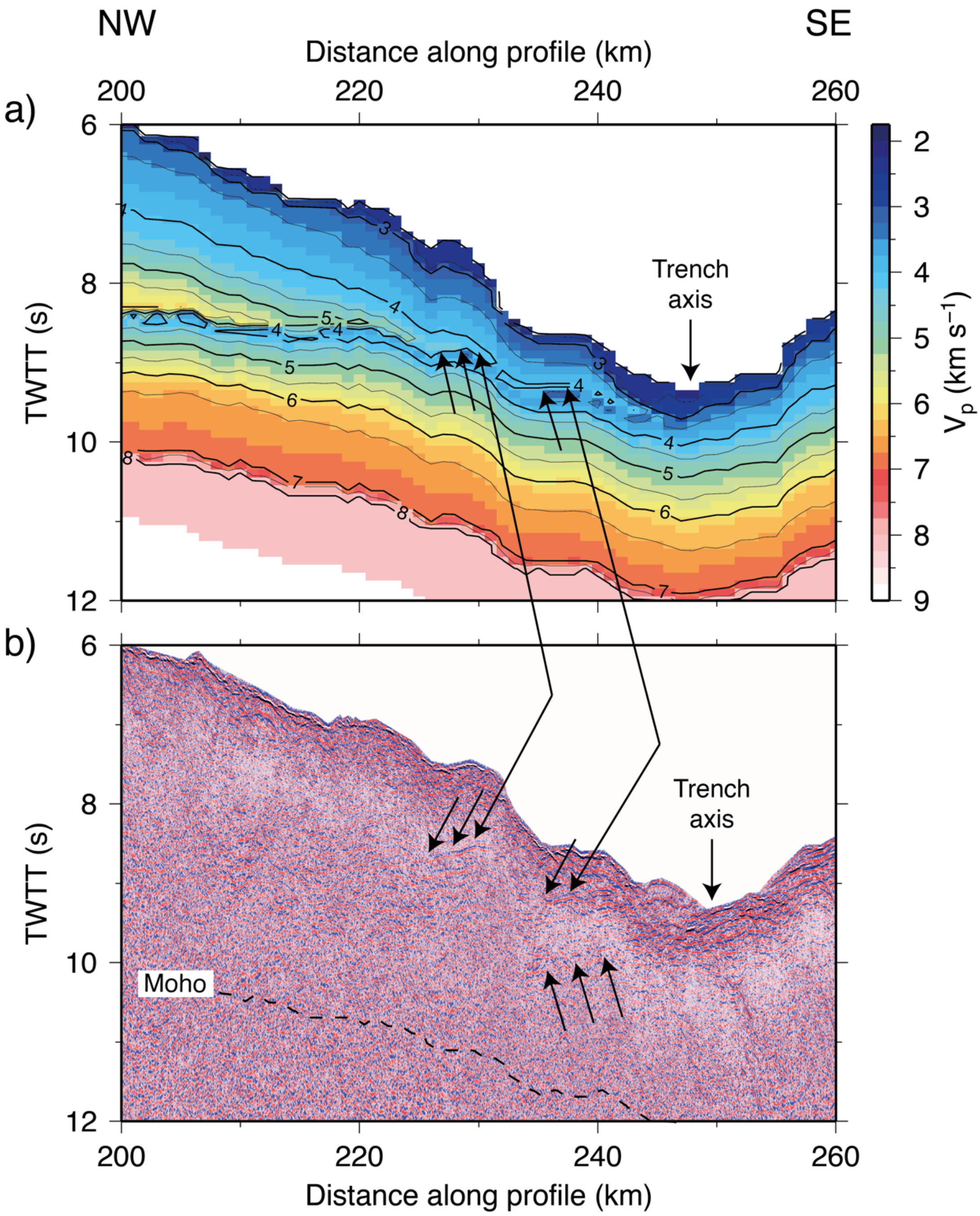

Figure 5.10: *Restacked MCS data in lower forearc region using the forward velocity model. a) Forward model converted to P-wave velocity-TWTT for trench/lower forearc region. b) MCS data restacked using forward model-derived stacking velocity-TWTT model. Arrows show the locations of reflectors which might be interpreted as representing possible continuations of the plate boundary, as comparison with the velocity structure in a) shows these to follow the plate boundary in TWTT.*

5.4.2. Is there evidence for seamount accommodation?

In Section 4.5.6, the positive FAA misfit, attributed above not to be related to a subducting seamount, was removed by modifying the geometry and density of crustal blocks in the *density model* (Fig. 4.31). The density reductions of 0.2 g cm^{-3} of the upper crustal block and 0.35 g cm^{-3} for the middle crustal block, between 180 km d.a.p. and the trench axis, correspond to velocity decreases of ~0.5 km s^{-1} and ~1.0 km s^{-1} respectively. These values lie outside the confidence limits of +0.4/-0.3 km s^{-1} calculated in Section 4.4, however, this is one of the parts of the model least well sampled by rays (Figs 3.33-3.35) and, hence, the velocity constraints may be expected to be poorer. Similar patterns of velocity reduction in the upper and middle crust of the overriding plate, where it is adjacent to the subduction interface, are also observed on other profiles in this region (Fig. 5.8). These lower velocities are typically associated with uplift and steepening of the lower forearc slope, and may be related to the development of fault networks which permit accommodation of subducting bathymetric features through plastic deformation of the overriding plate (Dominguez et al., 1998; Wang and Bilek, 2011). The step in bathymetry at ~185 km d.a.p. (~40 km d.p.t.), seen in Profiles A and C (Figs 5.8b,d and 5.9a) between the middle and lower forearc, is associated with a reduction in dip of the lower forearc trenchward-dipping normal faults (Fig. 5.9b), suggesting that this part of the forearc is uplifted from its trenchward end as it accommodates downgoing features.

5.5. Summary

In this chapter, the results of the combined geophysical data acquisition along Profile C have been described and interpreted. All of the interpretations of features which have been made have been accompanied by confidence limits on their dimensions and velocities, and where features lie either beyond these limits, or where these limits may inhibit potentially imageable features, this has been discussed. The interpretations made in this chapter are also informed by a series of additional profiles from the SO215 and *TOTAL* projects, which have allowed features to be compared either in a pseudo-three-dimensional sense (for the seamount chain) or in terms of along-margin structural variability (for the overriding plate region).

A number of important observations arise from the results of modelling the Profile C WA seismic data. Firstly, the elevated velocity seamount cores are a robust feature of the seamounts in which they are observed, lying within the calculated resolution and confidence limits. Not all of the seamounts along-chain appear to display this structure, and there appears to be a correlation between the observation of a shallow intrusive core and whether or not the profile traverses close to the centre of the edifice. Alternatively, the profile location may in itself put a maximum limit on the lateral dimension (size) that a core could have, if it exists. Overall, there does not appear to be any significant variation in the crustal thickness with distance along-chain, and there is no evidence for magmatic underplating.

It has not been possible, using the WA seismic dataset alone, to definitively argue for or against the presence of a seamount along the continuation of Profile C into the trench. However, the *forward model* does not show evidence for a seamount-type body in the plate boundary region, and this result is supported by the *inverse* and *density models*. Even if a seamount was present, the model resolution limits (determined through checkerboard testing in Section 4.3) compared to the typical sizes of the LRSC seamounts suggests it may not be possible to unequivocally resolve it. In addition, there is evidence that suggests that the seamounts may undergo some degree of disarticulation immediately prior to subduction, which would further inhibit imaging. Finally, the similarity between the velocity structure of seamount flank, intra-seamount saddle, and nearby oceanic crustal material may also make determination of the presence of a seamount difficult based on velocity alone.

Other lines of evidence may support or refute the presence of a seamount in the trench. Restacking the MCS data using the modelling-derived velocity structure reveals possible reflectors which may represent the plate boundary, and a comparison will be made between the geometry and location of these and a previously proposed seamount in the next chapter. In contrast, modelling of the FAA associated with the derived crustal velocity structure does not appear to support the presence of a higher density feature within the trench, instead requiring a reduction in density of the immediately overlying forearc which has been attributed to deformation caused by incoming subducting features either presently or in the past.

Chapter 6 – Discussion

6.1. Introduction

In Chapter 5, the results of this study were described and interpreted in the context of existing regional data profiles, which provide an insight into the pseudo-three-dimensionality and along-margin variability of the LRSC. A striking and robust observation made is that two of the large summit-traversed LRSC seamounts display elevated velocity (>6.0 km s^{-1}) intrusive cores which reach to within 1.0-1.5 km beneath their summits. In Section 6.2, how these dense cores form will be considered in relation to models that predict the formation of such features under certain conditions. It will, therefore, be considered whether the observed LRSC seamount structure can be explained by these simple models alone, or whether additional processes may be involved.

It has also been shown that, despite extensive evidence for subduction of the LRSC at the TKT, within the resolution of the modelled WA seismic data it is not possible to definitively argue for or against the presence of an already subducted seamount ahead of Osbourn, along the projection of Profile C into the forearc. It was additionally considered that outer-rise normal faulting may cause at least partial seamount breakup as they enter the trench, and this would further impede imaging the continuation of the chain. However, as the LRSC-TKT collisional region has only been sampled by a limited number of 2D WA seismic profiles, two crossing the trench and a further running trench-parallel over the forearc, it may be the case that the continuation of the LRSC does not lie on any of these profiles to a degree where it could be successfully imaged by them. In Section 6.3, the along-margin variability in forearc structure will be discussed with a view to determining both the pre-Osbourn strike of the seamount chain is (i.e. along what trend has the seamount historically subducted) and what evidence is there for the contiguity or breakup of seamounts as they subduct. As part of this, the forearc structural observations will be tied to temporal constraints on the history of LRSC subduction, including when and where along the margin this process began.

6.2. Seamount constructional processes

6.2.1. Formation of densely cored seamounts

The observation of discrete, high-velocity intrusive cores within two of the large, summit-traversed LRSC volcanoes (Section 5.3.1) is consistent with the Staudigel and Clague (2010) model for seamount construction, whereby initially high hydrostatic pressure predominantly favours volcanic intrusion over extrusion, although both may occur. With seamount growth, the nature of extrusive volcanism may evolve from more effusive in nature to more explosive, with a transition between these behaviours proposed to exist at 0.7-1.0 km water depth (McBirney, 1963; Peckover et al., 1973; Staudigel and Schminke, 1984). At this point, the reduced hydrostatic pressure permits more extensive and explosive degassing and the lower magma temperature, resulting from lengthening of the volcanic conduit (Bonatti and Harrison, 1988), promotes increased fracturing. The flat-topped (guyot) morphology of the LRSC seamounts is evidence that they were once emergent, and so must have passed through this transition zone.

The observation that the intrusive cores within Osbourn and 27.6°S seamounts are discrete in size suggests that, if this model for seamount core formation holds, the transition between dominantly intrusive and explosive-extrusive volcanism is itself sharp. Further to this, this result also indicates that intrusive seamount cores are limited in their spatial extent, having a radius of approximately a third to a half of that of their host seamount. This observation may explain the lack of evidence for an intrusive core where Canopus seamount is sampled by Profiles B and C, as neither profile directly crosses the seamount summit, instead traversing the ridge joining the two summits and the western flank at a distance of ~8 km from its centre respectively. However, the sampled velocity structure of Canopus seamount has been shown to be similar to that of the southeastern flank of the densely cored Osbourn seamount at a distance of ~14 km from its centre and ~8 km from the edge of the ‘summit’ of the core (Fig. 5.3e), which may suggest that the larger, more southerly, edifice of Canpous seamount could contain a similar core whose lateral dimension is constrained by the profile location off-summit.

Assuming the seamounts and intrusive cores are radially symmetrical, an estimate of the volumetric contribution of the latter to the former can be made, although this will be highly dependent on the velocity definition used for the transition between intrusive and extrusive materials (Houtz and Ewing, 1976; White et al., 1992;

Kopp et al., 2004) and the confidence limits on the size of the cores. From the results of this study, intrusive:extrusive volume proportions of 50-67% can be calculated for Osbourn seamount, using a range of velocity transitions between 6.0-6.5 km s^{-1}. Using the results of this study to calculate the intrusive:extrusive ratio for 27.6˚S seamount is challenging as Profile C does not traverse the centre of the seamount, so the assumption of radial symmetry does not hold. However, Contreras-Reyes et al. (2010) calculate, from their summit-traversing profile, that ~60% by volume of 27.6˚S seamount is associated with the intrusive core. The velocity structure determined for Profile C in this study shows a general consistency with the across-chain Profile P03, and so the Contreras-Reyes et al. (2010) estimate of ~60% may be regarded as indicative for all LRSC seamounts that contain elevated velocity cores.

In contrast, the fractured, vesiculated, and/or chemically altered nature of the volcanic, volcaniclastic and derived products comprising the upper and outer parts of the edifices, results in the expectation that these parts of the seamount will have a lower velocity relative to that of massive basalts of similar composition (e.g. Carlson and Herrick, 1990; Wilkens et al., 1991). These materials may, therefore, account for the thickening of the upper oceanic crustal layer (V_p <5 km s^{-1}) observed in between the seamounts (Fig. 5.6), and the sub-basement reflectivity observed in the saddles (Fig. 5.5). The abundance of this material in these locations, as well as in the flexural moat surrounding the seamount chain (Contreras-Reyes et al., 2010; Funnell et al., 2017) has an impact on the ability to resolve between these different settings based on P-wave velocity alone.

6.2.2. Δt and the LRSC

If the ‘plate age at time of volcanism’ (Δt) hypothesis (Gass et al., 1978; Pollack et al., 1981) holds then the LRSC may be considered a representing the small Δt end member of the structures this predicts. However, a Δt determination has remained elusive, largely due to a lack of magnetic reversals associated with Osbourn Trough spreading. Instead, a range of Δt values of 10-35 Ma has been proposed (Billen and Stock, 2000; Mortimer et al., 2006; Worthington et al., 2006; Downey et al., 2007). A lack of evidence for LRSC-related magmatic compositions in OT lavas supports the earlier proposed spreading cessation and, hence, larger Δt values (Beier et al., 2011). However, in contrast, Δt estimates of as little as ~4 Ma have been derived for 27.6˚S seamount using dense-core load flexural modelling (Kim and Wessel, 2010; Hwang and Kim, 2016). This value is significantly less than the ~20 Ma derived using the seamount ^{40}Ar/^{39}Ar age of 69.65 ± 0.48 Ma (Koppers et al., 2004, 2011) and crustal age of 89.65 ± 1.52 Ma (Müller et al., 2008). However, if the dated seamount samples are from close to the summit then they may represent late-stage volcanic products, and initial magmatism and loading may have occurred earlier. Eruptions have been shown to have occurred in close proximity in several locations along the LRSC over timescales up to 6 Ma (Koppers et al., 2011), indicating that seamount construction can occur over extensive timescales, which must be accounted for when considering geochronology and loading histories. If it is to be believed that the Louisville Ridge seamounts do have relatively extended loading histories, it may be more appropriate in flexural studies to consider models with more progressive loading sequences even if the relatively dense core does form relatively early on, as the entire edifice is not instantaneously emplaced at the time of volcanism. Hence, the values determined by Hwang and Kim (2016) may well represent an overestimate of the loading force on the young plate, resulting in smaller calculated values for T_e and Δt than actual reality. It may also be appropriate, if considering temporal effects on flexural studies, to consider the effects of viscoelastic stress relaxation (Watts and Zhong, 2000), especially given the relatively old age (~70 Ma) of 27.6°S seamount which means that a significant time has passed over which stress relaxation could occur.

If the ‘plate age at time of volcanism’ hypothesis holds then it would also be anticipated that at large Δt values, shallow vertical intrusion of magma into seamount edifices would no longer occur. This non-Louisville end member is well represented by the Hawaiian (Δt = 60-80 Ma – Watts et al., 1985; Watts and ten Brink, 1989) and Marquesas ($\Delta t \approx 50$ Ma – Caress et al., 1995) Islands, where significant thickening of the crust below the surface volcanic edifices is observed. This thickening appears as a magmatic underplate, with a P-wave velocity up to 7.9 km s^{-1}, intermediate between gabbroic (6.7-7.2 km s^{-1}) and peridotitic (7.8-8.3 km s^{-1}) velocities and suggestive of a mixed mafic-ultramafic composition. In both cases, the identification of mid-crustal reflectors consistent with the depth of normal oceanic crust is proposed to represent the pre-hotspot Moho, below which the mafic-ultramafic material has accreted. The presence of a pre-hotspot Moho underlain by a subcrustal intrusive complex has also been supported at a number of locations, including Hawaii, Tahiti, Kiribati and Rarotonga, by analysis of P-to-S conversion receiver functions (Leahy et al., 2005;

2010). The lack of an underplate beneath the LRSC, is, thus, consistent with the conclusion that its structure is representative of the low Δt end-member category.

6.2.3. Role of melting and crystallisation processes in crustal structural variability

Theoretical calculations of melting experiments, using established petrological codes and performed under an assumption of batch melting, show that melting pressure acts as a primary control on resultant density (e.g. Farnetani et al., 1996; Richards et al., 2013). Beneath older lithosphere, melting and melt equilibration with the surrounding mantle rocks occurs deeper than under younger lithosphere. The MgO content increases monotonically with melting pressure, with clinopyroxene and olivine replacing plagioclase in the crystallisation assemblage over a density range of 0.7-1.5 GPa (Hirose and Kushiro, 1993; Farnetani et al., 1996), corresponding to a change in melting depth from ~20 km to ~45 km. The crystallized densities relating to this change are 2.8-2.9 g cm^{-3} and >3.0 g cm^{-3} respectively, which correspond to P-wave velocities of 5.5-6.5 km s^{-1} and >7.0 km s^{-1} (Carlson and Raskin, 1984; Carlson and Herrick, 1990). Thus, these models are consistent with observations of the diversity in internal structure of vertically intruded (e.g. Contreras-Reyes et al., 2010; this study) and underplated (e.g. Watts et al., 1985; Caress et al., 1995) seamounts.

It is suggested that the Moho may be thought of as acting as a density filter (Richards et al., 2013). However, the fact that melt, which has a density likely to be in the range 2.7-2.8 g cm^{-3} (Stolper and Walker, 1980), can and does reach the surface requires that the level of neutral buoyancy (e.g. Ryan, 1987) is not a sole and strict barrier on surface-directed migration. Melt fractionation may produce some effect, particularly if relatively mafic-ultramafic magmas undergo extensive fractionation of dense Fe- and Mg-species prior to passing the Moho (Richards et al., 2013). In addition, there may be factors related to the rheology, stress regime, and pre-existing structure of the host crust which affect the resultant crustal structure (Parsons et al., 1992; Watanabe et al., 1999; Menand, 2011).

6.2.4. Seamount structures arising from alternative magmatic origins

Pre-existing structural weaknesses and actively evolving lithospheric stress conditions may provide an additional or primary control on intra-plate magmatism. Where these processes occur, it may be expected that the resultant seamount crustal structure does not necessarily reconcile with those discussed above. For example, the Marcus-Wake seamount chain displays similar, albeit smaller at 15-20% volume, intrusive cores to the LRSC (Kaneda et al., 2010), despite being located on much older lithosphere (163 ± 4 Ma, Müller et al., 2008) than its age of volcanism (~100-103 Ma, Koppers et al., 2000). This results in a Δt of ~60 Ma, which is similar to or greater than that calculated for La Reunion (Charvis et al., 1999) and larger than the Marquesas Islands (Caress et al., 1995), both of which show strong evidence for ultramafic underplating. It has been suggested, therefore, that the origin of the Marcus-Wake seamounts may be related to non-Wilson-Morgan (Wilson, 1963; Morgan, 1971) type processes. This is supported by the observation that these seamounts show a tendency to align with palaeofracture formations (Smoot, 1989). The short duration of magmatism and lack of evidence for age progressive volcanism (Winterer et al., 1993; Koppers et al., 2003) also strongly suggest that the structure and evolution of this feature is primarily governed by lithospheric and/or crustal controls rather than deep mantle melting anomalies. Additional examples of chains which may potentially be explained by these alternative formation mechanisms include the Marshall Islands and Gilbert Ridge (Koppers et al., 2003; Koppers et al., 2007), the Pukapuka Ridges (Lynch, 1999), the Cook-Austral Islands (McNutt et al, 1997), and the Line Islands (Davis et al., 2002). However, these have not necessarily had their crustal structure determined by robust (seismic) methods.

It may be necessary, therefore, to consider if there is any evidence for structural trends in the LRSC which may be related to either pre-existing structural features or dynamic stress conditions. The LRSC has formerly been proposed to be associated with the Eltanin fracture zone, due to the proximity of the younger end of the chain with this feature (Hayes and Ewing, 1971; Watts et al., 1988) and, if this were the case, then there may be a possibility that pre-existing structural fabrics and/or weaknesses may influence seamount formation and internal structure. However, this hypothesis for the LRSC's origin is now refuted, with the long history of LRSC magmatism with a near constant magmatic supply rate until 25 Ma (Lonsdale, 1986; Lonsdale, 1988; Koppers et al., 2004) and highly limited chemical and isotopic along-chain variability (Beier et al., 2011; Nichols et al., 2014) providing a strong case for a long-lived 'primary' hotspot source for the chain. Osbourn Trough spreading occurred in a broadly north-south direction (e.g. Billen and Stock, 2000; Müller et al., 2008), although there may have been a small (2-5°) rotation in spreading direction prior to the final ~900 km of crustal accretion (Downey et al., 2007). Osbourn Trough spreading segment offsets are small in size (≤20 km) and, hence, age discontinuities and, therefore, crustal properties across these will not be significantly different. Projecting the transforms southwards towards the LRSC shows that they do not appear to correlate with the changes in trend between the chain segments. Approximately 1000 km to the east, the Wishbone Scarp represents the boundary between crust formed by spreading at the OT and at the Pacific-Antarctic Ridge (Watts et al., 1988), and is the most significant spreading-parallel/OT-perpendicular structure in the region (Fig 1.5). The origin of the Wishbone Scarp is somewhat enigmatic, the western branch having been variously interpreted as a fracture zone, a fossil spreading centre, or an ~115 Ma intra-oceanic arc (Luyendyk, 1995; Billen and Stock, 2000; Mortimer et al., 2006), and the eastern branch proposed to be a remnant of a transform fault associated with an extinct spreading system (Sutherland and Hollis, 2001). Where it meets the LRSC south of 38°S, the seamounts appear to be smaller, more sparsely spaced, and display more variable lava, trace element and isotopic compositions (Lonsdale, 1988; Beier et al., 2011). However, rather than any apparent correlation with the Wishbone Scarp this instead appears to be associated with a seafloor age difference across this feature of ~50 Ma (Müller et al., 2008; Beier et al., 2011), suggesting that these differences are controlled by the plate age rather than any inherent plate structure. Overall, therefore, there does not appear to be good evidence to suggest that the LRSC formed by a mechanism other than classic Wilson-Morgan hotspot magmatism.

6.2.5 Additional controls on seamount structure

Studies of the diversity of seamounts indicate that their size follows an exponential distribution (Smith and Jordan, 1988), where the Hawaiian Islands are an extreme end-member. Hammer et al., (1994) suggest that, as a result of the first-order control of neutral buoyancy (Ryan, 1987), as seamounts grow the level within the edifice of the magma chamber and intrusive volcanic component will progressively rise as new material is added to the summit. Smaller seamounts are, therefore, dominantly extrusive, as they have insufficient overburden to support the development of shallow magma chambers and rift zones until they reach heights of ~2 km relative to the surrounding seafloor (Vogt and Smoot, 1984). However, it is also likely that as seamount size increases, the additional loading exerts changes on the local stress field, which may cause the neutral buoyancy first-order control to be overridden. Overall, therefore, it is not necessarily clear whether the control mechanisms governing seamount architecture can be extrapolated to all sizes.

Where seamount chains are underlain by large-scale magmatic underplates, it has been suggested that these may form late on during the period of volcanic activity (ten Brink and Brocher, 1987; Grevemeyer et al., 2001). The seismically constrained velocities of these features of >7.1-7.2 km s^{-1} indicates that they have a relatively high Mg content (as discussed above), which would prevent them from passing through the Moho density filter. This material is, therefore, intruded as sills, or is otherwise trapped in the crust–mantle boundary region. If underplating does represent a late stage process, it is possible that the tendency to image such a structure may be related to the plate velocity relative to the locus of magmatism (Pollack et al., 1981), as in order to accumulate such large volumes of melt at the base of the crust, the plate migration rate may need to be slower. However, underplating does not necessarily represent an exclusively late-stage process. Underplating beneath La Reunion appears to represent a similar proportion of the volcanic material as Hawaii, however here the process appears to be synchronous with volcanism (Charvis et al., 1999), in constrast to Hawaii where it is thought to post-date volcanism (ten Brink and Brocher, 1987).

6.3. Subduction of the LRSC

6.3.1. Behaviour and imaging of subducting seamounts

Large-scale bend-associated normal faulting of seamounts appears to be a relatively common process, with similar observations made where seamounts enter the Japan (Mogi and Nishizawa, 1980; Kobayashi et al., 1987), North Tonga (Coulbourn et al., 1989) and Izu-Bonin-Mariana (Fryer and Smoot, 1985) subduction systems, although it does appear to be limited to seamounts with a basal diameter of <40 km (Fryer and Smoot, 1985). In Section 5.4.1 it was argued that the modelling of Profile C does not provide evidence for an intact subducting seamount beneath the forearc, and even if it did it may push the limits of whole-model resolution in the trench region. In addition, if disarticulation, evidence by normal faulting of Osbourn observed in the bathymetric and MCS data, causes a seamount to enter the trench only in fragments, its 5-8 km wide blocks would not be imageable as they fall well below the minimum horizontal resolution of ~12-15 km determined for the model as a whole, even disregarding the more limited resolution found in the trench region.

The observation of throws of only 200-800 m on these normal faults, compared to up to 2 km to the north and south where there are no seamounts (Pelletier and Dupont, 1990; Crawford et al., 2003; Funnell et al., 2014; 2017), suggests that the LRSC at least partially resists bending and bend-related faulting. Despite the faulting patterns observed, it is not necessary that seamounts undergo total breakup upon entering the trench (Ballance et al., 1989), as a range of evidence supports at least some and in some cases significant integrity and/or contiguity. Accreted volcanic fragments in the Japan Trench are observed to be one-to-two orders of magnitude smaller than whole seamount edifices (Isozaki et al., 1990), indicating that whole-scale removal of the seamount from its host plate is relatively uncommon. Large-scale subducted seamount features have been imaged at a number of margins, including an 8-9 km-long, arcward-dipping reflector beneath the Tonga lower-trench slope at ~25.5 ˚S, along the projection of the LRSC, by a seismic reflection survey (Ballance et al., 1989), which will be discussed further in a following section, and at the Japan (Kodiara et al., 2000), Mediterranean Ridge (von Huene et al., 1997) and Mariana (Oakley et al., 2007, 2008) forearcs. Forearc slopes show morphological evidence for uplift, head scars, slumps, and re-entrant features along the projection of incoming seamount features at locations including the Mariana Trench (Fryer and Smoot, 1985), the Japan Trench (Lallemand and Le Pichon, 1987; Kobayashi et al., 1987), Costa Rica (Dominguez et al., 1998; Ranero and von Huene, 2000), and Tonga (Pontoise et al., 1986; Ballance et al., 1989). Magnetic anomalies have been traced into the overriding plates in the Japan (Cadet et al., 1987), Costa Rica (Barckhausen et al., 1998) and Cascadia (Tréhu et al., 2012) subduction zones.

6.3.2. Effects of LRSC subduction

6.3.2.1. Pre-collisional forearc structure

Lower forearc seismic velocities of 3-6 km s^{-1} are observed along the length of the subduction system (Crawford et al., 2003; Funnell et al., 2017), which indicate that the 'background' process governing forearc structure along the margin is subduction erosion (e.g. von Huene and Ranero, 2003; Sallares and Ranero, 2005). At the TKT, the incoming Pacific crust is characterised by a horst and graben structure with up to 2 km vertical throw and limited sedimentary fill (~0.2 s TWTT or ~200 m; Funnell et al., 2014). The subduction of graben provides a mechanism for allowing tectonic erosion, as these features cannot remain unfilled as they pass beneath the inner-trench slope, as this results in a space problem (Ballance et al., 1989 – Fig. 6.1a). Horst and graben can be traced along the plate boundary in MCS record sections from the LRSC-proximal pre-collisional zone for distances of up to 30 km arcward of the trench axis (von Huene and Scholl, 1991). The result of this background tectonic erosion is removal of material beneath the lower forearc slope, leading to steepening and extensional gravitationally-driven collapse into the trench along the margin (Fig. 6.1b – Lonsdale, 1986; Ballance et al., 1989; Pelletier and Dupont, 1990; Clift and MacLeod, 1999; Funnell et al., 2017). The crustal thickness in the pre-collisional forearc, as determined from Profile B (Funnell et al. 2017), is relatively low at ~13 km.

6.3.2.2. Syn-collisional forearc structure

The point of present LRSC-TKT intersection is marked by an ~4 km shallowing of the trench (Pontoise et al., 1986; Ballance et al., 1989). Directly arcward of the collision, the Tonga Ridge is uplifted by ~300 m relative to the bathymetry immediately to the north and south (Stratford et al., 2015). Locally, the lower forearc bulges by ~20 km toward the trench (Figs 6.1c, 6.2a) and is characterised by extensive small-scale normal faulting which accommodates the trenchward extension of this feature (e.g. Kukowski and Oncken, 2006). The trenchward bulging of the lower forearc, and associated uplift-related morphological merging of the mid- and lower-trench slopes morphologically (Stratford et al., 2015) may account for the apparent increase in distance between the trench and upper forearc slope transition. This lower-middle trench slope merger is in contrast to the more distinct slope breaks which are observed to the north (Contreras-Reyes et al., 2011) and south (Funnell et al., 2014; 2017), and indicates that this is only temporary, whilst this part of the forearc is supported from beneath by seamount subduction.

The middle forearc region is characterised by heterogeneous along-strike topography, which is manifest in Profile C as the ~800 m high transverse ridges which bound small, mostly unfilled sediment traps (Section 2.4 – Fig. 2.15). In plan view, these small ridges form the northern edge of a C-shaped ridge structure located on top of the bulge, which has an opening (or embayment) which faces toward the trench (Fig. 6.2a). An inner high within this C-shaped feature is correlated with free-air gravity (~60 mGal) and magnetic (~280 nT) anomaly peaks (Bassett, 2014; Bassett and Watts, 2015) The inner high and embayment lie approximately along a line joining

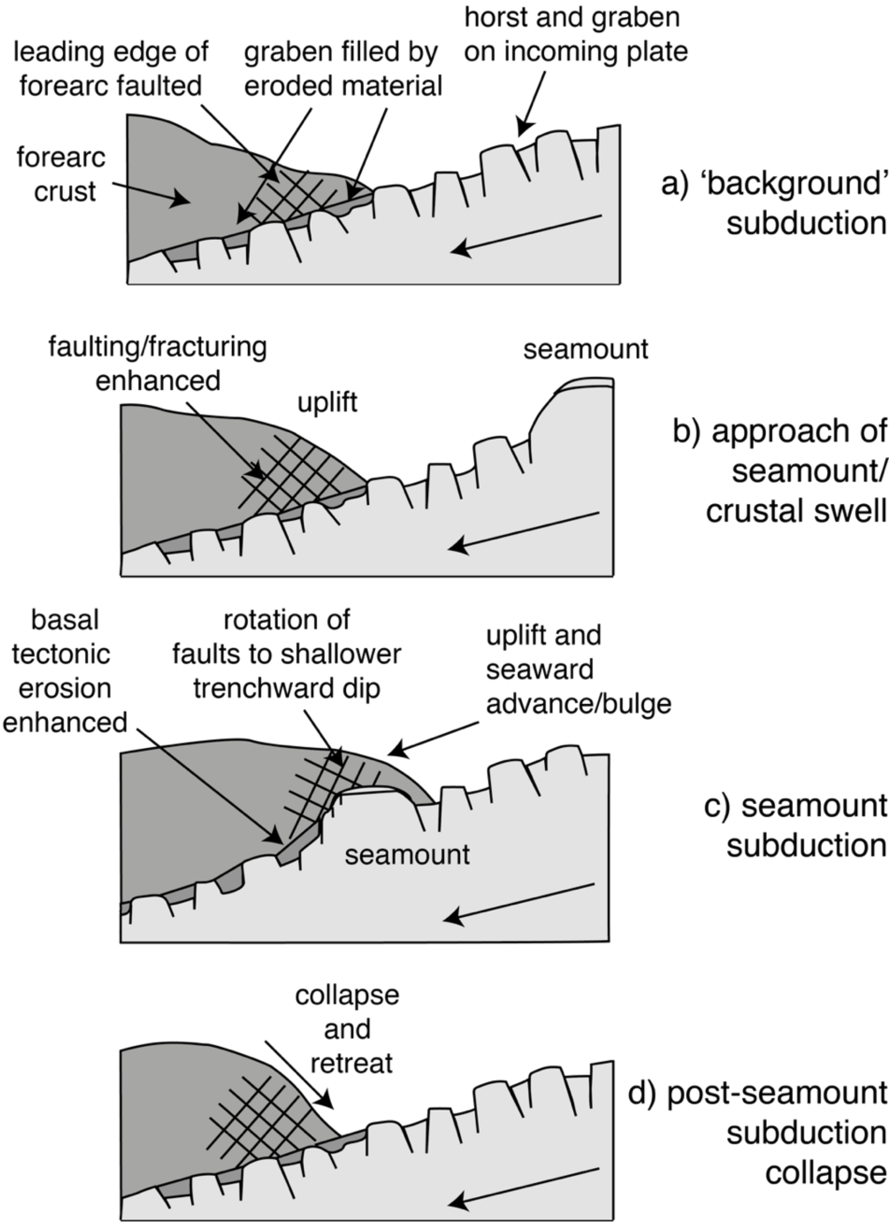

Figure 6.1: *Processes of tectonic erosion resulting from background plate and seamount subduction, adapted from Ballance et al. (1989). a) Horst and graben on the subducting plate cause partial frontal erosion of overriding plate, and basal erosion removes material which fills downgoing graben. b) As a subducting seamount approaches, subduction of the crustal swell initiates enhanced uplift, faulting and erosion of the lower forearc. c) As the seamount subducts, faulting is further enhanced. The forearc is uplifted and bulges towards the trench, with spreading accommodated on small, low-angle normal faults which are rotated by the uplift. d) Following seamount subduction the weakened forearc undergoes rapid gravitational collapse and retreats arcward.*

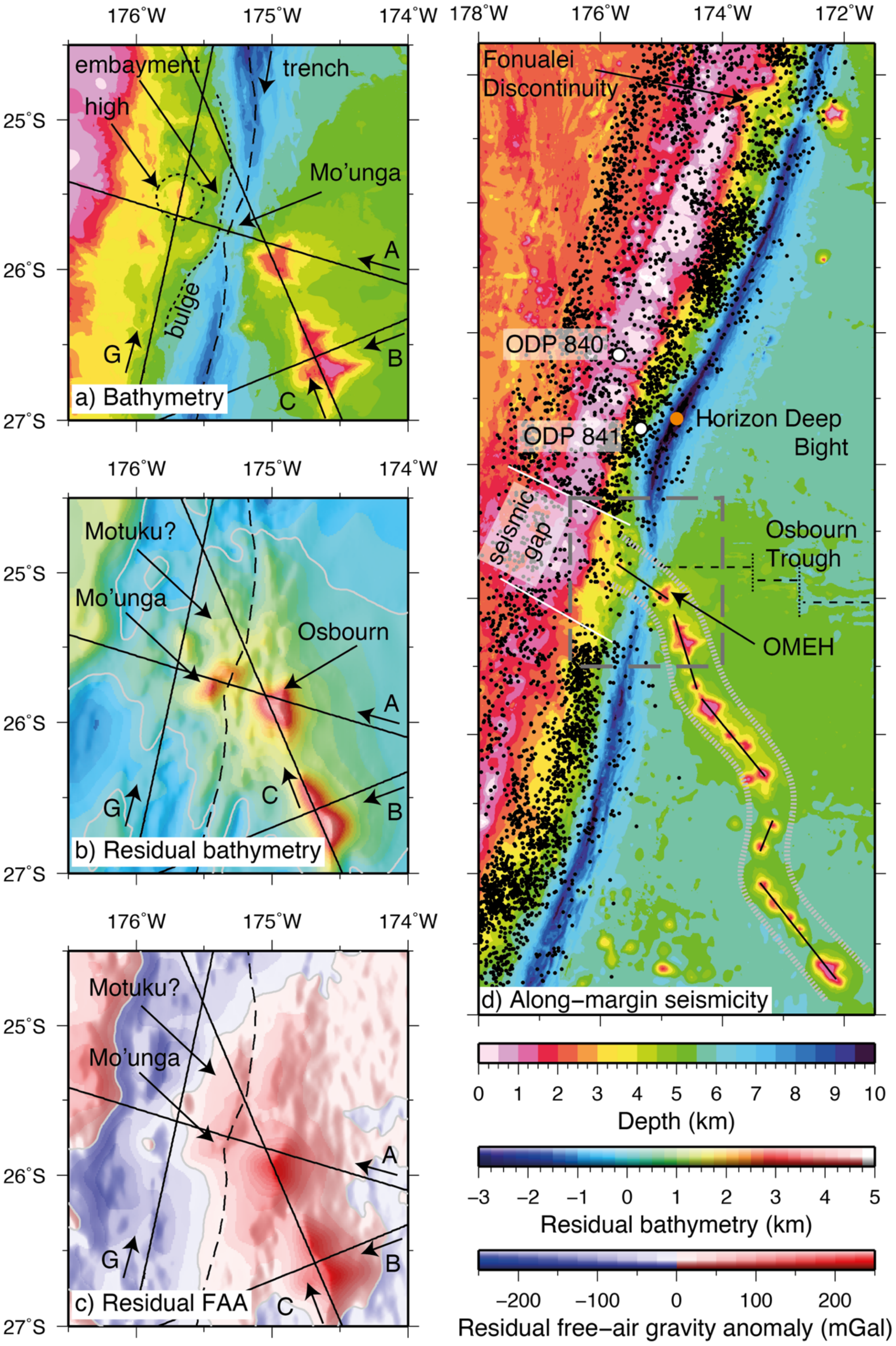
176˚W
175˚W
174˚W
25˚S
26˚S
27˚S
embayment
high
trench
Mo'unga
bulge
A
B
C
G
a) Bathymetry
Motuku?
Mo'unga
Osbourn
b) Residual bathymetry
c) Residual FAA
178˚W
172˚W
18˚S
20˚S
22˚S
24˚S
28˚S
30˚S
32˚S
Fonualei
Discontinuity
ODP 840
ODP 841
Horizon Deep
Bight
seismic
gap
Osbourn
Trough
OMEH
d) Along–margin seismicity
0 1 2 3 4 5 6 7 8 9 10
Depth (km)
–3 –2 –1 0 1 2 3 4 5
Residual bathymetry (km)
–200 –100 0 100 200
Residual free–air gravity anomaly (mGal)

Figure 6.2

the summits of Osbourn seamount and the inferred Mo'unga seamount, located in the trench (Fig. 6.2b). Bathymetric, gravity and magnetic data may support this Osbourn-Mo'unga-embayment-high lineation (OMEH – Fig. 6.2d) as a potential structural indicator of the LRSC continuation direction, which will be discussed further in a following section.

Together, these observations suggest that seamount-related deformation of the forearc may be superimposed on wider crustal-swell related deformation, where the 20 km lower forearc bulge represents the response to subduction of the crustal-scale LRSC, and the smaller embayment and high structure represent the accommodation of the protrusion of an intact or partially intact subducting seamount on top of the plate. As the LRSC represents a case where the height of the subducting bathymetric feature is not constant along its length, the presently observed forearc uplift may, therefore, directly correspond to an individual subducted seamount (Zeumann and Hampel, 2016) with the high representing an uplifted part of the forearc accommodating the topography on top of the plate, and the embayment associated with subsidence where the forearc directly overlies a gap between incoming seamounts.

Figure 6.2 (previous page): *Evidence for proposed continuation of the LRSC. a) Osbourn seamount-TKT region bathymetry. SO215 seismic profiles plotted as solid lines. Trench axis plotted as dashed line. Lower forearc bulge, embayment and high plotted as dotted lines and labelled. b) Residual bathymetric anomaly (RBA) from Bassett and Watts (2015). SO215 WA seismic profiles labelled as in a). Arrows show the locations of the two RBAs which are proposed to represent subducted continuations of the LRSC. A third, unnamed, RBA is traversed by Profile G. c) Residual free-air gravity anomaly (RFGA) from Bassett and Watts (2015), labelled as in b). The RFGA manifestation of Motuku is barely visible. d) 1960-2009 earthquake locations from the International Seismological Centre EHB (Engdahl et al., 1998) event catalogue (accessed 08/08/2017). Dashed grey box indicates the area shown in a-c). White lines show the limits of the Louisville seismic gap. Black lines over the LRSC represent the possible en-echelon segmentation, with that over Osbourn seamount extending over Mo'unga seamount in the trench to the lower forearc bulge and high (OMEH lineation, see text for more details). Osbourn Trough plotted as dashed black line between 25.5-26°S, with segment offsets shown as dotted black lines. Horizon Deep and ODP sites 840 and 841 labelled.*

6.3.3.3. Post-collisional forearc structure

The pre- to post-collisional structural transition occurs over an along-arc distance of ~180 km (Stratford et al., 2015) which, for an intersection migration rate of 120-180 mm yr^{-1} (Lonsdale, 1986; Ballance et al., 1989), results in transition timescales of 1.0-1.5 Ma. It has been estimated that subduction erosion due to the LRSC accounts for the removal of ~80 km of material from the leading edge of the overriding plate (Ballance et al., 1989; Clift and MacLeod, 1999; Wright et al., 2000), contributing to the formation of Horizon Deep, where the seafloor depth is ~10.8 km and the lower trench slope dips at >10˚ (Lonsdale, 1986). Arcward of Horizon Deep, observations of normal and reverse faults in cored sections from ODP Site 841 on the forearc slope (Ballance et al., 1989; MacLeod, 1994), support the interpretation that seamount subduction may be accommodated by permanent deformation of the overriding plate in the form of compression and uplift, followed by subsequent extension and gravitational collapse as the bathymetric feature is subducted beyond the base of this region (Dominguez et al., 1998). The location of Horizon Deep to the north of the syn-collisional zone, indicates that the maximum tectonic erosion of trench slope material occurs in the wake of LRSC subduction, taking place predominantly after the seamount chain and swell have migrated further to the south. This post-collisional collapse of the fractured and weakened forearc results in the steepening and rapid retreat of the lower forearc slope in this region (Fig. 6.1d).

Post-collisional trenchward tilting in the mid-slope basin regions has been shown to increase in the 0.5 Ma following LRSC passage, which is attributed to collapse of the trench slope in its wake (MacLeod, 1994). Both frontal and basal erosion of the weakened post-collisional forearc, due to the steepening of the inner trench wall and thinning of the crust respectively, lead to accelerated collapse and re-equilibration of the forearc in this region (Ballance et al., 1989). Sediment can continue to be deposited in small basins in the outer forearc for as long as 5 Ma following passage of the LRSC (Clift et al., 1998), indicating the timescale over which the return to a pre-LRSC equilibrium occurs. North of the present collision, incision of the forearc by canyons can be seen to be an important contributor to the redistribution of arc and upper forearc material towards the trench, and that it displays a waning influence over time (Clift et al., 1998).

North of ~22-23˚S, the trench slopes return to a more typical and constant along-strike structure, indicating that this represents the northerly limit of the LRSC-subduction affected zone (Stratford et al., 2015). Changes in forearc faulting patterns, which indicate a lack of pervasive deformation north of 22˚S, provide further evidence for the delimitation of the seamount subduction affected region being south of here (Herzer & Exon, 1985). Satellite FAA data indicates a co-incident ~20 km westward step in the trenchward edge of the buried Tonga Ridge (Funnell et al., 2017), which is proposed to be directly related to the onset of seamount subduction-related erosion following LRSC initial collision at ~5 Ma (e.g. Ruellan et al. 2003; Timm et al. 2013), rather than background tectonic erosional processes.

6.3.3.4. Arc and back arc structure

Bonnardot et al. (2007) observe that the dip of the subducting slab varies along strike, with the the dip being greater (58˚) at 26˚S, the present intersection point, than further to the north at 23˚S (52˚), suggesting that ridge subduction may cause flattening of the slab. It is also possible that this change in slab dip is linked to changing location of the active volcanic arc along the margin (England et al., 2004). North of the present collision zone the active Tofua Arc is located behind the Tonga forearc high (170-210 km d.p.t.), whereas to the south the Kermadec Arc is located on the peak of the high (150-180 km d.p.t. – Dupont and Herzer, 1985). Lallemand et al. (1992) propose the existence of a southward-migrating diffuse transfer zone which accommodates the shortening associated with LRSC impingement on the trench system. The existence of this zone is supported by stress inversions which show a segmentation between extensional Tonga and Kermadec domains separated by a small region of convergence-parallel compressive stress (Bonnardot et al., 2007), and supports the proposed southward propagation of Lau Basin spreading in the wake of the migrating intersection (Ruellan et al., 2003), the variable back arc spreading rates (Bevis et al., 1995), and the difference in morphology between the Lau Basin north of the intersection and the Havre Trough to the south (Wysoczanski et al., 2010). Subducting bathymetry has been proposed to play a role in the formation and evolution of other back arc systems. For example, at the Mariana Trench, which is pinned to the south by the Caroline Ridge and to the north by the Marcus–Necker Ridge (Vogt et al., 1976), subducting topography is suggested to lead to its arcuate shape.

6.3.4. Seismicity observations

The LRSC-TKT convergence is associated with a zone of relative seismic quiescence known as the Louisville Gap (Fig. 6.2d; Scholz and Small, 1997). Compared to the north and south of the TKT, the Louisville Gap shows a 40% reduction in shallow seismicity (0-100 km – Timm et al., 2013). Christensen and Lay (1988) also identified that there is a paucity of great subduction earthquakes associated with the LRSC-TKT collision. Some of the largest recorded earthquakes in the area (M_W >7 in 1919, 1975 and 1982 – Christensen and Lay, 1988; Pacheco and Sykes, 1992) are associated with outer-rise normal faulting rather than underthrusting.

The width of the Louisville Gap is approximately equal to that of the flexural moat around the seamount chain (150-200 km). The suggestion that LRSC volcanoes may be broken up during subduction (Section 5.3.5) does not, therefore, necessarily conflict with the observed seismicity, as it may not only be the presence of the bathymetric anomalies that causes it. Instead, the buoyancy and/or increased rigidity provided by the crustal-scale LRSC may provide the principal control. The gap is not centred on the point of present-day LRSC-TKT intersection, instead being offset to the south. This offset has been suggested as evidence for a change in strike of the seamount chain at this point (Timm et al., 2013; Bassett and Watts, 2015), which will be discussed further in a following section. The LRSC-TKT convergence is not the only location where a seismic gap is associated with a subducting bathymetric feature. A co-incidence between locations of subducting bathymetric highs and a reduction in the frequency of large earthquakes and the rupture lengths of those events is observed at a number of locations, including the Kuril, Ryukyu, Aleutian, Sunda and Ecuadorian subduction systems (Kelleher and McCann, 1976).

6.3.5. Continuation of the LRSC

Rather than continuing along its extant trend, it has been proposed that the present-day LRSC-TKT intersection may be coincident with an ~35° anticlockwise (westward) bend in the chain (Steinberger et al., 2004; Wessel and Kronke, 2009; Timm et al., 2013; Bassett, 2014), which may be analogous to an approximately contemporaneous bend north of Detroit seamount (75.8 ± 0.6 Ma, Duncan and Keller, 2004) at the northern end of the Emperor Seamount Chain. Potential field studies have identified a number of residual bathymetric (RBA) and free-air gravity (RFGA) anomalies, generated by removing the averaged trench-perpendicular bathymetry or gravity anomaly to enhance the short-wavelength features within the trench-forearc region to the west of Osbourn seamount (Fig. 6.2b,c – Bassett and Watts, 2015). Mo'unga seamount (Lonsdale, 1986; Pontoise et al., 1986; Ballance et al., 1989; Stratford et al., 2015), with dimensions of ~50 x 25 km and a residual bathymetric prominence of >2.5 km, the smaller inferred Motuku seamount (Ballance et al., 1989), and further small RBAs to the north and northwest of these, lie on or near WA seismic profiles collected as part of the SO215 experiment. However, despite crossing close to the summit of Mo'unga seamount, Profile A (Stratford et al., 2015) lacks convincing evidence for a seamount in this location, and the trench-parallel Profile G also does not show clear evidence for a similar feature (Bassett, 2014). It may be possible that the pre-Osbourn subducted seamount lies within the area bounded by Profiles A, C and G, which would not be inconsistent with the proposed chain rotation described above. If this is the case, then the lack of robust imaging of this feature may be a result of the difficulty of distinguishing seamount flank from ordinary oceanic crust on the basis of P-wave velocity alone (Section 5.3.2). It is also uncertain if any seamount located in the trench would show a similar velocity structure to Osbourn and 27.6 ˚S seamounts, especially given the potential control of edifice size on internal structural variability and the difficulty in quantifying the size of a subducting seamount. Finally, the results of checkerboard testing (Section 4.3) indicates that the minimum resolvable feature size beneath the lower forearc may be larger than the typical dimensions of an average LRSC seamount, and hence it is possible that WA seismic imaging alone would fail to robustly prove the existence of a subducted seamount on any of the SO215 profiles.

The clustering of Mo'unga, Motuku, and the un-named RBA to the west, may suggest that the continuation of the chain is not exactly linear, although Mo'unga seamount has a diameter and height (in terms of RBA) of at least two times that of the other anomalies. However, Motuku seamount is located at a similar along-ridge spacing from Osbourn as the latter is to the rest of the chain (Stratford et al., 2015). Observations of the extant part of the chain north of Hadar Guyot (169˚W) show that the LRSC could be described as a series of ~200 km-long en-echelon segments which represent a short wavelength weave superimposed on the long wavelength trend, rather than a purely linear chain (Koppers et al., 2011; Stratford et al., 2015). Projecting this pattern forward from the extant chain, the next oldest step may correspond to an apparent anticlockwise rotation of the chain of ~20-25˚. In Section 6.3.2.2 the OMEH lineation was identified as a potential structural consequence of the LRSC continuation direction based on bathymetry and gravity data. Whilst the forearc in this region has not definitively been shown to contain a subducted body (Bassett, 2014), where sampled by Profiles A and G the region shows a relatively thick (8-9 km) and slow (<5 km s^{-1}) crust which could be interpreted as representing high degrees of faulting and/or fluid. This highly fractured crust could result from the deformation associated with seamount collision (e.g. Dominguez et al., 1998; Wang and Bilek, 2011), with the broad lower forearc bulge representing the accommodation of the 'crustal' LRSC, and the small high within the C-shaped ridge representing uplift associated with an individual subducting seamount. This is further supported by the observation that the northern boundary of the Louisville seismic gap is associated with this deformation, suggesting that it represents the extent of the active collisional zone, and hence the continuation of the LRSC.

A previous MCS study at the Tonga margin by Ballance et al. (1989) identified an 8-9 km-long, arcward-dipping reflector beneath the Tonga lower-trench slope which was interpreted as representing the flat summit of a seamount, Motuku, along the continuation of the LRSC (Fig. 6.3a). The location of this feature at ~25.1˚S (Fig. 6.3a,b) approximately corresponds to a distance along Profile C of ~190 km d.a.p., which is 30-40 km arcward of where possible reflectors are observed in the MCS data (Fig. 5.10). This location corresponds to the northern part of the lower forearc bulge associated with the accommodation of the subducting LRSC (Fig. 6.3b,c) and would, therefore, correspond to continuation of the chain along the trend of its oldest extant portion, rather than it undergoing a westerly rotation as described above. This location does approximately correspond to the inferred Motuku RBA (Fig. 6.2b), however this is only a very weak feature, and is effectively absent in the RFGA (Fig. 6.2c) which may cast doubt over its significance. The origin of the Ballance et al. (1989) reflector could alternatively be explained as a continuation of the 'background' subducting plate, which may include a downgoing horst, although the downdip extent of ~10 km is greater than the general ~5-8 km normal fault spacing, and hence horst widths on the downgoing plate. To the north of this profile, a depth-migrated MCS section across Horizon Deep at ~23.5˚S, does display evidence for continuing horst and graben subduction, at distances of up to 30 km arcward of the trench axis (von Huene and Scholl; 1991).

6.3.6. Significance of the Osbourn Trough

Given the spatio-temporal proximity of Osbourn seamount to the Osbourn Trough palaeo-spreading centre, it is relevant to consider the potential effects this may have

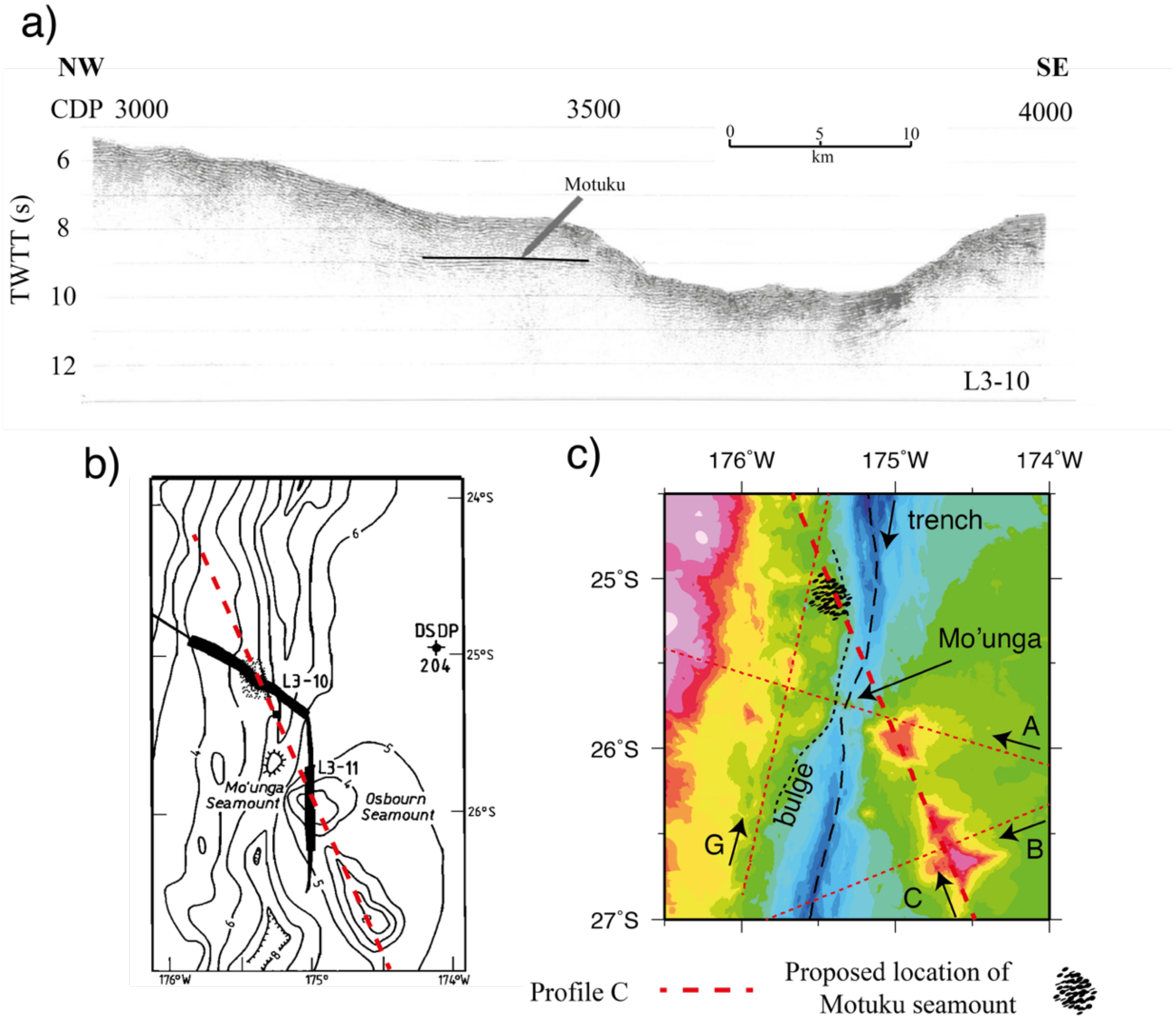

Figure 6.3: *Previous studies identifying a subducted seamount (Motuku) beneath the Tonga forearc. Original plots a) and b) are taken from Ballance et al. (1989), with annotation replaced for clarity. a) Multichannel seismic line L3-10 across the Tonga Trench and lower forearc slope. A package of approximately flat and planar reflectors, ~9 km in length and located at ~9 s TWTT, identified with a black line, are proposed to represent the summit of Motuku. b) Contoured bathymetry map showing location of seismic line L3-10. Location of SO215 Profile C is shown by dashed red line. Profiles intersect over a stippled area, which is suggested to represent the buried summit of Motuku. c) Combined swath-satellite bathymetry of LRSC-TKT collision zone. Location of SO215 Profile C shown by dashed red line and other SO215 profiles as dotted red lines. Corresponding location of Motuku seamount is shown as black stippling, located toward the northern edge of the lower forearc bulge.*

had on seamount constructional processes, or on the direction of the chain. A linear projection of the OT into the subduction zone lies proximal to the RBAs located in the trench (Fig. 6.2b,d). Studies of hotspot volcanic chains approaching active spreading systems have shown that the chain can be influenced over distances of up to 400 km (Small, 1995; Kopp et al., 2003). If the subducted portion of the LRSC had been influenced by and undergone deflection towards the Osbourn Trough, the resulting apparent change in trend, when viewed from the south, would be an anticlockwise (westerly) rotation (Sleep, 2002).

However, the lack of evidence for the presence of LRSC-related magmatic compositions in Osbourn Trough lavas (Beier et al., 2011) favours earlier ages for the cessation of spreading of up to 35 Ma before the passage of the Louisville hotspot, and strongly argues against any influence of the Osbourn Trough. In addition, there is no evidence for the uncoupling of the two systems in the trend of the extant LRSC. For example, there is no ‘gap’ as is sometimes seen for ridge-crossing hotspot trails (Sleep, 2002). However, even if the OT did not actively influence the LRSC plume, if it remained rheologically weak or continued to represent a pre-existing structural heterogeneity for a period post-extinction it may be preferentially exploited by magma reaching the surface.

6.3.7. Location of the initial collision

In addition to the uncertainty regarding the pre-Osbourn direction of the chain, there is debate over the location of initial LRSC-trench collision. Previously proposed locations for this include: the northern end of the subduction system (e.g. Lallemand et al. 1992; Ruellan et al. 2003); at the 18-19˚S Fonualei Discontinuity (Bonnardot et al., 2007); and north of Horizon Deep at 22.5˚S (Herzer and Exon, 1985; von Huene & Scholl 1991; Wright et al. 2000; Contreras-Reyes et al. 2011; Stratford et al. 2015; Funnell et al., 2017).

High $^{206}Pb/^{204}Pb$ values in LRSC samples provide a tracer which can be used to follow LRSC material through the subduction system (Cheng et al., 1987), thus providing a temporal constraint on when this material must have begun to be subducted. Samples from 1500 km to the north of the current intersection point, with an age of 3.0-3.5 Ma (Danyushevsky et al., 1995), contain Pb isotope signatures consistent with recycling of subducted LRSC material (Regelous et al., 2010). If Pb is released from the subducting slab, passes through the mantle wedge and erupts at the surface over timescales of approximately 2-3 Ma (Turner and Hawkesworth, 1997; Turner et al., 1997; Regelous et al., 1997), this indicates LRSC subduction occurred at the north of the Tonga Trench at around 4-5 Ma assuming limited trench-parallel migration of material.

Studies of the evolution of the Lau back arc basin in response to southward migration of the LRSC (Section 6.3.3.4 – Ruellan et al., 2003; Bonnardot et al., 2007) have assumed that the LRSC continues linearly along its extant trend. Therefore, if there is a westward bend in the trend of the chain (Section 6.3.5) then in order for the temporal constraints derived from these studies to fit, subduction of the LRSC must begin either earlier in time or further south than previously suggested, as the southward migration rate could decrease from 180 km Ma^{-1} to <45 km Ma^{-1} (Timm et al., 2013). However, it could also be argued that if initial collision occurred at 22˚S and there is a more westerly trend to the already subducted portion of the chain, southward migration of the intersection point may not be as significant in Lau Basin opening as has been previously suggested.

Overall, the strongest spatial and temporal evidence arising from all data sources appears to most strongly favour ~22˚S, to the north of Horizon Deep, as the most likely location for initial LRSC collision. If the timing of LRSC subduction initiation is held to be ~4-5 Ma to fit this location, a more westerly trend of the subducted chain (anticlockwise rotation) is required (Ballance et al., 1989; Ruellan et al., 2003).

6.4. Summary

The first goal of this study was to determine the internal structure of Louisville Ridge seamounts, and whether there is any significant along-ridge variation in crustal structure and/or thickness. Due to the complex geometry of the LRSC, the along-chain profile provides laterally limited insight into seamount internal structure. Where two large seamounts are crossed over their summits they display relatively high velocity (>6.0 km s^{-1}) intrusive cores which reach to within 1.0-1.5 km beneath their summits. As a result of the limited definitive age constraints on the spreading history of the Osbourn Trough which formed the crust on which the seamounts are hosted, it is unclear how much of an effect the ‘plate age at time of volcanism’ has had on their internal structure, and whether the LRSC represents an end-member or more intermediate structure. The observation that the Louisville Ridge seamounts are structurally distinctly different to, for example, the Hawaiian and Marquesas Islands, provides evidence that the 'plate age at time of volcanism' hypothesis holds. Conversely, however, their structural similarity with small, non-hotspot related seamounts indicates that other processes may be able to produce similar patterns to the LRSC, and indeed may have a very significant influence on seamount structure in general, and so the hypothesis either does not hold, or has significant caveats, such as a strong(er) correlation with the plate-hotspot migration rate, or the edifice size. However, there does not appear to be any strong evidence which points to a non-hotspot origin for the Louisville Ridge. The long and relatively homogenous magmatic history, where the variability can be well correlated to locations with different seafloor age, and the lack of suitable seafloor structural fabrics which could have been exploited by magmatism, do not appear to refute the predictions of the hypothesis.

It has not been possible using the combined SO215 and *TOTAL* WA seismic datasets to place definitive and robust constraint on the continuation direction of the LRSC. However, wide-ranging evidence, including along-margin observations of trench slope morphology and uplift history, the spatial extent of faulting and deformation patterns, present-day seismicity, and potential field data, do not appear to negate the possibility that the point of present LRSC-TKT collision is also co-incident with a westward bend in the chain. Based on geochemical data and seafloor structural observations there does not, however, appear to be any evidence for additional influence on either the structure of LRSC seamounts or the direction of continuation of the chain arising from the spatial proximity of the OT spreading system, thus ruling ridge-trench interaction out as a cause of any change in trend. Correlation between this bend and the similarly aged Detroit-Meiji bend in the Hawaii-Emperor Seamount Chain suggest that the origins of these bends may be linked by a change in absolute plate motion. Alternatively, however, it can be seen that there is some variability, or weave, in the trend of the LRSC (Fig. 6.2d) over length scales of~200 km, which may contribute to the change in direction for seamounts older than Osbourn.

The observations of the along-margin structural variability and evolution show that seamount-related deformation is superimposed on pre-existing crustal structures, and that the deformation associated with seamount subduction manifests as a wake-effect whose maximum is not fully observed until some time (1.0-1.5 Ma) after collision. Subduction of the LRSC represents a situation where large-scale deformation is caused by the wider crustal structural anomaly (the swell) which is more-or-less continuous along the length of the LRSC, with an additional, narrower band of deformation superimposed on top. This latter deformation is associated with the topographic prominences of the seamount chain, which exhibit a non-constant peak elevation and thus may result in more temporally variable patterns of uplift and subsidence.

7. Conclusions and Further Work

7.1. Seamount structure

The primary goals of this study were to determine the internal structure of the Louisville Ridge seamounts and determine the nature of along-ridge variation in crustal structure and/or thickness. The results of modelling Profile C have been integrated with additional profiles from the SO215 and *TOTAL* experiments to provide a pseudo-three dimensional understanding of the largest seamounts of the LRSC. The principal observations and conclusions arising from this part of the study are summarised below.

- High velocity (>6.0 km s^{-1}) intrusive cores exist within the interior of Osbourn and 27.6°S seamounts, reaching to within 1.0-1.5 km below their summits. These features appear to be discrete in lateral extent, have a diameter of between a third and a half of that of the seamount, and contribute ~60 % of the edifice volume. These observations are consistent with models of seamount constructional processes and the internal structures these produce, which suggests that the primary controlling factors on seamount structure are the age of the plate on which a seamount is formed and how the dominant mode of volcanism varies through time as seamounts grow.
- Canopus seamount is not crossed at its summit by Profile C, and does not display an intrusive core. However, this observation does not preclude the existence of an intrusive core within this seamount, and may instead provide an indication of the maximum size a core might have, if it existed. This, therefore, further affirms the observation that intrusive cores are discrete in lateral extent, and lends support to the validity of models of formation of intrusive cores within seamounts.
- The observation that Louisville Ridge seamounts are structurally distinct from, say, the Hawaiian and Marquesas Islands, provides strong evidence that the ‘plate age at time of volcanism’ hypothesis holds. For example, this study shows that there does not appear to be any evidence for magmatic underplating or significant thickening of the crust beneath the LRSC, which are characteristics shown by the large Δt end-members. However, given the limited

definitive age constraints on the spreading history of the Osbourn Trough, which formed the crust on which the seamounts sit, it is unclear to what extent the LRSC represents an end-member predicted by this hypothesis or is an intermediate structure

7.2. Subduction of the LRSC

The secondary aim of this study was to understand how LRSC seamounts behave and interact with the overriding plate during subduction, and how the overriding plate responds to subduction of large-scale bathymetric features, in addition, allowing determination of the most likely continuation direction of the LRSC beneath the forearc. The principal observations and conclusions resulting from this part of the study are summarised below.

- Osbourn seamount appears to be significantly affected by normal faulting associated with bending of the Pacific plate as it passes over the outer rise. It is possible that this faulting may lead to its disarticulation as it enters the trench, at a scale of the observed inter-fault spacing of ~5-8 km. If this is the case, then individual subducting seamount blocks would fall below the model resolution limits in and beneath the trench and lower forearc regions.
- Distinguishing between seamount flank and ordinary subducting crust based on P-wave velocity alone is challenging. Therefore, in order to unequivocally identify a subducted seamount at depth it would be necessary to image distinct features such as a high velocity intrusive core.
- Subduction of the LRSC appears to result in multiple scales of deformation being superimposed on top of each other. Large-scale deformation of the forearc, manifest as a trenchward bulge of the lower trench slope, is caused by the wider crustal structural anomaly (the swell) which is effectively continuous along the length of the LRSC. The topographic prominences of the seamount chain on top of the plate then result in an additional, narrower band of deformation. As the LRSC does not display a constant along-chain peak elevation, this latter deformation is more temporally variable, with patterns of uplift and subsidence relating to the passage of the seamounts beneath the forearc.

- Observations of along-margin structural variability and evolution show that seamount-related deformation is superimposed on pre-existing crustal structure. The maximum deformation associated with seamount subduction occurs in the wake of the migrating intersection point and is, therefore, observed to the north of the present-day intersection. Maximum deformation occurs ~1.0-1.5 Ma after collision, with re-equilibration of the trench and forearc structure continuing beyond this timescale.
- The continuation direction of the LRSC beneath the forearc remains unresolved. However, a range of evidence including along-margin observations of trench slope morphology and uplift history, the spatial extent of faulting and deformation patterns, seismicity, and potential field data, appear to support the suggestion that the point of present-day LRSC-TKT collision may be co-incident with a westward bend in the chain. This may correlate with the similarly aged Detroit-Meiji bend in the Hawaii-Emperor Seamount Chain, suggesting that the origins of these bends may be linked by a change in absolute plate motion. In addition, there appears to be variability (weave) in the trend of the LRSC over short length scales (~200 km), which is superimposed on the overall trend of the chain. It is possible that this weave may instead account for, or contribute to, the apparent change in direction for seamounts older than Osbourn.

7.3. Further work

In response to the unresolved questions arising from this research, two further potential studies are proposed, involving primarily the acquisition of WA seismic data. Each of these proposed studies could be achieved within a single research cruise

The first study seeks to better understand the along-chain consistency of seamount internal structure by targeting Canopus seamount. SO215 Profiles B and C did not cross either summit of this seamount in a location that would result in the imaging of an intrusive core, if one were present (Fig. 7.1a). The ~70 x 60 km footprint of Canopus seamount makes it a suitable target for a 3D tomographic study. In addition to revealing the internal structure directly beneath the summit of this seamount, this survey would also permit the results of the flank-crossing Profile C to be used as a proxy for determining whether other flank-crossed seamounts along the chain may also display a similar internal structure to those imaged in this study. In addition, an

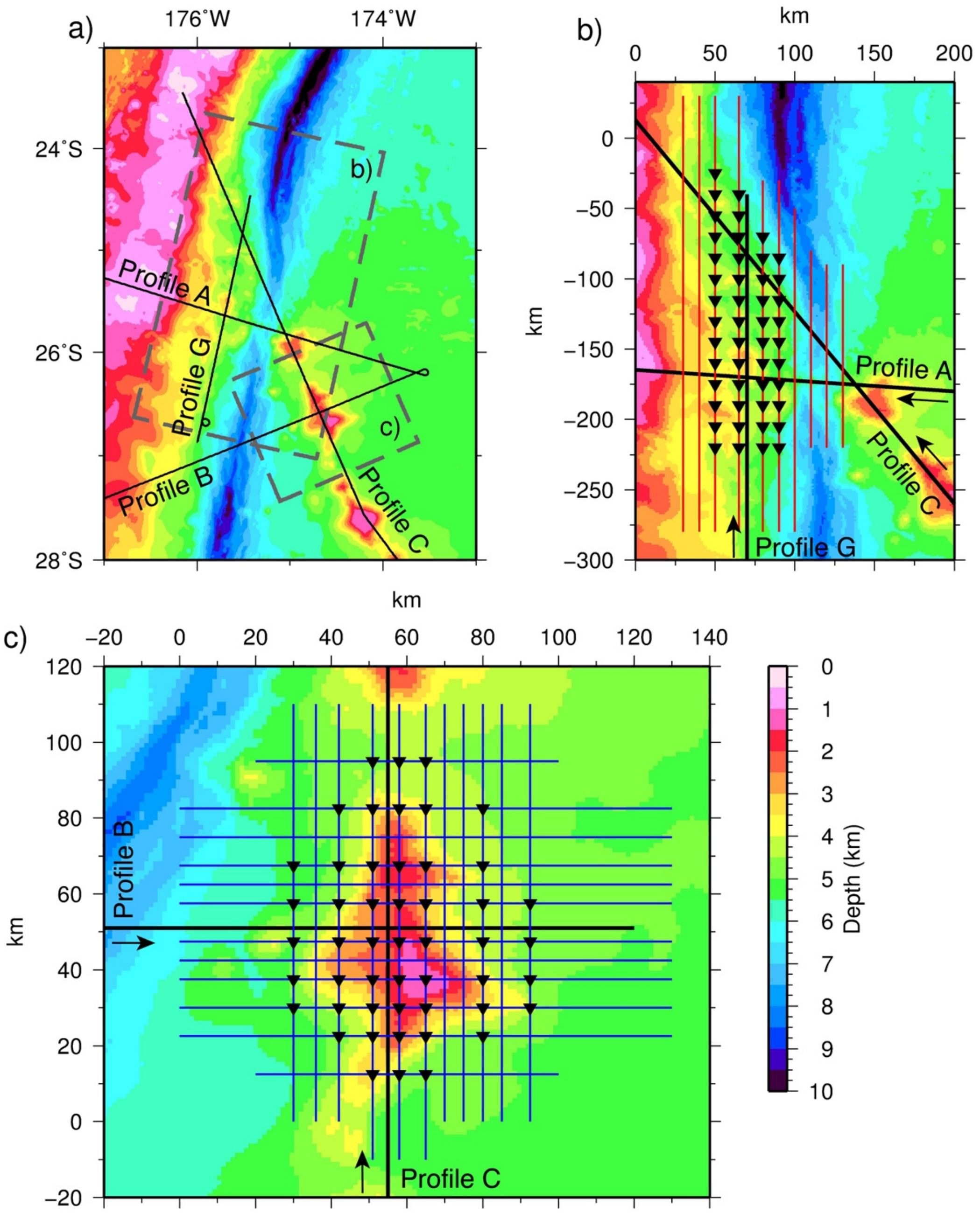

***Figure 7.1:** Potential further study locations in the LRSC-TKT intersection region. a) Bathymetry of the LRSC-TKT intersection region. SO215 WA seismic profiles plotted in black and labelled. Dashed grey boxes show locations of potential future study areas shown in b) and c). b) Tonga lower forearc region, rotated into km-offset space. SO215 WA seismic profiles plotted in black and labelled. Black inverted triangles show proposed OBS locations. Red lines show proposed seismic acquisition profiles. c) Canopus seamount region, rotated into km-offset space. SO215 WA seismic profiles plotted in black and labelled. Black inverted triangles show proposed OBS locations. Blue lines show proposed seismic acquisition profiles.*

understanding of the structure of the smaller, northern edifice of this seamount would be achieved, which may indicate whether it is an individual structure, or if the two edifices are connected at depth, and which may have implications for the understanding of intra-volcanic spacing along-chain. In addition, there remains a lack of certainty if edifice size controls whether or not a seamount contains an intrusive core, hence the imaging of this smaller feature may be useful in providing some insight. Finally, this study may also further assist in defining what velocity structure or characteristics, if observed, would be indicative of a subducting seamount in the trench/lower-forearc region.

Figure 7.1c shows a possible OBS deployment and profile acquisition geometry which would be suitable for achieving the above aims. The proposed profiles cross the summits of both the northern and southern parts of the seamount in both the along- and across-chain directions. The OBS array is relatively dense around both seamount summits to provide optimum resolution of the scale of any features likely to form a core. The across-chain shooting profiles extend >±60 km from the seamount centre, whilst the along-chain profiles are shorter (≤±50 km) as a result of the along-chain bathymetry which would add complication to the modelling by the necessity to incorporate these adjacent seamounts in the model. The dimensions of the survey are determined based on the observation from this study that the base of the crust is located at 15-16 km b.s.s., and a shot-receiver offset of >2.5 times the maximum depth to be imaged is taken as the rule of thumb to determine profile length. In order to increase the shot density within the grid, and thus the resolution of the resulting model, a number of shooting-only profiles are also located between OBS profiles.

The second further investigation focuses on the attempts to image an already subducted LRSC seamount, and determine the direction of continuation of the chain. The 'absolute plate motion change' model suggests that there could be a 35° westward (anticlockwise) bend at the point of current intersection, which corresponds to the Detroit-Meiji bend at the northern end of the Emperor Seamount Chain. Alternatively, the 'weaving' model for the LRSC suggests that short-wavelength changes in trend of ~20-25° are possible, and based on the direction of the last 'weave', the next would be expected to have a westward (clockwise) sense of rotation. It may also be possible that these two mechanisms for changing the trend of the chain could both be acting constructively, such that their effects are additive. Hence, the bend angle could be up to ~60°. It is most likely, therefore, that the continuation of the LRSC lies somewhere in the sector between Profiles A and C, which are separated by an angle of ~50°, or a short distance to the south of this.

In order to investigate this hypothesis, a series of trench-parallel, i.e. along the same orientation as SO215 Profile G (Fig. 7.1b), profiles are proposed. These profiles extend from ~20 km to the north of Profile C to ~50 km to the south of Profile A, with the acquisition survey footprint extending by ~50 km in each direction in order to provide sufficient depth penetration. The most trench-proximal profile is located as close to the trench as possible without the water depth becoming an inhibiting factor on instrument siting and, hence, profile length. This results in only part of the triangle between Profiles A, C and G being instrumented. To compensate for this, seismic shooting lines would be acquired in a trench-parallel direction across this region, so that arrivals can be traced laterally to the instruments. Further profiles may also be shot arcward of the OBS profiles, to the same effect.

7.4. Summary

This study has revealed the internal structure of the seamounts of the LRSC. It has also shown that each seamount has a unique internal structure, with each consistent with predictions of models explaining their mode of formation. When these seamounts are subducted, they are further deformed by plate-bending processes, becoming dissected at a scale of ~5-8 km along-chain. Subsequently, on subduction, the LRSC as a whole, and each seamount along it in particular, modify the background subduction deformation processes affecting the overriding plate, which occur both during and for a period of 1.0-1.5 Ma after subduction.

References

Abercrombie, R. E., M. Antolik, K. Felzer, and G. Ekstrom (2001), The 1994 Java tsunami earthquake: Slip over a subducting seamount, J. Geophys. Res., 106(B4), 6595–6607.

Ballance, P. F., D. W. Scholl, T. L. Vallier, A. J. Stevenson, H. Ryan, and R. H. Herzer (1989), Subduction of a Late Cretaceous Seamount of the Louisville Ridge at the Tonga Trench: A Model of Normal and Accelerated Tectonic Erosion, Tectonics, 8(5), 953–962.

Ballance, P. F., A. G. Ablaev, I. K. Pushchin, S. P. Pletnev, M. G. Birylina, T. Itaya, H. A. Follas, and G. W. Gibson (1999), Morphology and history of the Kermadec trench-arc-backarc basin-remnant arc system at 30 to 32°S: Geophysical profile, microfossil and K-Ar data, Mar. Geol., 159(1-4), 35–62.

Ballmer, M. D., J. van Hunen, G. Ito, P. J. Tackley, and T. A. Bianco (2007), Non-hotspot volcano chains originating from small-scale sublithospheric convection, Geophys. Res. Lett., 34, 1–5.

Bangs, N. L. B., S. P. S. Gulick, and T. H. Shipley (2006), Seamount subduction erosion in the Nankai Trough and its potential impact on the seismogenic zone, Geology, 34(8), 701–704.

Barckhausen, U., H. A. Roeser, and R. von Huene (1998), Magnetic signature of upper plate structures and subducting seamounts at the convergent margin off Costa Rica, J. Geophys. Res., 103, 7079–7093.

Bassett, D., and A. B. Watts (2015), Gravity anomalies, crustal structure, and seismicity at subduction zones: 1. Seafloor roughness and subducting relief, Geochem., Geophys., Geosyst., 16, 1508–1540.

Bassett, D., H. Kopp, R. Sutherland, S. Henrys, A. B. Watts, C. Timm, M. Scherwath, I. Grevemeyer, and C. E. J. Ronde (2016), Crustal structure of the Kermadec arc from MANGO seismic refraction profiles, J. Geophys. Res. Solid Earth, 121, 1–33.

Bassett, D. G. (2014), The Relationship Between Structure and Seismogenic Behaviour in Subduction Zones, University of Oxford.

Beier, C., L. Vanderkluysen, M. Regelous, J. J. Mahoney, and D. Garbe-Schönberg (2011), Lithospheric control on geochemical composition along the Louisville Seamount Chain, Geochem., Geophys., Geosyst., 12(9), Q0AM01.

Bell, R., C. Holden, W. Power, X. Wang, and G. Downes (2014), Hikurangi margin tsunami earthquake generated by slow seismic rupture over a subducted seamount, Earth Planet. Sci. Lett., 397, 1–9.

Bevis, M., F. W. Taylor, B. E. Schutz, J. Recy, B. L. Isacks, S. Helu, R. Singh, E. Kendrick, J. Stowell, and B. Taylor (1995), Geodetic observations of very rapid convergence and back-arc extension at the Tonga arc, Nature, 374, 249–251.

Bilek, S. L., S. Y. Schwartz, and H. R. Deshon (2003), Control of seafloor roughness on earthquake rupture behavior, Geology, 31, 455–458.

Billen, M. I., and J. M. Stock (2000), Morphology and origin of the Osbourn Trough, J. Geophys. Res., 105(B6), 13481–13489.

Birch, F. (1961), The velocity of compressional waves in rocks to 10 kilobars: 2., J. Geophys. Res., 66(7), 2199–2224.

Bird, P. (2003), An updated digital model of plate boundaries, Geochem., Geophys., Geosyst., 4(3), 1–52.

Bodine, J. H., and A. B. Watts (1979), On lithospheric flexure seaward of the Bonin and Mariana trenches, Earth Planet. Sci. Lett., 43(1), 132–148.

Bonatti, E. (1967), Mechanisms of Deep-sea Volcanism in the South Pacific, in Researches in geochemistry, Volume 2, ed. Abelson, P., pp. 453–491.

Bonatti, E., and C. G. A Harrison (1988), Eruption Styles of Basalt in Oceanic Spreading Ridges and Seamounts: Effect of Magma Temperature and Viscosity, J. Geophys. Res., 93(B4), 2967–2980.

Bonnardot, M.-A., M. Régnier, E. Ruellan, C. Christova, and E. Tric (2007), Seismicity and state of stress within the overriding plate of the Tonga-Kermadec subduction zone, Tectonics, 26, 1–15.

Box, G. E. P., and M. E. Muller (1958), A Note on the Generation of Random Normal Deviates, Ann. Math. Stat., 29(2), 610–611.

Buck, W. R., and E. M. M. Parmentier (1986), Convection beneath young oceanic lithosphere: Implications for thermal structure and gravity, J. Geophys. Res., 91(B2), 1961–1974.

Cadet, J. P., K. Kobayashi, J. Aubouin, J. Boulègue, C. Deplus, J. Dubois, R. von Huene, L. Jolivet, T. Kanazawa, J. Kasahara, K. Koizumi, S. Lallemand, Y. Nakamura, G. Pautot, K. Suyehiro, S. Tani, H. Tokuyama and T. Yamazaki (1987), The Japan Trench and its juncture with the Kuril Trench: cruise results of the Kaiko project, Leg 3, Earth Planet. Sci. Lett., 83(1-4), 267–284.

Calmant, S., J. Francheteau, and A. Cazenave (1990), Elastic layer thickening with age of the oceanic lithosphere: a tool for prediction of the age of volcanoes or oceanic crust, Geophys. J. Int., 100, 59–67.

Cande, S. C., and D. V Kent (1992), A New Geomagnetic Polarity Time Scale for the Late Cretaceous and Cenozoic, J. Geophys. Res., 97(B10), 13917–13951.

Caress, D. W., and D. N. Chayes (2006), Mapping the seafloor: Software for the processing and display of swath sonar data. www.mbari.org/data/mbsystem

Caress, D. W., M. K. McNutt, R. S. Detrick, and J. C. Mutter (1995), Seismic imaging of hotspot-related crust underplating beneath the Marquesas Islands, Nature, 373, 600–603.

Carlson, R. L., and C. N. Herrick (1990), Densities and porosities in the oceanic crust and their variations with depth and age, J. Geophys. Res., 95(B6), 9153.

Carlson, R. L., and D. J. Miller (2003), Mantle wedge water contents estimated from seismic velocities in partially serpentinized peridotites, Geophys. Res. Lett., 30(5), 12–15.

Carlson, R. L., and G. S. Raskin (1984), Density of the ocean crust, Nature, 311, 555–558.

Charvis, P., A. Laesanpura, J. Gallart, A. Hirn, J.-C. Lépine, B. de Voogd, T. A. Minshull, Y. Hello, and B. Pontoise (1999), Spatial distribution of hotspot material added to the lithosphere under La Réunion, from wide-angle seismic data, J. Geophys. Res., 104, 2875.

Chen, C.-Y., and F. A. Frey (1985), Trace Element and Isotopic Geochemistry of Lavas From Haleakala Volcano, East Maui, Hawaii' Implications for the Origin of Hawaiian Basalts, J. Geophys. Res., 90, 8743–8768.

Cheng, Q., K. Park, J. D. Macdougall, A. Zindler, H. Staudigel, J. Hawkins, and P. Lonsdale (1987), Isotopic Evidence for a Hotspot Origin of the Louisville Seamount Chain, in Seamounts, Islands, and Atolls, Geophys. Monogr. Ser., vol. 43, vol. 43, edited by B. H. Keating, P. Fryer, R. Batiza, and G. W. Boehlert, pp. 283–296.

Christensen, D. H., and T. Lay (1988), Large Earthquakes in the Tonga Region Associated with Subduction of the Louisville Ridge, J. Geophys. Res., 93(B11), 13367–13389.

Christensen, N.I., and W. D. Mooney (1995) Seismic velocity structure and composition of the continental crust: A global view, J. Geophys. Res., 100, 9761–9788.

Clague, D. A., and G. B. Dalrymple (1988), Age and petrology of alkalic postshield and rejuvenated-stage lava from Kauai, Hawaii, Contrib. to Mineral. Petrol., 202–218.

Clift, P. D., and C. J. Macleod (1999), Slow rates of subduction erosion estimated from subsidence and tilting of the Tonga forearc, Geology, 27(5), 411–414.

Clift, P., and P. Vannucchi (2004), Controls on tectonic accretion versus erosion in subduction zones: Implications for the origin and recycling of the continental crust, Rev. Geophys., 42.

Clift, P., C. J. Macleod, D. R. Tappin, D. J. Wright, and S. H. Bloomer (1998), Tectonic controls on sedimentation and diagenesis in the Tonga Trench and forearc, southwest Pacific, Geol. Soc. Am. Bull., 110(4), 483–496.

Cloos, M. (1992), Thrust-type subduction-zone earthquakes and seamount asperities: A physical model for seismic rupture, Geology, 20, 601–604.

Cloos, M., and R. L. Shreve (1996), Shear-zone thickness and the seismicity of Chilean- and Marianas-type subduction zones, Geology, 24(2), 107–110.

Cohen, J. K., and J. Stockwell (2000), SU: Seismic Unix, a free package for seismic research and processing. Center for Wave Phenomena, Colorado School of Mines.

Collot, J.-Y., and B. Davy (1998), Forearc structures and tectonic regimes at the oblique subduction zone between the Hikurangi Plateau and the southern Kermadec margin, J. Geophys. Res., 103(B4), 7107.

Contreras-Reyes, E., I. Grevemeyer, A. B. Watts, L. Planert, E. R. Flueh, and C. Peirce (2010), Crustal intrusion beneath the Louisville hotspot track, Earth Planet. Sci. Lett., 289(3-4), 323–333.

Contreras-Reyes, E., I. Grevemeyer, A. B. Watts, E. R. Flueh, C. Peirce, S. Moeller, and C. Papenberg (2011), Deep seismic structure of the Tonga subduction zone: Implications for mantle hydration, tectonic erosion, and arc magmatism, J. Geophys. Res., 116(B10), B10103.

Coulbourn, W. T., P. J. Hill, and D. D. Bergersen (1989), Machias Seamount, Western Samoa: Sediment remobilization, tectonic dismemberment and subduction of a guyot, Geo-Marine Lett., 9(3), 119–125.

Crawford, W. C., J. A. Hildebrand, L. M. Dorman, S. C. Webb, and D. A. Wiens (2003), Tonga Ridge and Lau Basin crustal structure from seismic refraction data, J. Geophys. Res., 108(B4), 2195.

Cummins, P. R., T. Baba, S. Kodaira, and Y. Kaneda (2002), The 1946 Nankai earthquake and segmentation of the Nankai trough, Phys. Earth Planet. Inter., 132(1-3), 75–87.

Danyushevsky, L. V, T. J. Falloon, and I. Alexander (1995), North Tongan High-Ca Boninite Petrogenesis: The Role of Samoan Plume and Subduction Zone-Transform Fault Transition, J. Geodyn., 20(3), 219–241.

Das, S., and A. B. Watts (2009), Subduction Zone Geodynamics, in Subduction Zone Geodynamics, edited by S. Lallemand and F. Funiciello, pp. 103–118, Springer Berlin Heidelberg, Berlin, Heidelberg.

Davis, A. S., L. B. Gray, D. A. Clague, and J. R. Hein (2002), The Line Islands revisited: New 40 Ar/ 39 Ar geochronologic evidence for episodes of volcanism due to lithospheric extension, Geochem., Geophys., Geosyst., 3(3), 1–28.

Devine, J. D., and H. Sigurdsson (1995), Petrology and eruption styles of Kick'em-Jenny submarine volcano, Lesser Antilles island arc, J. Volcanol. Geotherm. Res., 69(95), 35–58.

Dix, C. H. (1955), Seismic velocities from surface measurements, Geophysics, 20(1), 68–86.

Dixon, J. E., D. A. Clague, P. Wallace, and R. Poreda (1997), Volatiles in Alkalic Basalts from the North Arch Volcanic Field, Hawaii: Extensive Degassing of Deep Submarine-erupted Alkalic Series Lavas, J. Petrol., 38(7), 911–939.

Dominguez, S., S. E. Lallemand, J. Malavieille, and R. von Huene (1998), Upper plate deformation associated with seamount subduction, Tectonophysics, 293(3-4), 207–224.

Dominguez, S., J. Malavieille, and S. E. Lallemand (2000), Deformation of accretionary wedges in response to seamount subduction- Insights from sandbox experiments the features, Tectonics, 19(1), 182–196.

Downey, N. J., J. M. Stock, R. W. Clayton, and S. C. Cande (2007), History of the Cretaceous Osbourn spreading center, J. Geophys. Res., 112(B4), B04102.

Duncan, R. A., and R. A. Keller (2004), Radiometric ages for basement rocks from the Emperor Seamounts, ODP Leg 197, Geochem., Geophys., Geosyst., 5(8), 1–13.

Dupont, J., and R. H. Herzer (1985), Effect of Subduction of the Louisville Ridge on the Structure and Morphology of the Tonga Arc, in Geology and Offshore Resources of Pacific Island Arcs-Tonga Region, Circum-Pacific Council for Energy and Mineral Resources Earth Science Series v. 2, vol. 2, edited by D. W. Scholl and T. L. Vallier, pp. 323–332, Circum-Pacific Council for Energy and Mineral Resources, Houston, Texas.

Ellam, R. M. (1992), Lithospheric thickness as a control on basalt geochemistry, Geology, 20, 153–156.

Engdahl, E. R., R. Van Der Hilst, and R. Buland (1998), Global Teleseismic Earthquake Relocation with Improved Travel Times and Procedures for Depth Determination, Bull. Seismol. Soc. Am., 88(3), 722–743.

England, P., R. Engdahl, and W. Thatcher (2004), Systematic variation in the depths of slabs beneath arc volcanoes, Geophysical Journal International, 156(2), 377-408.

Farnetani, C. G., M. A. Richards, and M. S. Ghiorso (1996), Petrological models of magma evolution and deep crustal structure beneath hotspots and flood basalt provinces, Earth Planet. Sci. Lett., 143, 81–94.

Fisher, R. V, and H.-U. Schmincke (1984), Submarine Volcaniclastic Rocks, in Pyroclastic Rocks, pp. 265–296, Springer Berlin Heidelberg, Berlin, Heidelberg.

Fleury, J. M., M. Pubellier, and M. de Urreiztieta (2009), Structural expression of forearc crust uplift due to subducting asperity, Lithos, 113(1-2), 318–330.

Fryer, P., and N. C. Smoot (1985), Processes of Seamount Subduction in the Mariana and Izu-Bonin Trenches, Mar. Geol., 64(1550), 77–90.

Funnell, M. J., C. Peirce, W. R. Stratford, M. Paulatto, A. B. Watts, and I. Grevemeyer (2014), Structure and deformation of the Kermadec forearc in response to subduction of the Pacific oceanic plate, Geophys. J. Int., 199(2), 1286–1302.

Funnell, M. J., C. Peirce, and A. H. Robinson (2017), Structural variability of the Tonga-Kermadec forearc characterized using robustly constrained geophysical data, Geophys. J. Int., 210, 1681–1702.

Gass, I. G., D. S. Chapman, H. N. Pollack, R. S. Thorpe, and C. Froidevaux (1978), Geological and Geophysical Parameters of Mid-Plate Volcanism [and Discussion], Philos. Trans. R. Soc. A Math. Phys. Eng. Sci., 288(1355), 581–597.

Gill, J., P. Torssander, H. Lapierre, R. Taylor, K. Kaiho, M. Koyama, J. Aitchison, S. Cisowski, K. Dadey, K. Fujioka, A. Klaus, M. Lovell, K. Marsaglia, P. Pezard, B. Taylor, and K. Tazaki, Explosive Deep Water Basalt in the Sumisu Backarc Rift, Science, 248, 1214–1217.

Got, J.-L., V. Monteiller, J. Monteux, R. Hassani, and P. Okubo (2008), Deformation and rupture of the oceanic crust may control growth of Hawaiian volcanoes., Nature, 451, 453–456.

Grevemeyer, I., and E. R. Flueh (2008), FS Sonne Fahrtbericht / Cruise Report SO195 TOTAL, TOnga Thrust earthquake Asperity at Louisville Ridge.

Grevemeyer, I., E. R. Flueh, C. Reichert, J. Bialas, D. Kla, and C. Kopp (2001), Crustal architecture and deep structure of the Ninetyeast Ridge hotspot trail from active-source ocean bottom seismology, Geophys. J. Int., 144, 414–431.

Haase, K. M. (1996), The relationship between the age of the lithosphere and the composition of oceanic magmas: Constraints on partial melting, mantle sources and the thermal structure of the plates, Earth Planet. Sci. Lett., 144(1-2), 75–92.

Habermann, R. E., W. R. McCann, and B. Perin (1986), Spatial seismicity variations along convergent plate boundaries, Geophys. J. R. Astr. Soc., 85, 43–68.

Hammer, P. T. C., L. M. Donnan, J. A. Hildebrand, and B. D. Comuelle (1994), Jasper Seamount structure: Seafloor seismic refraction tomography, J. Geophys. Res., 99(B4), 6731–6752.

Hawkins, J. W., P. F. Lonsdale, and R. Batiza (1987), Petrologic evolution of the Louisville seamount chain, in Seamounts, Islands, and Atolls, Geophys. Monogr. Ser., vol. 43, vol. 43, edited by B. H. Keating, P. Fryer, R. Batiza, and G. W. Boehlert, pp. 235–254, AGU, Washington, D.C.

Haxby, W. F., and J. K. Weissel (1986), Evidence for Small-Scale Mantle Convection From Seasat Altimeter Data, J. Geophys. Res., 91(B3), 3507–3520.

Hayes, D. E., and M. Ewing (1971), The Louisville Ridge - A Possible Extension of the Eltanin Fracture Zone, Antarct. Oceanol. I, 15, 223–228.

Hayes, G. P., D. J. Wald, and R. L. Johnson (2012), Slab1.0: A three-dimensional model of global subduction zone geometries, J. Geophys. Res., 117, B01302.

Head, J. W., and L. Wilson (2003), Deep submarine pyroclastic eruptions: theory and predicted landforms and deposits, J. Volcanol. Geotherm. Res., 121, 155–193.

Hearn, T. M., and J. F. Ni (1994), Pn Velocities Beneath Continental Collision Zones: the Turkish-Iranian Plateau, Geophys. J. Int., 117(2), 273–283.

Herzer, R. H., and N. F. Exon (1985), Structure and basin analysis of the southern Tonga forearc, in Geology and Offshore Resources of Pacific Island Arcs-Tonga Region, Circum-Pacific Council for Energy and Mineral Resources Earth Science Series v. 2. edited by D. W. Scholl and T. L. Vallier, pp. 323–332, Circum-Pacific Council for Energy and Mineral Resources, Houston, Texas.

Hillier, J. K., and A. B. Watts (2007), Global distribution of seamounts from ship-track bathymetry data, Geophys. Res. Lett., 34(13), L13304.

Hirose, K., and I. Kushiro (1993), Partial melting of dry peridotites at high pressures: Determination of compositions of melts segregated from peridotite using aggregates of diamond, Earth Planet. Sci. Lett., 114, 477–489.

Houtz, R., and J. Ewing (1976), Upper crustal structure as a function of plate age, J. Geophys. Res., 81(14), 2490–2498.

Humphreys, E. R., and Y. Niu (2009), On the composition of ocean island basalts (OIB): The effects of lithospheric thickness variation and mantle metasomatism, Lithos, 112(1-2), 118–136.

Hwang, G., and S. Kim (2016), Tectonophysics Flexure and gravity anomalies of the oceanic lithosphere beneath the Louisville seamount, Tectonophysics, 686, 19–26.

IOC, IHO and BODC, 2003, "Centenary Edition of the GEBCO Digital Atlas", published on CD-ROM on behalf of the Intergovernmental Oceanographic Commission and the International Hydrographic Organization as part of the General Bathymetric Chart of the Oceans; British Oceanographic Data Centre, Liverpool.

Ishizuka, O., K. Tani, M. K. Reagan, K. Kanayama, S. Umino, Y. Harigane, I. Sakamoto, Y. Miyajima, M. Yuasa, and D. J. Dunkley (2011), The timescales of subduction initiation and subsequent evolution of an oceanic island arc, Earth Planet. Sci. Lett., 306(3-4), 229–240.

Isozaki, Y., S. Maruyama, and F. Furuoka (1990), Accreted oceanic materials in Japan, Tectonophysics, 181(1-4), 179–205.

Ito, G., and J. J. Mahoney (2005), Flow and melting of a heterogeneous mantle: 1. Method and importance to the geochemistry of ocean island and mid-ocean ridge basalts, Earth Planet. Sci. Lett., 230(1-2), 29–46.

Ivandic, M., I. Grevemeyer, J. Bialas, and C. J. Petersen (2010), Serpentinization in the trench-outer rise region offshore of Nicaragua: Constraints from seismic refraction and wide-angle data, Geophys. J. Int., 180(3), 1253–1264.

Kanamori, H. (1977), The Energy Release in Great Earthquakes, J. Geophys. Res., 82(20), 2981–2987.

Kanamori, H., and D. L. Anderson (1975), Theoretical basis of some empirical relations in seismology, Bull. Seismol. Soc. Am., 65, 1073–1095.

Kaneda, K., S. Kodaira, A. Nishizawa, T. Morishita, and N. Takahashi (2010), Structural evolution of preexisting oceanic crust through intraplate igneous activities in the Marcus-Wake seamount chain, Geochem., Geophys., Geosyst., 11(10), Q10014.

Kelleher, J., and W. R. McCann (1976), Buoyant Zones, Great Earthquakes, and Unstable Boundaries of Subduction, J. Geophys. Res., 81(26), 4885–4896.

Kim, S.-S., and P. Wessel (2010), Flexure modelling at seamounts with dense cores, Geophys. J. Int., 182, 583–598.

Kobayashi, K., J.-P. Cadet, J. Aubouin, J. Boulègue, C. Deplus, J. Dubois, R. von Huene, L. Jolivet, T. Kanazawa, J. Kasahara, K. Koizumi, S. Lallemand, Y. Nakamura, G. Pautot, K. Suyehiro, S. Tani, H. Tokuyama, and T. Yamazaki (1987), Normal faulting of the Daiichi-Kashima Seamount in the Japan Trench revealed by the Kaiko I cruise, Leg 3, Earth Planet. Sci. Lett., 83, 257–266.

Kodaira, S., N. Takahasi, A. Nakanishi, S. Miura, and Y. Kaneda (2000), Subducted Seamount Imaged in the Rupture Zone of the 1946 Nankaido Earthquake, Science (80-.)., 289(5476), 104–106.

Kokelaar, P. (1986), Magma-water interactions in subaqueous and emergent basaltic volcanism, Bull. Volcanol., 48, 275–289.

Kopp, H. (2013), Invited review paper: The control of subduction zone structural complexity and geometry on margin segmentation and seismicity, Tectonophysics, 589, 1–16.

Kopp, H., C. Kopp, J. P. Morgan, E. R. Flueh, W. Weinrebe, and W. J. Morgan (2003), Fossil hot spot-ridge interaction in the Musicians Seamount Province: Geophysical investigations of hot spot volcanism at volcanic elongated ridges, J. Geol., 108(B3), 1–20.

Kopp, H., E. R. Flueh, C. Papenberg, and D. Klaeschen (2004), Seismic investigations of the O'Higgins Seamount Group and Juan Fernández Ridge: Aseismic ridge emplacement and lithosphere hydration, Tectonics, 23(2), 1-21.

Koppers, A. A. P., H. Staudigel, and J. R. Wijbrans (2000), Dating crystalline groundmass separates of altered Cretaceous seamount basalts by the 40Ar/39Ar incremental heating technique, Chem. Geol., 166(1), 139–158.

Koppers, A. A. P., H. Staudigel, M. S. Pringle, and J. R. Wijbrans (2003), Short-lived and discontinuous intraplate volcanism in the South Pacific: Hot spots or extensional volcanism?, Geochem., Geophys., Geosyst., 4(10).

Koppers, A. A. P., R. a. Duncan, and B. Steinberger (2004), Implications of a nonlinear 40 Ar/ 39 Ar age progression along the Louisville seamount trail for models of fixed and moving hot spots, Geochem., Geophys., Geosyst., 5(6), Q06L02.

Koppers, A. A. P., H. Staudigel, J. P. Morgan, and R. A. Duncan (2007), Nonlinear 40 Ar/39Ar age systematics along the Gilbert Ridge and Tokelau Seamount Trail and the timing of the Hawaii-Emperor Bend, Geochem., Geophys., Geosyst., 8(6).

Koppers, A. A. P., M. D. Gowen, L. E. Colwell, J. S. Gee, P. F. Lonsdale, J. J. Mahoney, and R. a. Duncan (2011), New 40 Ar/ 39 Ar age progression for the Louisville hot spot trail and implications for inter-hot spot motion, Geochem., Geophys., Geosyst., 12(12), Q0AM02.

Koppers, A. A. P., T. Yamazaki, J. Geldmacher, and I. E. 330 S. Party (2013), IODP Expedition 330: Drilling the Louisville Seamount Trail in the SW Pacific, Sci. Drill., (15), 11–22.

Kukowski, N., and O. Oncken (2006), Subduction Erosion – the "Normal" Mode of Fore-Arc Material Transfer along the Chilean Margin?, in The Andes, pp. 217–236, Springer Berlin Heidelberg.

Kuo, B.-Y., and D. W. Forsyth (1988), Gravity anomalies of the ridge-transform system in the South Atlantic between 31 and 34.5°S: Upwelling centers and variations in crustal thickness, Mar. Geophys. Res., 10, 205–232.

Lallemand, E., J. Malavieille, and S. Calassou (1992), Effects of Oceanic Ridge Subduction on Accretionary Wedges: Experimental Modeling and Marine Obervations, Tectonics, 11(6), 1301–1313.

Lallemand, S., and X. Le Pichon (1987), Coulomb wedge model applied to the subduction of seamounts in the Japan Trench, Geology, 15, 1065–1069.

Leahy, G. M., and J. Park (2005), Hunting for oceanic island Moho, Geophys. J. Int., 160, 1020–1026.

Leahy, G. M., J. A. Collins, C. J. Wolfe, G. Laske, and S. C. Solomon (2010), Underplating of the Hawaiian Swell: evidence from teleseismic receiver functions, Geophys. J. Int., 183, 313–329.

Lonsdale, P. (1986), A Multibeam Reconnaissance of the Tonga Trench Axis and its Intersection with the Louisville Guyot Chain, Mar. Geophys. Res., 8, 295–327.

Lonsdale, P. (1988), Geography and history of the Louisville Hotspot Chain in the southwest Pacific, J. Geophys. Res., 93(B4), 3078–3104.

Ludwig, J. W., J. E. Nafe, and C. L. Drake (1970), Seismic refraction. In Maxwell, A. E. (ed.), The Sea, 53-84. Wiley-Interscience

Luyendyk, B. P. (1995), Hypothesis for Cretaceous rifting of east Gondwana caused by subducted slab capture, Geology, 23(4), 373–376.

Lynch, M. A. (1999), Linear ridge groups: Evidence for tensional cracking, J. Geophys. Res., 104(B12), 29321–29333.

Macleod, C. J. (1994), 20. Structure of the outer Tonga forearc at site 841, Proc. Ocean Drill. Program, Sci. Results, 135, 313–329.

MacPherson, G. J. (1983), The Snow Mountain Volcanic Complex: An On-Land Seamount in the Franciscan Terrain, California, J. Geol., 91(1), 73–92.

McBirney, A. R. (1973), Factors governing the intensity of explosive andesitic eruptions, Bull. Volcanol., 37(3), 443–453.

McCann, W. R., and R. E. Habermann (1989), Morphologic and Geologic Effects of the Subduction of Bathymetric Highs, Pure Appl Geophys., 129, 41–69.

McClain, J. S., and C. A. Atallah (1986), Thickening of the oceanic crust with age, Geology, 14, 574–576.

McGeary, S., A. Nur, and Z. Ben-Avraham (1985), Spatial gaps in arc volcanism: The effect of collision or subduction of oceanic plateaus, Tectonophysics, 119(1-4), 195–221.

McNutt, M. K., D. W. Caress, J. Reynolds, K. A. Jordahl, and R. A. Duncan (1997), Failure of plume theory to explain midplate volcanism in the southern Austral islands, Nature, 389, 479–482.

Meffre, S., T. J. Falloon, T. J. Crawford, R. A. Duncan, S. H. Bloomer, and D. J. Wright (2012), Basalts erupted along the Tongan fore arc during subduction initiation: Evidence from geochronology of dredged rocks from the Tonga fore arc and trench, Geochem., Geophys., Geosyst., 13(12), 1–17.

Menand, T. (2011), Physical controls and depth of emplacement of igneous bodies: A review, Tectonophysics, 500(1-4), 11–19.

Minshull, T.A., M. C. Sinha, and C. Peirce, C. (2005), Multi-disciplinary, sub-seabed geophysical imaging—a new pool of 28 seafloor instruments in use by the United Kingdom Ocean Bottom Instrument Consortium, Sea Technol., 46, 27–31.

Mitchell, N. C. (2001), Transition from circular to stellate forms of submarine volcanoes, J. Geophys. Res., 106(B2), 1987–2003.

Mogi, A., and K. Nishizawa (1980), Breakdown of a Seamount on the Slope of the Japan Trench, Proc. Jpn. Acad., 56B(5), 257–259.

Morgan, W. J. (1971), Convection Plumes in the Lower Mantle, Nature, 230, 42–43.

Mortimer, N., K. Hoernle, F. Hauff, J. M. Palin, W. J. Dunlap, R. Werner, and K. Faure (2006), New constraints on the age and evolution of the Wishbone Ridge, southwest Pacific Cretaceous microplates, and Zealandia-West Antarctica breakup, Geology, 34(3), 185–188.

Moscoso, E., and I. Grevemeyer (2015), Bending-related faulting of the incoming oceanic plate and its effect on lithospheric hydration and seismicity: A passive and active seismological study offshore Maule, Chile, J. Geodyn., 90, 58–70.

Müller, R. D., M. Sdrolias, C. Gaina, and W. R. Roest (2008), Age, spreading rates, and spreading asymmetry of the world's ocean crust, Geochem., Geophys., Geosyst., 9(4), 1–19.

Nafe, J. E., and C. L. Drake (1957), Variation With Depth in Shallow and Deep Water Marine Sediments of Porosity, Density and the Velocities of Compresional and Shear Waves, Geophysics, XXII(3), 523–552.

Nichols, A. R. L., C. Beier, P. A. Brandl, D. M. Buchs, and S. H. Krumm (2014), Geochemisty of volcanic glasses from the Louisville Seamount Trail (IODP Expedition 330): Implications for eruption environments and mantle melting, Geochem., Geophys., Geosyst., 15, 1718–1738.

Oakley, A. J., B. Taylor, P. Fryer, G. F. Moore, A. M. Goodliffe, and J. K. Morgan (2007), Emplacement, growth, and gravitational deformation of serpentinite seamounts on the Mariana forearc, Geophys. J. Int., 170(2), 615–634.

Oakley, A. J., B. Taylor, and G. F. Moore (2008), Pacific Plate subduction beneath the central Mariana and Izu-Bonin fore arcs: New insights from an old margin, Geochem., Geophys., Geosyst., 9(6), 1-28.

Orellana-Rovirosa, F., and M. Richards (2017), Rough vs. Smooth Topography along Oceanic Hotspot Tracks: Observations and Scaling Analysis, Geophys. Res. Lett., 44, 4074–4081.

Pacheco, J. F., and L. R. Sykes (1992), Seismic Moment Catalog of Large Shallow Earthquakes, 1900 to 1989, Bull. Seismol. Soc. Am., 82(3), 1306–1349.

Parsons, T., N. H. Sleep, and G. A. Thompson (1992), Host rock rheology controls on the emplacement of tabular intrusions: Implications for underplating of extending crust, Tectonics, 11(6), 1348–1356.

Peckover, R. S., D. J. Buchanan, and D. E. T. F. Ashby (1973), Fuel-Coolant Interactions in Submarine Vulcanism, Nature, 245(5424), 307–308.

Peirce, C., and A. B. Watts (2011), R/V Sonne SO215 Cruise Report.

Pellettier, B., and J. Dupont (1990), Effets de la subduction de la ride de Louisville sur l'arc de Tonga-Kermadec, Oceanol. Acta, 10, 57–76.

Phipps Morgan, J. (1999), Isotope topology of individual hotspot basalt arrays: Mixing curves or melt extraction trajectories?, Geochem., Geophys., Geosyst., 1(12), 1–15.

Planke, S., E. Alvestad, and O. Eldholm (1999), Seismic characteristics of basaltic extrusive and intrusive rocks, Leading Edge, 342-348

Pollack, H. N., I. G. Gass, R. S. Thorpe, and D. S. Chapman (1981), On the vulnerability of lithospheric plates to mid-plate volcanism: Reply to comments by P. R. Vogt, J. Geophys. Res., 86(B2), 961–966.

Pontoise, R., J. Aubouin, N. Raodry, P. Chotin, M. Diament, J. Dupont, J.-P. Kissen, R. Herzer, A. Lapouille, R. Louat, L. Ozouville, S. Soakai, and A. Stevenson (1986), La subduction de la ride de Louisville le long de la fosse des Tonga: premiers résultats de la campagne SEAPSO (Leg V), C. R. Acad. Sc. Paris, 303(10), 911–918.

Ranero, C. R., and R. von Huene (2000), Subduction erosion along the Middle America convergent margin, Nature, 404(6779), 748–752.

Ranero, C. R., and V. Sallarès (2004), Geophysical evidence for hydration of the crust and mantle of the Nazca plate during bending at the north Chile trench, Geology, 32(7), 549–552.

Ranero, C. R., J. P. Morgan, K. McIntosh, and C. Reichert (2003), Bending-related faulting and mantle serpentinization at the Middle America trench., Nature, 425(6956), 367–373.

Reagan, M. K., W. C. McClelland, G. Girard, K. R. Goff, D. W. Peate, Y. Ohara, and R. J. Stern (2013), The geology of the southern Mariana fore-arc crust: Implications for the scale of Eocene volcanism in the western Pacific, Earth Planet. Sci. Lett., 380, 41–51.

Regelous, M., K. D. Collerson, A. Ewart, and J. I. Wendt (1997), Trace element transport rates in subduction zones: evidence from Th, Sr and Pb isotope data for Tonga-Kermadec arc lavas, Earth Planet. Sci. Lett., 150, 291–302.

Regelous, M., J. A. Gamble, and S. P. Turner (2010), Mechanism and timing of Pb transport from subducted oceanic crust and sediment to the mantle source of arc lavas, Chem. Geol., 273(1-2), 46–54.

Richards, M., E. Contreras-Reyes, C. Lithgow-Bertelloni, M. Ghiorso, and L. Stixrude (2013), Petrological interpretation of deep crustal intrusive bodies beneath oceanic hotspot provinces, Geochem., Geophys., Geosyst., 14(3), 604–619.

Rosenbaum, G., and W. Mo (2011), Tectonic and magmatic responses to the subduction of high bathymetric relief, Gondwana Res., 19(3), 571–582.

Ruellan, E., J. Delteil, I. Wright, and T. Matsumoto (2003), From rifting to active spreading in the Lau Basin - Havre Trough backarc system (SW Pacific): Locking/unlocking induced by seamount chain subduction, Geochem., Geophys., Geosyst., 4(5), 1-21.

Ruff, L. J. (1989), Do Trench Sediments Affect Great Earthquake Occurrence in Subduction Zones?, PAGEOPH, 129(1/2), 263–282.

Ryan, P. (1987), Neutral buoyancy and the mechanical evolution of magmatic systems, Magmat. Processess Physiochemical Principles, The Geochemical Society Special Publication No. 1, 259-287

Sallarès, V., and C. R. Ranero (2005), Structure and tectonics of the erosional convergent margin off Antofagasta, north Chile (23°30′S), J. Geophys. Res., 110(6), 1–19.

Sandwell, D. T., E. L. Winterer, J. Mammerickx, R. A. Duncan, M. A. Lynch, D. A. Levitt, and C. L. Johnson (1995), Evidence for diffuse extension of the Pacific plate from Pukapuka ridges and cross-grain gravity lineations, J. Geophys. Res., 100(B8), 15087–15099.

Sandwell, D. T., R. D. Müller, W. H. F. Smith, E. Garcia, and R. Francis (2014), New global marine gravity model from CryoSat-2 and Jason-1 reveals buried tectonic structure, Science, 346(6205), 65–67.

Scales, J. A., P. Docherty, and A. Gersztenkorn (1990), Regularisation of nonlinear inverse problems: imaging the near-surface weathering layer, Inverse Probl., 6(1), 115.

Scholz, C. H., and C. Small (1997), The effect of seamount subduction on seismic coupling, Geology, 25(6), 487.

Schutt, D.L., and Lesher, C.E. (2006), Effects of melt depletion on the density and seismic velocity of garnet and spinel lherzolite, J. Geophys. Res., 111, B05401.

Singh, S. C., N. Hananto, M. Mukti, D. P. Robinson, S. Das, A. Chauhan, H. Carton, B. Gratacos, S. Midnet, Y. Djajadihardja, and H. Harjono (2011), Aseismic zone and earthquake segmentation associated with a deep subducted seamount in Sumatra, Nat. Geosci., 4(5), 308–311.

Sleep, N. H. (2002), Ridge-crossing mantle plumes and gaps in tracks, Geochem., Geophys., Geosyst., 3, 8505.

Small, C. (1995), Observations of ridge-hotspot interactions in the Southern Ocean, J. Geophys. Res., 100(B9), 17931.

Smith, D. K., and T. H. Jordan (1988), Seamount Statistics in the Pacific Ocean, J. Geophys. Res., 93, 2899–2918.

Smoot, N. C. (1989), The Marcus-Wake seamounts and guyots at paleo-fracture indicators and their relation to the Dutton Ridge, Mar. Geol., 88, 117–131.

Staudigel, H., and D. A. Clague (2010), The Geological History of Deep-Sea Volcanoes: Biosphere, Hydrosphere and Lithosphere Interactions, Oceanography, 23(1).

Staudigel, H., and H.-U. Schminke (1984), The Pliocene Seamount Series of La Palma / Canary Islands, J. Geophys. Res., 89(B13), 11195–11215.

Steinberger, B., R. Sutherland, and R. J. O'Connell (2004), Prediction of Emperor-Hawaii seamount locations from a revised model of global plate motion and mantle flow., Nature, 430, 167–173.

Stern, C. R. (2011), Subduction erosion: Rates, mechanisms, and its role in arc magmatism and the evolution of the continental crust and mantle, Gondwana Res., 20(2-3), 284–308.

Stolper, E. and Walker, D (1980), Melt Density and the Average Composition of Basalt, Contrib. Mineral. Petrol., 74, 7-12.

Stratford, W., C. Peirce, M. Paulatto, M. Funnell, A. B. Watts, I. Grevemeyer, and D. Bassett (2015), Seismic velocity structure and deformation due to the collision of the Louisville Ridge with the Tonga-Kermadec Trench, Geophys. J. Int., 200, 1503–1522.

Sutherland, R., and C. Hollis (2001), Cretaceous demise of the Moa plate and strike-slip motion at the Gondwana margin, Geology, 29(3), 279–282.

Talwani, M., J. L. Worzel, and M. Landisman (1959), Rapid Gravity Computations for Two-Dimensional Bodies with Application to the Mendocino Submarine Fracture Zone, J. Geophys. Res., 64(1), 49–59.

ten Brink, U. S., and T. M. Brocher (1987), Multichannel Seismic Evidence for a Subcrustal Intrusive Complex Under Oahu and a Model for Hawaiian Volcanism, J. Geophys. Res., 92(B13), 13687–13707.

ten Brink, U. (1991), Volcano spacing and plate rigidity, Geology, 19(4), 397–400.

Tetreault, J. L., and S. J. H. Buiter (2014), Future accreted terranes: a compilation of island arcs, oceanic plateaus, submarine ridges, seamounts, and continental fragments, Solid Earth, 5, 1243–1275.

Timm, C., D. Bassett, I. J. Graham, M. I. Leybourne, C. E. J. de Ronde, J. Woodhead, D. Layton-Matthews, and A. B. Watts (2013), Louisville seamount subduction and its implication on mantle flow beneath the central Tonga-Kermadec arc., Nat. Commun., 4, 1720.

Tréhu, A. M., R. J. Blakely, and M. C. Williams (2012), Subducted seamounts and recent earthquakes beneath the central Cascadia forearc, Geology, 40(2), 103–106.

Turner, S., and C. Hawkesworth (1997), Constraints on flux rates and mantle dynamics beneath island arcs from Tonga–Kermadec lava geochemistry, Nature, 389, 568–573.

Turner, S., C. Hawkesworth, N. Rogers, J. Bartleti, T. Worthington, J. Hergt, J. Pearce, and I. Smith (1997), 238U-230Th disequilibria, magma petrogenesis, and flux rates beneath the depleted Tonga-Kermadec island arc, Geochim. Cosmochim. Acta, 61(22), 4855–4884.

Vogt, P. R., and N. C. Smoot (1984), The Geisha Guyots: Multibeam Bathymetry and Morphometric Interpretation, J. Geophys. Res., 89(B13), 11085–11107.

Vogt, P. R., A. Lowrie, D. R. Bracey, and R. N. Hey (1976), Subduction of Aseismic Oceanic Ridges: Effects on Shape, Seismicity, and Other Characteristics of Consuming Plate Boundaries, Geol. Soc. Am. Spec. Pap., 172, 1–59.

von Huene, R., and C. R. Ranero (2003), Subduction erosion and basal friction along the sediment-starved convergent margin off Antofagasta, Chile, J. Geophys. Res., 108(B2), 1–17.

von Huene, R., and D. W. Scholl (1991), Observations at convergent margins concerning sediment subduction, subduction erosion, and the growth of continental crust, Rev. Geophys., 29(3), 279.

von Huene, R., T. Reston, N. Kukowski, G. A. Dehghani, and W. Weinrebe (1997), A subducting seamount beneath the Mediterranean Ridge, Tectonophysics, 271, 249–261.

von Huene, R., C. R. Ranero, W. Weinrebe, and K. Hinz (2000), Quaternary convergent margin tectonics of Costa Rica, segmentation of the Cocos Plate, and Central American volcanism, Tectonics, 19(2), 314–334.

Wang, J., M. Zhao, X. Qiu, J.-C. Sibuet, E. He, J. Zhang, and C. Tao (2016), 3D seismic structure of the Zhenbei-Huangyan seamounts chain in the East Sub-basin of the South China Sea and its mechanism of formation, Geol. J., 1-16.

Wang, K., and S. L. Bilek (2011), Do subducting seamounts generate or stop large earthquakes?, Geology, 39(9), 819–822.

Wang, K., and S. L. Bilek (2014), Invited review paper: Fault creep caused by subduction of rough seafloor relief, Tectonophysics, 610, 1–24.

Watanabe, T., T. Koyaguchi, and T. Seno (1999), Tectonic stress controls on ascent and emplacement of magmas, J. Volcanol. Geotherm. Res., 91, 65–78.

Watts, A. B. (1978), An Analysis of Isostasy in the World's Oceans 1. Hawaiian-Emperor Seamount Chain, J. Geophys. Res., 83(8), 5989.

Watts, A. B., and U. S. Brink (1989), Crustal structure, flexure, and subsidence history of the Hawaiian Islands, , 94(89).

Watts, A. B., and S. Zhong (2000), Observations of flexure and the rheology of oceanic lithosphere, Geophys. J. Int., 142, 855–875.

Watts, A. B., J. H. Bodine, and M. S. Steckler (1980), Observations of Flexure and the State of Stress in the Oceanic Lithosphere, J. Geophys. Res., 85(B11), 6369–6376.

Watts, A. B., U. S. ten Brink, P. Buhl, and T. M. Brocher (1985), A multichannel seismic study of lithospheric flexure across the Hawaiian-Emperor seamount chain, Nature, 315(6015), 105–111.

Watts, A. B., J. K. Weissel, R. A. Duncan, and R. L. Larson (1988), Origin of the Louisville Ridge and its relationship to the Eltanin Fracture Zone System, J. Geophys. Res., 93(B4), 3051.

Watts, A. B., D. Robinson, and A. A. P. Koppers (2010), Seamount Subduction and Earthquakes, Oceanography, 23(1), 166–173.

Weigel, W., and I. Grevemeyer (1999), The Great Meteor seamount: seismic structure of a submerged intraplate volcano, J. Geodyn., 28(1), 27–40.

Wessel, P. (2001), Global distribution of seamounts inferred from gridded Geosat/ERS-1 altimetry, J. Geophys. Res., 106(B9), 431–441.

Wessel, P., and L. W. Kroenke (2009), Observations of geometry and ages constrain relative motion of Hawaii and Louisville plumes, Earth Planet. Sci. Lett., 284(3-4), 467–472.

Wessel, P., and W. H. F. Smith (1991), Free software helps map and display data, EOS Trans AGU, 72(41), 441.

Wessel, P., A. B. Watts, and S. Kim (2014), Time-Dependent Flexural Deformation Beneath the Emperor Seamounts, Abstract MR23C-4362 presented at 2014 Fall Meeting, AGU, San Francisco, Calif., 15-19 Dec.

White, R. S., D. McKenzie, and K. O'Nions (1992), Oceanic Crustal Thickness from Seismic Measurements and Rare Earth Element Inversions, J. Geophys. Res., 97(B13), 19,683–19,715.

Wilkens, R. H., G. J. Fryer, and J. Karsten (1991), Evolution of Porosity and Seismic Structure of Upper Oceanic Crust: Importance of Aspect Ratios, J. Geophys. Res., 96(B11), 17981–17995.

Wilson, J. T. (1963), A Possible Origin of the Hawaiian Islands, Can. J. Phys., 41, 863–870.

Winterer, E. L., and D. T. Sandwell (1987), Evidence from en-echelon cross-grain ridges for tensional cracks in the Pacific Plate, Nature, 329(6139), 534–537.

Winterer, E. L., J. H. Natland, R. J. V. A. N. Waasbergen, and R. A. Duncan (1993), Cretaceous Guyots in the Northwest Pacific: an Overview of Their Geology and Geophysics, Mesozoic Pacific Geol. Tectonics Volcanism Geophys. Monogr. 77.

Worthington, T. J., R. Hekinian, P. Stoffers, T. Kuhn, and F. Hauff (2006), Osbourn Trough: Structure, geochemistry and implications of a mid-Cretaceous paleospreading ridge in the South Pacific, Earth Planet. Sci. Lett., 245, 685–701.

Wright, D. J., S. H. Bloomer, C. J. MacLeod, B. Taylor, and A. M. Goodlife (2000), Bathymetry of the Tonga Trench and Forearc: A map series, Mar. Geophys. Res., 21(5), 489–511.

Wysoczanski, R. J., E. Todd, I. C. Wright, M. I. Leybourne, J. M. Hergt, C. Adam, and K. Mackay (2010), Backarc rifting, constructional volcanism and nascent disorganised spreading in the southern Havre Trough backarc rifts (SW Pacific), J. Volcanol. Geotherm. Res., 190(1-2), 39–57.

Zelt, C. A. (1998), Lateral velocity resolution from three-dimensional seismic refraction data, Geophys. J. Int., 135(3), 1101–1112.

Zelt, C. A. (1999), Modelling strategies and model assessment for wide-angle seismic traveltime data, Geophys. J. Int., 139, 183–204.

Zelt, C. A., and P. J. Barton (1998), Three-dimensional seismic refraction tomography: A comparison of two methods applied to data from the Faeroe Basin, J. Geophys. Res. Solid Earth, 103(B4), 7187–7210.

Zelt, C. A., and R. B. Smith (1992), Seismic traveltime inversion for 2-D crustal velocity structure, Geophys. J. Int., 108(1), 16–34.

Zeumann, S., and A. Hampel (2016), Three-dimensional finite-element models on the deformation of forearcs caused by aseismic ridge subduction: The role of ridge shape, friction coefficient of the plate interface and mechanical properties of the forearc, Tectonophysics, 684, 76–91.

Appendix A - OBS Record Sections

This appendix contains plots of the OBS record sections for the instruments where these are not presented in Chapter 3. Plots of each OBS record section are presented in order of their location along the profile, beginning at the northwestern end on the uppermost Tonga forearc and progressing southeastwards.

Each figure is presented in the same manner as Figure 3.3, with part a) showing the OBS hydrophone record section after filtering using a minimum-phase Butterworth band-pass filter (2-3-20-30 Hz) and trace amplitude normalisation, and part b) showing the same with the picked arrivals overlaid using the same colours for each arrival phase as in Fig. 3.3, and modelled travel times in black. OBS record sections are plotted using a reducing velocity of 8 km s^{-1}. Part c) shows the rays which are traced through the model, with the colours for each arrival phase corresponding to those in b).

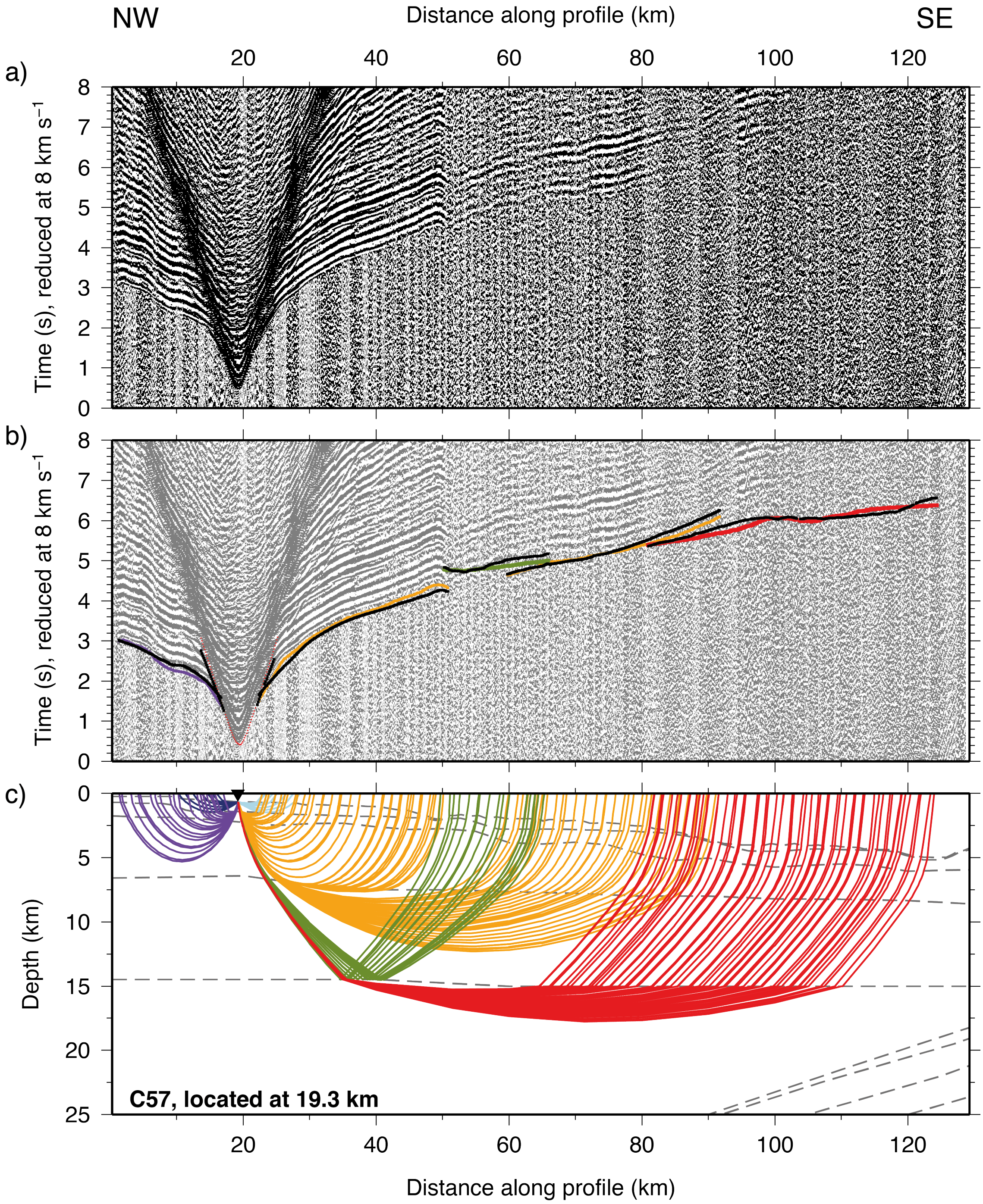

Figure A.1: *WA seismic data from OBS C57 hydrophone channel, located at 19.3 km d.a.p., on the Tonga upper forearc (see Fig. 3.8).*

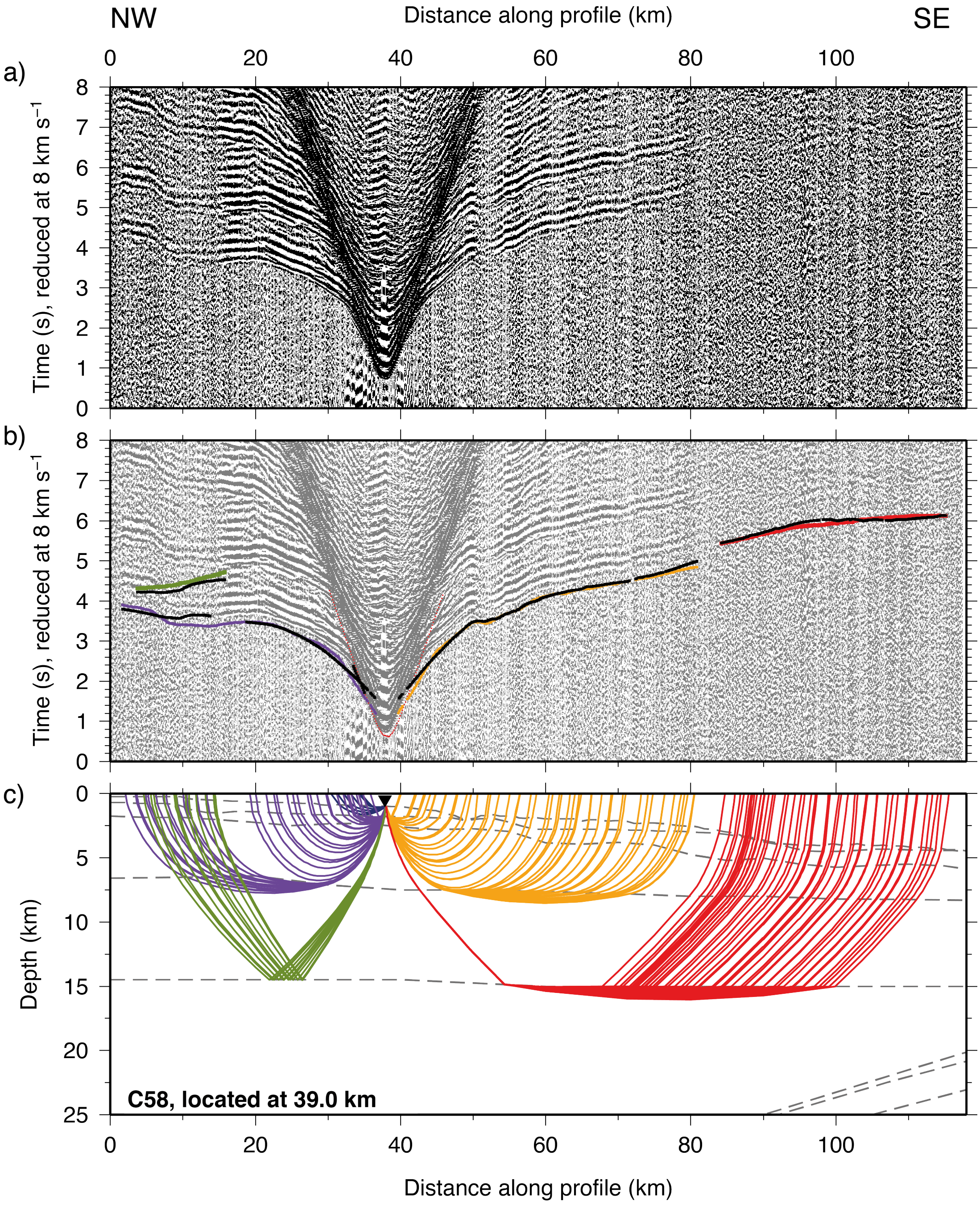

Figure A.2: *WA seismic data from OBS C58 hydrophone channel, located at 39.0 km d.a.p., on the Tonga upper forearc (see Fig. 3.8).*

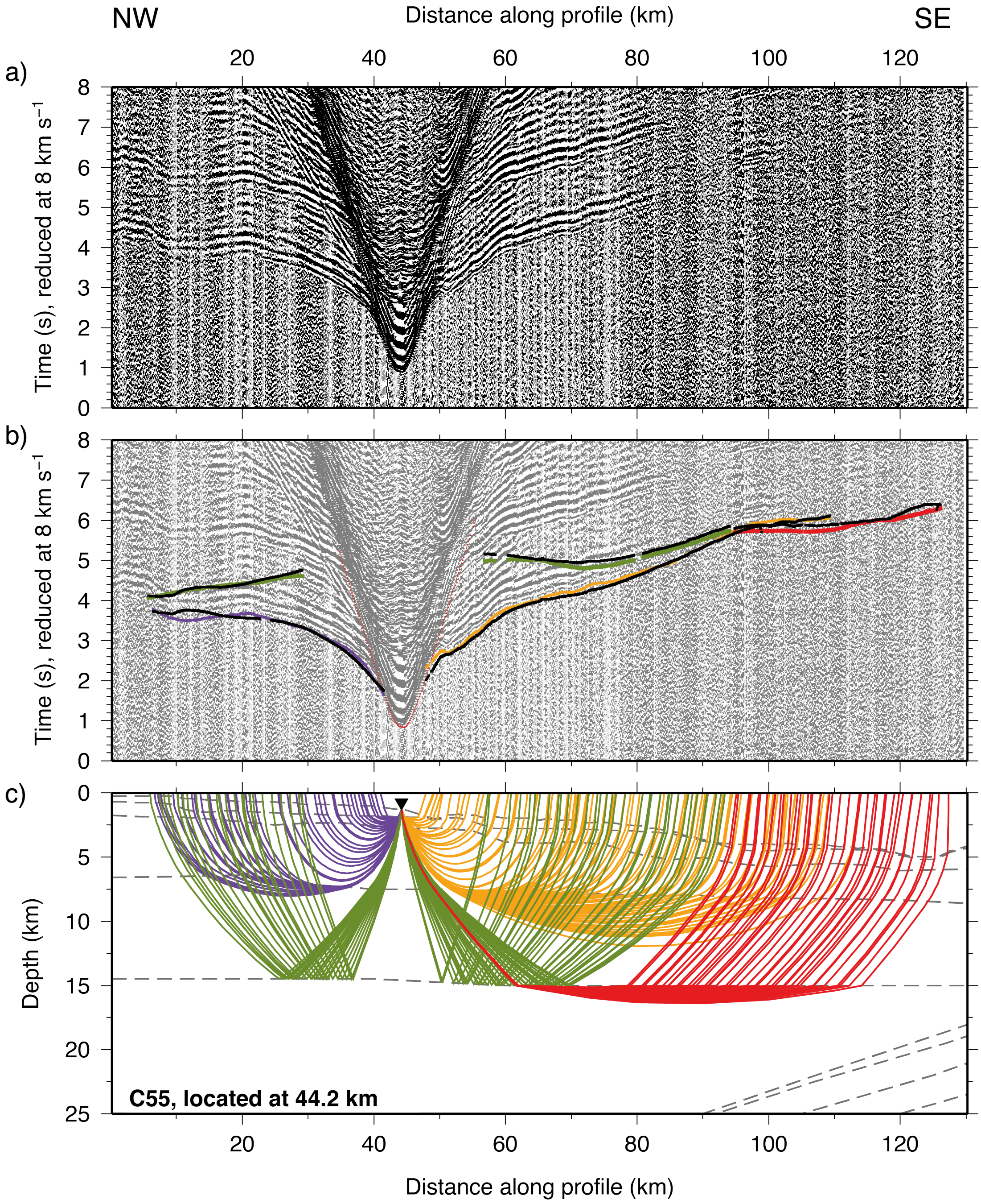

Figure A.3: *WA seismic data from OBS C55 hydrophone channel, located at 44.2 km d.a.p., on the Tonga upper forearc (see Fig. 3.8).*

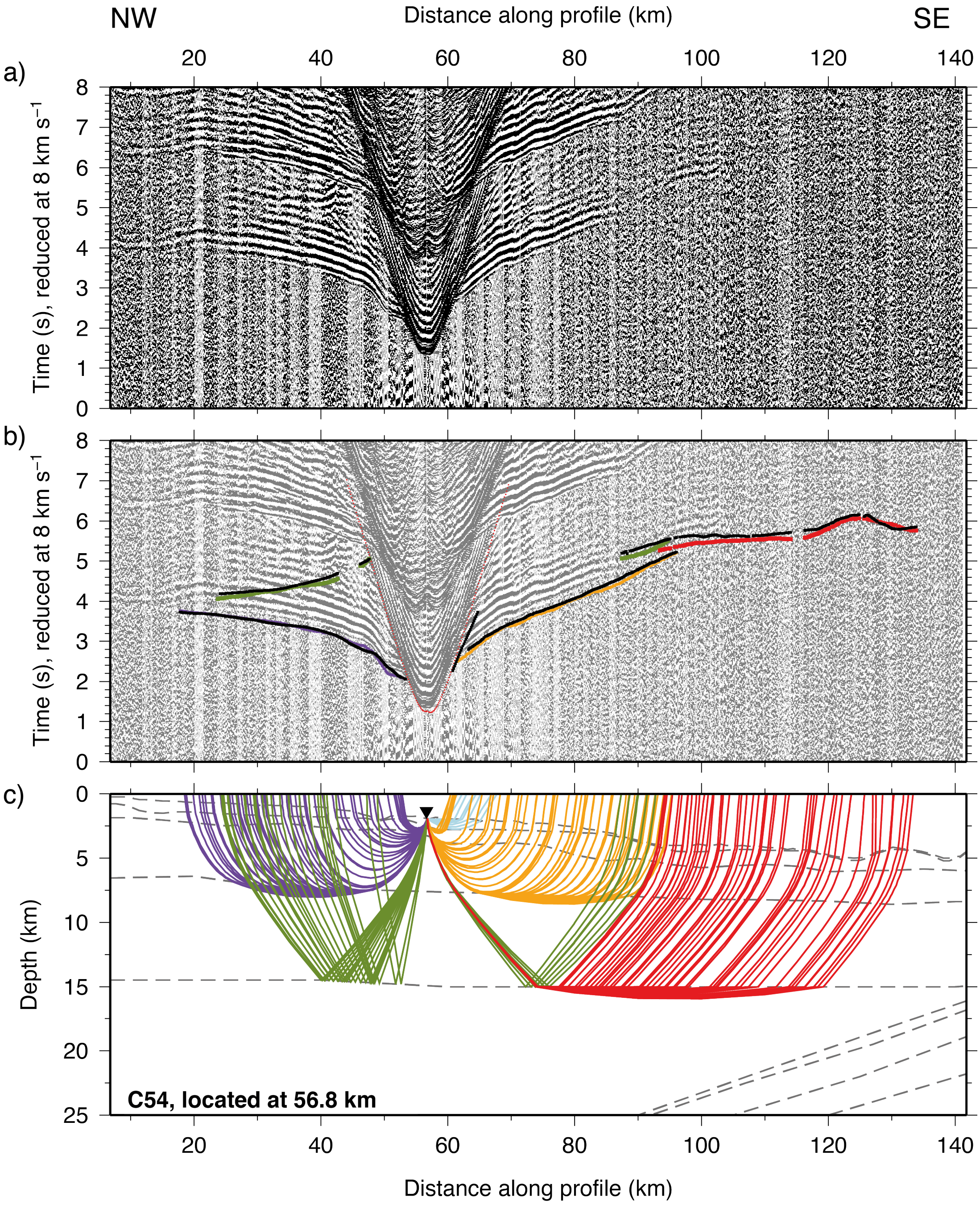

Figure A.4: *WA seismic data from OBS C54 hydrophone channel, located at 56.8 km d.a.p., on the Tonga upper forearc (see Fig. 3.8).*

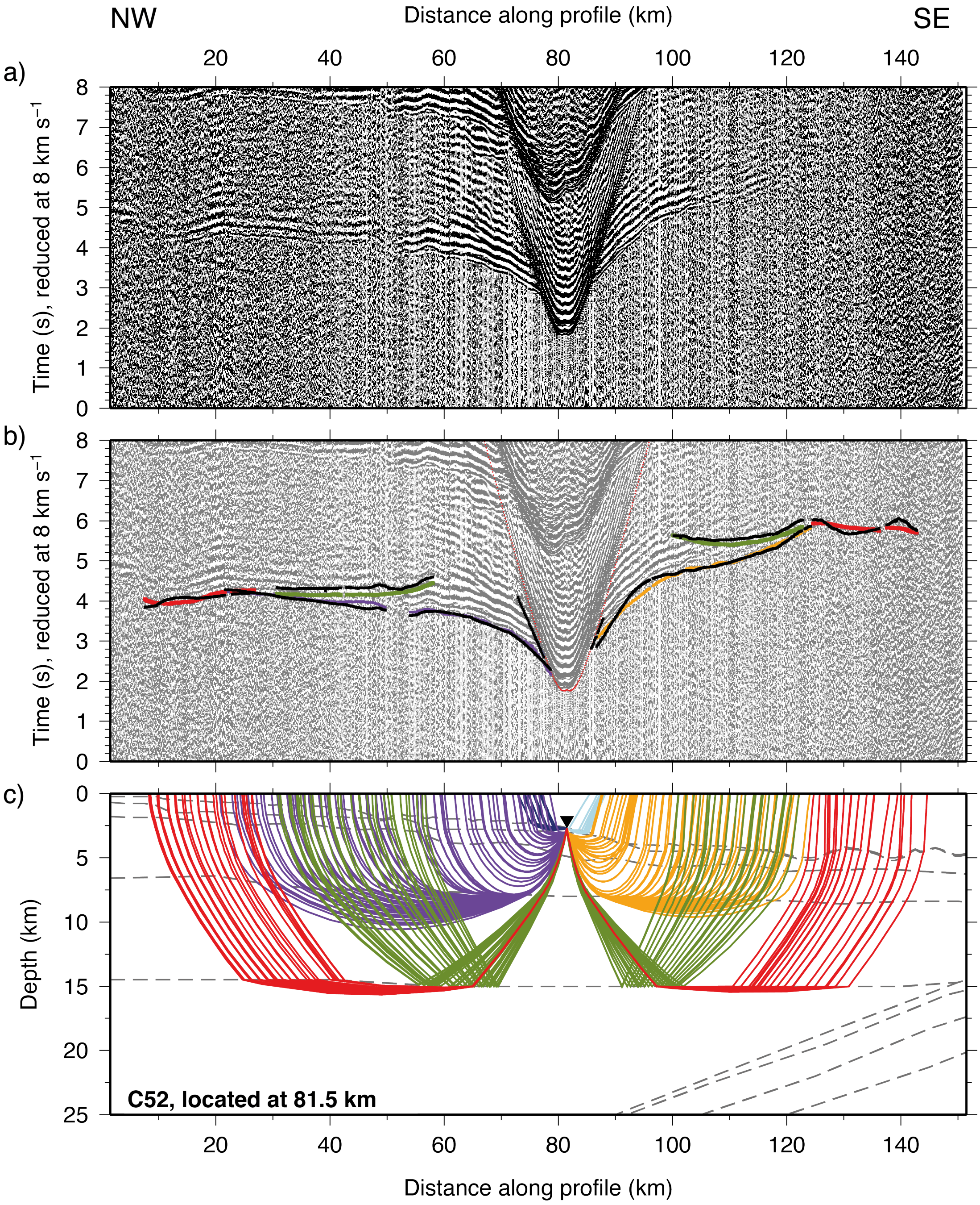

Figure A.5: *WA seismic data from OBS C52 hydrophone channel, located at 81.5 km d.a.p., on the Tonga upper forearc (see Fig. 3.8).*

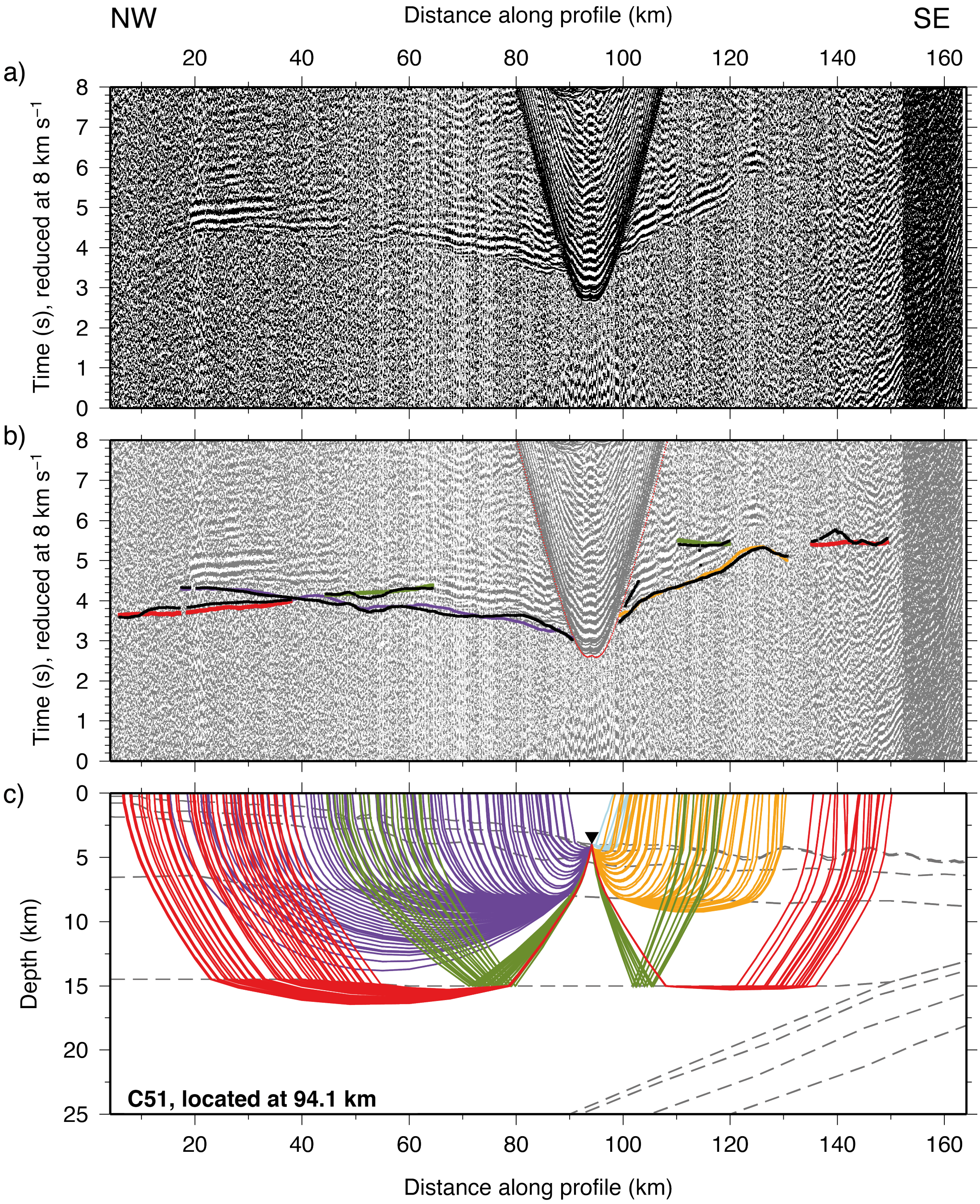

Figure A.6: *WA seismic data from OBS C51 hydrophone channel, located at 94.1 km d.a.p., on the Tonga upper forearc (see Fig. 3.8).*

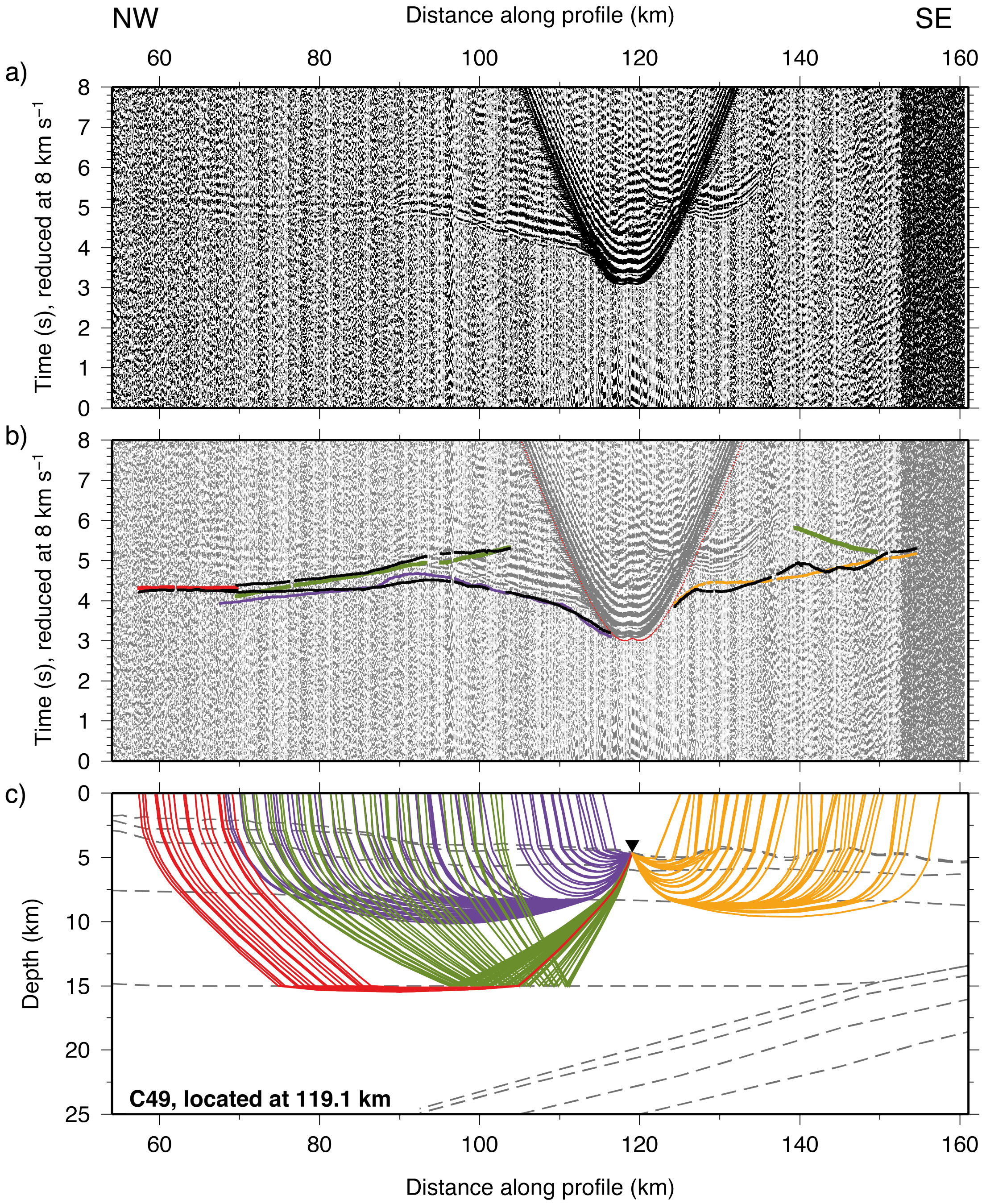

Figure A.7: *WA seismic data from OBS C49 hydrophone channel, located at 119.1 km d.a.p., on the Tonga middle forearc (see Fig. 3.11).*

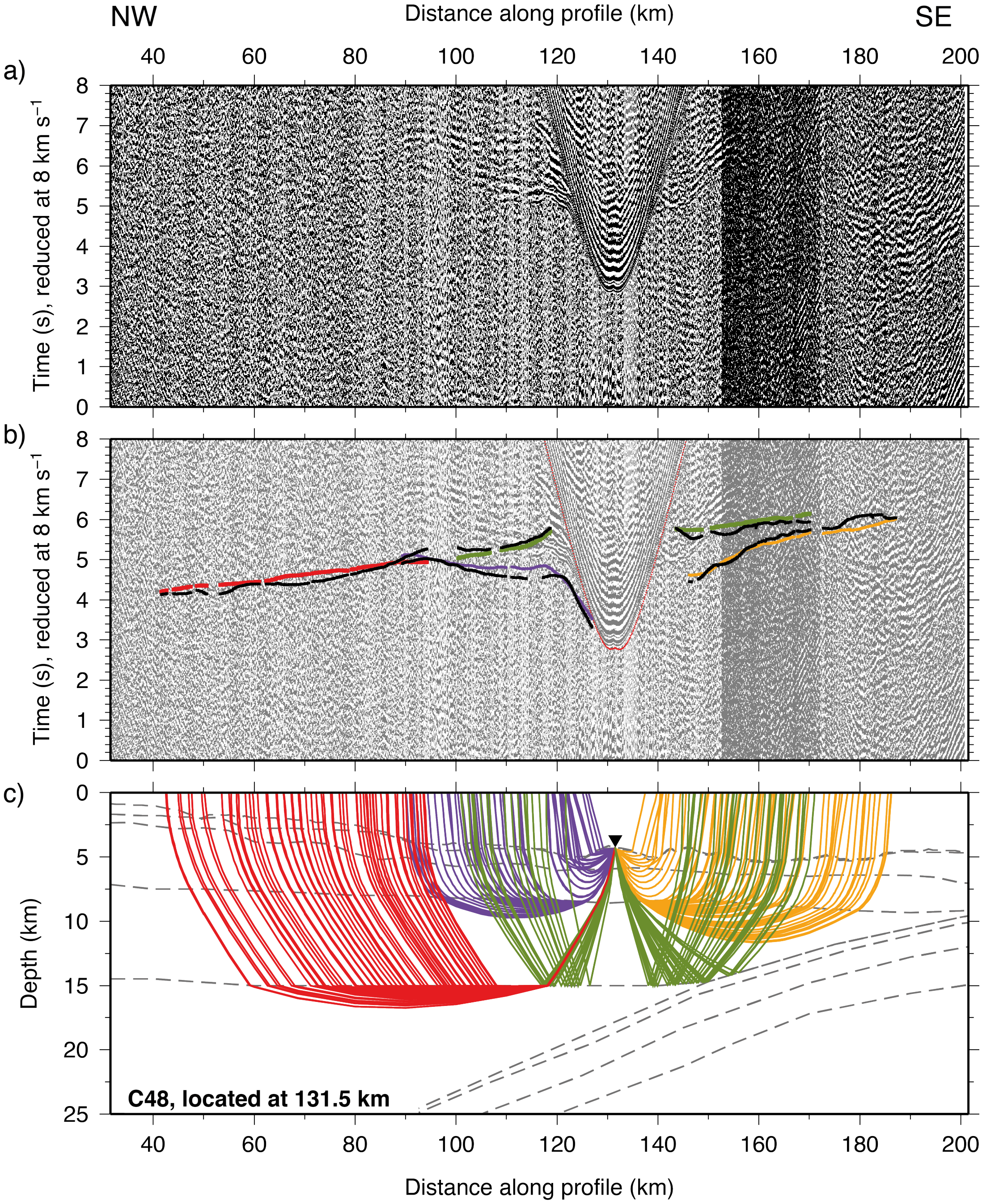

Figure A.8: *WA seismic data from OBS C48 hydrophone channel, located at 131.5 km d.a.p., on the Tonga middle forearc (see Fig. 3.11).*

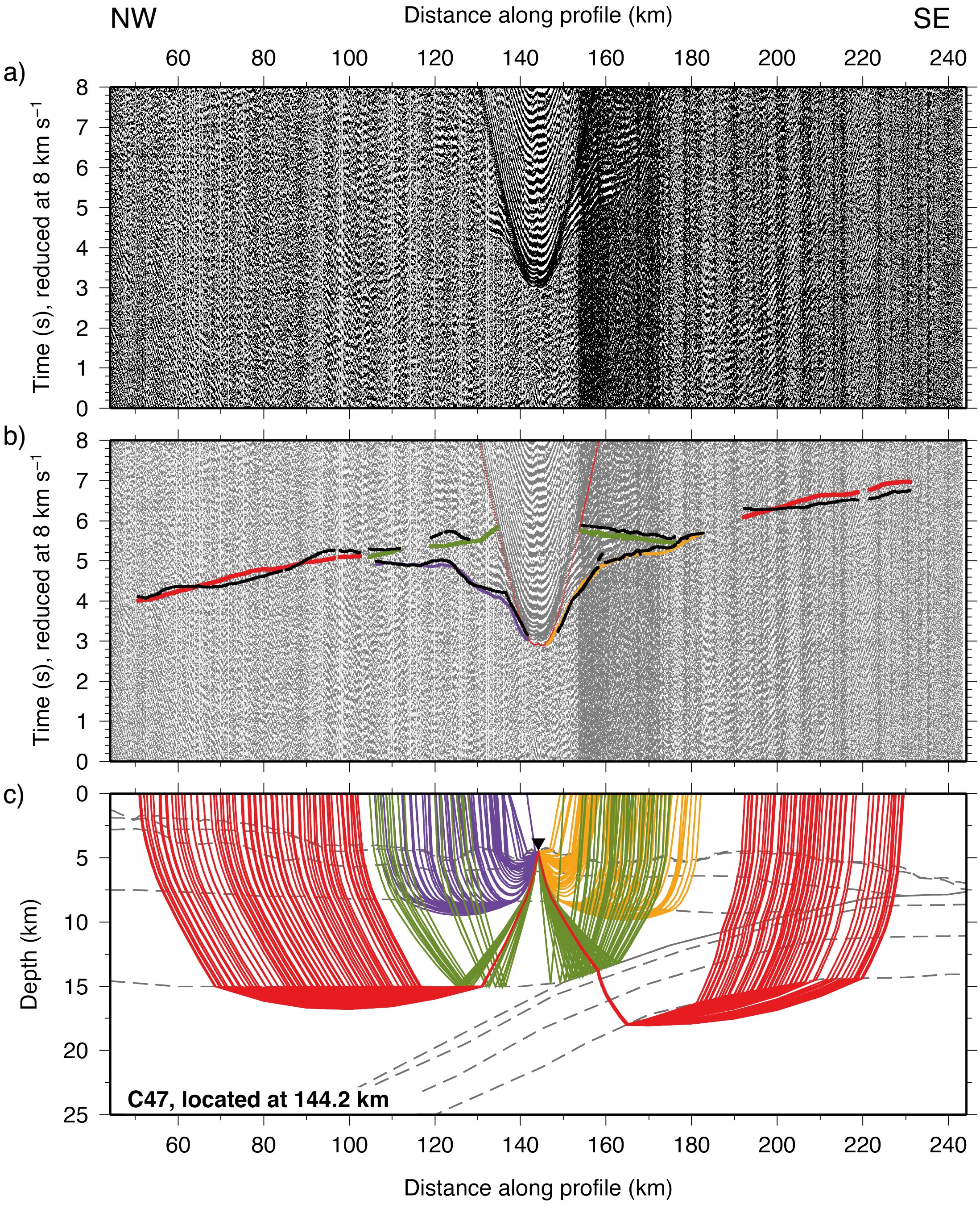

Figure A.9: *WA seismic data from OBS C47 hydrophone channel, located at 144.2 km d.a.p., on the Tonga middle forearc (see Fig. 3.11).*

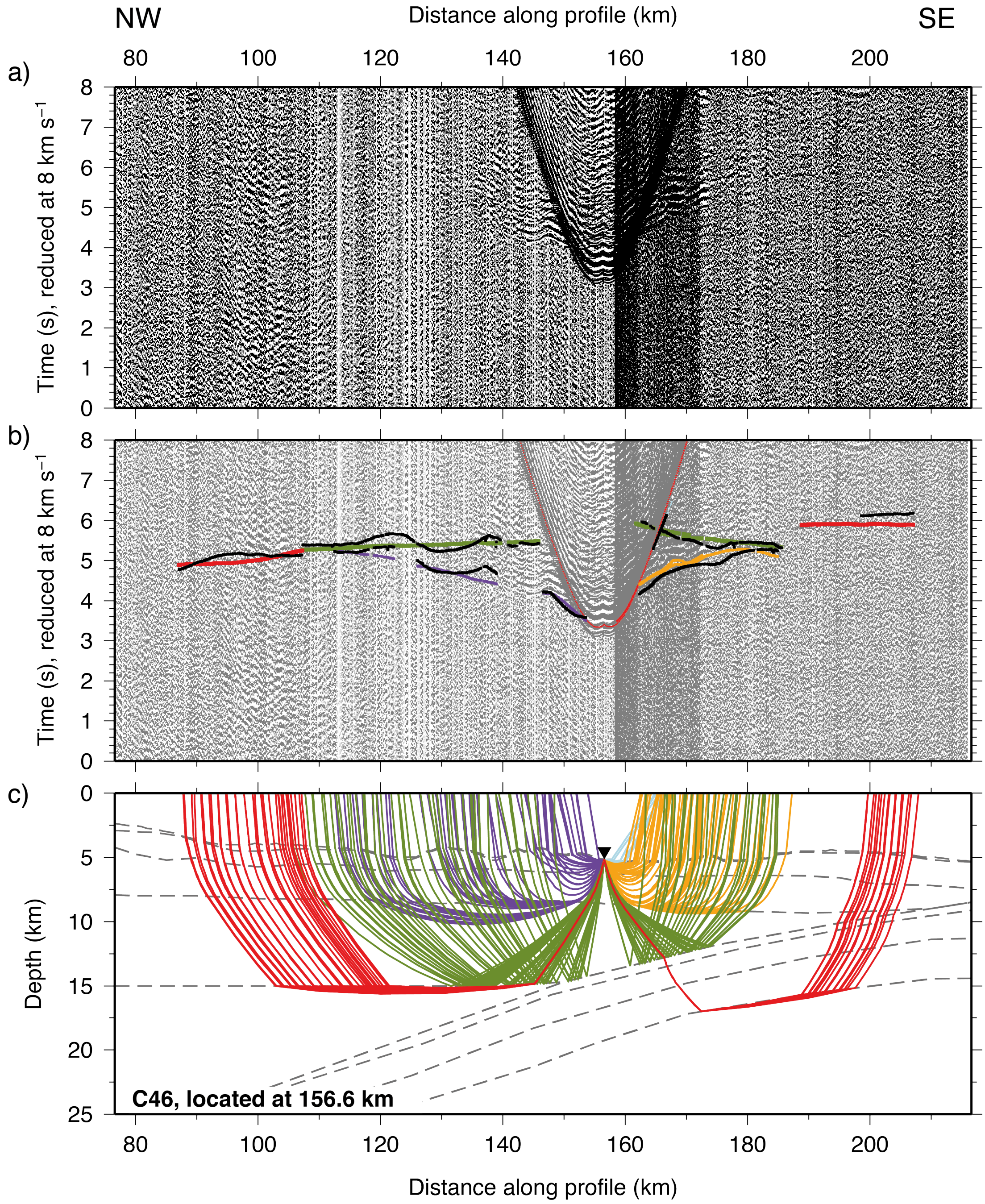

__Figure A.10:__ WA seismic data from OBS C46 hydrophone channel, located at 156.6 km d.a.p., on the Tonga middle forearc (see Fig. 3.11).

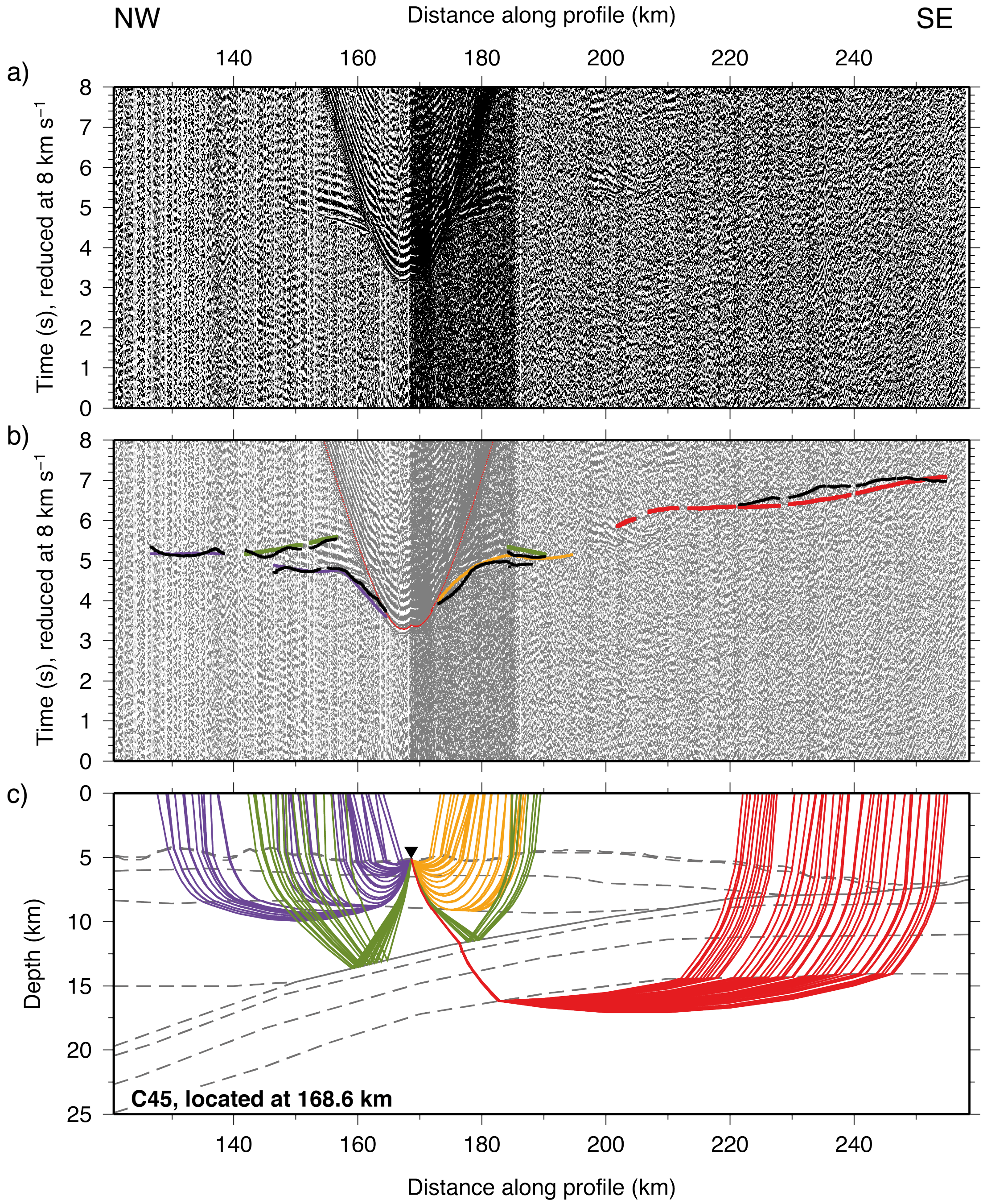

Figure A.11: *WA seismic data from OBS C45 hydrophone channel, located at 168.6 km d.a.p., on the Tonga middle forearc (see Fig. 3.11).*

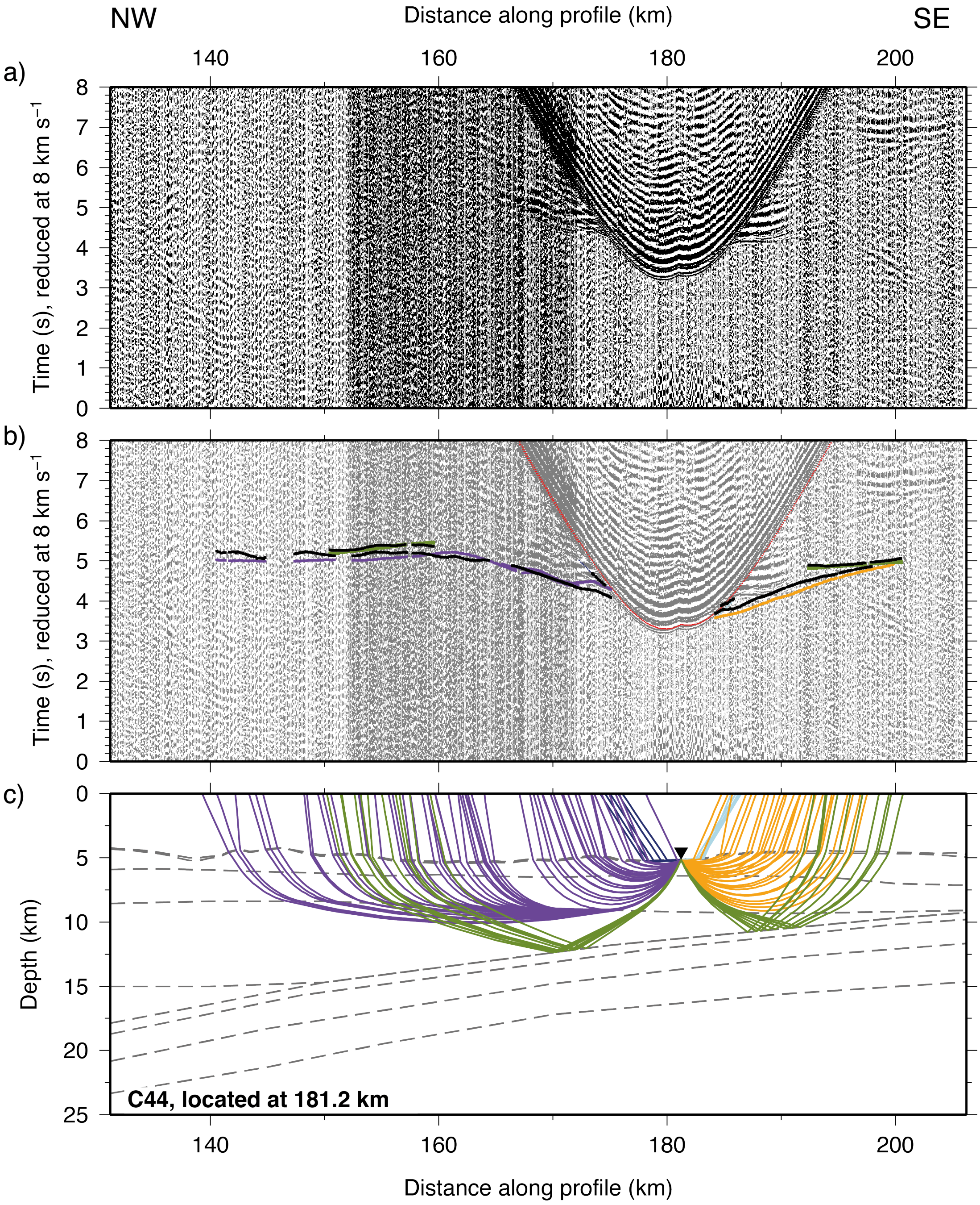

Figure A.12: *WA seismic data from OBS C44 hydrophone channel, located at 181.2 km d.a.p., on the Tonga middle forearc (see Fig. 3.11).*

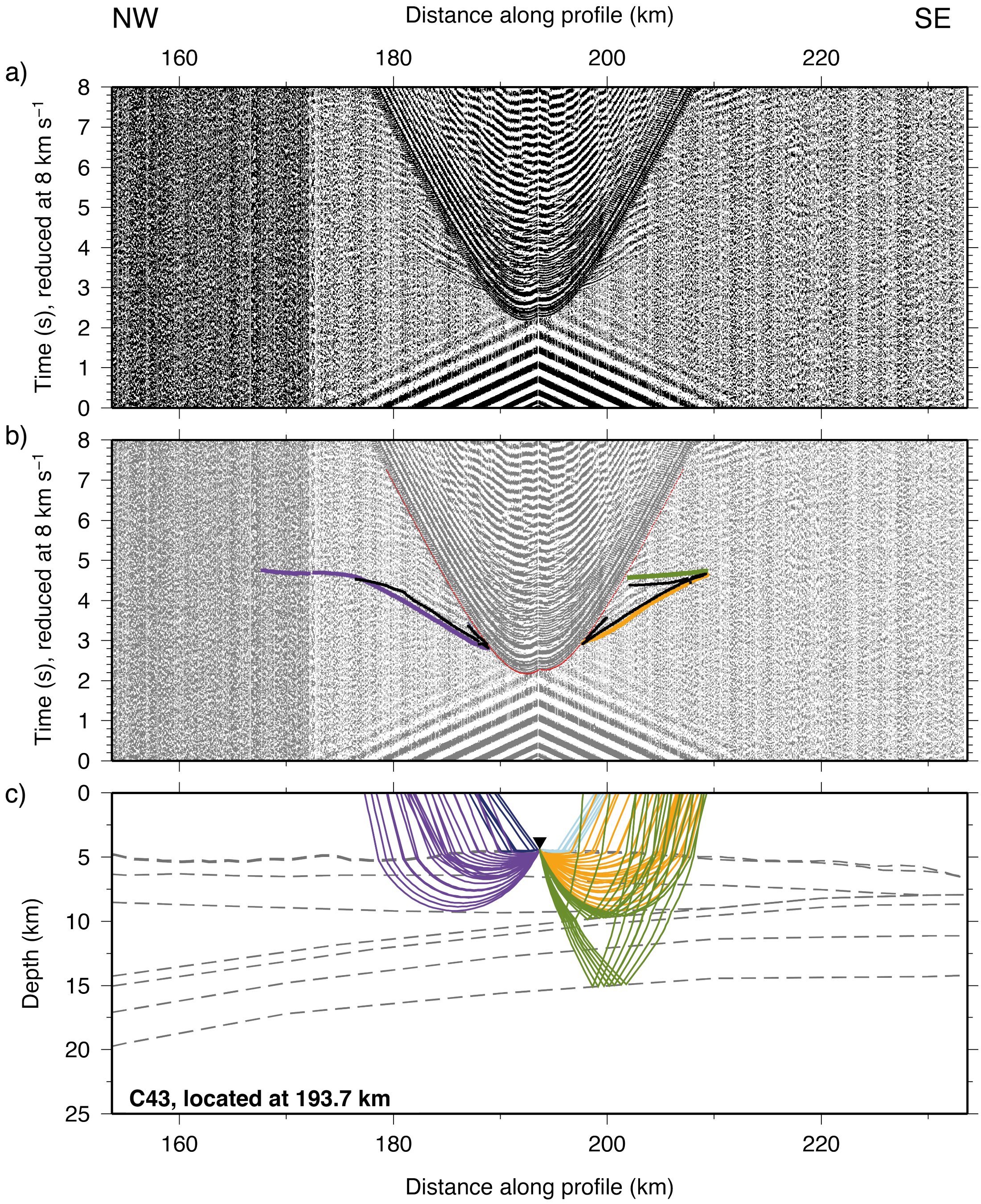

Figure A.13: *WA seismic data from OBS C43 hydrophone channel, located at 193.7 km d.a.p., on the Tonga lower forearc-trench region (see Fig. 3.13).*

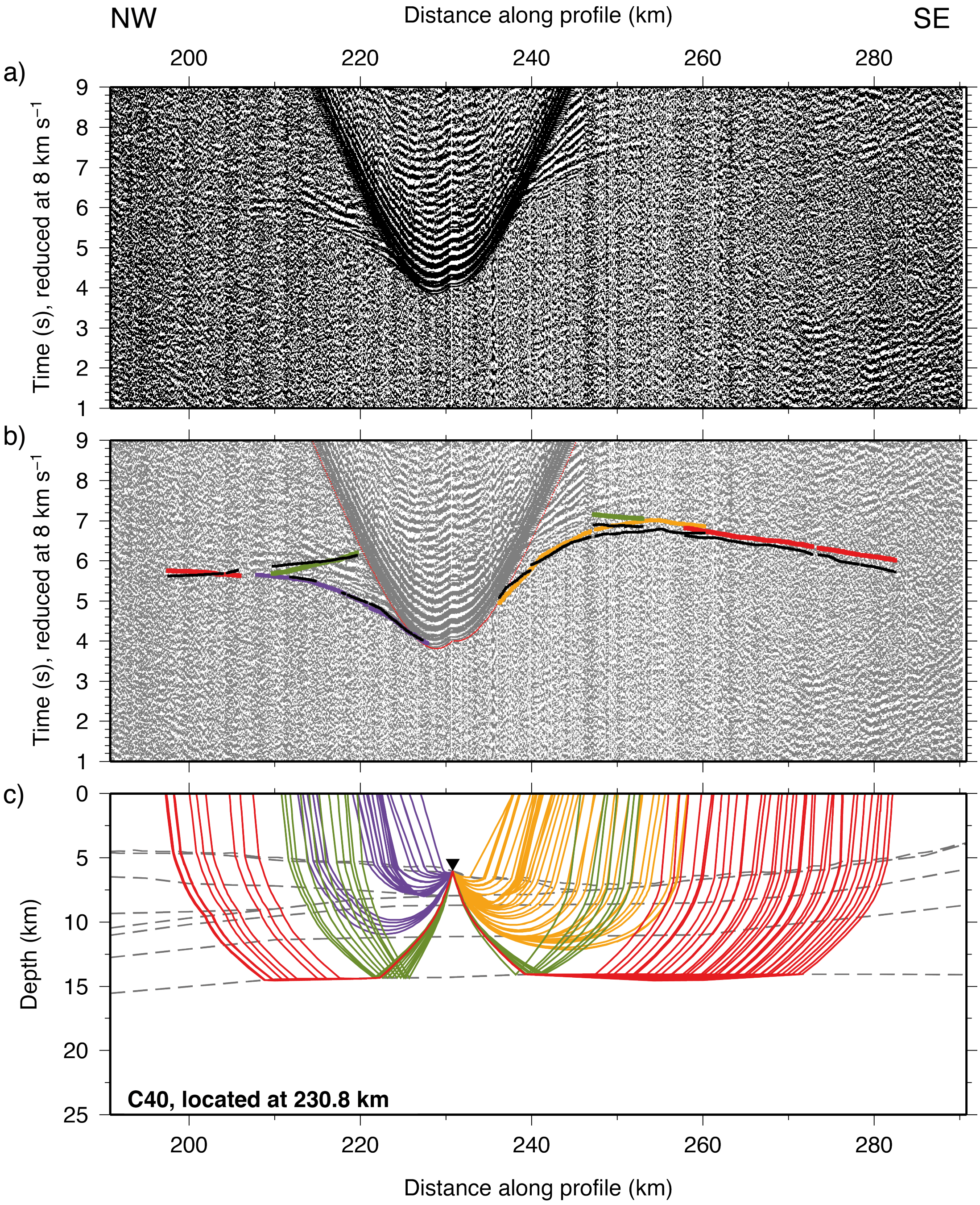

Figure A.14: *WA seismic data from OBS C40 hydrophone channel, located at 230.8 km d.a.p., on the Tonga lower forearc-trench region (see Fig. 3.13).*

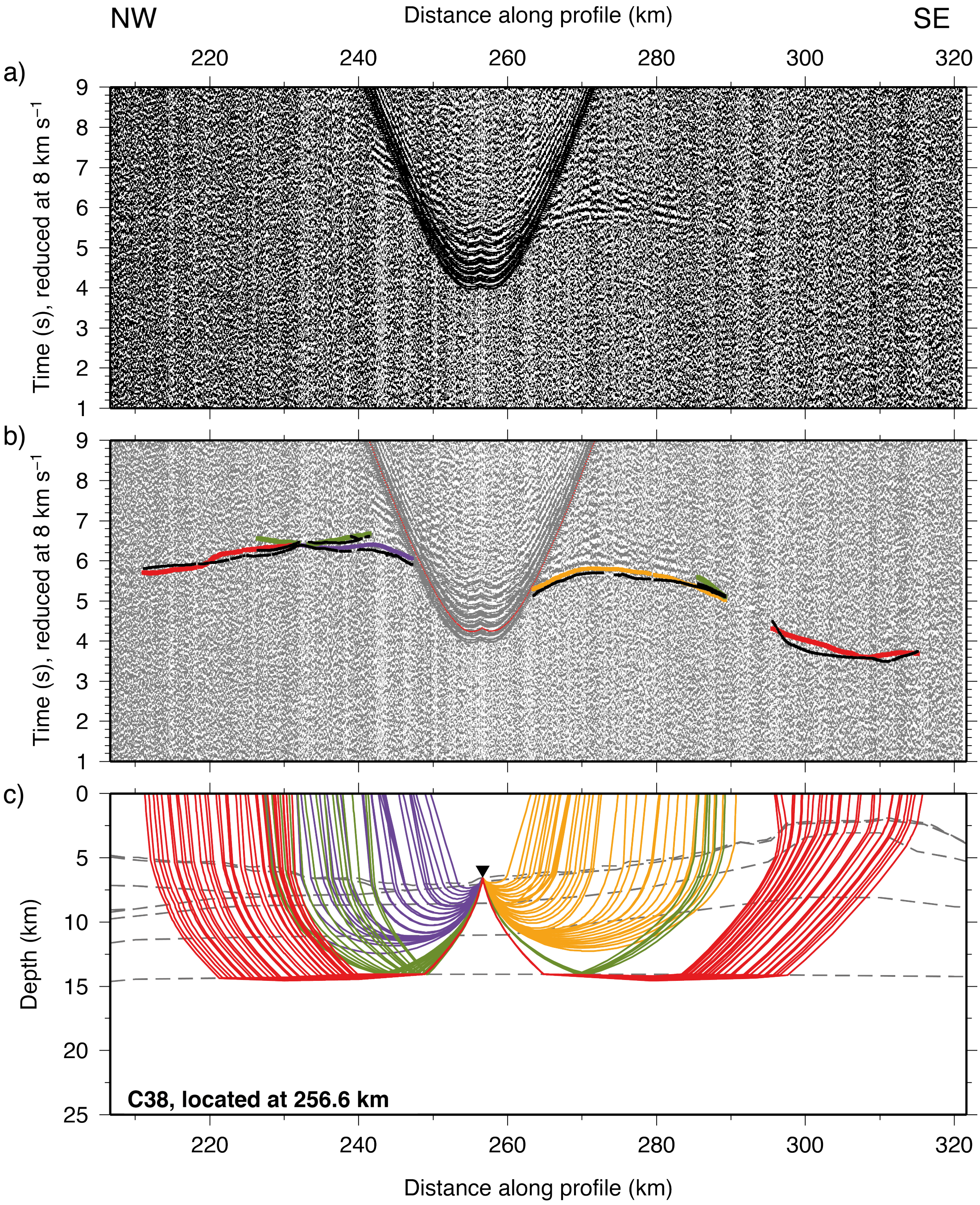

Figure A.15: *WA seismic data from OBS C38 hydrophone channel, located at 256.6 km d.a.p., on the trenchward flank of Osbourn seamount (see Fig. 3.13).*

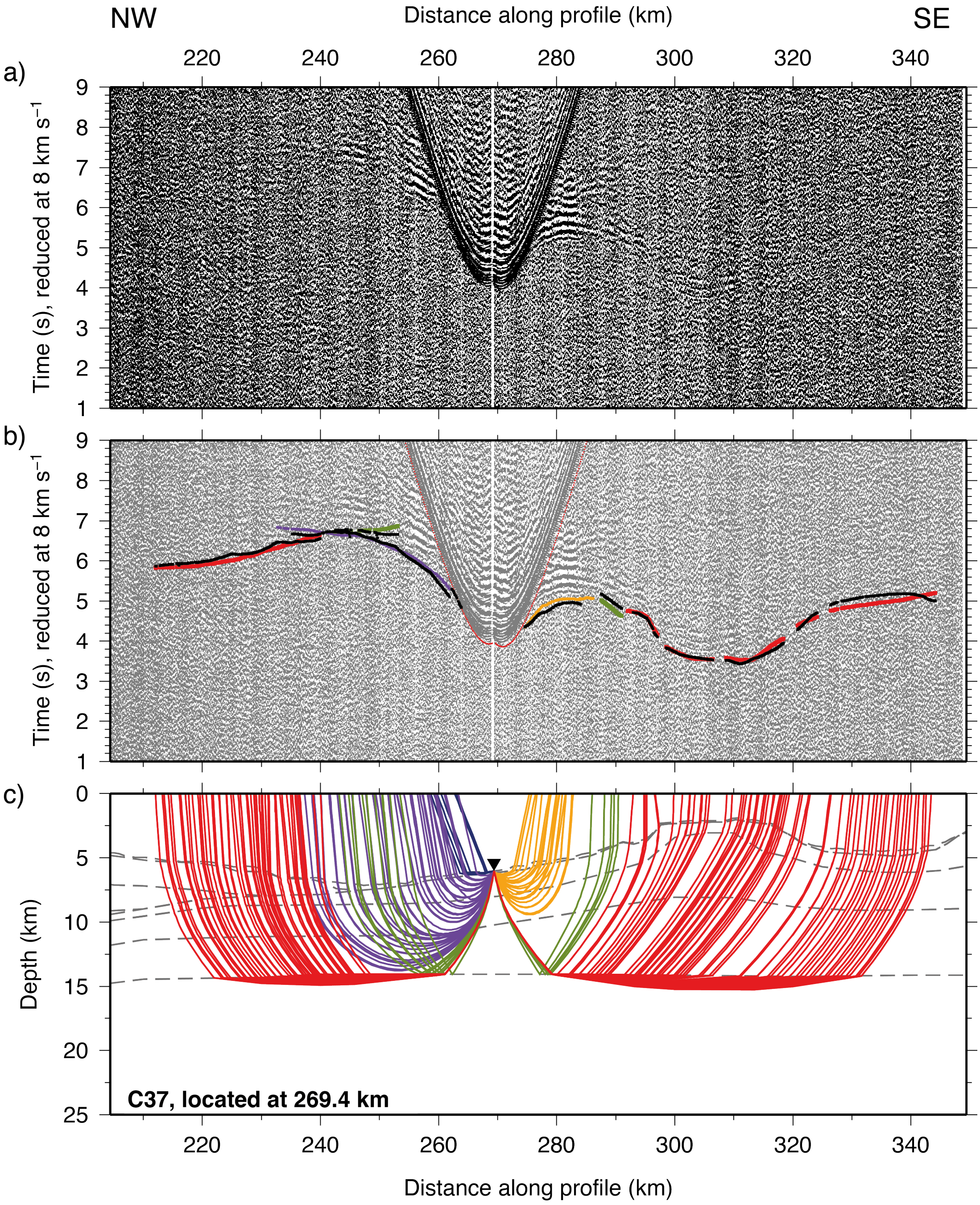

Figure A.16: *WA seismic data from OBS C37 hydrophone channel, located at 269.4 km d.a.p., on the trenchward flank of Osbourn seamount (see Fig. 3.13).*

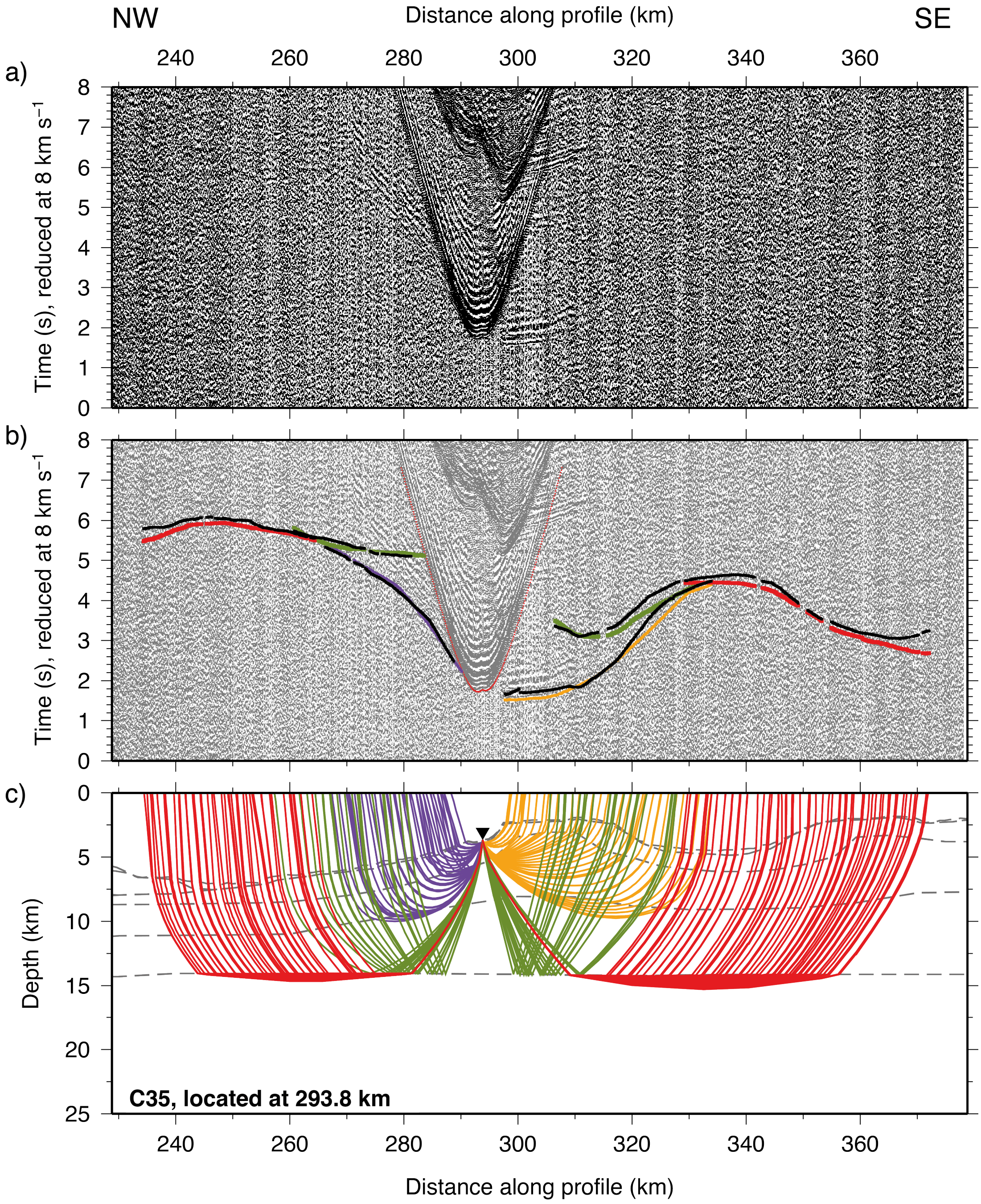

Figure A.17: *WA seismic data from OBS C35 hydrophone channel, located at 293.8 km d.a.p., on the northwestern/trenchward flank of Osbourn seamount (see Fig. 3.4).*

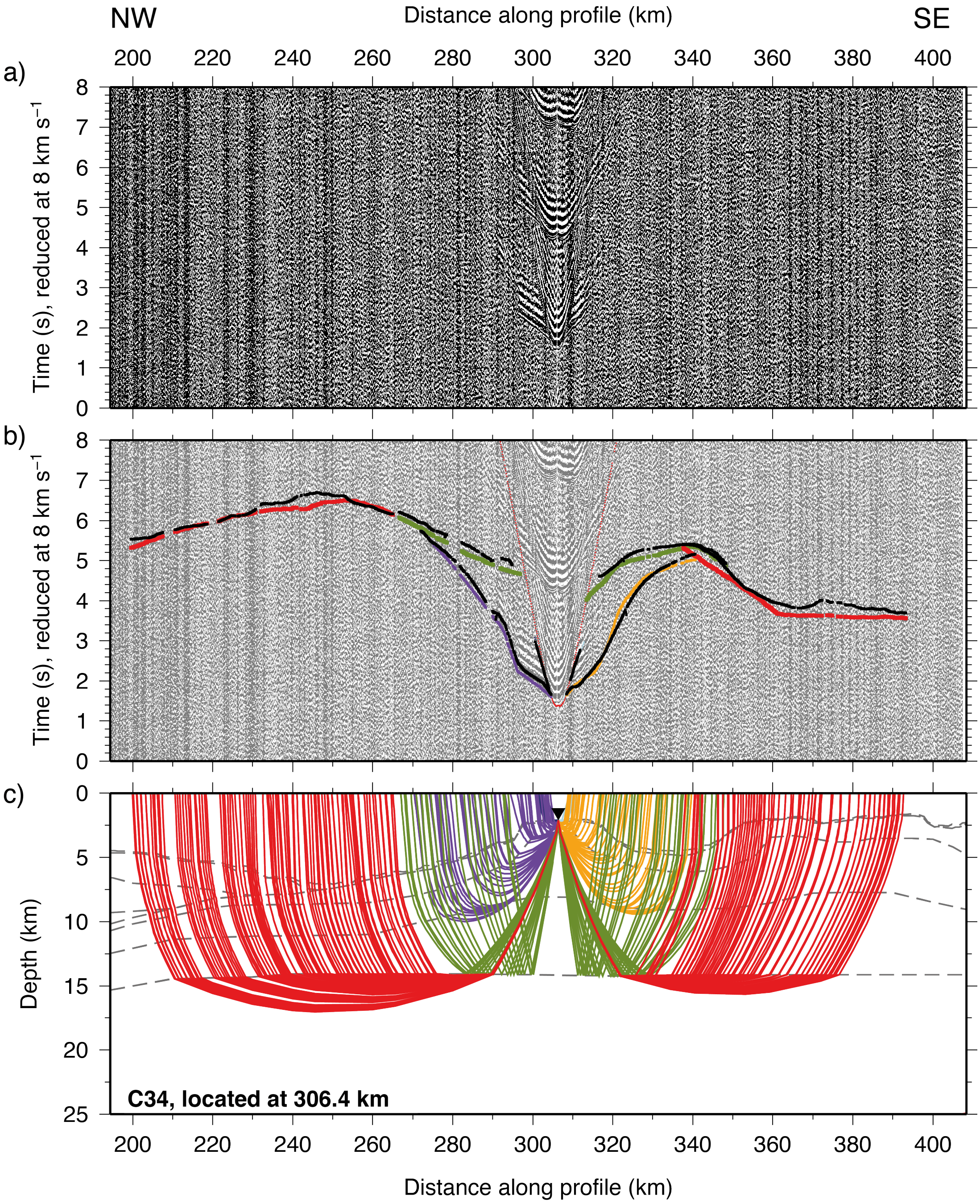

Figure A.18: *WA seismic data from OBS C34 hydrophone channel, located at 306.4 km d.a.p., on the summit of Osbourn seamount (see Fig. 3.4).*

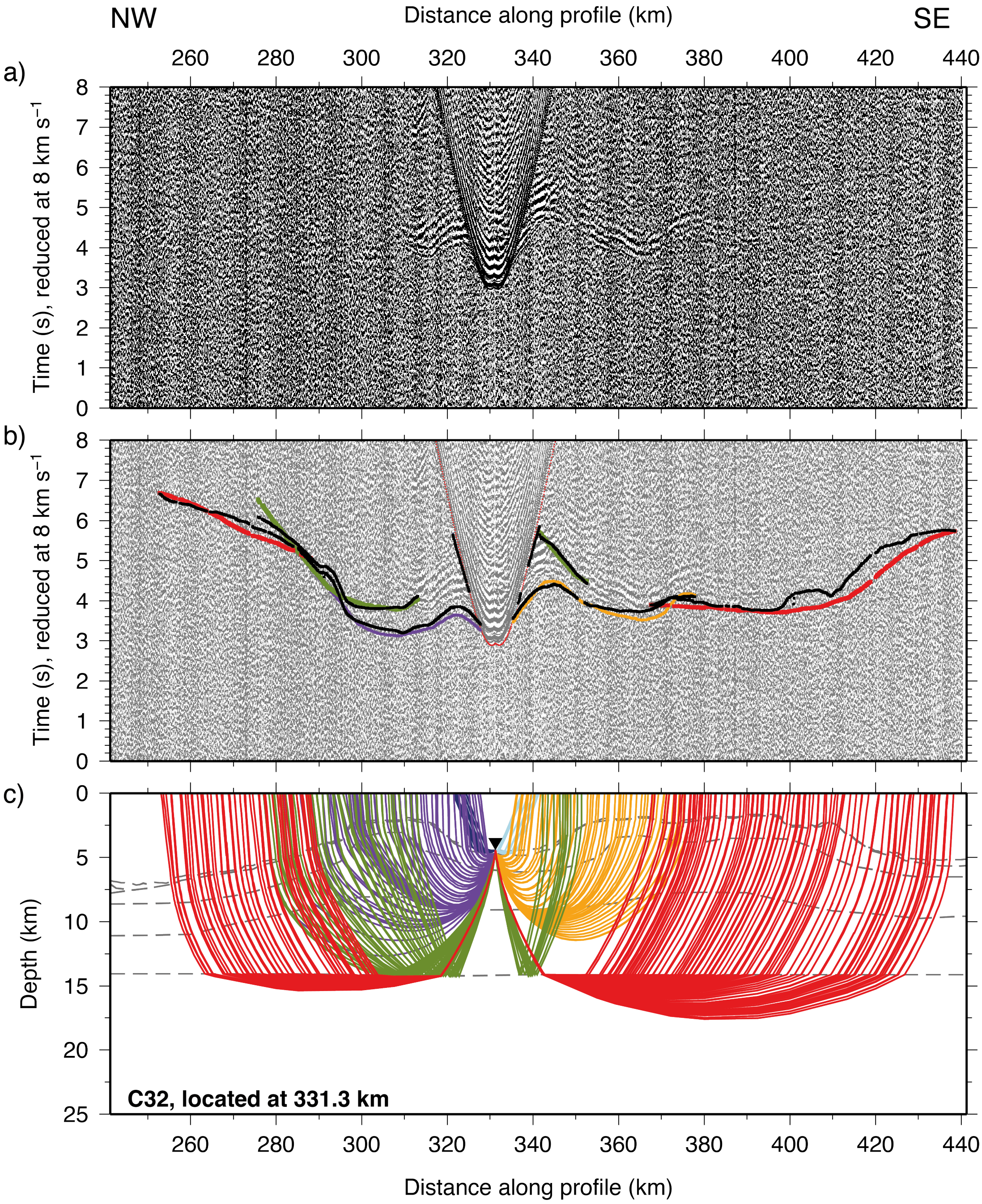

Figure A.19: *WA seismic data from OBS C32 hydrophone channel, located at 331.3 km d.a.p., between Osbourn and Canopus seamounts (see Fig. 3.4).*

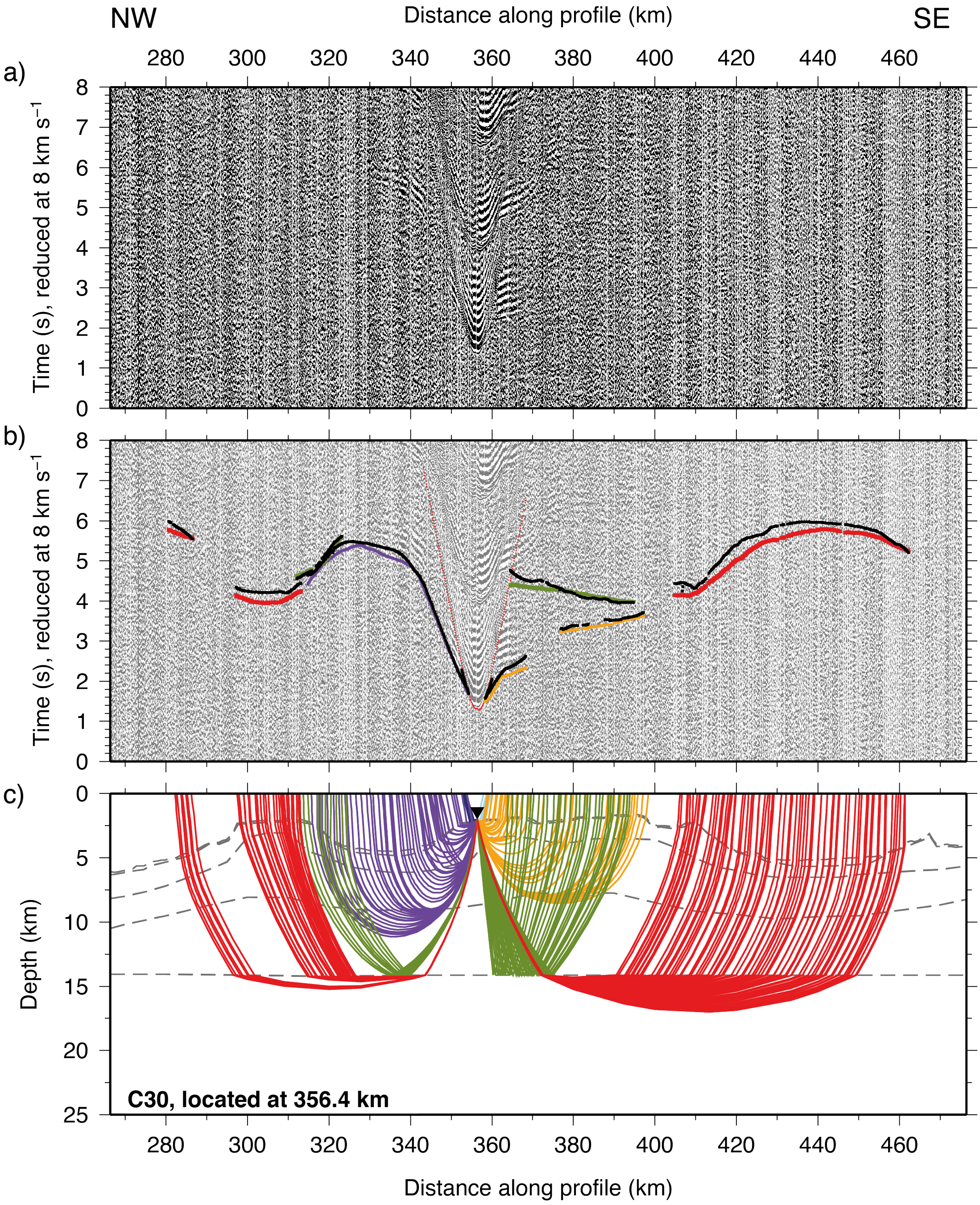

Figure A.20: *WA seismic data from OBS C30 hydrophone channel, located at 356.4 km d.a.p., on Canopus seamount (see Fig. 3.4).*

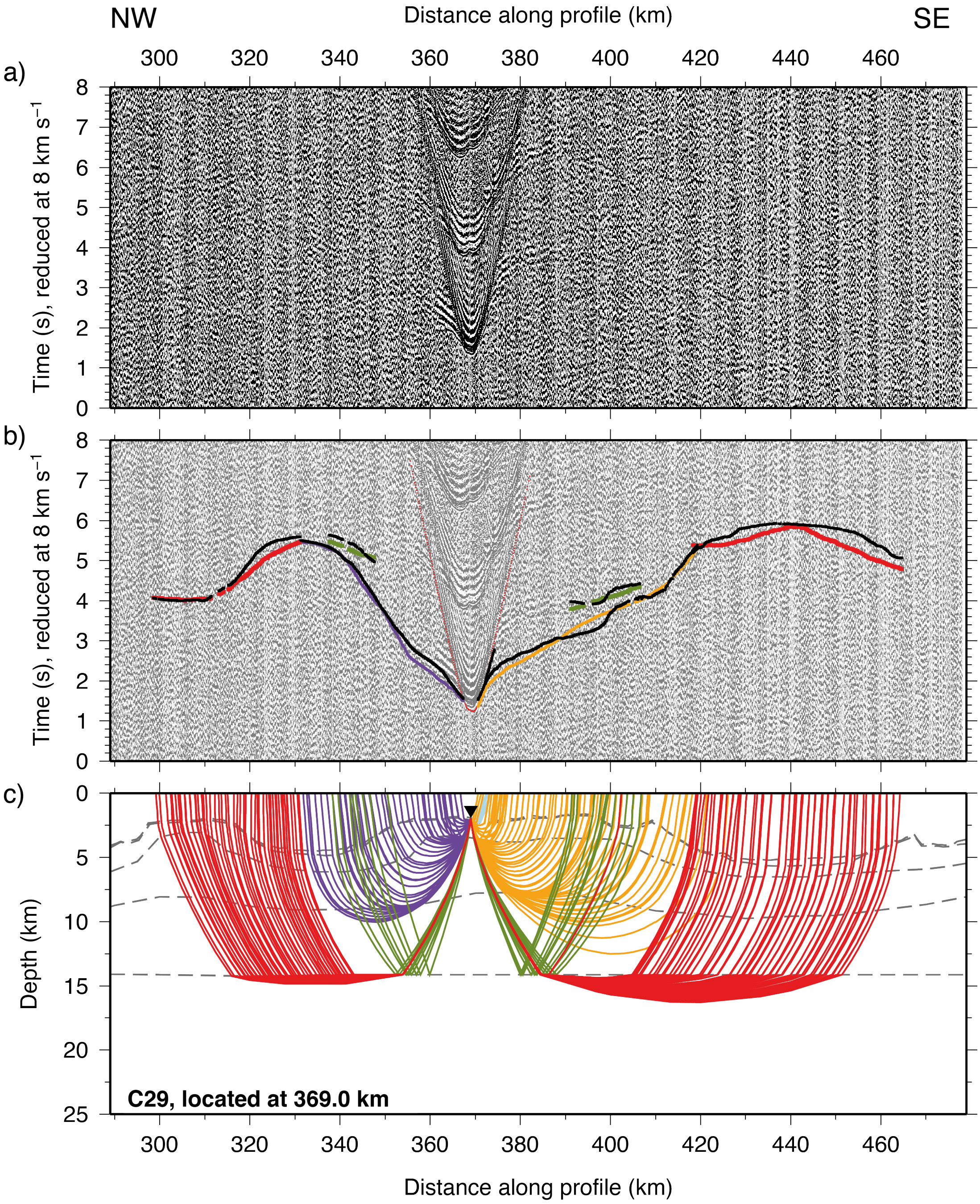

Figure A.21: *WA seismic data from OBS C29 hydrophone channel, located at 369.0 km d.a.p., on Canopus seamount (see Fig. 3.4).*

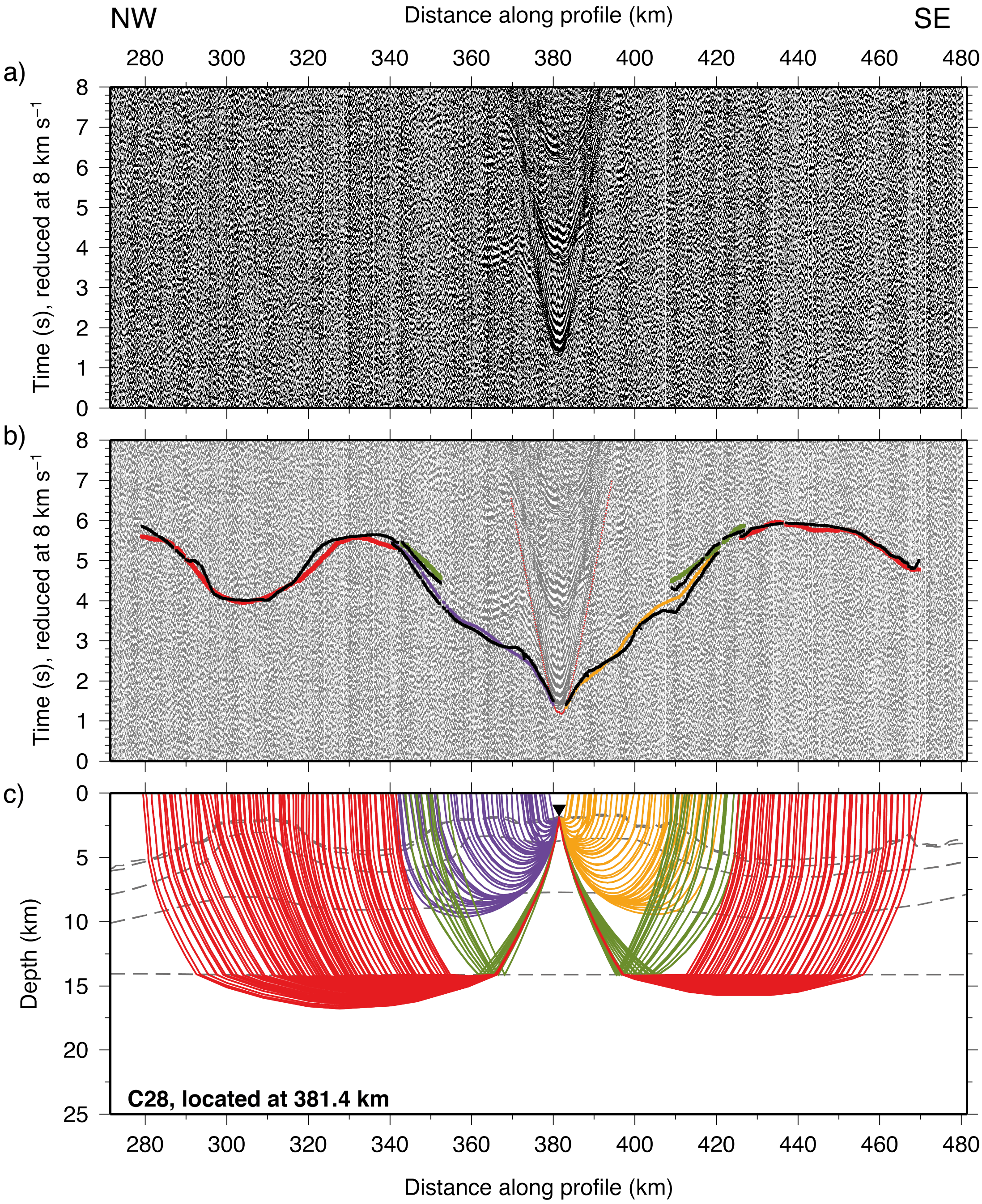

Figure A.22: *WA seismic data from OBS C28 hydrophone channel, located at 381.4 km d.a.p., on Canopus seamount (see Fig. 3.4).*

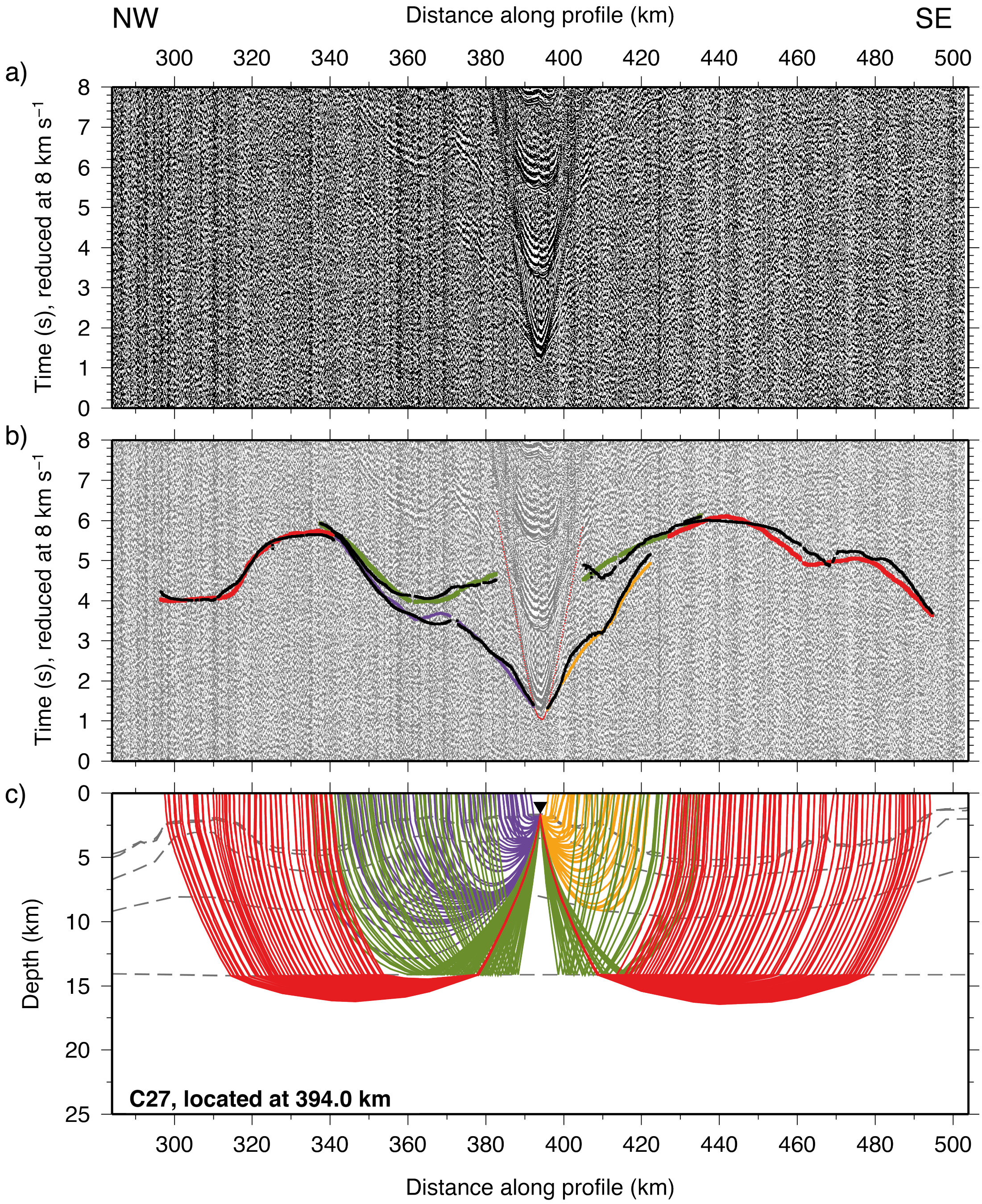

Figure A.23: *WA seismic data from OBS C27 hydrophone channel, located at 394.0 km d.a.p., on Canopus seamount (see Fig. 3.4).*

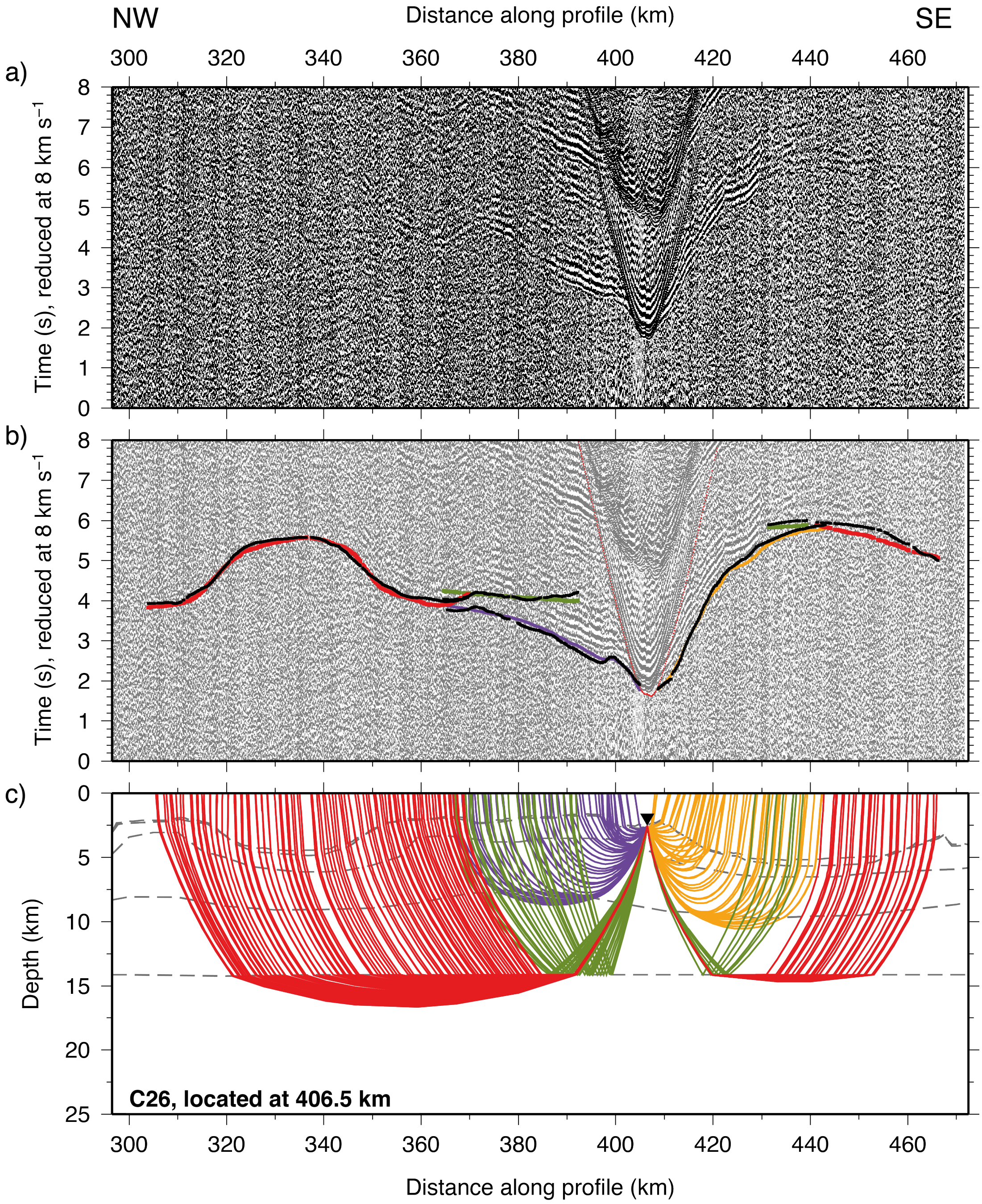

Figure A.24: *WA seismic data from OBS C26 hydrophone channel, located at 406.5 km d.a.p., on Canopus seamount (see Fig. 3.4).*

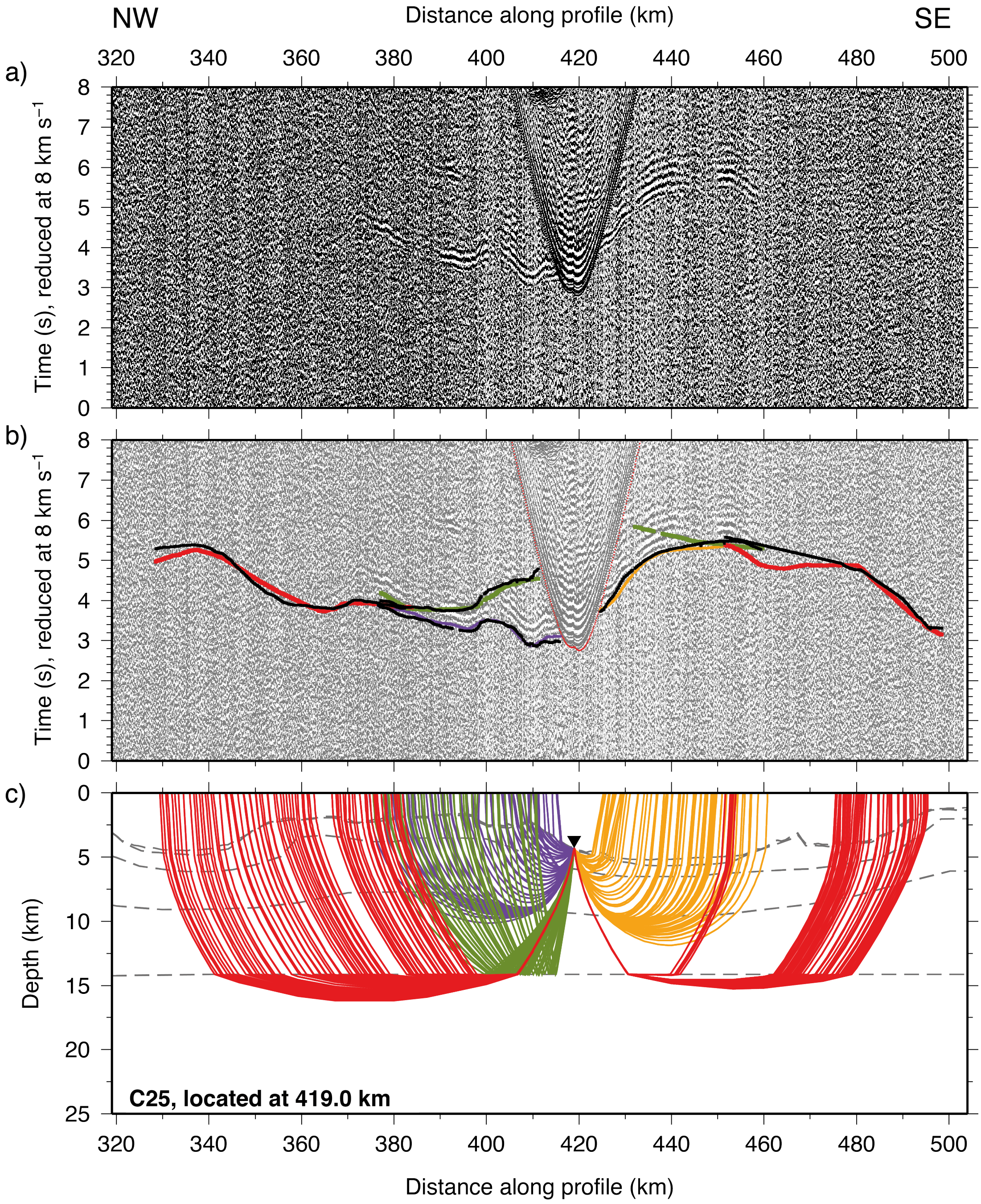

Figure A.25: *WA seismic data from OBS C25 hydrophone channel, located at 419.0 km d.a.p., between Canopus and 27.6° seamounts (see Fig. 3.4).*

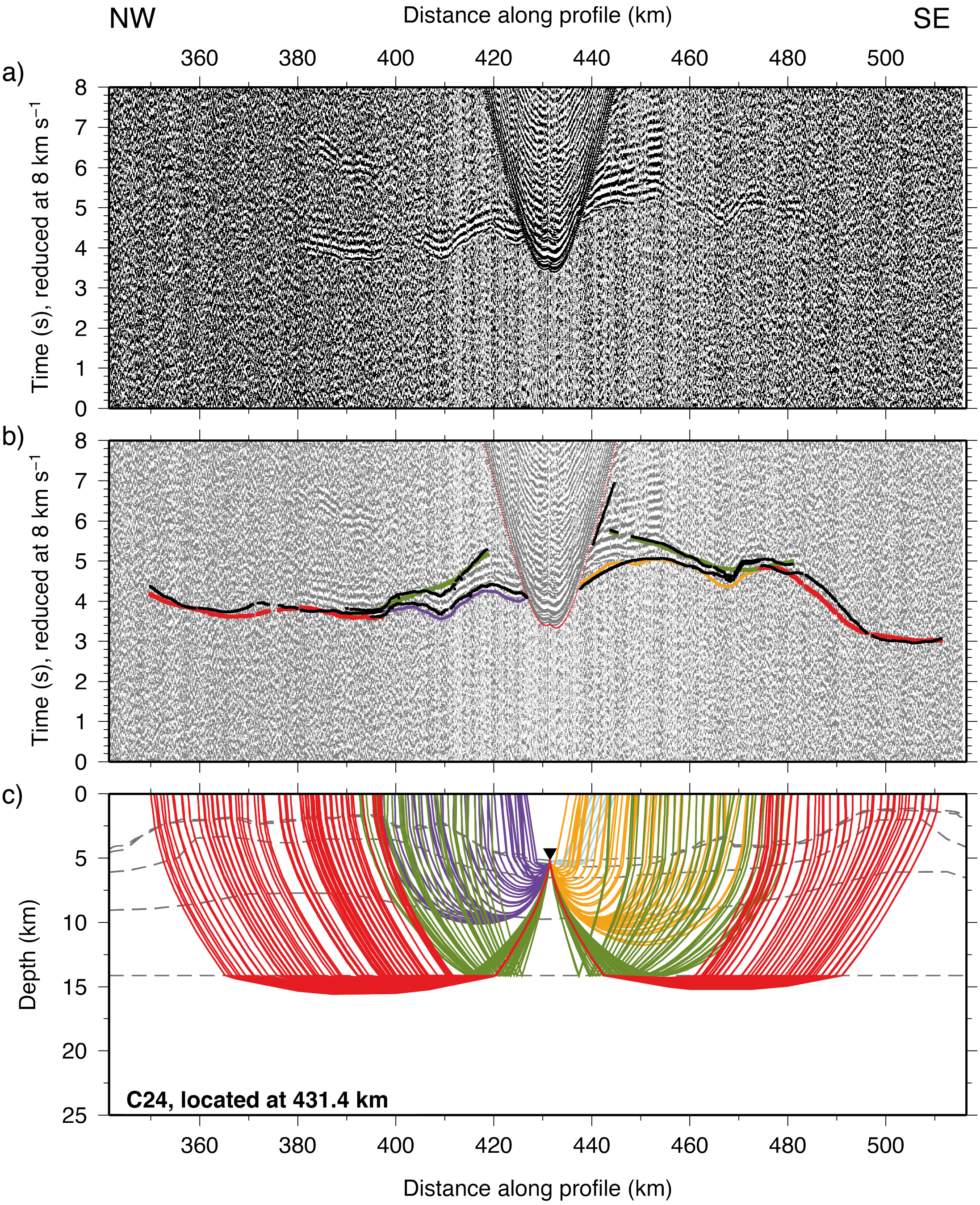

Figure A.26: *WA seismic data from OBS C24 hydrophone channel, located at 431.4 km d.a.p., between Canopus and 27.6° seamounts (see Fig. 3.4).*

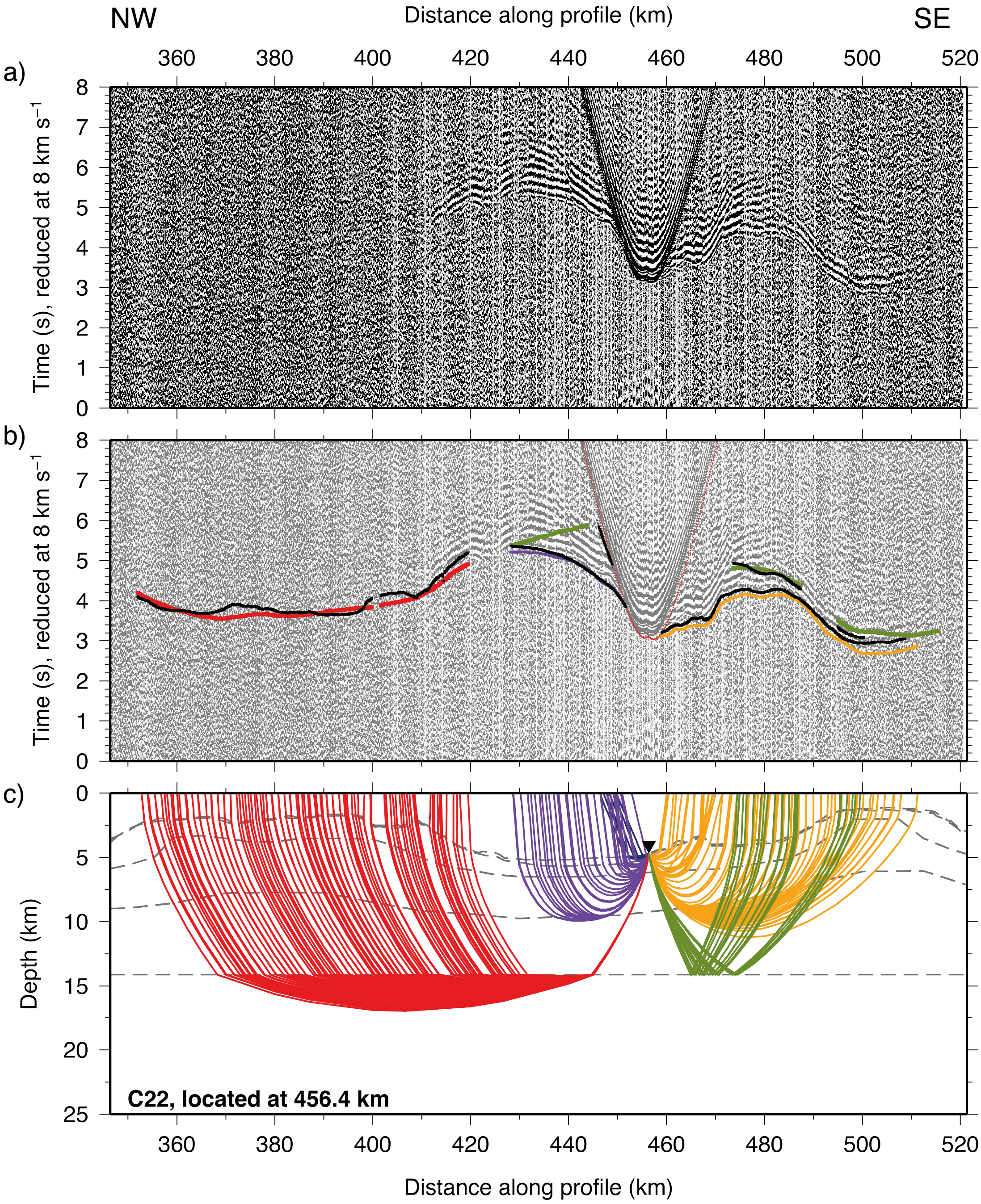

Figure A.27: *WA seismic data from OBS C22 hydrophone channel, located at 456.4 km d.a.p., between Canopus and 27.6° seamounts (see Fig. 3.4).*

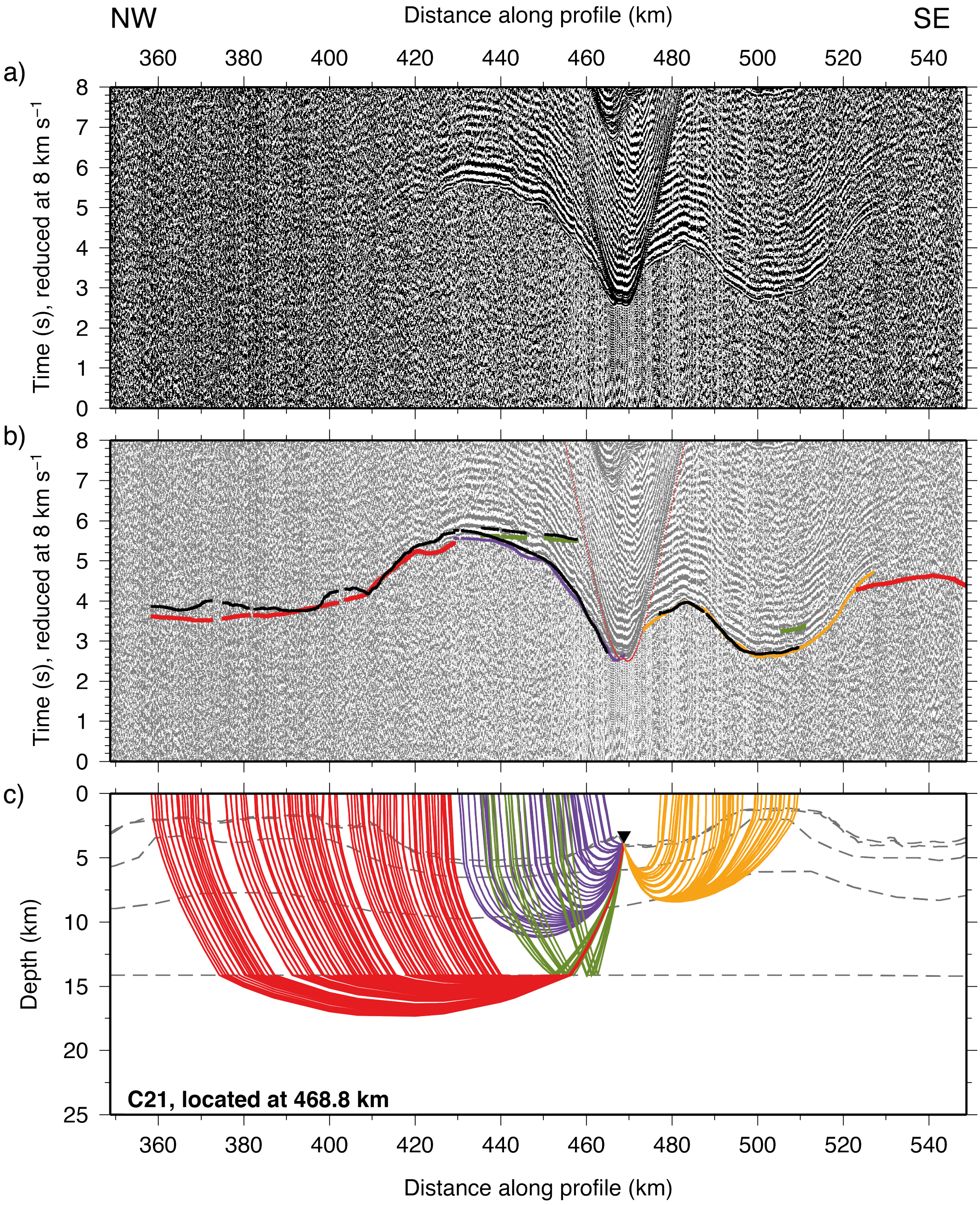

Figure A.28: *WA seismic data from OBS C21 hydrophone channel, located at 468.8 km d.a.p., between Canopus and 27.6° seamounts (see Fig. 3.4).*

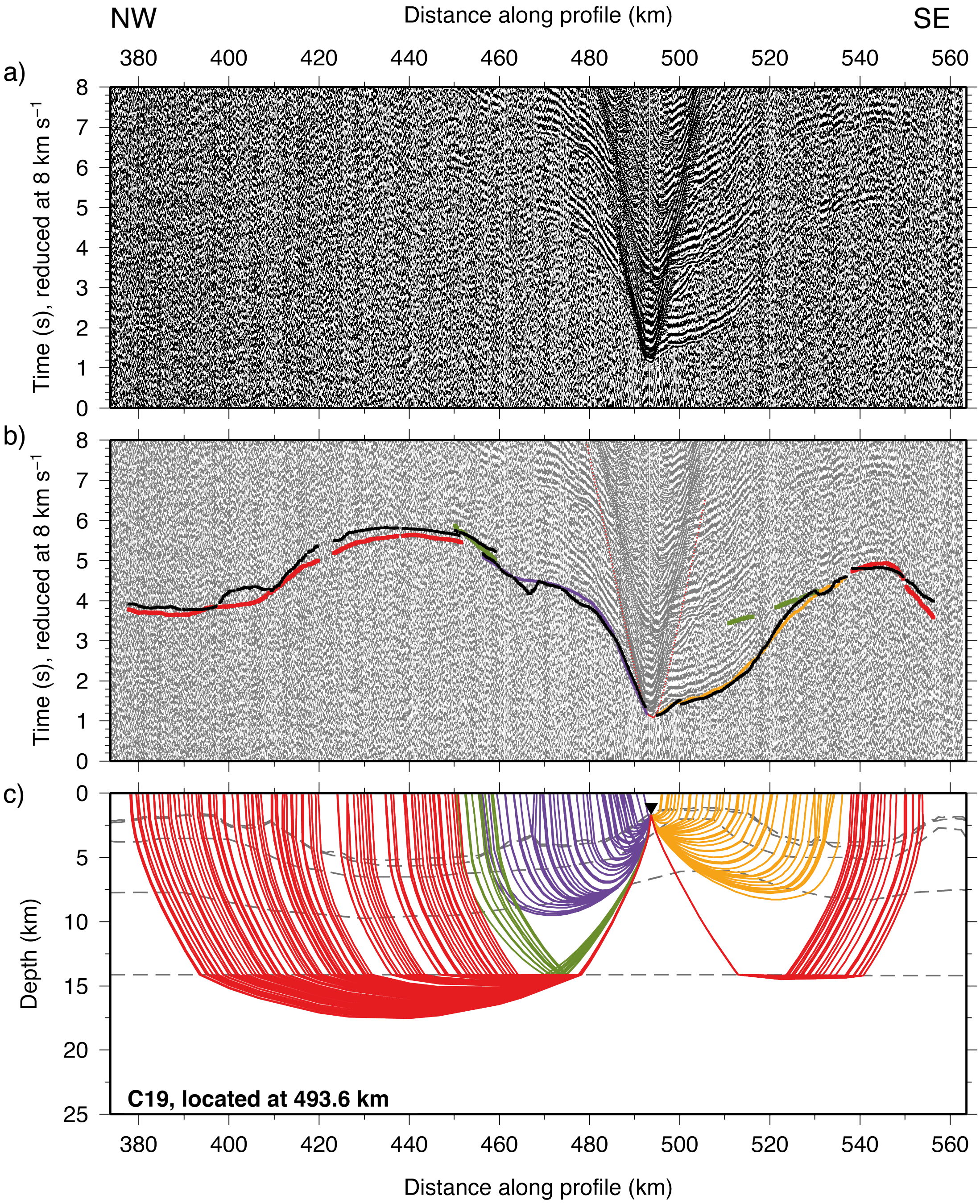

Figure A.29: *WA seismic data from OBS C19 hydrophone channel, located at 493.6 km d.a.p., on the summit of 27.6° seamount (see Fig. 3.4).*

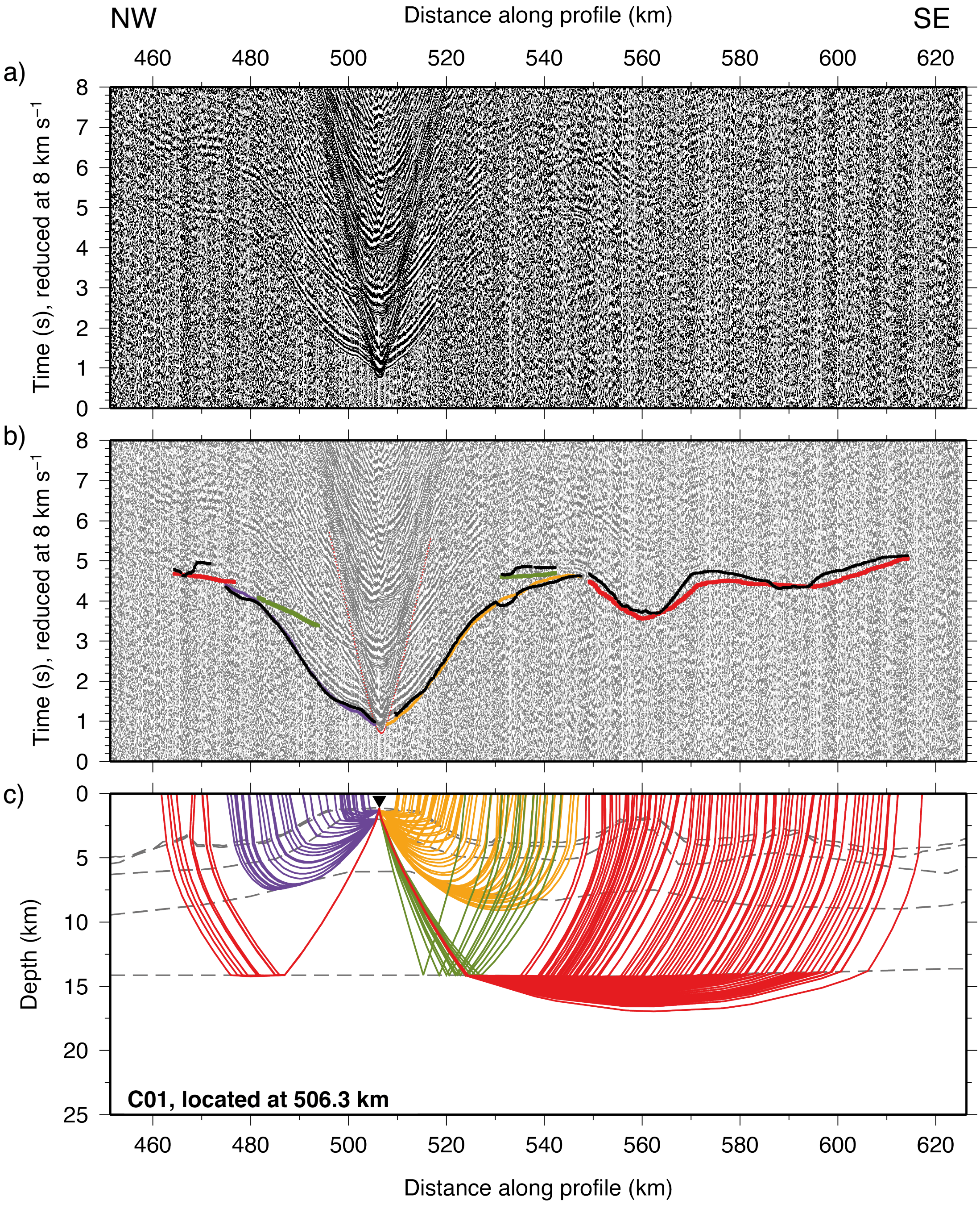

Figure A.30: *WA seismic data from OBS C01 hydrophone channel, located at 506.3 km d.a.p., on the summit of 27.6° seamount (see Fig. 3.4).*

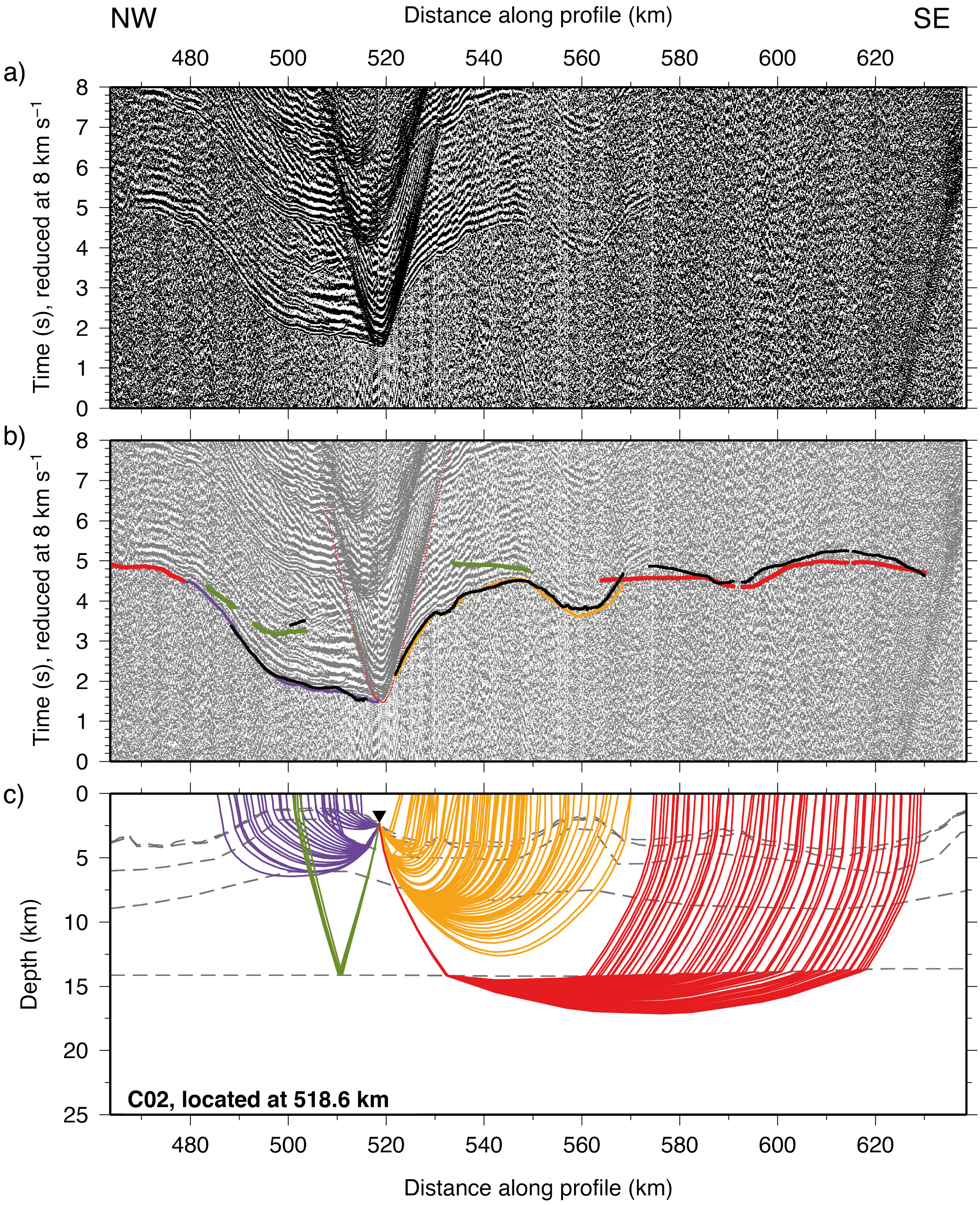

Figure A.31: *WA seismic data from OBS C02 hydrophone channel, located at 518.6 km d.a.p., on the flank of 27.6° seamount (see Fig. 3.4).*

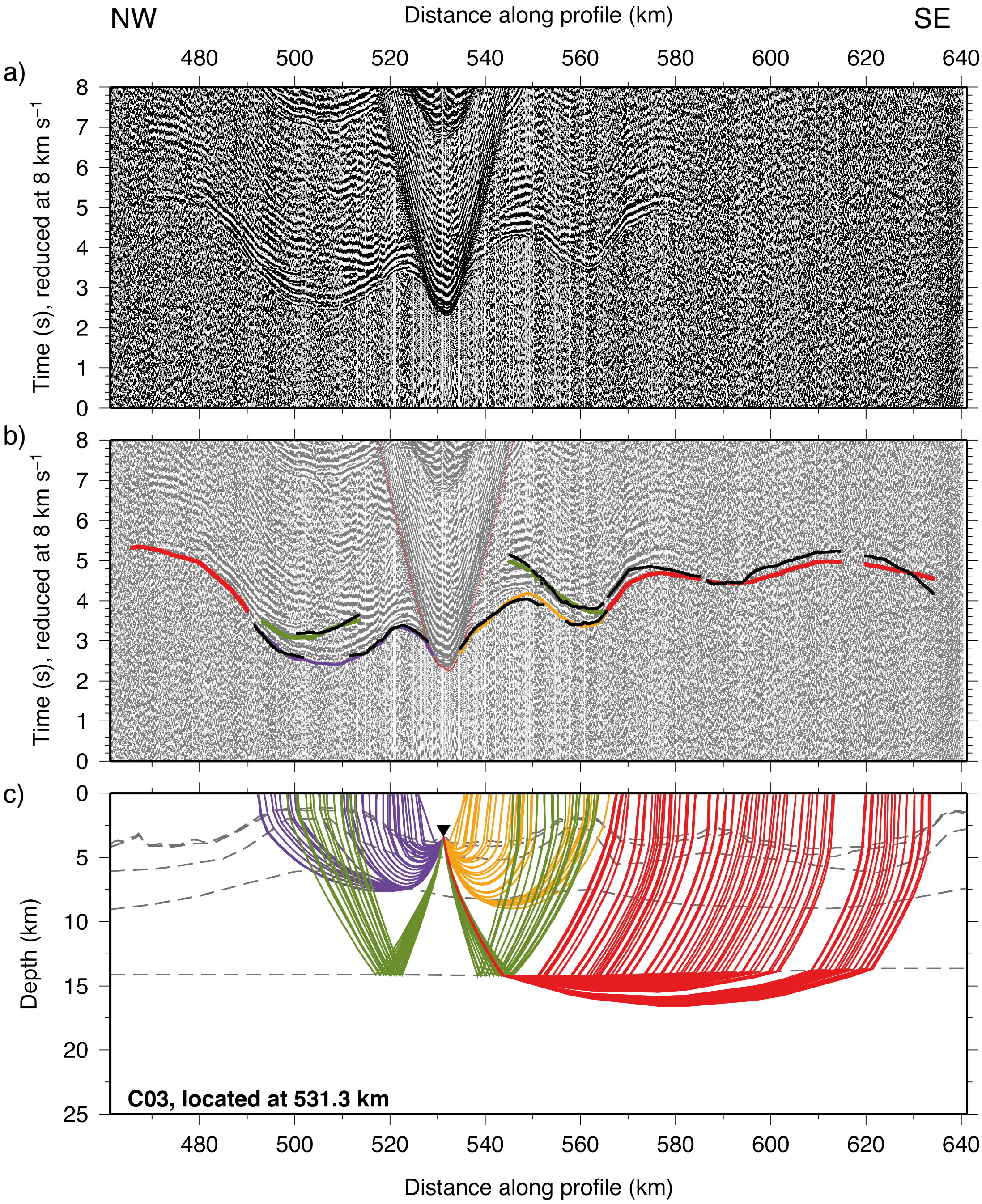

Figure A.32: *WA seismic data from OBS C03 hydrophone channel, located at 531.3 km d.a.p., on the southern part of Profile C (see Fig. 3.4).*

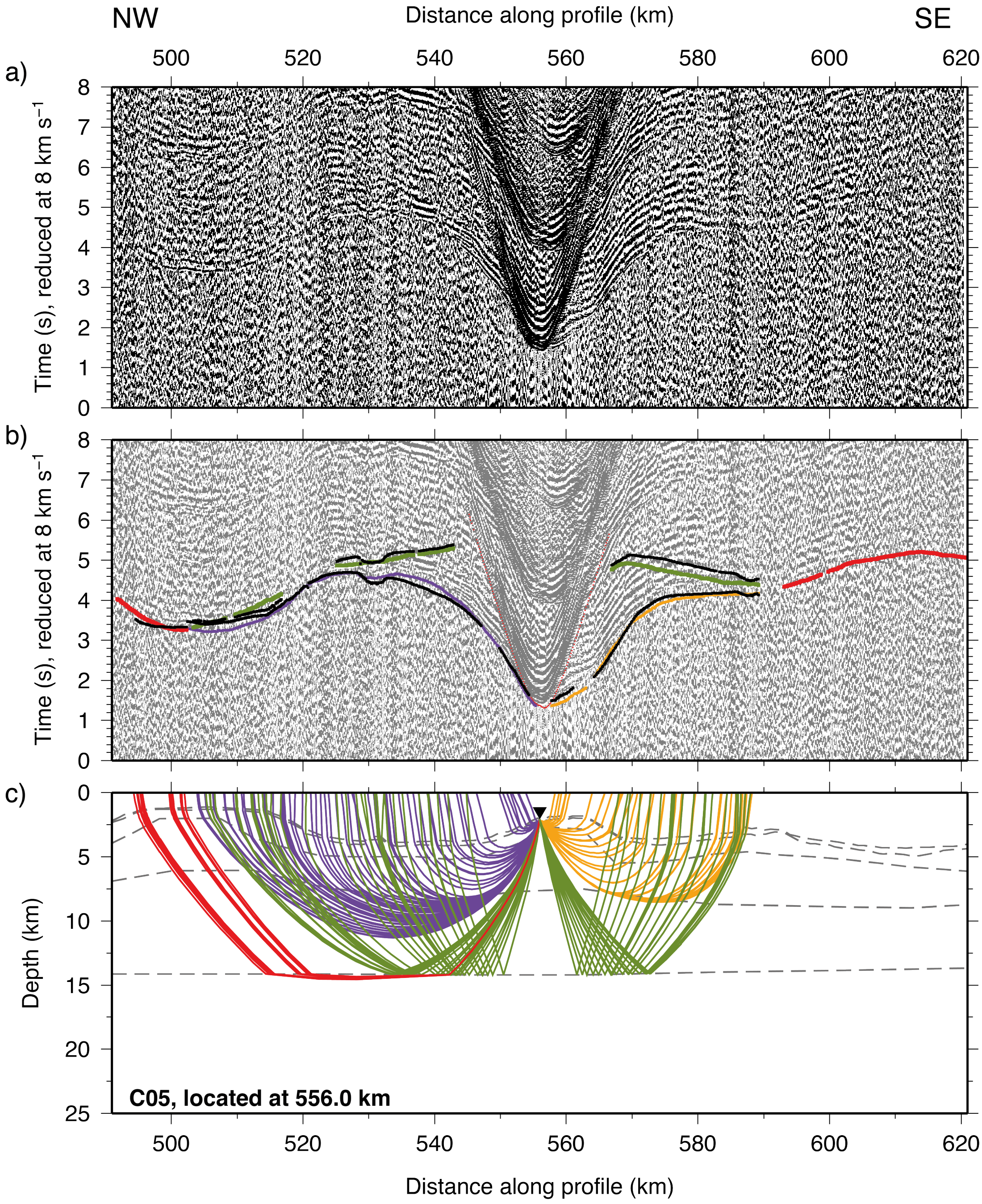

Figure A.33: *WA seismic data from OBS C05 hydrophone channel, located at 556.0 km d.a.p., on the southern part of Profile C (see Fig. 3.4).*

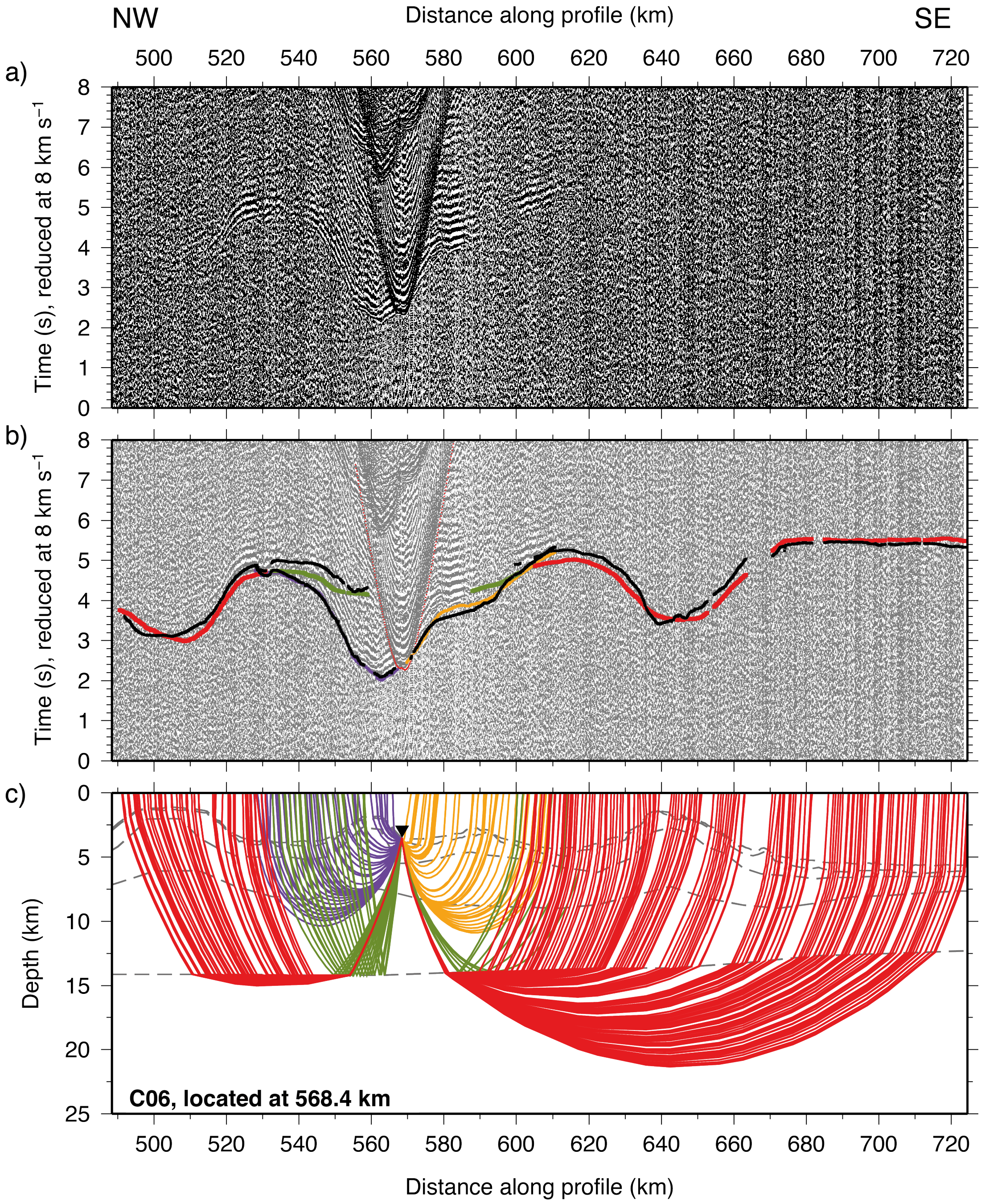

Figure A.34: *WA seismic data from OBS C06 hydrophone channel, located at 568.4 km d.a.p., on the southern part of Profile C (see Fig. 3.4).*

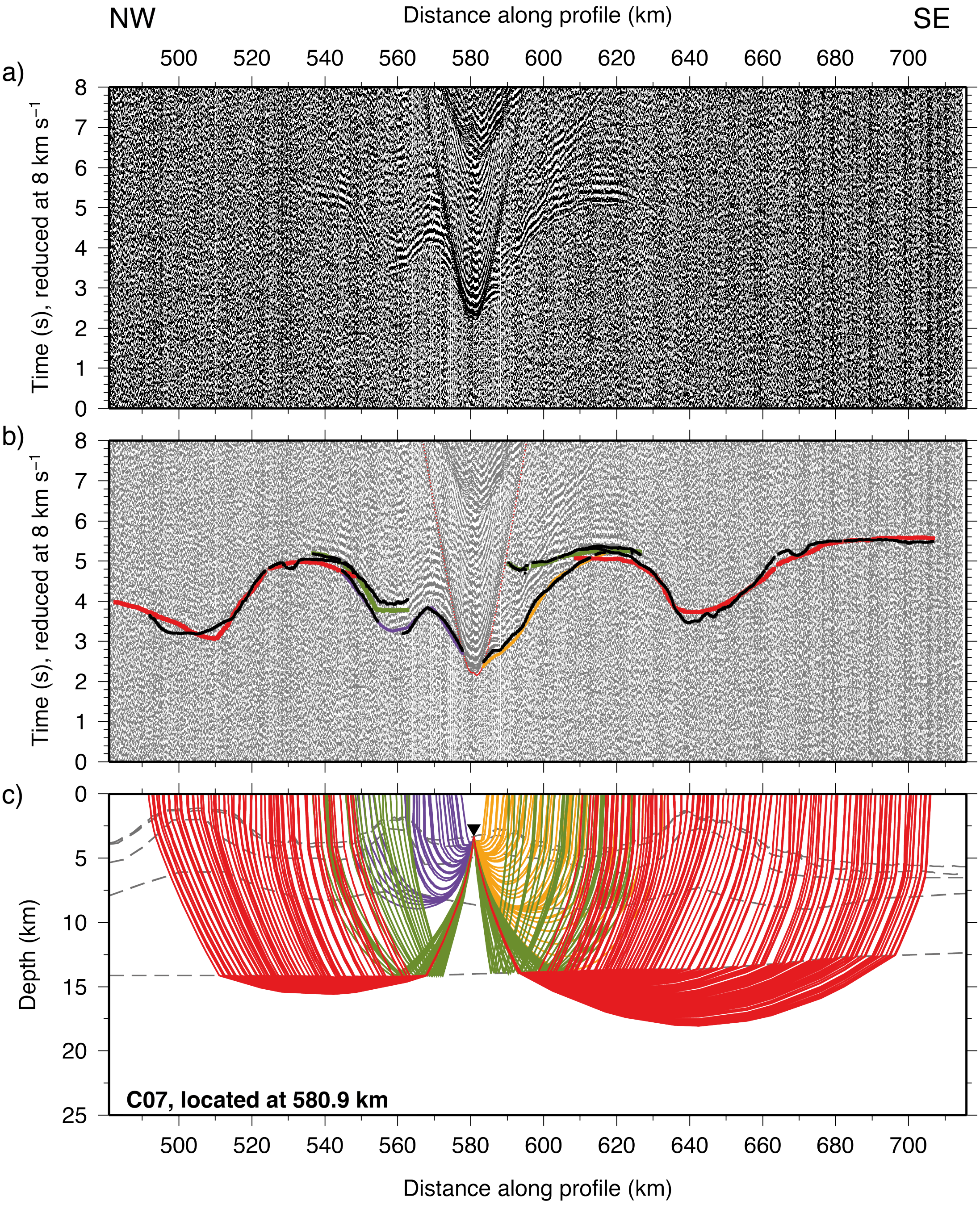

Figure A.35: *WA seismic data from OBS C07 hydrophone channel, located at 580.9 km d.a.p., on the southern part of Profile C (see Fig. 3.4).*

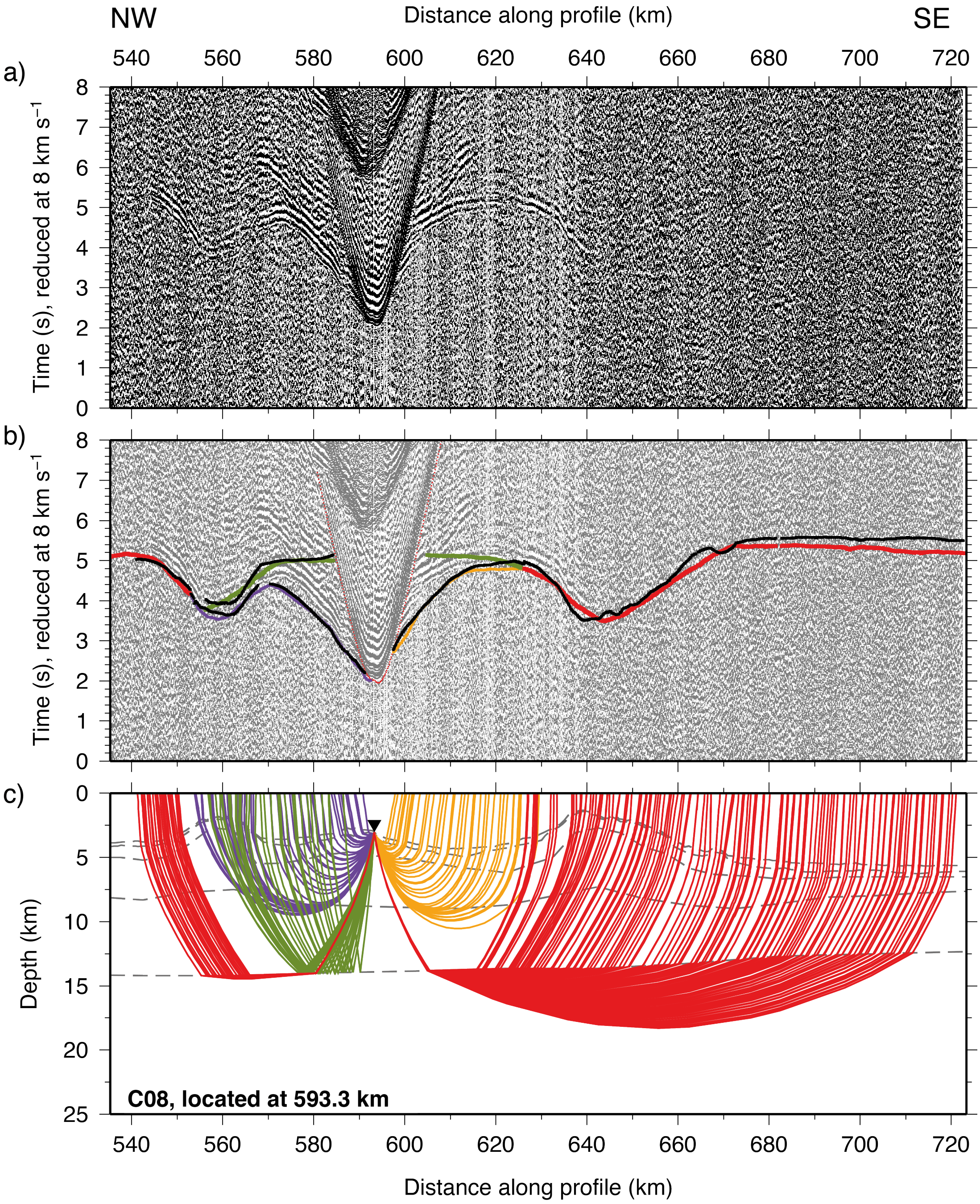

Figure A.36: *WA seismic data from OBS C08 hydrophone channel, located at 593.3 km d.a.p., on the southern part of Profile C (see Fig. 3.4).*

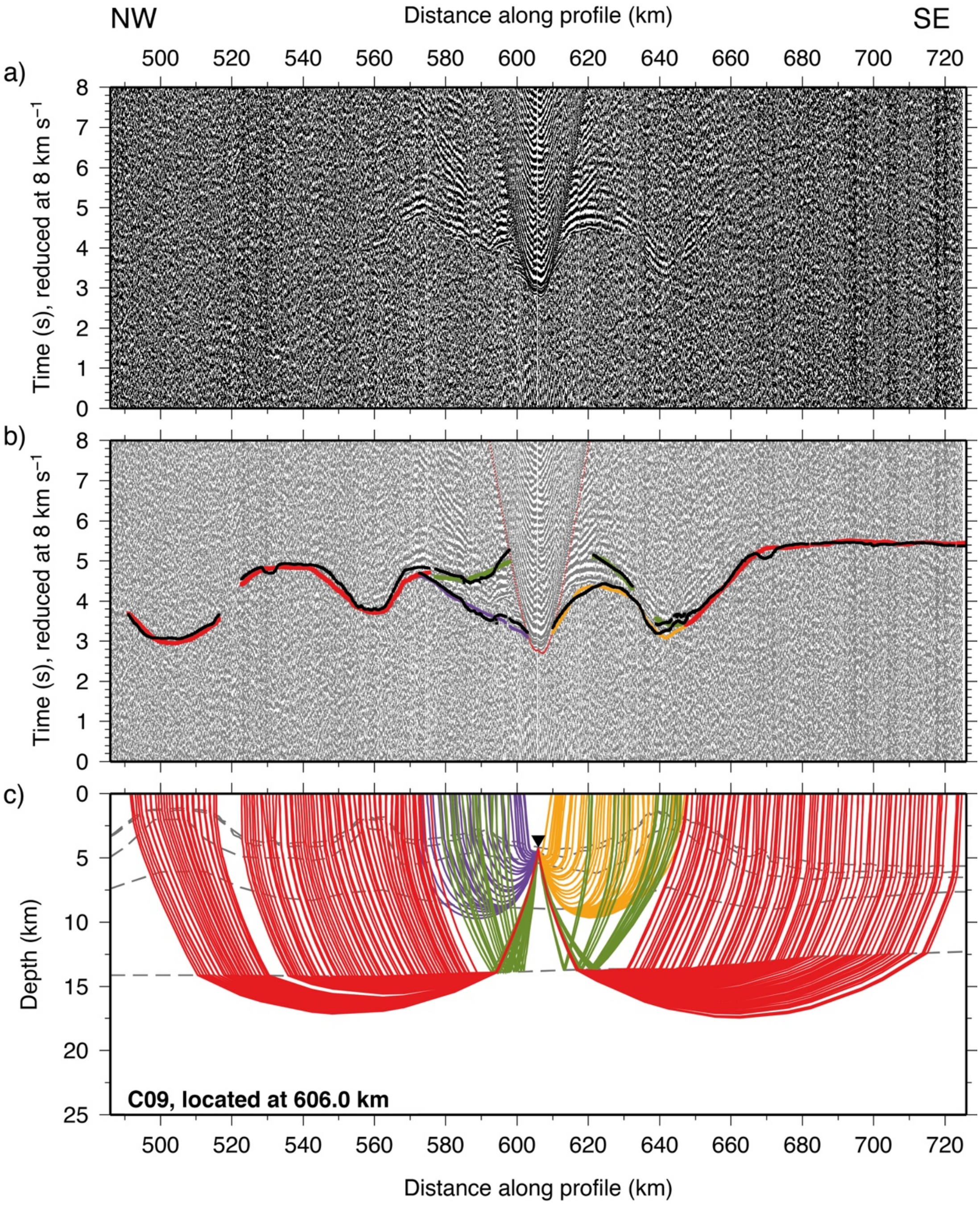

Figure A.37: *WA seismic data from OBS C09 hydrophone channel, located at 606.0 km d.a.p., on the southern part of Profile C (see Fig. 3.4).*

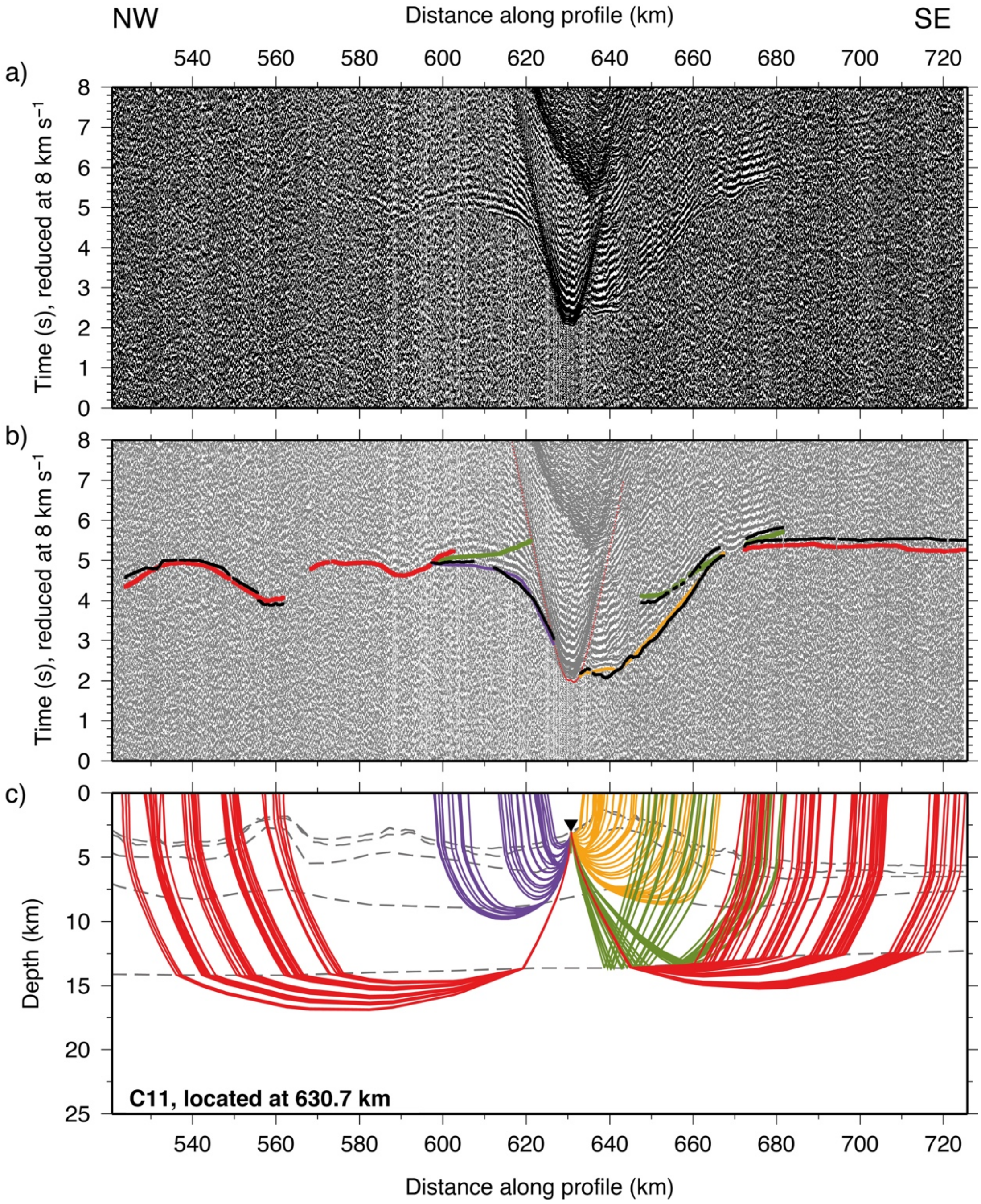

Figure A.38: *WA seismic data from OBS C11 hydrophone channel, located at 630.7 km d.a.p., on the southern part of Profile C (see Fig. 3.4).*

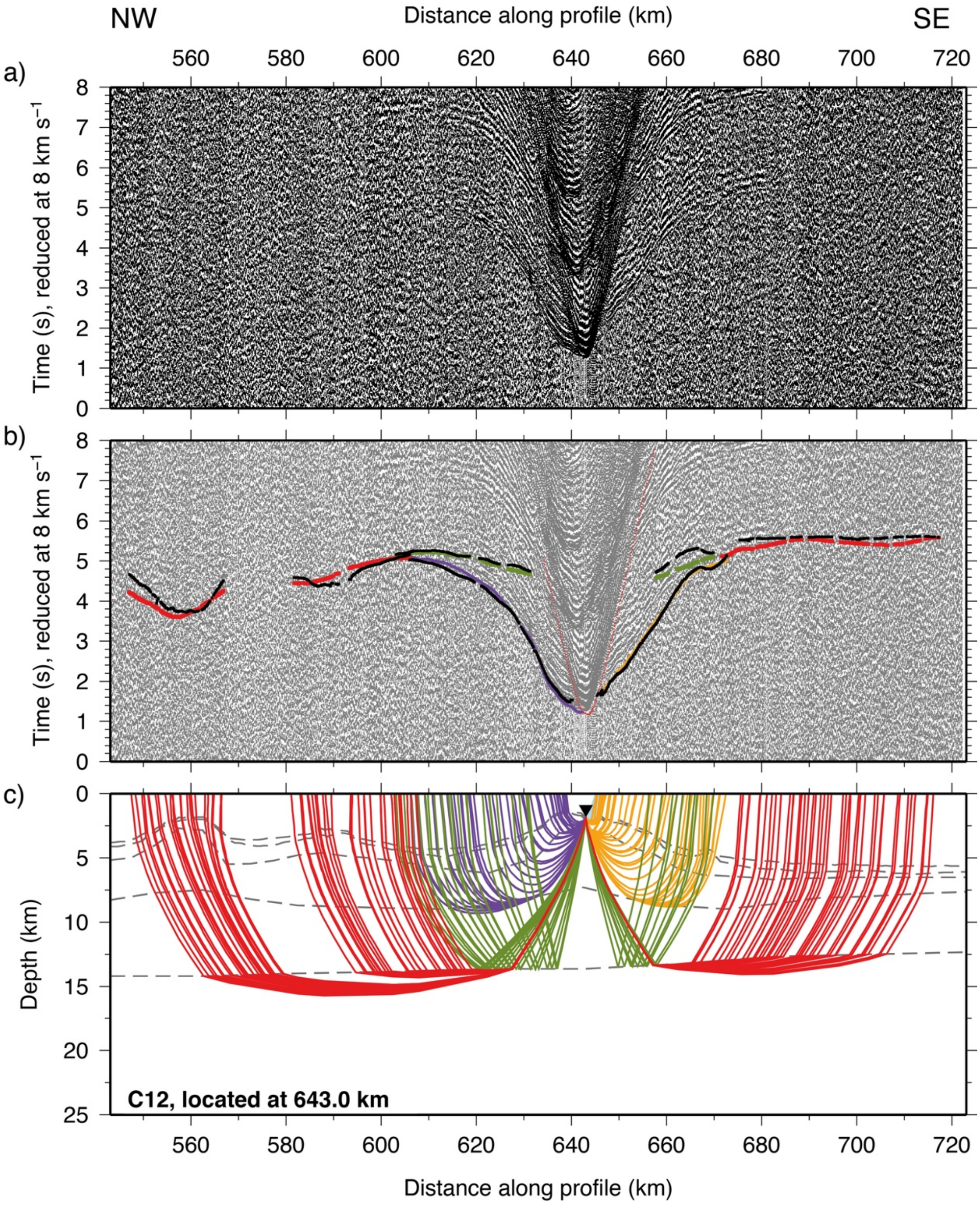

Figure A.39: *WA seismic data from OBS C12 hydrophone channel, located at 643.0 km d.a.p., on the southern part of Profile C (see Fig. 3.4).*

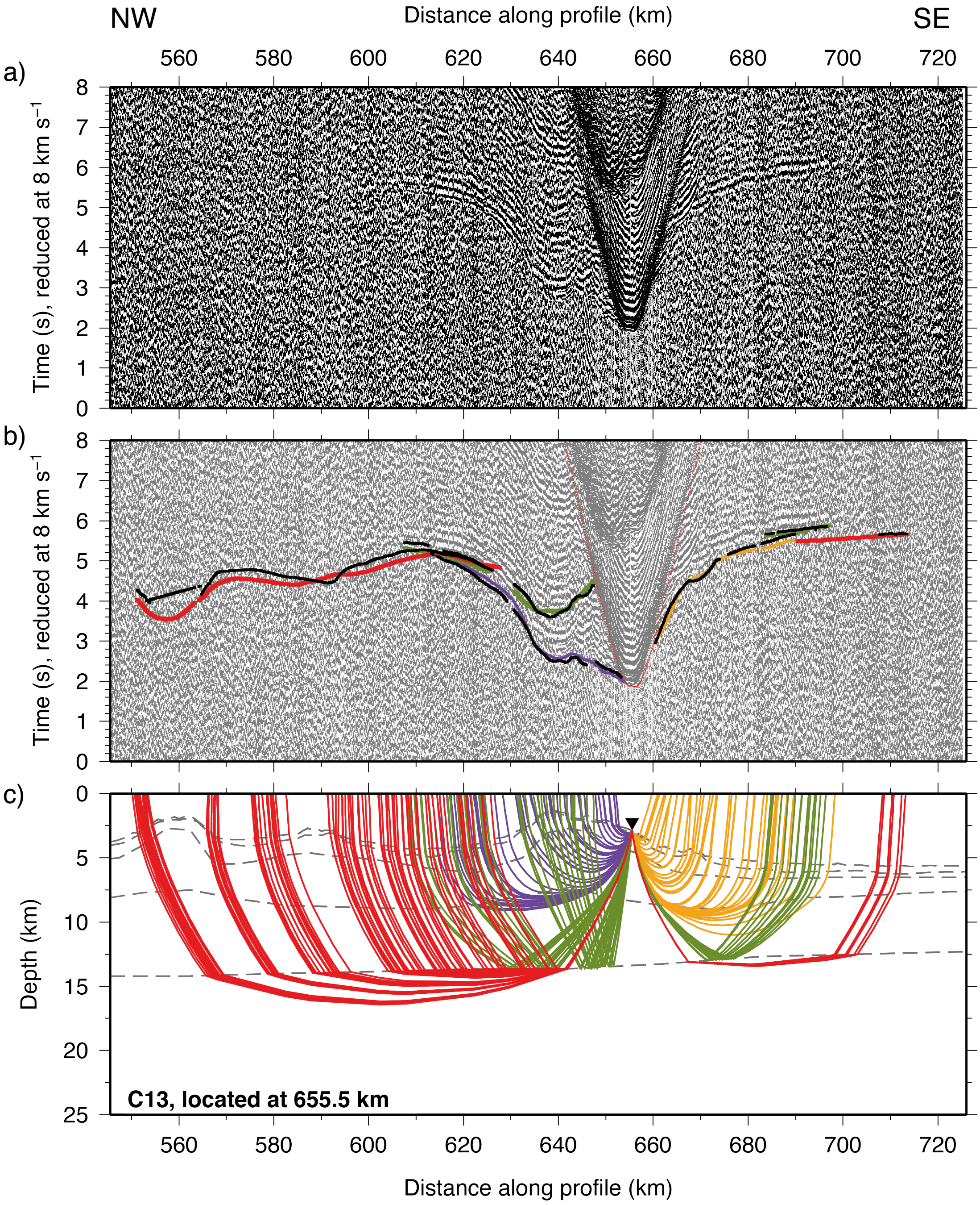

Figure A.40: *WA seismic data from OBS C13 hydrophone channel, located at 655.5 km d.a.p., on the southern part of Profile C (see Fig. 3.4).*

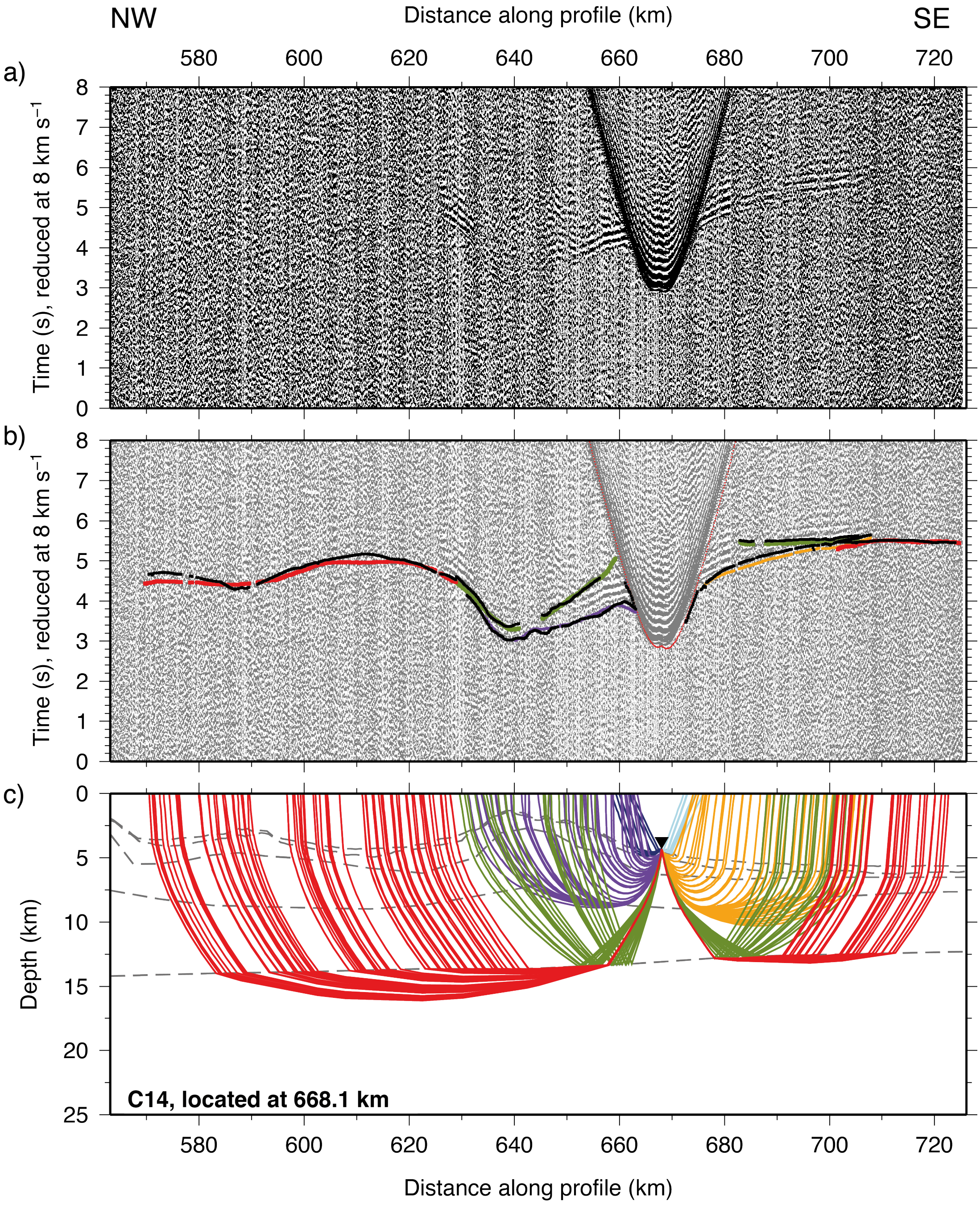

Figure A.41: *WA seismic data from OBS C14 hydrophone channel, located at 668.1 km d.a.p., on the 'background' Pacific plate (see Fig. 3.2).*

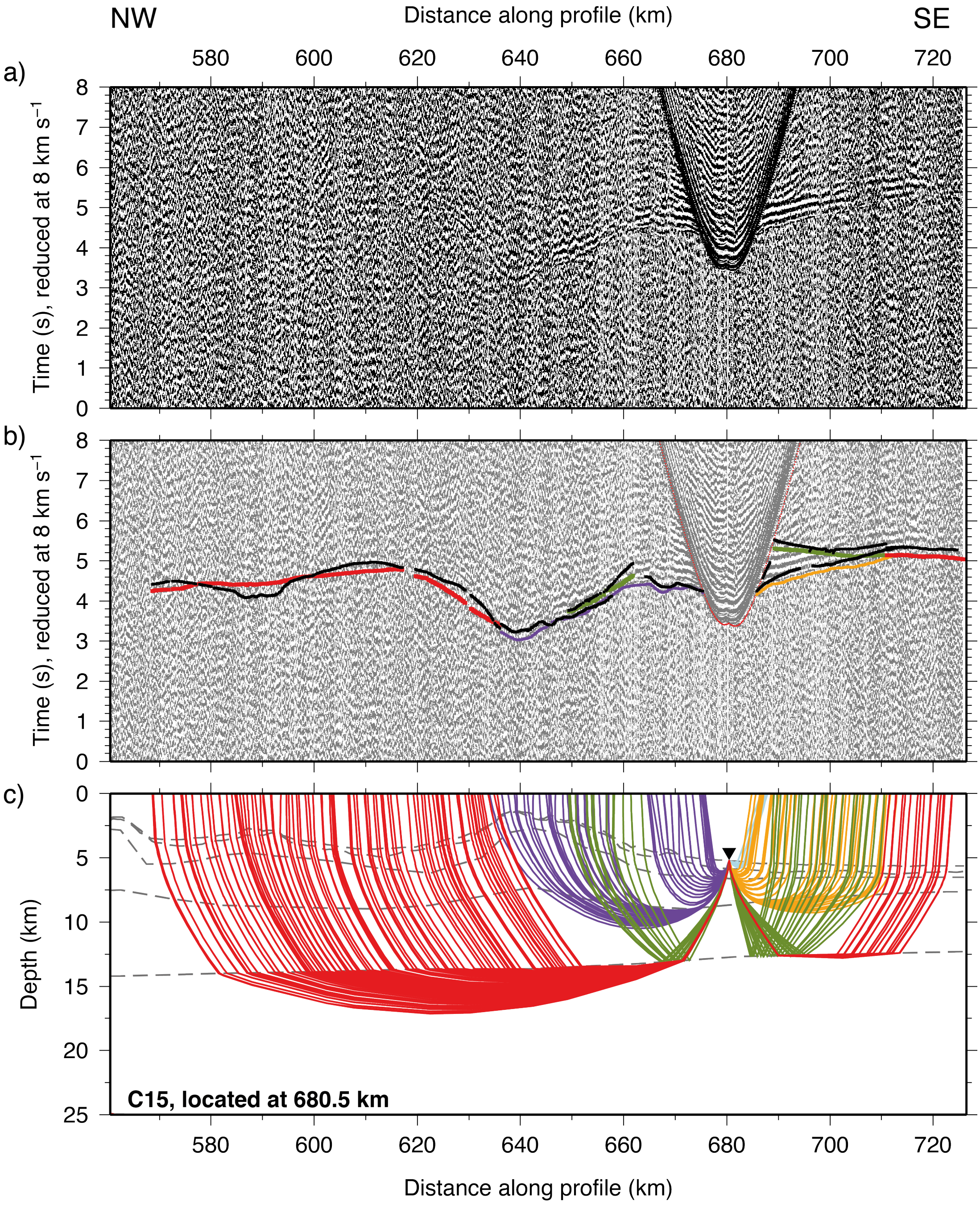

Figure A.42: *WA seismic data from OBS C15 hydrophone channel, located at 680.5 km d.a.p., on the 'background' Pacific plate (see Fig. 3.2).*

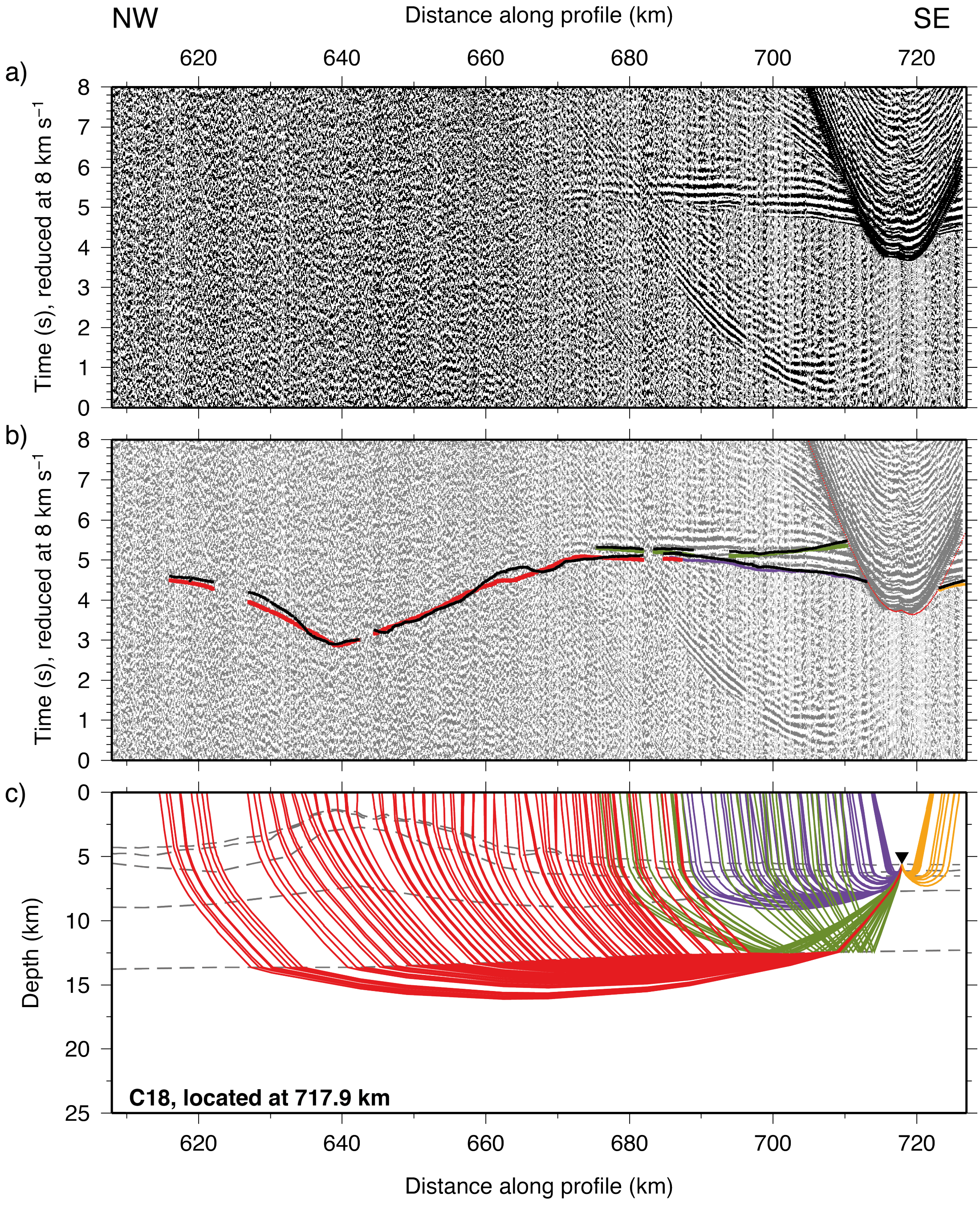

Figure A.43: *WA seismic data from OBS C18 hydrophone channel, located at 717.9 km d.a.p., on the 'background' Pacific plate (see Fig. 3.2).*

Appendix B - OBS Locations

Table B.1 (below) provides the locations of the OBSs deployed along Profile C during the SO215 wide-angle seismic experiment. The model positions and depths listed are those after instruments have been relocated using the method described in Section 3.5.3 onto the profile in the distance along profile rotated modelling space.

Table B.1: *OBS deployment and recovery locations, and relocated model positions (d.a.p.) and depths. Instruments are listed in order of distance along profile from northwest to southeast. OBSs C23 and C31, indicated by *, were not included in modelling as a result of failing to record usable data and significant drift off-profile and respectively. OBSs C10, C16, C39 and C42 were permanently installed.*

OBS No.	Deployment position			Recovery position		Model position (km)	Model depth (m)
	Latitude (° ' S)	Longitude (° ' W)	Depth (m)	Latitude (° ' S)	Longitude (° ' W)		
C57	23 35.561	176 05.335	637	23 35.663	176 05.506	19.29	647
C56	23 41.770	176 02.452	874	23 41.852	176 02.725	31.79	873
C58	23 44.858	176 01.083	991	23 44.913	176 01.347	37.99	981
C55	23 47.982	175 59.634	1292	23 47.954	175 59.900	44.20	1293
C54	23 54.184	175 56.758	1938	23 54.154	175 56.859	56.76	1889
C53	24 00.378	175 53.883	2153	24 00.237	175 53.893	69.15	2125
C52	24 06.597	175 51.051	2717	24 06.444	175 51.130	81.53	2699
C51	24 12.800	175 48.180	3974	24 12.724	175 48.217	94.15	3979
C50	24 18.996	175 45.324	4049	24 18.741	175 45.462	106.43	4011

C49	24 25.229	175 43.432	4612	24 24.927	175 42.574	119.07	4613
C48	24 31.418	175 39.545	4238	24 31.070	175 39.735	131.52	4242
C47	24 37.651	175 36.647	4442	24 37.101	175 36.878	144.17	4443
C46	24 43.860	175 33.675	5110	24 43.006	175 33.893	156.58	5126
C45	24 50.102	175 30.855	5054	24 49.403	175 31.160	168.61	5099
C44	24 56.277	175 27.974	5124	24 55.355	175 28.330	181.23	5132
C43	25 02.443	175 25.036	4540	25 01.530	175 25.150	193.68	4414
C42	25 08.630	175 22.082	4785	*Permanently installed*			
C41	25 14.801	175 19.201	5364	25 14.054	175 19.216	218.48	5292
C40	25 21.044	175 16.239	6109	25 19.503	175 16.476	230.79	6021
C39	25 27.303	175 13.330	6962	*Permanently installed*			
C38	25 33.502	175 10.429	6517	25 33.253	175 10.567	256.63	6551
C37	25 39.664	175 07.484	6049	25 39.911	175 07.842	269.40	6014
C36	25 45.896	175 04.559	5046	25 45.689	175 04.826	281.51	5045
C35	25 52.040	175 01.609	3629	25 51.884	175 01.759	293.80	3671
C34	25 58.205	174 58.626	2084	25 58.098	174 58.677	306.39	2090
C33	26 04.374	174 55.698	3050	26 04.260	174 55.743	318.77	3010
C32	26 10.625	174 52.760	4437	26 10.563	174 52.905	331.26	4446
C31*	26 16.774	174 49.889	4021	26 16.831	174 49.950	340.53	4332
C30	26 22.988	174 46.850	2000	26 23.024	174 46.908	356.38	1983
C29	26 29.186	174 43.810	1901	26 29.201	174 43.872	369.00	1916
C28	26 35.348	174 40.891	1823	26 35.423	174 40.990	381.41	1824
C27	26 41.560	174 37.883	1619	26 41.575	174 37.924	393.97	1623
C26	26 47.717	174 34.876	2547	26 47.784	174 34.879	406.48	2513
C25	26 52.908	174 31.870	4373	26 54.002	174 31.809	419.01	4278

C24	27 00.070	174 28.927	5154	27 00.257	174 28.896	431.45	5166
C23*	27 06.255	174 25.929	5081	27 06.289	174 25.818	443.77	5078
C22	27 12.439	174 22.846	4647	27 14.428	174 22.717	456.36	4687
C21	27 18.592	174 19.866	3788	27 18.714	174 19.586	468.78	3863
C20	27 24.773	174 16.896	3779	27 24.861	174 16.830	481.15	3787
C19	27 30.957	174 13.876	1652	27 31.075	174 13.815	493.64	1692
C1	27 36.771	174 10.092	1124	27 36.869	174 09.910	506.29	1130
C2	27 42.105	174 05.586	2173	27 42.150	174 05.403	518.62	2296
C3	27 47.528	174 01.029	3487	27 47.819	174 00.865	531.26	3414
C4	27 52.936	173 56.555	3804	27 53.190	173 56.434	543.58	3795
C5	27 58.288	173 51.992	1986	27 58.500	173 51.972	555.97	2052
C6	28 03.694	173 47.416	3453	28 03.814	173 47.369	568.42	3472
C7	28 09.075	173 42.860	3297	28 09.309	173 42.856	580.86	3312
C8	28 14.492	173 38.373	3010	28 14.705	173 38.262	593.31	3036
C9	28 19.926	173 33.824	4563	28 20.159	173 33.706	605.96	4173
C10	28 25.247	173 29.126	4195	*Permanently installed*			
C11	28 30.639	173 24.592	3078	28 30.829	173 24.420	630.72	3028
C12	28 35.981	173 20.056	1734	28 36.137	173 19.963	643.03	1815
C13	28 41.357	173 15.436	2839	28 41.430	173 15.421	655.53	2857
C14	28 46.747	173 10.854	4303	28 46.771	173 10.707	668.07	4310
C15	28 52.100	173 06.254	5148	28 51.999	173 05.996	680.46	5185
C16	28 57.493	173 01.608	5512	*Permanently installed*			
C17	29 02.854	172 57.062	5612	29 03.113	172 57.133	705.58	5612
C18	29 08.169	172 52.433	5626	29 08.405	172 52.696	717.92	5595

Appendix C – Results of checkerboard testing

In Section 4.3., the *inverse model* was tested for its ability to resolve feature sizes by applying a checkerboard testing approach. During this testing, each input checkerboard anomaly size had phase shifts applied in horizontal (along-model) and vertical (depth) directions, in order to test for the sensitivity of the results to checkerboard edge geometry versus bathymetric contrasts (Section 4.3.4).

This appendix provides an array of recovered checkerboards resulting from testing over a range of input anomaly size. The input anomaly is defined in terms of its width and depth. The top left panel of each figure shows the input checkerboard for the test size, without any phase shifts applied. The 16 recovered checkerboards arise from tests where phase shifts of 0.5, 1.0 and 1.5 times the width and depth were applied to the input checkerboard before this was added to the model for testing. Each recovered checkerboard is labelled with its phase shift in kilometres, with h indicating a horizontal shift, and where positive is towards the right or southeast of the model, and v indicating a vertical shift, where positive corresponds to an increase in depth.

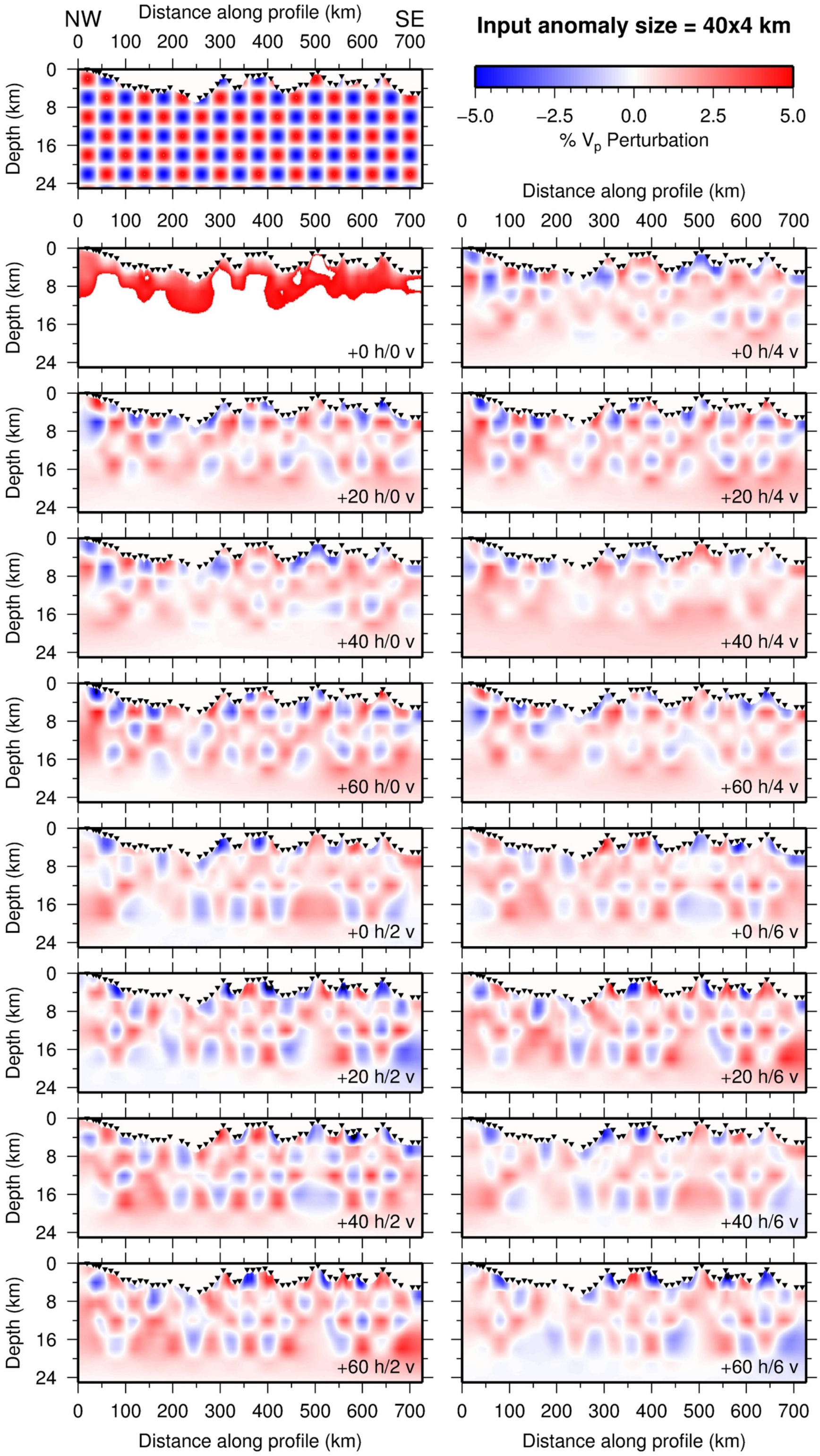

Fig. C.1: *Results of checkerboard testing for 40 x 4 km input anomaly*

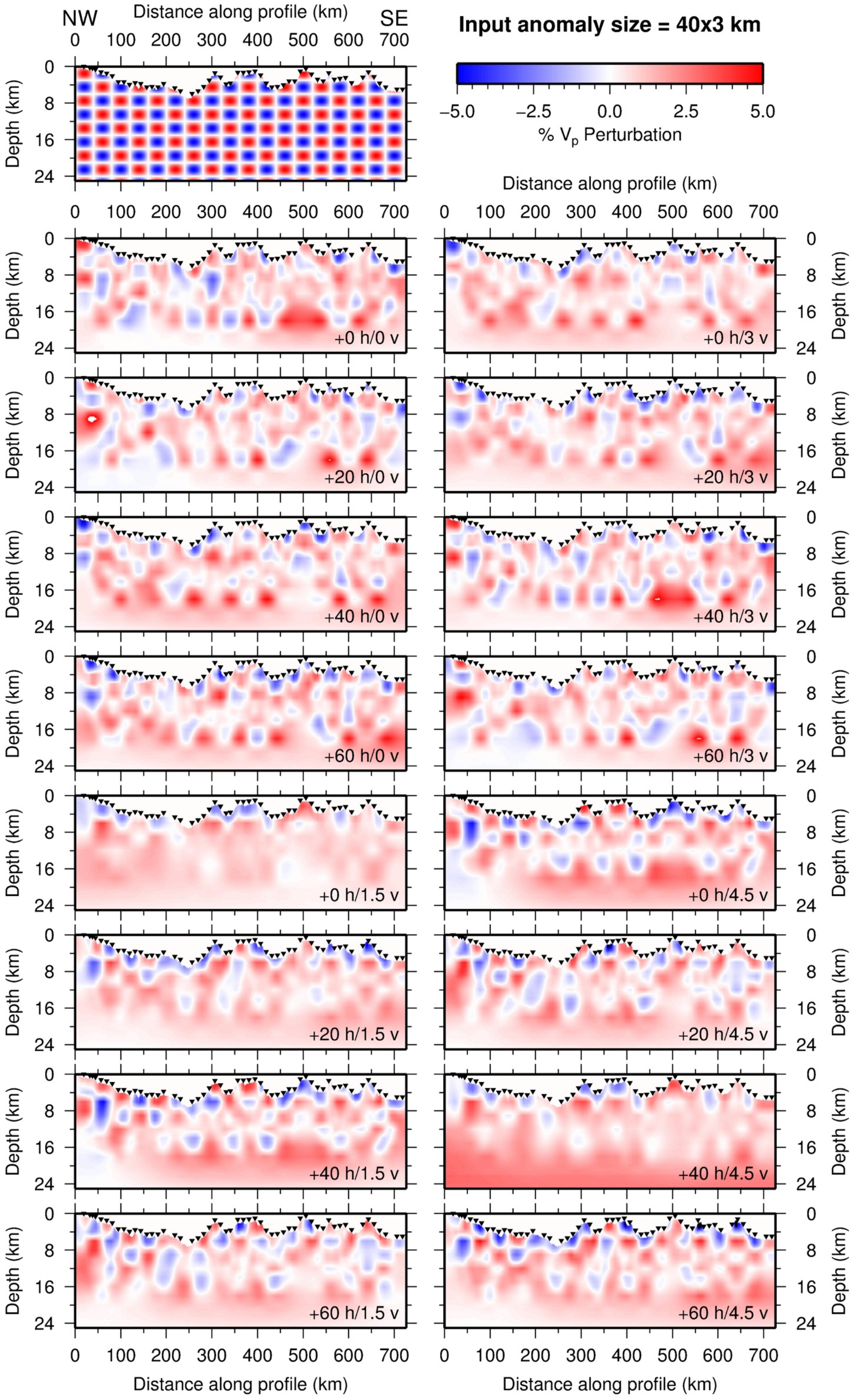

Fig. C.2: *Results of checkerboard testing for 40 x 3 km input anomaly*

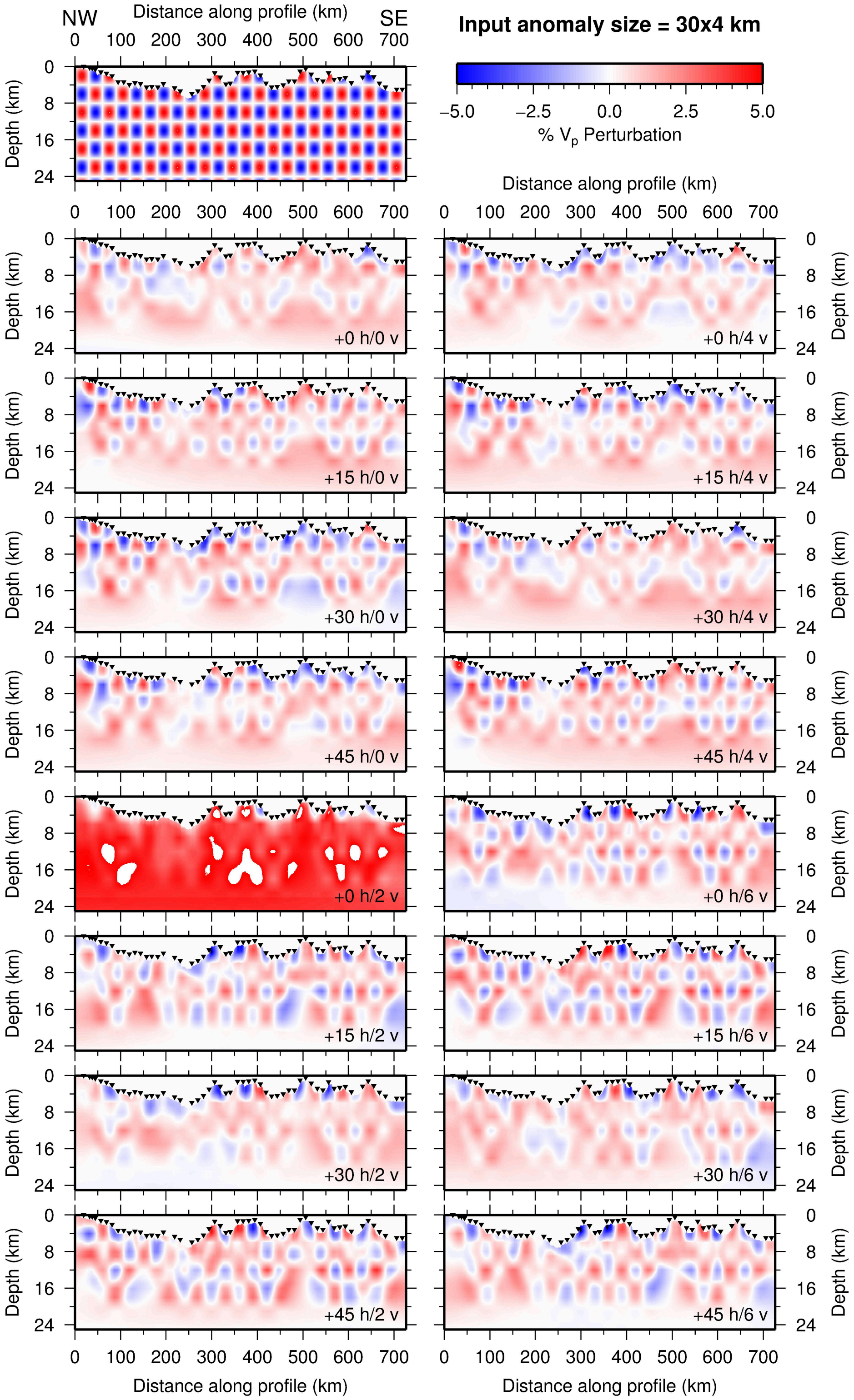

Fig. C.3: *Results of checkerboard testing for 30 x 4 km input anomaly*

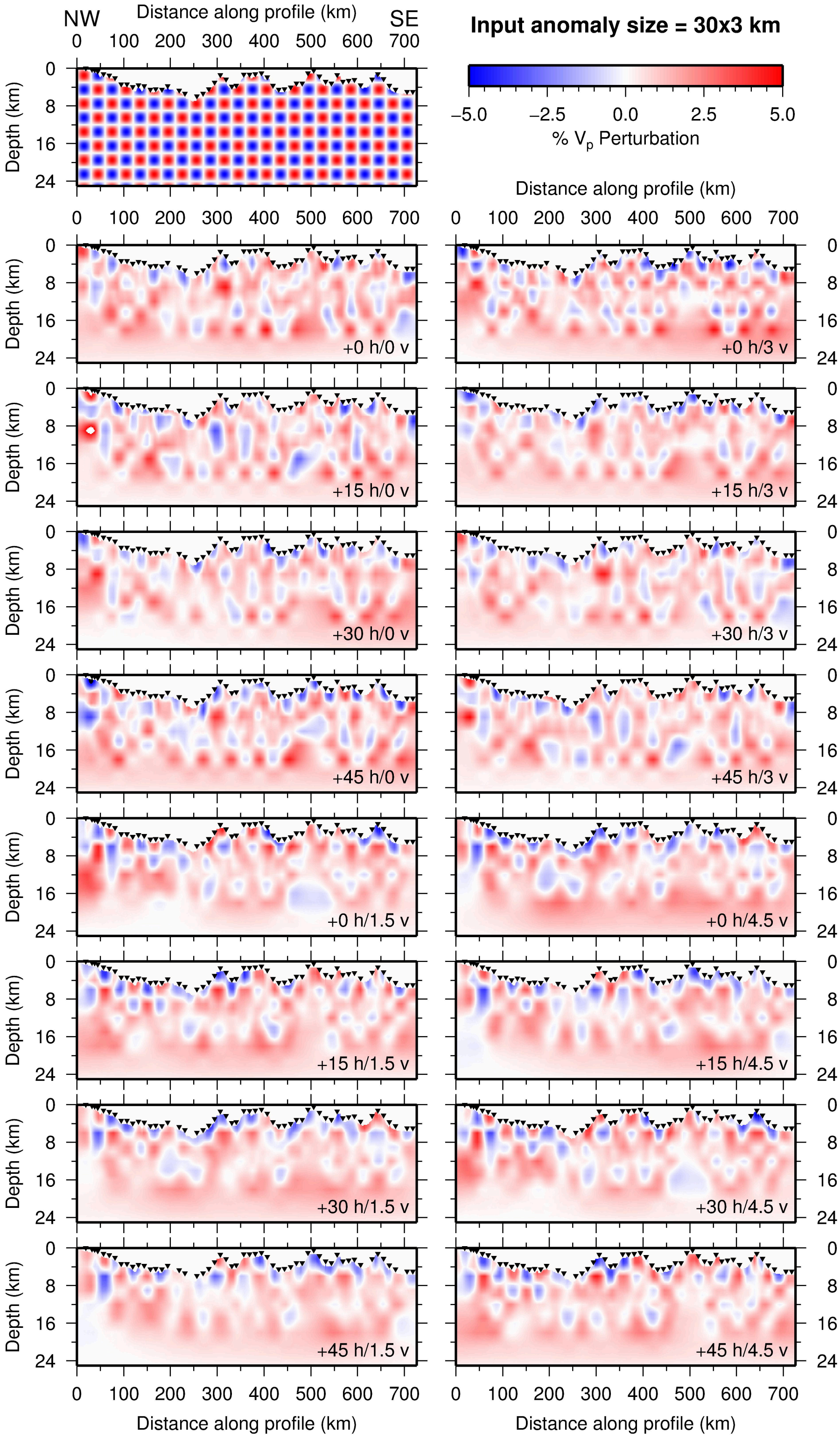

Fig. C.4: *Results of checkerboard testing for 30 x 3 km input anomaly*

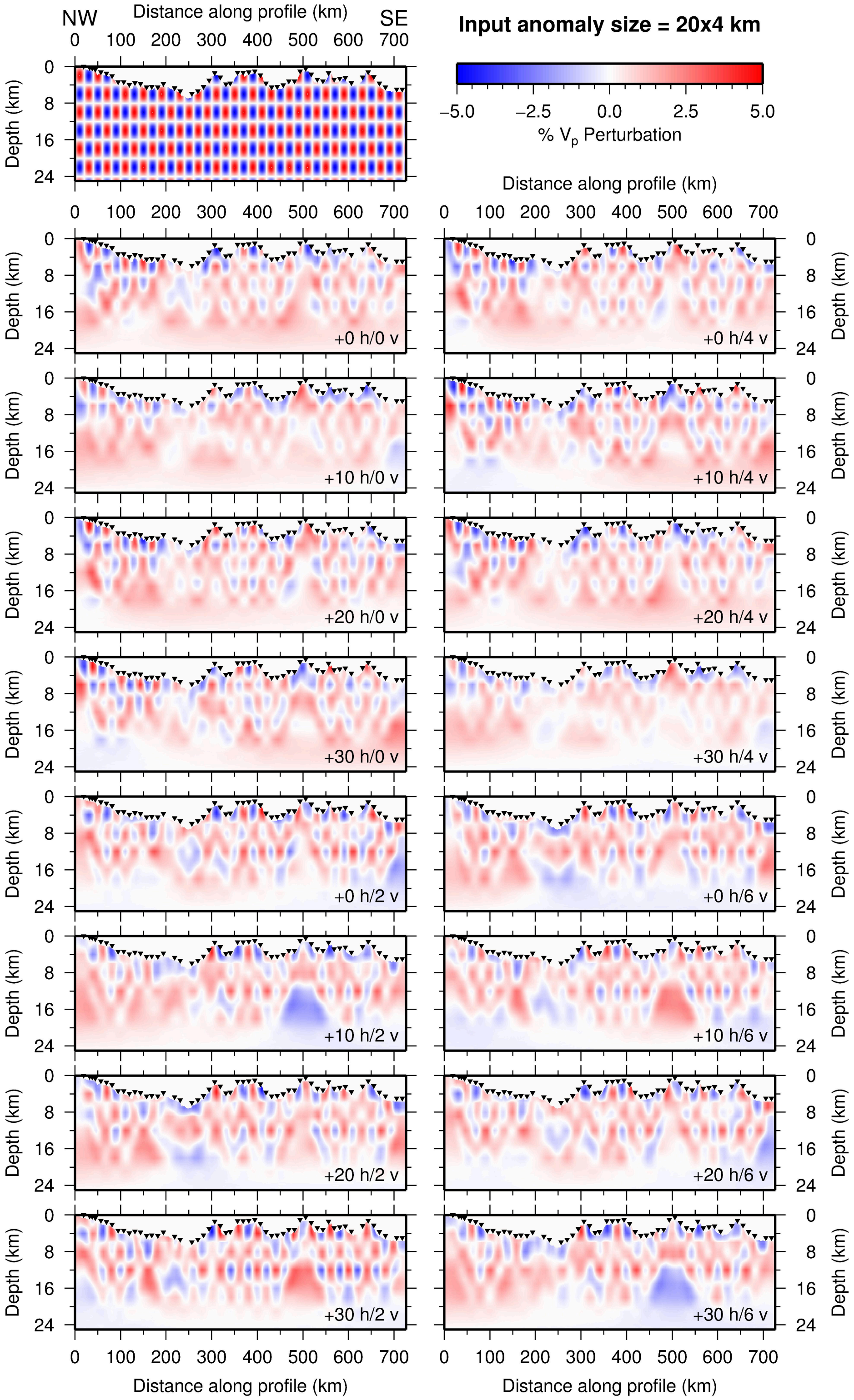

Fig. C.5: *Results of checkerboard testing for 20 x 4 km input anomaly*

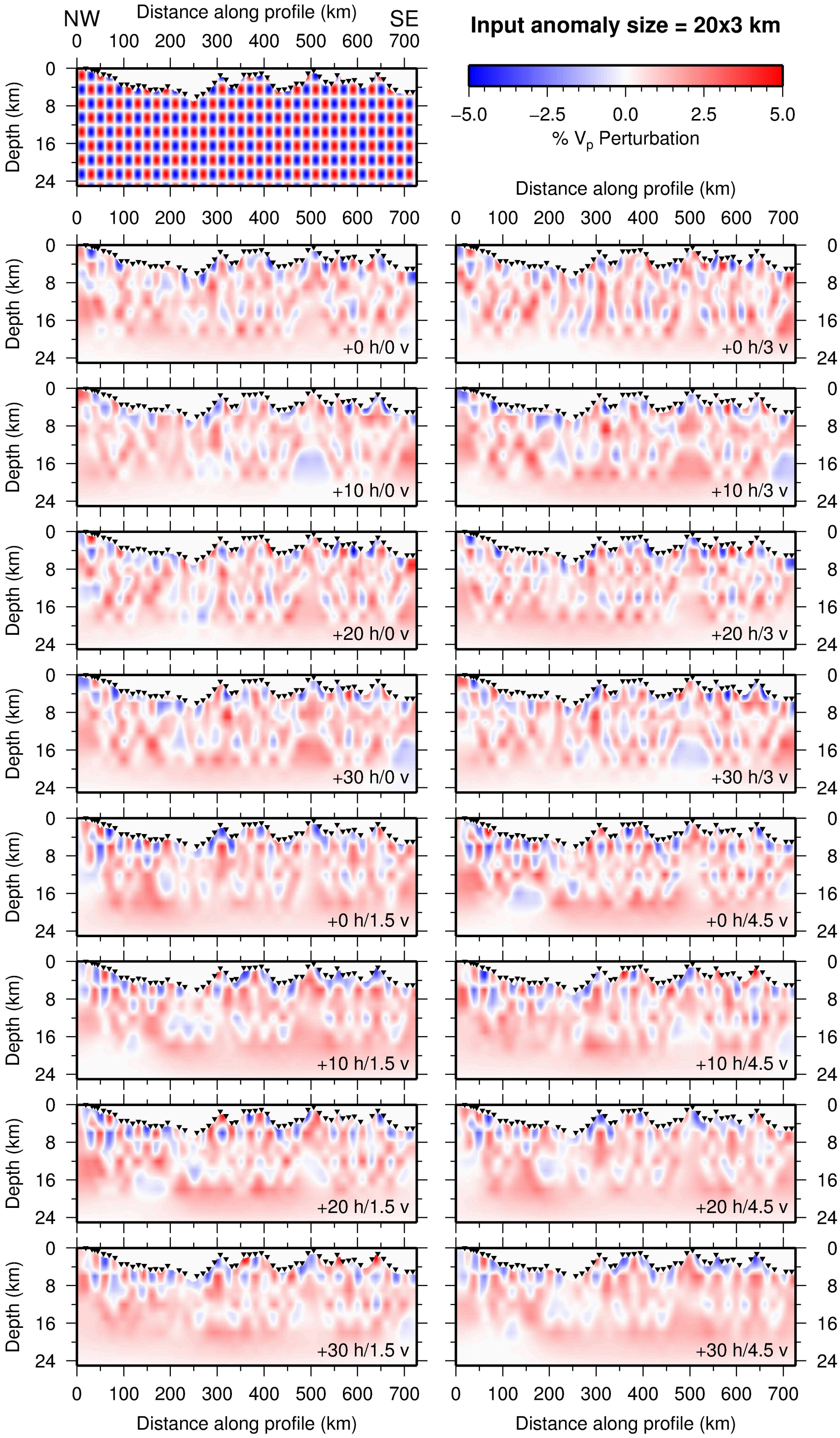

Fig. C.6: *Results of checkerboard testing for 20 x 3 km input anomaly*

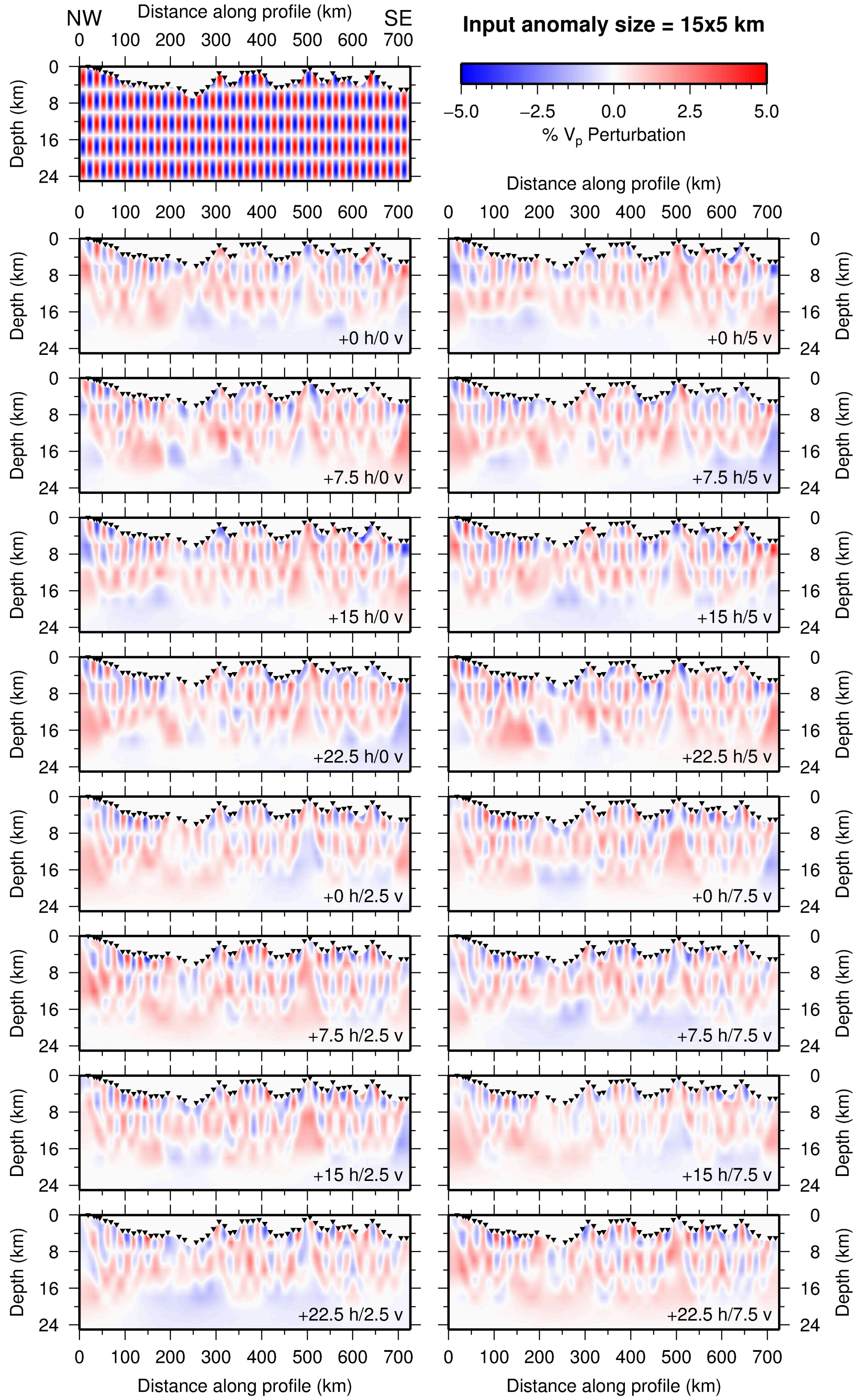

Fig. C.7: *Results of checkerboard testing for 15 x 5 km input anomaly*

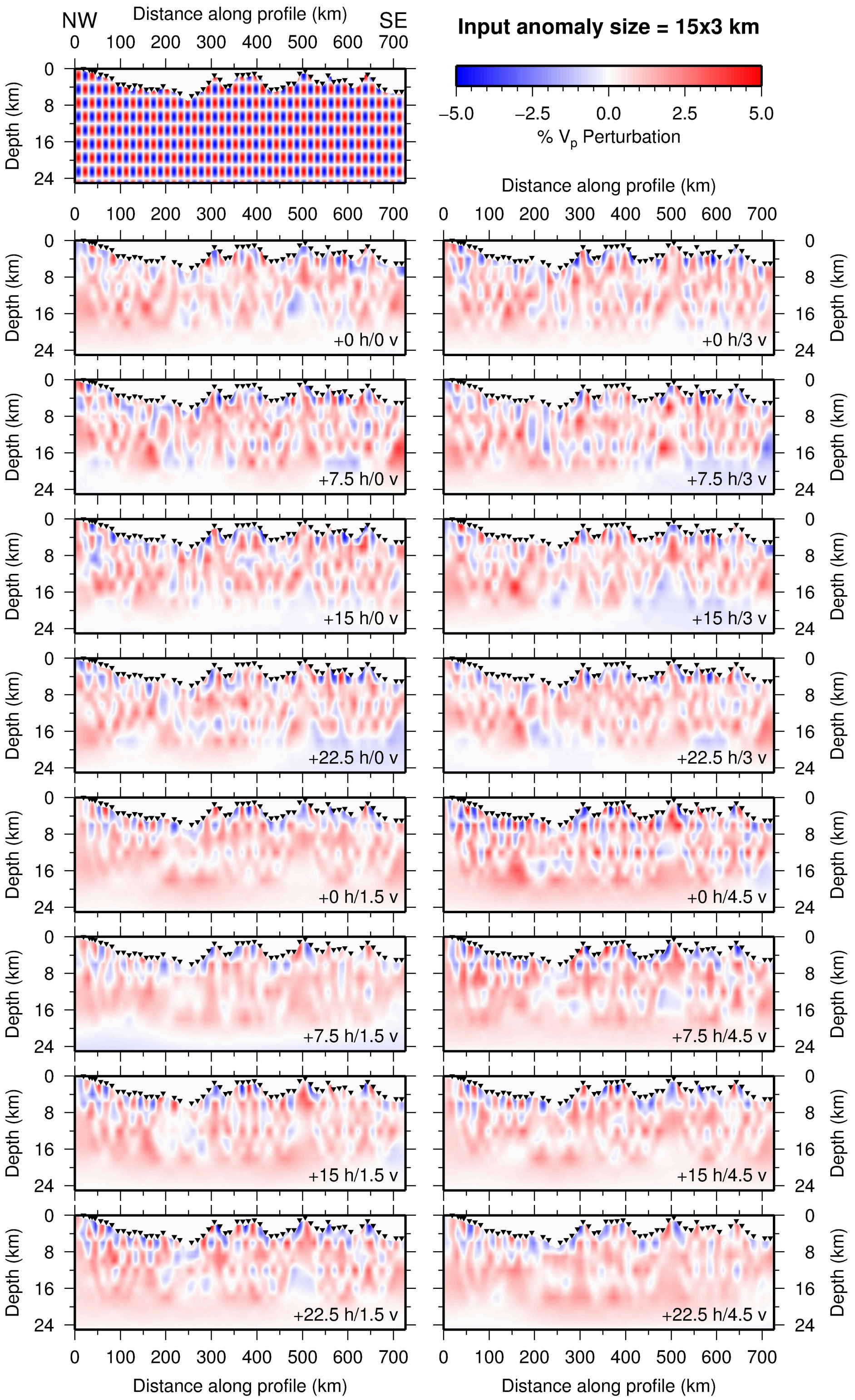

Fig. C.8: *Results of checkerboard testing for 15 x 3 km input anomaly*

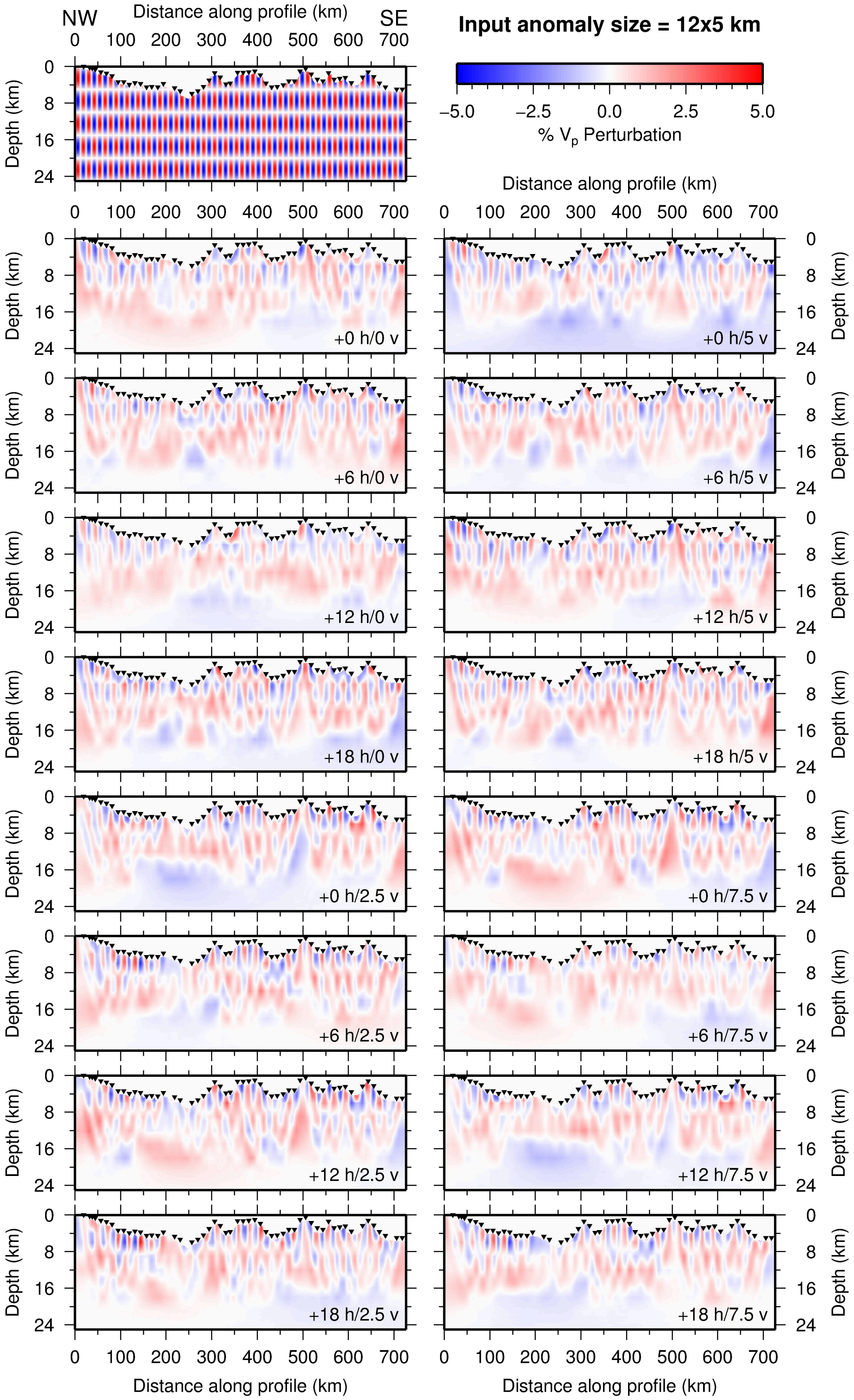

Fig. C.9: *Results of checkerboard testing for 12 x 5 km input anomaly*

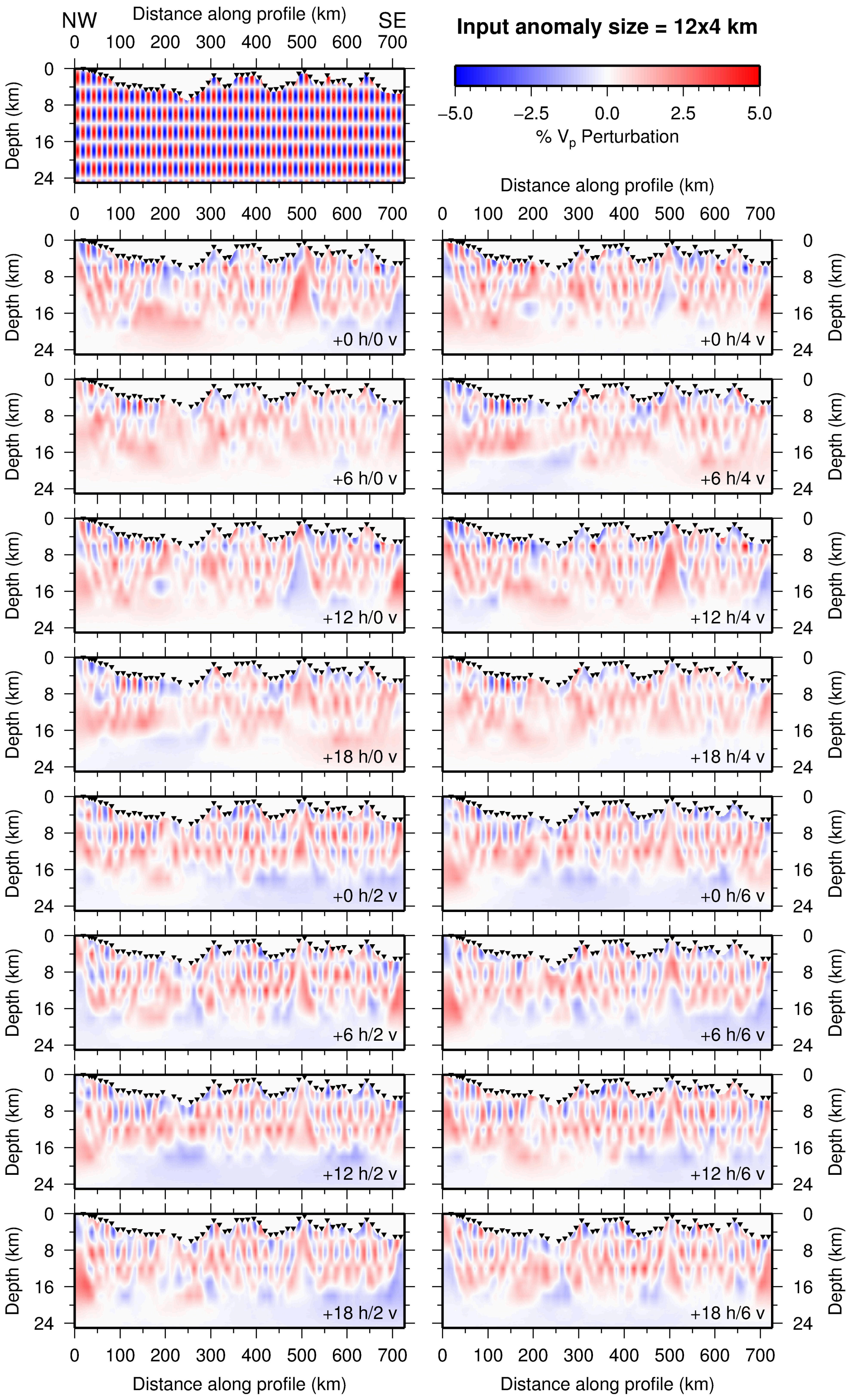

Fig. C.10: *Results of checkerboard testing for 12 x 4 km input anomaly*